Finland's 100,000-year tomb for nuclear waste p. 806

Machine learning tackles antibiotic resistance pp. 818 & 889

Michelson & *Science* Prize highlights autoantibodies in COVID-19 p. 829

Science

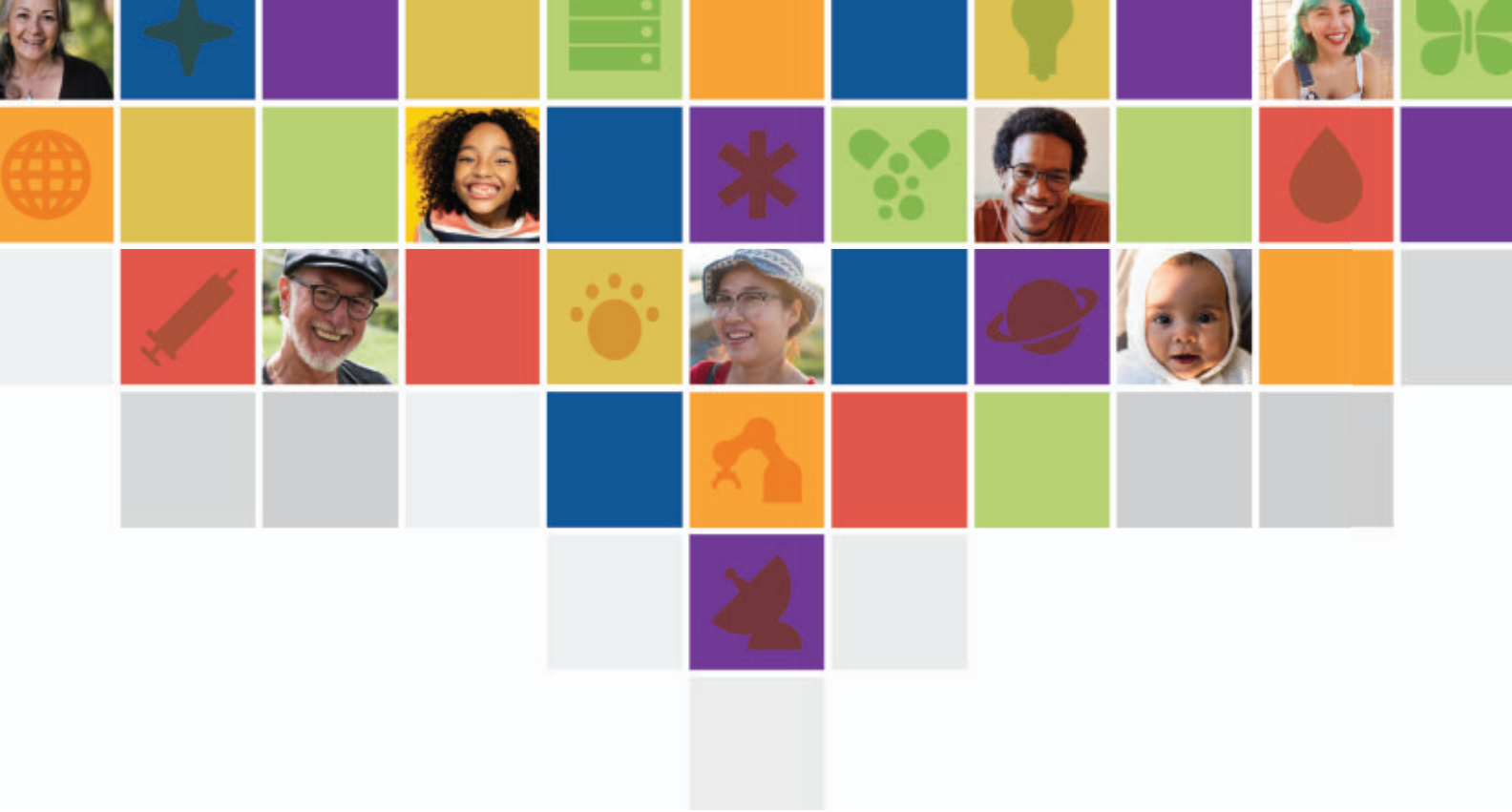
$15
25 FEBRUARY 2022
science.org

AAAS



GORDON RESEARCH CONFERENCES

Neural development, computational materials science, immunoengineering, and more p. 900



SCIENCE FOR HUMANITY

AAAS | ANNUAL MEETING

The scientific endeavor aims to provide findings, models, tools, and advances to better understand and address the myriad complex challenges facing society. Meeting this goal requires collective objectivity determined by a wealth of individual and diverse perspectives and experiences—a sample as broad as the diversity of disciplines in the scientific endeavor itself.

Highlighting the importance and just integration of our multiplicity, the 2023 AAAS Annual Meeting will feature groundbreaking multi-disciplinary research—research that advances knowledge and responds to the needs of humanity. Drawing from work ranging from astronomy to zoology, the program committee seeks proposals that highlight breakthroughs in science and technology and, in particular, those that incorporate the importance of diversity—in its investigators, subjects of study, and translational implications.

aaas.org/meetings | #AAASmtg

CONTENTS

25 FEBRUARY 2022 • VOLUME 375 • ISSUE 6583



NEWS

IN BRIEF

798 News at a glance

IN DEPTH

801 United Nations to tackle global plastics pollution
Research could gain from negotiations to reduce, reuse, and recycle the common material *By E. Stokstad*

802 Biden gets pans and praise for dividing top science positions
Francis Collins named as science adviser and Alondra Nelson as head of White House science office
By J. Mervis

803 Oldest genomes from Africa offer glimpse of complex past
Signs of ice age isolation match archaeological clues *By M. Price*

804 Glowing tumor marker hampers mouse cancer studies
Response to protein complicates immunotherapy research *By J. Kaiser*

805 Novel viruses highlight risks of Asia's wild animal trade
Sampling of game in China reveals many viral threats *By J. Cohen*

FEATURES

806 Final resting place
Finland is set to open the world's first permanent repository for high-level nuclear waste. How did it succeed when other countries stumbled? *By S. El-Showk*
PODCAST

INSIGHTS

BOOKS *ET AL.*

812 Science at Sundance 2022

PERSPECTIVES

816 Losing sleep with age
Hypocretin neuron hyperexcitability underlies disrupted sleep quality associated with age *By L. H. Jacobson and D. Hoyer*
RESEARCH ARTICLE p. 838



817 Inferring human evolutionary history
Unified genetic genealogy improves our understanding of how humans evolved
By J. Rees and A. Andrés
RESEARCH ARTICLE p. 836

818 Anticipating antibiotic resistance
Machine learning can use clinical history to lower the risk of infection recurrence
By J.-B. Lugagne and M. J. Dunlop
REPORT p. 889

820 Dimerization decrypts antibiotic activity
Direct dimerization simplifies the synthesis of himastatin and elucidates its mode of action
By M. Smith
REPORT p. 894

821 A crooked spinning black hole
New observations challenge the current understanding of black hole formation *By F. Patat and M. Mapelli*
REPORT p. 874

822 Flashing light with nanophotonics
Manipulation and enhancement of scintillation is achieved in nanophotonic structures *By R. Yu and S. Fan*
RESEARCH ARTICLE p. 837

824 C. Thomas Caskey (1938–2022)
A visionary architect of genomic medicine *By A. Ballabio and H. Zoghbi*

CREDITS: (PHOTO) TAPANI KARJANLAHTI/TVO; (ILLUSTRATION) HANNAH AGOSTA

POLICY FORUM

825 Streamlining ethics review for international health research
Single-site review means protection and efficiency *By Mark A. Rothstein* et al.

LETTERS

827 Plans to protect China's depleted groundwater
By C. Zheng and Z. Guo

827 Transparency crucial to Paris climate scenarios
By L. King et al.

828 Response
By Y. Ou et al.

PRIZE ESSAY

829 Why do people die from COVID-19?
Autoantibodies that neutralize type I interferons increase with age
By P. Bastard

RESEARCH

IN BRIEF

832 From *Science* and other journals

REVIEW

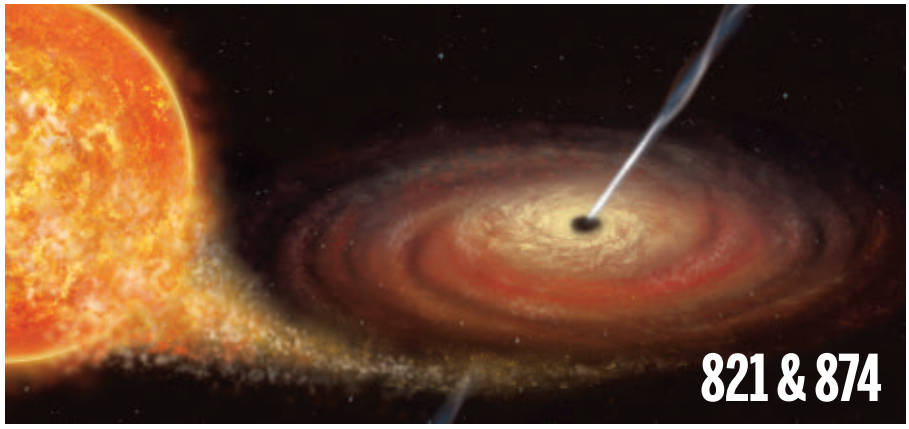
835 Solar cells
Rethinking the A cation in halide perovskites *J.-W. Lee* et al.
REVIEW SUMMARY; FOR FULL TEXT: DOI.ORG/10.1126/SCIENCE.ABJ1186

RESEARCH ARTICLES

836 Human evolution
A unified genealogy of modern and ancient genomes *A. W. Wohns* et al.
RESEARCH ARTICLE SUMMARY; FOR FULL TEXT: DOI.ORG/10.1126/SCIENCE.ABI8264
PERSPECTIVE p. 817

837 Nanophotonics
A framework for scintillation in nanophotonics *C. Roques-Carmes* et al.
RESEARCH ARTICLE SUMMARY; FOR FULL TEXT: DOI.ORG/10.1126/SCIENCE.ABM9293
PERSPECTIVE p. 822

838 Neuroscience
Hyperexcitable arousal circuits drive sleep instability during aging *S.-B. Li* et al.
RESEARCH ARTICLE SUMMARY; FOR FULL TEXT: DOI.ORG/10.1126/SCIENCE.ABH3021
PERSPECTIVE p. 816



839 Protein targeting
Mechanism of signal sequence handover from NAC to SRP on ribosomes during ER-protein targeting *A. Jomaa* et al.

845 Structural biology
Dynamics and mechanism of a light-driven chloride pump *S. Mous* et al.

852 Nanomaterials
Highly stretchable van der Waals thin films for adaptable and breathable electronic membranes *Z. Yan* et al.

REPORTS

859 Immunology
Trained ILC3 responses promote intestinal defense *N. Serafini* et al.

864 Coronavirus
Structural basis of SARS-CoV-2 Omicron immune evasion and receptor engagement *M. McCallum* et al.

869 Organic chemistry
Deracemization through photochemical *E*/*Z* isomerization of enamines *M. Huang* et al.

874 Black holes
Black hole spin–orbit misalignment in the x-ray binary MAXI J1820+070 *J. Poutanen* et al.
PERSPECTIVE p. 821

877 Cancer immunology
Molecular signatures of antitumor neoantigen-reactive T cells from metastatic human cancers *F. J. Lowery* et al.

884 Optics
Topological modes in a laser cavity through exceptional state transfer *A. Schumer* et al.

889 Antibiotic resistance
Minimizing treatment-induced emergence of antibiotic resistance in bacterial infections *M. Stracy* et al.
PERSPECTIVE p. 818

894 Organic chemistry
Total synthesis of himastatin *K. A. D'Angelo* et al.
PERSPECTIVE p. 820

DEPARTMENTS

797 Editorial
We are all Gang Chen *By G. Chen*

930 Working Life
It's not (all) about you *By J. R. Posselt*

ON THE COVER

A reconstruction of multiple optical slices from the developing eye of a fruit fly (*Drosophila melanogaster*) larva. Each observed photoreceptor neuron expresses one of three protein tags (either alone or in combination), corresponding to different colors. The neurons maintain their spatial proximity while sending projections to the brain. The Gordon Research Conference on Neural Development will be held from 7 to 12 August 2022 in Newport, Rhode Island. See page 900 for the Gordon Research Conferences schedule and preliminary programs. *Image: Amanda A. G. Ferreira*



GRAPHIC: KELLIE HOLOSKI/*SCIENCE*

Gordon Research Conferences 900
Science Careers 928

SCIENCE (ISSN 0036-8075) is published weekly on Friday, except last week in December, by the American Association for the Advancement of Science, 1200 New York Avenue, NW, Washington, DC 20005. Periodicals mail postage (publication No. 484460) paid at Washington, DC, and additional mailing offices. Copyright © 2022 by the American Association for the Advancement of Science. The title SCIENCE is a registered trademark of the AAAS. Domestic individual membership, including subscription (12 months): $165 ($74 allocated to subscription). Domestic institutional subscription (51 issues): $2212; Foreign postage extra: Air assist delivery: $98. First class, airmail, student, and emeritus rates on request. Canadian rates with GST available upon request, GST #125488122. Publications Mail Agreement Number 1069624. **Printed in the U.S.A.**
Change of address: Allow 4 weeks, giving old and new addresses and 8-digit account number. **Postmaster:** Send change of address to AAAS, P.O. Box 96178, Washington, DC 20090–6178. **Single-copy sales:** $15 each plus shipping and handling available from backissues.science.org; bulk rate on request. **Authorization to reproduce** material for internal or personal use under circumstances not falling within the fair use provisions of the Copyright Act can be obtained through the Copyright Clearance Center (CCC), www.copyright.com. The identification code for *Science* is 0036-8075. *Science* is indexed in the *Reader's Guide to Periodical Literature* and in several specialized indexes.

EDITORIAL

We are all Gang Chen

Rampant wrongful prosecutions terrorize innocent people—everywhere. The scientific community is not immune to this. I know because I was a victim. I am a professor at the Massachusetts Institute of Technology (MIT) who was accused by the US government of fraud and questionable connections to Chinese entities. Earlier this year, I was finally exonerated—it took 2 years. I am painfully aware, however, that I am the luckiest among the unlucky. Many other Chinese American scientists are being unfairly investigated for similar alleged "crimes." Or they are simply leaving the country to avoid being targeted. My ordeal taught me that politics affects science and scientists, and that universities and funding agencies must stand up for faculty who are wrongfully prosecuted.

I grew up in China and found my American dream at MIT, where I became a department head and led a vibrant research group. In January 2020, the dream turned into a nightmare. I was detained and interrogated at Boston's Logan Airport, and my electronic devices were confiscated. A year later, federal agents raided my home, arrested me, and interrogated my wife without an attorney present. My family lived in fear for 2 years, and members of my research group relocated. The accusations against me were absurd. They criminalized routine professional activities: reviewing research proposals, writing recommendations, and hosting visiting scientists. In January 2022, the US Department of Justice (DOJ) dropped all charges.

I was investigated under the DOJ's China Initiative, an effort launched in 2018 by the Trump administration to counter Chinese government's espionage and threats to national security. Andrew Lelling, a chief architect of the Initiative and the US Attorney for Massachusetts at the time, rushed my indictment through. Although he recently said, "The Initiative has drifted, and in some significant ways, lost its focus," similar prosecutions are still going on. Christopher Wray, director of the Federal Bureau of Investigation, said just weeks ago that the agency opens two new China Initiative investigations every day.

What gave me hope and ultimately saved me is a lesson for all universities. MIT leadership, under President L. Rafael Reif, supported me morally and financially after I was detained at the airport, and the university made its support public soon after I was arrested. MIT professor Yoel Fink organized faculty support, which led to an open letter, signed by over 200 MIT faculty. The letter used facts to tear apart the criminal complaint and ended with a rallying statement: "We are all Gang Chen." A similar online petition launched by Northwestern University professor G. Jeffrey Snyder was signed by 1380 individuals. In open letters, faculty from about 230 universities in the country called on the DOJ to stop the China Initiative. The fundraising that my daughter launched reached its goal in 1 day and helped raise awareness of other Chinese American scientists in a similar plight. New civil rights organizations joined forces with existing ones to fight for justice and eliminate the China Initiative. These collective voices helped compel the government to drop all charges.

> "...wrongful prosecutions terrorize innocent people—everywhere."

MIT has supported other faculty under similar investigation, but other universities have mostly remained silent. I urge university leaders, trustees, and alumni associations to protect their faculty from a campaign that is misdirected. The talent loss and terror lobbed upon faculty are weakening their institutions, supporting harmful bias, and ruining lives.

Funding agencies must also stand up for justice. Dr. Chris Fall, the former director of the Office of Science at the US Department of Energy (DOE), explained recently that in 2020, the DOE changed reporting rules regarding foreign ties. The government applied the 2020 rules to my 2017 DOE grant application. The 2021 indictment mentioned DOE 18 times, only to miss this basic fact. The DOE should have spoken up when it counted. That is a lesson for all federal agencies.

I've devoted my life to science and education and never thought that I would get involved in activism. But I am now. People need to raise their voices so that the government and public understand the evil of wrongful prosecutions. I call on Congress to investigate the wrongdoings of the government in my case and similar cases. And I call for continued vigilance to end the China Initiative, however it is repositioned by the DOJ. As Martin Luther King Jr. wrote from a Birmingham jail, "Injustice anywhere is a threat to justice everywhere."

–Gang Chen



PHOTO: MIT

Gang Chen is the Carl Richard Soderberg Professor of Power Engineering at the Massachusetts Institute of Technology, Cambridge, MA, USA. gchen2@mit.edu

10.1126/science.abo6697

> "[Hong Kong's] hospitals are sandcastles in a tsunami."
>
> **University of Hong Kong virologist Siddharth Sridhar**, in a tweet describing the impact of the recent COVID-19 surge on the city's health care system.



The presidents of Ghana, Rwanda, and Senegal visited a modular vaccine lab in Germany.

IN BRIEF

Edited by **Kelly Servick**

COVID-19

Africa builds mRNA vaccine capacity

The drive to help African countries produce vaccines with messenger RNA (mRNA) technology got big boosts last week from the World Health Organization (WHO) and the company BioNTech. The success of mRNA COVID-19 vaccines made by the Pfizer-BioNTech collaboration and Moderna led to intense global demand, but African countries have had little access because of limited supply and high prices. Campaigns by several governments and nongovernmental organizations failed to convince the companies to freely share their technologies with economically strapped countries. So last year WHO launched a hub in South Africa to produce mRNA vaccines independently. The agency, which hopes the hub licenses a product by 2024, last week announced plans to train scientists from South Africa, Egypt, Kenya, Nigeria, Senegal, and Tunisia. BioNTech, which has been criticized for trying to undermine the WHO effort, separately announced that later this year it will train local scientists and send modular, shipping container–size vaccine factories to Ghana, Rwanda, and Senegal.

Wild poliovirus back in Africa

INFECTIOUS DISEASE | In a setback for the global polio eradication campaign, a wild poliovirus has leapt from Pakistan to the African continent, where it has paralyzed a 3-year-old girl in Malawi. The case, announced on 17 February by the Malawi government, is the first wild polio case in the country since 1992. Pakistan and Afghanistan are the last two countries that are endemic for the wild virus, which means circulation there has never stopped. Occasionally, however, the virus spills over from these entrenched reservoirs. Africa's last known case of wild polio occurred in 2016 in Nigeria's Borno state. The continent is still battling big outbreaks of vaccine-derived polio, however, which occur in areas of low immunization when the live but attenuated virus in the oral polio vaccine regains its ability to paralyze and spread. The Global Polio Eradication Initiative is hopeful that it can stop the spread of the virus in Malawi quickly through a vaccination campaign, as it has done for several other "imported" wild polio outbreaks.

Winter study probes Great Lakes

ECOLOGY | Researchers from the United States and Canada last week used sleds, snowmobiles, airboats, and icebreakers to fan out across the Great Lakes in a bid to better understand how the five water bodies function in the dead of winter and how climate change is reshuffling their ecosystems. Scientists from 19 research institutions and government agencies participated in the Winter Grab, a weeklong push to collect data at some 30 sampling sites. Fewer than 5% of Great Lakes studies have been done in winter, in part because lakes were long considered relatively dormant when covered by ice—not to mention dangerous to access. As a result, scientists know relatively little about how lake organisms behave during winter or how nutrient cycles vary by season. As warmer winters shrink ice cover, Winter Grab researchers hope their findings will help spur more efforts to study lakes around the world during the coldest months.

Dinosaurs' death came in spring

PALEONTOLOGY | The beginning of the end for dinosaurs was likely one day in spring, according to a study of fish fossils excavated in North Dakota. To pinpoint the season of the Cretaceous-Paleogene mass extinction 66 million years ago, paleontologists analyzed the bones of filter-feeding fish from a site called Tanis. There, the asteroid impact that doomed dinosaurs kicked up a large river wave, burying countless late-Cretaceous era animals and plants. The fish had debris from the impact lodged in their gills, evidence that they had perished within minutes. The researchers used carbon isotopes in the bones to identify seasonal growth layers. (The fish grew faster in spring, when food

PHOTO: FABIAN BIMMER/REUTERS



An elliptical secondary crater on Sheep Mountain in Wyoming.

GEOLOGY

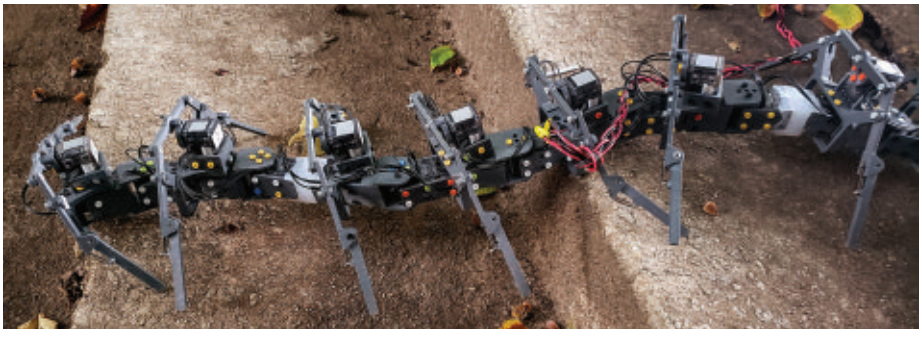
First secondary craters found on Earth point to giant asteroid impact

Scientists have identified a series of 31 craters in Wyoming with diameters from 10 to 70 meters, created 280 million years ago by boulders ejected from a previously unknown cosmic impact. Such "secondary" craters are common on airless moons and planets, but previously have never been identified on Earth. Many scientists suspected the planet's thick atmosphere would prevent their formation altogether by cracking up boulders on descent. The finding, published this month in the *Geological Society of America Bulletin*, also suggests a 60-kilometer-wide impact crater is likely buried some 2 kilometers below Wyoming's eastern border—potentially one of the largest known impacts in North American history.

was plentiful.) They report on 23 February in *Nature* that the fish—along with three-quarters of life on Earth—perished during spring in the Northern Hemisphere.

Centipedes inspire robot

BIOLOGY | Centipedes' ability to speed over rock, sand, and soil has led to a new robot that could prove handy to farmers. On land, centipedes move their legs in a wave that switches direction when they encounter obstacles, researchers reported this month at the virtual meeting of the Society of Integrative and Comparative Biology. In water, they wiggle their bodies to move forward. To better understand how the animals coordinate their legs and body in different environments, the researchers built a 70-centimeter robot model and determined the most efficient timing of leg and body movements. The robot was so adept at moving across a natural landscape that the team has formed a company to develop the device for finding and destroying weeds in agricultural fields.



A robot mimics the leg and body movements of centipedes to move efficiently over uneven terrain.

Psilocybin shows lasting effects

MENTAL HEALTH | The antidepressant effects of psilocybin-assisted therapy may last at least 1 year for some people, a small follow-up study suggests. In a clinical trial of 24 people with major depressive disorder, researchers found that two doses of the substance found in magic mushrooms, given approximately 2 weeks apart alongside psychotherapy, led to clinically significant reductions in depression severity in 18 participants and remission in 14 of them after 1 year. The results, reported last week in the *Journal of Psychopharmacology* and discussed in a panel at the annual meeting of AAAS,

PHOTOS: (TOP TO BOTTOM) KENT SUNDELL/CASPER COLLEGE; YASEMIN OZKAN-AYDIN/UNIVERSITY OF NOTRE DAME

THREE QS

European Commission pushes for gender equality

Effective this year, higher education and research organizations must have a gender equality plan to qualify for European Commission research grants. Among other commitments, grantees will be required to train staff about unconscious bias and collect data on staff and students for accountability. Anne Pépin, a physicist at the French national research agency, CNRS, and senior policy officer at the Commission, spoke with *Science* about the changes and structural barriers for female scientists. (A longer version of this interview is at https://scim.ag/GenderEqEurope.)

Q: What motivated you to get involved?
A: When I became a researcher, I was clearly a minority in physics. I didn't suffer from explicit discrimination. But it was more a cumulative effect—like sometimes people taking you for the postdoc when you're the permanent researcher. I've been involved in pioneering a gender equality plan at CNRS, and I think it can have long-lasting and multiplier effects. We were able to implement a range of actions—for example, sensitizing the recruitment and promotion committees to gender issues and allowing women to have 6 months off teaching duties to concentrate on their research after a maternity leave.

Q: Why make this a mandatory requirement?
A: To some extent, the voluntary implementation of gender equality plans over the last decade by European organizations was a success—we've accumulated a wealth of good practices and established practical tools. Still, changes are fragmented and very slow. We're roughly at gender parity among doctoral graduates, but women only represent 26% of full professors. The institutions will be responsible for identifying the most pressing areas to address based on their data.

Q: Are you optimistic for change?
A: There is still a lot of work ahead, and it's not all on the side of the European Commission. It also has to be a collective effort with everyone—women, men, gender-diverse individuals—getting onboard to further improve working conditions for all.

SCIENCE.ORG/NEWS
Read more news from *Science* online.

which publishes *Science*, offer the longest follow-up yet for a randomized study of psilocybin's antidepressant effect. They extend findings from the same trial, published in November 2020, that revealed improvements for 17 of the 24 participants after 1 month. Other factors may have contributed to the persistent benefit, the researchers note: One-third of participants began treatment with an antidepressant sometime over the course of follow-up study, and nearly half received some form of psychotherapy outside of the study.

Health equity fight loses pioneer

GLOBAL HEALTH | Paul Farmer, an infectious disease physician, anthropologist, and champion of global public health, died suddenly this week at age 62. At the time of his death, he was visiting the University of Global Health Equity in Butaro, Rwanda, that he helped found. Farmer, who was also a professor at Harvard Medical School, dedicated his career to bringing health care to poor and marginalized communities, in particular in Haiti and Rwanda. In 1987, he founded the nonprofit Partners in Health, focused on providing high-quality health care in resource-poor settings and advocating for human rights and social justice. Farmer's work also helped inspire global efforts to expand access to lifesaving treatments for HIV and other diseases.

Antarctic pollution melting snow

ENVIRONMENT | Burning of fossil fuels in Antarctica is hastening snow melt there, researchers have found. When soot, a byproduct of combustion, settles out of the air, the dark particles absorb sunlight and heat the snow. To estimate the impact, researchers measured soot in snow taken from 28 places across the northern Antarctic Peninsula, including sites near research bases and stops for ships that carry an average of 53,000 tourists per year to the continent. Melting from the ship soot amounts to hundreds of tons of snow loss per person, the group reports this week in *Nature Communications*. Per person losses are estimated to be an order of magnitude higher near research stations, because of generators, helicopters, and vehicles. In the most polluted areas, the snowpack has declined by 2.3 centimeters each summer. The researchers recommend limits on research infrastructure and surging tourism, as well as improvements in energy efficiency and renewable power.



PHOTO: POVILAS ŠIMONIS

SCIENCE AND ART

Yeasty dance video rises to top of Ph.D. contest

Lithuanian scientist Povilas Šimonis's colorful and catchy interpretation of the electrical stimulation of yeast cells is the winner of this year's "Dance Your Ph.D." contest. The annual competition, which is hosted by *Science* and sponsored by the artificial intelligence company Primer, invites researchers to interpret their theses through movement and to commit the act to video for cash prizes and nerd fame. Šimonis's doctoral work at Lithuania's Center for Physical Sciences and Technology and Vilnius University explores how the single-celled fungus that powers bread baking behaves when pulsed with electricity. The performance, which included original music and several sets, casts people as yeast cells prancing amid mouthwatering baked goods. The result beat out 29 other submissions to win both the overall award and the biology category. A judging panel of dancers, scientists, and artists also selected winners in chemistry, physics, and social sciences. See videos from all the winners at https://scim.ag/DancePhD.



IN DEPTH

Plastic waste piles up on a beach off Panama City. Nations will try to negotiate a new treaty aimed at reducing the global problem.

PHOTO: LUIS ACOSTA/AFP/GETTY IMAGES

ENVIRONMENTAL POLICY

United Nations to tackle global plastics pollution

Research could gain from negotiations to reduce, reuse, and recycle the common material

By **Erik Stokstad**

Each year, an estimated 11 million tons of plastic waste enter the ocean, equivalent to a cargo ship's worth every day. The rising tide—in the oceans and beyond—is just a symptom of much wider problems: unsustainable product design, short-sighted consumption, and insufficient waste management, scientists say. To curb the flood, says Jenna Jambeck, an environmental engineer at the University of Georgia, "we need to take more action and it needs to be further upstream" in the production process.

That's exactly what negotiators from 193 countries are setting out to do when they meet in Nairobi, Kenya, next week. Their ambitious goal: to create a negotiating committee that will try to hammer out, within 2 years, a new global treaty intended to curb plastic pollution.

An already released proposal, modeled on the United Nations's climate treaty, would have nations adopt action plans, set binding waste reduction targets, and establish monitoring systems and a new global scientific advisory body. "It's about time," says Chelsea Rochman, an ecologist at the University of Toronto who has called on nations to tackle the issue.

Existing international efforts to reduce marine litter and exposure to hazardous chemicals include some measures related to plastic pollution. But no global treaty tries to reduce pollution by targeting a product's entire life cycle, from its birth as a raw material to its death—if it becomes trash. Taking such a broad approach to plastics, says Anja Brandon, a policy analyst at the Ocean Conservancy, "is going to be a much bigger scientific endeavor."

For one thing, rigorous, comparable numbers on the scope and sources of the problem are scarce, making it difficult to identify pollution hot spots or detect trends. Nonprofit groups and government agencies use dozens of varying protocols for surveying beach litter, for example. Methods of counting microplastics in water—shed from synthetic fabrics, for example, or formed when large plastic objects degrade—also vary. "There are several holes in the data," Jambeck says.

The new treaty could help by promoting or establishing standard measuring and accounting methods. One such approach, called environmental economic accounting, is already being used in some countries to track various raw materials. And a method known as mass balance analysis, which tracks the amount of material entering and leaving production processes, holds promise for quantifying the amount of recycled plastic used in new products.

Even after scientists settle on standard metrics, collecting those numbers could be a challenge, Jambeck notes, especially in developing nations with relatively weak regulatory and research infrastructures. The United Nations Environment Programme (UNEP), which is hosting the upcoming meeting, has worked to increase monitoring capacity with training programs and online courses. Such efforts would be aided by a new treaty that encourages funding and technological advances. Remote sensing via satellites and drones, for example, could more easily identify plastic pollution trends, reducing the need for labor-intensive ground surveys.

More detailed industrial data on plastics production, transport, and consumption could also help nations curb pollution, researchers say. But many countries allow companies to keep such numbers private, making it difficult to calculate how plastic is moving through the economy and into the environment. And no one systematically tracks that information. The Ocean Conservancy, for example, has struggled to find out how much recycled plastic firms are using, Brandon says. Researchers are still pondering which numbers would be most useful, and how the treaty might help make that information more available.

Negotiators will also confront a key question: How much plastic pollution is too much? It's clear that plastic bags, discarded fishing gear, and microplastics can kill wildlife, but scientists are just beginning to figure out how to calculate the risks. The treaty could help catalyze such efforts, says Rochman, who recently helped California regulators devise protocols for setting microplastic thresholds to protect people and ecosystems.

The political will to reduce plastic waste will be much higher if it's known to harm humans, says Karen Raubenheimer, a policy researcher at the University of Wollongong. But she thinks any final agreement is unlikely to call for hard caps on new plastic. "It will be challenging in the short-term to stop using virgin plastic," Raubenheimer says.

A big reason is that many uses of plastic are seen as essential. Single-use plastic items are common in health care, for example, to prevent contamination and infections, and in the food industry to keep fruit, vegetables, and other products from spoiling. Even disposable bottles can be vital in areas without clean water.

Negotiators might call for the reduction or elimination of what UNEP has called "unnecessary, avoidable and problematic plastic," such as single-use shopping bags, takeout cutlery, or plastic beads in cosmetics. But analysts say nations must also focus on ways to reuse and recycle plastic materials. Currently, researchers estimate that less than 10% of plastic products are recycled. Smarter product designs that drive better waste management practices could boost that number, reducing the demand for virgin materials.

Trying to finalize the new treaty in just 2 years is "highly ambitious," UNEP admits. But researchers who have watched the plastic pile up are delighted that the talks are even getting started. "People are putting high level resources to try to solve this problem in a way that we didn't see a decade ago," says Kara Lavender Law, a physical oceanographer at the Sea Education Association. "It's actually astonishing." ■

U.S. GOVERNMENT

Biden gets pans and praise for dividing top science positions

Francis Collins named as science adviser and Alondra Nelson as head of White House science office

By **Jeffrey Mervis**

President Joe Biden's decision to name two people to temporarily fill the top science advice post in his administration—a job historically held by one appointee—is drawing mixed reactions from the U.S. research community, including opposing takes from two former presidential science advisers.

Biden said last week he is "doubling down on science" by appointing geneticist Francis Collins, former director of the National Institutes of Health (NIH), to serve as the president's science adviser and social scientist Alondra Nelson, deputy director of the White House Office of Science and Technology Policy, to serve as OSTP director. Both jobs were held by geneticist Eric Lander, who announced on 7 February he was resigning after a White House investigation found "credible evidence" that Lander had bullied and disrespected staffers.





Alondra Nelson (top) and Francis Collins (bottom) will share jobs previously held by Eric Lander, who stepped down last week.

Biden gave no timeline for nominating a permanent replacement for Lander, who took office in May 2021. (Neither Collins nor Nelson is in the running, sources say.) In the meantime, Biden said this temporary arrangement would "allow OSTP and [my] science and technology agenda to move seamlessly forward under proven leadership."

Others, however, aren't sure the new arrangement is a good idea. "I don't understand it, and it doesn't make any sense to me," says Neal Lane, an emeritus physics professor at Rice University who served as former President Bill Clinton's science adviser while leading OSTP in the late 1990s. Lane calls it "an unprecedented experiment" that could weaken the office's ability to serve the president.

But John Holdren, a physicist who served in both roles under former President Barack Obama, doesn't see the division of labor as a problem. "I think both Alondra and Francis are very collegial people and will work very well together," Holdren says. "If the president wants advice in domains where Francis is not an expert, I have no doubt that he will talk to Alondra. I don't see any glitches."

Collins, who led NIH for 12 years before stepping down in December 2021, will provide advice on "all things science," says an OSTP spokesperson, and will co-chair the President's Council of Advisors on Science and Technology. Collins will also work on two of Biden's research priorities: establishing a new biomedical research agency, the Advanced Research Projects Agency for Health (ARPA-H), and reinvigorating the Cancer Moonshot, which Biden led as Obama's vice president. Collins will not report to Nelson, the OSTP spokesperson says.

Nelson would be the first Black woman and first social scientist to lead OSTP. Trained as a sociologist, she was president of the Social Science Research Council before coming to OSTP 1 year ago as deputy director for science and society, where she managed programs to improve scientific integrity, broaden participation in science and engineering, and ensure equitable access to new technologies.

Nelson's promotion allows her to con-

PHOTOS: (TOP TO BOTTOM) REUTERS/KEVIN LAMARQUE; NATIONAL INSTITUTES OF HEALTH

tinue to use her expertise in those areas and also apply her skills as a manager, says one of her former mentors, Evelynn Hammonds, professor of African American studies and head of the history of science department at Harvard University. "I think it's a very good move by the president," Hammonds adds. "And I think that she and Francis could turn out to be a great team."

The 140-person OSTP staff provide technical expertise to the White House, coordinate research-related policies across the government, and produce a stream of congressionally mandated reports. Its health and life sciences division, for example, is helping coordinate governmentwide efforts on both ARPA-H and the Cancer Moonshot.

To Lane, that overlap is a formula for bureaucratic confusion, if not gridlock. "Who's in charge?" he asks. "If Francis isn't reporting to Alondra, that raises serious questions." Lane also worries that some senior administration officials might regard Nelson as Collins's deputy, while Collins assumes a more visible public role.

Holdren disagrees. He thinks bringing in Collins will bolster the White House science team. "Biden wanted someone of stature in biomedical research to lead the charge [on his priorities], and that is what Francis Collins represents," Holdren says. "Lander was doing that. But those issues are not in Alondra Nelson's wheelhouse."

Biomedical research advocates are also divided over the appointments. Collins's long government tenure and easy rapport with Congress make him an ideal candidate to push the health initiatives forward, says Ellen Sigal, founder and chair of Friends of Cancer Research. "There's no one better than Francis," she says.

At the same time, many lobbyists are unhappy with the administration's intent to house ARPA-H within NIH, a plan Collins has backed. They would prefer to see it have more independence by locating it within NIH's parent body, the Department of Health and Human Services. And several researchers complained about the Biden administration opting for yet another "old white dude" to be science adviser, reviving a criticism levied when Lander was named.

Neither Collins nor Nelson will get Lander's Cabinet seat. Science advocates applauded Biden's decision to elevate the OSTP director to the Cabinet, a status normally held by heads of major agencies who are Senate-confirmed. But an OSTP spokesperson says whoever Biden nominates for the permanent position will have Cabinet status once confirmed. ■

With reporting by Jocelyn Kaiser.



PHOTO: JACOB DAVIS

Archaeologists and fieldworkers excavate Malawi's Hora rock shelter, where two male infants had been buried.

HUMAN EVOLUTION

Oldest genomes from Africa offer glimpse of complex past

Signs of ice age isolation match archaeological clues

By **Michael Price**

Africa is the birthplace of our species, but ancient DNA from the continent has so far provided relatively few clues to our history there, partly because researchers have struggled to recover genetic samples that survived the hot, humid climate. Now, an analysis of ancient DNA from six individuals from southeastern Africa offers a glimpse of the lives, movements, and relations of people who occupied the continent between 18,000 and 5000 years ago; it also hints at the complex commingling of African populations even further back. For instance, the work suggests that during the last ice age, some African societies may have become more sedentary and isolated as their environments fragmented.

The study, published this week in *Nature*, is "terrific," says Susan Pfeiffer, an anthropologist emeritus at the University of Toronto. "It's like a little hint of what I hope will be a wonderfully rich story."

To get a clearer picture of ancient Africa, a team led by North American researchers and including 13 scientists from five African nations analyzed samples from the remains of four infants and two adults buried in Malawi, Tanzania, and Zambia. The team managed to extract enough DNA to partially sequence the genomes. Five samples came from inner ear bones, which are dense and preserve DNA well.

Two infant boys from the Hora rock shelter in Malawi were buried on their sides in a flexed position about 14,000 years ago. "I spent a lot of time thinking about the circumstances that led to them dying so young and … about how carefully their communities had interred them," says Yale University anthropologist Jessica Thompson, who led the Hora excavation in 2019. The most recent remains, of an adult woman from Zambia's Kalemba rock shelter, were radiocarbon dated to about 5000 years ago. The oldest remains belonged to a woman found in Tanzania's Mlambalasi rock shelter amid ostrich eggshell beads radiocarbon dated to about 18,000 years ago. Previously, the oldest human genome from sub-Saharan Africa was 9000 years old.

Thompson and colleagues analyzed the six new partial genomes plus 28 previously reported from across the continent. The team ran the data through a computer program that compares similar snippets of DNA to estimate relatedness; they reconstructed a rough family tree dating back 18,000 years.

Their model suggests the 34 individuals descend from three major source populations. Two of them, from northeastern Africa and southern Africa, were already known.

But the third population, from Central Africa and most closely related to people today who live a foraging lifestyle there, came as a surprise.

The distinct genetic signatures of those ancestral populations indicate they were mostly isolated from one another for vast amounts of time before eventually coming together, suggests David Reich, a population geneticist at Harvard Medical School who co-led the study. "If you look at Europeans and East Asians, maybe they're separated by 40,000 or 50,000 years," he says. "These three groups were basically separated 200,000 years ago, then come together … maybe 80,000 to 50,000 years ago." That range is only a rough estimate, Reich notes, given none of the new genomes dates beyond 20,000 years ago.

But that time frame for commingling matches developments in material culture, says co-author Mary Prendergast, an archaeologist at Rice University. In African artifacts of that period, "we see a ton of hints that people are connecting in different ways," she says, mixing and matching artifacts from distant places.

Considered in that context, the new DNA data suggest sometime after 20,000 years ago, ancient Africans stayed closer to home. Stone tools found in their rock shelters take on a local flair. And their DNA suggests that starting around this time, people traveled shorter distances to find mates.

That date range marks the Last Glacial Maximum, which affected climate worldwide, points out Rick Potts, a paleoanthropologist at the Smithsonian Institution's National Museum of Natural History. Across tropical Africa, forests contracted and grasslands grew in between, forming fragmented savannalike "islands" for many species—perhaps humans among them. "It's interesting to think about whether sub-Saharan African foragers were mapping onto a kind of refugium model."

The six new genomes are a welcome addition to Africa's sparse record of ancient DNA, says Sarah Tishkoff, a geneticist at the University of Pennsylvania. But she's not swayed by the team's ideas about what happened before 20,000 years ago. "There's a lot of assumptions in that analysis," she says, and it's not clear to her that the authors considered alternative explanations.

The analysis included some remains from museums, highlighting the key role of collections, says study co-author Maggie Katongo, a curator at Zambia's Livingstone Museum and a doctoral student at Rice University. "When you do this research, you want to give back to the community," she adds. "We want to make sure that whatever comes from this research is made public for all people in Zambia." ■

BIOMEDICINE

Glowing tumor marker hampers mouse cancer studies

Response to protein complicates immunotherapy research

By **Jocelyn Kaiser**

Cancer biologist Cyrus Ghajar was gearing up to study how the immune system can fight breast cancer when he hit a snag: The supposedly fast-spreading cancer cells he implanted in mice stayed put and sometimes even disappeared after about 11 days. Then, postdoc Candice Grzelak identified the culprit: the green fluorescent protein (GFP) the researchers were using to track the cells. The marker itself was stimulating the rodents' immune system to attack the tumor cells.

Ghajar's lab at the Fred Hutchinson Cancer Research Center got around this unexpected problem, which it described in a paper last month. But he and others say the experience reflects a broader issue in mouse studies of immunotherapies, treatments that harness the immune system to vanquish tumors: The glowing proteins biologists use to track the cancer cells, often borrowed from fireflies or jellyfish, may provoke their own immune attack on the cells.

> **"We wanted to draw attention to the problem and provide the field with reagents and metrics necessary to solve it."**
>
> **Cyrus Ghajar**, Fred Hutchinson Cancer Research Center

Other foreign proteins that are workhorses of lab studies, such as components of the genome editor CRISPR, could have the same effect. And the phenomenon could explain why labs sometimes can't reproduce immunotherapy findings from other groups, suggests Glenn Merlino, a cancer biologist at the National Cancer Institute.

As immunotherapy becomes more and more important, he adds, scientists need to be aware of confounding factors like this. "So many preclinical experiments do not end up telling you anything useful in the clinic," says Merlino, a co-author on commentary on the issue last week in *Cancer Cell*.

Although it's long been known that the immune system can sense marker proteins such as GFP as foreign, it didn't much matter for cancer studies. That's because most labs used mice lacking an immune system so they would not reject the transplanted human cancer cells often used to assess treatments.

But as immunotherapies have taken off in the past decade, more labs are working with mice that have intact immune systems. Ghajar and others shifted to mouse cancer cells, which aren't immediately rejected. Others use mice that have humanized immune systems and accept human cancer cells.

Ghajar's lab realized its mice were producing immune sentinels called T cells that attacked the GFP-labeled cells, blocking their growth. They lowered the levels of GFP, but the cancer cells still didn't metastasize. The group found the best solution was to trick the mouse immune system into thinking the GFP was a natural protein, by using mice engineered to produce GFP in certain immune cells known as dendritic cells, which induce tolerance. In these rodents, the breast cancer cells grew as expected, they reported in *Cancer Cell*.

"We wanted to draw attention to the problem and provide the field with reagents and metrics necessary to solve it," Ghajar says.

Merlino and his coauthors warn in their commentary that the same problematic immune response could arise in experiments using other glowing proteins from various species, viral proteins that cause cancer, and even Cas9, CRISPR's DNA-cutting enzyme, which comes from a bacterium. Researchers may need to find workarounds, such as mouse strains modified so they tolerate the foreign proteins, like the mice turned to by Ghajar's lab. Merlino calls for other researchers to share similar experiences, perhaps in a database.

Peter Friedl, who studies metastasis at Radboud University and the MD Anderson Cancer Center, says he, too, has had experiments fail because of an immune reaction to a nonmouse marker protein. Researchers have fingered other causes for cancer biology's replication problem, such as variations in mouse colony microbiomes. But the unexpected immune responses, Friedl says, "absolutely" could contribute. ■



PHOTO: SU SHUO

Raccoon dogs in China were found to harbor several novel coronaviruses.

COVID-19

Novel viruses highlight risks of Asia's wild animal trade

Sampling of game in China reveals many viral threats

By **Jon Cohen**

Wild animals that are sometimes on the menu in China harbor a bewildering panoply of viruses, including many novel ones that may be able to infect humans, a study published in *Cell* on 16 February has found. Although none is closely related to the coronavirus that caused the COVID-19 pandemic, the study sends a clear warning that other viral threats are lurking in the animal kingdom, scientists say.

"There is an enormous amount of unsampled viral diversity" in animals, says Harvard University evolutionary biologist William Hanage, who was not involved in the work. "We humans need to understand that for a virus, different mammal species can look pretty alike, provided their cells have appropriate receptors." Live-animal markets are known to have sparked outbreaks, such as severe acute respiratory syndrome (SARS) 2 decades ago. China has since clamped down on the sale of the animals sampled in the study, but other countries in the region have not.

The researchers, led by veterinarian Su Shuo of Nanjing Agricultural University, took samples from nearly 2000 animals representing 18 different species at fur farms, zoos, and natural habitats in China. Most were species traditionally eaten as delicacies in China, including civets, raccoon dogs, badgers, bamboo rats, and porcupines. Using a "metagenomics" technique, which probes samples for RNA transcripts that viruses make when they copy themselves, they identified 102 virus species from 13 different viral families in the animals' noses, feces, and tissues. The researchers deemed 21 of those as "high risk" to humans, because they had infected people in the past or had a history of readily jumping between species. Sixty-five viruses had never been described before.

"Our results provide important insights to those game animals and their viruses that might lead to the next pandemic," Su says.

Among the worrisome finds were several coronaviruses. For example, a hedgehog was infected with a virus resembling the one that causes Middle East respiratory syndrome in humans. Four canine coronaviruses found in raccoon dogs were about 94% similar to coronaviruses recently found in humans in Malaysia and Haiti. "These viruses can infect many animals," Su says.

Some of the sampled species could act as intermediary hosts that bat coronaviruses infect before they make the jump to humans. Indeed, a coronavirus close to one found in bats turned up in a civet. Most researchers think both SARS-CoV-2 and SARS-CoV-1—the cause of SARS—became human pathogens after passing through an intermediate host.

The researchers also detected several influenza viruses, another family that could trigger a new pandemic. In a finding "of considerable significance," they write, civets and Asian badgers carried H9N2, an influenza A virus that has become increasingly common in chickens and ducks. H9N2 does not transmit efficiently between people and a February 2020 report noted that fewer than 50 human infections have been documented. But researchers fear that the virus, by replicating in other mammals, has more opportunities both to infect humans and to adapt to them. The infected badgers had runny noses and presumably could transmit to humans through the respiratory route.

Other viruses detected in the study that can infect people include influenza B, Norwalk, human parainfluenza virus 2, rotaviruses, and orthoreoviruses.

Markets that sell live animals—often called "wet markets"—are ideal places for viruses to transmit to humans, both because of the density of animals and because the stress they suffer makes them prone to shedding viruses, says medical virologist Marietjie Venter of the University of Pretoria, Hatfield. The new findings "confirm that trade and consumption of these animals should be avoided and support the actions taken by China to ban the trade of many of these animals," says Venter, who is a member of the World Health Organization's Scientific Advisory Group for the Origins of Novel Pathogens.

After SARS, China made the sale of many of the animals sampled in the study illegal, but they were still readily available in Wuhan markets in 2019, just before the start of the pandemic, including at the Huanan Seafood Market, which had the earliest identified cluster of COVID-19 cases. Su says the government has cracked down hard on illegal sales since then. "With very strict legislation, as well as screening checks, it is now difficult to find wildlife" for sale, Su says. "What worries me is that it seems that in Southeast Asia, where the economy is lagging, this wild animal trade is continuing."

Evolutionary biologist Edward Holmes at the University of Sydney, a co-author of the new study, "strongly suspects" SARS-CoV-2 jumped into humans at the Huanan market. As long as wild animals are sold, the risk of other viruses making a similar jump is high, he says. "It's hard to think of a more effective way to ignite and fan the flames of an epidemic," Holmes says. "We keep allowing these things to flourish and it's only a matter of time before we get another outbreak and perhaps another pandemic." ■



FINAL RESTING PLACE

Finland is set to open the world's first permanent repository for high-level nuclear waste. How did it succeed when other countries stumbled?

By **Sedeer El-Showk**

After passing through a security gate, the van descends into a tunnel that burrows under the forests of Olkiluoto, an island off Finland's west coast. The wheels crunch on crushed stone as a gray, wet October day gives way to darkness. "Welcome to Onkalo," deadpans Antti Mustonen, a geologist here. Onkalo—"cavity" or "pit" in Finnish—will be the world's first permanent disposal site for high-level nuclear waste, and a triumph for Finland.

Safety lights guide the van down through switchback turns that lead to a cavernous chamber, its walls reinforced with spray-on concrete. In just a few years, spent reactor fuel rods, encased in giant copper casks as tall as giraffes, will arrive here via elevator before robotic vehicles take them to one of the dozens of dead-end disposal tunnels that will form an ant's nest in the bedrock. In a freshly excavated disposal tunnel, Mustonen explains over the roar of ventilator fans that the peculiar smell comes from rock dust mixed with a trace of explosives. It is muddy underfoot—not what you want to see in a place that shouldn't have leaks, but Mustonen says the water is only from the excavation effort.

In the blackness, bare bedrock glints in the meager light from the van. After 30 to 40 of the copper casks are buried in the tunnel floor, the holes will be plugged with bentonite, a water-absorbing clay. Each tunnel will be backfilled with more bentonite and sealed with concrete. The casks will then begin their long vigil. They must remain undisturbed for 100,000 years, even as the warming climate of coming centuries gives way to the next ice age. "It's final disposal," Mustonen says. "Right here, in stable Finnish bedrock, 430 meters belowground, 420 meters below sea level."

Although nuclear power is declining in many nations, Finland has embraced the carbon-free energy source, lobbying the European Union to label it as sustainable. Two of the country's four reactors are on Olkiluoto. After a new Olkiluoto reactor is connected to the grid later this year, nuclear power will account for more than 40% of Finland's electricity.

The emissions-free electricity comes with a downside: hot and highly radioactive spent uranium fuel rods. In Finland, the rods cool for decades in pools of water; other nations park them in concrete and steel "dry storage" casks. Either way, surface storage is vulnerable to accidents, leaks, or neglect during the thousands of years the waste remains dangerous, says Budhi Sagar, a nuclear expert formerly at the Southwest Research Institute. "It's not safe—some disaster will occur," he says, citing the groundwater contaminated by leaky waste tanks at the U.S. Department of Energy's (DOE's) Hanford Site in Washington state, where reactors produced plutonium for the first nuclear weapons.

Without a long-term solution, the waste is piling up. Finland had about 2300 tons of waste in 2019, and about 263,000 tons of spent fuel sit in interim storage facilities worldwide, a report this year from the International Atomic Energy Agency estimates. "In my view, that's an unacceptable legacy to leave to future generations," says Tom Isaacs, a strategic adviser for Canada's Nuclear Waste Management Organization (NWMO) and Southern California Edison. "We generated this electricity. We benefited from that."

Many experts view permanent deep repositories like Onkalo as the best solution, but getting community buy-in is often a deal breaker. Street protests have slowed down plans for a disposal site in France, and in 2009, after years of debate, then-President Barack Obama's administration gave up on plans to develop Nevada's Yucca Mountain as the U.S. national repository. "The U.S. approach didn't pay sufficient attention to community acceptance or engagement," says Isaacs, who was the lead adviser on a 2012 blue-ribbon report commissioned by DOE to chart a way forward. "The original approach led to conflict rather than cooperation."

Finland, however, has run into remarkably few problems with Onkalo, which the government approved as a site in 2000. It helped that the residents of Eurajoki, the town closest to Onkalo and the nearby reactors, were comfortable with nuclear power. "Almost everyone in Eurajoki has a friend or relative who has worked in the nuclear power plants, so they know how we operate," says Janne Mokka, CEO of Posiva, the nuclear waste company set up by two nuclear power utilities to develop and manage Onkalo.

But experts say the success of Onkalo also reflects unique cultural and political conditions in Finland: high trust in institutions, community engagement, a lack of state-level power centers, and a balance of power between industry and stakeholders. "If you tried to implement the same thing in a country with much lower levels of trust, it would probably fail," says Matti Kojo, a political science researcher at Tampere University in Finland.

"The Finns have been able to articulate a consistent message about what they're doing, why they believe this facility will be safe, and why it will be a major benefit to the well-being of certain communities," Isaacs says. In late December 2021, Posiva applied for a license to begin operations in 2024.

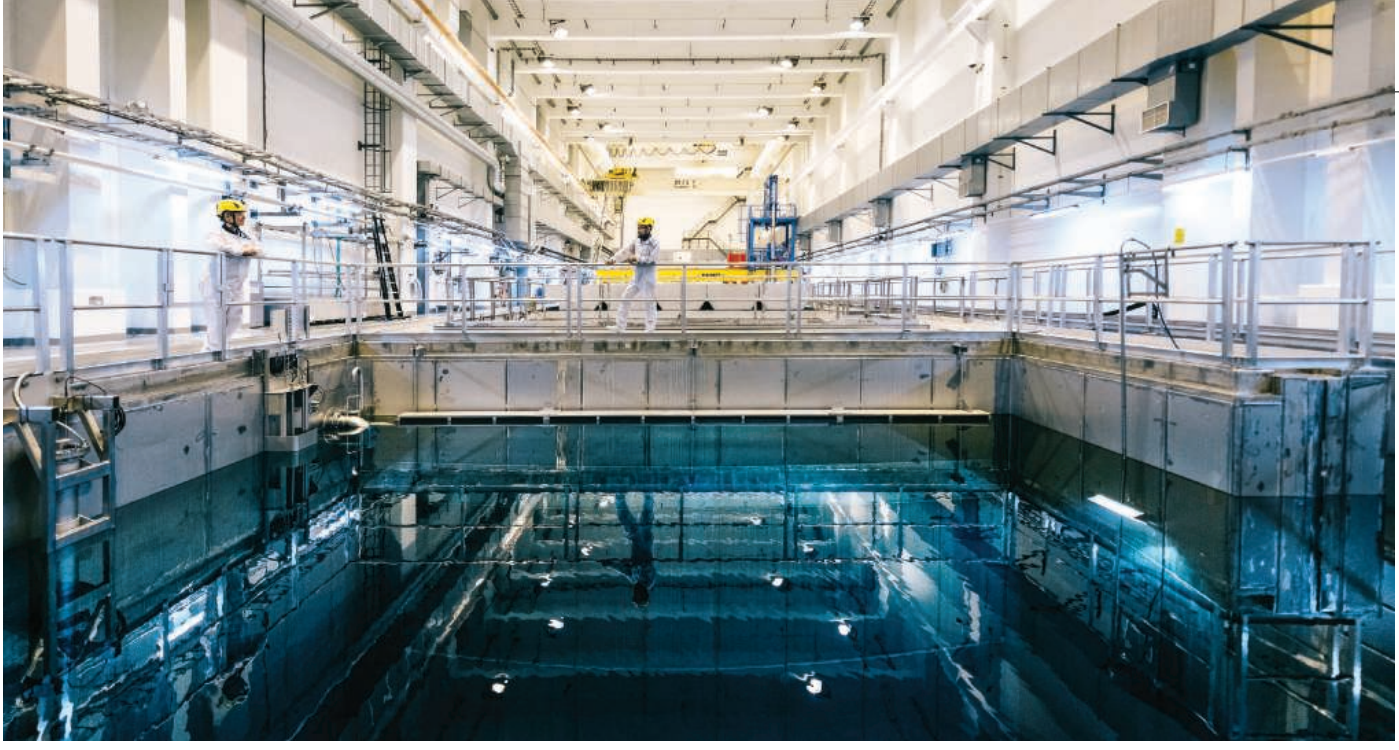
POSIVA BEGAN its search in the 1990s, with dozens of candidate sites, before narrowing the list to four with different geological characteristics. The final choice was



Spent uranium fuel rods will be sealed within thousands of tall, corrosion-resistant copper canisters.

About 100 nuclear waste disposal tunnels are being dug 430 meters underground at Onkalo.

PHOTOS: LEHTIKUVA/EMMI KORHONEN/VIA REUTERS; (OPPOSITE PAGE) TAPANI KARJANLAHTI/TVO



Spent fuel rods from Olkiluoto's nuclear power plants will cool off for several decades in interim storage pools before final burial at Onkalo.

between Olkiluoto and the area around the town of Loviisa, which houses the country's other nuclear power plants. In 1999, Posiva put forward the site that would become Onkalo.

The bedrock at Onkalo has been mostly stable for the past billion years, geologists say, although there is evidence of earthquakes during the past 10,000 years as massive glaciers retreated at the end of the last ice age and the bedrock rebounded. Posiva scientists don't expect significant earthquakes in the region until after the next ice age. Mustonen says Onkalo was purposefully situated between two parallel fault zones about 800 meters apart. If an earthquake were to occur, it would preferentially happen along those existing fault lines, he says. "They absorb the movement and nothing happens here in the area in between."

But earthquakes aren't the main threat. "The only way for things to move from the repository out to the surface and to impact people is to be carried by water," says Sarah Hirschorn, director of geoscience at NWMO. That means deep repositories are best situated in certain types of clay, salt, or hard crystalline rock, because they have small, disconnected pore spaces and are almost impermeable to water. At Onkalo, the nearly 2-billion-year-old bedrock is mostly gneiss, a hard rock formed at high temperatures and pressures.

Although decidedly nonporous, these rocks can still contain cracks, and Posiva had to map and avoid them as workers dug deeper. "It's these fractures which control the movement of water," says Neil Chapman, a geologist who has served as an independent consultant for Finland's nuclear regulator, the Radiation and Nuclear Safety Authority (STUK). If any significant fractures are discovered when drilling individual cask pits, he says, those holes won't be used.

If water were somehow able to seep into the repository, it would still have to get past the bentonite and copper to reach the spent fuel. "You're never relying on a single barrier," says Emily Stein, who researches deep geologic disposal at DOE's Sandia National Laboratories. "If one barrier fails, you have other barriers that can minimize or prevent radionuclide release."

After arriving at Onkalo, spent fuel will be unpacked in an encapsulation plant. In a stainless steel room surrounded by 1.3-meter-thick concrete walls, robots will vacuum away any water left on the fuel rods from their time in the storage pools, and seal them within a cast-iron canister nested inside a copper canister. Argon will be injected between the two canisters to provide an inert atmosphere, and the copper cask will be welded shut.

Copper is slow to corrode, and by the time any groundwater does reach Onkalo's depths, chemical or microbial reactions would have consumed all of its dissolved oxygen, making it less reactive. But Peter Szakálos, a chemist at the KTH Royal Institute of Technology in Stockholm, has concerns. In a 2007 study, he and colleagues found signs that copper can corrode even in pure, oxygen-free water. When the metal is exposed to water, Szakálos and his colleagues found it releases a whiff of hydrogen gas. He suspects the water reacts with the copper to form a "distorted" copper oxide crystal along with free hydrogen, which is either released or absorbed into the copper. Szakálos says any absorbed hydrogen would make the copper brittle and prone to cracking, and bronze would have been a safer choice. "It's just a matter of time—between decades and centuries—before unalloyed copper canisters start to crack at Onkalo."

Posiva and SKB, Sweden's nuclear waste management company, say Szakálos's experimental conditions are not relevant for the planned repositories. Even so, SKB contracted Uppsala University and the University of Toronto to try to replicate the findings. The Uppsala tests did not find evidence of any reaction with pure water, whereas the Toronto group observed one but said it was too slow to matter. "Making a measurement that tells you nothing happened is impossible," says David Shoesmith of the University of Western Ontario, a corrosion chemist who has consulted for SKB. "Based on what's been published, the answer to this question is that minimal things will happen."

Those concerns nevertheless delayed plans for what would be the world's second deep repository, near the Swedish coastal town of Forsmark. In 2018, Sweden's Land and Environment Court called for SKB to provide more evidence that copper corrosion would not undermine long-term safety. SKB submitted additional documentation to the Swedish Radiation Safety Authority, and in January, the Swedish government approved the facility based on the regulator's assessment that the other barriers would keep the repository safe.

PHOTO: TAPANI KARJANLAHTI/TVO

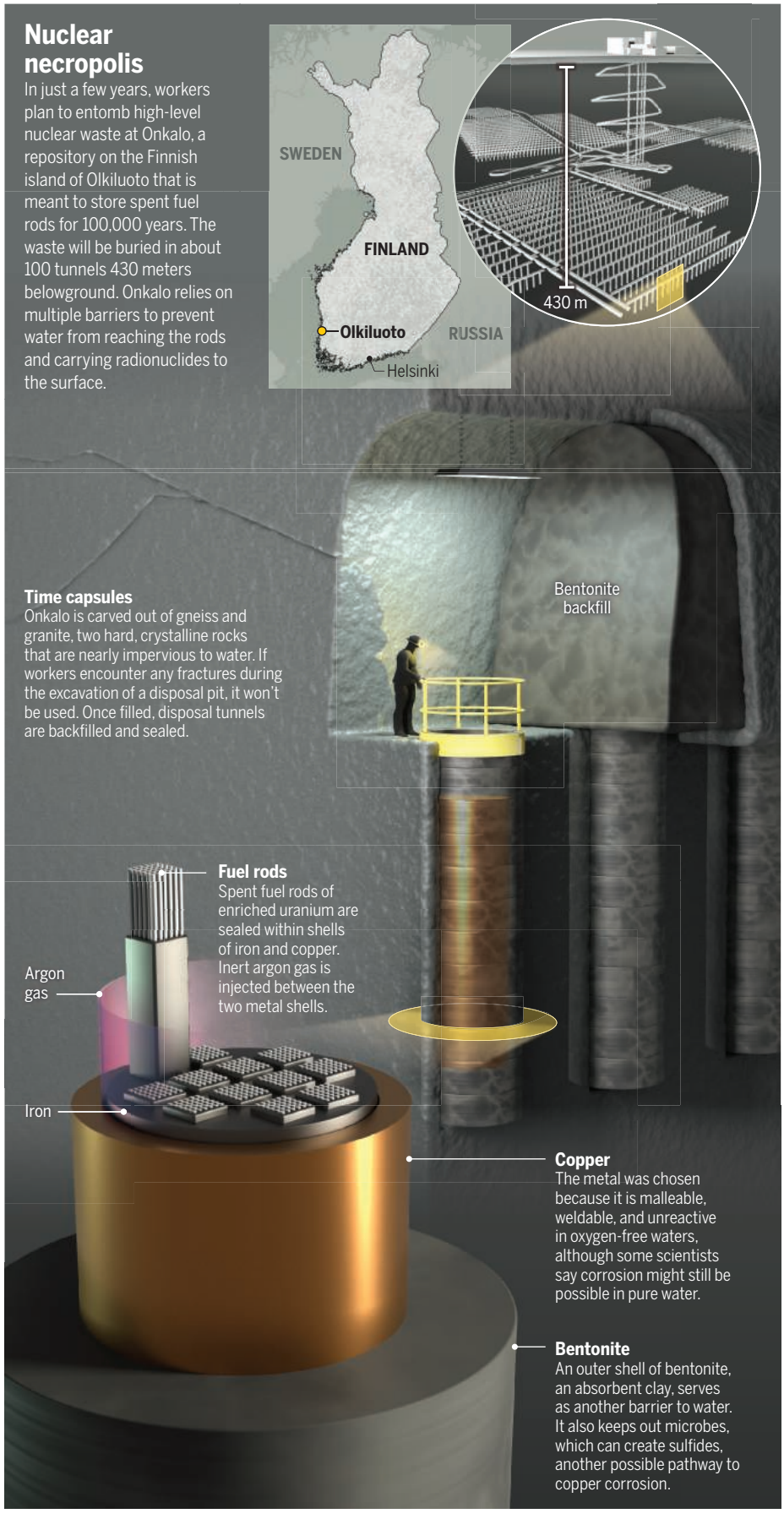
In addition to the casks themselves, the bentonite surrounding them will also prevent radionuclide escape, regulators say. The mineral not only keeps water away, but also prevents microbes from reaching the canister surface. Microbes can pose a threat, says Karsten Pedersen, CEO of Microbial Analytics Sweden, a company that researches their effect on deep repositories, because they can metabolize sulfates in groundwater and turn them into sulfides, which can slowly corrode copper. Posiva acknowledges that possibility, but the company's calculations suggest that even at elevated sulfide levels, the canisters would have a lifetime of more than 100,000 years.

Should all these barriers fail, escaping waste would face one last impediment: the decades it would take to migrate to the surface, with radioactivity levels dropping all the while. Sagar, who reviewed the long-term scenarios that were a part of STUK's overall safety assessment, says that even under worst-case assumptions the impact of leaking radionuclides would be minimal. For people living near the repository and drinking contaminated water from deep wells, the assessment found, the annual exposure would be well below the allowable limit set by STUK, which is about the same as the average background radiation exposure a person in Finland experiences today. "That's the point of a multibarrier system," Sagar says. "Even if some containers fail or a systematic construction error means they all have defects, the geology and other barriers are good enough that you're still within limits."

YET THE TRUE SECRET to Finland's success with Onkalo lies not so much in geology and engineering, but in the site selection process, the structure of government, and a culture of trust in institutions and expertise.

Finland's 1987 Nuclear Energy Act set up a nuclear waste management fund, financed by the nuclear operators, which incentivizes companies to develop waste disposal solutions. It also insulates the process from politics. Isaacs notes how this differs starkly from the situation in the United States, where DOE—which answers to the White House—runs the waste disposal program. "No matter how competent and well-intentioned people are, presidential and congressional elections are held regularly," he says. Important decisions can end up subject to political expedience, crippling a project that takes decades to build.

Another important difference, according to Isaacs, is the absence of strong state-level government in Finland. State governments, often far from disposal sites, see repositories more in terms of perceived



GRAPHIC: V. ALTOUNIAN/*SCIENCE*



Onkalo's encapsulation plant (white) sits atop an ant's nest of underground tunnels in this August 2021 photo. Olkiluoto's nuclear power plants can be seen in the distance.

PHOTO: TVO

costs rather than benefits, Isaacs says. Nevada officials—governors, senators, and others—have consistently opposed the development of the Yucca Mountain facility, blocking funding and throwing up other hurdles. More recently, state politicians in New Mexico have opposed a proposed temporary storage facility for nuclear waste in the state.

In Finland, without comparable power centers to play spoiler, Posiva and the national government could deal directly with communities like Eurajoki. Community acceptance was forged in the back and forth between Eurajoki and Posiva, Kojo says. "In the 1990s, the power companies knew that they really needed approval at the local level," he explains. Finnish law gave Eurajoki the right to veto disposal in the area. But Eurajoki officials were tempted by the tax revenue that would come from the third nuclear power plant if Posiva's parent company, TVO, decided to build it there. Posiva also funded the construction of a new senior center in town.

This approach—continual engagement with potential host communities—is rare in many other countries, including the United States. Even in Finland it is new. In the mid-1980s, Finland had a technical, top-down approach with no public participation that experts like Kojo and Isaacs call "decide-announce-defend." In 1986, TVO announced it would investigate the municipality of Ikaalinen as a final disposal site. However, local resistance, particularly in the wake of the catastrophic nuclear accident at Chernobyl in the former Soviet Union, foiled the plans. The company realized it would have to engage more and build local political support using an approach Kojo calls "mitigate-understand-mediate."

Once an agreement was reached, Eurajoki residents were largely willing to leave technical matters and safety questions to expert bodies. "In Finland, there is a very high level of trust in science and in the authorities," Kojo says. "If the national authority says the repository is safe, they don't need to worry about it." The process became a purely technocratic affair in the hands of Posiva and STUK.

Not everyone's concerns have been allayed. The Finnish Association for Nature Conservation (FANC) says it is worried about long-term ecotoxicity and bioaccumulation of the radioisotopes. It also cites concerns raised by retired geologist Matti Saarnisto, former director of research for the Geological Survey of Finland. In 2010, Saarnisto told Finland's national broadcaster that as the next ice age arrives, freezing soil and rock could create pressures that would damage the repository. In any case, Saarnisto argued, it is impossible to make predictions on the scale of 100,000 years.

Jari Natunen, a scientist with FANC, says the relationship between industry and regulators in Finland is far too cozy—a form of "structural corruption." "The authorities are biased to think that the industry's position is correct and valuable, and the concerns of civil society are not," says Natunen, who is also a member of Nuclear Transparency Watch, an antinuclear advocacy organization.

Natunen adds that the Finnish media's coverage of Onkalo has been too compliant. By contrast, in the United States, France, and Sweden, safety concerns remain a central part of the public debate. A 2020 study by Kojo and his colleagues, for example, found that France's *Le Monde* newspaper played a more critical role in debates about repositories, acting as a watchdog that challenged authorities, whereas Finland's leading daily, the *Helsingin Sanomat*, generally took a more positive approach that reflected the framing and confidence of the government and industry.

If getting the operating license goes smoothly, Posiva is on track to begin to bury nuclear waste deep in the Finnish bedrock in 2024 or 2025. Excavation will continue over the next century as new disposal tunnels are added. When the repository is filled to capacity, sometime around 2120, the entrance tunnel will be sealed shut. The encapsulation plant and other surface structures will be demolished. Nothing above will remain, not even a warning sign. Deep below the dismantled site, 6500 tons of spent fuel rods will lie in their tombs, quiet but still warm from radioactive decay.

"What we are doing really has meaning and is really important," Mustonen says. "For me, this is the reasonable thing to do with nuclear waste, and we need to make it as good as possible. The sense of responsibility to the next generation doesn't keep me awake at night, but it's there. It just is." ■

Sedeer El-Showk is a science journalist in Helsinki who joined the communications team at Aalto University at the end of 2021. His reporting was carried out independently.

eppendorf & Science

PRIZE FOR NEURO BIOLOGY



2021 Winner
Amber L. Alhadeff, Ph.D.
Monell Chemical Senses Center, USA
For research on the gut-brain control of hunger circuits

Tell the World About Your Work!

Application Deadline
June 15, 2022

Eppendorf & Science Prize for Neurobiology
The annual Eppendorf & Science Prize for Neurobiology is an international prize which honors young scientists for their outstanding contributions to neurobiological research based on methods of molecular and cell biology. The winner and finalists are selected by a committee of independent scientists, chaired by *Science's* Senior Editor, Dr. Peter Stern. If you are 35 years of age or younger and doing great research, now is the time to apply for this prize.

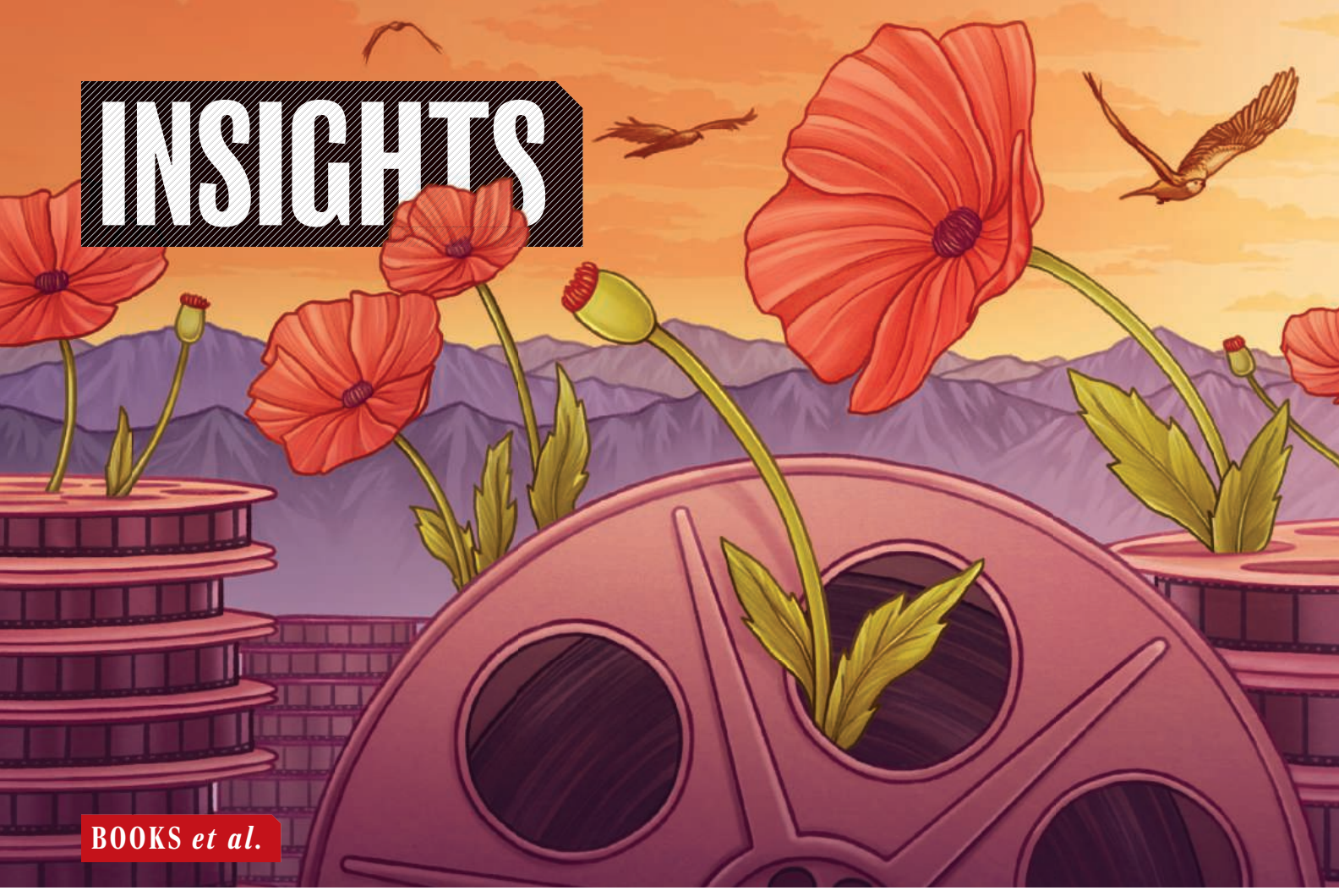
As the Grand Prize Winner, you could be next to receive
> Prize money of US$25,000
> Publication of your work in *Science*
> Full support to attend the Prize Ceremony held in conjunction with the Annual Meeting of the Society for Neuroscience in the USA
> 10-year AAAS membership and online subscription to *Science*
> Complimentary products worth US$1,000 from Eppendorf
> An invitation to visit Eppendorf in Hamburg, Germany

It's easy to apply! Write a 1,000-word essay and tell the world about your work. Learn more at:

eppendorf.com/prize

eppendorf Science AAAS

AAAS® and Science® are registered trademarks of the American Association for the Advancement of Science, USA. Eppendorf® and the Eppendorf Brand Design are registered trademarks of Eppendorf SE, Germany. All rights reserved, including graphics and images. Copyright © 2022 by Eppendorf SE. Photography: Happy Hour Headshot Philadelphia.



FILM

Science at Sundance 2022

Conceived of as a hybrid event during a period of pandemic optimism, the 2022 Sundance Film Festival pivoted at the last minute from partially in-person to fully online—a move that likely caused chaos behind the scenes but didn't faze our panel of virtual festival-goers. From a vivid documentary on the late volcanologists Maurice and Katia Krafft, featuring stunningly restored volcanic footage captured by the pair, to a melancholic meditation on the roles that social robots may soon play in our lives and families, this year's program featured a number of films with strong science, engineering, and technology themes. Read on to see what our reviewers thought of six of this year's offerings. **—Valerie Thompson**

To The End

Reviewed by **Sarah Roth**[1]

To The End, directed by Rachel Lears, traces the latest push to pass historic climate legislation in the United States amid record-breaking natural disasters, a global pandemic, and a racial justice reckoning. It follows a trailblazing group of young climate activists as they work to advance both climate and social policy.

The story picks up where Lears's 2018 film, *Knock Down the House,* left off, documenting the buzz surrounding the policy document known as the Green New Deal, which put forward a blueprint for reaching net-zero carbon emissions by 2030 while fueling job growth and investment in disadvantaged communities. In the words of congresswoman Alexandria Ocasio-Cortez: "The climate and environment piece is what we need to do, the justice and equality piece is how we do it."

The film weaves together the stories of three young women of color—Varshini Prakash of the youth-led "Sunrise movement," Alexandra Rojas of the progressive political action committee Justice Democrats, and Rhiana Gunn-Wright, policy director of the think tank New Consensus and coauthor of the Green New Deal—documenting their efforts to challenge a political system that favors the status quo along with their private moments of doubt and frustration. We witness these young activists and their collaborators soberly describing the stakes of the climate emergency, campaigning to elect progressive legislators, confronting elected officials, and even participating in a harrowing near-fatal hunger strike.

The film concludes at the end of 2021, when hopes run high for major climate legislation in the form of the Build Back Better bill. In congressional hearings and political debates, opponents argue that the bill is too costly. But graphic scenes throughout the film force viewers to confront the enormous costs associated with not addressing climate change. As the fate of this legislation re-

ILLUSTRATION: HANNAH AGOSTA



mains uncertain, the activists' expressions of anxiety and hope make clear that much work remains to be done.

Some of the film's most compelling moments emerge against the backdrop of archival footage documenting the rise of the New Deal out of the economic devastation of the Great Depression and the US mobilization to defeat fascism during World War II. Such scenes remind us that the social contract between Americans and their government has been rewritten before and can be again.

The views expressed herein are the author's own and do not necessarily reflect the opinions of the Environmental Law Institute.

To the End, *Rachel Lears, director,* Jubilee Films, 2022, 103 minutes.

All That Breathes

Reviewed by **Amit Chandra[2]**

In a working-class neighborhood of New Delhi's Muslim quarter, two brothers work tirelessly to rescue and rehabilitate local birds of prey. Winner of Sundance's World Cinema Grand Jury Prize: Documentary, *All That Breathes* paints an engrossing portrait of the siblings and the city's wildlife as they endure environmental and political turmoil.

Toxic air, poor visibility, and collisions with buildings and electrical wires make bird injuries a common occurrence in New Delhi. Brothers Nadeem Shehzad and Mohammad Saud began their journey into wildlife conservation in 2003, when they brought an injured black kite (*Milvus migrans*) to a local bird hospital, only to discover that the facility was unable to treat it. (The hospital, operated by vegetarian adherents of the Jain faith, refused to treat meat-eating animals.) The brothers returned home and cared for the bird themselves, building a makeshift infirmary in a basement that doubles as a factory for their soap dispenser business. They have since treated more than 20,000 birds.

Director Shaunak Sen captures the remarkable intimacy that exists between the two brothers as their informal search and rescue service becomes the primary focus of their lives. The pair invest the bulk of their assets into this activity, which they clearly see as crucial to their own survival. Meanwhile, long takes show viewers how the megacity in which the brothers' story is unfolding teems with life—a turtle crawls across plastic garbage, a snail crosses a busy street, a majestic bird glides effortlessly across the sky. These moments bring serenity and a wide lens to the drama surrounding the film's human and animal subjects.

The wildlife and the brothers alike serve as witnesses to the toxic accumulation of pollution in the city's air, water, soil, and even local politics. "Delhi is a gaping wound and we're a Band-aid on it," laments Shehzad. And yet they persevere.

As political tensions rise and riots erupt in the city around them, the brothers press on with their mission, propelled by new grant funding secured after their efforts are featured in the *New York Times*. The pair's delicate equilibrium is tested when Shehzad is invited to study animal rescue in the United States, an opportunity Saud initially resists but embraces by the end of the film.

The film's message is timely against the accelerating effects of pollution and climate change. Our fate is intertwined with the planet's biodiversity, insist the brothers. Quoting their deceased mother, they maintain that "we should not differentiate between all that breathes."

All That Breathes, *Shaunak Sen, director,* Rise Films, 2022, 91 minutes.

After Yang

Reviewed by **Lindsey Brown**[3]

Winner of the 2022 Alfred P. Sloan Feature Film Prize, *After Yang*, directed by Kogonada, is based on a short story with a very simple premise: the family robot, Yang, has unexpectedly broken. In the film, patriarch Jake (Colin Farrell)—a pensive tea purveyor—undertakes the task of getting Yang (Justin H. Min) fixed while his wife, Kyra (Jodie Turner-Smith)—the family breadwinner—is busy with work. Meanwhile, the couple's daughter, Mika (Malea Emma Tjandrawidjaja), for whom Yang was originally acquired, misses her best friend. Purchased refurbished when Mika, now in elementary school, was an infant, Yang is a "technosapien," designed to serve as a tool for linking Chinese children adopted into Western families with their cultural heritage.

After a certified repair shop declines to fix Yang, Jake secures the services of an unauthorized repairman, who suspects that the android has been equipped with spyware. Jake then takes Yang to the Museum of Technology, where curator Cleo (Sarita Choudhury) accesses a file filled with thousands of brief video clips captured by Yang throughout his time with the family. The robot's "memories" include his initial interactions with baby Mika, snippets from his life as her caretaker, and seemingly mundane moments such as taking a family photo—perspectives that sometimes contrast with the family's memories of Yang.

As Jake views the videos and reflects on his relationship with Yang, he notices the recurring appearance of a mysterious young woman. A deeper investigation reveals that Yang's interior life was far richer than Jake had imagined.

In the film's not-too-distant future, there have been many technological advances in the aftermath of an unspecified climate disaster: self-driving cars seem to be the norm, one can watch videos via eyeglasses, and human clones and biological robots are not uncommon. Far from a flashy, futuristic dystopia, however, *After Yang* is lush and quiet. Advanced technologies—some of which raise questions about the very nature of humanity—are all but invisible in the film, seamlessly woven into everyday life.

After Yang's distinctive perspective on the human experience prompts reflections on loss and grief and invites viewers to consider their connections to technology. It also asks unexpected questions: What are memories, if not simply a record of time? How are our identities formed and shaped? Are there patterns to the rules of attraction? Such queries, we learn, often have complex answers.

The views expressed herein are the author's own and do not necessarily reflect the opinions of the US Food and Drug Administration.

After Yang, *Kogonada, director,* A24, 2021, 96 minutes.

The Territory

Reviewed by **Gabrielle Kardon**[4]

In *The Territory*, directed by Alex Pritz, the Amazon is under siege. Motorcycles roar through the underbrush, chainsaws and fires demolish large swaths of trees, and the threat of violence is ever present. At the center of this conflict are 7000 square miles of rainforest, home of the Indigenous Uru-eu-wau-wau people and the illegal settlers and non-native farmers intent on seizing this land. The film, coproduced with the Uru-eu-wau-wau, is a riveting vérité-style documentary with unparalleled footage of the tinderbox that has been set aflame in Brazil.

Since they were first contacted in 1981, the Uru-eu-wau-wau have dwindled to less than 200 people. To survive, they must safeguard the rainforest that is not only their home but also the source of traditional foods and medicinal plants. Although the Uru-eu-wau-wau have been granted sovereignty over the disputed region, illegal deforestation and land theft have gradually chipped away at their territory. The film follows 19-year-old Bitaté as he is elected by the Uru-eu-wau-wau elders to lead them through the current conflict. Environmental activist Neidinha Bandeira plays an essential role as well, publicly admonishing intrusions into the protected area. Together, they brave violent threats and use drones and cameras to document incursions and deforestation.

The film also follows a group of farmers organized as the Association of the Rio Bonito, who see themselves as pioneers. In their view, building their own farms is their only means to escape poverty. The association, which has since disbanded, endeavored to establish guidelines to stake legal claims on the areas they clear. However, others—emboldened by the aggressive anti-environmental and anti-Indigenous rhetoric of President Jair Bolsonaro—operate clandestinely. Startling footage shows settler "Martin" setting fire to the forest, for example, an act he views as a way to "liberate" the land.

When the COVID pandemic begins, the Uru-eu-wau-wau retreat deeper into the forest. With recording equipment provided by Pritz, Bitaté and the Uru-eu-wau-wau start their own media team and take over filming, documenting confrontations with invaders and discovery of illegal settlements. Their footage provides a singular view of the conflict that they have begun to use to rally public support for the protection of Indigenous lands.

The Territory, which received an Audience Award and a Special Jury Award at Sundance, is a tightly edited documentary that explores the intimate relationship between people and land and captures the perspectives of each of a heated conflict's protagonists. It is also a testament to the power that film can have on environmental action and the protection of Indigenous peoples.

The Territory, *Alex Pritz, director,* Documist, 2022, 86 minutes.



Before he malfunctions, android Yang (right) serves as a cultural link for adoptee Mika (left) in *After Yang*.

PHOTO: CARA HOWE/COURTESY OF A24



Striking footage brings Katia and Maurice Krafft's passion for volcanoes to life in *Fire of Love*.

PHOTO: COURTESY OF SUNDANCE

Fire of Love

Reviewed by **Gabrielle Kardon**[4]

Two foil-clad figures dance incongruously in front of plumes of fiery lava in a scene that epitomizes the striking footage at the heart of the new documentary *Fire of Love*. Directed by Sara Dosa, the film showcases newly available archival recordings of volcanic eruptions captured by the late volcanologists Katia and Maurice Krafft, giving viewers a glimpse into their lives and their mutual love of volcanoes—a passion that would ultimately kill them.

Katia and Maurice came of age during the 1960s—an era that saw antiwar protests and shifting paradigms in the field of geology, the latter heralded by the discovery of plate tectonics and continental drift. In an interview that appears in the film, Maurice highlights how the cultural context of the moment influenced the pair's trajectory, explaining: "Katia and I got into volcanology because we were disappointed in humanity."

The Kraffts, who both grew up in the Alsace region of France, each cited childhood fascinations with volcanoes as early inspirations for their eventual careers. The pair met at the University of Strasbourg, began exploring volcanoes together in Iceland in 1968, were married in 1970, and soon were traveling the world to visit erupting volcanoes. At each location, they went dangerously close to collect samples and take spellbinding films and photos. Like their contemporary, Jacques Cousteau, the Kraffts cultivated an intrepid public image in which they cast themselves as "wandering volcanologists." The pair fortified their mythic personas with risky stunts and bold declarations ("I want to get closer, right into the belly of the volcano. It will kill me one day, but that does not bother me at all.").

Fire of Love fully embraces this myth. Influenced by French New Wave cinema, the film's narrator, Miranda July, expounds on the existential themes raised by the Kraffts' love and dangerous obsession.

In 1991, Maurice and Katia died together, engulfed by a pyroclastic flow while documenting the eruption of Japan's Unzen volcano. It is clear from the film that their legacy includes extraordinary footage of a myriad of volcanic eruptions that highlighted the dangers of living near a volcano. But did the pair's dangerous volcano-chasing lead to meaningful scientific contributions? Disappointingly, this fascinating question is left largely unexplored.

Fire of Love, *Sara Dosa, director,* Submarine, 2022, 93 minutes.

Downfall: The Case Against Boeing

Reviewed by **Lindsey Brown**[3]

The Boeing Company has long been regarded as one of the premier aircraft manufacturers in the world. But when Lion Air Flight 610 and Ethiopian Airlines Flight 302—both flown on Boeing's newest aircraft, the 737 MAX—crashed within 5 months of one another in 2018 and 2019, killing 346 people, the company's culture of safety and quality was called into question. *Downfall*, directed by Rory Kennedy, investigates what caused these tragedies, arguing that Boeing minimized its own responsibility and that it leveraged a campaign of plausible deniability, misinformation, and deception to deflect blame for the crashes.

The film's interviews with pilots, former employees, flight safety experts, legislators, and journalists paint a portrait of a company where safety is no longer paramount. Many of the film's subjects point to the 1997 merger with aerospace manufacturing corporation McDonnell Douglas as a time when corporate culture shifted from an emphasis on quality and care to messaging that profit should be prioritized above other considerations.

The film documents how, after losing market share to competitors, Boeing produced the 737 MAX, promising airlines that pilots would not require additional flight simulator training to operate the new aircraft. In the aftermath of the October 2018 Lion Air crash, a new feature known as the Maneuver Characteristics Augmentation System (MCAS) was implicated. Boeing initially blamed operator error and promised to implement MCAS training; however, data collected in the wake of the Ethiopian Airlines crash pointed to a critical malfunction of the system.

Moved to action by their losses, family members of the crash victims traveled from all over the world to Washington, DC, to pressure the US government to uncover the truth. In one riveting scene, CEO Dennis Muilenburg answers questions from Congress as family members carrying posters with photos of their loved ones look on silently.

Court documents would later reveal that Boeing had deceived the US Federal Aviation Administration by omitting crucial information about MCAS from official communications with the agency, and the company agreed to pay more than $2.5 billion under a deferred prosecution agreement. *Downfall*'s timeline clearly articulates the lead-up to, and fallout from, the 737 MAX crashes—two tragedies that emphasize the importance of prioritizing quality and safety in high-stakes settings.

The views expressed herein are the author's own and do not necessarily reflect the opinions of the US Food and Drug Administration.

Downfall: The Case Against Boeing, *Rory Kennedy, director,* Netflix, 2022, 89 minutes.

10.1126/science.abo3606

[1]Environmental Law Institute, Washington, DC 20036, USA. Email: sroth8@gmu.edu [2]Department of International Health, Georgetown University, Washington, DC 20057, USA. Email: amit.chandra@georgetown.edu [3]Division of Biotechnology Manufacturing, US Food and Drug Administration, Silver Spring, MD 20993, USA. Email: lindsey.james.brown@gmail.com [4]Department of Human Genetics, University of Utah, Salt Lake City, UT 84112, USA. Email: gkardon@genetics.utah.edu

PERSPECTIVES

NEUROSCIENCE

Losing sleep with age

Hypocretin neuron hyperexcitability underlies disrupted sleep quality associated with age

By **Laura H. Jacobson**[1,2,3] *and* **Daniel Hoyer**[1,2,4]



Sleep quality declines with aging. In mice, wake-promoting hypocretin neurons, normally silent during sleep, become hyperexcitable with age, resulting in intrusions of wakefulness into sleep. This discovery may lead to new therapies to improve sleep in aging and related disorders.

PHOTO: ENES EVREN/ISTOCKPHOTO.COM

Humans spend approximately one-third of their lives asleep, but this is not distributed equally across their life span. Sleep quantity and quality decline as age advances, and insomnia and sleep fractionation are common in older people (*1*, *2*). Sleep is essential for vitality and health. At any age, chronic sleep deprivation causes a range of issues, including disrupted cognition and memory (*3*). Correspondingly, sleep complaints in older people are associated with increased risks of impaired physical and mental health and with mortality (*4*). Beyond evidence of degenerating subcortical nuclei in age-associated sleep disturbances (*2*), the underlying mechanisms remain unclear despite decades of awareness of the problem and its consequences. On page 838 of this issue, Li *et al.* (*5*) report the hyperexcitability of hypocretin neurons as a core mechanism underlying sleep disruption in aged mice, explaining why sleep is punctuated by intruding wakefulness despite the loss of wake-promoting neurons.

Hypocretins, neuropeptides that are also called orexins, are produced by a few thousand neurons located exclusively in the lateral hypothalamus. These cells project widely across the brain, providing dense, stimulatory innervation to wake-promoting nuclei, such as the adrenergic locus coeruleus, histaminergic tuberomammillary nucleus, serotonergic raphe nuclei, and basal forebrain cholinergic neurons (*6*). Hypocretin neurons fire and release hypocretins during wakefulness and become inactive with sleep. Narcolepsy type 1 (NT1) is caused by the loss of hypocretinergic neurons and is characterized by unstable sleep, wakefulness, and cataplexy (loss of muscle tone) (*7*). Accordingly, hypocretin receptor antagonists, which block hypocretin-induced wakefulness, produce a more natural sleep architecture than classic hypnotics: benzodiazepines or "z-drugs" (e.g., zolpidem), which activate inhibitory γ-aminobutyric acid type A ($GABA_A$) receptors, and sedative antidepressants and antipsychotics, which act by globally dampening brain activity (*8*). Three dual orexin receptor antagonists (DORAs) are now approved for treating insomnia: suvorexant, lemborexant, and daridorexant.

Li *et al.* report age-dependent decreased hypocretin neuron density, which could be expected to destabilize sleep-wakefulness, as seen in NT1. Others have also observed decreased hypocretin neuron density with aging in various species, including humans (*9*). However, the detailed analyses of remaining hypocretin neurons by Li *et al.* provide a deeper level of understanding of the underlying mechanisms leading to disrupted sleep. Using fiber photometry and calcium imaging, Li *et al.* showed calcium peaks in hypocretin neurons associated with wakefulness. During the inactive (sleep dominant) phase, these calcium transients were more frequent and lower in amplitude in old versus young mice and were associated with increased wakefulness. This suggested a lower threshold to arousal in aged hypocretin neurons and increased hypocretin release. Indeed, this was confirmed by the increased wakefulness induced by optogenetic stimulation of hypocretin neurons and their electrophysiological hyperexcitability in aged mice.

Investigating possible causes of this intrinsic hyperexcitability, Li *et al.* discovered a reduced expression of subunit 2 of the KCNQ voltage-gated potassium channel. Channels composed of KCNQ subunits 2 and 3 are responsible for M-currents, which maintain the cell membrane potential below the threshold for action potentials, inhibiting neuronal activity. Li *et al.* found reduced M-currents in aged hypocretin neurons, explaining their hyperactivity. By selectively reducing KCNQ2/3 expression in hypocretin neurons using CRISPR-Cas9 in young mice, the authors mimicked aspects of hypocretin neuron hyperexcitability and non–rapid eye movement (NREM) sleep instability of old mice. Characterized by slower electroencephalographic (EEG) frequencies, NREM sleep is associated with learning and memory consolidation and is the most disrupted sleep state with age (*2*). The KCNQ channel blocker XE991 stimulated wakefulness in young mice, whereas in old mice, the KCNQ2/3 channel opener flupirtine improved NREM sleep quantity and stability and, notably, enhanced recognition memory. Increased NREM sleep stability was also induced by treating aged mice with the DORA MK6096.

Sleep is also disrupted in several neurodegenerative and neuropsychiatric diseases, including anxiety, depression, autism, posttraumatic stress disorder, and Parkinson's and Alzheimer's diseases. Li *et al.* show that despite commonalities such as hypocretin neuron loss and sleep-wakefulness fractionation in aging and NT1 (but not cataplexy), the disrupted sleep of older mice was mechanistically different from that of a mouse model of NT1 (although resting membrane potential of surviving hypocretin neurons was increased in both aging and early stages of hypocretin neuron loss in the NT1 mouse model, indicating some form of circuit-based compensation in both). Given the severe hypocretin neuron loss in advanced NT1, KCNQ2/3 channel openers or hypocretin receptor antagonists should not consolidate sleep in NT1 patients.

[1]Florey Institute of Neuroscience and Mental Health, Parkville, VIC, Australia. [2]Department of Biochemistry and Pharmacology, School of Biomedical Sciences, Faculty of Medicine, Dentistry and Health Sciences, The University of Melbourne, Parkville, VIC, Australia. [3]Melbourne Dementia Research Centre, The Florey Institute of Neuroscience and Mental Health and The University of Melbourne, Parkville, VIC, Australia. [4]Department of Molecular Medicine, The Scripps Research Institute, La Jolla, CA, USA.
Email: laura.jacobson@florey.edu.au; d.hoyer@unimelb.edu.au

Indeed, DORAs are contraindicated in NT1 owing to an increased risk of cataplexy (*8*). However, this leads to questions about the mechanisms underlying disrupted sleep in other pathologies.

Like aging, Alzheimer's disease is commonly accompanied by disrupted sleep, as well as hypocretin neuron loss (*10*) and increased hypocretinergic tone (*11*, *12*). It will thus be important to determine whether aging and Alzheimer's disease share KCNQ2/3 channel-induced hypocretin neuron hyperactivity as a common mechanism. NREM sleep is important for the clearance of toxic, misfolded brain peptides and proteins (*13*) such as β-amyloid (Alzheimer's disease), tau (tauopathies), and α-synuclein [Parkinson's disease (*14*)]. Because these products can also directly disrupt sleep, hypnotic-enhanced NREM sleep may further enhance sleep quality and delay disease progression by reducing their accumulation (*14*, *15*). However, classical hypnotics are unlikely to unlock such benefits. These broad-spectrum inhibitors of neuronal activity can induce cognitive complaints and falls and are thus contraindicated in such disorders and in older people in general. DORAs, by contrast, have a better side-effect profile in these domains (*8*). Together with Li *et al.*'s evidence of improved recognition memory with flupirtine in aged mice, selective targeting of hypocretinergic mechanisms may prove superior in reaping the rewards of pharmacologically enhanced sleep in older people in both health and disease.

The discovery by Li *et al.* reveals an age-dependent mechanism underlying sleep disruption and thus reopens the search for new, targeted strategies to combat sleep disturbances in older people, and future research has the potential to expand to neurodegenerative disorders. If translated clinically, these findings pave the way for the development of sleep medications that specifically dampen hypocretin neuron hyperactivity to improve sleep and mental and physical health in older people. ■

REFERENCES AND NOTES

1. D. Kocevska *et al.*, *Nat. Hum. Behav.* **5**, 113 (2021).
2. B. A. Mander, J. R. Winer, M. P. Walker, *Neuron* **94**, 19 (2017).
3. C. J. Lowe *et al.*, *Neurosci. Biobehav. Rev.* **80**, 586 (2017).
4. D. J. Foley *et al.*, *Sleep* **18**, 425 (1995).
5. S.-B. Li *et al.*, *Science* **375**, eabh3021 (2022).
6. T. E. Scammell *et al.*, *Neuron* **93**, 747 (2017).
7. C. L. A. Bassetti *et al.*, *Nat. Rev. Neurol.* **15**, 519 (2019).
8. D. Hoyer *et al.*, *Br. J. Clin. Pharmacol.* **86**, 244 (2020).
9. N. J. Hunt *et al. Neurobiol. Aging* **36**, 292 (2015).
10. J. Oh *et al.*, *Alzheimers Dement.* **15**, 1253 (2019).
11. Y. A. Dauvilliers *et al.*, *Front. Aging Neurosci.* **6**, 119 (2014).
12. C. Liguori *et al.*, *JAMA Neurol.* **71**, 1498 (2014).
13. M. Nedergaard, S. A. Goldman, *Science* **370**, 50 (2020).
14. M. M. Morawska *et al.*, *Sci. Transl. Med.* **13**, eabe7099 (2021).
15. B. P. Lucey, *Neurobiol. Dis.* **144**, 105031 (2020).

ACKNOWLEDGMENTS

L.H.J. has consulted for Eisai Co., Ltd.

10.1126/science.abo1822

GRAPHIC: K. FRANKLIN/*SCIENCE*

GENETICS

Inferring human evolutionary history

Unified genetic genealogy improves our understanding of how humans evolved

By **Jasmin Rees**[1,2] *and* **Aida Andrés**[1,2]

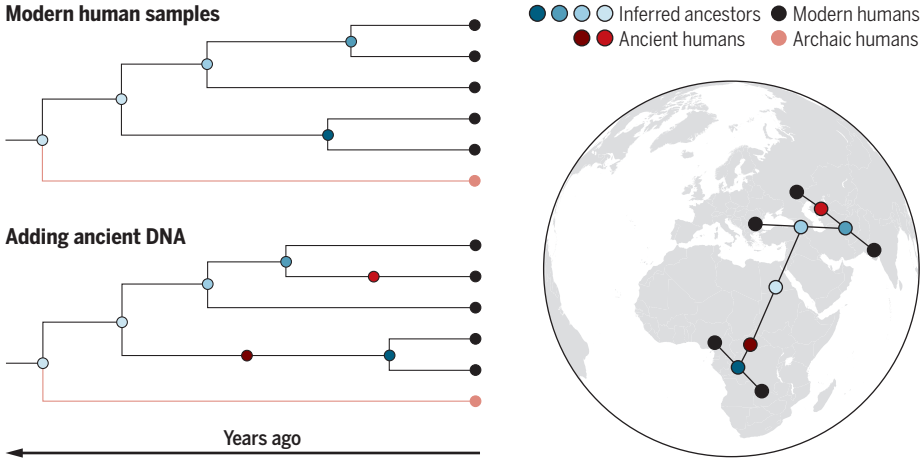
Genomes are invaluable tools for inferring the demographic and adaptive history of human populations, including migrations, population splits, admixture, and genetic adaptations. Growing datasets of modern and ancient genomes make this possible, but their massive size comes with important challenges, demanding techniques that analyze immense amounts of data in reasonable amounts of time while using as much information as possible. Combining genomes from different datasets poses perhaps an even greater challenge, especially when it comes to integrating ancient and modern genomes. On page 836 of this issue, Wohns *et al.* (*1*) report surmounting some of these challenges to construct the largest human genealogy to date, integrating modern and ancient genomes from multiple datasets to infer key events in human history together with their timings and geographical locations.

Phylogenetic trees are used to represent the evolutionary or genetic relationships among species. Similar trees can represent the relationships among individuals within a species, analogous to how family genealogies represent relationships between family members. However, because of the effects of recombination, each locus has a slightly different evolutionary history and therefore a different tree. Tree-recording methods (*2*) can infer these trees along the genome, with each tree representing what can be considered a nearly complete history of the locus. Consequently, tree recording is superior to most classical methods, which condense complicated evolutionary patterns in relatively simple summary statistics. By combining trees across the genome, a theoretical genealogy can be generated that embodies the genetic relationships among sampled individuals and their inferred ancestors, within and across populations. If the sampling of genomes was sufficiently comprehensive, such genealogy would in theory represent relationships over the entire species, capturing the genetic history of modern humans today.

Owing to a series of impressive theoretical and computational advances, genetic

Human genealogy reconstruction and geographical inference

By building the tree from modern human and high-quality ancient genomes, one can infer ancestral human relationships. Using additional ancient human samples to help infer the ages of alleles, Wohns *et al.* built a unified genealogy that also includes the geographical location of inferred ancestors, which gives information about populations and their migrations through human history.



trees can now be inferred for thousands of genomes (*3*–*7*). Analyses of these trees have already improved our knowledge of human demography (*4*, *5*, *8*, *9*) and promise to improve our ability to identify targets of natural selection (*5*, *8*, *10*–*12*). Further, high-quality ancient genomes can be directly integrated in the tree, which greatly increases the certainty of evolutionary processes by supporting inferences with data from the past. This is particularly helpful to study populations that are extinct or that contributed little to modern populations, such as Neanderthals and Denisovans (archaic humans) (*13*, *14*), and tree-based studies are helping to create a better understanding of the nature of interbreeding between modern and archaic groups (*5*, *8*, *9*).

Unfortunately, the DNA in ancient remains is usually highly degraded and most ancient genomes are not of sufficient quality to be fully incorporated into the trees. Wohns *et al.* present an approach that aims to skirt inaccuracies introduced by ancient DNA by using such ancient genomes only to help time the emergence of alleles (see the figure). This allows the use of hundreds of ancient genomes while limiting the effects of errors. They generated an impressive, unified human genealogy from >3500 modern and high-quality ancient genomes from >215 different human populations, using >3000 additional ancient genomes to improve inferences from the trees. With this unified genealogy, key events in history, such as population size changes, splits, or migrations, become clearly apparent. They identify well-resolved events, such as the out-of-Africa migration, and suggest multiple severe reductions in population size through human history.

Further, Wohns *et al.* propose a new method that, applied to the unified genealogy, allows them to estimate ancestral geographical locations of evolutionary events. Although there have been other efforts to place past events geographically (*15*), Wohns *et al.* use a nonparametric method to estimate the theoretical location of inferred human ancestors simply as the midpoint of the geographic coordinates of their descendants—with these calculations extended backward up the tree to reach a theoretical common ancestor of all individuals. Using this method, Wohns *et al.* infer an average ancestral location of all sampled humans in Northeast Africa by 72,000 years ago and until the oldest common ancestors of all individuals. This simple method works well to refine known ancestral locations and, as sampling improves, it has the potential to identify currently unknown human movements. More generally, the trees generated in this study will undoubtedly prove useful to those studying human evolution.

Although tree-recording methods represent an exciting and promising avenue of harmonizing datasets across time and space, as demonstrated by Wohns *et al.*, they are not without their limitations. There remains uncertainty in evolutionary parameters and ancient genomes, and it is unlikely that the use of low-quality ancient DNA will ever be without a degree of error, except when using rare high-quality genomes or if inferring missing data becomes substantially more accurate. Still, as genomic datasets continue to grow, genealogical methods will be increasingly useful to represent the wealth of genomic data. Perhaps most importantly, as larger numbers of modern and ancient genomes from underrepresented populations become available, our understanding of human demography, currently still biased to well-sampled populations, will improve in both detail and scope.

The power and resolution of tree-recording methods promise to help clarify the evolutionary history of humans and other species. It is likely that the most powerful ways to infer evolutionary history going forward will have their foundations firmly set in these methods. ■

[1]UCL Genetics Institute, Department of Genetics, Evolution and Environnment, University College London, London, UK. [2]Genetics and Genomic Medicine Programme, Great Ormond Street Institute of Child Health, University College London, London, UK. Email: a.andres@ucl.ac.uk

REFERENCES AND NOTES

1. A. W. Wohns *et al.*, *Science* **375**, eabi8264 (2022).
2. M. D. Rasmussen, M. J. Hubisz, I. Gronau, A. Siepel, *PLOS Genet.* **10**, e1004342 (2014).
3. J. Kelleher, A. M. Etheridge, G. McVean, *PLOS Comput. Biol.* **12**, e1004842 (2016).
4. J. Kelleher *et al.*, *Nat. Genet.* **51**, 1330 (2019).
5. L. Speidel, M. Forest, S. Shi, S. R. Myers, *Nat. Genet.* **51**, 1321 (2019).
6. K. Harris, *Nat. Genet.* **51**, 1306 (2019).
7. P. Ralph, K. Thornton, J. Kelleher, *Genetics* **215**, 779 (2020).
8. L. Speidel *et al.*, *Mol. Biol. Evol.* **38**, 3497 (2021).
9. N. K. Schaefer, B. Shapiro, R. E. Green, *Sci. Adv.* **7**, abc0776 (2021).
10. Y. Field *et al.*, *Science* **354**, 760 (2016).
11. A. J. Stern, P. R. Wilton, R. Nielsen, *PLOS Genet.* **15**, e1008384 (2019).
12. A. J. Stern, L. Speidel, N. A. Zaitlen, R. Nielsen, *Am. J. Hum. Genet.* **108**, 219 (2021).
13. M. Meyer *et al.*, *Science* **338**, 222 (2012).
14. K. Prüfer *et al.*, *Nature* **505**, 43 (2014).
15. M. M. Osmond, G. Coop, bioRxiv 10.1101/2021.07.13.452277 (2021).

ACKNOWLEDGMENTS

J.R. is funded by the National Institute for Health Research Great Ormond Street Hospital Biomedical Research Centre. A.A. is funded by University College London's Wellcome Institutional Strategic Support Fund 3 (204841/Z/16/Z).

10.1126/science.abo0498

MEDICINE

Anticipating antibiotic resistance

Machine learning can use clinical history to lower the risk of infection recurrence

By **Jean-Baptiste Lugagne**[1,2] *and* **Mary J. Dunlop**[1,2]

When a patient is diagnosed with a bacterial infection, clinicians perform antibiotic susceptibility tests in the laboratory and use the results to prescribe an appropriate antibiotic. But recurrence rates are high; for example, ~25% of women with urinary tract infections (UTIs) develop another infection within 6 months (*1*, *2*). On page 889 of this issue, Stracy *et al.* (*3*) reveal that recurrent infections are often driven by a different strain than the original infection. Although correctly prescribing a susceptibility-matched antibiotic reduces recurrence rates overall, it also increases the chances of developing a resistant infection caused by a different strain. Thus, treatment is a double-edged sword, in which susceptibility-matched treatments can pave the way for resistant strains lurking in the microbiota. The authors find that this risk can be minimized with a data-driven approach that incorporates population-wide statistics and the patient's personal history through a machine learning model to make antibiotic recommendations.

Key to this study is a large longitudinal dataset containing information about UTIs and wound infections, including antibiotic susceptibility profiles and prescribed antibiotics, for male and female patients of all ages in Israel's Maccabi Healthcare Services between 2007 and 2019. In most cases, antibiotic treatment of the initial infection is effective. However, in 10% of UTIs and 6% of wound infections, patients experience early recurrence, returning with another infection within 28 days of the original. Some of these early recurrences are the result of erroneous prescription of an antibiotic that the infection was resistant to, as can hap-

[1]Department of Biomedical Engineering, Boston University, Boston, MA, USA. [2]Biological Design Center, Boston University, Boston, MA, USA. Email: mjdunlop@bu.edu

pen when drugs are prescribed to provide rapid clinical intervention while awaiting results from susceptibility tests (*4*). However, a substantial fraction of cases fall into the insidious category of being appropriately treated with susceptibility-matched antibiotics and yet returning with an antibiotic-resistant infection.

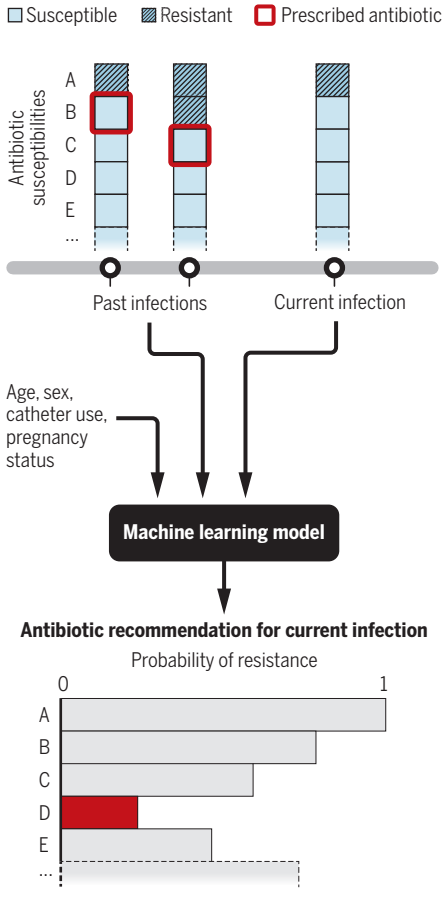
How do these resistant strains emerge? Stracy *et al.* carried out genomic sequencing of the bacteria, providing a detailed view of the strains and species of the original infection compared with the ones that caused it to recur. This analysis reveals an underappreciated path to reinfection, with the original species being treated and eliminated but with the treatment ultimately setting the stage for other resistant strains to emerge. Recent studies provide compelling examples of how a patient's microbiota serves as a reservoir, such as uropathogenic strains being harbored in the gut (*2*, *5*). This analysis also joins a growing list of studies that highlight the power and potential of integrating genome sequencing data with clinical records (*6*, *7*).

Building on the extensive dataset of infection and treatment histories, Stracy *et al.* develop a machine learning algorithm for patient-specific recommendations (see the figure). This strategy is successful because the patient's risk of developing a recurrent infection is strongly linked to their treatment and infection history. The authors use multivariate logistic regression, a powerful long-established tool for medical outcome predictions (*8*), to assess the risk of early recurrence for each antibiotic candidate. The algorithm then identifies the antibiotic that is least likely to cause an infection to recur early and be resistant to the prescribed antibiotic. Notably, the model uses only 13 parameters to fit the data for each UTI antibiotic, and eight in the case of wound infections, in which the parameters weight factors such as age, sex, pregnancy status, catheter use, and infection history.

These recommendation algorithms are evaluated against statistical models of early recurrence and are predicted to reduce the rate of early resistance recurrences of UTIs and wound infections by almost half compared with those of physicians' susceptibility-matched prescriptions. This is one of the great advantages of machine learning approaches: By systematically reviewing all available patient information, with a statistical model built on thousands of training samples, the algorithm can identify subtle patterns and provide valuable insights and recommendations to support physicians in their decisions (*4*, *9*). The algorithms are also predicted to significantly improve on current physician practices

Predicting resistance according to treatment history

A machine learning model built with data from thousands of patients with wound infections and urinary tract infections identified the factors that contribute to antibiotic resistance in recurrent infections. A patient's history of infections and antibiotic treatments can then be used with their demographic data to predict which candidate antibiotics would likely prevent a recurrent infection.



even when they are constrained to recommend different types of antibiotics at frequencies that match present-day practices. This is essential because other factors, such as side effects and ease of use, inform decisions about antibiotic selection. The risk assessment for each antibiotic and a quantified contribution profile for each patient risk factor, such as age or resistance history, can be retrieved. The decision is therefore interpretable, a critical step toward establishing trust in machine learning recommendation systems for health care (*10*, *11*).

However, these algorithms are not ready to prescribe antibiotics just yet. The algorithms were not evaluated on actual patients but against statistical estimates of the chances of early resistance recurrences. Further studies are required to assess whether resistant infections that extend beyond the 28-day window are also prevented. It is also unknown how large and diverse the training sets need to be and, once trained, how robust the recommendation system is, for example, to missing data points or clerical errors.

More generally, data-driven approaches to health care decisions face numerous social, legal, and ethical challenges, as highlighted recently by the World Health Organization (WHO) (*12*). Algorithms can entrench suboptimal or even discriminatory practices (*13*). Although the recommendation model presented by Stracy *et al.* is not fitted directly to the clinicians' decisions if, for example, the responses of 10- to 19-year old women to fosfomycin are underrepresented in the training set, predictions under these conditions will be less reliable. It is also unclear how the model will adapt to shifts in medical practices—for example, in the case of newly available antibiotics. Still, machine learning recommendation systems such as the one presented by Stracy *et al.* have the potential to substantially improve patient outcomes and could play a major role in mitigating antibiotic resistance.

The current wave of data-driven methods for health care presents an opportunity not only to tackle broad public health issues but to harness their power to introduce new data collection standards, evaluation metrics, and training paradigms (*14*, *15*). Essential to the success of these methods is the availability of both longitudinal datasets and interdisciplinary studies, such as those based on genomic sequence analysis, that provide fundamental insights into the mechanisms by which resistance emerges. ■

REFERENCES AND NOTES

1. A. L. Flores-Mireles, J. N. Walker, M. Caparon, S. J. Hultgren, *Nat. Rev. Microbiol.* **13**, 269 (2015).
2. B. M. Forde *et al.*, *Nat. Commun.* **10**, 3643 (2019).
3. M. Stracy *et al.*, *Science* **375**, 889 (2022).
4. I. Yelin *et al.*, *Nat. Med.* **25**, 1143 (2019).
5. K. L. Nielsen, P. Dynesen, P. Larsen, N. Frimodt-Møller, *J. Med. Microbiol.* **63**, 582 (2014).
6. X. Didelot, R. Bowden, D. J. Wilson, T. E. A. Peto, D. W. Crook, *Nat. Rev. Genet.* **13**, 601 (2012).
7. M. Magruder *et al.*, *Nat. Commun.* **10**, 5521 (2019).
8. P. W. F. Wilson *et al.*, *Circulation* **97**, 1837 (1998).
9. A. Rajkomar, J. Dean, I. Kohane, *N. Engl. J. Med.* **380**, 1347 (2019).
10. C. M. Cutillo *et al.*, *NPJ Digit. Med.* **3**, 47 (2020).
11. A. F. Markus, J. A. Kors, P. R. Rijnbeek, *J. Biomed. Inform.* **113**, 103655 (2021).
12. WHO, Ethics and governance of artificial intelligence for health: WHO guidance (WHO, 2021); www.who.int/publications/i/item/9789240029200.
13. Z. Obermeyer, B. Powers, C. Vogeli, S. Mullainathan, *Science* **366**, 447 (2019).
14. J. F. Rajotte *et al.*, *GoodIT 2021 Proc. 2021 Conf. Inf. Technol. Soc. Good*, 10.1145/3462203.3475875 (2021).
15. S. Hooker, *Patterns* **2**, 100241 (2021).

10.1126/science.abn9969

GRAPHIC: V. ALTOUNIAN/*SCIENCE*

ORGANIC CHEMISTRY

Dimerization decrypts antibiotic activity

Direct dimerization simplifies the synthesis of himastatin and elucidates its mode of action

By **Myles Smith**

With the emergence of drug-resistant bacteria that can evade current frontline therapeutics, the need for antibiotics with new modes of action is increasingly urgent (*1*). One emerging strategy to address this need is to revisit previously identified antibiotics of promise and apply modern medicinal chemistry and biochemical tools to improve their activity and unveil their often ill-defined modes of action (*2, 3*). Among such natural products is himastatin (**1**), a dimeric peptide antibiotic isolated in 1990 that shows good activity against Gram-positive bacteria, albeit through a largely unknown mode of action (*4*). On page 894 of this issue, D'Angelo *et al*. (*5*) develop an efficient chemical synthesis of himastatin through a bioinspired dimerization of its native monomeric units. This approach provides a blueprint to access not only this complex target and its derivatives, but also molecular probes that allow for its mode of action to be elucidated (*5*).

The most intuitive simplification in the retrosynthesis of a challenging dimeric target such as **1** would be to break its structure into two units of its monomer, depsipeptide **2**, by cleaving the central C5–C5′ bond. This approach reduces the synthetic task to the preparation of monomer **2**, provided a method could be found to unite the halves at the correct position. Such a dimerization is used by the producing organism in the biosynthesis of **1** through P450-catalyzed oxidative dimerization of **2**.

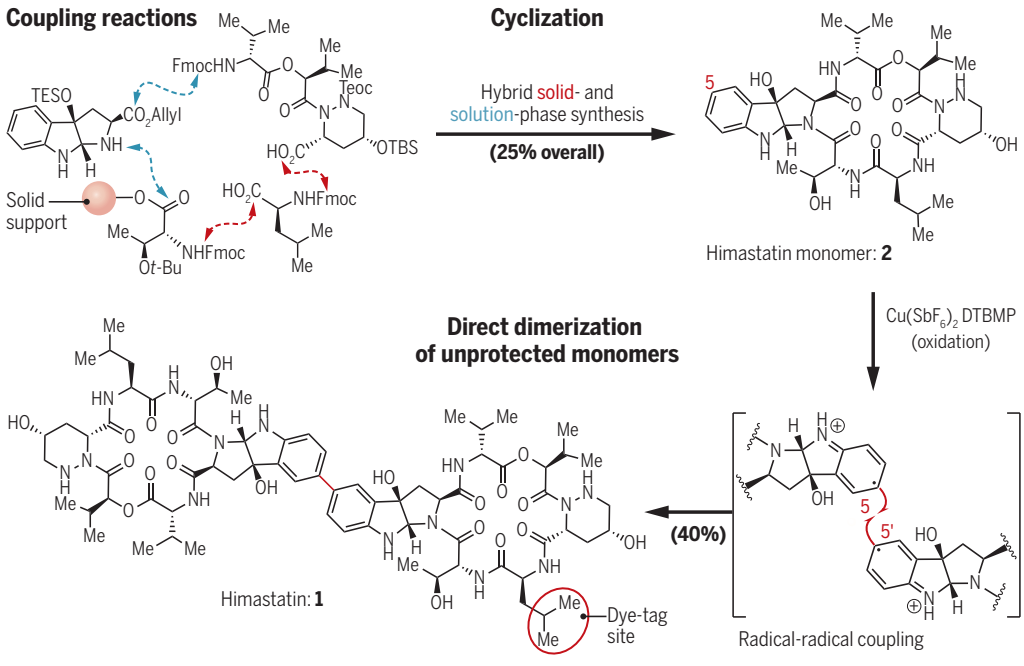
Being able to effect such a transformation by chemical means is a daunting challenge. Any developed method would need to tolerate the numerous functional groups in the complex peptide backbone of **2**, which might interfere through their reactive nitrogen and oxygen atoms, as well as forge the necessary carbon–carbon bond selectively at one specific position on each monomer. Prior approaches to natural products related to **1** had unsuccessfully attempted similar late-stage dimerizations, and lengthy two-directional strategies were used in which a simplified dimeric core is grown outward into each macrocyclic half. This approach was initially showcased in Kamenecka and Danishefsky's inaugural synthesis of **1** (*6*) and in later efforts for the synthesis of chloptosin (*7, 8*). From a biological standpoint, the dimeric structure of **1** is vital for its antibacterial properties, with monomeric compounds like **2** showing no activity (*6*).

Inspired by the simplicity of the biosynthetic route, D'Angelo *et al*. began by developing a dimerization process on simpler cyclotryptophan and cyclotryptamine compounds using either a silver(I)- or copper(II)-based oxidant to selectively arrive at C5–C5′ dimers in useful yields without the need for C5 prefunctionalization. Mechanistic studies showed that such couplings likely proceed through dimerization of an aniline radical cation, forming the new C–C bond at the most accessible C5 position. To prepare the necessary monomer **2**, they combined the convenience of solid-phase synthesis of a pentadepsipeptide with solution-phase coupling of the more tricky cyclotryptophan unit and a final macrolactamization to form the 18-membered ring in a highly efficient manner (see the figure). With monomer **2** in hand, the authors performed the dimerization with a stoichiometric copper(II) oxidant to deliver **1** in 40% yield.

Given the complexity of the substrate, the obtained yield is surprisingly high, and the efficiency of the dimerization is notable given the absence of any protecting groups in **2** that would typically be used to mask reactive groups that might otherwise risk being oxidized themselves or sequester the metal oxidant. The convergent synthesis of **2**

Streamlining dimerization

Chemical routes to forming large peptide dimers like himastatin (**1**) from its monomer (**2**) usually are unsuccessful. D'Angelo *et al*. report a bioinspired oxidative coupling route that performs this step in useful yields.



Abbreviations: Me, methyl; *t*-Bu, *tert*-butyl; Teoc, 2-(trimethylsilyl)ethoxycarbonyl; Fmoc, 9-fluorenylmethoxycarbonyl; TBS, *tert*-butyl(dimethyl)silyl; TES, triethylsilyl; and DTBMP, 2,6-di-*tert*-butyl-4-methylpyridine.

GRAPHIC: N. CARY/*SCIENCE*

Department of Biochemistry, University of Texas Southwestern Medical Center, Dallas, TX 75390, USA. Email: myles.smith@utsouthwestern.edu

made it straightforward and robust enough for the authors to prepare structural analogs of **2**, and in turn **1**, to probe their activity.

Assaying these compounds for antibacterial activity revealed interesting trends. For example, the sense of chirality of **1** had little effect, with its enantiomer *ent*-**1** and *meso*-diastereomer displaying a potency similar to that of natural **1**. The dependence on overall topology rather than absolute chirality points to a physical interaction underlying their activity.

Although it had been suggested that **1** may target bacterial membranes, no definitive evidence has been available (*9*). D'Angelo *et al.* prepared a himastatin probe in which one isopropyl group is replaced with a fluorescent dye. Antibacterial activity was only maintained when one half of the molecule bore this bulky tag. Prior two-directional approaches would have great difficulty accessing this heterodimer. Confocal microscopy experiments in *Bacillus subtilis* revealed that himastatin induces membrane defects that ultimately permeabilize the cell. This mode of action is reminiscent of that of daptomycin, a structurally unrelated cyclic peptide antibiotic (*10*).

The concise synthetic route of D'Angelo *et al.* should enable in-depth investigations of structural change to himastatin that could tune the potency and selectivity. Additionally, experiments that explore the molecular basis of the interaction with the bacterial membrane, as has recently begun to become apparent for daptomycin (*11*), could provide opportunities for both fundamental biophysical discoveries and inform designs of other molecules for membrane perturbation. From a synthetic standpoint, the bold dimerization showcased may inspire similarly direct approaches to complex dimeric or oligomeric natural products by coupling native monomers. ■

REFERENCES AND NOTES

1. H. W. Boucher *et al.*, *Clin. Infect. Dis.* **48**, 1 (2009).
2. G. D. Wright, *Can. J. Microbiol.* **60**, 147 (2014).
3. P. M. Wright, I. B. Seiple, A. G. Myers, *Angew. Chem. Int. Ed.* **53**, 8840 (2014).
4. K. S. Lam *et al.*, *J. Antibiot.* (Tokyo) **43**, 956 (1990).
5. K. A. D'Angelo, C. K. Schissel, B. L. Pentelute, M. Movassaghi, *Science* **375**, 894 (2022).
6. T. M. Kamenecka, S. J. Danishefsky, *Chemistry* **7**, 41 (2001).
7. S.-M. Yu, W.-X. Hong, Y. Wu, C.-L. Zhong, Z.-J. Yao, *Org. Lett.* **12**, 1124 (2010).
8. A. J. Oelke *et al.*, *Chemistry* **17**, 4183 (2011).
9. S. W. Mamber *et al.*, *Antimicrob. Agents Chemother.* **38**, 2633 (1994).
10. A. Pokorny, P. F. Almeida, *J. Membr. Biol.* **254**, 97 (2021).
11. R. Moreira, S. D. Taylor, *Angew. Chem. Int. Ed.* **61**, e202114858 (2022).

ACKNOWLEDGMENTS

The Welch Foundation (I-2045) and University of Texas Southwestern Medical Center (W. W. Caruth Jr. Scholarship) are acknowledged for funding.

10.1126/science.abn8327

GRAPHIC: KELLIE HOLOSKI/*SCIENCE*

ASTRONOMY

A crooked spinning black hole

New observations challenge the current understanding of black hole formation

By **Ferdinando Patat**[1] *and* **Michela Mapelli**[2]

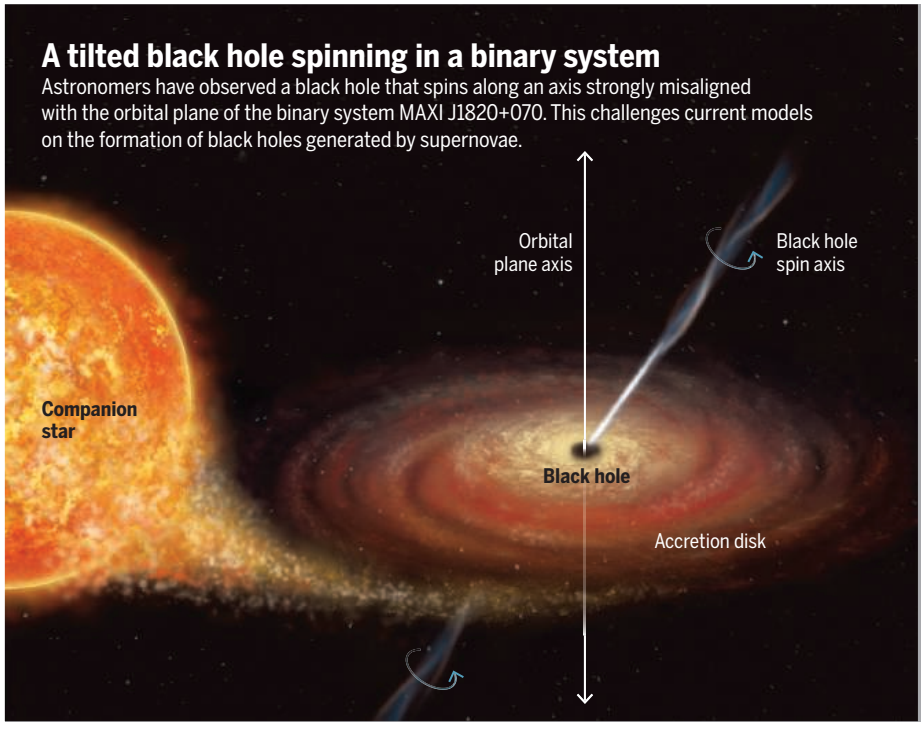
To different extents, all celestial bodies rotate, planets and stars alike. Things get particularly interesting when the objects are part of gravitationally bound configurations such as a binary system, in which the two bodies revolve around each other. In the absence of external perturbations, their rotation axes tend to be aligned with each other and perpendicular to the orbital plane. This trend is usually true even for exotic systems, such as x-ray binaries, in which a star revolves around a black hole. On page 874 of this issue, Poutanen *et al.* (*1*) present the case of x-ray binary system MAXI J1820+070, which counterintuitively has the spin axis of the black hole strongly misaligned to the orbital plane. This deeply challenges the current understanding of how black holes can be formed and indicates the presence of a powerful kick produced by the supernova that generated the black hole.

Our star, the Sun, has no companions. Although one may view this arrangement as the norm, a large fraction of stellar objects in a galaxy actually belong to binary or even triple systems. Multistar systems are more likely for heavier stars, with about 80% of stars with masses 15 times larger than that of the Sun (M_{sun}) being in a multiple system (*2*). Stars with masses >20M_{sun} are extremely short-lived, with a typical life span shorter than 10 million years. During their brief existence, massive stars in tight binary systems interact with the companion in several ways. For example, one of the two stars may transfer part of its matter to the other, changing the mass ratio and other orbital properties of the system. Tides can arise when the gravity force exerted by one star onto the other varies substantially from one point of the stars' surface to another, resulting in a tidal pull. Tides tend to align their rotation axes perpendicularly to the orbital plane of the system.

The death of a massive star, often accompanied by a formidable supernova explosion, is expected to leave behind a very compact and massive stellar object, such as a black hole. Because of the powerful asymmetric mass ejection, the newborn black hole receives what is known as a "natal kick." This kick might tilt the black hole's rotation axis, misaligning it with respect to the axis of the

A tilted black hole spinning in a binary system

Astronomers have observed a black hole that spins along an axis strongly misaligned with the orbital plane of the binary system MAXI J1820+070. This challenges current models on the formation of black holes generated by supernovae.



orbital plane. Under the most extreme circumstances, this kick can even unbind the binary system. In cases in which the binary system survives the supernova explosion and remains gravitationally bound, mass transfer from the smaller star to the black hole might ensue. This stripped-away mass from the star would take form in the shape of an accretion disk, which lies in the orbital plane around the black hole. Only part of this material would disappear below the event horizon—the point of no return—and falls into the black hole. The rest of the material is ejected at relativistic speeds in two symmetric, collimated jets, following the strong magnetic field along the spin axis of the black hole (*3*, *4*). This mechanism is unstable and undergoes erratic and powerful outbursts, producing radio and x-ray emissions that can be and have been observed (see the figure).

When the black hole was formed by the exploding massive star, as it collapsed inward its angular momentum was likely conserved. Therefore, as in the case of a ballet dancer bringing her arms closer to her body to increase the rotation velocity, the resulting spinning speed of the collapsing star is greatly increased and can reach more than a thousand rotations per second. This has important relativistic consequences, such as the modification of space-time around the eventual black hole. In the absence of external perturbations—for example, the gravitational pull from other stars in a multistar system or within a stellar cluster—mass transfer and tidal forces tend to align the rotation axes and keep the spin axis of everyone perpendicular to the orbital plane. This geometry is assumed, for example, when calculating the mass of the black hole.

However, the aforementioned alignment hypothesis is all but easy to verify in observational astronomy. Poutanen *et al*. have devised an ingenious technique that makes use of linear polarimetry and applied it to the x-ray binary system known as MAXI J1820+070. This system was discovered during an outburst by the All-Sky Automated Survey for Supernovae (ASAS-SN), and x-ray measurements were performed by the MAXI imager on board the International Space Station in July 2018 (*5*). At about 10,000 light-years from Earth, the system hosts a black hole with ~8 M_{sun}, which orbits around a star with ~0.5 M_{sun}. The axial offset between the black hole and the orbiting star in MAXI J1820+070 is more than 40°—the largest offset ever reported. This has crucial implications for theories of black hole formation (*6*). A substantial natal kick might either split the binary system or tilt the orbital plane with respect to its initial orientation (*7*). Because mass accretion (*8*) and tides (*9*) tend to align the spin axis to the orbital angular momentum of the binary system, the natal kick from the supernova is the main if not the only mechanism that can produce such a misalignment (*10*).

Although this explanation is very plausible, it is still a matter of debate (*11*). Alternatively, there are cases in which mass accretion does not necessarily result in spin alignment (*12*). Hence, measuring a substantial axial offset is to be considered as the smoking gun of either a large natal kick or a dynamical formation scenario for the binary system (*13*). Furthermore, finding a large axial offset in this system is particularly surprising because the evolution after the supernova explosion can only reduce the misalignment induced by the kick (*8*). This implies that it must have been even larger when the black hole was born.

When compared with the theoretical predictions, the reported lower limit of the misalignment angle is very high; this may call for the need of revising the existing models for these systems. Given the low mass of the companion star (*6*), MAXI J1820+070 will not evolve into a binary black hole. Nevertheless, the spin-orbit misalignment in MAXI J1820+070 is a crucial step forward for interpreting the observed distribution of spin tilts in Laser Interferometer Gravitational-wave Observatory (LIGO)–Virgo event candidates (*14*, *15*). ■

[1]European Southern Observatory, D-85748 Garching, Germany. [2]Physics and Astronomy Department "G. Galilei," University of Padova, 35122 Padova, Italy.
Email: fpatat@eso.org

REFERENCES AND NOTES

1. J. Poutanen *et al*., *Science* **375**, 874 (2022).
2. G. Duchêne, A. Kraus, *Annu. Rev. Astron. Astrophys.* **51**, 269 (2013).
3. J. C. McKinney, A. Tchekhovskoy, R. D. Blandford, *Science* **339**, 49 (2013).
4. P. Polko, J. C. McKinney, *Mon. Not. R. Astron. Soc.* **464**, 2660 (2017).
5. M. Espinasse *et al*., *Astrophys. J. Lett.* **895**, L31 (2020).
6. M. A. P. Torres *et al*., *Astrophys. J. Lett.* **882**, L21 (2019).
7. M. Mapelli, *Handbook of Gravitational Wave Astronomy* (Springer, 2021).
8. T. J. Maccarone, *Mon. Not. R. Astron. Soc.* **336**, 1371 (2002).
9. J. Hurley, C. A. Tout, O. Pols, *Mon. Not. R. Astron. Soc.* **329**, 897 (2002).
10. D. Gerosa *et al*., *Phys. Rev. D* **98**, 084036 (2018).
11. P. Atri *et al*., *Mon. Not. R. Astron. Soc.* **489**, 3116 (2019).
12. J. Stegmann, F. Antonini, *Phys. Rev. D* **103**, 063007 (2021).
13. C. L. Rodriguez, M. Zevin, C. Pankow, V. Kalogera, F. A. Rasio, *Astrophys. J. Lett.* **832**, L2 (2016).
14. D. Wysocki *et al*., *Phys. Rev. D* **97**, 043014 (2018).
15. R. Abbott *et al*., arXiv:2111.03606 [gr-qc] (2021).

ACKNOWLEDGMENTS

The authors thank S. Piranomonte for her help during the preparation of this article. M.M. acknowledges support from the European Research Council Consolidator grant DEMOBLACK, under contract 77001.

10.1126/science.abn5290

PHOTONICS

Flashing light with nanophotonics

Manipulation and enhancement of scintillation is achieved in nanophotonic structures

By **Renwen Yu** *and* **Shanhui Fan**

When a material is bombarded with high-energy particles, such as free electrons or x-ray photons, it may emit light in the visible frequency. This process, known as scintillation, is important for applications such as medical imaging and nondestructive inspection (*1*). For these applications, enhancing and controlling the light emission is of critical importance to improve their capabilities involving precision and resolution. Toward this goal, researchers are constantly looking for better scintillator materials (*2*) and better ways to control the scintillation processes. One way to improve the functionalities of scintillator materials is by introducing photonic structures to enhance scintillation (*3*). On page 837 of this issue, Roques-Carmes *et al*. (*4*) report a method to optimize scintillation using nanophotonic structures that can achieve orders-of-magnitude enhancement.

The scintillation process that occurs inside a solid material can be broken down into three smaller steps. In the first step of the process, the incoming high-energy particles create a nonequilibrium distribution of electrons inside the material. In the second step, the now-excited electrons diffuse through the material to create a steady-state density distribution of secondary electrons. In the final step, these secondary electrons radiatively decay at certain sites in the material, shedding their excess energy as light.

There is extensive research on how to manipulate electromagnetic fields using nanophotonic structures, such as nanostructures with periodically varying refractive indices, for controlling and enhancing these light emissions (*5*). Consequently, by integrating the scintillator with or patterning it into a nanophotonic structure, it should be pos-

sible to enhance the scintillation yield and control the emitted light spectrum. However, to design nanophotonics-enhanced scintillation requires a comprehensive understanding of the complex process involving both electron and photon dynamics.

Roques-Carmes *et al.* provide a complete model for the entire scintillation process involving the use of nanophotonic structures. They modeled the process of electron excitation as a result of the incoming high-energy particles, as well as the subsequent excitation and spatial transportation of secondary electrons (*6*). The model can produce the density distribution of the nonequilibrium secondary electrons that is responsible for the ultimate scintillation. To model the radiative decay of these electrons at specific crystal defect sites where scintillation occurs, the model also computes the electronic levels of these defect sites and models the radiative transition (*7*) between these electronic levels.

From these electronic simulations, the scintillation source can be described as a spatial distribution of fluctuating dipoles that results from the radiative transition. Although the light emission from fluctuating dipoles can be modeled, in principle, using a typical electromagnetic field solver that solves Maxwell's equations (*8*), this brute force approach is computationally costly and often impractical. Roques-Carmes *et al.* simplify this computation process by exploiting electromagnetic reciprocity, which states that the relationship between a fluctuating dipole and the resulting electric field remains the same if their positions are interchanged (*9*). Based on this exploit, the emission enhancement can then be computed by simulating the absorption of an electromagnetic plane wave. Finally, the scintillation can be described by combining emission-enhancement distribution obtained from photonic simulations with the power of the scintillation source as obtained from electronic simulations.

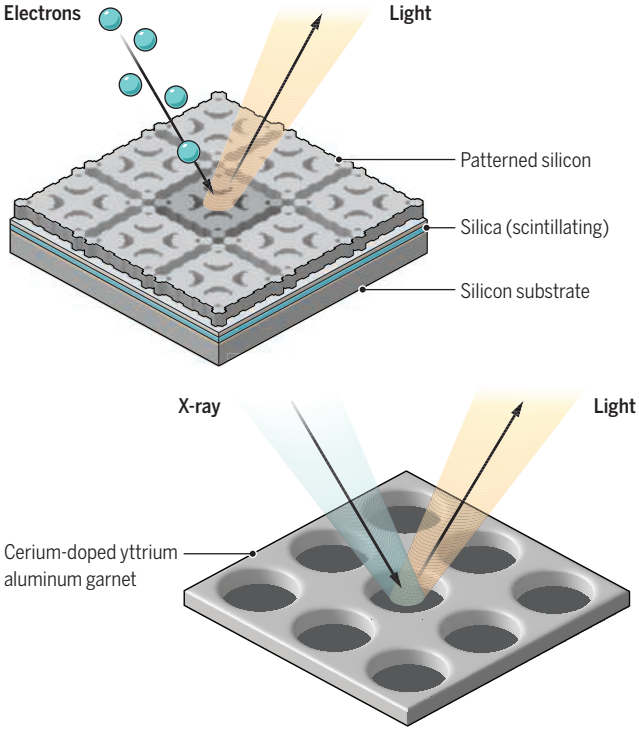
Based on their framework of theoretical modeling, Roques-Carmes *et al.* design and demonstrate several nanophotonics-enhanced scintillators (see the figure). In one set of experiments, they investigate the scintillation from a silicon-on-silica device bombarded by an electron beam. Scintillation in the device is emitted by the defects in the silica layer (*10*), and the silicon layer is designed to provide scintillation enhancement. They compare results from similar scintillators where the silicon layer is uniform with the enhanced version where the silicon layer has a lattice of specially patterned cuts. The scintillation emission from the patterned samples shows very strong and wavelength-dependent enhancement. Overall, the patterned sample shows up to sixfold enhancement compared with the sample that has the unstructured silicon layer, with the additional ability to tune the scintillation spectra by changing the cut depth. Electronic dynamics can also play a role in controlling the scintillation process. The authors also measure the scintillation emission in both red and green wavelength ranges. By changing either the energy or the power of the incident free electrons, the ratio of green to red scintillation peak powers can be controlled, which can be understood by using the rate equations to describe the microscopic transition dynamics.

In another set of experiments, Roques-Carmes *et al.* demonstrate a roughly ninefold enhancement over the measured scintillation spectrum in a patterned cerium-doped yttrium aluminum garnet scintillator under x-ray compared with an unpatterned sample. The higher efficiency is beneficial for scintillation applications where x-ray exposure is of concern. Moreover, by using the inverse-design technique (*11*) together with electromagnetic reciprocity, further enhancements beyond what has been demonstrated in the experiments may be achievable. For both experiments, their results show good agreement with the back-to-back theoretical modeling that incorporates both electronic and photonic processes.

The demonstrated nanophotonic scintillators show that one can engineer and enhance the performance of a given scintillating material through nanostructures. The work of Roques-Carmes *et al.* points to new possibilities for applications ranging from high-resolution x-ray detectors used in medical imaging to efficient ultraviolet-light sources. The developed comprehensive theoretical framework can be applied to explore other light-emission phenomena, such as harmonic generation and surface-enhanced Raman spectroscopy, where the understanding of both electron and photon dynamics is important. Finally, the present theoretical framework relies upon the use of reciprocity. It is known that nonreciprocal nanophotonic structures can exhibit unusual thermal emission (*12*) and cathodoluminescence (*13*) properties. It may therefore be of interest to explore scintillation in nonreciprocal nanophotonic structures. ■

Improving scintillator capabilities with cutouts

By stacking patterned cutouts of silicon on a silica layer and creating patterned dimples on cerium-doped yttrium aluminum garnet, researchers improved the efficiency of, and offered wavelength-dependent tunability to, the two scintillation devices.



GRAPHIC: A. MASTIN/*SCIENCE*

Ginzton Laboratory, Department of Electrical Engineering, Stanford University, Stanford, CA, USA.
Email: shanhui@stanford.edu

REFERENCES AND NOTES

1. J. A. Sorenson, M. E. Phelps, *Physics in Nuclear Medicine* (Grune & Stratton, ed. 2, 1987).
2. P. Lecoq, A. Gektin, M. Korzhik, *Inorganic Scintillators for Detector Systems* (Springer, 2017).
3. P. Pignalosa, B. Liu, H. Chen, H. Smith, Y. Yi, *Opt. Lett.* **37**, 2808 (2012).
4. C. Roques-Carmes *et al.*, *Science* **375**, eabm9293 (2022).
5. S. Noda, M. Fujita, T. Asano, *Nat. Photonics* **1**, 449 (2007).
6. H. Demers *et al.*, *Scanning* **33**, 135 (2011).
7. F. J. García de Abajo, *Rev. Mod. Phys.* **82**, 209 (2010).
8. C. Luo, A. Narayanaswamy, G. Chen, J. D. Joannopoulos, *Phys. Rev. Lett.* **93**, 213905 (2004).
9. V. S. Asadchy, M. S. Mirmoosa, A. Diaz-Rubio, S. Fan, S. A. Tretyakov, *Proc. IEEE* **108**, 1684 (2020).
10. S. Girard *et al.*, *Rev. Phys.* **4**, 100032 (2019).
11. S. Molesky *et al.*, *Nat. Photonics* **12**, 659 (2018).
12. L. Zhu, S. Fan, *Phys. Rev. B* **90**, 220301 (2014).
13. R. Yu, A. Konečná, F. J. García de Abajo, *Phys. Rev. Lett.* **127**, 157404 (2021).

10.1126/science.abn8478

RETROSPECTIVE

C. Thomas Caskey (1938–2022)

A visionary architect of genomic medicine

By **Andrea Ballabio**[1,2,3,4] and **Huda Zoghbi**[3,4,5]

Renowned molecular and human geneticist C. Thomas Caskey died on 13 January. He was 83 years old. Tom transformed biomedical research in both academic medical centers and the pharmaceutical industry, effortlessly moving between the two worlds and catalyzing new ideas and applications. His discovery of trinucleotide repeats and their role in dynamic mutations helped overturn a century's worth of assumptions about genetic inheritance. A visionary physician-scientist, he also had a gift for nurturing talent and building programs that would themselves redraw the boundaries of scientific possibility.

Born in Lancaster, South Carolina, on 22 September 1938, Tom never lost his relaxed southern charm. He studied chemistry at the University of South Carolina for 2 years before transferring into the Duke University School of Medicine. There, he spent a year researching purine biosynthesis and the genetics of gout under the mentorship of physician James B. Wyngaarden before receiving an MD in 1963. In 1965, after completing a residency in internal medicine, he joined geneticist Marshall Nirenberg's lab at the National Institutes of Health. Tom's experiments demonstrated the universality of the genetic code from bacteria through mammals and identified the proteins that terminate translation of mRNA. During this time, he mentored Arthur L. Beaudet, Edward Scolnick, and Joseph Goldstein, physicians who later became pioneers in their own right. In 1971, Caskey left for Baylor College of Medicine in Houston, Texas, where he started the division of genetics that eventually became the Department of Molecular and Human Genetics.

Although Tom was a physician, he did not overprioritize human genetics—instead, he recruited scientists working in diverse species, so that yeast, fly, mouse, and human genetics researchers were constantly rubbing shoulders in the hallways, at seminars, and at journal clubs. Cross-species collaborations became the norm at Baylor. Tom also had a keen sense for which new technologies would be most important in advancing genetic research. For example, he brought in viral gene therapy and sequencing technologies and persuaded Allan Bradley to come all the way from England, bringing embryonic stem cell technology with him. All this helped the department become renowned as a cradle for discoveries. When we joined the faculty in the late 1980s, we benefited tremendously from this intellectual and technological vibrancy.

Tom's early work in enzymology bore fruit in 1982 when he cloned the gene that encodes hypoxanthine-guanine phosphoribosyltransferase, the enzyme whose loss causes gout and Lesch-Nyhan syndrome. His greatest scientific contribution, however, was the discovery of tri- and tetranucleotide repeats in the genome. These repeats form tracts of variable length in healthy individuals but over a certain threshold can become subject to further expansions. In 1991, three teams (one of which included Tom) showed that fragile X syndrome was caused by an unstable CGG repeat tract that expands on germline transmission. This "dynamic mutation" explained how a disease could become more severe with each generation. We now know of 60 distinct disorders caused by dynamic mutations, including myotonic dystrophy, the mutation for which was discovered by Ying-Hui Fu, then a postdoc in Tom's lab. Tom also recognized that short tandem repeats could have a socially beneficial use: Because the length of these repeat tracts varies between healthy individuals, they provide a shortcut for identifying genetic material. He used this approach to identify 32 Gulf War casualties, and the method forms the basis of the Federal Bureau of Investigation's Combined DNA Index System for identifying suspects in crimes.



The Caskey lab contributed to the discovery of more than two dozen human disease genes, but Tom had wider ambitions. He rallied his faculty to each contribute their own skills and interests to mapping discrete regions of the genome. This call to action spurred Richard Gibbs to establish the Baylor College of Medicine Human Genome Sequencing Center, one of the five sites that collaborated to assemble the human genome reference sequence.

In 1994, Tom relinquished the position he'd held since 1976 as a Howard Hughes Medical Institute investigator to join Merck Research Laboratories as senior vice president of research, where he incorporated human genetics into drug development. In 2006, he returned to Houston and founded the Institute of Molecular Medicine at the University of Texas Health Science Center, and in 2011 he returned to Baylor and launched one of the first programs in precision medicine. He performed whole-genome sequencing on 1190 volunteers, identifying risk variants that he used to guide interventions to forestall the development of disease.

Tom served as president of the American Society of Human Genetics, and in 2021 the society honored him with the William Allan Award. He was also elected to the National Academy of Sciences and the National Academy of Medicine. Despite his stature in the field, his interactions with faculty and the more than 90 postdocs and graduate students he trained at Baylor were characterized by warmth and humor. He could be tough, but he also took pains to give encouragement. We mostly remember the twinkle in his eyes when he asked an unexpected question and walked off, leaving you to ponder what you were missing. Whether or not you figured out what he intended, he always made you think.

Tom had a zeal for life. He was an avid sailor and often took his family and friends out on the water. He and Peggy, his wife of 62 years, frequently opened their home for lab and faculty gatherings and invited trainees to celebrate holidays with them. His memorable lab parties usually involved people swimming in his pool and Tom sporting a cowboy hat. Those of us lucky enough to know Tom learned to be more ambitious about improving human health and serving society but, above all, to cherish the people around us. He will be remembered as an innovative scientist, a dedicated mentor, and an enthusiastic man who loved life in all its forms. ■

10.1126/science.abo3949

PHOTO: BAYLOR COLLEGE OF MEDICINE

[1]Telethon Institute of Genetics and Medicine, Pozzuoli, Italy. [2]Department of Translational Medicine, University of Naples Federico II, Naples, Italy. [3]Neurological Research Institute, Texas Children's Hospital, Houston, TX, USA. [4]Department of Molecular and Human Genetics, Baylor College of Medicine, Houston, TX, USA. [5]Howard Hughes Medical Institute, Baylor College of Medicine, Houston, TX, USA. Email: ballabio@tigem.it; hzoghbi@bcm.edu

POLICY FORUM

RESEARCH ETHICS

Streamlining ethics review for international health research

Single-site review means protection and efficiency

By **Mark A. Rothstein[1], Ma'n H. Zawati[2], Adrian Thorogood[2], Michael J. S. Beauvais[2], Yann Joly[2], Kyle B. Brothers[1], Michael Lang[2], Pamela Andanda[3], Calvin Ho[4], Rosario Isasi[5], Jane Kaye[6], Won Bok Lee[7], Obiajulu Nnamuchi[8], Andrea Saltzman[9], Bartha Maria Knoppers[2]**

International biomedical research, in which projects span borders and engage participants from multiple countries, has increased substantially during the last several decades. Despite the proven value of large, geographically, and ethnically diverse studies, further advancements are being impeded by the burden of submitting separate, and often numerous, applications for research ethics approval in compliance with country-specific laws or varied policy frameworks. To address this, we see promise in applying the international concept of "adequacy," contained in the European Union (EU) General Data Protection Regulation (GDPR) (*1*), to ethics review of international health research. We advocate for countries to publish their prior determinations about the adequacy of ethics review requirements in other countries to enable review by one institutional review board (IRB) or comparable body ("single-site" review) in the researcher's country, streamlining ethics review while safeguarding the welfare of local research participants.

Research ethics rules in nearly every country were developed when health research was small-scale, domestic, and clinical. Some of the most restrictive laws were enacted in response to a history of colonialism (or "ethics dumping") (*2*), economic imperialism, or ethically questionable research practices. Adding to these concerns were issues of national sovereignty and the entrenched system of single-country review.

There is general agreement about the criteria for research ethics review, but each country has its own procedures. Researchers planning international recruitment of participants must first overcome a dearth of information about ethics review in multiple countries. Although some compilations of international laws, regulations, and guidelines are published (*3*), obtaining accurate and current information about the ethics review requirements of numerous countries remains difficult (*4*). The lack of easily available resources means that researchers often must retain lawyers or research ethics consultants in their own country—and possibly in the prospective participants' countries—to discern the substantive and procedural elements of research ethics approvals. This often substantial and unexpected expense can create unnecessary delay. Thus, an essential starting point is ensuring access to continually updated and expertly translated online resources of research ethics materials.

Even then, researchers face the prospect of separate ethics reviews in each country. Multiple reviews are arduous, involving substantial and compounding costs and delays without necessarily improving protections for research participants. It is particularly impractical when recruiting small numbers of participants from multiple countries. Furthermore, multiple ethics reviews, even in the same country, are often inconsistent (*5*).

A recent study illustrates challenges that researchers face in such a balkanized system. The authors of this article were part of a team that surveyed laws in 31 diverse countries and detailed how common approaches to ethics review processes could facilitate international direct-to-participant (DTP) genomic research (*6*) in which researchers use the internet to recruit and enroll research participants, without using physicians, hospitals, or biobanks. As part of that study, we asked legal experts in these countries questions in the context of international DTP genomic research (*6*). Two conclusions from this survey are of particular interest (recognizing that the opinions of individual legal experts that we engaged might not be shared unanimously by others in the surveyed countries).

First, most of the experts reported that there was no official legal determination of how research ethics review requirements in their own country applied to foreign-based research. They could at best merely predict how existing laws would be interpreted. Second, experts from only five countries (Australia, Canada, Germany, Japan, and Spain) reported that approval by a review body in the researcher's country is sufficient, although exceptions may exist for clinical trials.

EQUIVALENCY, ADEQUACY, RECIPROCITY

Our proposal for single-site ethics review is based on international adoption of three fundamental concepts: equivalency, adequacy, and reciprocity. Equivalency means that the essential standards of ethical research with human participants are substantially equivalent from one country to another in theory and practice. Adequacy means that research ethics review in other countries is adequate to safeguard the interests of research participants and the national interests of their countries. Reciprocity means that one country recognizes the research ethics processes of another country, or two or more countries mutually agree to recognize each other's research ethics processes.

The possibility of eliminating multiple ethics reviews for international research is supported by the considerable equivalence in the national procedures and benchmarks for review of IRBs and similar bodies. Given this compatibility, it should be possible to identify a set of core criteria for appropriate ethics review that, if followed in one country, could be recognized as appropriate for review internationally. For example, the Global Alliance for Genomics and Health (GA4GH) compiled substantive elements and procedures for research ethics review around the globe (*7*) (see the table).

Moreover, there is consistency on the common values governing research ethics that need to be addressed by researchers in their protocols irrespective of jurisdiction (*8*). These "classical ethical" considerations are endorsed by respected international bodies, including the United Nations Educational, Scientific, and Cultural Organization (UNESCO) (*9*). The elements include informed consent, privacy/confidentiality, benefit/risk ratio, return of results, commercialization (if applicable), protection of the interests of vulnerable persons/communities, and research integrity and safety.

[1]Institute for Bioethics, Health Policy and Law, University of Louisville School of Medicine, Louisville, KY, USA. [2]Centre of Genomics and Policy, McGill University Faculty of Medicine and Health Sciences, Montreal, QC, Canada. [3]University of Witswatersrand, Johannesburg, South Africa. [4]Centre for Medical Ethics and Law and the Department of Law, University of Hong Kong, Pokfulam, Hong Kong, PRC. [5]Department of Human Genetics and John P. Hussman Institute for Human Genomics, University of Miami School of Medicine, Miami, FL, USA. [6]Oxford University, Oxford, UK. [7]Ewha Law School, Seoul, South Korea. [8]Centre for Health, Bioethics and Human Rights, Faculty of Law, University of Nigeria, Enugu, Nigeria. [9]Office of Research Subject Protection, The Broad Institute, Cambridge, MA, USA. Email: mark.rothstein@louisville.edu

Equivalence of international standards and processes makes single-site ethics review a promising alternative to multisite, multicountry review. Single-site ethics review has been shown to be more efficient and consistent on a national basis, including in the United Kingdom (*10*) and Canada (*11*). It is now required in the United States (*12*).

An international "adequacy" model, already used in the domain of data protection and international data transfer, could serve to frame, guide, and coordinate decisions as to whether biomedical research ethics review and oversight are essentially equivalent between two jurisdictions. For example, an adequacy decision by the European Commission recognizes that the data protection regime in a country offers an essentially equivalent level of data protection and can be considered as achieving a similar outcome as if Europe's GDPR (*1*) were followed.

Likewise, under a research ethics adequacy approach, researchers could "have their IRB approvals recognized in another country if the health research norms of both countries are demonstrated to be essentially equivalent, both in terms of their purpose and their effectiveness" (*13*). In this way the framework of single-site ethics review in the researcher's country is generalizable and serves to streamline ethics review while protecting the welfare of diverse participants in international health research.

We outline four recommendations for an international adequacy model of single-site research ethics review: (i) International research approved by an ethics review body in the researcher's country should be deemed approved in the participant's country if the overall ethics review regime in the researcher's country has been determined to be adequate by the local participant's country; (ii) a list of countries for which an ethics review undertaken by a competent foreign ethics review body is deemed adequate should be posted on the website of the regulatory authority responsible for the ethical conduct of research with human participants in each country; (iii) regulatory authorities responsible for the ethical conduct of research with human participants should inform ethics review bodies under their jurisdiction of the approval criteria for international health research; and (iv) in applying this framework, special attention should be given to the specific ethical provisions required by the participants' country as well as the sociocultural traditions or vulnerabilities of various population subgroups in the participants' country, including minority and Indigenous populations.

In assessing these recommendations, a key element is that the approval process begins in the participant's country. Only if research regulatory officials in the participant's country have made a prior determination that ethics review in the researcher's country is adequate does the researcher-country–based ethics review body have authorization to consider the research protocol.

Furthermore, any country may add limitations or conditions to an adequacy decision and require approval of certain types of research in their country. Requirements may include local approval for clinical research, collaboration with a local researcher, community engagement with certain participants, specific consent procedures in accordance with cultural expectations, additional privacy and confidentiality protections, special provisions on data access, a requirement of insurance or other compensation in the event of injury, or more general benefit sharing (*14*). Thus, within this broad framework of equivalent research ethics criteria, countries can require additional features deemed essential to protecting the well-being and interests of participants in their countries.

Procedural elements of effective ethics review

Drawn from (*7*).

- Established norms of conduct, including authority and independence
- Resources to carry out the work
- Competence of members
- Understandable procedures and forms
- Equitable treatment of the protocols of all researchers
- Attention to vulnerable populations and cultural differences
- Record of due diligence
- Transparency of decisions
- Continuing oversight of approved protocols
- Accountability of all reviewers and public authorities

IMPLEMENTATION CHALLENGES

Implementation of this proposal will be challenging. Each country would need to formalize legislation, regulations, or professional guidance recognizing the ethics review processes of other countries. Endorsement of the recommendations in the ethical guidelines and best practices of international organizations could generate momentum for global adoption. Some key organizations include the Council of Europe, the Council for International Organizations of Medical Services, the World Health Organization, the Africa Union Development Agency–New Partnership for Africa's Development, UNESCO, and the World Medical Association. Funders of international research, such as the Bill & Melinda Gates Foundation and the Wellcome Trust, also could play an important role in harmonizing international standards for the ethical conduct of health research.

It is important to recognize that, at least initially, the countries mainly benefiting from single-site ethics review in the researcher's country are likely to be high-income countries that perform most international health research. Low- and middle-income countries might stand to lose the most if single-site ethics review means a loss of research partnerships and ethics review capacity building (*15*).

Successful implementation strategies could include initial implementation between high-income, major research countries; limiting international ethics review to IRBs and similar bodies that have special training and receive certification to evaluate international research protocols; or phasing in single-site review after a period of systematically comparing the results of ethics review of the same protocol by ethics review bodies in different countries. Ultimately, adoption of a new way of conducting international ethics review will depend on equal measures of altruism, trust, and hope in realizing the possibilities of biomedical research. ■

REFERENCES AND NOTES

1. Regulation (EU) 2016/679 of the European Parliament.
2. D. Schroeder, J. Cook, F. Hirsch, S. Fenet, "Ethics Dumping: Introduction," in *Ethics Dumping Case Studies from North-South Research Collaborations*, D. Schroeder, J. Cook, S. Fenet, V. Mythuswamy, Eds. (Springer, 2018), pp. 99–106.
3. Office of Human Research Protections, International Compilation of Human Research Standards, www.hhs.gov/ohrp/international/compilation-human-research-standards/index.html.
4. P. Andanda, J. Wathuta, K. Leising, D. Schroeder, National and International Compliance Tools, A Report for TRUST, http://trust-project.eu/wp-content/uploads/2017/02/TRUST-664771-National-and-International-Compliance-Tools-Final.pdf.
5. D. Resnik, *J. Clin. Res. Best Pract.* **10**, 1 (2014).
6. M. A. Rothstein *et al.*, *J. Law Med. Ethics* **47**, 705 (2019).
7. Global Alliance for Genomics and Health, "Enabling responsible genomic data sharing for the benefit of human health," www.ga4gh.org.
8. M. H. Zawati *et al.*, *J. Law Med. Ethics* **47**, 582 (2019).
9. UNESCO, https://unesdoc.unesco.org/ark:/48223/pf0000146180.
10. Royal College of Physicians, *Guidelines on the Practice of Ethics Committees in Medical Research with Human Participants* (Royal College of Physicians, 2007).
11. J. V. Lavery, M. McDonald, E. M. Meslin, *Health Law Rev.* **13**, 86 (2005).
12. Code of Federal Regulations, Title 45, sec. 46.114.
13. A. Thorogood, M. J. S. Beauvais, *Philosophies* **6**, 93 (2021).
14. E. S. Dove *et al.*, *Science* **351**, 1399 (2016).
15. COVID-19 Clinical Research Coalition, Ethics Review Mutual Recognition and Multinational Research Collaboration in Pandemic Response Settings, (2021); https://covid19crc.org/wp-content/uploads/2021/03/Covid19-Ethics-Working-Group-Report_FINAL_.pdf.

ACKNOWLEDGMENTS

Research support was provided by the U.S. National Institutes of Health.

10.1126/science.abn0675



LETTERS

Groundwater overexploitation in China has led to rapid declines in the water table, drying up rivers like this one.

PHOTO: CHUNMIAO ZHENG

Edited by **Jennifer Sills**

Plans to protect China's depleted groundwater

Groundwater is a hidden resource that can store 100 times as much as global freshwater lakes and rivers (*1*). In China, groundwater serves as the primary source for drinking water for 70% of the population (*2*). Historically, China has lagged behind developed countries in managing and protecting groundwater. Over the past several decades, China has rapidly depleted groundwater reserves (*2*). Overexploitation of groundwater for domestic, agricultural, and industrial uses, exacerbated by climate change, has resulted in about 920,000 km^2 with substantial land subsidence (*3*) and more than 10,000 km^2 of coastal areas affected by seawater intrusion (*4*). It has also contributed to the loss of more than 16,000 km^2 of wetlands (*5*) and to more than half of the country's 50,000 rivers drying up (*6*). Overuse has left China's groundwater in a perpetual state of crisis (*7*).

In November 2021, Chinese Premier Li Keqiang signed the Regulation on Groundwater Management (*8*). The legislation was created to comprehensively and explicitly address groundwater-related issues, including investigation and planning, monitoring, risk assessment, overdraft control, pollution prevention, site remediation, regulatory oversight, and sustainable management. The plan requires ongoing consideration of groundwater quantity and quality and their relations to ecosystems, climate change, and sustainability. National coordination and enforcement will facilitate the implementation of management strategies, and clear division of responsibilities and jurisdictions for different government agencies will help to minimize bureaucratic red tape. These changes mark an important first step to sustainable groundwater management.

To ensure that China's efforts toward sustainable groundwater supplies are successful, the government should mandate equitable funding to support groundwater research and protection. For example, out of several hundred "state key laboratories" in science, engineering, and medicine, not one is currently devoted primarily to groundwater. Enactment of protective legislation should go hand-in-hand with strict enforcement of existing regulations. Finally, data-sharing in the field of groundwater should become a norm rather than an exception to promote management transparency and scientific advances.

Chunmiao Zheng* and Zhilin Guo*
State Environmental Protection Key Laboratory of Integrated Surface Water-Groundwater Pollution Control, School of Environmental Science and Engineering, Southern University of Science and Technology, Shenzhen, China.
*Corresponding author. Email: zhengcm@sustech.edu.cn; guozl@sustech.edu.cn

REFERENCES AND NOTES

1. R. Taylor *et al.*, "Groundwater and global hydrological change-current challenges and new insight," IAHS Publ. 338 (2010), pp. 51–61.
2. F. Hu, "Groundwater under pressure" (2015); www.chinawaterrisk.org/resources/analysis-reviews/groundwater-under-pressure/.
3. China Institute of Geo-Environment Monitoring, "Map of land subsidence in China" (2019).
4. Y. Luo, *Bull. Chin. Acad. Sci.* **31**, 133 (2016).
5. W. Meng *et al.*, *Ocean Coast. Manage.* **146**, 50 (2017).
6. K. Ravilious, "How vulnerable is China's water?" *Physics World* (2019).
7. C. Dagbegnon, S. Djebou, V. P. Singh, *Environ. Soc. Psychol.* **1**, 16 (2016).
8. The State Council of the People's Republic of China. "Regulation on Groundwater Management (000014349/2021-00106)" (2021).

10.1126/science.abn8377

Transparency crucial to Paris climate scenarios

In their Policy Forum "Can updated climate pledges limit warming well below 2°C?" (5 November 2021, p. 693), Y. Ou and coauthors explain that the updated pledges submitted as part of the Paris Agreement process, although an improvement, will only result in a ~33% chance of staying within 2°C of warming. We agree with Ou *et al.* that more ambition is required, but we think even the low chance of success they estimate is overly optimistic. The mitigation pathways based on Paris Agreement pledges lack transparency and immediacy, making them difficult to evaluate and decreasing the chances of success.

The updated pledges, if executed as written, will result in negligible global emission reductions of 1% by 2030, according to Ou *et al.* Substantive reductions are postponed until after 2030 on the assumption that countries will fulfill their softer commitment to "long-term strategies." In line with earlier studies using integrated assessment models (*1*), these strategies heavily depend on negative-emissions technologies. For example, US fossil fuels and industry emissions are expected to fall from 2.7 $GtCO_2$ to –1.1 $GtCO_2$ between 2030 and 2050 according to the "Updated pledges-Continued ambition" scenario proposed by Ou *et al.* However, implementing negative-emissions technologies at such a large scale remains highly speculative and would present serious challenges to other sustainability dimensions (*2*). Analyses of this nature need to be transparent about the extent to which negative-emissions technologies are used. Only then can we evaluate the inherent risk of this goal not being achieved.

Other uncertainties merit structural attention as well. An energy transition to low-carbon alternatives could result in a lower average energy return, leading to

additional energy costs and indirect emissions (*3*). Moreover, modeled transitions rely on decoupling gross domestic product and energy at a faster rate than historical trends, which underestimates rebound effects caused by energy-efficiency policies (*4*). In addition, differing levels of pledge ambition could lead to carbon leakage, where emissions are transferred to countries with weaker policies (*5*). The extent to which these neglected uncertainties are captured in current and future integrated assessment model studies of the Paris Agreement pathways needs to be transparent and, ideally, quantified.

Lewis King[1]*, Jeroen van den Bergh[1,2,3], Giorgos Kallis[1,2]
[1]Institute of Environmental Science and Technology, Universitat Autonoma de Barcelona, 08193 Bellaterra, Catalonia, Spain. [2]ICREA, 08010 Barcelona, Catalonia, Spain. [3]Vrije Universiteit Amsterdam, 1081 HV Amsterdam, The Netherlands.
*Corresponding author.
Email: lewiscarl.king@uab.cat

REFERENCES AND NOTES

1. A. A. Fawcett *et al.*, *Science* **350**, 1168 (2015).
2. K. Anderson, G. Peters, *Science* **354**, 182 (2016).
3. L. C. King, J. C. J. M. van den Bergh, *Nat. Energ.* **3**, 334 (2018).
4. P. E. Brockway, S. Sorrell, G. Semieniuk, M. K. Heun, V. Court, *Renew. Sustain. Energ. Rev.* **141**, 110781 (2021).
5. L. C. King, J. C. J. M. van den Bergh, *Clim. Change* **165**, 52 (2021).

10.1126/science.abn7998

Response

King *et al.* raise important issues, several of which pertain to the broader policy discourse surrounding international climate negotiations and countries' climate pledges rather than the modeling conducted in our Policy Forum. We agree with King *et al.* that the updated Paris Agreement pledges could paint an overly optimistic picture of the future, especially if their success depends on postponing deeper reductions until after 2030. To illustrate a less-optimistic future, our Policy Forum includes scenarios showing what would happen if countries continued to implement current policies alone. The "Current policy" scenarios in the Policy Forum result in less than a 10% chance of limiting global warming to below 2°C this century, whereas the "Updated pledges" scenarios result in at least a 33% chance of achieving the same temperature goal. Additional policy measures could help bridge emission gaps between current policies, updated pledges, and the global emission levels needed to cost-effectively achieve the Paris Agreement's climate goals (*1*).

We also agree with King *et al.* that greater near-term ambition is necessary, particularly to set up the technological, political, and financial infrastructures required to achieve the long-term strategies and net-zero pledges (*2*). Delaying emission reductions would substantially reduce the likelihood of achieving the Paris temperature goal (*3*) and could prove to be very expensive (*4*). However, we disagree that the updated 2021 pledges result in negligible global emission reductions. Our Policy Forum suggests that the updated pledges alone—if successfully implemented—could result in a reduction of 2030 global greenhouse gas emissions of about 6.6 $GtCO_2$ (12%) compared with the 2015 pledges. The United Nations Environment Programme suggests reductions of 4 $GtCO_2$ (7.5%) (*5*).

The "Updated pledges-Continued ambition" scenario in our Policy Forum assumes that countries with net-zero pledges achieve those pledges in the specified target years. Achieving net-zero pledges will require large-scale deployment of negative-emissions technologies (*6*, *7*). Our study assumes the availability of bioenergy with carbon capture and storage (BECCS) and direct air capture (DAC) technologies in addition to terrestrial sinks and makes conservative assumptions about their deployment compared to the literature (*7*). Our assumptions about BECCS and DAC are transparently documented in several publications [e.g., (*8*, *9*)]. Moreover, the entire model code and data files used in our study are publicly available (*10*). Future research should explore the implications of alternative assumptions about the type and scale of negative-emissions technologies.

Our Policy Forum addressed uncertainties in the climate system, but we only focused on one source of uncertainty in emissions trajectories: stringency of climate policy. The minimum decarbonization rate assumption (2% per year) in our "Continued ambition" scenarios is on the conservative side of historical trends [fig. S2 in (*11*)] and conservative compared to developed countries with decarbonization policies (tables S14 to S17 in our Policy Forum). By contrast, our "Increased ambition" scenarios assume a higher minimum decarbonization rate (5%), which is on the higher end of historically observed rates [fig. S2 in (*11*)]. Many other uncertainties—including and beyond those highlighted by King *et al.*—could affect future emissions trajectories (*12*). Future research should also explore the implications of these variables.

Yang Ou[1], Gokul Iyer[1], James Edmonds[1], Allen Fawcett[2], Nathan Hultman[3], Jim McFarland[3], Stephanie Waldhoff[1], Matthew Gidden[4,5], Haewon McJeon[1]*
[1]Joint Global Change Research Institute, Pacific Northwest National Laboratory and University of Maryland, College Park, MD 20740, USA. [2]US Environmental Protection Agency, Washington, DC 20004, USA. [3]Center for Global Sustainability, School of Public Policy, University of Maryland, College Park, MD 20742, USA. [4]Climate Analytics, Berlin, Germany. [5]International Institute for Applied Systems Analysis, Laxenburg, Austria.
*Corresponding author.
Email: haewon.mcjeon@pnnl.gov

REFERENCES AND NOTES

1. L. B. Baptista *et al.*, *Glob. Environ. Change* **73**, 102472 (2022).
2. G. Iyer *et al.*, *Nat. Clim. Change* **7**, 871 (2017).
3. Climate Action Tracker, "Glasgow's 2030 credibility gap: Net zero's lip service to climate action," *Warming Projections Global Update November 2021* (2021).
4. G. C. Iyer *et al.*, *Environ. Res. Lett.* **10**, 125002 (2015).
5. United Nations Environment Programme, "Emissions gap report 2021: The heat is on—a world of climate promises not yet delivered" (2021).
6. G. Iyer *et al.*, *Energ. Clim. Change* **2**, 100043 (2021).
7. Intergovernmental Panel on Climate Change, "Global warming of 1.5°C" (2018); https://www.ipcc.ch/sr15/.
8. J. Fuhrman *et al.*, *Environ. Res. Lett.* **16**, 114012 (2021).
9. M. Muratori *et al.*, *Environ. Res. Lett.* **11**, 095004 (2016).
10. Y. Ou, "Source code and data for Ou et al. (2021) Updates to Paris climate pledges improve chances of limiting global warming to well below 2°C [Data set]," Zenodo (2021).
11. A. A. Fawcett *et al.*, *Science* **350**, 1168 (2015).
12. L. Clarke *et al.*, in *Climate Change 2014: Mitigation of Climate Change. Contribution of Working Group III to the Fifth Assessment Report of the Intergovernmental Panel on Climate Change,* O. Edenhofer *et al.*, Eds. (Cambridge University Press, 2014), chap. 6.

10.1126/science.abn9667

NEXTGEN VOICES: SUBMIT NOW

Rules every PI should follow

Add your voice to *Science*! Our new NextGen Voices survey is now open:
Imagine that you can write one rule that every principal investigator (PI) must follow to improve the experience of young scientists in their lab. What rule would you enact?

To submit, go to www.science.org/nextgen-voices
Deadline for submissions is 4 March. A selection of the best responses will be published in the 1 April issue of *Science*. Submissions should be no more than 50 words. Anonymous submissions will not be considered.

PRIZE ESSAY



Medical personnel in an overcrowded intensive care unit battle SARS-CoV-2 in critically ill patients.

PHOTO: ANDREW TESTA/PANOS PICTURES

IMMUNOLOGY

Why do people die from COVID-19?

Autoantibodies that neutralize type I interferons increase with age

By **Paul Bastard**[1,2,3]

The past 2 years have witnessed the infection of millions of people with severe acute respiratory syndrome coronavirus 2 (SARS-CoV-2). The course of infection is highly variable. Some young patients have died, while several centenarians, having already lived through the 1918 influenza pandemic, have survived SARS-CoV-2 infection—without experiencing severe respiratory symptoms.

These anecdotal observations belie a key risk factor that emerged early on: The risk of death doubles for every 5 years of age (*1, 2*). Comorbid conditions have also been shown to affect outcome, but with a lower relative risk (*3*). Risk factors are not causal explanations, and the question remains: Why is SARS-CoV-2 infection fatal in more than 10% of people over 80 years old but in fewer than 0.001% of individuals below 18 years old?

Since the onset of the pandemic, the COVID Human Genetic Effort (CHGE) has recruited patients infected with SARS-CoV-2 who exhibit either mild infection or severe and/or critical COVID-19 pneumonia (i.e., requiring oxygen supplementation) (*4*). We sequenced these patients' exomes to test our hypothesis that some individuals with life-threatening COVID-19 have underlying inborn errors of immunity (IEI) (*5*).

Mutations in interferon regulatory factor 7 (IRF7) are already known to underlie severe viral infections such as fulminant influenza pneumonia (*6*). In patients with life-threatening COVID-19 pneumonia, including previously healthy adults, we found IEI that affect Toll-like receptor 3 (TLR3)– and IRF7-dependent type I interferon (IFN) immunity with complete or autosomal-recessive IRF7 or IFN-α/β receptor subunit 1 (IFNAR1) deficiency. A parallel unbiased genome-wide approach found loss-of-function variants of X-linked gene *TLR7* in more than 1% of men with life-threatening COVID-19, leading to deficient type I IFN production (*7*). On this genetic basis, could other types of type I IFN pathway deficiencies account for life-threatening COVID-19 in other patients (*8*)?

MICHELSON PHILANTHROPIES & Science PRIZE FOR IMMUNOLOGY

[1]Laboratory of Human Genetics of Infectious Diseases, Imagine Institute, University of Paris and INSERM U1163, Paris, France. [2]The Rockefeller University, New York, NY, USA. [3]Department of Pediatrics, Necker Hospital for Sick Children, AP-HP, Paris, France.
Email: paul.bastard@institutimagine.org

Autoantibodies (auto-Abs) have been described for IFN-γ, interleukin-6 (IL-6), IL-17A, and IL-17F and associated with susceptibility to infection (*9*). We first tested for the presence of auto-Abs in a cohort of 987 individuals with critical COVID-19 compared with more than 663 asymptomatic patients (*10*). In patients with critical COVID-19, 10% had immunoglobulin G (IgG) auto-Abs that neutralized high amounts of IFN-ω and/or the 13 individual types of IFN-α. Further, these auto-Abs prevented IFN-α2 from blocking SARS-CoV-2 in vitro.

In autoimmune polyglandular syndrome type-1 (APS-1), affected individuals produce auto-Abs against type I IFNs from early childhood onward. Among a group of APS-1 patients, aged 8 to 48 years, infected with SARS-CoV-2, we found that most were hospitalized for COVID-19 pneumonia, with a fatal outcome for 18% (*11*). In a separate study of over 4000 patients with severe and/or critical COVID-19, we detected auto-Abs that neutralized more physiological concentrations of IFN-α2 and/or IFN-ω in over 15% of patients with critical COVID-19 pneumonia, including more than 20% of patients over 80 years, and ~20% of those who died (*12*). Notably, another 1% of the patients only had auto-Abs against IFN-β. When we looked at a group of 34,000 uninfected individuals, we found that the prevalence of auto-Abs that neutralized high concentrations of type I IFNs increased markedly with age. Auto-Abs were present in 0.18% of those 18 to 69 years, 1.1% of those 70 to 80 years, and 3.4% of those over 80 years. The proportion of patients that produced auto-Abs neutralizing physiological concentrations (i.e., 100-fold lower) was even greater, with 1% of those under 70 years, 2.3% of those 70 to 80 years, and 6.4% of those over 80 years.

The findings outlined here provide clues to the reasons why COVID-19 is fatal for some individuals 70 years and older (*8*). The presence of preexisting auto-Abs against type I IFNs can account for severe disease in some older individuals, as it does in many younger patients presenting with life-threatening COVID-19. Since discovering the role of auto-Abs to type I IFNs in COVID-19 in 2020, I have focused on leading the studies of these auto-Abs in our laboratory and performing studies on COVID-19 as part of the effort led by Qian Zhang and Jean-Laurent Casanova within the CHGE (*4*). Our observations have several important medical implications: Patients infected with SARS-CoV-2 could be tested for auto-Abs against type I IFNs (e.g., IFN-α2, IFN-ω, IFN-β), and in individuals in at-risk groups (e.g., people 70 years and older, or patients with autoimmune conditions), these tests could be performed at any time (*5, 9, 10, 12*). Auto-Ab–positive patients should be vaccinated against SARS-CoV-2 as a matter of priority, but not with a live attenuated vaccine (*13, 14*). In cases of infection, these patients should be hospitalized and would benefit from early treatment with antiviral compounds, monoclonal antibodies (*15–17*), and/or IFN-β, provided they have neither pneumonia nor auto-Abs against IFN-β (*18*). Early administration of type I IFNs in patients infected with SARS-CoV-2 could prevent viral growth and uncontrolled infection, which can lead to a cytokine storm and life-threatening COVID-19. Other treatments designed to enhance the type I IFN pathway, or to replicate its antiviral effects, are of potential interest for the treatment of SARS-CoV-2 infection.

Beyond COVID-19, many other viral diseases increase in severity with age, suggesting a possible role of auto-Abs against type I IFNs in their severity. We have shown previously that auto-Abs that neutralize type I IFNs underlie one-third of adverse reactions to the live-attenuated yellow fever virus vaccine (*11*). It therefore appears likely that these auto-Abs also underlie other viral infections, especially those for which severity increases with age. Influenza affects millions of people worldwide every year, causing between 200,000 and 650,000 deaths (*19*). It remains unclear why deaths from influenza disproportionately affect the elderly (*20*), but some of these deaths could be due to auto-Abs that neutralize type I IFNs. Why does the prevalence of auto-Abs against IFNs increase with age? The answer might provide hints to targeted treatments for preventing auto-Abs from being produced in the first place, or for their targeted removal prior to infection. It might also help to explain other issues, from the redundancy of type I IFNs to the causes of various autoimmune diseases. ■

REFERENCES AND NOTES

1. A. T. Levin *et al.*, *Eur. J. Epidemiol.* **35**, 1123 (2020).
2. M. O'Driscoll *et al.*, *Nature* **590**, 140 (2021).
3. E. J. Williamson *et al.*, *Nature* **584**, 430 (2020).
4. J. L. Casanova, H. C. Su, *Cell* **181**, 1194 (2020).
5. Q. Zhang *et al.*, *Science* **370**, abd4570 (2020).
6. M. J. Ciancanelli *et al.*, *Science* **348**, 448 (2015).
7. T. Asano *et al.*, *Sci. Immunol.* **6**, abl4348 (2021).
8. J. L. Casanova, L. Abel, *Science* **374**, 1080 (2021).
9. C.-L. Ku, C.-Y. Chi, H. von Bernuth, R. Doffinger, *Hum. Genet.* **139**, 783 (2020).
10. P. Bastard *et al.*, *Science* **370**, abd4585 (2020).
11. P. Bastard *et al.*, *J. Exp. Med.* **218**, e20210554 (2021).
12. P. Bastard *et al.*, *Sci. Immunol.* **6**, abl4340 (2021).
13. L. Sanchez-Felipe *et al.*, *Nature* **590**, 320 (2021).
14. P. Bastard *et al.*, *J. Exp. Med.* **218**, e20202486 (2021).
15. P. Chen *et al.*, *N. Engl. J. Med.* **384**, 229 (2021).
16. D. M. Weinreich *et al.*, *N. Engl. J. Med.* **384**, 238 (2021).
17. E. M. N. Ferré *et al.*, *Front. Immunol.* **12**, 720205 (2021).
18. P. Bastard *et al.*, *J. Clin. Immunol.* **41**, 931 (2021).
19. J. Paget *et al.*, *J. Glob. Health* **9**, 020421 (2019).
20. F. Krammer *et al.*, *Nat. Rev. Dis. Primers* **4**, 3 (2018).

10.1126/science.abn9649



GRAND PRIZE WINNER

Paul Bastard

Paul Bastard, MD, PhD, is currently working as a chief resident in the Department of Pediatrics at the Necker Hospital for Sick Children (AP-HP, Paris, France) while also doing research in the Necker branch of the laboratory of Jean-Laurent Casanova, located at the Imagine Institute (University of Paris and INSERM) and the Rockefeller University (New York, USA). His research focuses on the genetic and immunological determinants of severe viral diseases, including the causes and consequences of autoantibodies against type I interferons.



FINALIST

Scott Biering

Scott Biering received undergraduate degrees from the University of California, Los Angeles, and a PhD in microbiology from the University of Chicago. He is currently a postdoctoral scholar at the University of California, Berkeley, in the laboratory of Eva Harris. His present research investigates the role of viral proteins like flavivirus nonstructural protein 1 (NS1) and SARS-CoV-2 spike (S) in inducing viral pathogenesis and promoting viral dissemination. **www.science.org/doi/10.1126/science.abn9651**



FINALIST

Lisa Wagar

Lisa Wagar received a BSc from the University of Ontario Institute of Technology and a PhD from the University of Toronto. After completing her postdoctoral fellowship at Stanford University, she started her laboratory in 2020 in the Department of Physiology and Biophysics at the University of California, Irvine, where she is currently an assistant professor. Her research focuses on translational human immunology and the use of organoids to understand the complex interactions that occur between immune cells upon vaccination and infection in humans. **www.science.org/doi/10.1126/science.abn9652**

PHOTOS: (TOP TO BOTTOM) COURTESY OF QUENTIN LEMAIRE/INSTITUT IMAGINE; COURTESY OF SCOTT BIERING; ANDREW SORN

PRIZE ESSAY



FINALIST

Scott Biering

Scott Biering received undergraduate degrees from the University of California, Los Angeles, and a PhD in microbiology from the University of Chicago. He is currently a postdoctoral scholar at the University of California, Berkeley, in the laboratory of Eva Harris. His present research investigates the role of viral proteins like flavivirus nonstructural protein 1 (NS1) and SARS-CoV-2 spike (S) in inducing viral pathogenesis and promoting viral dissemination. **www.science.org/doi/10.1126/science.abn9651**

PHOTO: COURTESY OF SCOTT BIERING

IMMUNOLOGY

One antibody to treat them all

Conserved flavivirus protein holds potential as target for versatile vaccines and therapies

By **Scott B. Biering**

MICHELSON PHILANTHROPIES & Science PRIZE FOR IMMUNOLOGY

The *Flaviviridae* are a family of medically important viral pathogens that include dengue virus serotypes 1 to 4 (DENV1 to DENV4) as well as Zika virus (ZIKV), West Nile virus (WNV), and yellow fever virus (YFV). Together, these mosquito-borne human pathogens impose a tremendous global disease burden (ranging from nonsevere to potentially fatal cases) with devastating economic effects (*1*). Almost half of the world's population lives within the tropical and subtropical habitats of the *Aedes* mosquito vectors that transmit these viruses. As global temperatures continue to climb, the habitats of *Aedes* will expand further, resulting in even more people being at risk for flavivirus infection. Thus, the development of therapeutics and vaccines to treat or prevent severe flavivirus infections is urgently needed.

There are currently no flavivirus therapeutics available, and the lone licensed dengue vaccine, Dengvaxia, is approved only for individuals with preexisting DENV immunity because of the risk of predisposing DENV-naïve recipients to severe disease, presumably from antibody-dependent enhancement (ADE) (*2*, *3*). This risk of vaccine-induced ADE is a problem for all current dengue vaccine candidates because they target the envelope (E) protein, making the production of a vaccine challenging. Targeting other viral proteins that contribute to severe disease is now a major avenue of investigation (*4*). Further, a pan-flavivirus therapeutic or vaccine directed to a conserved viral protein critical for disease is highly attractive given the prevalence of multiple flaviviruses in many *Aedes*-endemic areas. Previous work from my team's laboratory and others has implicated the flavivirus nonstructural protein 1 (NS1) as such a target (*5*, *6*).

NS1 is well conserved among flaviviruses, exhibiting 20 to 40% identity and 60 to 80% similarity. This protein is essential for viral replication as an intracellular dimer and is secreted from infected cells as a hexamer containing lipid cargo (*7*, *8*). Secreted NS1 circulates in the blood of infected individuals, where it is used clinically for diagnosis and as a biomarker of disease severity (*9*). NS1 also functions as a virulence factor through interactions with immune cells, leading to the secretion of proinflammatory and vasoactive cytokines as well as interactions with endothelial cells, which result in endothelial barrier dysfunction and vascular leak (*5*, *6*, *10*–*12*). A cytokine storm and vascular leak are hallmarks of severe DENV infection (*13*). My colleagues and I have shown that multiple flavivirus NS1 proteins can trigger vascular leak independently of viral infection (*14*). Further, immunization and passive transfer of anti-NS1 antibodies protects mice from lethal flavivirus challenge, making NS1 a promising target for therapeutic intervention against pan-flavivirus infection with no risk of ADE (*5*, *15*, *16*).

In 2021, we published a proof of concept for achieving pan-flavivirus protection, reporting the structural basis of protection of a pan-flavivirus anti-NS1 monoclonal antibody (mAb) 2B7 (*17*). This antibody was isolated from mice immunized with DENV2 NS1 as part of an immunology course taught at the University of California, Berkeley, by P. Robert Beatty in conjunction with the laboratory of Eva Harris more than 20 years ago. Today, our laboratory and many others frequently use 2B7 as a molecular tool to study DENV. As the role of flavivirus NS1 in promoting pathogenesis became apparent, we investigated whether 2B7 could protect against lethal vascular leak syndrome in our mouse model and found that it did (*17*). To investigate the mechanism by which 2B7 inhibits NS1 pathogenesis, we teamed up with Janet Smith, an expert NS1 structural biologist at the University of Michigan, to resolve a crystal structure of NS1 complexed with 2B7. We reasoned that visualizing the interaction between NS1 and 2B7 could elucidate why 2B7 was protective and potentially how NS1 contributes to disease. Structures of DENV NS1 in complex with 2B7 revealed the possibility that 2B7 may inhibit two domains of NS1 at once.

Flavivirus NS1 has three domains, including the amino-terminal β-roll, the wing do-

Division of Infectious Diseases and Vaccinology, School of Public Health, University of California, Berkeley, Berkeley, CA 94720, USA. Email: sbiering@berkeley.edu

main, and the carboxyl-terminal β-ladder (*18*). The crystal structure of NS1 complexed with 2B7 revealed that 2B7 bound the β-ladder directly but at an angle so that 2B7 ended up blocking the wing domain as well (*17*). This structure predicted that 2B7 would inhibit the NS1 β-ladder domain to which it bound while indirectly hindering the wing domain from interacting with endothelial cells. We tested this prediction by producing recombinant NS1 proteins with mutations in the β-ladder or wing domains and found that these were defective in mediating pathology. We concluded that 2B7 simultaneously blocked residues in the wing domain of NS1 critical for cell binding as well as directly binding to residues in the β-ladder essential for pathogenesis downstream of cell binding (*17*).

Continued examination of 2B7 and its NS1 binding site revealed that this domain is highly conserved among flaviviruses. We tested whether 2B7 bound to diverse flavivirus NS1 proteins and found that 2B7 bound strongly to NS1 proteins from multiple flaviviruses, including DENV1 to DENV4, ZIKV, and WNV (*17*). The possibility that the strong flavivirus cross-reactivity of 2B7 would confer cross-flavivirus protection against NS1 pathogenesis warranted further study. We conducted in vitro endothelial dysfunction assays and in vivo lethal flavivirus challenge experiments, revealing that 2B7 inhibited DENV, ZIKV, and WNV NS1 in vitro and was protective in in vivo lethal challenge models of both DENV and ZIKV. Years of research initiated by multiple laboratories culminated in our revealing not only critical domains for NS1 pathogenesis but also a highly conserved flavivirus epitope within the NS1 β-ladder, with the potential to serve as a molecular road map for the rational design of NS1-targeted therapeutics.

Therapeutic approaches focused on NS1 are a viable alternative strategy to targeting the E protein, given the risk of ADE, and focusing on highly conserved sites within NS1 can achieve flavivirus cross-protection. Further, antagonizing multiple domains of NS1 simultaneously may achieve greater protective efficacy. Ultimately, our study of 2B7 holds the potential to shift the current flavivirus vaccine and therapeutic design paradigm to one that incorporates NS1 and prompts further examination of simultaneous cross-protection against multiple flavivirus infections. ■

REFERENCES AND NOTES

1. T. C. Pierson, M. S. Diamond, *Nat. Microbiol.* **5**, 796 (2020).
2. S. Sridhar *et al.*, *N. Engl. J. Med.* **379**, 327 (2018).
3. L. C. Katzelnick *et al.*, *Science* **358**, 929 (2017).
4. D. A. Muller, P. R. Young, *Antiviral Res.* **98**, 192 (2013).
5. P. R. Beatty *et al.*, *Sci. Transl. Med.* **7**, 304ra141 (2015).
6. N. Modhiran *et al.*, *Sci. Transl. Med.* **7**, 304ra142 (2015).
7. I. Gutsche *et al.*, *Proc. Natl. Acad. Sci. U.S.A.* **108**, 8003 (2011).
8. P. Scaturro, M. Cortese, L. Chatel-Chaix, W. Fischl, R. Bartenschlager, *PLOS Pathog.* **11**, e1005277 (2015).
9. S. A. Paranavitane *et al.*, *BMC Infect. Dis.* **14**, 570 (2014).
10. H. Puerta-Guardo, D. R. Glasner, E. Harris, *PLOS Pathog.* **12**, e1005738 (2016).
11. D. R. Glasner *et al.*, *PLOS Pathog.* **13**, e1006673 (2017).
12. C. Wang *et al.*, *PLOS Pathog.* **15**, e1007938 (2019).
13. S. B. Halstead, *Lancet* **370**, 1644 (2007).
14. H. Puerta-Guardo *et al.*, *Cell Rep.* **26**, 1598 (2019).
15. D. A. Espinosa *et al.*, *J. Immunol.* **202**, 1153 (2019).
16. A. C. Brault *et al.*, *Sci. Rep.* **7**, 14769 (2017).
17. S. B. Biering *et al.*, *Science* **371**, 194 (2021).
18. D. L. Akey *et al.*, *Science* **343**, 881 (2014).

10.1126/science.abn9651

PRIZE ESSAY



FINALIST

Lisa Wagar

Lisa Wagar received a BSc from the University of Ontario Institute of Technology and a PhD from the University of Toronto. After completing her postdoctoral fellowship at Stanford University, she started her laboratory in 2020 in the Department of Physiology and Biophysics at the University of California, Irvine, where she is currently an assistant professor. Her research focuses on translational human immunology and the use of organoids to understand the complex interactions that occur between immune cells upon vaccination and infection in humans.

www.science.org/doi/10.1126/science.abn9652

PHOTO: ANDREW SORN

IMMUNOLOGY

Small centers of defense

Deciphering immune responses to viruses and vaccines using human tonsil organoids

By **Lisa Wagar**

MICHELSON PHILANTHROPIES & Science PRIZE FOR IMMUNOLOGY

The investigation of how the specialized microenvironment of lymphoid tissues regulates adaptive immune responses forms the foundation of my laboratory's research. At present, I am using human tonsil organoids to predict immunogenicity and immunodominance for vaccines and infectious diseases and then leveraging this new information to improve vaccine design. We are also using tumor organoids (derived from primary human biopsies or excisional surgeries) to investigate the dynamics of tumor–immune cell interactions to dissect the mechanisms by which immunotherapies contribute to tumor control.

At present, there are two major challenges that limit our ability to rationally design new immune therapeutics for humans. First, although numerous animal models exist to study adaptive immunity, translating these foundational discoveries into vaccines and immunotherapies remains inefficient. Vaccine efficacy for some of the most well-studied human pathogens (e.g., HIV, *Mycobacterium tuberculosis*, *Plasmodium falciparum*, influenza) ranges from 0 to 60%, indicating our inability to predict in vivo immunogenicity on the basis of preclinical data. The second major challenge is that most preclinical studies fail to adequately account for the extent of interindividual immune variation. I have studied the effects of demographic and environmental factors (e.g., age, sex, immune history, microbial environment) on human adaptive immunity and repeatedly found that they play a crucial role (*1*–*3*). Studying this variability can help us to understand why some people respond differently to the same drug as well as to develop more broadly effective immune therapeutics. Immune organoids are an optimal strategy to overcome these challenges because they enable us to study the factors that contribute to adaptive immunity in a high-throughput way while controlling for interindividual variation.

Organoid technologies have revolutionized our ability to study complex tissues in a physiologically relevant microenvironment. Immune organoid models offer a distinctive opportunity to track the early events in lymphoid tissues that lead to protective responses. In the laboratory, we use tonsils as a source of accessible lymph node–like tissues from humans. Tonsillectomy surgeries are common, and the excised tissue is usually discarded. Lymph nodes are one of the most important tissue types for understanding the maturation of vaccine-induced adaptive immunity. Tonsils are exposed to both respiratory and alimentary antigens and are a key access point for studying the response to both oral and nasal vaccines. We developed an immune organoid model, derived from primary human lymphoid tissues (principally tonsils but also lymph nodes and spleen), to improve the translational value of preclinical vaccine studies and to increase our appreciation of how interindividual differences contribute to immune variation (*4*). Our organoids are derived from tonsil tissue collected from children (≥2 years old) and adults of ethnically diverse backgrounds, with males and females represented equally. Tonsils are collected from relatively healthy individuals, but we do not exclude those with common conditions such as diabetes and heart disease. We are now screening a large panel of US Food and Drug Administration–approved vaccines in tonsil organoids to build an integrated model of vaccine immunogenicity and make predictions about the magnitude and quality of the response in people.

Previous techniques for producing in vitro models of human adaptive immunity, though successful, have not been widely adopted because of reliance on specialized equipment, challenging technical protocols, poor throughput, a lack of evidence for antigen-specific responses, and/or the absence of cells known to be crucial to important features of adaptive immunity (*5*–*12*). Contrary to previous immune organoid methods, our tonsil organoid system holistically captures the original cell composition and complete functional capabilities of donor tissues.

Research published last year details how these immune organoids respond to influenza and other viral vaccines and patho-

Institute for Immunology, University of California, Irvine, Irvine, CA 92697, USA. Email: lwagar@uci.edu

gens (*4*). The organoid cultures recapitulate the key features of an adaptive immune response, including T and B cell activation and differentiation, antigen-specific T and B cell expansion, somatic hypermutation, class switching, and specific antibody secretion. Major advantages of the organoid system are that both cellular and humoral immunity can be studied simultaneously and longitudinally and that hundreds of conditions can be tested on a single individual's cells, revealing intra- and interindividual sources of immune-response variance. We showed that tonsil-derived immune organoids stimulated with vaccines produce antibody responses. Further, using B cell receptor repertoire analysis, we demonstrated antigen-driven B cell maturation through germinal centers within the organoids. The role of T cell help can also be quantified because T follicular helper cells, which are critical for B cell selection; T cell activation; and antigen-specific CD8 T cell expansion were well recapitulated in the organoids.

My laboratory is now using immune organoids to study the human adaptive immune response to vaccines and infectious diseases—including influenza, Epstein Barr virus, and severe acute respiratory syndrome coronavirus 2 (SARS-CoV-2)—to understand why some individuals respond better than others to a given antigen. Interindividual variation in the magnitude and quality of the antibody response is observable, and we are using clinical and demographic data to explain this variability. The spatial organization of lymphoid tissues plays a key role in orchestrating adaptive immune responses by regulating what cell types are sufficiently proximal to interact and signal one another. The germinal center, where B cells undergo selection and affinity maturation, is structurally complex. The formation and dissolution of germinal centers is dynamic, with changes occurring within minutes and across multiple days. Because some features of the germinal center are preserved in organoid cultures, we have an unprecedented opportunity to visualize the dynamics of these structures in human samples.

Our long-term goal for immune organoid development is to use them to investigate the mechanisms involved in human adaptive immune responses, enable more informed decision-making about what drugs to take to clinical trial, and accelerate vaccine design. ■

REFERENCES AND NOTES

1. L. E. Wagar *et al.*, *Front. Immunol.* **10**, 2239 (2019).
2. L. E. Wagar *et al.*, *PLOS ONE* **6**, e28063 (2011).
3. L. E. Wagar, B. Gentleman, H. Pircher, J. E. McElhaney, T. H. Watts, *PLOS ONE* **6**, e23698 (2011).
4. L. E. Wagar *et al.*, *Nat. Med.* **27**, 125 (2021).
5. W. Béguelin *et al.*, *Nat. Commun.* **8**, 877 (2017).
6. A. M. Byers, T. M. Tapia, E. R. Sassano, V. Wittman, *Biologicals* **37**, 148 (2009).
7. C. Giese, U. Marx, *Adv. Drug Deliv. Rev.* **69-70**, 103 (2014).
8. C. Giese *et al.*, *Artif. Organs* **30**, 803 (2006).
9. I. Kuzin *et al.*, *Biotechnol. Bioeng.* **108**, 1430 (2011).
10. A. Purwada, A. Singh, *Nat. Protoc.* **12**, 168 (2017).
11. A. Purwada *et al.*, *Biomaterials* **198**, 27 (2019).
12. A. Purwada *et al.*, *Biomaterials* **63**, 24 (2015).

10.1126/science.abn9652



Pushing the Boundaries of Knowledge

As AAAS's first multidisciplinary, open access journal, *Science Advances* publishes research that reflects the selectivity of high impact, innovative research you expect from the *Science* family of journals, published in an open access format to serve a vast and growing global audience. Check out the latest findings or learn how to submit your research: **science.org/journal/sciadv**

Science Advances
AAAS

GOLD OPEN ACCESS, DIGITAL, AND FREE TO ALL READERS

RESEARCH

IN *SCIENCE* JOURNALS

Edited by **Michael Funk**



False-color scanning electron microscope image of a human natural killer cell

CANCER

Naturally killing leukemia

Natural killer (NK) cells are innate immune cells that are under investigation as a cell therapy for multiple types of cancer. A challenge for NK cell–based therapies is ensuring that the cells persist and remain functional long-term. Berrien-Elliott *et al.* generated cytokine-induced memory-like NK (ML NK) cells as a therapeutic for leukemia and investigated their functional capacity and persistence in patients receiving human leukocyte antigen–haploidentical hematopoietic cell transplantation (HCT). The authors showed that ML NK cells derived from the same donor as the HCT persisted for at least 2 months after HCT and were highly functional ex vivo. Together, these findings support the use of ML NK cells as a component of HCT for leukemia. —CSM *Sci. Transl. Med.* **14**, eabm1375 (2022).

OPTICS

An exceptional laser cavity

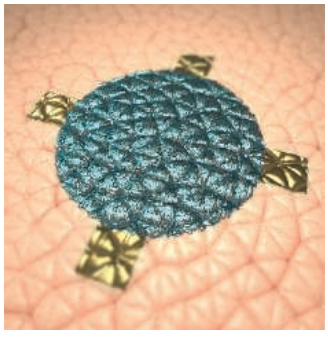
Laser cavities are typically simple structures in the sense that the pump light oscillates between the cavity walls symmetrically, ideally with a single resonant output mode. More complex cavity designs exploiting materials exhibiting gain and loss can be realized that result in an exceptional point at which the output mode can effectively be tuned. Schumer *et al*. designed a cavity in which the pump light encircles the exceptional point as it propagates back and forth within the cavity. The result is a laser capable of simultaneously emitting in two different, but topologically linked, transverse profiles, each from a different facet of the cavity. The approach provides flexibility in designing topologically robust laser cavities. —ISO

Science, abl6571, this issue p. 884

NANOMATERIALS

Weaker interfaces enable conformal films

Rigid materials become more flexible when cast as thin sheets, but they will still bump and buckle when subjected to in-plane rotation or twisting motions and thus cannot conformally cover a curved and mobile surface. Yan *et al*. formed roughly 10-nanometer-thick freestanding sheets by spin coating films containing flakes of semiconducting materials. The flakes attract each other through bond-free van der Waals interfaces to enable mechanical stretchability and malleability as well as permeability and breathability. These properties make them suitable for bioelectronic membranes that can monitor and amplify a range of electrophysiological signals, including demonstrations of electrocardiography and electroencephalography. —MSL



A flexible, wearable film containing semiconducting flakes is well suited for application to skin.

Science, abl8941, this issue p. 852

PROTEIN TARGETING

NAC acts as a gatekeeper on the ribosome

In eukaryotes, signal recognition particle (SRP) targets membrane and secretory proteins to the endoplasmic reticulum (ER) while they are being synthesized on the ribosome. To prevent erroneous targeting of proteins to the ER, access of SRP is

IMAGES: (TOP TO BOTTOM) NIAID/SCIENCE SOURCE; YAN *ET AL.*

regulated by the nascent polypeptide–associated complex (NAC). Jomaa *et al*. investigated how NAC can prevent SRP from binding ribosomes that are synthesizing cytosolic and mitochondrial proteins while at the same time recruiting SRP to ribosomes translating an ER protein client. Their findings reveal the role of NAC as a key sorting factor for nascent chains that helps to ensure the specificity of membrane and secretory protein localization in eukaryotes. —SMH

Science, abl6459, this issue p. 839

DARK MATTER

The search for axion dark matter

The hypothetical "axion" particle is gaining momentum as a candidate for explaining the ever enigmatic "dark matter," which is thought to account for about 85% of the matter in the universe. Chadha-Day *et al.* reviewed what this particle is, and Semertzidis and Youn reviewed how scientists are trying to detect it. Axion dark matter is proposed to consist of an oscillating radiofrequency field coupled to ordinary matter with charge-parity violating interactions. Detection experiments use magnetic fields to try to convert dark matter axions into weak signals of radiofrequency photons. New experimental typologies and advances in precision measurement have dramatically expanded the range of detectability, and hopes are high that they may succeed in discovering the axion in the near future. —MNA

Sci. Adv. 10.1126/sciadv.abj3618 (2022), 10.1126/sciadv.abm9928 (2022).

STRUCTURAL BIOLOGY

Movie of a moving chloride ion

Biological pumps that use retinal isomerization to move protons across a membrane have been studied extensively, but the mechanisms involved in moving chloride ions, which have both a different charge and different coordination requirements, are less well understood. Mous *et al.* combined time-resolved x-ray crystallography, spectroscopy, and computational simulations to generate a molecular movie of chloride transport through a chloride-pumping halorhodopsin. Ion uptake from the extracellular environment is supported by interactions with the retinal, and transport through a space generated by retinal isomerization occurs within about 1 microsecond of excitation. Release of chloride and blockage of backward flow is mediated by a salt bridge that forms an electrostatic gate at the intracellular face. These insights are important for understanding ion transport in these pumps, which are important tools for optogenetic silencing of neurons. —MAF

Science, abj6663, this issue p. 845

CANCER IMMUNOLOGY

Shared states of tumor-specific T cells

Adoptive cell therapy is a type of cancer immunotherapy in which an individual's immune system is trained to eliminate their tumor. This process involves genetically engineering T cells, but it requires the challenging identification of T cell receptors (TCRs) that can recognize cancer-specific alterations. Lowery and Krishna examined TCRs from human metastatic tumors, including those of breast, melanoma, and colon origin. Using TCR and single-cell sequencing technology, the authors found a conserved phenotypic state common to known tumor mutation–specific T cells. Gene signatures were able to predict the tumor reactivity of TCRs from independent samples and discriminate them from bystander T cells. Such strategies may enable more streamlined identification of tumor-specific TCRs for patient immunotherapy. —PNK

Science, abl5447, this issue p. 877

IN OTHER JOURNALS

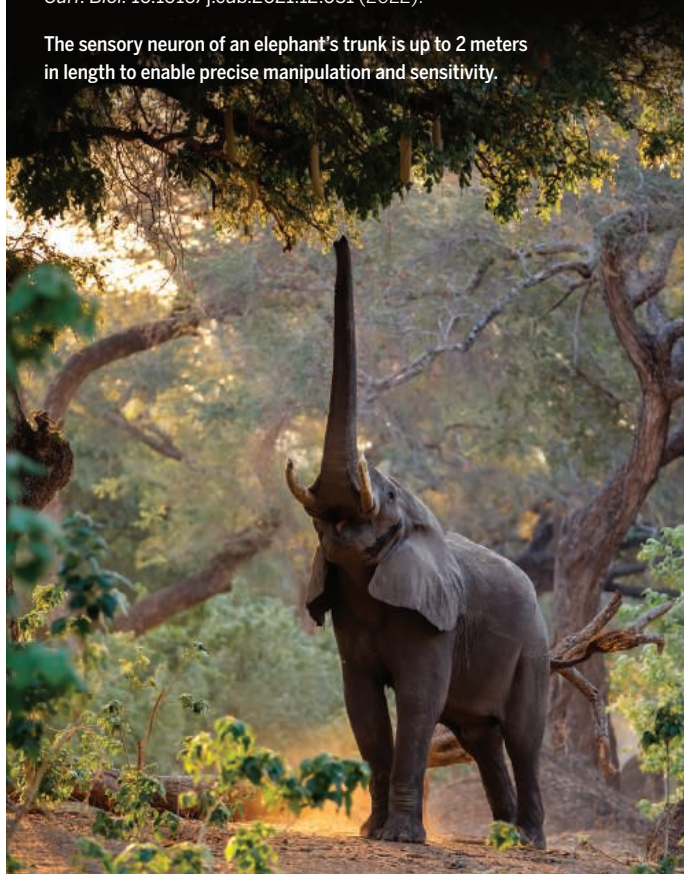
Edited by **Caroline Ash** *and* **Jesse Smith**

NEUROSCIENCE

The elephant's trunk

In the trigeminal ganglion reside cell bodies of neurons that serve the face. For the elephant, this includes its trunk. Purkart *et al.* have made an anatomical analysis of the trigeminal system in Asian and African bush elephants. A trunk sensory neuron can be as much as 2 meters in length and is exuberantly supported by glial cells. The elephant's trigeminal ganglion is larger in diameter than its spinal cord. The infraorbital nerve, which serves the trunk, is thicker than those serving the eye or inner ear. The authors suggest that the unusually thick axons in the trigeminal nerve support temporal precision, highlighting the trunk not only for its utility in manipulating the elephant's environment but also for its contribution of sensory input for the elephant. —PJH

Curr. Biol. 10.1016/j.cub.2021.12.051 (2022).



The sensory neuron of an elephant's trunk is up to 2 meters in length to enable precise manipulation and sensitivity.

PHOTO: HENK BOGAARD/ISTOCK.COM

PHYSIOLOGY

How exercise supports the brain

How does exercise enhance neurogenesis in the adult hippocampus? The effect may in part result from increased amounts of the selenium transport protein selenoprotein P (SEPP1) in the serum of exercised animals. Leiter *et al.* screened for proteins that increased in abundance in mice that exercised on a running wheel. One of them was SEPP1, which helps provide selenium to the brain. Genetic depletion of SEPP1 or its receptor reduced the effect of exercise on neural precursor cell proliferation. Dietary



BEHAVIORAL GENETICS

Nature-loving inheritance

Why some people spend more time outdoors could be explained by factors such as place of residence, parental influence, and childhood experience. Chang *et al.* found that genetics also plays a part in determining the strength of an individual's desire to experience nature. Of 1100 pairs of twins in the TwinsUK panel, comparing those who were raised together with twins raised apart and nonidentical twins revealed that nature-loving behavior has a significant inheritable component. Like genes make like minds. —DJ *PLOS Biol.* **20**, e3001500 (2022).

Twins Tashi and Nungshi Malik, who have climbed Everest, likely share a genetic component in their love of the outdoors.

supplementation of selenium mimicked the effect of exercise and reduced some of the cognitive defects brought on by aging. Understanding the mechanism of these effects might allow treatments that reproduce the exercise benefit. In the meantime, the authors note that selenium is found in foods such as nuts, dairy products, and grains. —LBR

Cell Metab. 10.1016/j.cmet.2022.01.005 (2022).

BIOCHEMISTRY

Avoiding assembly by negative design

Many diseases are caused by mutations that affect how proteins self-assemble or localize in cells, but mapping these relationships is challenging. Seisdedos *et al.* randomly mutated three residues at the surface of each of two homo-oligomeric complexes from *Escherichia coli*. In both cases, some mutants triggered nuclear localization and the formation of puncta or fibers. For one complex, this was driven by so-called positive design, changes that drive association by increasing surface hydrophobicity or stickiness. The other complex provides an example of negative design, in which removing negatively charged residues drives aberrant association. The effect of alanine mutations in additional complexes indicates that such negative design is common. The resulting changes in protein assembly and localization could be important in both normal physiology and disease. —VV

Proc. Natl. Acad. Sci. U.S.A. **119**, e2101117119 (2022).

HYDROGELS

Swelling polymers with polymers

Hydrogels consist of highly cross-linked polymers heavily swollen with water. These soft, squishy materials have thus found use in biomedical applications, but they are limited by their lack of toughness and the need to keep their water from evaporating over time. Wang *et al.* developed gels based on cross-linked poly(hydroxyethyl methacrylate–co–acrylic acid) polymerized in the presence of short polyethylene glycol chains. This combination results in gels with high stretchability and toughness and the ability for rapid self-healing and long-term stability under ambient conditions. This combination of properties make these gels suitable for pneumatically driven soft actuators useful for a robotic gripper. —MSL

Adv. Mat. 10.1002/adma.202107791 (2022).

SCIENTIFIC WORKFORCE

Not all postdocs are created equal

Using National Science Foundation data, Denton *et al.* shed light on employment implications for physical sciences and engineering (PSE) and life sciences (LS) postdocs in government, industry, and academia. The authors found that for each sector, PSE postdocs are shorter and offer higher salaries than LS postdocs. Further, transitioning from a postdoc to permanent employment occurred more frequently within sectors than between sectors, although a substantial number of academic postdocs transitioned to different sectors. Finally, the data showed that the least frequent reason for engaging in a postdoc was the lack of other options, refuting a common narrative that postdocs are a last resort for some. Collectively, these results provide data with which to reconsider career development advice provided to PhD candidates and postdocs. —MMc

PLOS One 10.1371/journal.pone.0263185 (2022).

POROUS FRAMEWORKS

Alkane separations branch out

Microporous materials such as metal-organic frameworks (MOFs) can enable hydrocarbon isomer separations and have been used to separate linear from monobranched isomers. Yu *et al*. report that a ytrrium-based MOF containing two types of structure-building units is effective for separating three types of hexane isomers. The use of less-symmetrical 5,5′-azanediyldiisophthalic acid linkers enabled the coexistence of hexanuclear $Y_6(OH)_8(COO)_8$ secondary building units and mononuclear $Y(COO)_4$ primary building units and created a MOF with a new topology. The pores absorbed the more branched 2,2-dimethyl butane more readily than 3-methylpentane, which in turn was adsorbed preferentially compared with linear *n*-hexane. —PDS

J. Am. Chem. Soc. 10.1021/jacs.1c12068 (2022).

PHOTO: VIRENDER SINGH MALIK/WIKIMEDIA COMMONS/CC BY-SA

ALSO IN *SCIENCE* JOURNALS

Edited by **Michael Funk**

NEUROSCIENCE

Aging and sleep disruption

In humans, the deterioration of sleep quality during aging is one of the most prevalent complaints. In an animal model, Li *et al*. found that aging correlated with enhanced spontaneous activity of wake-promoting brain areas during sleep (see the Perspective by Jacobson and Hoyer). Hypocretin-expressing neurons were more active during sleep, raising the chances of brief arousals and thus causing sleep to be more fragmented. The excitability of hypocretin neurons in aged brain tissue was heightened, possibly because of decreased expression of a subpopulation of potassium channels. Aging-related sleep fragmentation may therefore be due to altered intrinsic excitability of arousal-promoting neurons. —PRS

Science, abh3021, this issue p. 838; see also abo1822, p. 816

IMMUNOLOGY

Trained ILC3: Better, faster, stronger!

Type 3 innate lymphoid cells (ILC3s) are enriched in the intestinal tract and play important roles in mucosal homeostasis, host defense, and the organization of lymphoid tissues. Although certain innate immune cell populations can adopt new long-term phenotypes in response to inflammatory signals ("trained immunity"), whether this is also true of ILC3s is unclear. Serafini *et al*. report that after mice were infected with *Citrobacter rodentium*, a subset of activated ILC3s persisted for months. These "trained" ILC3s (Tr-ILC3s) showed superior activation and controlled infection better than "naïve" ILC3s after pathogen rechallenge. The initial encounter with *C. rodentium* durably rewired the metabolic pathways of Tr-ILC3s, endowing them with an enhanced capacity to proliferate and secrete cytokines such as interleukin-22. —STS

Science, aaz8777, this issue p. 859

CORONAVIRUS

Ongoing adaptation of SARS-CoV-2

Two years into the COVID-19 pandemic, several variants of severe acute respiratory syndrome coronavirus 2 (SARS-CoV-2) have arisen that show increased infectivity or evade immunity. The Omicron variant of concern has 37 mutations in the spike protein, which is responsible for host cell entry. Most of these mutations are in two domains targeted by neutralizing antibodies, the receptor-binding domain (RBD), and the N-terminal domain (NTD). McCallum *et al*. present structures of the viral spike bound to S309, a therapeutic antibody that maintains neutralizing activity against Omicron, and structures of the RBD bound to S309 and the human ACE2 receptor. The structures show how Omicron retains high-affinity binding to ACE2 while greatly reducing binding to other therapeutic antibodies. —VV

Science, abn8652, this issue p. 864

ORGANIC CHEMISTRY

Twisting enamines through the mirror

Separating enantiomers, or mirror-image molecules, is essential to pharmaceutical synthesis. Enriching an equal mixture of them by selectively converting one to the other is not possible using catalysis alone. Recently, however, an approach pairing catalysis with energy injection from light absorption has proven feasible. Huang *et al*. report a variant of this strategy whereby a chiral amine catalytically cycles chiral aldehydes through enamine derivatives. Selective activation by a light-absorbing sensitizer then tilts the equilibrium of enamine isomers to favor net conversion of a single aldehyde enantiomer into its counterpart. —JSY

Science, abl4922, this issue p. 869

BLACK HOLES

Misaligned spin in an x-ray binary

If a black hole is in a close enough binary system with a star, it rips material off the companion. As that material falls into the black hole, it forms an accretion disk that is hot enough to emit optical and x-ray radiation. Poutanen *et al*. used optical polarimetry to determine the orbital axis of a black hole x-ray binary (see the Perspective by Patat and Mapelli). Combining these observations with previous measurements of the black hole spin showed that the two are misaligned by at least 40 degrees. This high misalignment must have been generated during the formation of the black hole, because accretion always brings the two axes closer together. —KTS

Science, abl4679, this issue p. 874; see also abn5290, p. 821

ANTIBIOTIC RESISTANCE

Personal histories of past resistance

A serious infection may initially be diagnosed as antibiotic susceptible but subsequently become drug resistant—and life threatening. Rather than de novo resistance mutation occurring, it is more likely that a resistant strain or species persisting in the patient's gut or skin replaces the susceptible strain. From this starting point, Stracy *et al*. built machine-learning models that predict individual risks of gaining resistance to specific antibiotics using 8 years of records on more than 200,000 patients' microbiome profiles (see the Perspective by Lugagne and Dunlop). Data on antibiotic use for urinary tract and wound infections were used to train the algorithms and to develop personalized antibiotic treatment strategies. For most patients, there was an alternative susceptibility-matched antibiotic that had a lower predicted risk of resistance emerging compared with the antibiotic prescribed by the physician. —CA

Science, abg9868, this issue p. 889; see also abn9969, p. 818

ORGANIC CHEMISTRY

A late coupling for himastatin

Himastatin is a bacterial natural product that has been studied over the past several decades for its antibiotic properties and intriguing structure. The compound is a dimer of peptide macrocycles linked through a bond between the aryl rings of two cyclotryptophan residues. D'Angelo *et al*. report a comparatively efficient synthesis of himastatin as well as its unnatural enantiomer and several other derivatives (see the Perspective by Smith). The key step is a late-stage dimerization relying on oxidation of the monomers by a copper salt. Fluorescent tagging sheds light on the compound's cell membrane–disrupting mechanism of action. —JSY

Science, abm6509, this issue p. 894; see also abn8327, p. 820

INTERFERON SIGNALING

From bone marrow to hemorrhage

Hemorrhaging is a potentially fatal outcome of arenaviral infections and is related to increased interferon-α (IFN-α) production. Aiolfi *et al.* found that bleeding from arenaviral infection in mice resulted from IFN-α triggering the formation of defective platelets through a pathway that did not act directly on platelets, which lack IFN receptors.

Instead, IFN-α decreased the expression of genes involved in platelet formation and function in megakaryocytes, the bone marrow cells that generate platelets. Infected mice produced fewer platelets, and those that were produced were less functional. —WW

Sci. Signal. **15**, eabb0384 (2022).

ALLERGY

Stress leads to IL-9 danger

Interleukin-9 (IL-9) can promote type 2 lung inflammation during allergic responses to inhaled allergens, but the direct cellular targets of IL-9 are not well characterized. Fu *et al.* showed that pulmonary macrophages are a major population of immune cells responding to IL-9 produced in mouse models of allergic airway disease. Mice deficient in the IL-9 receptor had impaired expansion of monocyte-derived interstitial macrophages that promoted airway inflammation dependent on arginase expression. IL-9 signaling also promoted macrophage production of the eosinophil-attracting chemokine CCL5, which was elevated in the serum of patients with asthma and correlated with IL-9 levels. These results identify lung macrophages as key cellular targets of IL-9 during allergic disease that subsequently amplify type 2 inflammatory responses. —CO

Sci. Immunol. **7**, eabi9768 (2022).

SOLAR CELLS

Optimizing perovskite A sites

In the organic-inorganic lead halide perovskites (OLHPs) used in optoelectronics, the monovalent A site was thought initially to have little effect on band edge states compared with the divalent lead or tin cations and halide anions. However, the recent improvement performance breakthroughs for OLHP solar cells have largely come from modifications of A site cations. Lee *et al*. reviewed their expanded roles and versatility in three-dimensional OLHPs, especially for structural stabilization, mitigation of ion migration, and surface functionalization for interface modification and trap passivation. —PDS

Science, abj1186, this issue p. 835

HUMAN EVOLUTION

Genomics and human ancestral genealogy

Hundreds of thousands of modern human genomes and thousands of ancient human genomes have been generated to date. However, different methods and data quality can make comparisons among them difficult. Furthermore, every human genome contains segments from ancestries of varying ages. Wohns *et al*. applied a tree recording method to ancient and modern human genomes to generate a unified human genealogy (see the Perspective by Rees and Andrés). This method allows for missing and erroneous data and uses ancient genomes to calibrate genomic coalescent times. This permits us to determine how our genomes have changed over time and between populations, informing upon the evolution of our species. —LMZ

Science, abi8264, this issue p. 836; see also abo0498, p. 817

NANOPHOTONICS

Scintillating nanophotonics

When a high-energy particle collides with a material, the energy is transferred to atoms in the material, and light can be emitted. This scintillation process is used in many detector applications ranging from medical imaging to high-energy particle physics. Roques-Carmes *et al*. integrated scintillating materials with nanophotonic structures to enhance and control their light emission (see the Perspective by Yu and Fan). The authors show how nanophotonic structures enable the ability to shape the spectral, angular, and polarization characteristics of scintillation. This approach should enable the development of brighter, faster, and higher-resolution scintillators. —ISO

Science, abm9293, this issue p. 836; see also abn8478, p. 822

REVIEW SUMMARY

SOLAR CELLS

Rethinking the A cation in halide perovskites

Jin-Wook Lee†, Shaun Tan†, Sang Il Seok*, Yang Yang*, Nam-Gyu Park*

BACKGROUND: Organic-inorganic lead halide perovskites (OLHPs) represent a family of semiconducting materials that have attracted wide interest for their optoelectronic applications. By combining notable electronic and photophysical properties with low-temperature solution processability using earth-abundant materials, the field has experienced rapid breakthroughs over the past decade. OLHP-based optoelectronic devices have now been established as an independent field of study. In particular, solar cells that use OLHPs as the photoactive layer have exceeded 25% power conversion efficiency, which is competitive with photovoltaics based on traditional inorganic semiconductors such as silicon. However, unanswered questions remain to be addressed regarding the fundamental properties and our understanding of OLHP materials.

ADVANCES: OLHPs have the general chemical formula of ABX_3, where A represents a monovalent cation, B represents the divalent lead cation, and X is a halide anion. During its initial development, the A cation was limited to mainly three candidates, namely methylammonium (MA^+), formamidinium (FA^+), and cesium (Cs^+), which were determined by size and structural constraints to fit within the spaces of the OLHP crystal lattice. Because the A cation, by itself, does not directly contribute to the OLHP band-edge construction, it was traditionally believed to hardly affect the optoelectronic properties of OLHPs.

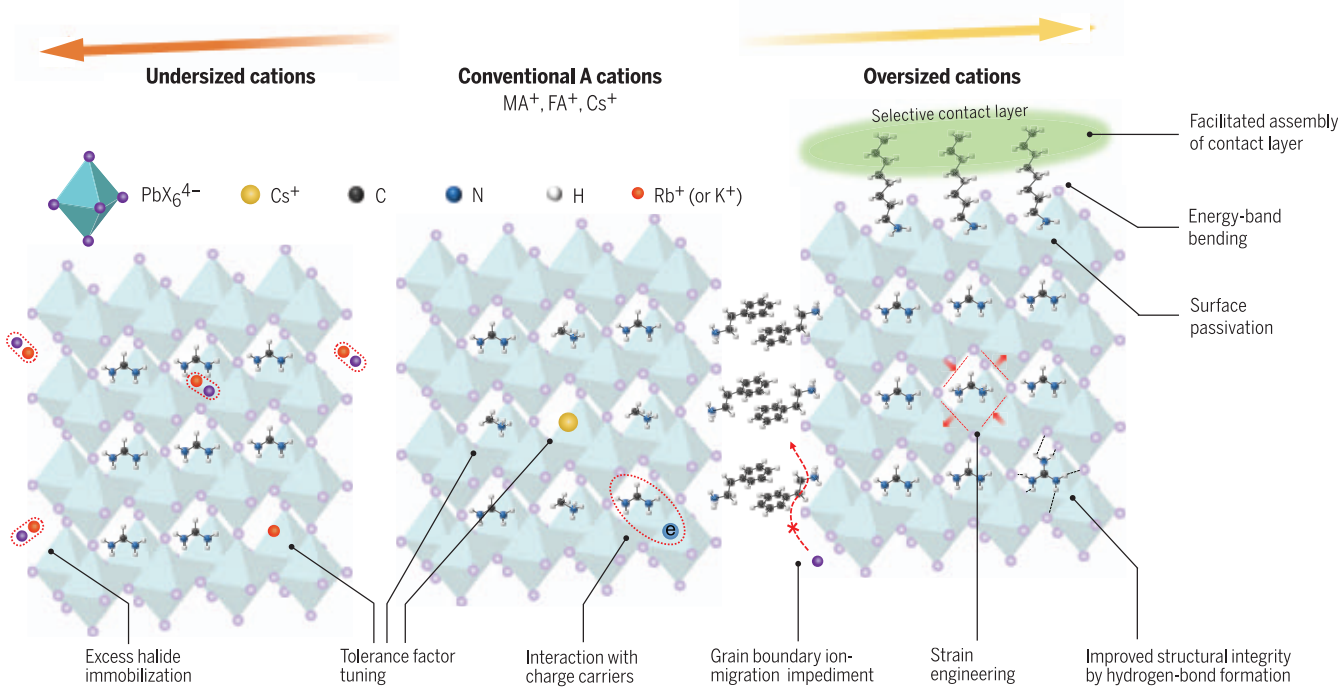
In contrast to these presumptions, advancements in recent years have unraveled the critical role of the A cation in determining the optoelectronic and physicochemical properties of OLHPs. Major breakthroughs in the field have been realized by using A cations to fine-tune the properties of OLHPs, including for (i) thermodynamic or kinetic stabilization of desirable OLHP phases, especially the metastable cubic formamidinium lead triiodide polymorph; (ii) impeding the migration of ions by electrostatic interactions and/or steric effects; and (iii) surface and interface functionalization and modification. These topics are now at the forefront of OLHP research, ultimately dictating the utility, function, performance, and stability of OLHP-based optoelectronic devices.

In this review, we examine the important developments enabled by the expanded role of the A cation. To highlight its importance, the vast majority of the record-breaking performances for OLHP-based photovoltaics have been enabled by breakthroughs related to the versatility of the A cation, which we discuss. Moreover, recently, bulky conjugated A cations have even been demonstrated to participate in constructing the OLHP band-edge structure, further challenging a long-held traditional notion regarding the role of the A cation.

OUTLOOK: Future opportunities entail either discovering new uses for existing A cation species or identifying new A cations for existing applications, or both simultaneously. When looking toward improving the commercialization readiness of OLHPs, A cation applications that involve addressing the module scale-up challenges and long-term operational instability issues must be further explored. This necessitates a more comprehensive understanding of the structure-property-performance-stability correlations conferred by the A cation by combining systematic experimental approaches with first-principles theoretical studies. ■

The list of author affiliations is available in the full article online.
*Corresponding author. Email: seoksi@unist.ac.kr (S.I.S.); yangy@ucla.edu (Y.Y.); npark@skku.edu (N.-G.P.)
†These authors contributed equally to this work.
Cite this article as J.-W. Lee *et al.*, *Science* 375, eabj1186 (2022). DOI: 10.1126/science.abj1186

READ THE FULL ARTICLE AT
https://doi.org/10.1126/science.abj1186



Modifying perovskites through A site cations. In recent years, important breakthroughs have been enabled by the expanded role and function of the A cation in tailoring the physicochemical and optoelectronic properties of OLHPs. These advances ultimately dictate the utility, function, and performance of OLHP-based optoelectronic devices.

REVIEW

SOLAR CELLS

Rethinking the A cation in halide perovskites

Jin-Wook Lee[1]†, Shaun Tan[2,3]†, Sang Il Seok[4]*, Yang Yang[2,3]*, Nam-Gyu Park[5]*

The A cation in ABX_3 organic-inorganic lead halide perovskites (OLHPs) was conventionally believed to hardly affect their optoelectronic properties. However, more recent developments have unraveled the critical role of the A cation in the regulation of the physicochemical and optoelectronic properties of OLHPs. We review the important breakthroughs enabled by the versatility of the A cation and highlight potential opportunities and unanswered questions related to the A cation in OLHPs.

Organic-inorganic lead halide perovskites (OLHPs) have the general stoichiometry formula of ABX_3, with A as the monovalent organic or inorganic cation, B as the divalent Pb^{2+} cation, and X as the halide anion. Any of the A, B, and X sites can be occupied by a mixture of constituents to afford OLHPs a wide compositional breadth and tuneability toward different applications (*1*, *2*). The Goldschmidt tolerance factor can be useful to predict structural formability and the resulting crystal phase based on ionic size considerations; it is defined by

$$t = \frac{r_A + r_X}{\sqrt{2}(r_B + r_X)}$$

where r_A, r_B, and r_X are the ionic radii of the A, B, and X species, respectively. The perovskite phase is desired for many practical optoelectronic applications and empirically observed to form at $0.8 < t < 1.0$. The crystal structure consists of an inorganic BX_6^{4-} octahedra network that is three-dimensionally connected through the corner halides, with structural stabilization contributed by the A cations that occupy the cuboctahedral spaces surrounded by eight BX_6^{4-} octahedra. For $APbI_3$-based stoichiometries, three A cations are known to definitively fit this geometric constraint, namely methylammonium ($CH_3NH_3^+$, or MA^+), formamidinium [$HC(NH_2)_2^+$, or FA^+], and cesium (Cs^+), albeit $FAPbI_3$ ($t \sim 0.99$) and $CsPbI_3$ ($t \sim 0.80$) are at the edges of the t limits.

[1]SKKU Advanced Institute of Nanotechnology (SAINT) and Department of Nanoengineering, Sungkyunkwan University, Suwon 16419, Republic of Korea. [2]Department of Materials Science and Engineering, University of California, Los Angeles, CA 90095, USA. [3]California NanoSystems Institute, University of California, Los Angeles, CA 90095, USA. [4]Department of Energy Engineering, School of Energy and Chemical Engineering, Ulsan National Institute of Science and Technology, Ulsan 44919, Republic of Korea. [5]School of Chemical Engineering and Center for Antibonding Regulated Crystals, Sungkyunkwan University, Suwon 16419, Republic of Korea.
***Corresponding author. Email: seoksi@unist.ac.kr (S.I.S.); yangy@ucla.edu (Y.Y.); npark@skku.edu (N.-G.P.)**
†These authors contributed equally to this work.

Traditionally, the A cation was not believed to directly contribute to the OLHP band-edge construction, which is primarily composed of orbital states from the B and X species (*3*). Resultantly, the A cation was not thought to substantially affect the optoelectronic properties of OLHPs. However, progress in recent years has since challenged this notion. Furthermore, the A cation has been shown to critically influence the physiochemical properties and the intrinsic and extrinsic stability of OLHPs.

In this review, we evaluate the expanded role of the A cation (Fig. 1), which has enabled many important breakthroughs for high-performance and stable OLHP optoelectronics. Many of these developments were made possible by the introduction of oversized ($t > 1$) or undersized ($t < 0.8$) cations that may not necessarily fit the structural constraints of the lattice bulk. Conversely, such missized cations may occupy the A sites along the surfaces and/or grain boundaries, which are free from the bulk steric constraints. By themselves, the oversized cations typically form lower-dimensional phases, such as the two-dimensional (2D) A_2PbI_4 perovskites, whereas the undersized cations are used to form the ABO_3 oxide perovskite structures. We focus only on their utility to and function in tuning the properties of three-dimensional (3D) OLHPs.

Revisiting the conventional roles of the A cation: Progress and challenges

Crystal symmetries and crystal phases

The size and geometry of the A cation affect the bond length and angle between the B and X species to alter the arrangement of the surrounding BX_6^{4-} octahedra and thus the resulting crystal symmetry and phase of the perovskite. The molecular orbitals of the A cation constitute deep energy states within the conduction and valence bands and thus do not directly affect the band-edge carrier properties (*4*). Consequently, A cation engineering has been considered as a useful approach to fine-tune the crystal structure (orthorhombic, tetragonal, and cubic) and physicochemical properties of OLHPs without substantially altering their optoelectronic properties.

The organic A cations interact with the surrounding BX_6^{4-} octahedra through weak secondary hydrogen bonding, with bonding energies lower than 0.1 eV per bond (*5*). Owing to such weak interaction energies, the reorientation of the organic cation can be thermally activated at a finite temperature. [The residence time at room temperature is on the order of ~10^2 femtoseconds to picoseconds (*6*–*8*).] The activated reorientation of the organic A cation and its coupling with the surrounding inorganic framework result in a temperature-dependent order-disorder–type phase transition between the orthorhombic, tetragonal, and cubic phases (*9*, *10*). For example, $MAPbBr_3$ crystallizes in the orthorhombic phase at low temperatures (<180 K) where the MA^+ cations are ordered. As the temperature increases to more than 180 K, the MA^+ cation becomes disordered with anisotropic thermal motion, which is coupled to the surrounding $PbBr_6^{4-}$ octahedra to induce the crystal phase transition to the tetragonal symmetry (Fig. 2A) (*11*). Contribution of the A cation thermal motion in relation to the OLHP phase behavior has also been discussed for $FAPbI_3$. The FA^+ cation, which has a larger ionic radius than MA^+, cannot be stabilized in the cubic symmetry at temperatures below ~390 K, and thus it forms a hexagonal nonperovskite polymorph. At temperatures beyond ~390 K, the activated thermal motion of the FA^+ cation contributes entropic stabilization to the cubic perovskite polymorph, which is subsequently retained as a metastable phase at temperatures lower than the phase conversion temperature (*12*). Because the thermal motion of the organic A cation and its coupling with the surrounding inorganic sublattice dictates the crystal structure of the OLHP system and its stability at operating temperatures, not only the static geometry of the A cation but also its dynamic structure should be considered in designing the A cation. In this regard, to predict structural formability, the effective ionic radii of the nonspherical organic cations have been estimated by assuming rotational freedom about the center of mass, by adding the distance from the center of mass to the outermost ion (excluding hydrogen) to the radius of the ion (*13*). However, the recalculated t values for many organic cations are still not correlated with experimental results (*14*). Introducing other geometrical factors such as globularity improved the correlation, but the versatility of these approaches has not yet been confirmed (*14*). Further work is needed to enhance the accuracy of calculating t, which may include additional corrections to account for molecular symmetry and hydrogen-bond strength, as well as the A cation dipole.

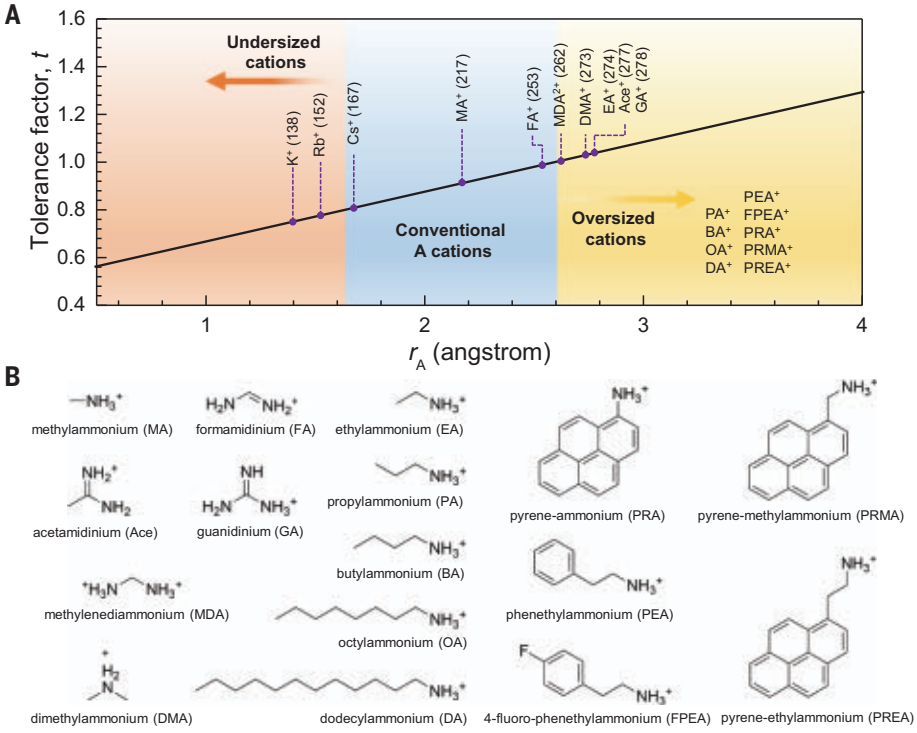


Fig. 1. Expanded role of A cations. (**A**) Selection of A cations that have enabled important breakthroughs in the field of OLHPs, classified by their cationic radius and corresponding tolerance factor based on the $APbI_3$ lattice framework. The number in parentheses indicates the cation radius. (**B**) Molecular structures of the organic cations listed in (A).

Compositional breadth and tunability for bandgap engineering

State-of-the-art, high-performance single-junction perovskite solar cells (PSCs) primarily incorporate Pb^{2+} and I^- in their B and X sites, respectively, because of the desirable bandgaps of such stoichiometries, which are closer to the ideal Shockley-Queisser theoretical value (~1.34 eV). Conversely, wide-bandgap OLHPs (~1.7 eV) are actively investigated for fabricating the top subcell of perovskite-based tandem solar cells by halide compositional tuning (*15*). However, continuous halide compositional tuning is not achievable for $FAPb(I_{1-x}Br_x)_3$ because the t value of $FAPbI_3$ is close to the cubic phase limit, and Br incorporation further increases t and reduces the A cuboctahedral space to aggravate structural formability. This results in the formation of an amorphous phase with high energetic disorder, low absorption, and inferior carrier mobility (~1 $cm^2\ V^{-1}$) compared with the pure iodide phase (~20 $cm^2\ V^{-1}$) (*16*, *17*). By contrast, A cation compositional engineering offers a solution to enable access to the wider bandgap range. Partial replacement of FA^+ with the smaller MA^+ or Cs^+ cation reduces the t value to compensate for the increase in t owing to the Br incorporation (*18*, *19*). This enables the formation of crystalline wide-bandgap compositions such as $FA_{0.83}Cs_{0.17}Pb(Br_{0.4}I_{0.6})_3$, with an optical bandgap of ~1.74 eV and mobility of 21 $cm^2\ V^{-1}$. Such multication mixed-halide compositions are now widely used for fabricating high-efficiency perovskite-silicon or perovskite-perovskite tandems (*20*–*22*).

Although widely used, the multication mixed-halide compositions suffer from spontaneous photo-induced phase segregation (*23*). The compositional engineering of A cations offers an advantage in this regard. In addition to compensating for t changes by halide substitution as discussed, more recently, A cation compositional engineering has been used to directly modulate the bandgap of the perovskite without changing the halide composition. $CsPbI_3$ has a suitable bandgap of ~1.7 eV, but its cubic phase is thermodynamically unstable at room temperature because of its low t value. Additive engineering has enabled the synthesis of thermodynamically stabilized $CsPbI_3$ with a power conversion efficiency (PCE) exceeding 19%, where $CsPbI_3$ is synthesized using dimethylammonium iodide (DMAI) or $HPbI_3$ (*24*, *25*). Quasi-2D perovskites that incorporate oversized ($t > 1$) ammonium cations are another class of wide-bandgap OLHPs that have been broadly explored (*26*). The bulky insulating ammonium cations that are intercalated between the 3D OLHP layers induce charge-carrier quantum confinement to enable bandgap engineering by varying the number of 3D layers (Fig. 2B) (*27*). However, the anisotropic charge transport and poor phase purity have limited the performance of such PSCs (*28*). Further developments are necessary for effective methods to grow phase-pure quasi-2D OLHPs with a desired orientation, because they might be promising active material candidates for the top subcell of perovskite-based tandems owing to their superior stability compared with conventional 3D OLHPs.

Charge-carrier dynamics

Although band-edge carrier transport is mediated through the BX_6^{4-} network, the thermally activated reorientational motion of dipolar A cations and coupled BX_6^{4-} octahedra may interact with charge carriers to affect their dynamics (*7*). It was suggested that the formation of (ferroelectric) large polarons, that is, charge carriers dressed by long-range lattice deformations (Fig. 2C), may be the possible origin of the long carrier lifetimes of OLHPs (*29*, *30*). The hot-carrier lifetime in OLHPs was found to be ~10^2 ps, which is exceptionally long compared with the ~10^2 fs lifetime of conventional polar semiconductors (*7*, *31*). This further suggests the potential application of OLHPs to hot-carrier solar cells, which remain relatively unexplored. It was proposed that the ultrafast reorientational motion of the A cation in response to the photogeneration of charge carriers may form large polarons, resulting in an effective screening of the Coulomb potential to diminish hot-carrier scattering (*7*). The long-lived hot carriers are observed in $MAPbBr_3$ and $FAPbBr_3$, but not $CsPbBr_3$. However, separate studies show an opposite trend, where the slower hot-carrier cooling of $CsPbBr_3$ is attributed to a relatively weak charge carrier–phonon coupling compared with its hybrid counterparts (*32*). Nevertheless, these studies highlight the importance of the dynamic motion of the A cation.

The role of the A cation in the band-edge carrier dynamics is still under debate. In contrast to initial reports correlating polaronic stabilization with A cations (*7*), recent consensus seems to be that the generation of large polarons is more closely associated with the dipolar BX_6^{4-} sublattice rather than the A cation, which is supported by the similar radiative recombination kinetics of band-edge carriers in $MAPbBr_3$, $FAPbBr_3$, and $CsPbBr_3$ (*33*). Conversely, experimental observations still indicate that the lifetimes of band-edge carriers are greatly affected by the A cation composition. For example, $FAPbI_3$-based compositions have demonstrated much longer charge-carrier lifetimes compared with that of $MAPbI_3$, irrespective of the former's generally inferior crystallinity and poor phase purity (*34*, *35*). Based on solid-state nuclear magnetic resonance (NMR) investigations, there exists a correlation between the faster reorientation

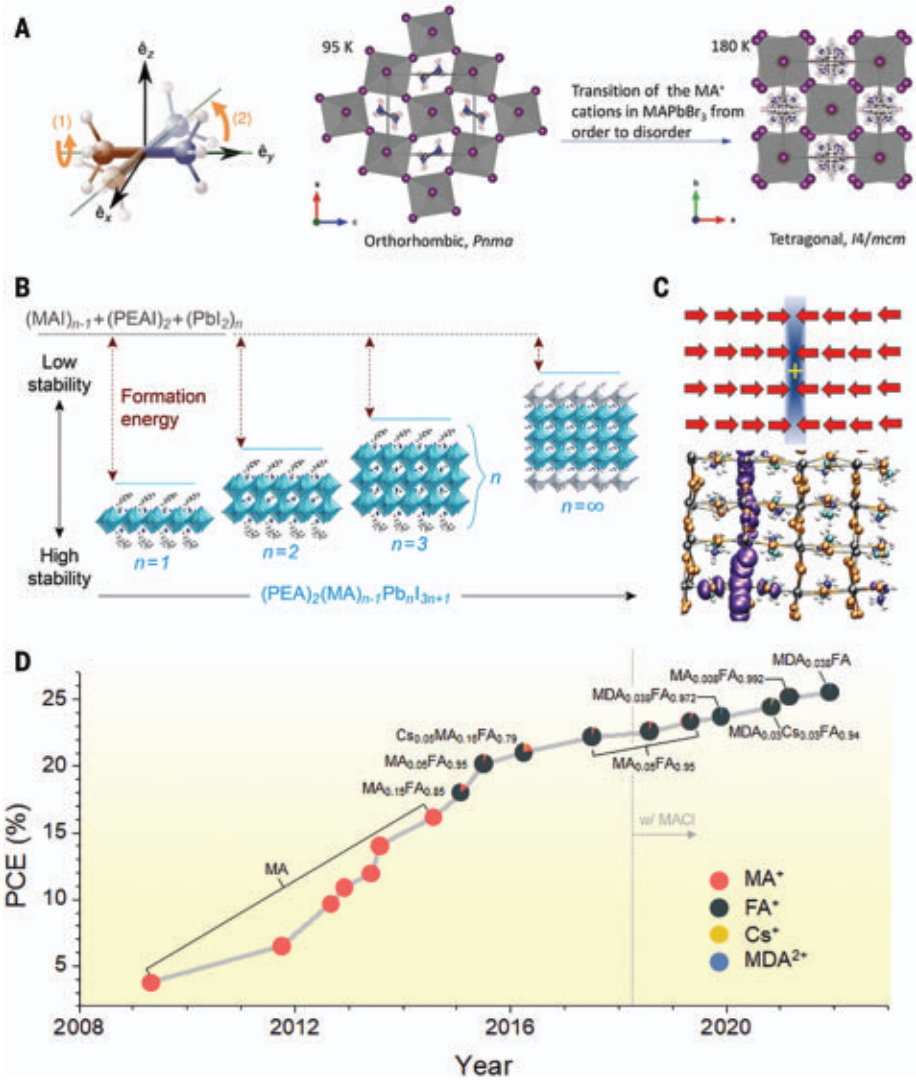


Fig. 2. Revisiting the conventional roles of the A cation. (**A**) Schematics illustrating the dynamic motion of the MA^+ cation (left) and temperature-dependent order-disorder–type phase transition of $MAPbBr_3$ induced by the MA^+ cation motion (right). Adapted with permission from (*6*) and (*11*). Labels (1) and (2) on the left figure indicate the two reorientation modes: (1) methyl and/or ammonium rotation around the C–N axis (carbon and nitrogen atoms are depicted in blue and brown, respectively, and the axis is indicated by the green dotted lines); and (2) whole-molecule reorientation via rotation of the C–N axis itself. (**B**) Low-dimensional $PEA_2MA_{n-1}Pb_nI_{3n+1}$ perovskites and their corresponding relative formation energy and stability. Adapted with permissions from (*27*). (**C**) Schematic of the ferroelectric large polarons and molecular dynamics simulation of the corresponding isodensity representation of holes, showing sheet-like charge localization in tetragonal $MAPbI_3$. Adapted with permission from (*29*). (**D**) History of the record PSC performance and the A cation compositions that were used. The PCE data and compositions are retrieved from their respective publications (*1*, *2*, *19*, *45*, *49*–*51*, *87*, *102*–*110*). The PCEs are plotted based on publication date. This panel conveniently summarizes the composition evolution of state-of-the-art PSCs with time, but we note that the final PSC efficiency is not solely determined by composition alone.

dynamics of the A cation and longer charge-carrier lifetimes (*36*). The temperature and resulting phase-dependent charge-carrier lifetime have also been correlated with the rotational entropy of the A cation (*37*). Recent computational studies proposed that charge carriers are weakly localized by the fluctuating organic A cation, although the subsequent energetic stabilization to form polarons is mediated by the BX_6^{4-} sublattice (*38*). It was also suggested that polaron hopping is related to the random reorientation of the organic cations. This again implies that the dynamic structure of the organic A cation plays a crucial role in affecting OLHP optoelectronic properties. However, all the observed carrier dynamics could have also manifested from composition-dependent defect type, density, and energetics. Therefore, further studies are required to unravel the correlations between the A cation and charge-carrier dynamics, which are essential for designing OLHP compositions.

Expanded role of the A cation

Phase stabilization of desired perovskite polymorphs

More recent record-breaking PSCs contain continuously increasing proportions of FA^+ in their compositions (Fig. 2D). Compared with the prototypical $MAPbI_3$, $FAPbI_3$-dominant compositions generally boast longer carrier lifetimes, superior thermal and photostability, and a bandgap closer to the ideal for photovoltaic applications (*3*). Stabilization of the metastable cubic $FAPbI_3$ phase at room temperature has become an important focus of ongoing research in the community (Fig. 3A).

Initially, substitution with the smaller MA^+ cation was widely used to lower the *t* value of $FAPbI_3$. Replacement of FAI with MAI or MABr in the precursor solution contributes to cubic phase stabilization at room temperature (*19*, *39*). The $(FAPbI_3)_{1-x}(MAPbI_3)_x$ or $(FAPbI_3)_{1-x}(MAPbBr_3)_x$ compositions demonstrated superior optoelectronic properties and stability compared with pure $MAPbI_3$ or $FAPbI_3$, resulting in several record-breaking certified efficiencies around 2015 (Fig. 2D) (*3*). However, MA^+ forms a smaller number of hydrogen bonds than FA^+ with the surrounding PbI_6^{4-} inorganic framework, and its consequent volatile nature aggravates the thermal and photo instability of the OLHP films (*40*, *41*). This motivated the development of alternative cations to stabilize the cubic polymorph. The inorganic Cs^+ and Rb^+ cations have a smaller ionic radius than FA^+ but form stronger primary chemical bonding with the BX_6^{4-} framework. Consequently, Cs^+ and Rb^+ effectively stabilize the cubic phase at lower temperatures while simultaneously enhancing the environmental stability of the films (*41*–*43*). It was also suggested that A cation mixing contributes entropic stabilization to the system (*44*), which motivated the development of more complex triple or quadruple cation systems such as $FA_{1-x-y}MA_xCs_y$- or $FA_{1-x-y-z}MA_xCs_yRb_z$-based compositions (*45*, *46*). Regardless of the improved phase stability of most $FAPbI_3$-based compositions by substitution with MA^+, Br^-, or Cs^+, however, these approaches inevitably increase the bandgap to sacrifice the photocurrent.

Recently, the focus of the community has shifted to phase-stabilization strategies that can preserve the inherent bandgap of cubic $FAPbI_3$. To minimize the bandgap penalty, "additive removal" approaches have been developed by using the smaller MA^+ cation to first form a highly crystalline perovskite phase and then removing it afterward. MACl is, at present, the most widely used additive among

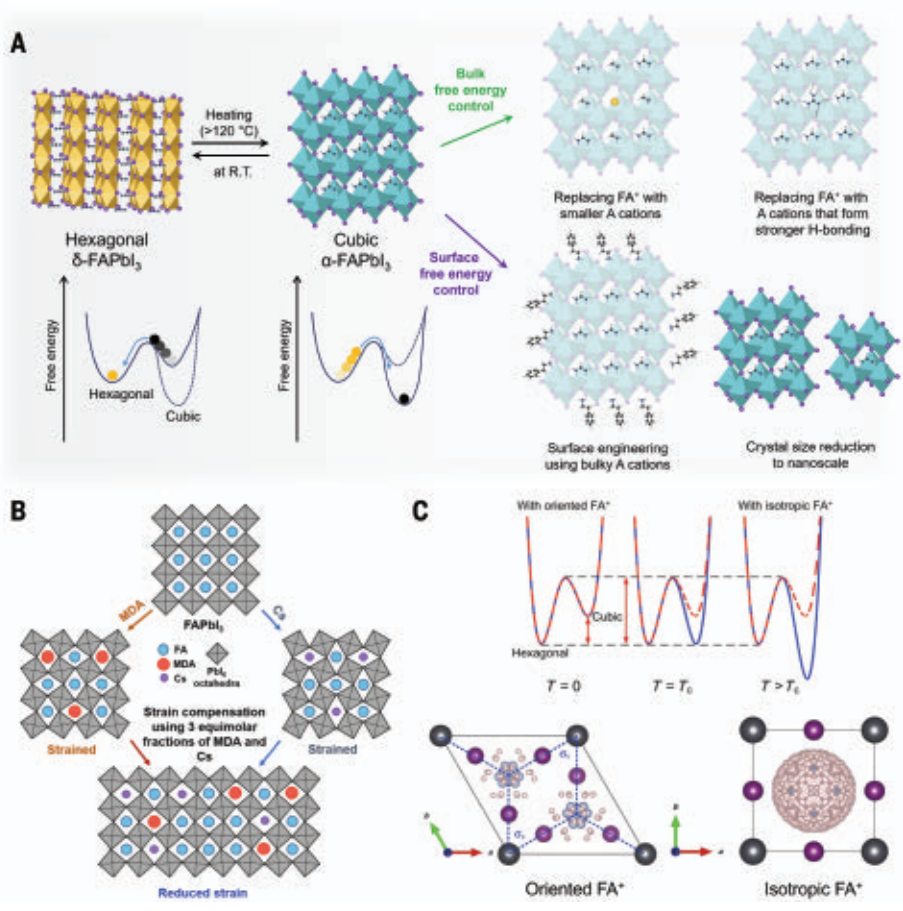


Fig. 3. Stabilization of the cubic $FAPbI_3$ phase by A cation engineering. (**A**) Schematics illustrating the metastability of the cubic α-$FAPbI_3$ phase and its corresponding free-energy diagram (left) and approaches to stabilize the cubic α-$FAPbI_3$ phase by tuning the bulk or surface free energy (right). R.T., room temperature. (**B**) Schematic illustration of lattice strain engineering by using MDA^{2+} and Cs^+ cations. Adapted with permission from (*51*). (**C**) Schematics showing the free-energy diagrams at different temperatures and refined structures of $FAPbI_3$ at the corresponding temperatures. At temperatures lower than the phase-transition temperature (T_c), the FA^+ cation is oriented within the hexagonal crystal structure, whereas its orientation becomes isotropic (random) in the cubic crystal structure at temperatures higher than T_c, contributing to the entropy of the system. Adapted with permission from (*12*).

these approaches (*47*, *48*). The MA^+ cation from the added MACl initially participates in forming the perovskite intermediate phase at room temperature. During the subsequent annealing process, the intermediate phase is converted into the perovskite crystals with the vaporization of MACl. The slow vaporization of MACl and thus retarded crystal growth kinetics promote the growth of highly crystalline perovskite crystals. Regardless of the high molar concentrations of the excess MACl (~40 mol %) in the precursor solution, the final OLHP films contain only a small amount of residual MA^+ (~5 mol %) (*49*), and thus their bandgaps (~1.50 to 1.53 eV) are comparable to that of pure $FAPbI_3$. This approach enables the formation of phase-pure and highly crystalline $FAPbI_3$-based films, and it has been broadly used in studies that report record-efficiency PSCs (vertical dashed line in Fig. 2D) (*50*, *51*). Relatedly, the dual combination of MACl and CsCl was also found to effectively stabilize the perovskite phase (*52*). A similar approach was developed by using gaseous methylammonium thiocyanate (MASCN) (*53*). It was reported that MASCN is incorporated onto the surface of hexagonal $FAPbI_3$ crystals to assist in the conversion of the hexagonal phase into the cubic polymorph. For either MACl or MASCN, the counter anions were also reported to contribute to stabilizing the $FAPbI_3$ perovskite phase. Further developments may elucidate the different roles of the counter anions as well as explore alternative cations or counter anions that can impart additional functionalities.

The phase energetics of materials is governed by the Gibbs free energy of the phase, which is in turn determined by the summation of the bulk and surface free energies. Therefore, the phase conversion of metastable OLHP phases can be modulated by surface-energy manipulation. For example, it was demonstrated that the metastable $CsPbI_3$ perovskite phase can be stabilized by synthesizing nanosized crystals where the surface-energy contribution becomes dominant compared with that of its bulk counterpart (*54*). Such an approach was found to be also valid for $FAPbI_3$, where nanocrystalline $FAPbI_3$ demonstrated a superior phase stability compared with its corresponding bulk crystals (*55*). Surface-energy modulation can also be achieved by adopting surface-functionalizing oversized A cations (*56*–*58*). Bulky ammonium cations, such as phenethylammonium (PEA^+), butylammonium (BA^+), or isopropylammonium, are spontaneously expelled to the grain boundaries and surfaces during perovskite crystallization because of their inability to incorporate into the crystalline lattice bulk. The bulky cations are free from steric constraints at the surface and thus can coordinate with the surface A site by bonding with the surface BX_6^{4-}. Such surface functionalization was suggested to modulate the crystal surface energy to stabilize the cubic perovskite phase. This approach allows for the stabilization of metastable OLHP phases without changing its bulk composition and inherent bandgap.

The phase energetics of OLHPs were also suggested to be dependent on the hydrogen-bond number and bond strength between the A cation and surrounding inorganic framework (*5*). This is illustrated by using the divalent methylenediammonium (MDA^{2+}) cation that can form a greater number of hydrogen bonds with the BX_6^{4-} lattice than FA^+ (*50*). Compared with MA^+, lower concentrations of MDA^{2+} are required to stabilize the cubic phase of $FAPbI_3$, even though the ionic radius of MDA^{2+} is slightly oversized compared with that of FA^+. The incorporation of $MDACl_2$ may generate FA vacancy and interstitial Cl defects to maintain charge neutrality but, importantly, without forming deep trap states. It is noteworthy that the PSC performance and stability improved regardless of the generated additional defects, but further investigations may be necessary to decouple their full consequences. Nevertheless, incorporation of MDA^{2+} inadvertently induces tensile lattice strain as a result of its large cation radius. A direct correlation between residual lattice strain and a detrimental effect on the OLHP charge carrier dynamics has been reported (*59*). To compensate for the residual strain, it was further reported that the smaller Cs^+ cation can be incorporated in equimolar amounts with MDA^{2+} (Fig. 3B) (*51*). Tensile strain relaxation by Cs^+ incorporation resultingly increased the carrier lifetime owing to a reduced defect concentration in the film. The case of MDA^{2+} illustrates the possibility of expanding into higher-valency cations for use in OLHPs, although

their exact phase-stabilization mechanisms still need to be explored.

More generally, the vast majority of $FAPbI_3$ stabilization strategies now reported could be considered kinetic stabilization approaches, such that the cubic $FAPbI_3$ phase only remains metastable and still spontaneously degrades into the equilibrium hexagonal phase. Although kinetic stabilization is effective in retarding phase degradation, true thermodynamic stabilization of cubic $FAPbI_3$ as the equilibrium phase remains the elusive goal. To achieve this, understanding the many overlapping factors that affect the thermodynamic energetic landscape of OLHPs is required. For example, the thermally activated random motion of the FA^+ cation and its entropic contribution to the phase energetics were found to have a crucial role in stabilizing the cubic phase (Fig. 3C) (*12*, *60*), but the entropic contribution of the different A cations has barely been explored. Also, the effects of strain on OLHP thermodynamics and energetics have not been fully elucidated and require further systematic investigations. Defect states must also be correlated with the thermodynamic energetics of metastable OLHPs, which has been shown to affect the phase degradation of $FAPbI_3$ (*61*).

Impeding ion migration by steric and electrostatic interactions

The charged ionic constituents of OLHPs are mobile under an electric field and accelerated under illumination or at increased temperatures. An ion displaced from its original lattice site becomes a crystal defect (or Schottky, Frenkel defect pairs). Ion (or defect) migration are known to cause the current-voltage hysteresis, phase segregation, and chemical corrosion of reactive functional layers, which are responsible for PSC degradation during operation. Strategies to inhibit ion migration can be broadly categorized as reducing the density of mobile ions and/or increasing the activation energy barrier (E_a) for ions to migrate.

Relative to single-cation compositions, substitutional doping to create mixed-cation compositions is broadly observed to alleviate PSC hysteresis. In mixed-cation compositions, the local lattice mismatch caused by A cations with different sizes was reported to distort the ion-migration pathways (Fig. 4, A and B) (*62*). This steric impediment effect was shown to increase E_a to suppress ion migration, which consequently improved the thermal and photostabilities of PSCs. Conversely, excessive lattice strain may detrimentally lower E_a, because ion redistribution constitutes a driving force to relieve residual strain (*51*, *63*). This is especially relevant for pure $CsPbI_3$ and $FAPbI_3$ owing to their extreme t values. The intrinsic strain in $FAPbI_3$ was also shown to promote the formation of Schottky vacancy defects as a compensating strain relaxation mechanism (*64*). As a solution, partially substituting FA^+ in $FAPbI_3$ with smaller Cs^+ and/or MA^+ relaxes the intrinsic strain to suppress ion migration and defect formation (*41*, *51*). Such strain relaxation using Cs^+ has also been widely adopted to prevent phase segregation for wide-bandgap mixed-halide compositions (Fig. 4C) (*65*). Substitutional doping can also increase E_a by strengthening the structural integrity of the OLHP lattice. This is achieved by increasing the bond number and/or decreasing the bond length between the A cation and the BX_6^{4-} framework. This is illustrated by partial substitution of guanidinium (GA^+) into $MAPbI_3$, where GA^+ forms a greater number of effective hydrogen bonds than MA^+ (GA^+, seven bonds; MA^+, three bonds) with the PbI_6^{4-} lattice (*62*, *66*). Molecular dynamics simulations have further indicated that ion migration is affected by the A cation polarity (*67*). The study suggests that more-polar A cations (e.g., MA^+ is more polar than FA^+) may detrimentally assist halide migration because of a reorientation and charge-screening mechanism.

The undersized alkali cations, focusing on Rb^+ and K^+, are widely used as additive dopants to reduce ion migration. The strongly electropositive cations can bind and immobilize excess and undercoordinated halides to suppress their unwanted migration (*68*). Theoretical simulations also indicate that alkali cation doping increases the formation energy of mobile halide interstitial defects (*69*). Additionally, assuming incorporation into the A

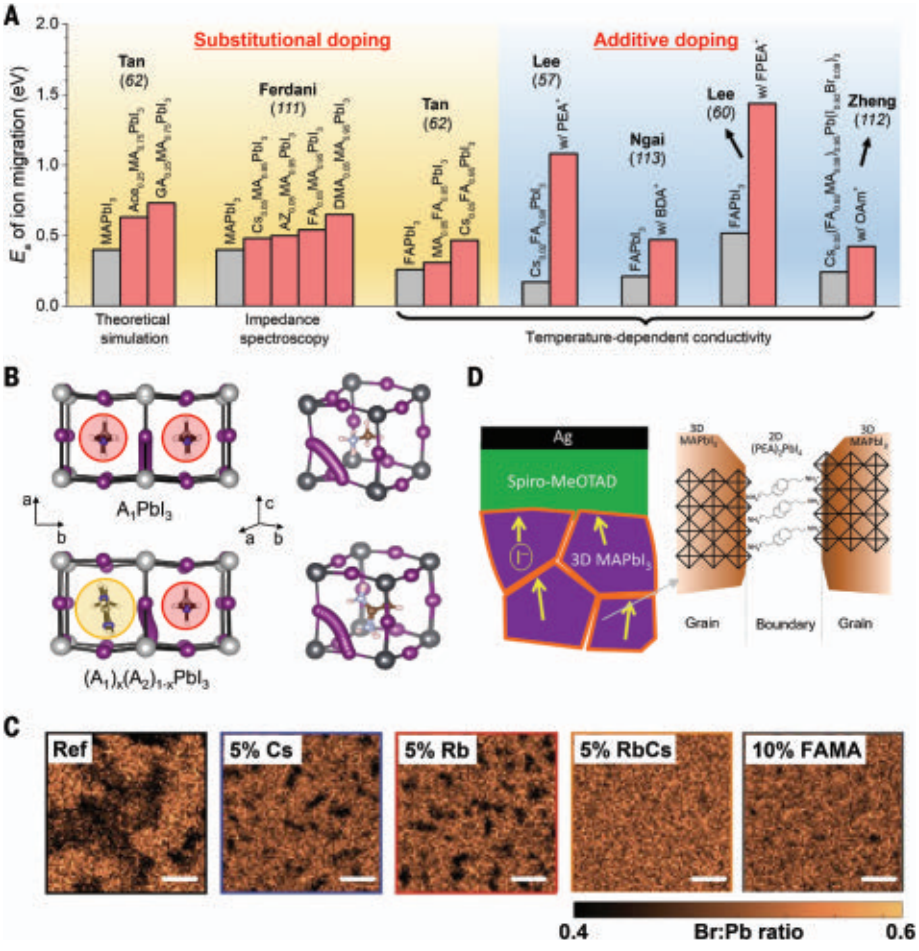


Fig. 4. Impeding ion migration. (**A**) Summary of reported E_a enhancements by A cation engineering, including the measurement and calculation methodologies. (AZ, azetidinium; BDA, 1,4-butanediamonium; OAm, oleylaminium). The PCE data and compositions are retrieved from their respective publications (*57*, *60*, *62*, *111*–*113*). (**B**) Theoretically simulated iodide migration pathway for single-cation (top row) or mixed-cation (bottom row) compositions. The simulations were performed using the nudged elastic band and constrained energy minimization methodology. Adapted with permission from (*62*). (**C**) X-ray fluorescence mapping of the halide distribution of various mixed-halide perovskite films with different A cation compositions. Scale bars indicate 2 μm. Adapted with permission from (*65*). Ref, reference; FAMA, mixture of 8.3% FAI and 1.7% MAI. (**D**) Schematic illustrating the suppressed ion migration by grain boundary 2D $(PEA)_2PbI_4$. Adapted with permission from (*77*).

site, the resultant lattice contraction decreases the ionic interaction distances to improve the structural integrity of the OLHP lattice (*43*, *46*). There is ongoing debate regarding the residing location of the undersized cations, especially for Rb^+. Experimental observations have been interpreted as incorporation into the lattice A site (*43*, *46*). Based on *t* values, their ionic radii should be too small to fit into the A site of the $APbI_3$ lattice. Theoretical calculations suggest that interstitial site occupation is energetically favorable (*70*–*72*). Conversely, solid-state NMR results suggest that Rb^+ and K^+ are entirely immiscible (even at the interstitial sites) and segregate into secondary photoinactive phases (*73*). These discrepancies may perhaps be related to varying miscibility limits of different OLHP compositions. For example, K^+ incorporation may be facilitated by Br^- in mixed-halide $APbI_{3-x}Br_x$ stoichiometries (*74*). Particularly, if assuming the undersized cations are indeed expelled from the A site, alternative mechanisms that do not involve lattice occupancy must be elucidated to explain their ion-migration impediment effects. For example, interstitial site occupancy has been suggested to prevent lattice iodine from displacing into the filled interstitial sites, which inhibits the formation of mobile iodide Frenkel defects (iodine interstitial-vacancy pairs) (*70*, *75*).

Oversized organic A cations are often used as additive dopants into the precursor solution. As discussed, the bulky cations segregate at the grain boundaries and surfaces, possibly forming lower-dimensional phases depending on the specific species. The bulky cations can act as physical barriers to increase E_a by blocking the low-energy ion-migration channels through the grain boundaries (Fig. 4D) (*76*, *77*). The $-NH_3^+$ functional group of ammonium-based cations can also bind with negatively charged defects (e.g., A cation vacancies, undercoordinated halides) by electrostatic interactions to inhibit their migration and deactivate their charge-trapping ability. In an alternate perspective, the replacement of defective grain-boundary regions with lower-dimensional phases equivalently decreases the overall defect density, thus reducing the overall concentration of mobile defective species. Functional groups can be introduced to the A cation chain to strengthen the bonding interaction between adjacent cations along the grain boundary to improve structural rigidity. This is exemplified by incorporating a carboxyl tail into BA^+, forming 5-ammoniumvaleric acid (5-AVA). Adjacent 5-AVA cations interact through stronger hydrogen bonding rather than the van der Waals interaction between BA^+ cations. Resultantly, doping of 5-AVA into $MAPbI_3$ was reported to dramatically suppress the loss of MAI by ion migration–driven volatilization (*78*). Despite using the supposedly unstable $MAPbI_3$ base composition, carbon-based 10-cm–by–10-cm solar modules doped with AVA^+ were shown to sustain their performance for more than 10,000 hours under continuous illumination at 55°C (*79*).

Bulky cyclic cation additives, including 1-butyl-1-methylpiperidinium (BMP) and 1-butyl-3-methylimidazolium (BMIM), have been reported to dramatically inhibit ion migration and OLHP decomposition even at increased temperatures (*80*, *81*). It was proposed that BMP may simultaneously reduce the density of mobile iodide Frenkel defects and inhibit the migration of iodine interstitial defects, which quenched the formation rate of harmful I_2 that catalyzes perovskite degradation (*81*). Ion migration–facilitated formations of δ-$FAPbI_3$ and segregated $FAPbBr_3$ impurity phases during degradation may also be suppressed by BMP addition (*81*). Interestingly, BMIM was observed to aggregate predominantly at the buried interface, whereas BMP was distributed along the grain boundaries. It was suggested that the segregation of BMIM modified its interface dynamics to become incompatible with poly-TPD [poly(*N*,*N*′-bis-4-butylphenyl-*N*,*N*′-bisphenyl)benzidine] as the bottom transport layer, whereas BMP addition was not affected by this problem. This comparison highlights the fact that additive doping can possibly incur unintentional side effects to negatively alter the perovskite crystallization dynamics or interfacial energy alignments. More generally, this emphasizes the importance of locating the distribution of different additive dopants within and around the OLHP layer.

Ion migration is fundamentally a defect-driven process. Theoretical studies show that halide migration, mediated by vacancy defects, is the lowest-energy transport mechanism, with an E_a between 0.1 and 0.6 eV (*82*). However, the vast majority of mitigation strategies in the literature fall short of pinpointing the specific defect species that are immobilized or suppressed. Further studies are necessary to investigate the binding and interaction of A cations with the complex defect landscape of OLHPs to mechanistically explain their ion-migration impediment effects.

Surface functionalization and interfacial modification

The OLHP surface is typically BX_2-rich owing to a combination of volatilization of organic FA^+ or MA^+ during thermal annealing, dissolution of FA^+ or MA^+ by the deposition of solvent during surface posttreatment, or excess BX_2, particularly excess PbI_2, intentionally added to the precursor solution (*83*–*85*). Degradation initiation and nonradiative recombination losses predominantly occur at the OLHP top surface region as a result of an abundance of defective states (*61*, *86*). Consequently, surface modification by posttreatments using A cations has become an essential processing step for state-of-the-art PSCs in recent years (Fig. 5, A and B). Unlike additive doping into the precursor solution that was discussed previously, surface treatments do not interfere with the initial perovskite crystallization process, which enables a larger variety of candidate cations to be used. An additional secondary annealing step typically follows deposition, which may facilitate a chemical reaction with BX_2 to form thin lower-dimensional phases at the surface. The deposition of PEA^+ is a notable exception that omits the secondary annealing step. Formation of the 2D $(PEA)_2PbI_4$ was indeed observed to weaken the trap passivation effect (*87*). This distinction for different A cations, of whether formation of the lower-dimensional crystalline phase is preferred, is still not fully understood.

Surface functionalization of A cations often confers beneficial trap passivation and environmental protection effects. For the former, various functional groups on the cation can coordinate with surface defects to passivate their charge-trapping ability. Most commonly, the $-NH_3^+$ group of ubiquitous ammonium-based cations interacts with negatively charged defects (*85*). Chemical and structural tailoring of the cation backbone is often used to enhance its binding and interaction with surface traps. This is illustrated by the incorporation of the *tert*-butyl moiety (*25*, *88*), which also has the additional benefit of improving the interfacial contact with spiro-MeOTAD [2,2′,7,7′-tetrakis(4,4′-dimethoxy-3-methyldiphenylamino)-9,9′-spirobifluorene] to facilitate hole extraction (*88*). Conversely, the $-NH_3^+$ functionality is insensitive to positively charged defects, such as halide vacancies, which readily form at the OLHP surface. This can be remedied by using zwitterions to simultaneously coordinate with both oppositely charged defects, for instance, by incorporating carboxyl or phosphate groups into the ammonium chain (*25*, *89*). Regarding environmental protection, bulky A cations with hydrophobic chains that orient out of plane with the surface can repel H_2O and O_2 ingression while simultaneously limiting the escape of the OLHP constituents from the active layer. Well-known hydrophobic groups include tertiary or quaternary hydrocarbons (e.g., tetra-ethylammonium) (*88*–*90*) and/or electron-withdrawing fluorine moieties, such as in 4-fluorophenylethylammonium or pentafluorophenylethylammonium (*60*, *91*). In general, a large variety of useful backbone-chain modifications can be found in the literature to enhance such desirable effects. However, despite these successes, concrete selection and design rules still need to be established to avoid

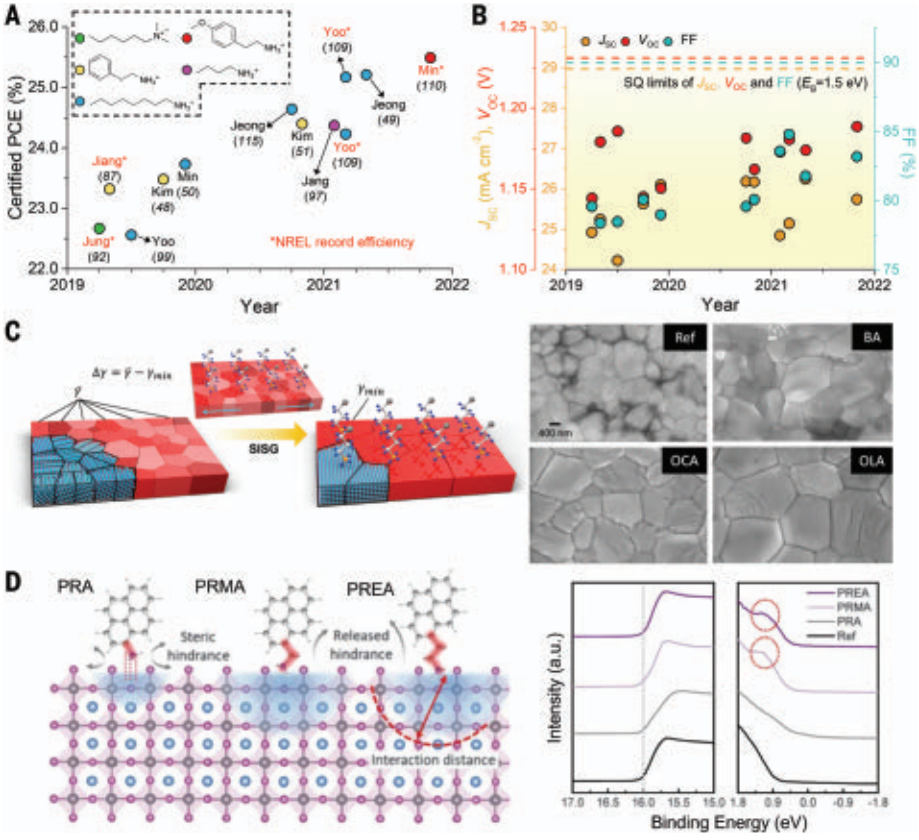


Fig. 5. Surface and interface modification by oversized A cations. (**A**) Summary of state-of-the-art PSCs with certified performance since 2019, highlighting the surface functionalization by the oversized A cations that were used. The data are plotted based on publication date. NREL, National Renewable Energy Laboratory. (**B**) Corresponding photovoltaic parameters from (A), with the horizontal dashed lines marking the theoretical Shockley-Queisser limits of each parameter for a bandgap of 1.5 eV. J_{SC}, short-circuit current; V_{OC}, open-circuit voltage; FF, fill factor. (**C**) Schematic of the surface-induced secondary grain growth (SISG) process by using alkylammonium functionalization to control the surface-energy anisotropy (left). Top-view scanning electron microscopy images of the perovskite films treated with various alkylammonium cations of different chain lengths (right). Adapted with permission from (*93*). γ, surface energy; OCA, octylammonium; OLA, oleylammonium. (**D**) Schematic illustrating the interactions of different pyrene-based ammonium cations with the OLHP film surface (left). Ultraviolet photoelectron spectroscopy spectra of OLHP films treated with the different cations (right). Red circles indicate the additional electronic states. Adapted with permission from (*96*). a.u., arbitrary units; PRA, pyrene-ammonium; PRMA, pyrene-methylammonium; PREA, pyrene-ethylammonium.

the utility of trial-and-error approaches and to maximize beneficial improvements.

In addition to their contributions to hydrophobicity and defect passivation, important breakthroughs in recent years have been realized by A cation surface modification. The top surface of OLHP films forms a carrier-extraction interface with a contacting charge-selective layer, typically a hydrophobic organic material. Surface modification by A cations can be used to aid the assembly of the charge-transporting layer and improve interfacial contact, by tailoring the interaction between the charge-transporting layer species and specific moieties on the A cation. This is exemplified by the use of *n*-hexyl-trimethylammonium (HTA^+) to facilitate the self-assembly of poly(3-hexylthiophene) (P3HT) (*92*). Interdigitation of the hydrophobic hexyl ($-C_6H_{13}$) backbone chains contained on both HTA^+ and P3HT promoted the growth of P3HT with a fibril structure. The fibril structure was suggested to enhance the charge-extraction capability of P3HT as a dopant-free hole-transporting material. This notable breakthrough resulted in one of the previous world-record performance PSCs (green dot in Fig. 5A). Relatedly, A cations can also be used to manipulate the OLHP surface energy. This can be exploited to induce the preferential growth of specific crystallographic planes with lower energy. During a secondary grain-growth process, BA^+, octylammonium, and oleylammonium progressively decreased the (100) plane surface energy to promote the recrystallization of highly textured (100) grains with greatly enlarged grain sizes (Fig. 5C) (*93*). Secondary surface grain growth has also been reported for A cations paired with Br^- as the counter anion, including GABr (*84*), FABr (*83*), and MABr (*94*). Such grain recrystallization can effectively minimize surface pinhole and/or PbI_2 formation (*84*). More generally, rather than the ubiquitous I^- (or Br^-), pairing A cations with alternative counter anions presents further opportunities to modify the OLHP surface, in addition to avoiding the possible formation of iodine interstitial defects as a side effect (*61*). For instance, sulfate (SO_4^{2-}) and phosphate (PO_4^{3-}) counter anions [paired with octylammonium (OA^+)] were reported to form thin (<5 nm) $PbSO_4$ or $Pb_3(PO_4)_2$ layers on the OLHP surface, which effectively inhibited ion migration owing to the strong chemical binding with the surface (*95*). Elsewhere, trifluoroacetate (CF_3COO^-) as a counter anion was reported to interact more strongly with halide vacancies on the surface (*61*).

As discussed, it was traditionally believed that A cations do not directly participate in constructing the OLHP band-edge electronic structure. This notion has since been challenged by the use of bulky polycyclic pyrene-based ammonium cations, where the frontier orbital separation of the cations was lowered by electron delocalization in the π-conjugated pyrene tails (Fig. 5D) (*96*). This enabled the orbitals of pyrene-methylammonium and pyrene-ethylammonium to overlap the I 5p and Pb 6s band-edge orbitals to contribute electronic states to the valence-band maximum, which increased hole mobility at the surface. Future works might explore whether the conjugated cations may have distorted the PbX_6^{4-} octahedra differently, which could have contributed to altering the band dispersion.

Surface functionalization typically alters the OLHP energy-level alignment, which can beneficially promote carrier extraction by a contacting charge-selective layer. To maximize built-in potential, a pressure-assisted, solid-state growth strategy was reported by transfer from an as-grown $(BA)_2PbI_4$ template with annealing (*97*). The method was capable of growing a highly crystalline and phase-pure 2D $(BA)_2PbI_4$ layer on top of the 3D perovskite. Thickness control was demonstrated by simply changing the annealing temperature or by an iteration process. Conversely, different studies have reported the formation of either type I or type II band alignments for identical or similar A cation species (*92*, *97*–*100*). Further mechanistic studies are necessary to explain the conflicting results. One possibility may be related to varying A cation distribution and orientation at the surface, which shift the OLHP band energetics differently (*100*). Both type I or type II alignments beneficially repel electrons away from a hole-selective interface, but type I alignments may represent an extraction barrier for holes. Relatedly, the chain groups of bulky A cations are typically electrically insulating. This effect manifests where,

for example, with increasing alkylammonium chain length, the higher cation dipole moment enhances its interaction with traps to further reduce nonradiative recombination losses, but conversely, the longer insulating chain increases series resistance, which is detrimental for charge extraction (*99*, *101*). Likewise, it is often observed that with increasingly higher A cation surface density, the PSC open-circuit voltage typically increases monotonously but the fill factor peaks at an optimum concentration before subsequently decreasing as the insulating surface layer becomes too thick. It is therefore crucial to carefully design the A cation chain group and elucidate its density, distribution, and orientation on the OLHP surface to maximize its beneficial effects while ensuring that carrier extraction is not compromised.

Perspectives

The structural flexibility of OLHPs has enabled A cation engineering to be a versatile approach to tailor and improve the properties of OLHPs for different applications. Future opportunities can be generally categorized as discovering new uses for existing A cation species or identifying new A cations for existing applications.

The former category necessitates a more comprehensive understanding of the structure-interaction-property-performance-stability correlations conferred by A cations. A fundamental understanding of the atomistic and mechanistic origins of reported beneficial improvements conferred by A cation engineering is still lacking. This includes understanding the physicochemical interactions of A cations with the lattice constituents, band structure, and charge carriers, as well as their assembly, occupancy, and distribution within the OLHP layer. For instance, the correlation between the dynamic A cation motion and OLHP charge-carrier dynamics is still under debate. This understanding may enable the design of targeted A cation compositions for different device applications, such as solar cells, photodetectors, or light-emitting diodes. Also, the spontaneous expulsion and assembly of oversized cations along the surfaces and grain boundaries are poorly understood but crucial to understand because of the generally insulating nature of the organic side chains.

For the latter category, despite the increasing number of candidates of oversized and undersized cations, only a limited number of cations can be bulk-incorporated into the lattice A site, limiting compositional diversity. Considerable efforts during the early days of OLHP research were devoted to identifying cations for bulk occupancy, but these have essentially ceased. This is related to an absence of working selection and design rules. The ideal bulk A cation should be slightly smaller than FA^+ but free of the volatility issues of MA^+. Besides size considerations, chemical design principles also include polarity, stereochemistry, coordination, and bonding. The characteristic dynamic nature of organic A cations should also be taken into account. These criteria are also applicable to chain-group modification of bulky organic cations. Chemical design of the A cation must further be correlated with the structural and thermodynamic stability of the lattice and its binding and interaction with the ionic and defective constituents of OLHPs. Particularly, cation polarity has been investigated relatively less but profoundly influences ion migration (*67*), surface energy (*93*), trap passivation, and charge extraction (*99*, *101*). Machine-learning methodologies have been gaining traction in the community, which may prove useful for accelerated screening and discovery.

Relatedly, to date, ammonium-based species constitute most of the A cations applied to OLHPs. However, the protic (acidic) ammonium group is susceptible to deprotonation by hydrogen donation, rendering it chemically vulnerable to water and radical and basic species. Therefore, the environmental stability of ammonium species is inherently limited by their proticity, despite the presence of hydrophobic chain groups. In this regard, replacing ammoniums with their analogous, aprotic sulfonium cations may offer a solution because of their lower acidity. It will be necessary to understand the likely different formability and interactions of sulfonium cations with the OLHP constituents and processing solvents, in consideration of the different polarity between sulfoniums and their ammonium counterparts.

More generally, for OLHP optoelectronics to achieve market readiness, the challenge should now be focused on addressing their long-term operational instability issues, which remain far short of the acceptable lifetime guarantees of commercial products. Engineering of A cations has contributed immensely to the stabilization improvements to date, but further progress is required. Reducing the device-to-module upscaling gap of OLHP technology is another crucial hurdle, and it is necessary to investigate the application and adaptability of A cation engineering strategies at the module scale. It is also important to investigate the applicability of Pb-based A cation engineering strategies when extending toward Sn or Pb-Sn stoichiometries, which are attractive for tandem applications or to reduce toxic Pb usage. There is still much work left to be done, and it will be important to fully understand the role and contribution of the A cation.

REFERENCES AND NOTES

1. H.-S. Kim *et al*., Lead iodide perovskite sensitized all-solid-state submicron thin film mesoscopic solar cell with efficiency exceeding 9%. *Sci. Rep.* **2**, 591 (2012). doi: 10.1038/srep00591; pmid: 22912919
2. J.-H. Im, C.-R. Lee, J.-W. Lee, S.-W. Park, N.-G. Park, 6.5% efficient perovskite quantum-dot-sensitized solar cell. *Nanoscale* **3**, 4088–4093 (2011). doi: 10.1039/c1nr10867k; pmid: 21897986
3. J. Y. Kim, J.-W. Lee, H. S. Jung, H. Shin, N.-G. Park, High-efficiency perovskite solar cells. *Chem. Rev.* **120**, 7867–7918 (2020). doi: 10.1021/acs.chemrev.0c00107; pmid: 32786671
4. S. Tao *et al*., Absolute energy level positions in tin- and lead-based halide perovskites. *Nat. Commun.* **10**, 2560 (2019). doi: 10.1038/s41467-019-10468-7; pmid: 31189871
5. K. L. Svane *et al*., How strong is the hydrogen bond in hybrid perovskites? *J. Phys. Chem. Lett.* **8**, 6154–6159 (2017). doi: 10.1021/acs.jpclett.7b03106; pmid: 29216715
6. A. M. Leguy *et al*., The dynamics of methylammonium ions in hybrid organic–inorganic perovskite solar cells. *Nat. Commun.* **6**, 7124 (2015). doi: 10.1038/ncomms8124; pmid: 26023041
7. H. Zhu *et al*., Screening in crystalline liquids protects energetic carriers in hybrid perovskites. *Science* **353**, 1409–1413 (2016). doi: 10.1126/science.aaf9570; pmid: 27708033
8. A. A. Bakulin *et al*., Real-time observation of organic cation reorientation in methylammonium lead iodide perovskites. *J. Phys. Chem. Lett.* **6**, 3663–3669 (2015). doi: 10.1021/acs.jpclett.5b01555; pmid: 26722739
9. F. Brivio *et al*., Lattice dynamics and vibrational spectra of the orthorhombic, tetragonal, and cubic phases of methylammonium lead iodide. *Phys. Rev. B* **92**, 144308 (2015). doi: 10.1103/PhysRevB.92.144308
10. J.-W. Lee *et al*., Dynamic structural property of organic-inorganic metal halide perovskite. *iScience* **24**, 101959 (2020). doi: 10.1016/j.isci.2020.101959; pmid: 33437939
11. B. Yang *et al*., Real-time observation of order-disorder transformation of organic cations induced phase transition and anomalous photoluminescence in hybrid perovskites. *Adv. Mater.* **30**, e1705801 (2018). doi: 10.1002/adma.201705801; pmid: 29660765
12. T. Chen *et al*., Entropy-driven structural transition and kinetic trapping in formamidinium lead iodide perovskite. *Sci. Adv.* **2**, e1601650 (2016). doi: 10.1126/sciadv.1601650; pmid: 27819055
13. G. Kieslich, S. Sun, A. K. Cheetham, Solid-state principles applied to organic–inorganic perovskites: New tricks for an old dog. *Chem. Sci.* **5**, 4712–4715 (2014). doi: 10.1039/C4SC02211D
14. S. Gholipour *et al*., Globularity-selected large molecules for a new generation of multication perovskites. *Adv. Mater.* **29**, 1702005 (2017). doi: 10.1002/adma.201702005; pmid: 28833614
15. J. H. Noh, S. H. Im, J. H. Heo, T. N. Mandal, S. I. Seok, Chemical management for colorful, efficient, and stable inorganic-organic hybrid nanostructured solar cells. *Nano Lett.* **13**, 1764–1769 (2013). doi: 10.1021/nl400349b; pmid: 23517331
16. W. Rehman *et al*., Charge-carrier dynamics and mobilities in formamidinium lead mixed-halide perovskites. *Adv. Mater.* **27**, 7938–7944 (2015). doi: 10.1002/adma.201502969; pmid: 26402226
17. L. M. Herz, Charge-carrier mobilities in metal halide perovskites: Fundamental mechanisms and limits. *ACS Energy Lett.* **2**, 1539–1548 (2017). doi: 10.1021/acsenergylett.7b00276
18. D. P. McMeekin *et al*., A mixed-cation lead mixed-halide perovskite absorber for tandem solar cells. *Science* **351**, 151–155 (2016). doi: 10.1126/science.aad5845; pmid: 26744401
19. N. J. Jeon *et al*., Compositional engineering of perovskite materials for high-performance solar cells. *Nature* **517**, 476–480 (2015). doi: 10.1038/nature14133; pmid: 25561177
20. A. Al-Ashouri *et al*., Monolithic perovskite/silicon tandem solar cell with >29% efficiency by enhanced hole extraction. *Science* **370**, 1300–1309 (2020). doi: 10.1126/science.abd4016; pmid: 33303611
21. D. Kim *et al*., Efficient, stable silicon tandem cells enabled by anion-engineered wide-bandgap perovskites. *Science* **368**, 155–160 (2020). doi: 10.1126/science.aba3433; pmid: 32217753
22. G. E. Eperon *et al*., Perovskite-perovskite tandem photovoltaics with optimized band gaps. *Science* **354**, 861–865 (2016). doi: 10.1126/science.aaf9717; pmid: 27856902

23. D. J. Slotcavage, H. I. Karunadasa, M. D. McGehee, Light-induced phase segregation in halide-perovskite absorbers. *ACS Energy Lett.* **1**, 1199–1205 (2016). doi: 10.1021/acsenergylett.6b00495
24. X. Chang *et al*., Printable $CsPbI_3$ perovskite solar cells with PCE of 19% via an additive strategy. *Adv. Mater.* **32**, e2001243 (2020). doi: 10.1002/adma.202001243; pmid: 32864773
25. Y. Wang *et al*., Thermodynamically stabilized β-$CsPbI_3$-based perovskite solar cells with efficiencies >18. *Science* **365**, 591–595 (2019). doi: 10.1126/science.aav8680; pmid: 31395783
26. H. Tsai *et al*., High-efficiency two-dimensional Ruddlesden-Popper perovskite solar cells. *Nature* **536**, 312–316 (2016). doi: 10.1038/nature18306; pmid: 27383783
27. L. N. Quan *et al*., Ligand-stabilized reduced-dimensionality perovskites. *J. Am. Chem. Soc.* **138**, 2649–2655 (2016). doi: 10.1021/jacs.5b11740; pmid: 26841130
28. C. Liang *et al*., Two-dimensional Ruddlesden–Popper layered perovskite solar cells based on phase-pure thin films. *Nat. Energy* **6**, 38–45 (2021). doi: 10.1038/s41560-020-00721-5
29. F. Wang *et al*., Solvated electrons in solids—Ferroelectric large polarons in lead halide perovskites. *J. Am. Chem. Soc.* **143**, 5–16 (2021). doi: 10.1021/jacs.0c10943; pmid: 33320656
30. X. Y. Zhu, V. Podzorov, Charge carriers in hybrid organic-inorganic lead halide perovskites might be protected as large polarons. *J. Phys. Chem. Lett.* **6**, 4758–4761 (2015). doi: 10.1021/acs.jpclett.5b02462; pmid: 26575427
31. N. Balkan, *Hot Electrons In Semiconductors: Physics and Devices* (Oxford Univ. Press, 1998).
32. J. Chen, M. E. Messing, K. Zheng, T. Pullerits, Cation-dependent hot carrier cooling in halide perovskite nanocrystals. *J. Am. Chem. Soc.* **141**, 3532–3540 (2019). doi: 10.1021/jacs.8b11867; pmid: 30685969
33. H. Zhu *et al*., Organic cations might not be essential to the remarkable properties of band edge carriers in lead halide perovskites. *Adv. Mater.* **29**, 1603072 (2017). doi: 10.1002/adma.201603072; pmid: 27792264
34. G. E. Eperon *et al*., Formamidinium lead trihalide: A broadly tunable perovskite for efficient planar heterojunction solar cells. *Energy Environ. Sci.* **7**, 982–988 (2014). doi: 10.1039/c3ee43822h
35. G. Xing *et al*., Long-range balanced electron- and hole-transport lengths in organic-inorganic $CH_3NH_3PbI_3$. *Science* **342**, 344–347 (2013). doi: 10.1126/science.1243167; pmid: 24136965
36. D. J. Kubicki *et al*., Formation of stable mixed guanidinium–methylammonium phases with exceptionally long carrier lifetimes for high-efficiency lead iodide-based perovskite photovoltaics. *J. Am. Chem. Soc.* **140**, 3345–3351 (2018). doi: 10.1021/jacs.7b12860; pmid: 29429335
37. T. Chen *et al*., Origin of long lifetime of band-edge charge carriers in organic-inorganic lead iodide perovskites. *Proc. Natl. Acad. Sci. U.S.A.* **114**, 7519–7524 (2017). doi: 10.1073/pnas.1704421114; pmid: 28673975
38. F. Ambrosio, D. Meggiolaro, E. Mosconi, F. De Angelis, Charge localization, stabilization, and hopping in lead halide perovskites: Competition between polaron stabilization and cation disorder. *ACS Energy Lett.* **4**, 2013–2020 (2019). doi: 10.1021/acsenergylett.9b01353
39. A. Binek, F. C. Hanusch, P. Docampo, T. Bein, Stabilization of the trigonal high-temperature phase of formamidinium lead iodide. *J. Phys. Chem. Lett.* **6**, 1249–1253 (2015). doi: 10.1021/acs.jpclett.5b00380; pmid: 26262982
40. A. Amat *et al*., Cation-induced band-gap tuning in organohalide perovskites: Interplay of spin-orbit coupling and octahedra tilting. *Nano Lett.* **14**, 3608–3616 (2014). doi: 10.1021/nl5012992; pmid: 24797342
41. J. W. Lee *et al*., Formamidinium and cesium hybridization for photo-and moisture-stable perovskite solar cell. *Adv. Energy Mater.* **5**, 1501310 (2015). doi: 10.1002/aenm.201501310
42. Z. Li *et al*., Stabilizing perovskite structures by tuning tolerance factor: Formation of formamidinium and cesium lead iodide solid-state alloys. *Chem. Mater.* **28**, 284–292 (2016). doi: 10.1021/acs.chemmater.5b04107
43. Y. H. Park *et al*., Inorganic rubidium cation as an enhancer for photovoltaic performance and moisture stability of $HC(NH_2)_2PbI_3$ perovskite solar cells. *Adv. Funct. Mater.* **27**, 1605988 (2017). doi: 10.1002/adfm.201605988
44. C. Yi *et al*., Entropic stabilization of mixed A-cation ABX_3 metal halide perovskites for high performance perovskite solar cells. *Energy Environ. Sci.* **9**, 656–662 (2016). doi: 10.1039/C5EE03255E
45. M. Saliba *et al*., Cesium-containing triple cation perovskite solar cells: Improved stability, reproducibility and high efficiency. *Energy Environ. Sci.* **9**, 1989–1997 (2016). doi: 10.1039/C5EE03874J; pmid: 27478500
46. M. Saliba *et al*., Incorporation of rubidium cations into perovskite solar cells improves photovoltaic performance. *Science* **354**, 206–209 (2016). doi: 10.1126/science.aah5557; pmid: 27708053
47. Z. Wang *et al*., Additive-modulated evolution of $HC(NH_2)_2PbI_3$ black polymorph for mesoscopic perovskite solar cells. *Chem. Mater.* **27**, 7149–7155 (2015). doi: 10.1021/acs.chemmater.5b03169
48. M. Kim *et al*., Methylammonium chloride induces intermediate phase stabilization for efficient perovskite solar cells. *Joule* **3**, 2179–2192 (2019). doi: 10.1016/j.joule.2019.06.014
49. J. Jeong *et al*., Pseudo-halide anion engineering for α-$FAPbI_3$ perovskite solar cells. *Nature* **592**, 381–385 (2021). doi: 10.1038/s41586-021-03406-5; pmid: 33820983
50. H. Min *et al*., Efficient, stable solar cells by using inherent bandgap of α-phase formamidinium lead iodide. *Science* **366**, 749–753 (2019). doi: 10.1126/science.aay7044; pmid: 31699938
51. G. Kim *et al*., Impact of strain relaxation on performance of α-formamidinium lead iodide perovskite solar cells. *Science* **370**, 108–112 (2020). doi: 10.1126/science.abc4417; pmid: 33004518
52. I. S. Yang, N. G. Park, Dual additive for simultaneous improvement of photovoltaic performance and stability of perovskite solar cell. *Adv. Funct. Mater.* **31**, 2100396 (2021). doi: 10.1002/adfm.202100396
53. H. Lu *et al*., Vapor-assisted deposition of highly efficient, stable black-phase $FAPbI_3$ perovskite solar cells. *Science* **370**, eabb8985 (2020). doi: 10.1126/science.abb8985; pmid: 33004488
54. A. Swarnkar *et al*., Quantum dot-induced phase stabilization of α-$CsPbI_3$ perovskite for high-efficiency photovoltaics. *Science* **354**, 92–95 (2016). doi: 10.1126/science.aag2700; pmid: 27846497
55. J. Xue *et al*., Surface ligand management for stable $FAPbI_3$ perovskite quantum dot solar cells. *Joule* **2**, 1866–1878 (2018). doi: 10.1016/j.joule.2018.07.018
56. Y. Fu *et al*., Stabilization of the metastable lead iodide perovskite phase via surface functionalization. *Nano Lett.* **17**, 4405–4414 (2017). doi: 10.1021/acs.nanolett.7b01500; pmid: 28595016
57. J.-W. Lee *et al*., 2D perovskite stabilized phase-pure formamidinium perovskite solar cells. *Nat. Commun.* **9**, 3021 (2018). doi: 10.1038/s41467-018-05454-4; pmid: 30069012
58. B. Park *et al*., Stabilization of formamidinium lead triiodide α-phase with isopropylammonium chloride for perovskite solar cells. *Nat. Energy* **6**, 419–428 (2021). doi: 10.1038/s41560-021-00802-z
59. S.-G. Kim *et al*., How antisolvent miscibility affects perovskite film wrinkling and photovoltaic properties. *Nat. Commun.* **12**, 1554 (2021). doi: 10.1038/s41467-021-21803-2; pmid: 33692346
60. J.-W. Lee *et al*., Solid-phase hetero epitaxial growth of α-phase formamidinium perovskite. *Nat. Commun.* **11**, 5514 (2020). doi: 10.1038/s41467-020-19237-3; pmid: 33139740
61. S. Tan *et al*., Shallow iodine defects accelerate the degradation of α-phase formamidinium perovskite. *Joule* **4**, 2426–2442 (2020). doi: 10.1016/j.joule.2020.08.016
62. S. Tan *et al*., Steric impediment of ion migration contributes to improved operational stability of perovskite solar cells. *Adv. Mater.* **32**, e1906995 (2020). doi: 10.1002/adma.201906995; pmid: 32017283
63. J. Zhao *et al*., Strained hybrid perovskite thin films and their impact on the intrinsic stability of perovskite solar cells. *Sci. Adv.* **3**, eaao5616 (2017). doi: 10.1126/sciadv.aao5616; pmid: 29159287
64. M. I. Saidaminov *et al*., Suppression of atomic vacancies via incorporation of isovalent small ions to increase the stability of halide perovskite solar cells in ambient air. *Nat. Energy* **3**, 648–654 (2018). doi: 10.1038/s41560-018-0192-2
65. J. P. Correa-Baena *et al*., Homogenized halides and alkali cation segregation in alloyed organic-inorganic perovskites. *Science* **363**, 627–631 (2019). doi: 10.1126/science.aah5065; pmid: 30733417
66. A. D. Jodlowski *et al*., Large guanidinium cation mixed with methylammonium in lead iodide perovskites for 19% efficient solar cells. *Nat. Energy* **2**, 972–979 (2017). doi: 10.1038/s41560-017-0054-3
67. E. Mosconi, F. De Angelis, Mobile ions in organohalide perovskites: Interplay of electronic structure and dynamics. *ACS Energy Lett.* **1**, 182–188 (2016). doi: 10.1021/acsenergylett.6b00108
68. M. Abdi-Jalebi *et al*., Maximizing and stabilizing luminescence from halide perovskites with potassium passivation. *Nature* **555**, 497–501 (2018). doi: 10.1038/nature25989; pmid: 29565365
69. L. Qiao, W. H. Fang, R. Long, O. V. Prezhdo, Extending carrier lifetimes in lead halide perovskites with alkali metals by passivating and eliminating halide interstitial defects. *Angew. Chem. Int. Ed.* **59**, 4684–4690 (2020). doi: 10.1002/ange.201911615; pmid: 31873979
70. D. Y. Son *et al*., Universal approach toward hysteresis-free perovskite solar cell via defect engineering. *J. Am. Chem. Soc.* **140**, 1358–1364 (2018). doi: 10.1021/jacs.7b10430; pmid: 29300468
71. J. Cao, S. X. Tao, P. A. Bobbert, C. P. Wong, N. Zhao, Interstitial occupancy by extrinsic alkali cations in perovskites and its impact on ion migration. *Adv. Mater.* **30**, e1707350 (2018). doi: 10.1002/adma.201707350; pmid: 29736912
72. N. X. Li *et al*., Cation and anion immobilization through chemical bonding enhancement with fluorides for stable halide perovskite solar cells. *Nat. Energy* **4**, 408–415 (2019). doi: 10.1038/s41560-019-0382-6
73. D. J. Kubicki *et al*., Phase segregation in Cs-, Rb- and K-doped mixed-cation $(MA)_x(FA)_{1-x}PbI_3$ hybrid perovskites from solid-state NMR. *J. Am. Chem. Soc.* **139**, 14173–14180 (2017). doi: 10.1021/jacs.7b07223; pmid: 28892374
74. Y. El Ajjouri, V. S. Chirvony, M. Sessolo, F. Palazon, H. J. Bolink, Incorporation of potassium halides in the mechanosynthesis of inorganic perovskites: Feasibility and limitations of ion-replacement and trap passivation. *RSC Advances* **8**, 41548–41551 (2018). doi: 10.1039/C8RA08823C
75. S.-G. Kim *et al*., Potassium ions as a kinetic controller in ionic double layers for hysteresis-free perovskite solar cells. *J. Mater. Chem. A Mater. Energy Sustain.* **7**, 18807–18815 (2019). doi: 10.1039/C9TA07595J
76. Z. P. Wang *et al*., Efficient ambient-air-stable solar cells with 2D-3D heterostructured butylammonium-caesium-formamidinium lead halide perovskites. *Nat. Energy* **2**, 17135 (2017). doi: 10.1038/nenergy.2017.135
77. J. Chen, D. Lee, N.-G. Park, Stabilizing the Ag electrode and reducing *J–V* hysteresis through suppression of iodide migration in perovskite solar cells. *ACS Appl. Mater. Interfaces* **9**, 36338–36349 (2017). doi: 10.1021/acsami.7b07595; pmid: 28952714
78. A. Y. Mei *et al*., Stabilizing perovskite solar cells to IEC61215:2016 standards with over 9,000-h operational tracking. *Joule* **4**, 2646–2660 (2020). doi: 10.1016/j.joule.2020.09.010
79. G. Grancini *et al*., One-year stable perovskite solar cells by 2D/3D interface engineering. *Nat. Commun.* **8**, 15684 (2017). doi: 10.1038/ncomms15684; pmid: 28569749
80. S. Bai *et al*., Planar perovskite solar cells with long-term stability using ionic liquid additives. *Nature* **571**, 245–250 (2019). doi: 10.1038/s41586-019-1357-2; pmid: 31292555
81. Y. H. Lin *et al*., A piperidinium salt stabilizes efficient metal-halide perovskite solar cells. *Science* **369**, 96–102 (2020). doi: 10.1126/science.aba1628; pmid: 32631893
82. C. Eames *et al*., Ionic transport in hybrid lead iodide perovskite solar cells. *Nat. Commun.* **6**, 7497 (2015). doi: 10.1038/ncomms8497; pmid: 26105623
83. K. T. Cho *et al*., Highly efficient perovskite solar cells with a compositionally engineered perovskite/hole transporting material interface. *Energy Environ. Sci.* **10**, 621–627 (2017). doi: 10.1039/C6EE03182J
84. D. Luo *et al*., Enhanced photovoltage for inverted planar heterojunction perovskite solar cells. *Science* **360**, 1442–1446 (2018). doi: 10.1126/science.aap9282;pmid: 29954975
85. S. Tan *et al*., Surface reconstruction of halide perovskites during post-treatment. *J. Am. Chem. Soc.* **143**, 6781–6786 (2021). doi: 10.1021/jacs.1c00757; pmid: 33915050
86. Z. Ni *et al*., Resolving spatial and energetic distributions of trap states in metal halide perovskite solar cells. *Science* **367**, 1352–1358 (2020). doi: 10.1126/science.aba0893; pmid: 32193323
87. Q. Jiang *et al*., Surface passivation of perovskite film for efficient solar cells. *Nat. Photonics* **13**, 460–466 (2019). doi: 10.1038/s41566-019-0398-2; pmid: 33416305

88. H. Zhu *et al*., Tailored amphiphilic molecular mitigators for stable perovskite solar cells with 23.5% efficiency. *Adv. Mater.* **32**, e1907757 (2020). doi: 10.1002/adma.201907757; pmid: 32068922
89. X. P. Zheng *et al*., Defect passivation in hybrid perovskite solar cells using quaternary ammonium halide anions and cations. *Nat. Energy* **2**, 17102 (2017). doi: 10.1038/nenergy.2017.102
90. S. Yang *et al*., Functionalization of perovskite thin films with moisture-tolerant molecules. *Nat. Energy* **1**, 15016 (2016). doi: 10.1038/nenergy.2015.16
91. Y. Liu *et al*., Ultrahydrophobic 3D/2D fluoroarene bilayer-based water-resistant perovskite solar cells with efficiencies exceeding 22. *Sci. Adv.* **5**, eaaw2543 (2019). doi: 10.1126/sciadv.aaw2543; pmid: 31187060
92. E. H. Jung *et al*., Efficient, stable and scalable perovskite solar cells using poly(3-hexylthiophene). *Nature* **567**, 511–515 (2019). doi: 10.1038/s41586-019-1036-3; pmid: 30918371
93. J. Xue *et al*., Crystalline liquid-like behavior: Surface-induced secondary grain growth of photovoltaic perovskite thin film. *J. Am. Chem. Soc.* **141**, 13948–13953 (2019). doi: 10.1021/jacs.9b06940; pmid: 31403287
94. M. Yang *et al*., Facile fabrication of large-grain $CH_3NH_3PbI_{3-x}Br_x$ films for high-efficiency solar cells via CH_3NH_3Br-selective Ostwald ripening. *Nat. Commun.* **7**, 12305 (2016). doi: 10.1038/ncomms12305; pmid: 27477212
95. S. Yang *et al*., Stabilizing halide perovskite surfaces for solar cell operation with wide-bandgap lead oxysalts. *Science* **365**, 473–478 (2019). doi: 10.1126/science.aax3294; pmid: 31371610
96. J. Xue *et al*., Reconfiguring the band-edge states of photovoltaic perovskites by conjugated organic cations. *Science* **371**, 636–640 (2021). doi: 10.1126/science.abd4860; pmid: 33542138
97. Y. W. Jang *et al*., Intact 2D/3D halide junction perovskite solar cells via solid-phase in-plane growth. *Nat. Energy* **6**, 63–71 (2021). doi: 10.1038/s41560-020-00749-7
98. K. T. Cho *et al*., Selective growth of layered perovskites for stable and efficient photovoltaics. *Energy Environ. Sci.* **11**, 952–959 (2018). doi: 10.1039/C7EE03513F
99. J. J. Yoo *et al*., An interface stabilized perovskite solar cell with high stabilized efficiency and low voltage loss. *Energy Environ. Sci.* **12**, 2192–2199 (2019). doi: 10.1039/C9EE00751B
100. R. Quintero-Bermudez *et al*., Ligand-induced surface charge density modulation generates local type-II band alignment in reduced-dimensional perovskites. *J. Am. Chem. Soc.* **141**, 13459–13467 (2019). doi: 10.1021/jacs.9b04801; pmid: 31366193
101. H. Kim *et al*., Optimal interfacial engineering with different length of alkylammonium halide for efficient and stable perovskite solar cells. *Adv. Energy Mater.* **9**, 1902740 (2019). doi: 10.1002/aenm.201902740
102. A. Kojima, K. Teshima, Y. Shirai, T. Miyasaka, Organometal halide perovskites as visible-light sensitizers for photovoltaic cells. *J. Am. Chem. Soc.* **131**, 6050–6051 (2009). doi: 10.1021/ja809598r; pmid: 19366264
103. M. M. Lee, J. Teuscher, T. Miyasaka, T. N. Murakami, H. J. Snaith, Efficient hybrid solar cells based on meso-superstructured organometal halide perovskites. *Science* **338**, 643–647 (2012). doi: 10.1126/science.1228604; pmid: 23042296
104. J. H. Heo *et al*., Efficient inorganic–organic hybrid heterojunction solar cells containing perovskite compound and polymeric hole conductors. *Nat. Photonics* **7**, 486–491 (2013). doi: 10.1038/nphoton.2013.80
105. J. Burschka *et al*., Sequential deposition as a route to high-performance perovskite-sensitized solar cells. *Nature* **499**, 316–319 (2013). doi: 10.1038/nature12340; pmid: 23842493
106. W. S. Yang *et al*., High-performance photovoltaic perovskite layers fabricated through intramolecular exchange. *Science* **348**, 1234–1237 (2015). doi: 10.1126/science.aaa9272; pmid: 25999372
107. W. S. Yang *et al*., Iodide management in formamidinium-lead-halide-based perovskite layers for efficient solar cells. *Science* **356**, 1376–1379 (2017). doi: 10.1126/science.aan2301; pmid: 28663498
108. N. J. Jeon *et al*., A fluorene-terminated hole-transporting material for highly efficient and stable perovskite solar cells. *Nat. Energy* **3**, 682–689 (2018). doi: 10.1038/s41560-018-0200-6
109. J. J. Yoo *et al*., Efficient perovskite solar cells via improved carrier management. *Nature* **590**, 587–593 (2021). doi: 10.1038/s41586-021-03285-w; pmid: 33627807
110. H. Min *et al*., Perovskite solar cells with atomically coherent interlayers on SnO_2 electrodes. *Nature* **598**, 444–450 (2021). doi: 10.1038/s41586-021-03964-8; pmid: 34671136
111. D. W. Ferdani *et al*., Partial cation substitution reduces iodide ion transport in lead iodide perovskite solar cells. *Energy Environ. Sci.* **12**, 2264–2272 (2019). doi: 10.1039/C9EE00476A
112. X. Zheng *et al*., Managing grains and interfaces via ligand anchoring enables 22.3%-efficiency inverted perovskite solar cells. *Nat. Energy* **5**, 131–140 (2020). doi: 10.1038/s41560-019-0538-4
113. K. H. Ngai *et al*., Enhanced electrochemical stability by alkyldiammonium in Dion–Jacobson perovskite toward ultrastable light-emitting diodes. *Adv. Opt. Mater.* **9**, 2100243 (2020). doi: 10.1002/adom.202100243
114. M. Saliba *et al*., Incorporation of rubidium cations into perovskite solar cells improves photovoltaic performance. *Science* **354**, 206–209 (2016). doi: 10.1126/science.aah5557; pmid: 27708053
115. M. Jeong *et al*., Stable perovskite solar cells with efficiency exceeding 24.8% and 0.3-V voltage loss. *Science* **369**, 1615–1620 (2020). doi: 10.1126/science.abb7167; pmid: 32973026

ACKNOWLEDGMENTS

Funding: This work was supported by a Korea Institute of Energy Technology Evaluation and Planning (KETEP) grant funded by the Korean government (MOTIE) under award numbers 20213030010400 and 20214000000640 (J.-W.L.); by National Research Foundation of Korea grants NRF-2018R1A3B1052820 (S.I.S.) and NRF-2021R1A3B1076723 (N.-G.P.); and by the US Department of Energy's Office of Energy Efficiency and Renewable Energy (EERE) under the Solar Energy Technologies Office under award number DE-EE0008751 (S.T. and Y.Y.) **Competing interests:** The authors declare that they have no competing interests.

10.1126/science.abj1186

RESEARCH ARTICLE SUMMARY

HUMAN EVOLUTION

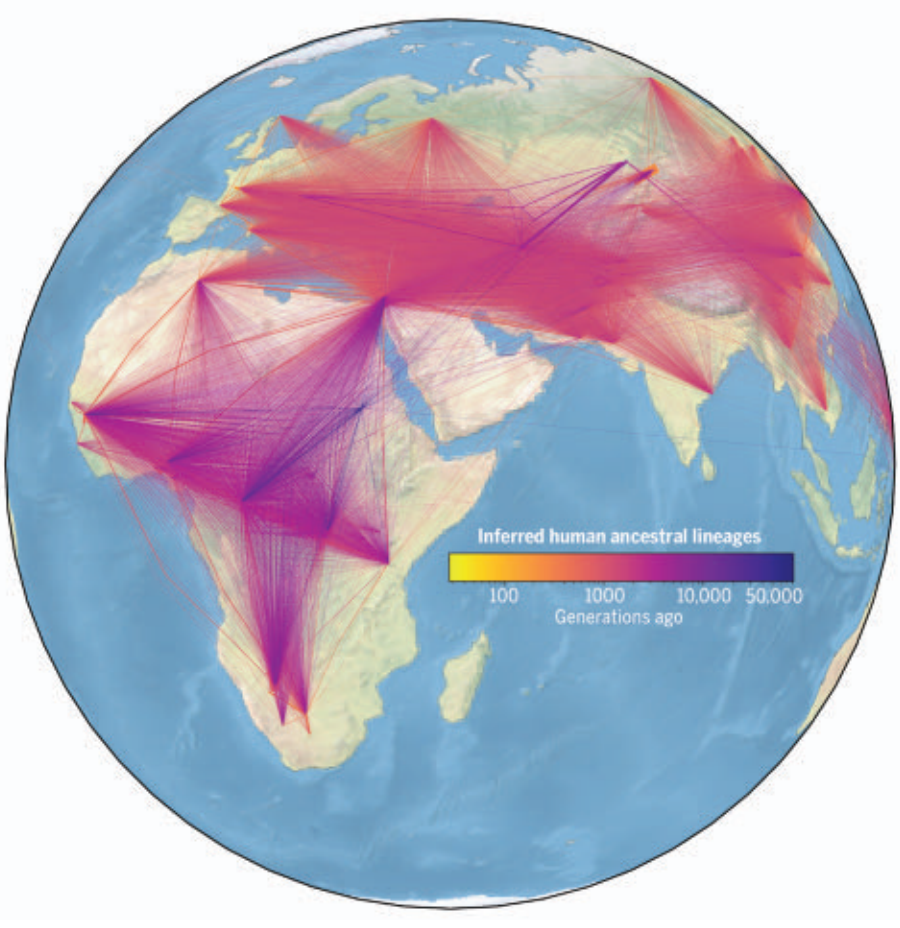
A unified genealogy of modern and ancient genomes

Anthony Wilder Wohns, Yan Wong†, Ben Jeffery, Ali Akbari, Swapan Mallick, Ron Pinhasi, Nick Patterson, David Reich, Jerome Kelleher†, Gil McVean*†

INTRODUCTION: The characterization of modern and ancient human genome sequences has revealed previously unknown features of our evolutionary past. As genome data generation continues to accelerate—through the sequencing of population-scale biobanks and ancient samples from around the world—so does the potential to generate an increasingly detailed understanding of how populations have evolved.

However, such genomic datasets are highly heterogeneous. Samples from diverse times, geographic locations, and populations are processed, sequenced, and analyzed using a variety of techniques. The resulting datasets contain genuine variation but also complex patterns of missingness and error. This makes combining data challenging and hinders efforts to generate the most complete picture of human genomic variation.

RATIONALE: To address these challenges, we use the foundational notion that the ancestral relationships of all humans who have ever lived can be described by a single genealogy or tree sequence, so named because it encodes the sequence of trees that link individuals to one another at every point in the genome. This tree sequence of humanity is immensely complex, but estimates of the structure are a powerful means of integrating diverse datasets and gaining greater insights into human genetic diversity. In this work, we introduce statistical and computational methods to infer such a unified genealogy of modern and ancient samples, validate the methods through a mixture of computer simulation and analysis of empirical data, and apply the methods to reveal features of human diversity and evolution.



Visualizing inferred human ancestral lineages over time and space. Each line represents an ancestor-descendant relationship in our inferred genealogy of modern and ancient genomes. The width of a line corresponds to how many times the relationship is observed, and lines are colored on the basis of the estimated age of the ancestor.

RESULTS: We present a unified tree sequence of 3601 modern and eight high-coverage ancient human genome sequences compiled from eight datasets. This structure is a lossless and compact representation of 27 million ancestral haplotype fragments and 231 million ancestral lineages linking genomes from these datasets back in time. The tree sequence also benefits from the use of an additional 3589 ancient samples compiled from more than 100 publications to constrain and date relationships.

Using simulations and empirical analyses, we demonstrate the ability to recover relationships between individuals and populations as well as to identify descendants of ancient samples. We calculate the distribution of the time to most recent common ancestry between the 215 populations of the constituent datasets, revealing patterns consistent with substantial variation in historical population size and evidence of archaic admixture in modern humans.

The tree sequence also offers insight into patterns of recurrent mutation and sequencing error in commonly used genetic datasets. We find pervasive signals of sequencing error as well as a small subset of variant sites that appear to be erroneous.

Finally, we introduce an estimator of ancestor geographic location that recapitulates key features of human history. We observe signals of very deep ancestral lineages in Africa, the out-of-Africa event, and archaic introgression in Oceania. The method motivates improved spatiotemporal inference methods that will better elucidate the paths and timings of historic migrations.

CONCLUSION: The profusion of genetic sequencing data creates challenges for integrating diverse data sources. Our results demonstrate that whole-genome genealogies provide a powerful platform for synthesizing genetic data and investigating human history and evolution. ■

The list of author affiliations is available in the full article online.
*Corresponding author. Email: gil.mcvean@bdi.ox.ac.uk
†These authors contributed equally to this work.
Cite this article as A. W. Wohns *et al.*, *Science* **375**, eabi8264 (2022). DOI: 10.1126/science.abi8264

READ THE FULL ARTICLE AT
https://doi.org/10.1126/science.abi8264

RESEARCH ARTICLE

HUMAN EVOLUTION

A unified genealogy of modern and ancient genomes

Anthony Wilder Wohns[1,2], Yan Wong[2]†, Ben Jeffery[2], Ali Akbari[1,3,4], Swapan Mallick[1,5], Ron Pinhasi[6], Nick Patterson[1,3,4,5], David Reich[1,3,4,5], Jerome Kelleher[2]†, Gil McVean[2]*†

The sequencing of modern and ancient genomes from around the world has revolutionized our understanding of human history and evolution. However, the problem of how best to characterize ancestral relationships from the totality of human genomic variation remains unsolved. Here, we address this challenge with nonparametric methods that enable us to infer a unified genealogy of modern and ancient humans. This compact representation of multiple datasets explores the challenges of missing and erroneous data and uses ancient samples to constrain and date relationships. We demonstrate the power of the method to recover relationships between individuals and populations as well as to identify descendants of ancient samples. Finally, we introduce a simple nonparametric estimator of the geographical location of ancestors that recapitulates key events in human history.

Our ability to determine relationships among individuals, populations, and species is being transformed by population-scale biobanks of medical samples (*1*, *2*), collections of thousands of ancient genomes (*3*), and efforts to sequence millions of eukaryotic species for comparative genomic analyses (*4*). Such relationships, and the resulting distributions of genetic and phenotypic variation, reflect the complex set of selective, demographic, and molecular processes and events that have shaped species such as our own (*5*–*8*).

However, learning about evolutionary events and processes from the totality of genomic variation, in humans or other species, is challenging. Combining information from multiple datasets, even within a species, is technically demanding: Discrepancies between cohorts due to error (*9*), differing sequencing techniques (*10*, *11*), and variant processing (*12*) can lead to noise that can easily obscure genuine signal. Furthermore, few tools can cope with the vast datasets that arise from the combination of multiple sources (*13*). Also, statistical analysis typically relies on data-reduction techniques (*14*, *15*) or the fitting of parametric models (*16*–*19*), which may provide an incomplete picture of the complexities of evolutionary history. Finally, data access and governance restrictions often limit the ability to combine data sources (*20*).

[1]Broad Institute of MIT and Harvard, Cambridge, MA 02142, USA. [2]Big Data Institute, Li Ka Shing Centre for Health Information and Discovery, University of Oxford, Oxford OX3 7LF, UK. [3]Department of Human Evolutionary Biology, Harvard University, Cambridge, MA 02138, USA. [4]Department of Genetics, Harvard Medical School, Boston, MA 02115, USA. [5]Howard Hughes Medical Institute, Harvard Medical School, Boston, MA 02115, USA. [6]Department of Evolutionary Anthropology, University of Vienna, 1090 Vienna, Austria.
*Corresponding author. Email: gil.mcvean@bdi.ox.ac.uk
†These authors contributed equally to this work.

The succinct tree sequence data structure provides a potential solution to many of these problems (*13*, *21*). Tree sequences extend the fundamental concept of a phylogenetic tree to multiple correlated trees along the genome, which is necessary when considering genealogies within recombining organisms (*22*). Notably, the tree sequence and the mapping of mutation events to it reflects the totality of what is knowable about genealogical relationships and the evolutionary history of individual variants. A tree sequence is defined as a graph with a set of nodes representing sampled chromosomes and ancestral haplotypes, edges connecting nodes representing lines of descent, and variable sites containing one or more mutations mapped onto the edges (Fig. 1A). Recombination events in the ancestral history of the sample create different edges and thus distinct but highly correlated trees along the genome. Tree sequences can not only be used to compress genetic data (*13*) but also lead to highly efficient algorithms for calculating population genetic statistics (*23*).

A unified genealogy of modern and ancient human genomes

Here, we introduce, validate, and apply nonparametric methods for inferring time-resolved tree sequences from multiple heterogeneous sources to efficiently infer a single, unified tree sequence of ancient and contemporary human genomes. Although humans are the focus of this study, the methods and approaches we introduce are valid for most recombining organisms.

To generate a unified genealogy of modern and ancient human genomes, we integrated data from three modern datasets: the 1000 Genomes Project (TGP), which contains 2548 sequenced individuals from 26 populations (*6*); the Human Genome Diversity Project (HGDP), which consists of 929 sequenced individuals from 54 populations (*8*); and the Simons Genome Diversity Project (SGDP), with 278 sequenced individuals from 142 populations (*7*). In total, 154 individuals appear in more than one of these datasets (*24*). Additionally, we included data from three high-coverage sequenced Neanderthal genomes (*25*–*27*), a single Denisovan genome (*28*), and high-coverage whole-genome data from a nuclear family of four (a mother, a father, and their two sons, with average coverages of 10.8×, 25.8×, 21.2×, and 25.3×, respectively) from the Afanasievo culture, who lived ~4.6 thousand years ago (ka) in the Altai Mountains of Russia (table S1). Finally, we used 3589 published ancient samples from >100 publications compiled by the Reich Laboratory (*24*) and three sequenced ancient samples—Loschbour, LBK-Stuttgart, and Ust'-Ishim (*5*, *29*)—to constrain allele age estimates. These ancient genomes were not included in the final tree sequence because of the lack of reliable phasing for most of the samples.

We built a unified genealogy from these datasets using an iterative approach (Fig. 1B). We first merged the modern datasets and inferred a tree sequence for each autosome using *tsinfer*, version 0.2 (*24*, *30*). We then estimated the age of ancestral haplotypes with *tsdate*, a Bayesian approach that infers the age of ancestral haplotypes with good accuracy and scaling properties (Fig. 1C and figs. S1 to S5) (*24*, *31*). Notably, *tsdate* can be used to date any valid tree sequence, not only those inferred by *tsinfer*. *tsdate* can also use ancient samples to improve date estimates (Fig. 1D). We identified 6,412,717 variants present in both ancient and modern samples. A lower bound on variant age is provided by the estimated archaeological date of the oldest ancient sample in which the derived allele is found. Where this was inconsistent with the initial inferred value (for 559,431 or 8.7% of variants), we used the archaeological date as the variant age.

Finally, we integrated the Afanasievo family and four archaic sequences with the modern samples and reinferred the tree sequence. The Afanasievo family has high coverage and comparably reliable haplotype phasing and was included to demonstrate the ability of our approach to incorporate high-quality ancient samples.

The integrated tree sequences of each autosome combined contain 26,958,720 inferred ancestral haplotype fragments, 231,073,278 edges, 91,172,114 variable sites, and 245,631,834 mutations. We infer that 38.7% of variant sites require more than one change in allelic state in the tree sequence to explain the data. This may indicate either recurrent mutations or errors, all of which are represented by additional mutations in the tree sequence. If we discount mutations that are likely indicative of sequencing errors (*24*), we find that

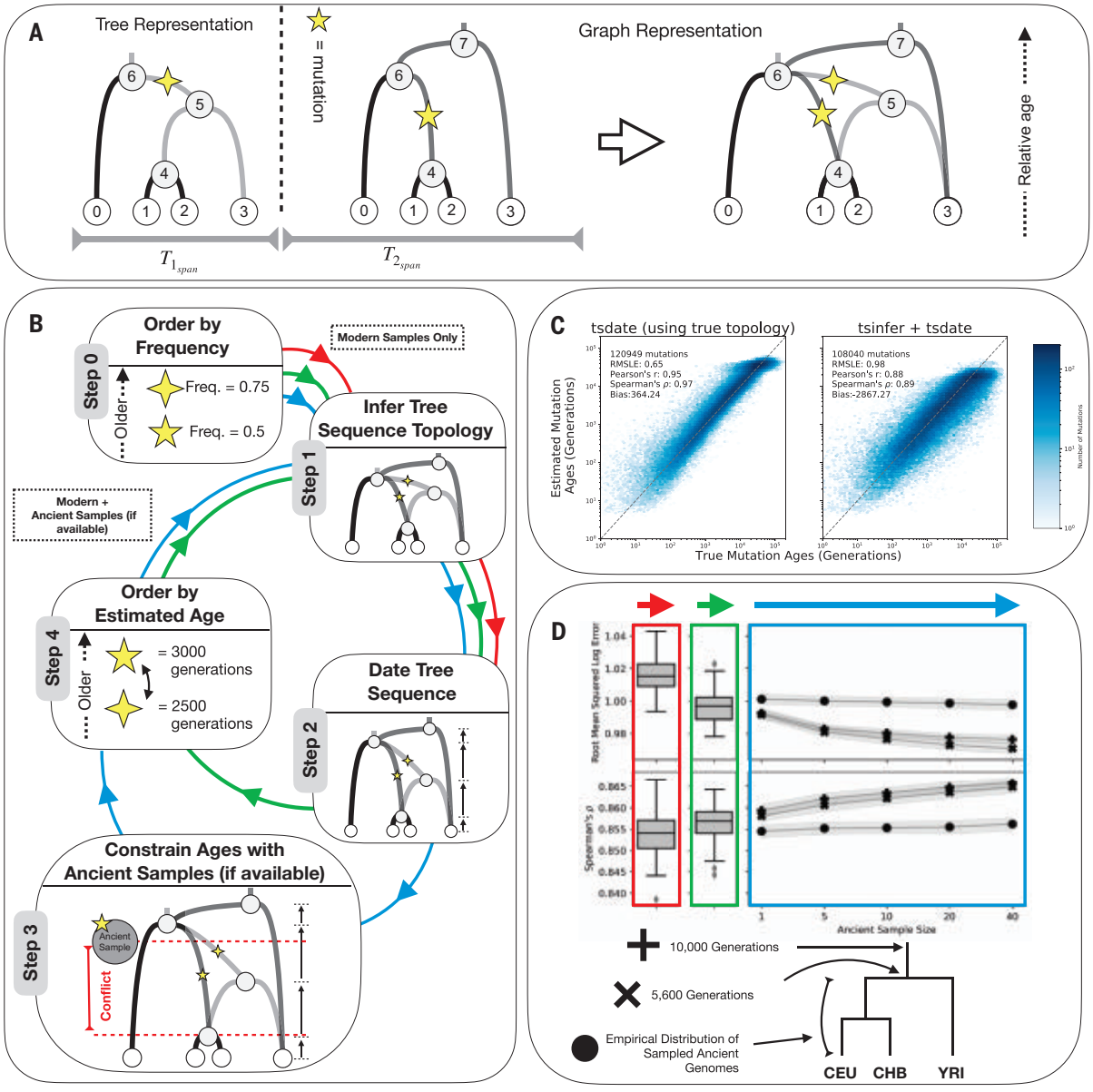


Fig. 1. Schematic overview and validation of the inference methodology. (**A**) An example tree sequence topology with four samples (nodes 0 to 3), two marginal trees, four ancestral haplotypes (nodes 4 to 7), and two mutations. T_{span} measures the genomic span of each marginal tree topology, with the dotted line indicating the location of a recombination event. The graph representation is equivalent to the tree representation. (**B**) Schematic representation of the inference methodology. Step 0: Alleles are ordered by frequency (freq.); the mutation represented by the four-point star is considered to be older. Step 1: The tree sequence topology is inferred with *tsinfer* using modern samples. Step 2: The tree sequence is dated with *tsdate*. Step 3: Node date estimates are constrained with the known age of ancient samples. Step 4: Ancestral haplotypes are reordered by the estimated age of their focal mutation; the five-pointed star mutation is now inferred to be older. The algorithm returns to step 1 to reinfer the tree sequence topology with ancient samples. Arrows refer to modes of operation: steps 0, 1, and 2 only (red); steps 0, 1, 2, 4, 1, and 2 (green); or steps 0, 1, 2, 3, 4, 1, and 2 (blue) (*24*). (**C**) Scatter plots and accuracy metrics comparing simulated (*x* axis) and inferred (*y* axis) mutation ages from *msprime* neutral coalescent simulations, using *tsdate* with the simulated topology (left) and inferred topology from *tsinfer* (right). RMSLE, root mean squared log error. (**D**) Accuracy metrics, RMSLE (top), and Spearman rank correlation coefficient (*r*) (bottom), with modern samples only (first panel), after one round of iteration (second panel), and with increasing numbers of ancient samples (third panel) [colored arrows as in (B)]. Ancient samples from three eras of human history are considered, as in the schematic (*24*). CEU, Utah residents with Northern and Western European Ancestry; CHB, Han Chinese; YRI, Yorubans.

13,513,873 sites contain at least two mutations affecting more than one sample, which implies that up to 17.5% of variable sites could result from more than one ancestral mutation. A high proportion of sites with more than ~100 mutations on chromosome 20 have sequencing or alignment quality issues as defined by the TGP accessibility mask (*6*) or are in minimal linkage disequilibrium to their surrounding sites (fig. S6), which suggests that they are largely erroneous. Moreover, analysis of data simulated with an empirically calibrated error profile and evaluation of the enrichment of multiple mutations at sites with known elevated mutation rates suggests that most of

the multiple mutations we identify are likely explained by error, but a minority (~20%) are the result of genuine recurrence or back mutation (*24*). We chose to retain such sites so that our inferred tree sequences are lossless representations of the original data sources; however, future iterative approaches to the removal of such probable errors are likely to improve use cases, such as imputation.

To characterize fine-scale patterns of relatedness between the 215 populations of the constituent datasets, we estimated the time to the most recent common ancestor (TMRCA) between pairs of haplotypes from these populations at the 122,637 distinct trees in the tree sequence of chromosome 20 (~300 billion pairwise TMRCAs). In this and other analyses, we present data from this chromosome because they are representative of genome-wide patterns. After performing hierarchical clustering on the average pairwise TMRCA values, we find that samples do not cluster by data source (which would indicate artifacts) but reflect patterns of global relatedness (Fig. 2 and the external interactive figure). We conclude that our method of integrating datasets is therefore robust to biases introduced by different datasets.

In this genealogy, numerous features of human history are immediately apparent, such as the deep divergence of archaic and modern humans, the effects of the out-of-Africa event (Fig. 2A), and a subtle increase in Oceanian and

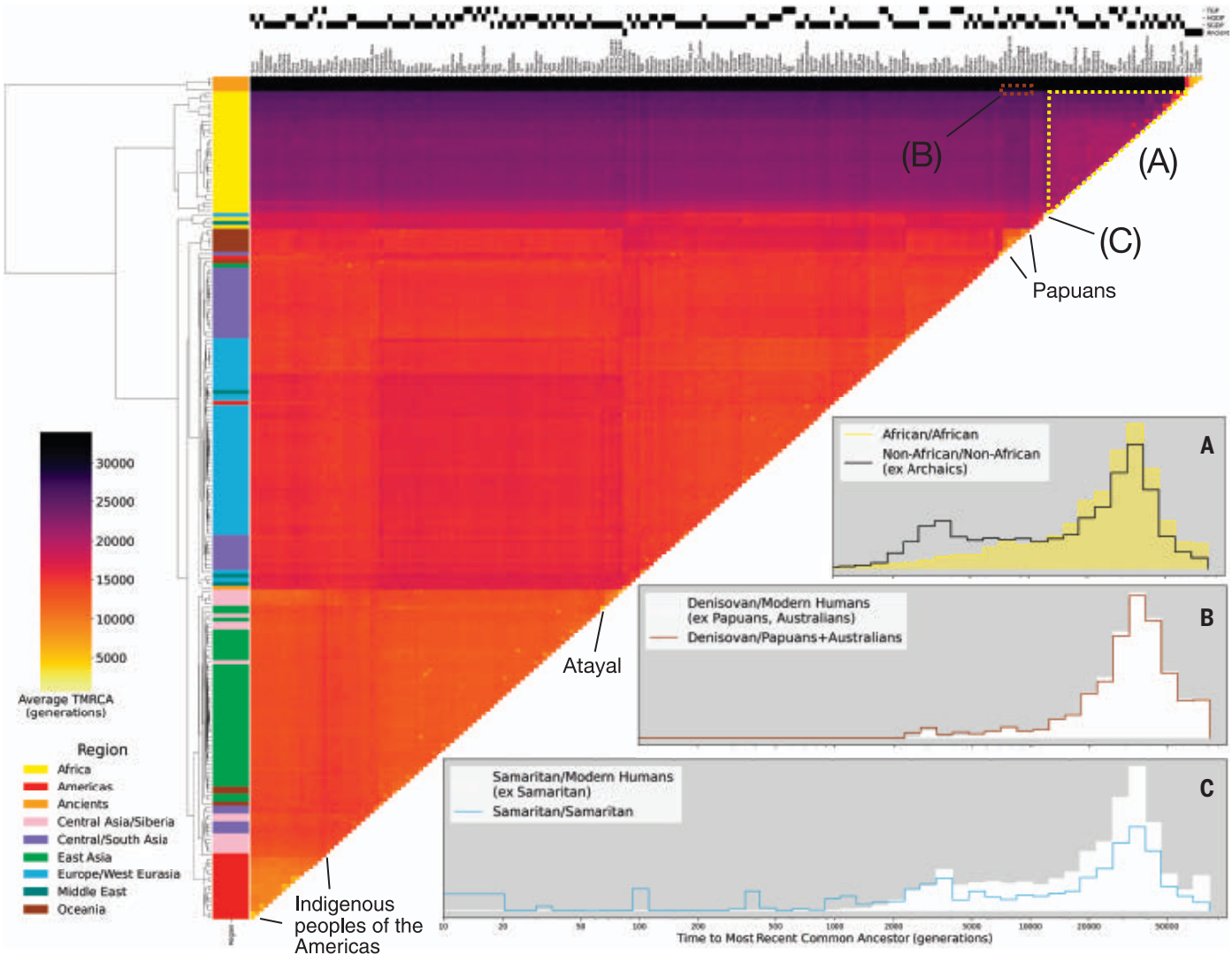


Fig. 2. Clustered heatmap showing the average TMRCA on chromosome 20 for haplotypes within pairs of the 215 populations in the HGDP, TGP, SGDP, and ancient samples. Each cell in the heatmap is colored by the logarithmic mean TMRCA of samples from the two populations. Hierarchical clustering of rows and columns has been performed using the unweighted pair group method with arithmetic mean (UPGMA) algorithm on the value of the pairwise average TMRCAs. Row colors are given by the region of origin for each population, as shown in the legend. The source of genomic samples for each population is indicated in the shaded boxes above the column labels. Three population relationships are highlighted using span-weighted histograms of the TMRCA distributions: (**A**) Average distribution of TMRCAs between all non-African populations (black line) compared with African/African TMRCAs (solid yellow). (**B**) Denisovan and Papuan/Australian TMRCAs (solid line) compared with the Denisovan against all nonarchaic populations (solid white). This subtle but specific signal of elevated recent ancestry between the Denisovan and Papuans/Australians is particularly evident in the external interactive figure. (**C**) TMRCAs between the two Samaritan chromosomes (solid line) compared with the Samaritans/all other modern humans (solid white). Selected populations with particularly recent within-group TMRCAs are indicated. Duplicate samples appearing in more than one modern dataset are included in this analysis. The external interactive figure is an interactive version of this figure that is available at https://awohns.github.io/unified_genealogy/interactive_figure.html.

Denisovan most recent common ancestor (MRCA) density from 2000 to 5000 generations ago (Fig. 2B). Multiple populations show recent within-group TMRCAs, which is suggestive of recent bottlenecks or consanguinity. The most extreme cases occur when a population consists of a single individual in our dataset, such as the Samaritan individual from the SGDP, where we see a logarithmic average within-group TMRCA of ~1000 generations, which is caused by multiple MRCAs at very recent times (Fig. 2C) and is consistent with a severe bottleneck and consanguinity in recent centuries (*32*). Indigenous populations in the Americas, an Atayal individual from Taiwan, and Papuans also exhibit particularly recent within-group TMRCAs (Fig. 2).

Tree sequence–based analysis of descent from ancient sequences

To validate the dating methodology, we used simulations to show that the integration of ancient samples improves derived allele age estimates under a range of demographic histories (Fig. 1D). To provide empirical validation of the method, we tested how best to infer allele ages that are consistent with observations from ancient samples. Thus, we inferred and dated a tree sequence of TGP chromosome 20 (without using ancient samples) and compared the resulting point estimates and upper and lower bounds on allele age with results from *GEVA* (*33*) and *Relate* (*34*). This resulted in a set of 659,804 variant sites where all three methods provide an allele age estimate. Of these, 76,889 derived alleles are observed within the combined set of 3734 ancient genome samples, thus putting a lower bound on allele age. The estimated allele ages from *tsdate* and *Relate* showed the greatest compatibility with ancient lower bounds, despite the fact that the mean age estimate from *tsdate* is more recent than that of *Relate* (Fig. 3A) (*24*).

Next, to assess the ability of the unified tree sequence to recover known relationships between ancient and modern populations, we considered the patterns of descent to modern samples from Archaic sequences on chromosome 20. Simulations indicate that this approach detects introgressed genetic material from Denisovans at a precision of ~86% with a recall of ~61% (*24*). We find descendants among nonarchaic individuals, including both modern individuals and the Afanasievo, for 13% of the span of the Denisovan haplotypes on chromosome 20. The highest degree of descent among modern humans is in Oceanian populations, as previously reported (*28*, *35*–*37*) (Fig. 3B). However, the tree sequence also reveals how both the extent and nature of descent from Denisovan haplotypes vary greatly among modern humans. In particular, we find that Papuans and Australians carry multiple fragments of Denisovan haplotypes that are largely specific to the individual (Fig. 3C). By contrast, other modern descendants of Denisovan haplotypes have fewer blocks that are more widely shared, often between geographically distant individuals.

Examining the other ancient samples in the unified genealogy, we find the greatest amount of descent from the haplotypes of the Afanasievo

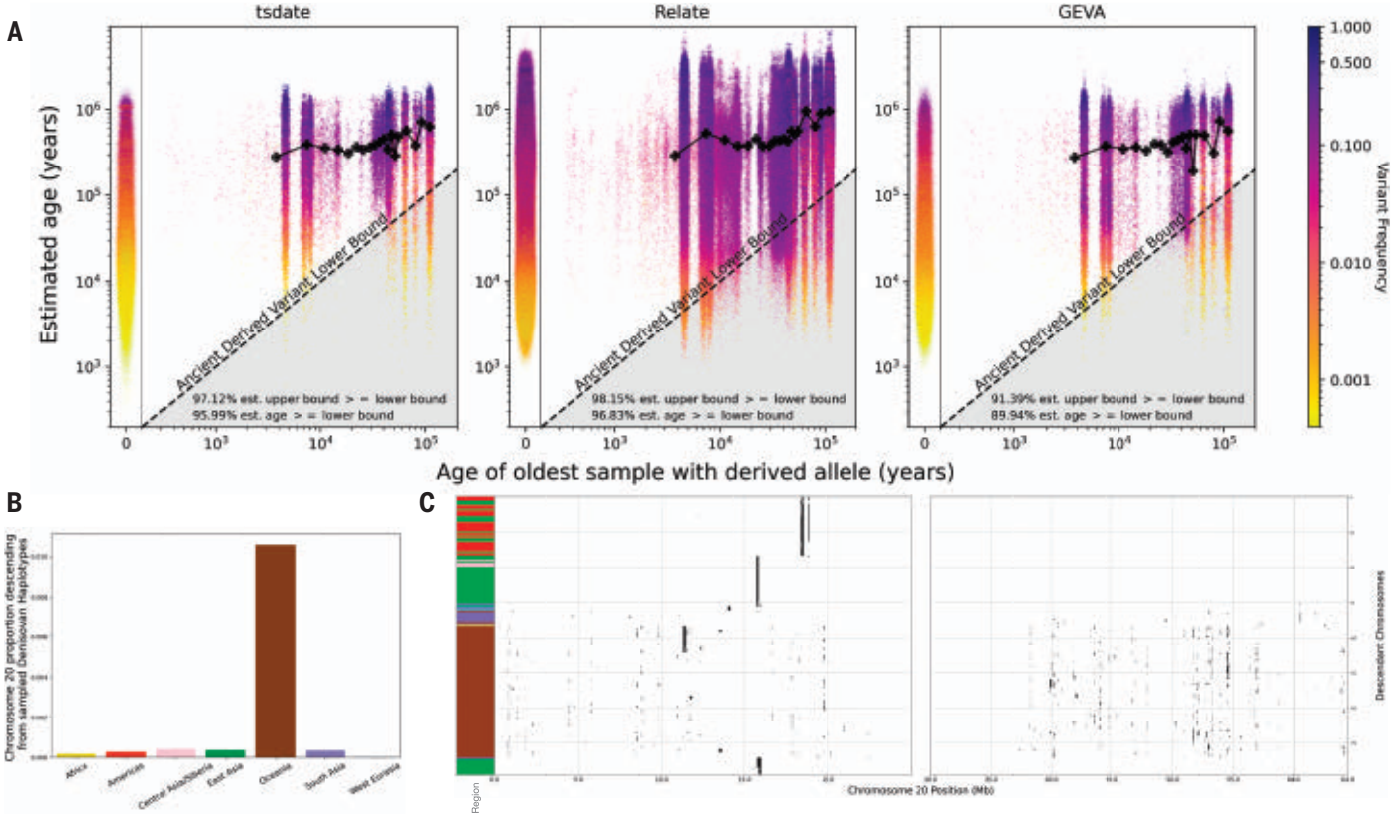


Fig. 3. Validation of inference methods using ancient samples. (**A**) Comparison of mutation age estimates from *tsdate*, *Relate*, and *GEVA* with 3734 ancient samples at 76,889 variants on chromosome 20 (note that *Relate* estimates ages separately for each population in which a variant is found). The radiocarbon-dated age of the oldest ancient sample carrying a derived allele at each variant site in the TGP is used as the lower bound on the age of the mutation (diagonal lines). Mutations below this line have an estimated age that is inconsistent with the age of the ancient sample. Black lines on each plot show the moving average of allele age estimates from each method as a function of oldest ancient sample age. Plots to the left show the distribution of allele age estimates for modern-only variants from each respective method. Additional metrics are reported in each plot. (**B**) Percentage of chromosome 20 for modern samples in each region that is inferred to descend from Denisovan haplotypes, calculated with the genomic descent statistic (*57*). (**C**) Tracts of descent along chromosome 20 descending from Denisovan haplotypes in modern samples with at least 100 kilobases (kb) of total descent (colors as in Fig. 2).

family among individuals in Western Eurasia and South Asia (fig. S7A), consistent with findings from the genetically similar Yamnaya peoples and supporting a contemporaneous diffusion of Afanasievo-like genetic material via multiple routes (*38*). For the Neanderthals, where there are three samples of different ages, our simulations indicate that interpretation of the descent statistics is complicated by varying levels of precision and recall among lineages. Nevertheless, recall is highest at regions where introgressing and sampled archaic lineages share more recent common ancestry, and precision is higher for the Vindija sample, which is more closely related to introgressing lineages. Examining patterns of descent from Vindija haplotypes across autosomes indicates that modern non-African groups carry similar levels of Vindija-like material (fig. S8), which supports suggestions that the proportions are similar between East Asians and West Eurasians (*39*) and is inconsistent with other studies (*26*, *40*).

Nonparametric inference of spatiotemporal dynamics in human history

Tree sequence–based analysis of ancient samples demonstrates an ability to characterize patterns of recent descent. We developed a simple estimator of ancestor spatial location that uses the coordinates of descendants of a node combined with the structure of the tree sequence to provide an estimate of ancestors' geographic position (*24*). Briefly, this is accomplished by determining the coordinates of a parent node in the tree sequence as the midpoint of its immediate children (*24*), an approach that performs well in simple simulations (fig. S9). The approach can use information on the location of ancient samples, although it does not attempt to capture the geographical plausibility of different locations and routes. The inferred locations are thus a model-free estimate of ancestors' locations, informed by the tree sequence topology and geographic distribution of samples.

We applied our method to the unified tree sequence of chromosome 20, excluding TGP individuals (which lack precise location information). We found that the inferred ancestor location recovers multiple key events in human history (Fig. 4 and movie S1). Despite the fact that the geographic center of sampled individuals is in Central Asia, by 72 ka, the average location of ancestral haplotypes is in Northeast Africa and remains there until the oldest common ancestors are reached. In fact, the inferred geographic center of gravity of the 100 oldest ancestral haplotypes (which have an average age of ~2 million years) is located in Sudan at 19.4°N, 33.7°E. These findings reflect the depth of African lineages in the inferred tree sequence and are compatible with well-dated early modern human fossils from eastern and northern Africa (*41*, *42*). We caution that if we analyzed data from a grid sampling of populations in Africa, the geographic center of gravity of independent lineages at different time depths would shift. Additionally, migrations occurring within the past few thousand years (*43*, *44*) mean that present-day distributions of groups in Africa and elsewhere may not represent those of their ancestors, and thus we may have a distorted picture of ancient geographic distributions (*45*). Nevertheless, the deep tree structure is geographically centered in Africa in autosomal data, just as it is for mitochondrial DNA and Y chromosomes (*46*, *47*).

By 280 ka, the estimated geographic center of human ancestors is still located in Africa, but many ancestors are also observed in the Middle East and Central Asia, and a few are located in Papua New Guinea. At 140 ka, more ancestors

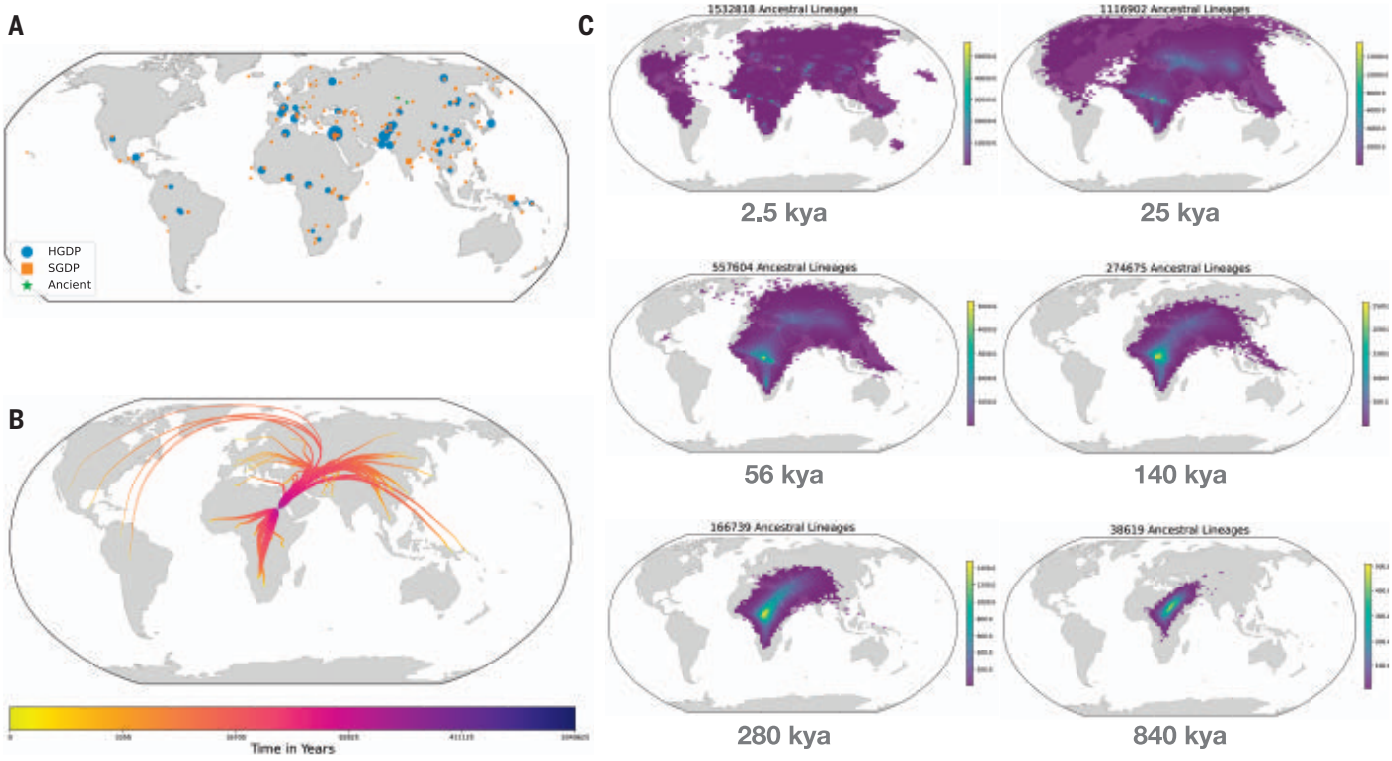


Fig. 4. Visualization of the nonparametric estimator of ancestor geographic location for HGDP, SGDP, Neanderthal, Denisovan, and Afanasievo samples on chromosome 20. (**A**) Geographic location of samples used to infer ancestral geography. The size of each symbol is proportional to the number of samples in that population. (**B**) The average location of the ancestors of each HGDP population from time t = 0 to ~2 million years ago. The width of lines is proportional to the number of ancestors of each population over time. The ancestor of a population is defined as an inferred ancestral haplotype with at least one descendant in that population. (**C**) Two-dimensional histograms showing the inferred geographical location of HGDP ancestral lineages at six time points. Histogram bins with <10 ancestors are not shown. The geographic concentration of ancestors at more recent times is an artifact of uneven sampling and our geographic inference method.

are found in Papua New Guinea. This is almost 100 thousand years before the earliest documented human habitation of the region (*48*). However, our findings are potentially consistent with the proposed time scales of deeply diverged Denisovan lineages specific to Papuans (*37*) and possibly with admixture with unsampled ghost lineages. At 56 ka, some ancestral lineages are observed in the Americas, which is earlier than the estimated migration times to the Americas (*49*). This effect is possibly attributable to the presence of ancestors that predate the migration and did not live in the Americas but whose descendants now exist solely in this region (*50*); the same effect may also explain observations from Papua New Guinea. Additional ancient samples and more-sophisticated inference approaches are required to distinguish between these hypotheses because there remains considerable uncertainty about the true age of any single ancestor (*24*). Nevertheless, these results demonstrate the ability of inference methods applied to tree sequences to capture key features of human history in a manner that does not require complex parametric modeling.

Discussion

A central theme in evolutionary biology is how best to represent and analyze genomic diversity to learn about the processes, forces, and events that have shaped organismal history. Historically, many modeling approaches have focused on the temporal behavior of individual mutation frequencies in idealized populations (*51*, *52*). More recently, modeling techniques have shifted to focus on the genealogical history of sampled genomes and the correlation structures that arise through recombination (*22*, *53*). Notably, a single (albeit extremely complex) set of ancestral relationships exists that, coupled with how mutation events have altered genetic material through descent, describes what we observe today.

However, developing efficient methods for inferring the underlying genealogy has proved challenging (*54*, *55*). The methods described here produce high-quality dated genealogies that include thousands of modern and ancient samples. These genealogies cannot be entirely accurate; nevertheless, they enable a wealth of analyses that reveal features of human evolution (*23*, *56*–*60*). That our highly simplistic geographic estimator captures key events suggests that more-sophisticated approaches, coupled with the ongoing program of sequencing ancient samples, will continue to generate insights into our history. Specifically, the methods developed here provide a framework for testing different models of human migration and demographic history, such as Neanderthal absorption models (*61*), using a parametric and explicitly spatial simulation framework. However, the accuracy of any ancestral geographic inference method will be limited when the distribution of sampled individuals does not reflect the location of the samples' ancestors.

Our study also highlights the importance of accommodating genotype error and recurrent mutation in the analysis of genomic variation. Although a large number of sites are inferred to carry multiple mutations, we find that most of these likely reflect genotype error and potentially errors arising from paralogy (particularly at sites requiring high numbers of mutations), although there remains a substantial signal of recurrent mutation, as previously reported (*62*, *63*). Similarly, we find some evidence for certain classes of error in ancient sequences leading to false correction of variant ages. We choose to retain all additional mutations in the analyses described in this paper, including those that are highly likely to reflect sequencing error, because this reflects the input data used to build the tree sequence, and any effort to remove mutations corresponding to errors will itself introduce bias. We caution that the absolute ages we report have some degree of error, in part as a result of these errors in the sequencing datasets. Estimates from simulations show that genotype error may cause an upward bias of up to 16% in age estimates derived from modern samples (fig. S3), but we also find that removing sites that are highly likely to be erroneous has a marginal effect on age estimates (fig. S10). Improving methods to detect and correct or mitigate against the effect of genotype errors is an important direction for future research.

Because the tree sequence approach aims to capture the structure of human relationships and genomic diversity, it provides a principled basis for combining data from multiple different sources, not just correcting errors but also enabling tasks such as imputing missing data. Although additional work is required to integrate other types of mutation, a reference tree sequence for human variation—along with the tools to use it appropriately (*13*, *23*)—potentially represents a basis for harmonizing much larger and wider sets of genomic data sources and enabling cross–data source analyses. We note that reference tree sequences could also enable data sharing and preserve privacy in genomic analysis (*20*) through the compression of cohorts against such a reference structure.

There exists room for improvement as well as opportunities for genomic analyses that use the dated tree sequence structure. Our approach requires phased genomes, a particular challenge for ancient samples. However, it should be possible to use a diploid version of the matching algorithm in *tsinfer* to jointly solve phasing and imputation. This also has the potential to alleviate biases introduced by using modern and genetically distant reference panels for ancient samples (*64*). Additionally, our approach to age inference within *tsdate* only provides an approximate solution to the cycles that are inherent in genealogical histories (*65*) and could be extended to model heterogeneity in mutation rates. There are also many possible approaches for improving the sophistication of spatiotemporal ancestor inference.

The unified genealogy presented in this work represents a foundation for building a comprehensive understanding of human genomic diversity, including both modern and ancient samples, which enables applications ranging from improving genome interpretation to deciphering our earliest roots. Although much work is still required to build the genealogy of everyone, the methods presented here provide a solution to this fundamental task.

Materials and methods summary

Dated tree sequences were constructed from the TGP (*6*), the SGDP (*7*), the HGDP (*8*), three Neanderthal genomes (*25*–*27*), and the Denisovan genome (*28*), and we added a dataset from a nuclear family of four from the Afanasievo culture who lived ~4.6 ka, sequenced to a depth of between 10.8× and 25.8×. First, tree sequence topologies were estimated using *tsinfer* (*13*), updated (version 0.2.0) to handle missing data and detect potential genotype errors and recurrent mutations. Subsequently, the dates of ancestral haplotypes were obtained with a new algorithm, *tsdate*—an approximate Bayesian method that estimates a joint posterior distribution for the nodes in a tree sequence using mutations inferred from the input sequences, inferred ancestors, and tree sequence topology. Ages in the unified genealogy were constrained by radiocarbon-dated ancient samples from the Allen Ancient DNA resource (*5*–*7*, *18*, *24*, *25*, *26*, *28*, *29*, *38*, *44*, *50*, *66*–*172*) as well as from the Loschbour, LBK-Stuttgart, and Ust'-Ishim (*5*, *29*) sequenced ancient samples. The geographic location of ancestral haplotypes was estimated from the inferred tree sequence topology using a weighted sum of the daughter node geographic locations converted to Cartesian coordinates. Coalescent simulations for method evaluation were performed using *msprime* (*21*) and *stdpopsim* (*173*). Full details of algorithms, data sources, data processing steps, and simulations are provided in the supplementary materials.

REFERENCES AND NOTES

1. C. Bycroft *et al*., The UK Biobank resource with deep phenotyping and genomic data. *Nature* **562**, 203–209 (2018). doi: 10.1038/s41586-018-0579-z; pmid: 30305743
2. D. Taliun *et al*., Sequencing of 53,831 diverse genomes from the NHLBI TOPMed Program. *Nature* **590**, 290–299 (2021). doi: 10.1038/s41586-021-03205-y; pmid: 33568819
3. D. Reich, *Who We Are and How We Got Here: Ancient DNA and the New Science of the Human Past* (Oxford Univ. Press, 2018).
4. H. A. Lewin *et al*., Earth BioGenome Project: Sequencing life for the future of life. *Proc. Natl. Acad. Sci. U.S.A.* **115**, 4325–4333 (2018). doi: 10.1073/pnas.1720115115; pmid: 29686065

5. I. Lazaridis *et al*., Ancient human genomes suggest three ancestral populations for present-day Europeans. *Nature* **513**, 409–413 (2014). doi: 10.1038/nature13673; pmid: 25230663
6. 1000 Genomes Project Consortium, A global reference for human genetic variation. *Nature* **526**, 68–74 (2015). doi: 10.1038/nature15393; pmid: 26432245
7. S. Mallick *et al*., The Simons Genome Diversity Project: 300 genomes from 142 diverse populations. *Nature* **538**, 201–206 (2016). doi: 10.1038/nature18964; pmid: 27654912
8. A. Bergström *et al*., Insights into human genetic variation and population history from 929 diverse genomes. *Science* **367**, eaay5012 (2020). doi: 10.1126/science.aay5012; pmid: 32193295
9. S. Belsare *et al*., Evaluating the quality of the 1000 genomes project data. *BMC Genomics* **20**, 620 (2019). doi: 10.1186/s12864-019-5957-x; pmid: 31416423
10. L. Shi *et al*., Long-read sequencing and de novo assembly of a Chinese genome. *Nat. Commun.* **7**, 12065 (2016). doi: 10.1038/ncomms12065; pmid: 27356984
11. A. M. Wenger *et al*., Accurate circular consensus long-read sequencing improves variant detection and assembly of a human genome. *Nat. Biotechnol.* **37**, 1155–1162 (2019). doi: 10.1038/s41587-019-0217-9; pmid: 31406327
12. S. Hwang, E. Kim, I. Lee, E. M. Marcotte, Systematic comparison of variant calling pipelines using gold standard personal exome variants. *Sci. Rep.* **5**, 17875 (2015). doi: 10.1038/srep17875; pmid: 26639839
13. J. Kelleher *et al*., Inferring whole-genome histories in large population datasets. *Nat. Genet.* **51**, 1330–1338 (2019). doi: 10.1038/s41588-019-0483-y; pmid: 31477934
14. L. L. Cavalli-Sforza, M. W. Feldman, The application of molecular genetic approaches to the study of human evolution. *Nat. Genet.* **33**, 266–275 (2003). doi: 10.1038/ng1113; pmid: 12610536
15. N. Patterson, A. L. Price, D. Reich, Population structure and eigenanalysis. *PLOS Genet.* **2**, e190 (2006). doi: 10.1371/journal.pgen.0020190; pmid: 17194218
16. J. K. Pritchard, M. Stephens, P. Donnelly, Inference of population structure using multilocus genotype data. *Genetics* **155**, 945–959 (2000). doi: 10.1093/genetics/155.2.945; pmid: 10835412
17. D. J. Lawson, G. Hellenthal, S. Myers, D. Falush, Inference of population structure using dense haplotype data. *PLOS Genet.* **8**, e1002453 (2012). doi: 10.1371/journal.pgen.1002453; pmid: 22291602
18. N. Patterson *et al*., Ancient admixture in human history. *Genetics* **192**, 1065–1093 (2012). doi: 10.1534/genetics.112.145037; pmid: 22960212
19. J. K. Pickrell, J. K. Pritchard, Inference of population splits and mixtures from genome-wide allele frequency data. *PLOS Genet.* **8**, e1002967 (2012). doi: 10.1371/journal.pgen.1002967; pmid: 23166502
20. L. Bonomi, Y. Huang, L. Ohno-Machado, Privacy challenges and research opportunities for genomic data sharing. *Nat. Genet.* **52**, 646–654 (2020). doi: 10.1038/s41588-020-0651-0; pmid: 32601475
21. J. Kelleher, A. M. Etheridge, G. McVean, Efficient Coalescent Simulation and Genealogical Analysis for Large Sample Sizes. *PLOS Comput. Biol.* **12**, e1004842 (2016). doi: 10.1371/journal.pcbi.1004842; pmid: 27145223
22. R. R. Hudson, Properties of a neutral allele model with intragenic recombination. *Theor. Popul. Biol.* **23**, 183–201 (1983). doi: 10.1016/0040-5809(83)90013-8; pmid: 6612631
23. P. Ralph, K. Thornton, J. Kelleher, Efficiently Summarizing Relationships in Large Samples: A General Duality Between Statistics of Genealogies and Genomes. *Genetics* **215**, 779–797 (2020). doi: 10.1534/genetics.120.303253; pmid: 32357960
24. Materials and methods are available as supplementary materials online.
25. K. Prüfer *et al*., The complete genome sequence of a Neanderthal from the Altai Mountains. *Nature* **505**, 43–49 (2014). doi: 10.1038/nature12886; pmid: 24352235
26. K. Prüfer *et al*., A high-coverage Neandertal genome from Vindija Cave in Croatia. *Science* **358**, 655–658 (2017). doi: 10.1126/science.aao1887; pmid: 28982794
27. F. Mafessoni *et al*., A high-coverage Neandertal genome from Chagyrskaya Cave. *Proc. Natl. Acad. Sci. U.S.A.* **117**, 15132–15136 (2020). doi: 10.1073/pnas.2004944117; pmid: 32546518
28. M. Meyer *et al*., A high-coverage genome sequence from an archaic Denisovan individual. *Science* **338**, 222–226 (2012). doi: 10.1126/science.1224344; pmid: 22936568
29. Q. Fu *et al*., Genome sequence of a 45,000-year-old modern human from western Siberia. *Nature* **514**, 445–449 (2014). doi: 10.1038/nature13810; pmid: 25341783
30. J. Kelleher, Y. Wong, B. Jeffery, A. W. Wohns, I. Rebollo, D. Rodriguez Fernandez, tskit-dev/tsinfer: 0.2.1, version 0.2.1, Zenodo (2021); https://doi.org/10.5281/zenodo.5168051.
31. A. W. Wohns, Y. Wong, B. Jeffery, tskit-dev/tsdate: Minor feature and bugfix release, version 0.1.4, Zenodo (2021); https://doi.org/10.5281/zenodo.5168040.
32. B. Bonne, The Samaritans: A demographic study. *Hum. Biol.* **35**, 61–89 (1963). pmid: 13968819
33. P. K. Albers, G. McVean, Dating genomic variants and shared ancestry in population-scale sequencing data. *PLOS Biol.* **18**, e3000586 (2020). doi: 10.1371/journal.pbio.3000586 pmid: 31951611
34. L. Speidel, M. Forest, S. Shi, S. R. Myers, A method for genome-wide genealogy estimation for thousands of samples. *Nat. Genet.* **51**, 1321–1329 (2019). doi: 10.1038/s41588-019-0484-x; pmid: 31477933
35. D. Reich *et al*., Genetic history of an archaic hominin group from Denisova Cave in Siberia. *Nature* **468**, 1053–1060 (2010). doi: 10.1038/nature09710; pmid: 21179161
36. D. Reich *et al*., Denisova admixture and the first modern human dispersals into Southeast Asia and Oceania. *Am. J. Hum. Genet.* **89**, 516–528 (2011). doi: 10.1016/j.ajhg.2011.09.005; pmid: 21944045
37. G. S. Jacobs *et al*., Multiple Deeply Divergent Denisovan Ancestries in Papuans. *Cell* **177**, 1010–1021.e32 (2019). doi: 10.1016/j.cell.2019.02.035; pmid: 30981557
38. V. M. Narasimhan *et al*., The formation of human populations in South and Central Asia. *Science* **365**, eaat7487 (2019). doi: 10.1126/science.aat7487; pmid: 31488661
39. L. Chen, A. B. Wolf, W. Fu, L. Li, J. M. Akey, Identifying and Interpreting Apparent Neanderthal Ancestry in African Individuals. *Cell* **180**, 677–687.e16 (2020). doi: 10.1016/j.cell.2020.01.012; pmid: 32004458
40. J. D. Wall *et al*., Higher levels of neanderthal ancestry in East Asians than in Europeans. *Genetics* **194**, 199–209 (2013). doi: 10.1534/genetics.112.148213; pmid: 23410836
41. I. McDougall, F. H. Brown, J. G. Fleagle, Stratigraphic placement and age of modern humans from Kibish, Ethiopia. *Nature* **433**, 733–736 (2005). doi: 10.1038/nature03258; pmid: 15716951
42. J.-J. Hublin *et al*., New fossils from Jebel Irhoud, Morocco and the pan-African origin of *Homo sapiens*. *Nature* **546**, 289–292 (2017). doi: 10.1038/nature22336; pmid: 28593953
43. K. Wang *et al*., Ancient genomes reveal complex patterns of population movement, interaction, and replacement in sub-Saharan Africa. *Sci. Adv.* **6**, eaaz0183 (2020). doi: 10.1126/sciadv.aaz0183; pmid: 32582847
44. M. E. Prendergast *et al*., Ancient DNA reveals a multistep spread of the first herders into sub-Saharan Africa. *Science* **365**, eaaw6275 (2019). doi: 10.1126/science.aaw6275; pmid: 31147405
45. A. Kalkauskas *et al*., Sampling bias and model choice in continuous phylogeography: Getting lost on a random walk. *PLOS Comput. Biol.* **17**, e1008561 (2021). doi: 10.1371/journal.pcbi.1008561
46. L. Vigilant, M. Stoneking, H. Harpending, K. Hawkes, A. C. Wilson, African populations and the evolution of human mitochondrial DNA. *Science* **253**, 1503–1507 (1991). doi: 10.1126/science.1840702; pmid: 1840702
47. P. A. Underhill *et al*., The phylogeography of Y chromosome binary haplotypes and the origins of modern human populations. *Ann. Hum. Genet.* **65**, 43–62 (2001). doi: 10.1046/j.1469-1809.2001.6510043.x; pmid: 11415522
48. J. F. O'Connell, J. Allen, The process, biotic impact, and global implications of the human colonization of Sahul about 47,000 years ago. *J. Archaeol. Sci.* **56**, 73–84 (2015). doi: 10.1016/j.jas.2015.02.020
49. B. Llamas *et al*., Ancient mitochondrial DNA provides high-resolution time scale of the peopling of the Americas. *Sci. Adv.* **2**, e1501385 (2016). doi: 10.1126/sciadv.1501385; pmid: 27051878
50. J. V. Moreno-Mayar *et al*., Early human dispersals within the Americas. *Science* **362**, eaav2621 (2018). doi: 10.1126/science.aav2621; pmid: 30409807
51. R. A. Fisher, *The Genetical Theory of Natural Selection* (Clarendon, 1930).
52. S. Wright, Evolution in Mendelian populations. *Genetics* **16**, 97–159 (1931). doi: 10.1093/genetics/16.2.97; pmid: 17246615
53. J. F. C. Kingman, The coalescent. *Stochastic Process. Appl.* **13**, 235–248 (1982). doi: 10.1016/0304-4149(82)90011-4
54. G. A. T. McVean, N. J. Cardin, Approximating the coalescent with recombination. *Phil. Trans. R. Soc. B* **360**, 1387–1393 (2005). doi: 10.1098/rstb.2005.1673; pmid: 16048782
55. M. D. Rasmussen, M. J. Hubisz, I. Gronau, A. Siepel, Genome-wide inference of ancestral recombination graphs. *PLOS Genet.* **10**, e1004342 (2014). doi: 10.1371/journal.pgen.1004342; pmid: 24831947
56. K. Harris, From a database of genomes to a forest of evolutionary trees. *Nat. Genet.* **51**, 1306–1307 (2019). doi: 10.1038/s41588-019-0492-x; pmid: 31477932
57. C. L. Scheib *et al*., East Anglian early Neolithic monument burial linked to contemporary Megaliths. *Ann. Hum. Biol.* **46**, 145–149 (2019). doi: 10.1080/03014460.2019.1623912; pmid: 31184205
58. A. J. Stern, L. Speidel, N. A. Zaitlen, R. Nielsen, Disentangling selection on genetically correlated polygenic traits via whole-genome genealogies. *Am. J. Hum. Genet.* **108**, 219–239 (2021). doi: 10.1016/j.ajhg.2020.12.005; pmid: 33440170
59. L. Speidel *et al*., Inferring population histories for ancient genomes using genome-wide genealogies. *Mol. Biol. Evol.* **38**, 3497–3511 (2021). doi: 10.1093/molbev/msab174
60. N. K. Schaefer, B. Shapiro, R. E. Green, An ancestral recombination graph of human, Neanderthal, and Denisovan genomes. *Sci. Adv.* **7**, eabc0776 (2021). doi: 10.1126/sciadv.abc0776; pmid: 34272242
61. R. Nielsen *et al*., Tracing the peopling of the world through genomics. *Nature* **541**, 302–310 (2017). doi: 10.1038/nature21347; pmid: 28102248
62. J. J. Michaelson *et al*., Whole-genome sequencing in autism identifies hot spots for de novo germline mutation. *Cell* **151**, 1431–1442 (2012). doi: 10.1016/j.cell.2012.11.019; pmid: 23260136
63. A. V. Nesta, D. Tafur, C. R. Beck, Hotspots of Human Mutation. *Trends Genet.* **37**, 717–729 (2021). doi: 10.1016/j.tig.2020.10.003; pmid: 33199048
64. R. Hui, E. D'Atanasio, L. M. Cassidy, C. L. Scheib, T. Kivisild, Evaluating genotype imputation pipeline for ultra-low coverage ancient genomes. *Sci. Rep.* **10**, 18542 (2020). doi: 10.1038/s41598-020-75387-w; pmid: 33122697
65. K. P. Murphy, Y. Weiss, M. I. Jordan, in *Proceedings of the Fifteenth Conference on Uncertainty in Artificial Intelligence*, K. B. Laskey, H. Prade, Eds. (Morgan Kaufmann Publishers Inc., 1999), pp. 467–475.
66. M. E. Allentoft *et al*., Population genomics of Bronze Age Eurasia. *Nature* **522**, 167–172 (2015). doi: 10.1038/nature14507; pmid: 26062507
67. C. E. G. Amorim *et al*., Understanding 6th-century barbarian social organization and migration through paleogenomics. *Nat. Commun.* **9**, 3547 (2018). doi: 10.1038/s41467-018-06024-4; pmid: 30206220
68. M. L. Antonio *et al*., Ancient Rome: A genetic crossroads of Europe and the Mediterranean. *Science* **366**, 708–714 (2019). doi: 10.1126/science.aay6826; pmid: 31699931
69. S. Brace *et al*., Ancient genomes indicate population replacement in Early Neolithic Britain. *Nat. Ecol. Evol.* **3**, 765–771 (2019). doi: 10.1038/s41559-019-0871-9; pmid: 30988490
70. F. Broushaki *et al*., Early Neolithic genomes from the eastern Fertile Crescent. *Science* **353**, 499–503 (2016). doi: 10.1126/science.aaf7943; pmid: 27417496
71. L. M. Cassidy *et al*., Neolithic and Bronze Age migration to Ireland and establishment of the insular Atlantic genome. *Proc. Natl. Acad. Sci. U.S.A.* **113**, 368–373 (2016). doi: 10.1073/pnas.1518445113; pmid: 26712024
72. P. B. Damgaard *et al*., 137 ancient human genomes from across the Eurasian steppes. *Nature* **557**, 369–374 (2018). doi: 10.1038/s41586-018-0094-2; pmid: 29743675
73. P. de Barros Damgaard *et al*., The first horse herders and the impact of early Bronze Age steppe expansions into Asia. *Science* **360**, eaar7711 (2018). doi: 10.1126/science.aar7711; pmid: 29743352
74. S. S. Ebenesersdóttir *et al*., Ancient genomes from Iceland reveal the making of a human population. *Science* **360**, 1028–1032 (2018). doi: 10.1126/science.aar2625; pmid: 29853688
75. M. Feldman *et al*., Late Pleistocene human genome suggests a local origin for the first farmers of central Anatolia. *Nat. Commun.* **10**, 1218 (2019). doi: 10.1038/s41467-019-09209-7; pmid: 30890703
76. M. Feldman *et al*., Ancient DNA sheds light on the genetic origins of early Iron Age Philistines. *Sci. Adv.* **5**, eaax0061 (2019). doi: 10.1126/sciadv.aax0061; pmid: 31281897

77. C. de la Fuente *et al*., Genomic insights into the origin and diversification of late maritime hunter-gatherers from the Chilean Patagonia. *Proc. Natl. Acad. Sci. U.S.A.* **115**, E4006–E4012 (2018). doi: 10.1073/pnas.1715688115; pmid: 29632188
78. D. M. Fernandes *et al*., A genomic Neolithic time transect of hunter-farmer admixture in central Poland. *Sci. Rep.* **8**, 14879 (2018). doi: 10.1038/s41598-018-33067-w; pmid: 30291256
79. P. Flegontov *et al*., Palaeo-Eskimo genetic ancestry and the peopling of Chukotka and North America. *Nature* **570**, 236–240 (2019). doi: 10.1038/s41586-019-1251-y; pmid: 31168094
80. R. Fregel *et al*., Ancient genomes from North Africa evidence prehistoric migrations to the Maghreb from both the Levant and Europe. *Proc. Natl. Acad. Sci. U.S.A.* **115**, 6774–6779 (2018). doi: 10.1073/pnas.1800851115; pmid: 29895688
81. Q. Fu *et al*., A revised timescale for human evolution based on ancient mitochondrial genomes. *Curr. Biol.* **23**, 553–559 (2013). doi: 10.1016/j.cub.2013.02.044; pmid: 23523248
82. Q. Fu *et al*., An early modern human from Romania with a recent Neanderthal ancestor. *Nature* **524**, 216–219 (2015). doi: 10.1038/nature14558; pmid: 26098372
83. Q. Fu *et al*., The genetic history of Ice Age Europe. *Nature* **534**, 200–205 (2016). doi: 10.1038/nature17993; pmid: 27135931
84. C. Gamba *et al*., Genome flux and stasis in a five millennium transect of European prehistory. *Nat. Commun.* **5**, 5257 (2014). doi: 10.1038/ncomms6257; pmid: 25334030
85. G. González-Fortes *et al*., Paleogenomic Evidence for Multi-generational Mixing between Neolithic Farmers and Mesolithic Hunter-Gatherers in the Lower Danube Basin. *Curr. Biol.* **27**, 1801–1810.e10 (2017). doi: 10.1016/j.cub.2017.05.023; pmid: 28552360
86. G. González-Fortes *et al*., A western route of prehistoric human migration from Africa into the Iberian Peninsula. *Proc. Biol. Sci.* **286**, 20182288 (2019). doi: 10.1098/rspb.2018.2288; pmid: 30963949
87. T. Günther *et al*., Population genomics of Mesolithic Scandinavia: Investigating early postglacial migration routes and high-latitude adaptation. *PLOS Biol.* **16**, e2003703 (2018). doi: 10.1371/journal.pbio.2003703; pmid: 29315301
88. T. Günther *et al*., Ancient genomes link early farmers from Atapuerca in Spain to modern-day Basques. *Proc. Natl. Acad. Sci. U.S.A.* **112**, 11917–11922 (2015). doi: 10.1073/pnas.1509851112; pmid: 26351665
89. M. Haber *et al*., Continuity and Admixture in the Last Five Millennia of Levantine History from Ancient Canaanite and Present-Day Lebanese Genome Sequences. *Am. J. Hum. Genet.* **101**, 274–282 (2017). doi: 10.1016/j.ajhg.2017.06.013; pmid: 28757201
90. M. Haber *et al*., A Transient Pulse of Genetic Admixture from the Crusaders in the Near East Identified from Ancient Genome Sequences. *Am. J. Hum. Genet.* **104**, 977–984 (2019). doi: 10.1016/j.ajhg.2019.03.015; pmid: 31006515
91. M. Hajdinjak *et al*., Reconstructing the genetic history of late Neanderthals. *Nature* **555**, 652–656 (2018). doi: 10.1038/nature26151; pmid: 29562232
92. É. Harney *et al*., Ancient DNA from Chalcolithic Israel reveals the role of population mixture in cultural transformation. *Nat. Commun.* **9**, 3336 (2018). doi: 10.1038/s41467-018-05649-9; pmid: 30127404
93. É. Harney *et al*., Ancient DNA from the skeletons of Roopkund Lake reveals Mediterranean migrants in India. *Nat. Commun.* **10**, 3670 (2019). doi: 10.1038/s41467-019-11357-9; pmid: 31431628
94. Z. Hofmanová *et al*., Early farmers from across Europe directly descended from Neolithic Aegeans. *Proc. Natl. Acad. Sci. U.S.A.* **113**, 6886–6891 (2016). doi: 10.1073/pnas.1523951113; pmid: 27274049
95. M. Järve *et al*., Shifts in the Genetic Landscape of the Western Eurasian Steppe Associated with the Beginning and End of the Scythian Dominance. *Curr. Biol.* **29**, 2430–2441.e10 (2019). doi: 10.1016/j.cub.2019.06.019; pmid: 31303491
96. C. Jeong *et al*., The genetic history of admixture across inner Eurasia. *Nat. Ecol. Evol.* **3**, 966–976 (2019). doi: 10.1038/s41559-019-0878-2; pmid: 31036896
97. C. Jeong *et al*., Long-term genetic stability and a high-altitude East Asian origin for the peoples of the high valleys of the Himalayan arc. *Proc. Natl. Acad. Sci. U.S.A.* **113**, 7485–7490 (2016). doi: 10.1073/pnas.1520844113; pmid: 27325755
98. C. Jeong *et al*., Bronze Age population dynamics and the rise of dairy pastoralism on the eastern Eurasian steppe. *Proc. Natl. Acad. Sci. U.S.A.* **115**, E11248–E11255 (2018). doi: 10.1073/pnas.1813608115; pmid: 30397125
99. E. R. Jones *et al*., Upper Palaeolithic genomes reveal deep roots of modern Eurasians. *Nat. Commun.* **6**, 8912 (2015). doi: 10.1038/ncomms9912; pmid: 26567969
100. E. R. Jones *et al*., The Neolithic Transition in the Baltic Was Not Driven by Admixture with Early European Farmers. *Curr. Biol.* **27**, 576–582 (2017). doi: 10.1016/j.cub.2016.12.060; pmid: 28162894
101. H. Kanzawa-Kiriyama *et al*., A partial nuclear genome of the Jomons who lived 3000 years ago in Fukushima, Japan. *J. Hum. Genet.* **62**, 213–221 (2017). doi: 10.1038/jhg.2016.110; pmid: 27581845
102. A. Keller *et al*., New insights into the Tyrolean Iceman's origin and phenotype as inferred by whole-genome sequencing. *Nat. Commun.* **3**, 698 (2012). doi: 10.1038/ncomms1701; pmid: 22426219
103. D. J. Kennett *et al*., Archaeogenomic evidence reveals prehistoric matrilineal dynasty. *Nat. Commun.* **8**, 14115 (2017). doi: 10.1038/ncomms14115; pmid: 28221340
104. G. M. Kılınç *et al*., The Demographic Development of the First Farmers in Anatolia. *Curr. Biol.* **26**, 2659–2666 (2016). doi: 10.1016/j.cub.2016.07.057; pmid: 27498567
105. T. S. Korneliussen, A. Albrechtsen, R. Nielsen, ANGSD: Analysis of Next Generation Sequencing Data. *BMC Bioinformatics* **15**, 356 (2014). doi: 10.1186/s12859-014-0356-4; pmid: 25420514
106. M. Krzewińska *et al*., Genomic and Strontium Isotope Variation Reveal Immigration Patterns in a Viking Age Town. *Curr. Biol.* **28**, 2730–2738.e10 (2018). doi: 10.1016/j.cub.2018.06.053; pmid: 30146150
107. M. Krzewińska *et al*., Ancient genomes suggest the eastern Pontic-Caspian steppe as the source of western Iron Age nomads. *Sci. Adv.* **4**, eaat4457 (2018). doi: 10.1126/sciadv.aat4457; pmid: 30417088
108. T. C. Lamnidis *et al*., Ancient Fennoscandian genomes reveal origin and spread of Siberian ancestry in Europe. *Nat. Commun.* **9**, 5018 (2018). doi: 10.1038/s41467-018-07483-5; pmid: 30479341
109. I. Lazaridis *et al*., Genomic insights into the origin of farming in the ancient Near East. *Nature* **536**, 419–424 (2016). doi: 10.1038/nature19310; pmid: 27459054
110. I. Lazaridis *et al*., Genetic origins of the Minoans and Mycenaeans. *Nature* **548**, 214–218 (2017). doi: 10.1038/nature23310; pmid: 28783727
111. J. Lindo *et al*., Ancient individuals from the North American Northwest Coast reveal 10,000 years of regional genetic continuity. *Proc. Natl. Acad. Sci. U.S.A.* **114**, 4093–4098 (2017). doi: 10.1073/pnas.1620410114; pmid: 28377518
112. J. Lindo *et al*., The genetic prehistory of the Andean highlands 7000 years BP though European contact. *Sci. Adv.* **4**, eaau4921 (2018). doi: 10.1126/sciadv.aau4921; pmid: 30417096
113. M. Lipson *et al*., Population Turnover in Remote Oceania Shortly after Initial Settlement. *Curr. Biol.* **28**, 1157–1165.e7 (2018). doi: 10.1016/j.cub.2018.02.051; pmid: 29501328
114. M. Lipson *et al*., Parallel palaeogenomic transects reveal complex genetic history of early European farmers. *Nature* **551**, 368–372 (2017). doi: 10.1038/nature24476; pmid: 29144465
115. M. Lipson *et al*., Ancient West African foragers in the context of African population history. *Nature* **577**, 665–670 (2020). doi: 10.1038/s41586-020-1929-1; pmid: 31969706
116. M. Lipson *et al*., Ancient genomes document multiple waves of migration in Southeast Asian prehistory. *Science* **361**, 92–95 (2018). doi: 10.1126/science.aat3188; pmid: 29773666
117. M. Gallego Llorente *et al*., Ancient Ethiopian genome reveals extensive Eurasian admixture in Eastern Africa. *Science* **350**, 820–822 (2015). doi: 10.1126/science.aad2879; pmid: 26449472
118. A.-S. Malaspinas *et al*., Two ancient human genomes reveal Polynesian ancestry among the indigenous Botocudos of Brazil. *Curr. Biol.* **24**, R1035–R1037 (2014). doi: 10.1016/j.cub.2014.09.078; pmid: 25455029
119. H. Malmström *et al*., The genomic ancestry of the Scandinavian Battle Axe Culture people and their relation to the broader Corded Ware horizon. *Proc. Biol. Sci.* **286**, 20191528 (2019). doi: 10.1098/rspb.2019.1528; pmid: 31594508
120. R. Martiniano *et al*., Genomic signals of migration and continuity in Britain before the Anglo-Saxons. *Nat. Commun.* **7**, 10326 (2016). doi: 10.1038/ncomms10326; pmid: 26783717
121. R. Martiniano *et al*., The population genomics of archaeological transition in west Iberia: Investigation of ancient substructure using imputation and haplotype-based methods. *PLOS Genet.* **13**, e1006852 (2017). doi: 10.1371/journal.pgen.1006852; pmid: 28749934
122. I. Mathieson *et al*., Genome-wide patterns of selection in 230 ancient Eurasians. *Nature* **528**, 499–503 (2015). doi: 10.1038/nature16152; pmid: 26595274
123. I. Mathieson *et al*., The genomic history of southeastern Europe. *Nature* **555**, 197–203 (2018). doi: 10.1038/nature25778; pmid: 29466330
124. H. McColl *et al*., The prehistoric peopling of Southeast Asia. *Science* **361**, 88–92 (2018). doi: 10.1126/science.aat3628; pmid: 29976827
125. A. Mittnik *et al*., The genetic prehistory of the Baltic Sea region. *Nat. Commun.* **9**, 442 (2018). doi: 10.1038/s41467-018-02825-9; pmid: 29382937
126. A. Mittnik *et al*., Kinship-based social inequality in Bronze Age Europe. *Science* **366**, 731–734 (2019). doi: 10.1126/science.aax6219; pmid: 31601705
127. M. Mondal *et al*., Genomic analysis of Andamanese provides insights into ancient human migration into Asia and adaptation. *Nat. Genet.* **48**, 1066–1070 (2016). doi: 10.1038/ng.3621; pmid: 27455350
128. J. V. Moreno-Mayar *et al*., Terminal Pleistocene Alaskan genome reveals first founding population of Native Americans. *Nature* **553**, 203–207 (2018). doi: 10.1038/nature25173; pmid: 29323294
129. A. G. Nikitin *et al*., Interactions between earliest Linearbandkeramik farmers and central European hunter gatherers at the dawn of European Neolithization. *Sci. Rep.* **9**, 19544 (2019). doi: 10.1038/s41598-019-56029-2; pmid: 31863024
130. C. Ning *et al*., Ancient Genomes Reveal Yamnaya-Related Ancestry and a Potential Source of Indo-European Speakers in Iron Age Tianshan. *Curr. Biol.* **29**, 2526–2532.e4 (2019). doi: 10.1016/j.cub.2019.06.044; pmid: 31353181
131. I. Olalde *et al*., A Common Genetic Origin for Early Farmers from Mediterranean Cardial and Central European LBK Cultures. *Mol. Biol. Evol.* **32**, 3132–3142 (2015). doi: 10.1093/molbev/msv181; pmid: 26337550
132. I. Olalde *et al*., Derived immune and ancestral pigmentation alleles in a 7,000-year-old Mesolithic European. *Nature* **507**, 225–228 (2014). doi: 10.1038/nature12960; pmid: 24463515
133. I. Olalde *et al*., The Beaker phenomenon and the genomic transformation of northwest Europe. *Nature* **555**, 190–196 (2018). doi: 10.1038/nature25738; pmid: 29466337
134. I. Olalde *et al*., The genomic history of the Iberian Peninsula over the past 8000 years. *Science* **363**, 1230–1234 (2019). doi: 10.1126/science.aav4040; pmid: 30872528
135. A. Omrak *et al*., Genomic Evidence Establishes Anatolia as the Source of the European Neolithic Gene Pool. *Curr. Biol.* **26**, 270–275 (2016). doi: 10.1016/j.cub.2015.12.019; pmid: 26748850
136. J. K. Pickrell *et al*., The genetic prehistory of southern Africa. *Nat. Commun.* **3**, 1143 (2012). doi: 10.1038/ncomms2140; pmid: 23072811
137. C. Posth *et al*., Reconstructing the Deep Population History of Central and South America. *Cell* **175**, 1185–1197.e22 (2018). doi: 10.1016/j.cell.2018.10.027; pmid: 30415837
138. C. Posth *et al*., Language continuity despite population replacement in Remote Oceania. *Nat. Ecol. Evol.* **2**, 731–740 (2018). doi: 10.1038/s41559-018-0498-2; pmid: 29487365
139. M. Raghavan *et al*., Upper Palaeolithic Siberian genome reveals dual ancestry of Native Americans. *Nature* **505**, 87–91 (2014). doi: 10.1038/nature12736; pmid: 24256729
140. M. Raghavan *et al*., The genetic prehistory of the New World Arctic. *Science* **345**, 1255832 (2014). doi: 10.1126/science.1255832; pmid: 25170159
141. M. Raghavan *et al*., Genomic evidence for the Pleistocene and recent population history of Native Americans. *Science* **349**, aab3884 (2015). doi: 10.1126/science.aab3884; pmid: 26198033
142. M. Rasmussen *et al*., Ancient human genome sequence of an extinct Palaeo-Eskimo. *Nature* **463**, 757–762 (2010). doi: 10.1038/nature08835; pmid: 20148029
143. M. Rasmussen *et al*., The genome of a Late Pleistocene human from a Clovis burial site in western Montana. *Nature* **506**, 225–229 (2014). doi: 10.1038/nature13025; pmid: 24522598

144. M. Rasmussen *et al*., The ancestry and affiliations of Kennewick Man. *Nature* **523**, 455–458 (2015). doi: 10.1038/nature14625; pmid: 26087396
145. R. Rodríguez-Varela *et al*., Genomic Analyses of Pre-European Conquest Human Remains from the Canary Islands Reveal Close Affinity to Modern North Africans. *Curr. Biol.* **27**, 3396–3402.e5 (2017). doi: 10.1016/j.cub.2017.09.059; pmid: 29107554
146. L. Saag *et al*., Extensive Farming in Estonia Started through a Sex-Biased Migration from the Steppe. *Curr. Biol.* **27**, 2185–2193.e6 (2017). doi: 10.1016/j.cub.2017.06.022; pmid: 28712569
147. L. Saag *et al*., The Arrival of Siberian Ancestry Connecting the Eastern Baltic to Uralic Speakers further East. *Curr. Biol.* **29**, 1701–1711.e16 (2019). doi: 10.1016/j.cub.2019.04.026; pmid: 31080083
148. C. L. Scheib *et al*., Ancient human parallel lineages within North America contributed to a coastal expansion. *Science* **360**, 1024–1027 (2018). doi: 10.1126/science.aar6851; pmid: 29853687
149. F. Sánchez-Quinto *et al*., Megalithic tombs in western and northern Neolithic Europe were linked to a kindred society. *Proc. Natl. Acad. Sci. U.S.A.* **116**, 9469–9474 (2019). doi: 10.1073/pnas.1818037116; pmid: 30988179
150. V. J. Schuenemann *et al*., Ancient Egyptian mummy genomes suggest an increase of Sub-Saharan African ancestry in post-Roman periods. *Nat. Commun.* **8**, 15694 (2017). doi: 10.1038/ncomms15694; pmid: 28556824
151. S. Schiffels *et al*., Iron Age and Anglo-Saxon genomes from East England reveal British migration history. *Nat. Commun.* **7**, 10408 (2016). doi: 10.1038/ncomms10408; pmid: 26783965
152. C. M. Schlebusch *et al*., Southern African ancient genomes estimate modern human divergence to 350,000 to 260,000 years ago. *Science* **358**, 652–655 (2017). doi: 10.1126/science.aao6266; pmid: 28971970
153. H. Schroeder *et al*., Origins and genetic legacies of the Caribbean Taino. *Proc. Natl. Acad. Sci. U.S.A.* **115**, 2341–2346 (2018). doi: 10.1073/pnas.1716839115; pmid: 29463742
154. H. Schroeder *et al*., Unraveling ancestry, kinship, and violence in a Late Neolithic mass grave. *Proc. Natl. Acad. Sci. U.S.A.* **116**, 10705–10710 (2019). doi: 10.1073/pnas.1820210116; pmid: 31061125
155. A. Seguin-Orlando *et al*., Genomic structure in Europeans dating back at least 36,200 years. *Science* **346**, 1113–1118 (2014). doi: 10.1126/science.aaa0114; pmid: 25378462
156. V. Shinde *et al*., An Ancient Harappan Genome Lacks Ancestry from Steppe Pastoralists or Iranian Farmers. *Cell* **179**, 729–735.e10 (2019). doi: 10.1016/j.cell.2019.08.048; pmid: 31495572
157. M. Sikora *et al*., The population history of northeastern Siberia since the Pleistocene. *Nature* **570**, 182–188 (2019). doi: 10.1038/s41586-019-1279-z; pmid: 31168093
158. M. Sikora *et al*., Ancient genomes show social and reproductive behavior of early Upper Paleolithic foragers. *Science* **358**, 659–662 (2017). doi: 10.1126/science.aao1807; pmid: 28982795
159. P. Skoglund *et al*., Reconstructing Prehistoric African Population Structure. *Cell* **171**, 59–71.e21 (2017). doi: 10.1016/j.cell.2017.08.049; pmid: 28938123
160. P. Skoglund *et al*., Genetic evidence for two founding populations of the Americas. *Nature* **525**, 104–108 (2015). doi: 10.1038/nature14895; pmid: 26196601
161. P. Skoglund *et al*., Genomic insights into the peopling of the Southwest Pacific. *Nature* **538**, 510–513 (2016). doi: 10.1038/nature19844; pmid: 27698418
162. P. Skoglund *et al*., Genomic diversity and admixture differs for Stone-Age Scandinavian foragers and farmers. *Science* **344**, 747–750 (2014). doi: 10.1126/science.1253448; pmid: 24762536
163. V. Slon *et al*., The genome of the offspring of a Neanderthal mother and a Denisovan father. *Nature* **561**, 113–116 (2018). doi: 10.1038/s41586-018-0455-x; pmid: 30135579
164. M. Unterländer *et al*., Ancestry and demography and descendants of Iron Age nomads of the Eurasian Steppe. *Nat. Commun.* **8**, 14615 (2017). doi: 10.1038/ncomms14615; pmid: 28256537
165. C. Valdiosera *et al*., Four millennia of Iberian biomolecular prehistory illustrate the impact of prehistoric migrations at the far end of Eurasia. *Proc. Natl. Acad. Sci. U.S.A.* **115**, 3428–3433 (2018). doi: 10.1073/pnas.1717762115; pmid: 29531053
166. M. van de Loosdrecht *et al*., Pleistocene North African genomes link Near Eastern and sub-Saharan African human populations. *Science* **360**, 548–552 (2018). doi: 10.1126/science.aar8380; pmid: 29545507
167. C. M. van den Brink *et al*., A Late Bronze Age II clay coffin from Tel Shaddud in the Central Jezreel Valley, Israel: Context and historical implications. *Levant* **49**, 105–135 (2017). doi: 10.1080/00758914.2017.1368204
168. K. R. Veeramah *et al*., Population genomic analysis of elongated skulls reveals extensive female-biased immigration in Early Medieval Bavaria. *Proc. Natl. Acad. Sci. U.S.A.* **115**, 3494–3499 (2018). doi: 10.1073/pnas.1719880115; pmid: 29531040
169. D. N. Vyas, A. Al-Meeri, C. J. Mulligan, Testing support for the northern and southern dispersal routes out of Africa: An analysis of Levantine and southern Arabian populations. *Am. J. Phys. Anthropol.* **164**, 736–749 (2017). doi: 10.1002/ajpa.23312; pmid: 28913852
170. C.-C. Wang *et al*., Ancient human genome-wide data from a 3000-year interval in the Caucasus corresponds with eco-geographic regions. *Nat. Commun.* **10**, 590 (2019). doi: 10.1038/s41467-018-08220-8; pmid: 30713341
171. M. A. Yang *et al*., 40,000-Year-Old Individual from Asia Provides Insight into Early Population Structure in Eurasia. *Curr. Biol.* **27**, 3202–3208.e9 (2017). doi: 10.1016/j.cub.2017.09.030; pmid: 29033327
172. P. Zalloua *et al*., Ancient DNA of Phoenician remains indicates discontinuity in the settlement history of Ibiza. *Sci. Rep.* **8**, 17567 (2018). doi: 10.1038/s41598-018-35667-y; pmid: 30514893
173. J. R. Adrion *et al*., A community-maintained standard library of population genetic models. *eLife* **9**, e54967 (2020). doi: 10.7554/eLife.54967; pmid: 32573438
174. J. Kelleher *et al*., tskit-dev/tskit: C API 0.99.14, version C_0.99.14, Zenodo (2021); https://doi.org/10.5281/zenodo.5465773.
175. A. W. Wohns, Y. Wong, B. Jeffery, awohns/unified_genealogy_paper: Revised manuscript, version 0.1.1, Zenodo (2021); https://doi.org/10.5281/zenodo.5784137.
176. A. W. Wohns *et al*., A unified genealogy of modern and ancient genomes: Unified, inferred tree sequences of 1000 Genomes, Human Genome Diversity, and Simons Genome Diversity Projects, version 1.0.0, Zenodo (2021); https://doi.org/10.5281/zenodo.5495535.
177. A. W. Wohns *et al*., A unified genealogy of modern and ancient genomes: Unified, inferred tree sequences of 1000 Genomes, Human Genome Diversity, and Simons Genome Diversity Projects with ancient samples, version 1.0.0, Zenodo (2021); https://doi.org/10.5281/zenodo.5512994.

ACKNOWLEDGMENTS

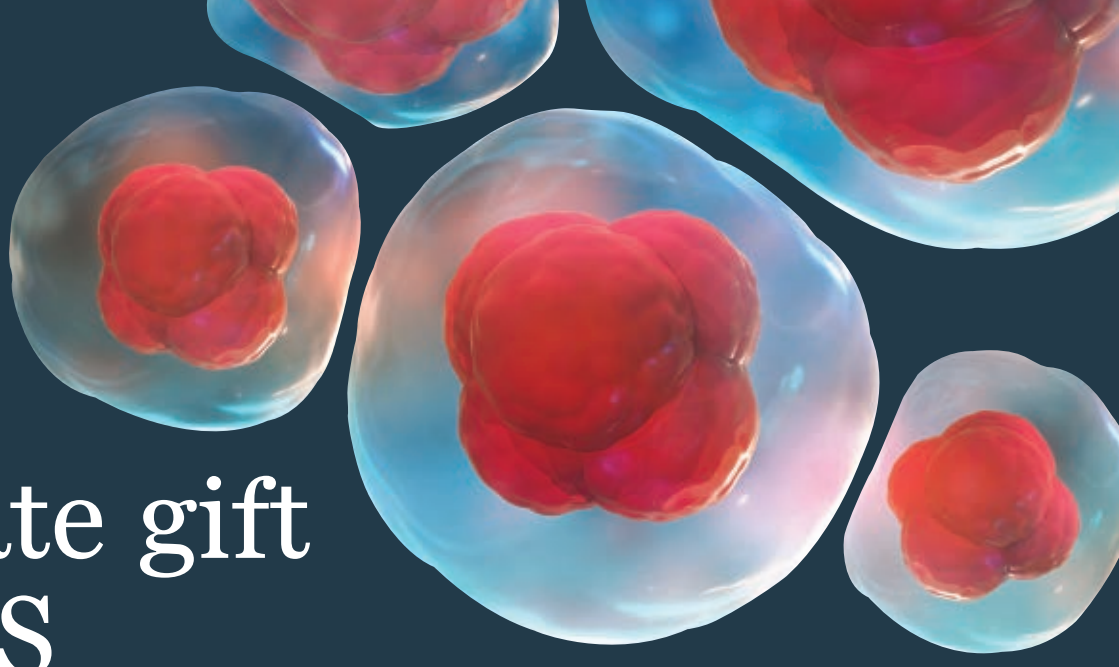
We thank the Oxford Big Data research computing team, specifically A. Huffman and R. Esnouf, as well as D. Lieberman, K. Lohse, and E. Castedo Ellerman for comments. **Funding:** This work was supported by Wellcome Trust grant 100956/Z/13/Z (to G.M.), the Li Ka Shing Foundation (to G.M.), the Robertson Foundation (to J.K.), the Rhodes Trust (to A.W.W.), NIH (NIGMS) grant GM100233 (to D.R.), the Paul Allen Foundation (to D.R.), the John Templeton Foundation grant 61220 (to D.R.), and the Howard Hughes Medical Institute (to D.R.). The computational aspects of this research were supported by the Wellcome Trust (core award 203141/Z/16/Z) and the NIHR Oxford BRC. The views expressed are those of the authors and not necessarily those of the NHS, the NIHR, or the Department of Health. **Author contributions:** Conceptualization: A.W.W., Y.W., J.K., and G.M. Methodology: A.W.W., Y.W., A.A., S.M., N.P., J.K., and G.M. Software: A.W.W., Y.W., and J.K. Investigation: A.W.W., Y.W., B.J., R.P., and D.R. Formal analysis: A.W.W., Y.W., B.J., A.A., and S.M. Validation: A.W.W., Y.W., and B.J. Visualization: A.W.W., Y.W., and B.J. Data curation: A.W.W., Y.W., B.J., A.A., and S.M. Resources: A.W.W., Y.W., A.A., S.M., R.P., D.R., and J.K. Funding acquisition: D.R., J.K., and G.M. Project administration: A.W.W. and D.R. Supervision: Y.W., D.R., J.K., and G.M. Writing–original draft: A.W.W., Y.W., and G.M. Writing–review and editing: A.W.W., Y.W., D.R., J.K., and G.M. **Competing interests:** G.M. is a director of and shareholder in Genomics plc and a partner in Peptide Groove LLP. The authors declare no other competing interests. **Data and materials availability:** Newly reported sequencing data from the Afanasievo family are available from the European Nucleotide Archive, accession number PRJEB43093, and phased variant data for the family are available from the European Variation Archive, accession number PRJEB46983. All publicly available datasets used in this paper are available from their original publications. *tsinfer* is deposited to Zenodo (*30*) and is available at https://tsinfer.readthedocs.io/ under the GNU General Public License v3.0, *tsdate* is deposited to Zenodo (*31*) and is available at https://tsdate.readthedocs.io/ under the MIT License, and *tskit* is deposited to Zenodo (*174*) and is available at https://tskit.readthedocs.io/ under the MIT License. All code used to perform analyses in this paper is deposited to Zenodo (*175*) and can be found at https://github.com/awohns/unified_genealogy_paper. Unified tree sequences of the HGDP, SGDP, and TGP autosomes are available from Zenodo (*176*). Unified tree sequences of the HGDP, SGDP, TGP, and high-coverage ancient autosomes are available from Zenodo (*177*). Tree sequences were compressed using the *tszip* utility; see the documentation at https://tszip.readthedocs.io/ for further details.

SUPPLEMENTARY MATERIALS

science.org/doi/10.1126/science.abi8264
Materials and Methods
Supplementary Text
Figs. S1 to S21
Tables S1 to S3
References (*178*–*208*)
Movie S1

9 April 2021; accepted 23 December 2021
10.1126/science.abi8264

1848 SOCIETY
AAAS



An estate gift to AAAS

Going all the way back to 1848, our founding year, the American Association for the Advancement of Science (AAAS) has been deeply committed to advancing science, engineering and innovation around the world for the benefit of all people.

Today, we are dedicated to advocating for science and scientific evidence to be fully and positively integrated into public policy and for the community to speak with one voice to advance science and engineering in the United States and around the world.

By making AAAS a beneficiary of your will, trust, retirement plan or life insurance policy, you will become a member of our 1848 Society and will help fuel our work on behalf of science and society – including publishing the world's most promising, innovative research in the *Science* family of journals and engaging in the issues that matter locally, nationally and around the world.

"As a teacher and instructor, I bear responsibility for the younger generations. If you have extra resources, concentrate them on organizations, like AAAS, that are doing work for all."

—Prof. Elisabeth Ervin-Blankenheim, 1848 Society member

If you intend to include AAAS in your estate plans, provide this information to your lawyer or financial adviser:

Legal Name: American Association for the Advancement of Science
Federal Tax ID Number: 53-0196568
Address: 1200 New York Avenue, NW, Washington, DC 20005

If you would like more information on making an estate gift to AAAS, cut out and return the form below or send an email to philanthropy@aaas.org. Additional details are also available online at **www.aaas.org/1848Society**.

AMERICAN ASSOCIATION FOR THE ADVANCEMENT OF SCIENCE

cut here

Yes, I would like more information about joining the AAAS 1848 Society.

1848 SOCIETY
AAAS

PLEASE CONTACT ME AT:

Name: _____

Address: _____

City: _____ State: _____ Zip code: _____ Country: _____

Email: _____ Phone: _____

RETURN THIS FORM TO:
AAAS Office of Philanthropy and Strategic Partnerships • 1200 New York Avenue, NW • Washington, DC 20005 USA

RESEARCH ARTICLE SUMMARY

NANOPHOTONICS

A framework for scintillation in nanophotonics

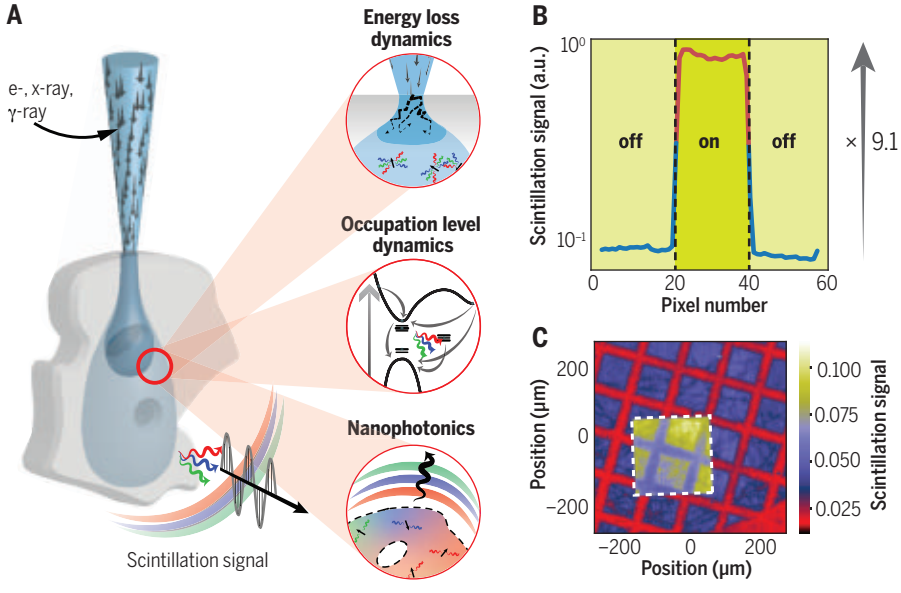
Charles Roques-Carmes*†, Nicholas Rivera*†, Ali Ghorashi, Steven E. Kooi, Yi Yang, Zin Lin, Justin Beroz, Aviram Massuda, Jamison Sloan, Nicolas Romeo, Yang Yu, John D. Joannopoulos, Ido Kaminer, Steven G. Johnson, Marin Soljačić

INTRODUCTION: Bombardment of materials by high-energy particles often leads to light emission in a process known as scintillation. Scintillators, being broadly applicable to the detection of ionizing radiation, have widespread applications, including in x-ray detectors for medical imaging and nondestructive inspection, gamma-ray detectors for positron emission tomography, phosphor screens in night vision systems and electron microscopes, and electromagnetic calorimeters in high-energy physics experiments. Accordingly, there is great interest in the development of "better scintillators" with greater photon yields and improved spatial and energy resolution. Better scintillators in general would lead to definite improvements in all of the above use cases. One example application is medical imaging, where brighter scintillators could enable very-low-dose x-ray imaging, therefore reducing potential harm to patients. Most research into the problem of improving scintillators involves the synthesis of new materials with better intrinsic scintillating properties.

RATIONALE: The conversion of a high-energy particle into photons is a complex, multiphysics process in which the incident particle creates a cascade of secondary electron excitations in the scintillator. These secondary excitations then relax into a non-equilibrium distribution before emitting scintillation photons. By creating spatial inhomogeneities in the scintillator on the scale of the scintillation photon wavelength, and thus modulating the optical properties of the material on the wavelength scale, one can control and enhance the light emission. In such "nanophotonic scintillators," it is then possible for the light-emitting electrons in the scintillator to emit light much more rapidly due to enhancement of the local density of optical states available to the electrons for light emission. It is also possible to use these nanophotonic structures to "steer" trapped light out of the scintillator, enabling more light to be detected. Both of these effects lead to enhanced rates of scintillation photon emission. These nanophotonic effects are material-agnostic, enabling in principle any scintillator to be enhanced, and these effects can also be in principle observed for any type of high-energy particle.

RESULTS: We developed a first-principles theory of nanophotonic scintillators, taking into account the complex processes leading to electron excitation as well as the light emission by non-equilibrium electrons in arbitrary nanophotonic structures. Using the theory as a guide, we experimentally demonstrated order-of-magnitude scintillation enhancements in two different platforms: electron-induced scintillation by silica defects, and x-ray–induced scintillation by rare-earth dopants in conventional scintillators. The enhancements in both cases were enabled by two-dimensionally periodic etching of either the scintillator or the material above the scintillator to create a two-dimensional photonic crystal slab geometry. The theory accounted for the enhancements observed experimentally, as well as other effects that required first-principles description of the underlying microscopic kinetics of the emission process. For example, we could explain the observed spectral shaping as a function of geometrical parameters of the photonic crystal slab. Additionally, using the framework, we could account for nonlinear relationships of the signal on the incident particle flux, as well as effects where the dominant scintillation wavelength could change as a function of high-energy particle flux. Beyond, we used a nanopatterned x-ray scintillator to record x-ray scans of various specimens and observed an increase in image brightness. This directly translates into faster scans, or equivalently a lower x-ray dose required to achieve a given brightness.

CONCLUSION: Our framework can be directly applied to model nanophotonic scintillation in many existing experiments, accounting for arbitrary types of high-energy particles, scintillator materials, and nanophotonic environments. Beyond this, our framework also allows the discovery of optimal nanophotonic structures for enhancing scintillation. We show how topology optimization and other types of nanophotonic structures can be used to find structures that could present even larger scintillation enhancements. We expect that the concept demonstrated here could be deployed in all of the application areas where scintillators are used, with compelling applications throughout, including medical imaging, night vision, and high-energy physics experiments. ■



Nanophotonic scintillators. (**A**) Nanophotonic scintillators consist of nanophotonic structures integrated with scintillators. Scintillation can be modeled, tailored, and optimized by combining energy loss dynamics, occupation level dynamics, and nanophotonics modeling. (**B**) Order-of-magnitude x-ray scintillation enhancement with a photonic crystal nanophotonic scintillator. (**C**) X-ray scan taken with a nanophotonic scintillator (white dashed square).

The list of author affiliations is available in the full article online.
*Corresponding author. Email: chrc@mit.edu (C.R.-C.); nrivera@mit.edu (N.R.)
†These authors contributed equally to this work.
Cite this article as C. Roques-Carmes *et al.*, *Science* **375**, eabm9293 (2022). DOI: 10.1126/science.abm9293

READ THE FULL ARTICLE AT
https://doi.org/10.1126/science.abm9293

RESEARCH ARTICLE

NANOPHOTONICS

A framework for scintillation in nanophotonics

Charles Roques-Carmes[1]*†, Nicholas Rivera[2]*†, Ali Ghorashi[2], Steven E. Kooi[3], Yi Yang[1,2,4], Zin Lin[5], Justin Beroz[2], Aviram Massuda[6], Jamison Sloan[1], Nicolas Romeo[2], Yang Yu[7], John D. Joannopoulos[2,3], Ido Kaminer[8], Steven G. Johnson[2,4], Marin Soljačić[1,2]

Bombardment of materials by high-energy particles often leads to light emission in a process known as scintillation. Scintillation has widespread applications in medical imaging, x-ray nondestructive inspection, electron microscopy, and high-energy particle detectors. Most research focuses on finding materials with brighter, faster, and more controlled scintillation. We developed a unified theory of nanophotonic scintillators that accounts for the key aspects of scintillation: energy loss by high-energy particles, and light emission by non-equilibrium electrons in nanostructured optical systems. We then devised an approach based on integrating nanophotonic structures into scintillators to enhance their emission, obtaining nearly an order-of-magnitude enhancement in both electron-induced and x-ray–induced scintillation. Our framework should enable the development of a new class of brighter, faster, and higher-resolution scintillators with tailored and optimized performance.

Scintillation, the process by which high-energy particles (HEPs, also known as ionizing radiation) bombarding a material convert their kinetic energy into light, is among the most commonly occurring phenomena in the interaction of ionizing radiation with matter. It enables a number of technologies, including x-ray detectors used in medical imaging and nondestructive inspection, γ-ray detectors in positron emission tomography scanners, phosphor screens in night-vision systems, electron detectors in electron microscopes, and electromagnetic calorimeters in high-energy physics experiments (*1*, *2*). Scintillation appears under many different guises. For example, when the "high-energy" particle is a visible or ultraviolet (UV) photon, the scintillation is better known as photoluminescence. When the incident particles are energetic electrons, scintillation is also known as incoherent cathodoluminescence. When the high-energy particle is an x-ray or γ-ray, the phenomenon is almost exclusively referred to as scintillation (*1*). Because of scintillation's broad applications, there is interest in the development of "better scintillators" with greater photon yields as well as greater spatial and energy resolution. Such enhanced scintillators could translate into enhanced functionalities. One such example is in medicine: Brighter and higher-resolution scintillators could enable medical imaging (e.g., computed tomography) with higher resolution and a substantially lower radiation dose. Current approaches to improve scintillation are mostly oriented toward the growth of higher-quality materials (e.g., single-crystalline, controlled creation of defect sites) as well as the identification of new materials [e.g., ceramics and metal halide perovskites (*3*)] with faster and brighter intrinsic scintillation.

We have developed a different approach to this problem, which we refer to as "nanophotonic scintillators." By patterning a scintillator on the scale of the wavelength of light, it is possible to strongly enhance, as well as control, the scintillation yield, spectrum, directivity, and polarization response. The motivation for our approach was the observation that the light emitted in scintillation is effectively spontaneous emission (*4*). An enormous amount of effort in multiple fields has gone into controlling and enhancing spontaneous emission through the density of optical states (*5*, *6*), with corresponding impact in those fields (*7*), including photovoltaics (*8*), sensing (*9*, *10*), light-emitting diodes (LEDs) (*11*, *12*), thermal emission (*13*), and free-electron radiation sources (*14*–*23*). In the context of scintillation, nanophotonic enhancements could in principle take two forms: (i) through direct enhancement of the rate of spontaneous emission by shaping the density of optical states (*4*), or (ii) through improved light extraction from bulk scintillators. Early work demonstrated enhanced light extraction provided by a photonic crystal coating atop a bulk scintillator (*24*–*30*). Nonetheless, the prospect of enhancing scintillation through the local density of states, as well as the prospect of large scintillation enhancements, by either mechanism remains unrealized. Moreover, the type of nanophotonic structures that could even in principle realize such effects is unknown.

Part of the reason for the lack of progress in this field so far entails a theoretical gap associated with the complex, multiphysics nature of scintillation emission (Fig. 1, A to D). The process of scintillation is composed of several complex parts spanning a wide range of length and energy scales (*1*): (i) ionization of electrons by HEP followed by production and diffusion of secondary electrons (Fig. 1B) (*31*, *32*); (ii) establishment of a non-equilibrium steady state (Fig. 1C) (*33*, *34*); and (iii) recombination, leading to light emission (Fig. 1D). The final step of light emission is particularly complex to model, especially in nanophotonic settings, as it results from fluctuating, spatially distributed dipoles with a non-equilibrium distribution function that strongly depends on the previous steps of the scintillation process.

A general theory of nanophotonic scintillation

First, we present a unified theory of nanophotonic scintillators. The theory we have developed is ab initio: It can, from first principles, predict the angle- and frequency-dependent scintillation from arbitrary scintillators (established and nascent), taking into account the three steps illustrated in Fig. 1, B to D. It takes into account the energy loss dynamics of HEPs through arbitrary materials, the non-equilibrium steady state and electronic structure of the scintillating electrons, and the nanostructured optical environment (i.e., the electrodynamics of the light emission by this non-equilibrium electron distribution).

Consider the situation depicted in Fig. 1A, in which a HEP beam deposits energy into a scintillating material (Fig. 1B). The material may be in proximity to a nanophotonic structure or integrated with it (as in both cases for which we present experiments). The interaction of the beam with the scintillating material will generally lead to a process of electron excitation in the scintillator, followed by relaxation into an excited state (Fig. 1C).

After this relaxation occurs, the occupations of electrons and holes are typically in an approximate equilibrium (*34*) (referred to as a non-equilibrium steady state). This equilibrium is well defined because it occurs on picosecond time scales, which are effectively instantaneous relative to the excited-state depletion time scales (nanoseconds) (*31*). Under these assumptions, the radiative recombination may be described in terms of emission from fluctuating currents in the material, not unlike thermal radiation (in which the electrons are in a true equilibrium). The key difference from thermal radiation is that the

[1]Research Laboratory of Electronics, Massachusetts Institute of Technology, Cambridge, MA 02139, USA. [2]Department of Physics, Massachusetts Institute of Technology, Cambridge, MA 02139, USA. [3]Institute for Soldier Nanotechnologies, Massachusetts Institute of Technology, Cambridge, MA 02139, USA. [4]Department of Physics, University of Hong Kong, Hong Kong, China. [5]Department of Mathematics, Massachusetts Institute of Technology, Cambridge, MA 02139, USA. [6]Microsystems Technology Laboratories, Massachusetts Institute of Technology, Cambridge, MA 02139, USA. [7]Raith America Inc., Troy, NY 12180, USA. [8]Department of Electrical and Computer Engineering, Technion, Haifa 32000, Israel.
*Corresponding author. Email: chrc@mit.edu (C.R.-C.); nrivera@mit.edu (N.R.)
†These authors contributed equally to this work.

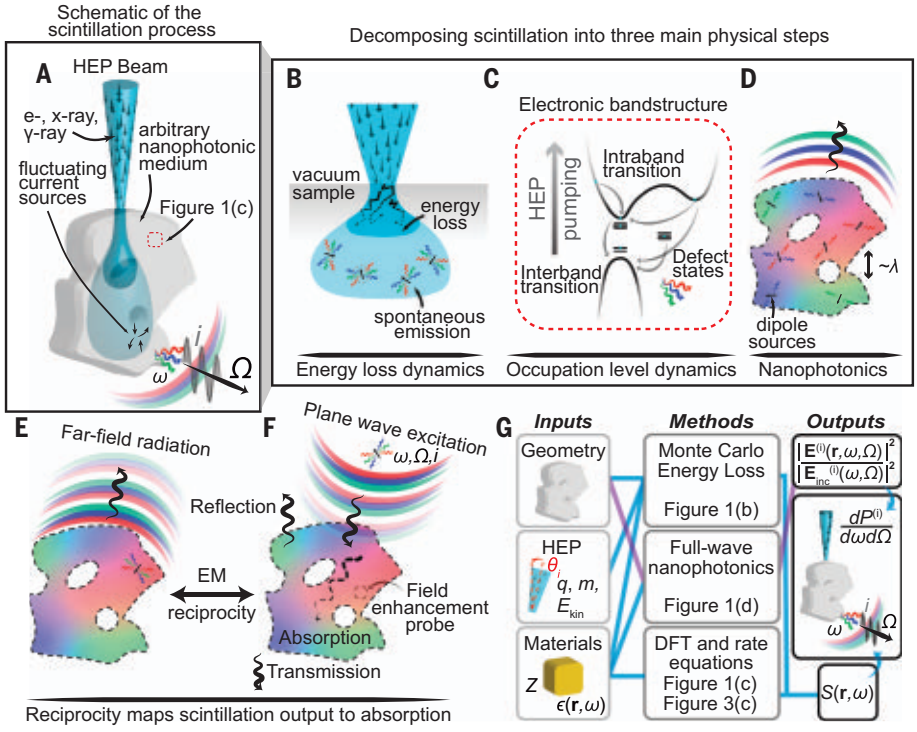


Fig. 1. A general framework for scintillation in nanophotonics. (**A**) We consider the case of high-energy particles (HEPs) bombarding an arbitrary nanophotonic medium, emitting scintillation photons at frequency ω (free-space wavelength λ), propagation angle Ω, and polarization *i*. (**B**) Subsequent HEP energy loss results in excitation of radiative sites (darker blue region in sample), which may diffuse before spontaneously emitting photons (lighter-blue region in sample). (**C**) The framework also accounts for different types of microscopic emitters. (**D**) The emitters may emit in arbitrary nanophotonic environments. (**E** and **F**) Electromagnetic reciprocity maps far-field radiation calculations from the stochastic many-body ensemble in a single electromagnetic simulation of plane-wave scattering (E) by calculating the effective spatially dependent field enhancement (F). (**G**) Summarized framework. Links indicate forward flow of information. The purple links indicate the possibility of backward flow (inverse design) in our current implementation. *q*, particle charge; *m*, mass; E_{kin}, kinetic energy; θ_i, incidence angle; $\varepsilon(\mathbf{r},\omega)$, material permittivity; *Z*, effective *Z*-number; $S(\mathbf{r},\omega)$, spatially varying intrinsic scintillation spectral function; $dP^{(i)}/d\omega d\Omega$, scintillation spectral-angular power density at polarization *i*. See (*39*) for an expanded and elaborated version of this panel.

occupation functions that determine the current-current correlations (which in turn determine the emission) are no longer governed by the Bose-Einstein distribution, but are instead dependent on the material and the HEP pump (and therefore spatially dependent).

Despite the nonuniversality of the current-current correlations, the otherwise strong similarity to thermal radiation inspires a key simplification that also gives rise to simple and powerful numerical methods for modeling and optimizing scintillation. This key simplification is electromagnetic reciprocity, which relates the following two quantities: (i) the emitted scintillation from the structure (at a given frequency ω, direction Ω, and polarization *i*) and (ii) the intensity of the field induced in the scintillator by sending a plane wave at it (of frequency ω, propagating along direction Ω into the structure, and polarization *i*). The intensity of the field induced in the structure at a given point is proportional to the local absorption, so the "emission" (i) is related to "absorption" of a plane wave (ii). As a result of this relation, it is possible to calculate the scintillation at some angle and frequency by calculating absorption of light incident from the far field at that frequency, angle, and polarization. We note that this relation makes use of the Lorentz reciprocity of Maxwell's equations only for the nanophotonic structure, and thus makes no assumption about the electronic transitions responsible for scintillation (we assume that the non-equilibrium electrons only weakly change the material's optical properties). Lorentz reciprocity can be broken in several classes of systems such as magnetic, nonlinear, and time-modulated materials (*35*). Such nonreciprocal photonic structures, which are of great recent interest, require extension of the framework but may allow many new phenomena [as in nonreciprocal effects in thermal radiation (*36*)]. Direct modeling of light emission by means of calculating the emission from an ensemble of fluctuating dipoles, as considered in the past [e.g., for thermal emission (*37*)], is extremely resource-intensive from a computational perspective (*38*). The effect of the spatial distribution of the scintillating centers is captured by integrating this spatial distribution against the spatially dependent absorption in the scintillating structure. In this way, the spatial information can be obtained "all-at-once" from a single absorption "map."

We use this simplification to quantify scintillation, which we represent in terms of the scintillation power per unit frequency $d\omega$ and solid angle $d\Omega$ along the *i*th polarization (e.g., $i = s,p$): $dP^{(i)}/d\omega d\Omega$ [where $dP/d\omega d\Omega = \sum_i (dP^{(i)}/d\omega d\Omega)$ is the total scintillation power density]. In most cases, the current-current correlations in the scintillator are isotropic [a condition that we relax in (*39*)], and we get

$$\frac{dP^{(i)}}{d\omega d\Omega} = \frac{\omega^2}{8\pi^2\varepsilon_0 c^3}\int d\mathbf{r}\,\frac{\left|\mathbf{E}^{(i)}(\mathbf{r},\omega,\Omega)\right|^2}{\left|\mathbf{E}^{(i)}_{\mathrm{inc}}(\omega,\Omega)\right|^2}\,S(\mathbf{r},\omega) \tag{1}$$

where the quantity $\mathbf{E}^{(i)}_{\mathrm{inc}}(\omega,\Omega)$ denotes the electric field of an incident plane wave of frequency ω, incident from a direction Ω, with polarization *i*. The quantity $\mathbf{E}^{(i)}(\mathbf{r},\omega,\Omega)$ denotes the total electric field at position $\mathbf{r}$ resulting from the incident field, and their ratio is thus the field enhancement. The function $S(\mathbf{r},\omega)$ in Eq. 1 is the spectral function encoding the frequency and position dependence of the current-current correlations, given by

$$S(\mathbf{r},\omega) = \frac{1}{3}\sum_{\alpha,\beta}\mathrm{tr}\left[\mathbf{J}^{\alpha\beta}(\mathbf{r})\mathbf{J}^{\beta\alpha}(\mathbf{r})\right]\times f_\alpha(\mathbf{r})\left[1-f_\beta(\mathbf{r})\right]\delta(\omega-\omega_{\alpha\beta}) \tag{2}$$

In this spectral function, f_α is the occupation factor of microscopic state α with energy E_α, $\mathbf{J}^{\alpha\beta}$ represents the matrix element of the current density operator $[\mathbf{J} \equiv (e/m)\psi^\dagger(-i\hbar\nabla)\psi]$, $\omega_{\alpha\beta} = [E_\alpha - E_\beta]/\hbar$, and tr denotes matrix trace. Besides the position dependence of the current density matrix element, the occupation functions can also depend on position, as they depend on the HEP energy loss density (specifically, how much energy is deposited in the vicinity of $\mathbf{r}$). Interestingly, Eq. 1 would be proportional to the strength of thermal emission upon substitution of $S(\mathbf{r},\omega)$ by the imaginary part of the material permittivity, multiplied by the Planck function. However, here the primary difference is that $S(\mathbf{r},\omega)$ describes a non-equilibrium state rather than the thermal equilibrium state of the material.

To better understand the core components of nanophotonic scintillation enhancement, let us simplify it further by considering the case where the density of excited states is uniform over some scintillating volume V_S [in which case we may drop the spatial dependence of *S* such that $S(\mathbf{r},\omega) \rightarrow S(\omega)$]. This volume can be thought of as the characteristic volume

over which excited electrons are created (as in Fig. 1B). Then we may write

$$\frac{dP^{(i)}}{d\omega d\Omega} = \frac{\pi}{\varepsilon_0 \omega} \times S(\omega) \times \frac{V_{\text{eff}}^{(i)}(\omega, \Omega)}{\lambda^3} \quad (3)$$

where

$$V_{\text{eff}}^{(i)}(\omega, \Omega) = \int_{V_S} d\mathbf{r} \frac{\left|\mathbf{E}^{(i)}(\mathbf{r}, \omega, \Omega)\right|^2}{\left|\mathbf{E}_{\text{inc}}^{(i)}(\omega, \Omega)\right|^2} \quad (4)$$

Because $V_{\text{eff}}^{(i)}(\omega, \Omega)$ has dimensions of volume and is proportional to the absorbed power over V_S (in the limit of weak absorption, so as not to perturb the field solutions), we often refer to this term (shortened as V_{eff}) as the effective volume of field enhancement or the effective volume of absorption. Equation 3 states that under this approximation, the scintillation spectrum is a simple product of a microscopic factor [which is set by the non-equilibrium spectral function $S(\omega)$] and an effective absorption volume V_{eff} [which is set only by the (structured) optical medium surrounding the scintillating medium].

Our framework to calculate scintillation according to Eq. 1 consists of three components, as illustrated in Fig. 1, B, C, D, and G: energy loss of a beam of HEPs, creation of excited electrons, and subsequent light emission (which is computed by calculating field enhancement from incident plane waves via electromagnetic reciprocity). As a technical matter, we note that we compute the HEP energy loss density by Monte Carlo simulations of energy loss [as is standard; see (*40*)], the electron energy levels and spectral function through density functional theory (DFT), and the nanophotonic field enhancement through finite-difference time-domain and rigorous coupled-wave analysis methods. In principle, these components are coupled together (*39*).

More details on each component of the workflow depicted in Fig. 1G can be found in (*39*). The description of scintillation provided here—using calculations of electronic structure, energy loss, and electromagnetic response—is, to the best of our knowledge, the first to provide an ab initio and end-to-end account of scintillation in nanophotonic structures.

Enhancement and shaping of electron beam–induced scintillation

We first experimentally demonstrate scintillation from silicon-on-insulator nanophotonic structures due to bombardment by electrons (here, with energies in the range of 10 to 40 keV). Electrons with a few tens of keV energies are a convenient platform to demonstrate nanophotonic scintillation, as they readily lose almost all of the energy to the nanophotonic structure. Such lower-energy particles penetrate materials less deeply, leading to a strong overlap between the spatial region of HEP energy loss density and the region of high field enhancement (the latter of which is within a few hundred nanometers of the surface).

Our experimental setup to measure scintillation is based on a modified scanning electron microscope (SEM) [an earlier version of which was reported in (*15*–*17*, *19*)], shown in Fig. 2, A and E: A focused electron beam of tunable energy (10 to 40 keV) excites the sample at a shallow (~1°) angle, and the resulting radiation is collected and analyzed with a set of free-space optics. The light is collected by an objective lens that accepts radiation emitted in a cone of half-angle 17.5°. Under the shallow-angle conditions of electron incidence in our experiments, the effective penetration depth of the electrons is on the scale of a few hundred nanometers (Fig. 2B), far below the nominal mean free paths of 40-keV electrons in silica or silicon, which are on the order of 20 μm. This leads to strong overlap of the energy loss with regions of field enhancement. Control over the incidence angle also enables tuning of this overlap between the HEP energy loss density and V_{eff}.

The first structure we consider is a thin film of 500 nm of Si atop 1 μm of SiO_2 atop a Si substrate. The second structure differs from the first in that the top Si layer is patterned to form a square lattice (design period ~430 nm; see Fig. 2C) of air holes (diameter ~260 nm) of various etch depths (~25, 35, and 45 nm). We refer to them as "thin film" (TF) and "photonic crystal" (PhC) samples, respectively. Scintillation in these structures occurs in the buried silica layer, and in particular among a class of commonly occurring defects called self-trapped holes (STHs) (*41*). Such defects have been studied extensively because of their consequences for silica fibers. They display distinct emission at red and green wavelengths, which, in addition to our other observations, enable us to attribute our observations to STH scintillation [and thus rule out other mechanisms of electron beam–induced emission, such as coherent cathodoluminescence (*39*)].

We now show how nanophotonic structures shape and enhance scintillation in silica. The scintillation spectrum of the sample in the visible range, for both TF and PhC samples, is shown in Fig. 2D. The TF scintillation measurements shown in black in Fig. 2, F and G, display two main sets of features at green (~500 nm) and red (~625 to 675 nm) wavelengths. At red wavelengths, there is a clear double-peak structure; at green wavelengths, the scintillation spectrum displays multiple peaks. These multiply peaked spectra differ considerably from prior observations of STH scintillation (*41*): Although they occur at roughly the same wavelength, prior observations show only one peak at the red and green wavelengths (*42*). The multiple peaks of the spectrum (and even its shoulders) are well accounted for at both red and green wavelengths even by the simplified Eq. 3, and specifically by multiplying the shape of the STH spectrum in bulk by the V_{eff} calculated for the TF. The bulk spectrum is inferred from previous observations (*41*) and is confirmed by our DFT calculations (Fig. 3D). The multiply peaked structure of V_{eff} thus arises from thin-film resonances, which enhance the absorption of light in the buried silica layer. The agreement between theory and experiment in Fig. 2, F and G, unambiguously indicates a strong degree of spectral control over scintillation even in the simplest possible "nanostructure" (namely, a thin film).

In contrast to the TF scintillation, the scintillation from the PhC samples displays very strong and spectrally selective enhancement. We report an enhancement of the red scintillation peak in the PhC sample, relative to the TF, by a factor of ~6 (peak at 674 nm) and a factor of ~3 integrated over the main red peak (665 ± 30 nm), as shown in Fig. 2D. This feature is reproduced by our theoretical framework via enhancement of V_{eff} around the red scintillation peak, using the same fitting parameters as those taken from the TF results of Fig. 2, F and G. Comparatively, the green peak remains at a value similar to those in the TF spectra. As a result of the high losses at those shorter wavelengths, little enhancement is expected for the green wavelength.

The observed enhancement can readily be attributed theoretically to the presence of high–quality factor (high-Q) resonances at the red wavelength, which lead to enhanced absorption of light in the far field. The positions of the many subpeaks in the scintillation spectra are accounted for by the peaks of V_{eff}. Somewhat larger uncertainties are introduced in the patterned structure because of the strong degree of angular shaping of the radiation associated with certain wave vectors in the PhC band structure (Fig. 2G, inset, shows the predicted scintillation spectrum at normal emission). As a result, the spectrum depends on the exact angular acceptance function of the objective. There is also a more sensitive dependence on the exact distribution of electron energy loss relative to the thin-film case; this is due to the well-localized nature of the resonances leading to scintillation in the patterned structure.

Having shown scintillation control and enhancement based on nanophotonic structures, we now explore another core element of our general framework for scintillation: the microscopic transition dynamics associated with the scintillation process, their effect on the non-equilibrium occupation functions, and the corresponding effect on observable properties of the scintillation spectrum. In the specific case of silica defects, we can make use of spectral observables such as dependence of the

scintillation on the electron energy, as well as the ratio of green to red scintillation peak powers (defined as η) as a function of deposited HEP energy, to test assumptions about the microscopic properties of the scintillation mechanism. We can even infer the energy level structure of the scintillating defects by combining these measurements with first-principles electronic structure calculations and models of the excited electron kinetics (e.g., rate equations).

Figure 3A shows the evolution of the scintillation spectrum for various energies. At high-energy pumping (~40 keV), red scintillation in the PhC sample dominates; decreasing the pumping energy results in a gradual increase of the green peak scintillation (and of η). We took similar measurements for high- and low-current pumping (at a constant pumping energy of 40 keV) of PhC and TF samples. Our results are compiled in Fig. 3E, where the green peak scintillation always dominates ($\eta > 1$) for the TF sample, whereas a crossover is seen for a certain value of the deposited beam power (represented by η crossing unity) for the PhC sample.

To account for these observations, we consider a description of the defect levels in terms of a three-level Fermi system, featuring two lowest occupied levels (denoted 1 and 2 in Fig. 3C) coupled to an upper "pump" level (denoted 3) through the high-energy electron beam, which acts as a pump. These three levels correspond to energy levels from our electronic structure calculations of the STH defects in silica [based on DFT (*39*)]. The relative rates of the transitions $3 \rightarrow 1$ (Γ_{31}) and $3 \rightarrow 2$ (Γ_{32})—which depend on the pump strength and the emission rates (which in turn depend on V_{eff})—dictate the strength of the green and red emission, respectively. We arrive at the results of Fig. 3E by solving for the steady-state values of these transition rates using rate equations (*39*) and extracting the corresponding η as a function of the incident beam power.

The agreement between theory and experiment enables us to understand the crossover as resulting from a combination of (i) the relative enhancement of red transitions from the PhC, and (ii) the nonlinear transition dynamics of excited electrons in the defect. In particular, data from both samples indicate that the pump rate for the "green transition," Γ_{13}, is faster than its red counterpart, Γ_{23} (with consistent ratio values of ~3.2 for the TF and ~3.35 for the PhC). The existence of a crossover-deposited beam power between domains where $\eta > 1$ and $\eta < 1$ translates into an enhancement of the ratio of decay rates Γ_{32}/Γ_{31} in the PhC sample. After comparing model parameters

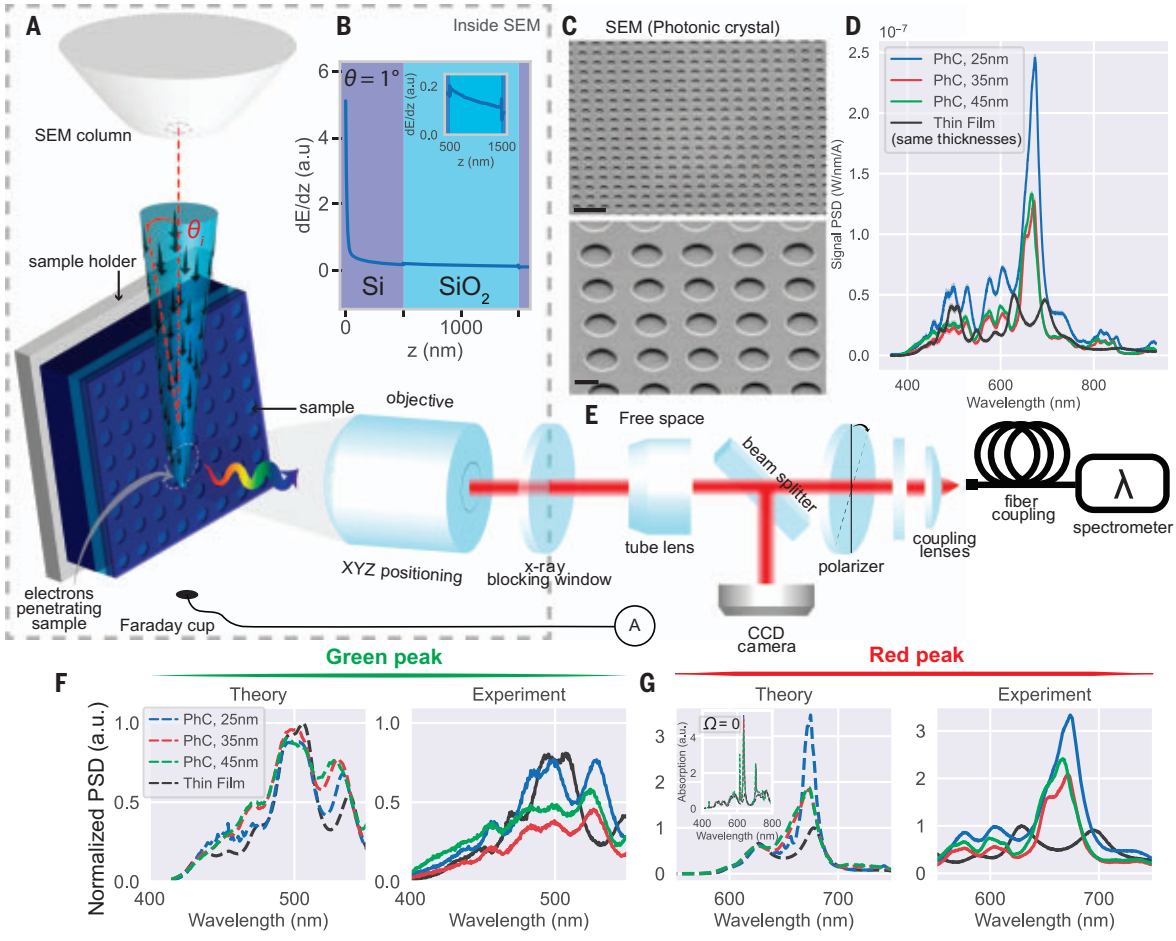


Fig. 2. Experimental demonstration of nanophotonic shaping and enhancement of electron beam–induced scintillation. (**A**) A modified scanning electron microscope (SEM) is used to induce and measure scintillation from electron beams (10 to 40 keV) bombarding scintillating nanophotonic structures. (**B**) Electron energy loss in the silicon-on-insulator wafer is calculated via Monte Carlo simulations. Inset: Zoomed-in electron energy loss in the scintillating (silica) layer. a.u., arbitrary units. (**C**) SEM images of photonic crystal (PhC) sample (etch depth 35 nm). Tilt angle 45°. Scale bars, 1 μm (top), 200 nm (bottom). (**D**) Scintillation spectrum from thin-film and PhC samples with varying etch depths (but same thickness). PSD, power spectral density. (**E**) The scintillation signal is coupled out of the vacuum chamber with an objective and then imaged on a camera and analyzed with a spectrometer. (**F** and **G**) Comparison between theoretical (left) and experimental (right) scintillation spectra for green and red scintillation peaks. Inset: Calculated scintillation spectra (per solid angle) at normal emission direction, showing the possibility of much larger enhancements over a single angle of emission.

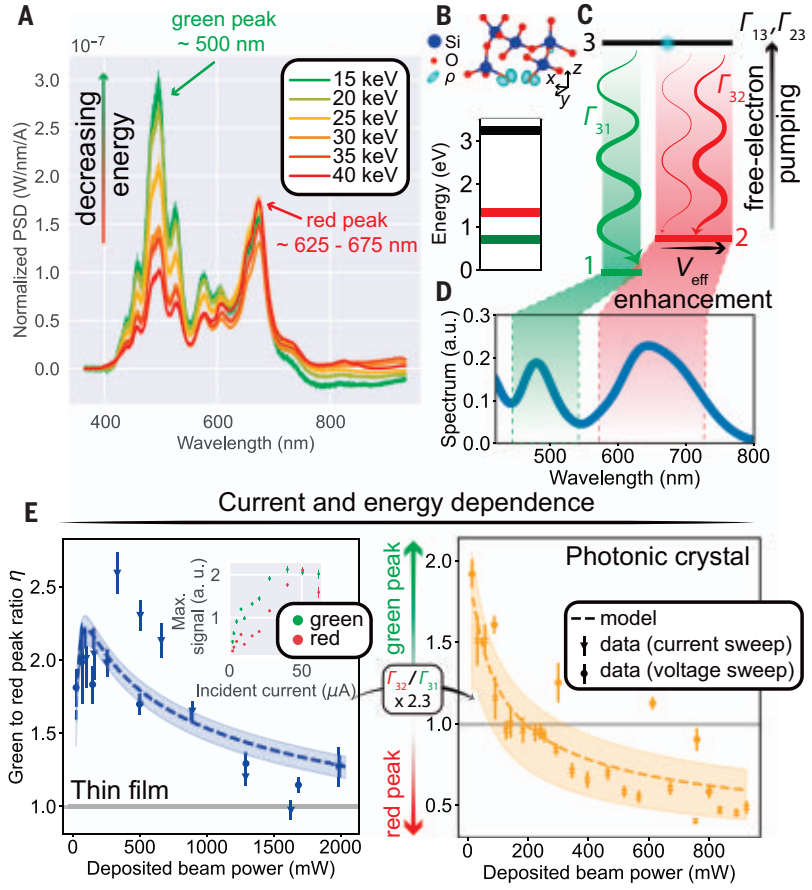


Fig. 3. Probing the microscopics of electron beam–induced scintillation in silica. (**A**) Energy-dependent scintillation spectra (PhC sample, etch 25 nm). (**B**) Top: 3D molecular model of STH defect in silica; ρ, spin-polarized density. Bottom: Calculated STH defect energy levels via density functional theory (DFT). (**C**) Simplified three-level system modeling the microscopics of scintillation from STH defects in silica. (**D**) Bulk scintillation spectrum calculated with DFT (dipole matrix elements). (**E**) Thin film (left) and PhC (right) scintillation peak ratios as a function of deposited beam powers through electron pumping. The dashed line corresponds to the mean model prediction and the shaded area to the prediction from the model parameters ± SD [defined as the uncertainty on Γ_{31}/Γ_{32}, the ratio of rates shown in (B), bottom]. Inset: Maximum signal of green and red scintillation peaks versus current in TF sample.

fitting the TF experimental data to models fitting the PhC data, we estimate that the decay rate ratio is enhanced by a factor of ~2.3 ± 1.0. This value is in agreement with the V_{eff} enhancement predicted by our theory and by our observation of enhanced scintillation from the red defects in the experimental data.

By patterning nanophotonic scintillators, one can thus tailor microscopic properties and selectively enhance scintillation from microscopic defects. This also suggests that scintillation rates can be selectively enhanced using nanophotonic structures, a feature that is particularly sought after in some medical imaging modalities (*43*). Moreover, our results indicate that the measured scintillation may be used to sort out competing models of the electronic structure, especially in complex defects such as this one, where self-interaction effects lead to modeling difficulties (*39*).

Observation of strongly enhanced scintillation induced by x-rays

We now consider another example of a nanophotonic scintillator designed using our theoretical framework, showing its application to enhancing scintillation induced by high-energy photons such as x-rays. Such HEPs lose their energy much differently from massive charged particles (such as electrons).

In our experimental configuration (Fig. 4A), x-rays traverse a specimen, leading to spatially dependent absorption of the incident x-ray flux. This absorption pattern is geometrically magnified until it encounters the cerium-doped yttrium-aluminum-garnet (YAG:Ce) scintillator. The pattern is then translated into scintillation photons, which are imaged with an objective and a charge-coupled device (CCD) camera. The nanopatterned scintillator is constructed by etching a two-dimensional PhC into YAG [via focused ion beam (FIB) lithography (*39*)] at the surface of the scintillator facing the objective. The PhC period is 430 nm and the total patterned area is 215 μm × 215 μm (Fig. 4) or 430 μm × 430 μm (Fig. 5).

In the case of YAG:Ce, the intrinsic scintillation properties have long been characterized and our experiments reveal only weak dependence of the scintillation on incident x-ray energy (*39*). Thus, the full theoretical apparatus we demonstrate for electron scintillation is not needed to adequately describe our results. Primarily, the electromagnetic response (using reciprocity) is needed to account for the experimental results and is the part of our general framework that leads us to order-of-magnitude enhancement of x-ray scintillation (*39*).

According to the scintillation framework developed above, nanophotonic scintillation enhancement is to be expected when the absorption of light is enhanced. In Fig. 4B, we show the calculated wavelength-dependent scintillation in YAG:Ce (averaged over the angular acceptance of the objective, as in Fig. 2) for an unpatterned self-standing thick (20 μm) film, as well as for the PhC sample. Here, the calculated enhancement is by a factor of ~9.3 ± 0.8 over the measured scintillation spectrum. In our calculations, we attribute the main error bar to the uncertainty on the hole depth [±10 nm, as can be extracted from our atomic force microscopy (AFM) measurements, shown fully in Fig. 4A (right) and in cross sections in (*39*)]. However, there are several other sources of uncertainty in the fabricated samples: the hole diameter, the hole periodicity, and the optical absorption of YAG:Ce (taken in our calculations to be the value provided by the wafer supplier). We also measured, and compared to our theory, scintillation enhancements from multiple nanophotonic scintillators with various thicknesses, hole shapes, depths, and patterned areas (table S1) (*39*).

Here, the x-ray scintillation enhancement originates in light out-coupling enhancement (or, by reciprocity, in-coupling enhancement). In particular, the PhC allows more channels (i.e., a plane-wave coupling to a resonance) into the scintillator crystal than would be achievable with a flat interface. The multiple channels translate into sharp resonant peaks in the calculated absorption spectrum [see (*39*) for raw signal]. This is to be contrasted with the origin of electron beam–induced scintillation enhancement in silica, where the enhancement can be tied to the presence of one or a small number of high-*Q* resonances. This effect is of the type often leveraged to design more efficient LEDs and solar cells that approach the "Yablonovitch limit" in both ray-optical (*44*, *45*) and nanophotonic (*46*, *47*) settings. There, it is well known that the device efficiency is optimized by designing a structure

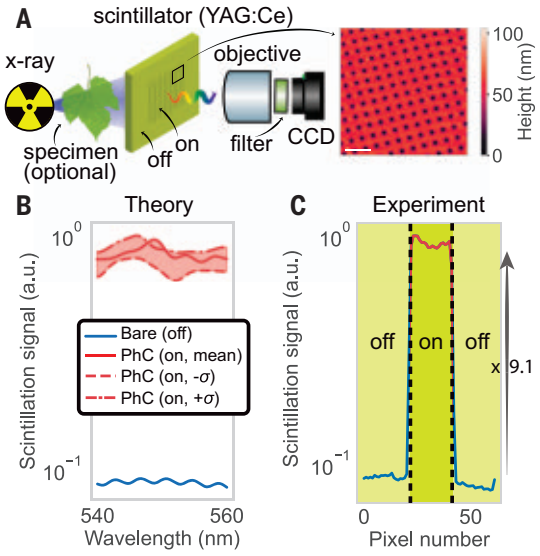


Fig. 4. Nanophotonic enhancement of x-ray scintillation. (**A**) Left: X-ray scintillation experimental setup. Light generated by x-ray bombardment of a YAG:Ce scintillator is imaged with a set of free-space optics. A specimen may be positioned between the source and the scintillator to record an x-ray scan of the specimen. Right: AFM image of patterned YAG:Ce scintillator (thickness, 20 μm). Scale bar, 1 μm. (**B**) Calculated scintillation spectrum of the PhC, integrated over the experimental angular aperture. Calculations are performed for measured etching depths ± SD (corresponding to 40, 50, and 60 nm). The shaded area corresponds to possible scintillation enhancements between those values. The calculated spectra are convolved with a moving-mean filter of width 1.33 nm [raw signal shown in (*39*)]. (**C**) Measured scintillation along a line of the sample, including regions on (red) and off (blue) the PhC. The scintillation from the PhC region is on average higher than the unpatterned region by a factor of ~9.1. All signals were recorded with x-ray source settings of 40 kVp, 3 W.

that leads to strong absorption over the spectral range of the emission (*44*, *48*).

In Fig. 4C, we show the experimentally measured scintillation scanned along a line of the sample. The regions "off" indicate unpatterned regions of the YAG:Ce, whereas "on" indicates the PhC region. Here, the signal is enhanced on average by a factor of ~9.1 over the unpatterned region, consistent with the predictions of Fig. 4B.

To demonstrate the potential of our approach to x-ray imaging, we fabricated a larger-scale pattern on a 50-μm wafer, which exhibits a scintillation enhancement of 2.3 (*39*). We recorded single-shot x-ray scans of biological and inorganic specimens through the PhC, showing no evident decrease in resolution, while increasing the image brightness by the same factor. Equivalently, the required x-ray dose or exposure time to get a given number of counts on the detector is reduced [shown experimentally in (*39*)].

Our framework allows us to further gain understanding of the scintillation mechanism at play, directly leveraging known techniques in absorption enhancement. For certain structures, one could expect even greater scintillation enhancements on the order of ~$4n^2$ in the ray-optics approximation (*44*) or ~$4\pi n^2$ for periodic structures on the wavelength scale (*46*, *47*) (where n is the index of refraction). For example, for a thin high-index material such as doped GaAs, which also scintillates at room temperature (*49*), enhancements on the order of ~50 and ~150 could be respectively achieved in the two regimes (over a 2π collection solid angle).

Discussion

We have presented a general framework to model, tailor, and enhance scintillation by means of nanophotonic structures integrated into scintillating materials (nanophotonic scintillators). Although we mainly focused on the demonstration of spectral shaping and enhancement of scintillation, our results could be extended to show angular and polarization control as well. We have demonstrated nanophotonic scintillators enhancing electron beam–induced and x-ray–induced scintillation. The theoretical framework we used to describe our experimental results combines Monte Carlo simulations of the energy loss density (*40*) with DFT calculations of the microscopic structure and full-wave calculations of the electromagnetic response of the nanophotonic structures probed in this work.

We note that this type of "full" analysis, to the best of our knowledge, has not been performed to explain scintillation (nor incoherent cathodoluminescence) experiments, likely because of the prohibitively expensive computations associated with simulating ensembles of dipoles radiating in 3D structures. The reciprocity framework we use [also commonly used in areas of thermal radiation, LEDs, and photoluminescence (*34*, *50*–*54*)] strongly simplifies the analysis, and makes a full modeling of the scintillation problem tractable. We conclude by outlining a few promising avenues of future work that are enabled by the results provided here. [See (*39*) for further elaboration and initial results for each of these avenues.]

The first area, inspired by our simplified calculations based on reciprocity, is numerical optimization of nanophotonic scintillators. Our framework, which relies on the calculation of V_{eff} (which is relatively amenable, even in three dimensions), enables the inverse design of nanophotonic scintillators. [See (*39*) for methods to calculate the forward (V_{eff} given a nanophotonic structure) and backward (gradients of V_{eff} with respect to degrees of freedom describing the nanophotonic structure) problems.] The experimentally reported enhancements can be further improved upon by inverse-designing the nanophotonic structure via topology optimization of V_{eff} (*55*). In (*39*), we show the kind of results that could be expected from topology-optimized nanophotonic scintillators: We find that selective enhancements of scintillation in particular topology-optimized photonic structures by one to nearly two orders of magnitude are possible. By considering different emission linewidths and frequencies, one can selectively design optimized nanophotonic structures that enhance one of the scintillating peaks, at a single frequency or over the entire scintillation bandwidth. Beyond our reciprocity-based approach, low-rank methods can be used for the inverse design of nanophotonic scintillators with very large angular ranges (*56*, *57*). Beyond scintillation, our techniques may find applicability in other imaging modalities involving random incoherent emitters, such as surface-enhanced Raman scattering (*58*).

Another promising area of research enabled by our findings is nanophotonically enhanced and controlled UV light sources. In (*39*) we show how UV scintillation in patterned materials such as hBN enables strongly enhanced scintillation with a spectrum that can be controlled simply by the position of the electron beam relative to the patterned features in the hBN arising from changes in the overlap between the HEP loss density and V_{eff}. The prospect of realizing optimized and compact nanophotonic UV scintillation sources is particularly exciting for applications in water purification and sanitization (*59*).

Nanophotonic scintillators provide a versatile approach for controlling and enhancing the performance of scintillating materials for a wide range of applications. The framework developed here applies to arbitrary scintillating

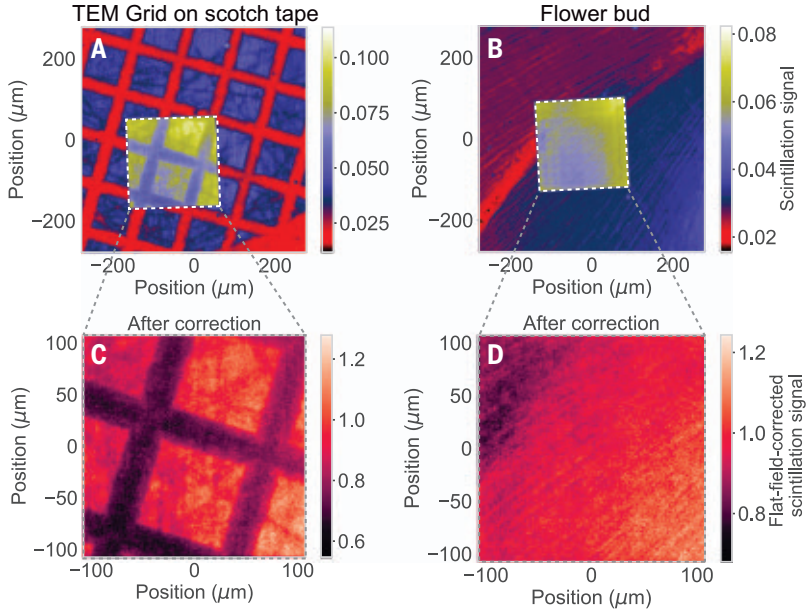


Fig. 5. X-ray scintillation imaging with nanophotonic scintillators. (**A** and **B**) Measured x-ray images of a TEM grid on scotch tape (A) and a flower bud (B). The white square delimits the PhC area. (**C** and **D**) Flat field–corrected zoom-in of the x-ray image in the PhC area. Geometric magnification on those images is ~2. Relative to the unpatterned regions, the images are brighter above the PhC region, showing no evident decrease in resolution. The particular nanophotonic scintillator used for this experiment was patterned over an area of 430 μm × 430 μm and resulted in a scintillation enhancement of ×2.3 (measured with respect to an unpatterned scintillator of same thickness). All signals were recorded with x-ray source settings of 60 kVp, 5 W.

materials, nanophotonic structures, and HEPs, solving for the process end-to-end using first-principles methods. The electron-beam and x-ray scintillation experiments provide the proof-of-concept tests of the promising prospects of this field. Our work may open a panoply of exciting applications, from high-resolution, low-dose x-ray imaging to efficient UV electron beam–pumped light sources.

REFERENCES AND NOTES

1. A. Gektin, M. Korzhik, *Inorganic Scintillators for Detector Systems* (Springer, 2017).
2. S. Cherry, J. Sorenson, M. Phelps, *Physics in Nuclear Medicine* (Wiley, 2012).
3. Q. Chen *et al*., All-inorganic perovskite nanocrystal scintillators. *Nature* **561**, 88–93 (2018). doi: 10.1038/s41586-018-0451-1; pmid: 30150772
4. Y. Kurman, A. Shultzman, O. Segal, A. Pick, I. Kaminer, Photonic-Crystal Scintillators: Molding the Flow of Light to Enhance X-Ray and γ-Ray Detection. *Phys. Rev. Lett.* **125**, 040801 (2020). doi: 10.1103/PhysRevLett.125.040801; pmid: 32794818
5. E. Yablonovitch, Inhibited spontaneous emission in solid-state physics and electronics. *Phys. Rev. Lett.* **58**, 2059–2062 (1987). doi: 10.1103/PhysRevLett.58.2059; pmid: 10034639
6. J. D. Joannopoulos, S. G. Johnson, J. N. Winn, R. D. Meade, *Photonic Crystals: Molding the Flow of Light* (Princeton Univ. Press, 2011).
7. M. Pelton, Modified spontaneous emission in nanophotonic structures. *Nat. Photonics* **9**, 427–435 (2015). doi: 10.1038/nphoton.2015.103
8. A. Polman, H. A. Atwater, Photonic design principles for ultrahigh-efficiency photovoltaics. *Nat. Mater.* **11**, 174–177 (2012). doi: 10.1038/nmat3263; pmid: 22349847
9. P. Anger, P. Bharadwaj, L. Novotny, Enhancement and quenching of single-molecule fluorescence. *Phys. Rev. Lett.* **96**, 113002 (2006). doi: 10.1103/PhysRevLett.96.113002; pmid: 16605818
10. J. B. Jackson, N. J. Halas, Surface-enhanced Raman scattering on tunable plasmonic nanoparticle substrates. *Proc. Natl. Acad. Sci. U.S.A.* **101**, 17930–17935 (2004). doi: 10.1073/pnas.0408319102; pmid: 15608058
11. E. F. Schubert *et al*., Highly efficient light-emitting diodes with microcavities. *Science* **265**, 943–945 (1994). doi: 10.1126/science.265.5174.943; pmid: 17782147
12. A. A. Erchak *et al*., Enhanced coupling to vertical radiation using a two-dimensional photonic crystal in a semiconductor light-emitting diode. *Appl. Phys. Lett.* **78**, 563–565 (2001). doi: 10.1063/1.1342048
13. J.-J. Greffet *et al*., Coherent emission of light by thermal sources. *Nature* **416**, 61–64 (2002). doi: 10.1038/416061a; pmid: 11882890
14. R. Remez *et al*., Spectral and spatial shaping of Smith-Purcell radiation. *Phys. Rev. A* **96**, 061801 (2017). doi: 10.1103/PhysRevA.96.061801
15. Y. Yang *et al*., Maximal spontaneous photon emission and energy loss from free electrons. *Nat. Phys.* **14**, 894–899 (2018). doi: 10.1038/s41567-018-0180-2
16. I. Kaminer *et al*., Spectrally and Spatially Resolved Smith-Purcell Radiation in Plasmonic Crystals with Short-Range Disorder. *Phys. Rev. X* **7**, 011003 (2017). doi: 10.1103/PhysRevX.7.011003
17. C. Roques-Carmes *et al*., Towards integrated tunable all-silicon free-electron light sources. *Nat. Commun.* **10**, 3176 (2019). doi: 10.1038/s41467-019-11070-7; pmid: 31320664
18. F. Liu *et al*., Integrated Cherenkov radiation emitter eliminating the electron velocity threshold. *Nat. Photonics* **11**, 289–292 (2017). doi: 10.1038/nphoton.2017.45
19. A. Massuda *et al*., Smith-Purcell radiation from low-energy electrons. *ACS Photonics* **5**, 3513–3518 (2018). doi: 10.1021/acsphotonics.8b00743
20. F. J. García de Abajo, Optical excitations in electron microscopy. *Rev. Mod. Phys.* **82**, 209–275 (2010). doi: 10.1103/RevModPhys.82.209
21. G. Li, B. P. Clarke, J.-K. So, K. F. MacDonald, N. I. Zheludev, Holographic free-electron light source. *Nat. Commun.* **7**, 13705 (2016). doi: 10.1038/ncomms13705; pmid: 27910853
22. C. I. Osorio, T. Coenen, B. J. M. Brenny, A. Polman, A. F. Koenderink, Angle-Resolved Cathodoluminescence Imaging Polarimetry. *ACS Photonics* **3**, 147–154 (2015). doi: 10.1021/acsphotonics.5b00596
23. Y. Yang *et al*., Observation of enhanced free-electron radiation from photonic flatband resonances. arXiv 2110.03550 (2021).
24. X. Chen *et al*., Enhanced light extraction of plastic scintillator using large-area photonic crystal structures fabricated by hot embossing. *Opt. Express* **26**, 11438–11446 (2018). doi: 10.1364/OE.26.011438; pmid: 29716062
25. A. Knapitsch *et al*., Results of Photonic Crystal Enhanced Light Extraction on Heavy Inorganic Scintillators. *IEEE Trans. Nucl. Sci.* **59**, 2334–2339 (2012). doi: 10.1109/TNS.2012.2184556
26. A. Knapitsch, P. Lecoq, Review on photonic crystal coatings for scintillators. *Int. J. Mod. Phys. A* **29**, 1430070 (2015). doi: 10.1142/S0217751X14300701
27. Z. Zhu *et al*., Enhanced light extraction of scintillator using large-area photonic crystal structures fabricated by soft-X-ray interference lithography. *Appl. Phys. Lett.* **106**, 241901 (2015). doi: 10.1063/1.4922699
28. P. Pignalosa, B. Liu, H. Chen, H. Smith, Y. Yi, Giant light extraction enhancement of medical imaging scintillation materials using biologically inspired integrated nanostructures. *Opt. Lett.* **37**, 2808 (2012). doi: 10.1364/OL.37.002808; pmid: 22825141
29. Z. Zhu *et al*., Improved light output from thick β-Ga_2O_3 scintillation crystals via graded-refractive-index photonic crystals. *Opt. Express* **29**, 18646 (2021). doi: 10.1364/OE.428671; pmid: 34154117
30. X. Ouyang *et al*., Enhanced light output of CsI(Na) scintillators by photonic crystals. *Nucl. Instrum. Methods Phys. Res. A* **969**, 164007 (2020). doi: 10.1016/j.nima.2020.164007
31. C. A. Klein, Bandgap Dependence and Related Features of Radiation Ionization Energies in Semiconductors. *J. Appl. Phys.* **39**, 2029 (1968). doi: 10.1063/1.1656484
32. A. Polman, M. Kociak, F. J. García de Abajo, Electron-beam spectroscopy for nanophotonics. *Nat. Mater.* **18**, 1158–1171 (2019). doi: 10.1038/s41563-019-0409-1; pmid: 31308514
33. P. Wurfel, The chemical potential of radiation. *J. Phys. C* **15**, 3967–3985 (1982). doi: 10.1088/0022-3719/15/18/012
34. J. J. Greffet, P. Bouchon, G. Brucoli, F. Marquier, Light Emission by Nonequilibrium Bodies: Local Kirchhoff Law. *Phys. Rev. X* **8**, 021008 (2018). doi: 10.1103/PhysRevX.8.021008
35. D. L. Sounas, A. Alù, Non-reciprocal photonics based on time modulation. *Nat. Photonics* **11**, 774–783 (2017). doi: 10.1038/s41566-017-0051-x
36. L. Zhu, S. Fan, Persistent Directional Current at Equilibrium in Nonreciprocal Many-Body Near Field Electromagnetic Heat Transfer. *Phys. Rev. Lett.* **117**, 134303 (2016). doi: 10.1103/PhysRevLett.117.134303; pmid: 27715122
37. D. L. C. Chan, M. Soljacić, J. D. Joannopoulos, Direct calculation of thermal emission for three-dimensionally periodic photonic crystal slabs. *Phys. Rev. E* **74**, 036615 (2006). doi: 10.1103/PhysRevE.74.036615; pmid: 17025772
38. This issue is compounded by the sensitivity of the results to assumptions about the spatial and spectral distributions of the dipoles, which are related to the microscopic details of the defect electronic structure, as well as the mechanism of high-energy particle energy transfer into the material.
39. See supplementary materials.
40. H. Demers *et al*., Three-dimensional electron microscopy simulation with the CASINO Monte Carlo software. *Scanning* **33**, 135–146 (2011). doi: 10.1002/sca.20262; pmid: 21769885
41. S. Girard *et al*., Overview of radiation induced point defects in silica-based optical fibers. *Rev. Phys.* **4**, 100032 (2019). doi: 10.1016/j.revip.2019.100032
42. In principle, one would want to compare V_{eff} in the TF to a "truly intrinsic" or "bulk" silica case. In that case, one would compare to silica of the same thickness (1000 nm). However, because this reference case is a thin film as well, nanophotonic shaping effects in the spectrum will inevitably be present. Comparing the V_{eff} in the thin-film case of Fig. 2 to thin films without (i) the top Si layer or (ii) without both Si layers (see fig. S1), one finds that the TF of Fig. 2 presents slightly smaller absorption enhancement at the red peak, possibly due to the high reflectivity of the top Si layer (suppressing the amount of field that can be absorbed by the material). However, the PhC sample still shows strong shaping and enhancement relative to all TF cases.
43. P. Lecoq *et al*., Roadmap toward the 10 ps time-of-flight PET challenge. *Phys. Med. Biol.* **65**, 21RM01 (2020). doi: 10.1088/1361-6560/ab9500; pmid: 32434156
44. E. Yablonovitch, Statistical ray optics. *J. Opt. Soc. Am.* **72**, 899 (1982). doi: 10.1364/JOSA.72.000899
45. P. Campbell, M. A. Green, The limiting efficiency of silicon solar cells under concentrated sunlight. *IEEE Trans. Electron Dev.* **33**, 234–239 (1986). doi: 10.1109/T-ED.1986.22472

46. R. N. Raman, M. J. Matthews, J. J. Adams, S. G. Demos, Monitoring annealing via CO_2 laser heating of defect populations on fused silica surfaces using photoluminescence microscopy. *Opt. Express* **18**, 15207–15215 (2010). doi: 10.1364/OE.18.015207; pmid: 20640006
47. Z. Yu, A. Raman, S. Fan, Fundamental limit of nanophotonic light trapping in solar cells. *Proc. Natl. Acad. Sci. U.S.A.* **107**, 17491–17496 (2010). doi: 10.1073/pnas.1008296107; pmid: 20876131
48. A. I. Zhmakin, Enhancement of light extraction from light emitting diodes. *Phys. Rep.* **498**, 189–241 (2011). doi: 10.1016/j.physrep.2010.11.001
49. S. Derenzo, E. Bourret, C. Frank-Rotsch, S. Hanrahan, M. Garcia-Sciveres, How silicon and boron dopants govern the cryogenic scintillation properties of N-type GaAs. *Nucl. Instrum. Methods Phys. Res. A* **989**, 164957 (2021). doi: 10.1016/j.nima.2020.164957
50. S. Liu *et al*., Light-Emitting Metasurfaces: Simultaneous Control of Spontaneous Emission and Far-Field Radiation. *Nano Lett.* **18**, 6906–6914 (2018). doi: 10.1021/acs.nanolett.8b02808; pmid: 30339762
51. K. M. Schulz, D. Jalas, A. Y. Petrov, M. Eich, Reciprocity approach for calculating the Purcell effect for emission into an open optical system. *Opt. Express* **26**, 19247–19258 (2018). doi: 10.1364/OE.26.019247; pmid: 30114183
52. Y. Sheng *et al*., Čerenkov third-harmonic generation in $\chi^{(2)}$ nonlinear photonic crystal. *Appl. Phys. Lett.* **98**, 241114 (2011). doi: 10.1063/1.3602312
53. S. Zhang *et al*., Calculation of the emission power distribution of microstructured OLEDs using the reciprocity theorem. *Synth. Met.* **205**, 127–133 (2015). doi: 10.1016/j.synthmet.2015.03.035
54. A. C. Overvig, S. A. Mann, A. Alù, Thermal Metasurfaces: Complete Emission Control by Combining Local and Nonlocal Light-Matter Interactions. *Phys. Rev. X* **11**, 021050 (2021). doi: 10.1103/PhysRevX.11.021050
55. S. Molesky *et al*., Inverse design in nanophotonics. *Nat. Photonics* **12**, 659–670 (2018). doi: 10.1038/s41566-018-0246-9
56. A. G. Polimeridis *et al*., Fluctuating volume-current formulation of electromagnetic fluctuations in inhomogeneous media: Incandescence and luminescence in arbitrary geometries. *Phys. Rev. B* **92**, 134202 (2015). doi: 10.1103/PhysRevB.92.134202
57. W. Yao, F. Verdugo, R. E. Christiansen, S. G. Johnson, Trace formulation for photonic inverse design with incoherent sources. arXiv 2111.13046 (2021).
58. R. E. Christiansen, J. Michon, M. Benzaouia, O. Sigmund, S. G. Johnson, Inverse design of nanoparticles for enhanced Raman scattering. *Opt. Express* **28**, 4444–4462 (2020). doi: 10.1364/OE.28.004444; pmid: 32121681
59. K. Watanabe, T. Taniguchi, T. Niiyama, K. Miya, M. Taniguchi, Far-ultraviolet plane-emission handheld device based on hexagonal boron nitride. *Nat. Photonics* **3**, 591–594 (2009). doi: 10.1038/nphoton.2009.167
60. C. Roques-Carmes *et al*., Data for "A framework for scintillation in nanophotonics" (2021); https://github.com/charlesrc/nanoscint.

ACKNOWLEDGMENTS

We thank T. Savas for assistance in fabricating the sample used for electron-beam scintillation; I. Shestakova and O. Philip (Crytur) for helpful discussions on x-ray scintillators; C. Graf vom Hagen, X. Xu, and J. Treadgold (Zeiss) for feedback on micro-CT scanner experiments; R. Sundararaman (Rensselaer Polytechnic Institute) and J. Coulter (Harvard University) for assistance with DFT calculations; and Y. Salamin and S. Pajovic (MIT) for stimulating discussions. **Funding:** This material is based on work supported in part by the US Army Research Laboratory and the US Army Research Office through the Institute for Soldier Nanotechnologies under contract W911NF-18-2-0048. This material is also in part based on work supported by the Air Force Office of Scientific Research under awards FA9550-20-1-0115 and FA9550-21-1-0299. This work was performed in part on the Raith VELION FIB-SEM in the MIT.nano Characterization Facilities (award DMR-2117609) C.R.-C. acknowledges funding from the MathWorks Engineering Fellowship Fund by MathWorks Inc. **Author contributions:** C.R.-C., N.Ri., N.Ro., I.K., and M.S. conceived the original idea; N.Ri. developed the theory with inputs from C.R.-C. and A.G.; C.R.-C. and S.E.K. performed the electron-beam and x-ray experiments; C.R.-C. and N.Ri. analyzed the experimental data and fitted them to the theory; C.R.-C. and S.E.K. built the electron-beam experimental setup with contributions from J.B., A.M., J.S., Y.Ya., I.K., and M.S.; N.Ri. performed energy loss calculations; C.R.-C. performed absorption map calculations; A.G. performed DFT calculations; C.R.-C. wrote code for optimizing nanophotonic scintillators with inputs from N.Ri., Z.L., and S.G.J.; Y.Yu and C.R.-C. fabricated the x-ray scintillation sample; and J.D.J., I.K., S.G.J., and M.S. supervised the project. The manuscript was written by C.R.-C. and N.Ri. with inputs from all authors. **Competing interests:** The authors declare the following potential competing financial interests: C.R.-C., N.Ri., A.G., S.E.K., Y.Ya., Z.L., J.B., N.Ro., J.D.J., I.K., S.G.J., and M.S. are seeking patent protection for ideas in this work (provisional patent application no. 63/178,176). C.R.-C., N.Ri., Z.L., and M.S. are seeking patent protection for ideas in this work (provisional patent application no. 63/257,611). **Data and materials availability:** The data and codes that support the plots within this paper and other findings of this study are available online (*60*).

SUPPLEMENTARY MATERIALS

science.org/doi/10.1126/science.abm9293
Materials and Methods
Supplementary Text
Figs. S1 to S19
Table S1
References (*61*–*82*)

21 October 2021; accepted 22 December 2021
10.1126/science.abm9293

RESEARCH ARTICLE SUMMARY

NEUROSCIENCE

Hyperexcitable arousal circuits drive sleep instability during aging

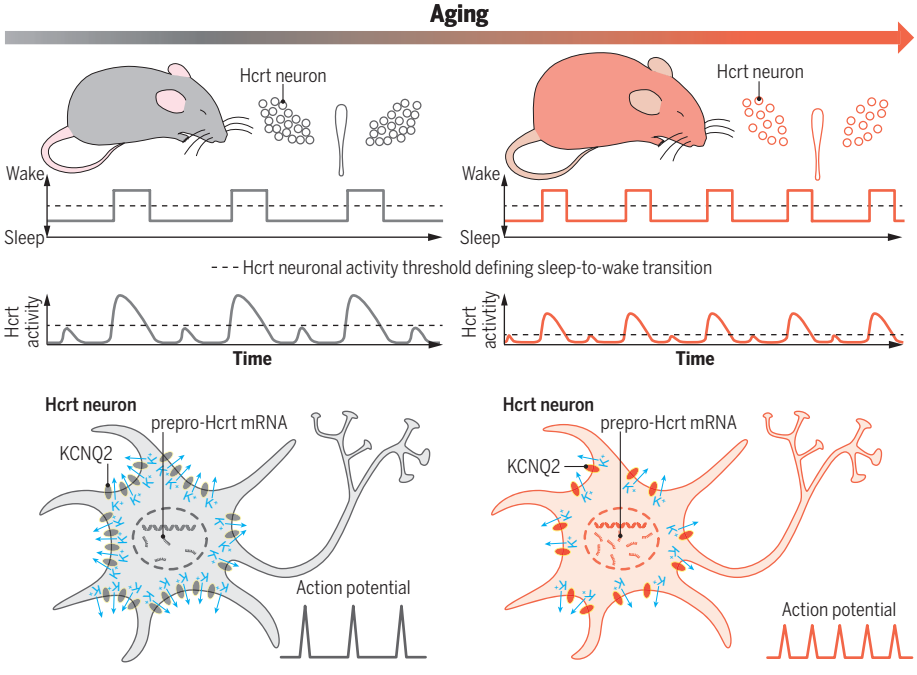
Shi-Bin Li†, Valentina Martinez Damonte†, Chong Chen, Gordon X. Wang, Justus M. Kebschull, Hiroshi Yamaguchi, Wen-Jie Bian, Carolin Purmann, Reenal Pattni, Alexander Eckehart Urban, Philippe Mourrain, Julie A. Kauer, Grégory Scherrer, Luis de Lecea*

INTRODUCTION: Sleep destabilization is strongly associated with aging and cognitive function decline. Despite sleep fragmentation being central to the most prevalent complaints of sleep problems in elderly populations, the mechanistic underpinnings of sleep instability remain elusive. Fragmented sleep during aging has been observed across species, indicating conserved underlying mechanisms across the phylogenetic tree. Therefore, understanding why the aging brain fails to consolidate sleep may shed light on translational applications for improving the sleep quality of aged individuals.

RATIONALE: We hypothesized that the decline in sleep quality could be due to malfunction of the neural circuits associated with sleep/wake control. It has been established that hypocretin/orexin (Hcrt/OX) neuronal activity is tightly associated with wakefulness and initiates and maintains the wake state. In this study, we investigated whether the intrinsic excitability of Hcrt neurons is altered, leading to a destabilized control of sleep/wake states during aging.

RESULTS: Aged mice exhibited sleep fragmentation and a significant loss of Hcrt neurons. Hcrt neurons manifested a more frequent firing pattern, driving wake bouts and disrupting sleep continuity in aged mice. Aged Hcrt neurons were capable of eliciting more prolonged wake bouts upon optogenetic stimulations. These results suggested that hyperexcitability of Hcrt neurons emerges with age. Patch clamp recording in genetically identified Hcrt neurons revealed distinct intrinsic properties between the young and aged groups. Aged Hcrt neurons were hyperexcitable with depolarized membrane potentials (RMPs) and a smaller difference between RMP and the firing threshold. Aged Hcrt neurons expressing ChR2-eYFP were more sensitive to optogenetic stimulations, with a smaller-amplitude attenuation upon repetitive light pulse stimulations. More spikelets were generated in aged Hcrt neurons upon current injections. Recording from non-Hcrt neurons postsynaptic to Hcrt neurons revealed that optogenetic stimulation of Hcrt neurons expressing ChR2-eYFP reliably evoked time-locked postsynaptic currents (PSCs) after optogenetic stimulation more often in the aged group. Aged Hcrt neurons were characterized with a functional impairment of repolarizing M-current mediated by KCNQ2/3 channels and an anatomical loss of KCNQ2, revealed with array tomography at ultrastructural resolution. Single-nucleus RNA-sequencing (snRNA-seq) revealed molecular adaptions, including up-regulated prepro-*Hcrt* mRNA expression and a smaller fraction of *Kcnq* family subtypes *Kcnq1/2/3/5* in aged Hcrt neurons. CRISPR/SaCas9–mediated disruption of *Kcnq2/3* genes selectively in Hcrt neurons was sufficient to recapitulate the aging-associated sleep fragmentation trait in young mice. Pharmacological augmentation of M-current repolarized the RMP, suppressed spontaneous firing activity in aged Hcrt neurons, and consolidated sleep stability in aged mice. Sleep fragmentation in a narcolepsy mouse model with genetic ablation of Hcrt neurons at young ages manifested a mechanism other than hyperexcitable arousal-promoting Hcrt neurons that drives sleep fragmentation during healthy aging.

CONCLUSION: Our data indicate that emerging hyperexcitability of arousal-promoting Hcrt neurons is strongly associated with fragmented sleep in aged mice, which display a lowered sleep-to-wake transition threshold defined for Hcrt neuronal activity. We have demonstrated that the down-regulation of KCNQ2/3 channels compromising repolarization drives Hcrt neuronal hyperexcitability, which leads to sleep instability during aging. Pharmacological remedy of sleep continuity through targeting KCNQ2/3 channels in aged mice confers a potential translational therapy strategy for improving sleep quality in aged individuals. ■



Hyperexcitable Hcrt neurons drive sleep instability during aging. Elevated excitability of Hcrt neurons with depolarized RMPs and adaptive up-regulation of prepro-*Hcrt* mRNA expression converge to drive sleep/wake instability in the aged brain with substantial Hcrt neuron loss. Hyperexcitable aged Hcrt neurons express functional impairment of KCNQ2/3 channel–mediated M-current and an anatomical loss of KCNQ2, compromising the neurons to repolarize.

The list of author affiliations is available in the full article online.
*Corresponding author. Email: llecea@stanford.edu
†These authors contributed equally to this work.
Cite this article as S.-B. Li *et al.*, *Science* 375, eabh3021 (2022). DOI: 10.1126/science.abh3021

READ THE FULL ARTICLE AT
https://doi.org/10.1126/science.abh3021

RESEARCH ARTICLE

NEUROSCIENCE

Hyperexcitable arousal circuits drive sleep instability during aging

Shi-Bin Li[1,2]†, Valentina Martinez Damonte[1,2]†, Chong Chen[3,4], Gordon X. Wang[1], Justus M. Kebschull[5]‡, Hiroshi Yamaguchi[1,2]§, Wen-Jie Bian[1,2], Carolin Purmann[1,6], Reenal Pattni[1,6], Alexander Eckehart Urban[1,6], Philippe Mourrain[1,7], Julie A. Kauer[1,2], Grégory Scherrer[3,4], Luis de Lecea[1,2]*

Sleep quality declines with age; however, the underlying mechanisms remain elusive. We found that hyperexcitable hypocretin/orexin (Hcrt/OX) neurons drive sleep fragmentation during aging. In aged mice, Hcrt neurons exhibited more frequent neuronal activity epochs driving wake bouts, and optogenetic activation of Hcrt neurons elicited more prolonged wakefulness. Aged Hcrt neurons showed hyperexcitability with lower KCNQ2 expression and impaired M-current, mediated by KCNQ2/3 channels. Single-nucleus RNA-sequencing revealed adaptive changes to Hcrt neuron loss in the aging brain. Disruption of *Kcnq2/3* genes in Hcrt neurons of young mice destabilized sleep, mimicking aging-associated sleep fragmentation, whereas the KCNQ-selective activator flupirtine hyperpolarized Hcrt neurons and rejuvenated sleep architecture in aged mice. Our findings demonstrate a mechanism underlying sleep instability during aging and a strategy to improve sleep continuity.

Sleep quality correlates with cognitive function (*1*, *2*), and decline in sleep quality is among the most prevalent complaints during aging in humans (*3*, *4*). Aging is associated with alterations in sleep architecture, prominently sleep fragmentation, which prevents restorative sleep (*3*, *5*). The ability to sustain sleep/wake states during aging is heavily impaired across species (*5*–*7*), suggesting that the underlying mechanisms are conserved across the phylogenetic tree. However, the cellular and molecular underpinnings of sleep instability during aging are unknown. A plausible mechanism underlying aging-related sleep fragmentation is that elevated intrinsic excitability of arousal-promoting circuits emerges with age, disrupting sleep stability.

Hypocretin/orexin (Hcrt/OX) neurons (*8*, *9*) in the lateral hypothalamus (LH) play a pivotal role in sleep/wake control (*10*, *11*). Optogenetic stimulation of Hcrt neurons during sleep triggers sleep-to-wake transition (*12*, *13*), whereas optogenetic suppression of Hcrt neuronal activity induces non–rapid eye movement (NREM) sleep (*14*). Furthermore, genetic Hcrt neuron depletion (*15*) or Hcrt receptor 2 (HcrtR2) mutation (*16*) leads to narcolepsy with cataplexy, a condition in which patients suffer sleep and wake fragmentation (*17*). In vivo electrophysiological recordings demonstrate that Hcrt neuronal activity is correlated with wakefulness and initiates and maintains wake state (*18*, *19*). We thus hypothesized that emerging hyperexcitability of Hcrt neurons drives sleep instability during aging.

[1]Department of Psychiatry and Behavioral Sciences, Stanford University School of Medicine, 1201 Welch Road, Stanford, CA 94305, USA. [2]Wu Tsai Neurosciences Institute, Stanford University, Stanford, CA 94305, USA. [3]Department of Cell Biology and Physiology, University of North Carolina at Chapel Hill, Chapel Hill, NC 27599, USA. [4]UNC Neuroscience Center, University of North Carolina at Chapel Hill, Chapel Hill, NC 27599, USA. [5]Department of Biology, Stanford University, Stanford, CA 94305, USA. [6]Department of Genetics, Stanford University School of Medicine, Stanford, CA 94305, USA. [7]INSERM 1024, Ecole Normale Supérieure, Paris, France.
*Corresponding author. Email: llecea@stanford.edu
†These authors contributed equally to this work.
‡Present address: Department of Biomedical Engineering, Johns Hopkins University, Baltimore, MD 21205, USA.
§Present address: Department of Neuroscience II, Research Institute of Environmental Medicine, Nagoya University, Nagoya 464-8601, Japan.

Results

Aged mice exhibit fragmented sleep and significant loss of Hcrt neurons

We compared the sleep/wake patterns between young (3 to 5 months) and aged (18 to 22 months) wild-type (WT) mice implanted with electroencephalogram (EEG)–electromyography (EMG) electrodes. Wake and NREM but not REM sleep were more fragmented in aged mice (fig. S1). We next determined the number of Hcrt neurons in these mice and found a significant loss (~38%) of Hcrt neurons in aged mice compared with young mice (fig. S2), indicating a high vulnerability of these neurons in the aging brain.

Fragmented sleep pattern with increased Hcrt neuronal activity in aged mice

We monitored the intrinsic activity of Hcrt neurons using fiber photometry recording of GCaMP6f signals in both young and aged Hcrt::Cre mice (*20*) while simultaneously recording EEG-EMG signals (Fig. 1) during the light phase, when mice exhibited a stable sleep/wake pattern (fig. S1). We found scattered Hcrt neuronal GCaMP6f transients during sleep (G^S) and GCaMP6f epochs associated with wakefulness (G^W) in both young and aged mice. The GCaMP6f amplitude change (*Z* score) was smaller in the aged group (Fig. 1, C and D), indicating that the threshold of Hcrt neuronal activity that defines sleep-to-wake transition is lower in aged mice. The frequency of G^W was significantly higher in aged mice (young, 16.1 ± 0.7 counts/hour versus aged, 22.8 ± 1.4 counts/hour) (Fig. 1D, bottom right). The G^W epoch frequencies of Hcrt neurons matched the wake bout counts recorded during the same time window in young and aged WT mice, respectively (fig. S1B). The peak and duration of both G^S (Fig. 1C, middle right) and G^W (Fig. 1D, middle right) were smaller in aged mice. In the same amount of recording time during the same circadian phase, the mean bout duration of sleep, wake, and sleep-wake (S-W) episodes was shorter in aged mice (Fig. 1E); a fragmented sleep/wake pattern was associated with age. Correlation analysis with a linear fit revealed that sleep bout duration negatively correlates with Hcrt G^W epoch frequency (Fig. 1F), suggesting the possibility that sleep bout shortening is driven by Hcrt neuron hyperactivity.

Longer wakefulness upon optogenetic activation of aged Hcrt neurons

We then injected adeno-associated virus (AAV) vectors encoding ChR2–enhanced yellow fluorescent protein (eYFP) in the LH of young (3 to 5 months) and aged (18 to 22 months) Hcrt::Cre mice (fig. S3, A and B) and implanted fiber optics and EEG-EMG electrodes. After recovery with sufficient virus expression, we stimulated Hcrt neurons in both young and aged mice with a range of blue light intensities (1, 5, 10, 15, and 20 mW) and frequencies (1, 5, 10, 15, and 20 Hz) within 30 s from either NREM onset (Fig. 2, A to F, and fig. S3) or REM sleep onset (Fig. 2, G to L, and fig. S3). Stimulation with high light intensities and frequencies elicited immediate NREM/REM sleep-to-wake transitions in both young and aged mice (Fig. 2, A and G). The sleep-to-wake transition latency is generally shorter in aged mice according to condition-matched comparison (Fig. 2, B and H) and data aggregated for individual mouse (Fig. 2, C and I). Activation of Hcrt neurons evoked significantly longer durations of wakefulness in aged mice as revealed by comparisons based on each stimulation condition (Fig. 2, E and K) and data aggregated for the individual mouse (Fig. 2, F and L) for optogenetic stimulation during either NREM (young, 162.7 ± 5.4 s versus aged, 292.0 ± 8.3 s) (Fig. 2F) or REM sleep (young, 69.0 ± 3.5 s versus aged, 134.0 ± 2.5 s) (Fig. 2L). The surface plots of in vivo optogenetic data demonstrated that compared with the aged mice, the young mice required stronger stimulation to elicit wake bouts with identical lengths, as

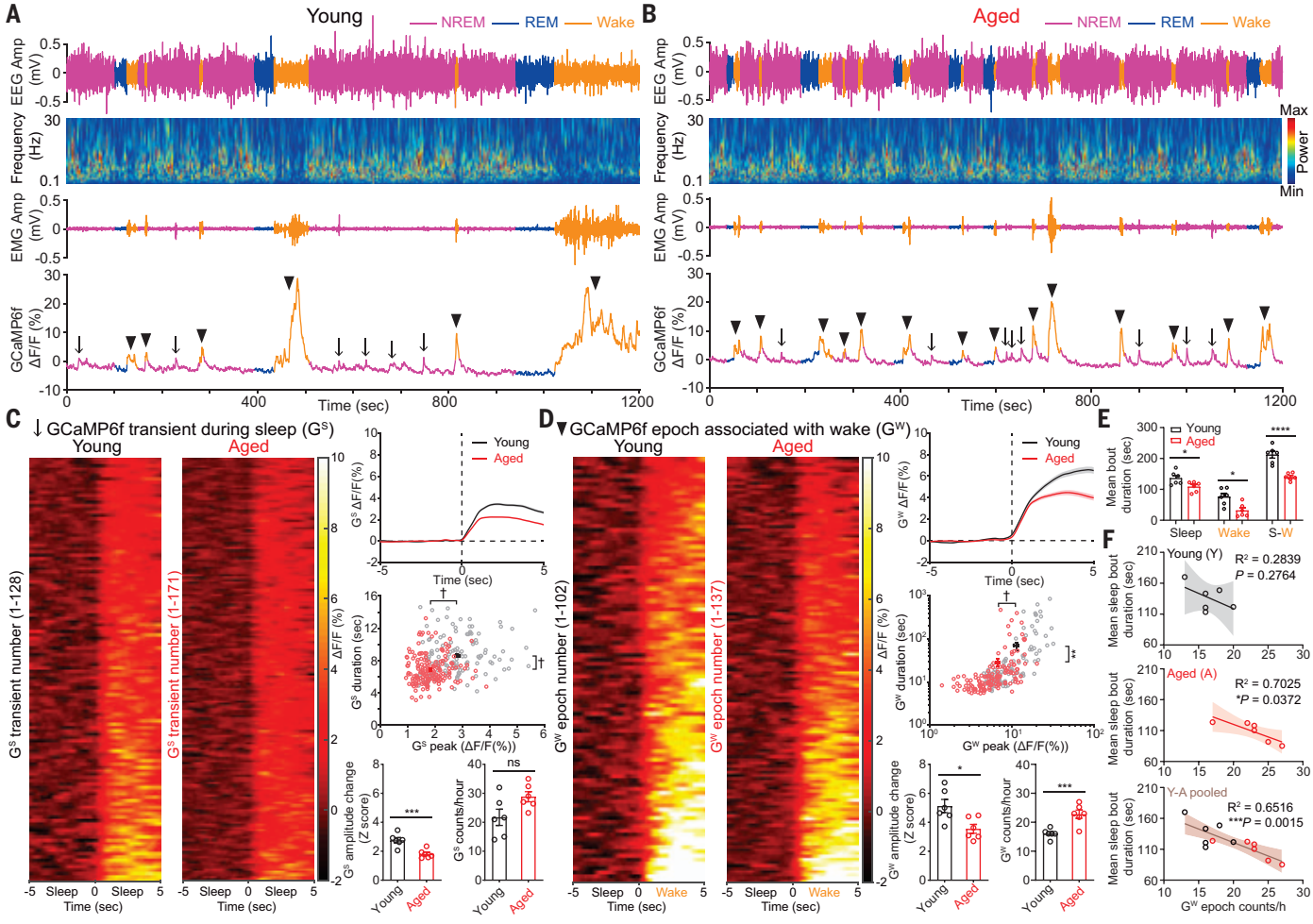


Fig. 1. Spontaneous activity of Hcrt neurons across sleep/wake states in young and aged mice. (**A** and **B**) Representative EEG, EEG power spectra, EMG, simultaneous Hcrt GCaMP6f signals from (A) young and (B) aged mice. The arrows indicate GCaMP6f transients during sleep (G^S), and the black triangles indicate GCaMP6f epochs associated with wakefulness (G^W). (**C**) Staged G^S signals during 10 s around the start of G^S transients from identical length (6 hours, 1 hour/mouse) of recorded GCaMP6f signals from young and aged mice (n = 6 mice each group), respectively, during light phase, averaged trace plot (right top), scatter plot of individual G^S duration against G^S peak (young, n = 128; aged, n = 171) (right middle), animal-based comparison of G^S signals for Z score and G^S frequency (right bottom). (**D**) Staged G^W signals during 10 s around start of G^W epochs from identical length (6 hours, 1 hour/mouse) of recorded GCaMP6f signals from young and aged mice, averaged trace plot (right top), scatter plot of individual G^W duration against G^W peak (young, n = 102; aged, n = 137) (right middle), animal-based comparison of G^W signals for Z score and G^W frequency (right bottom). (**E**) Animal-based comparison of mean bout duration for sleep, wake, and entire S-W episodes (n = 6 mice each group). (**F**) Correlation for mean sleep bout duration against G^W bout counts/hour in young, aged, and pooled datasets. Data represent mean ± SEM. In (C) to (E) unpaired t test with Welch's correction; (F), Spearman correlation, linear fit and 95% confidence band; *P < 0.05, **P < 0.01, ***P < 0.005, ****P < 0.001, †P < 0.0005; statistical details see supplementary text.

indicated by the cutaway surface (Fig. 2, D and J) for the mean value of wake duration in aged mice (Fig. 2, F and L). These results demonstrate that the threshold of Hcrt neuronal activity defining the sleep-to-wake transition was lower in aged mice, which is consistent with the hypothesis that aged Hcrt neurons are hyperexcitable.

Elevated intrinsic excitability of aged Hcrt neurons

To determine directly whether the intrinsic excitability of Hcrt neurons differs with age, we recorded spontaneous neuronal activity from ChR2-eYFP–labeled Hcrt neurons with whole-cell patch clamp recording in brain slices from young and aged Hcrt::Cre mice (Fig. 3). Immunostaining against Hcrt1 confirmed that the recorded neurons infused with biocytin were Hcrt1-positive (Fig. 3A). A higher fraction of aged versus young Hcrt neurons exhibited spontaneous firing (young, 12 of 33 versus aged, 9 of 21) (Fig. 3B). Despite comparable input resistances between young and aged Hcrt neurons (Fig. 3D), the resting membrane potential (RMP) of aged Hcrt neurons was more depolarized than young Hcrt neurons (young, −60.5 ± 1.9 mV versus aged, −51.5 ± 3.1 mV) (Fig. 3E). Ion channels that determine the firing threshold remained unchanged with age because the most negative voltage that must be reached for all-or-none firing to occur (*21*) was comparable between young and aged Hcrt neurons (young, −34.2 ± 1.6 mV versus aged, −36.3 ± 1.8 mV) (Fig. 3F). The difference between RMP and firing threshold was smaller in aged Hcrt neurons (young, 19.8 ± 2.6 mV versus aged, 11.4 ± 1.5 mV) (Fig. 3G), priming aged Hcrt neurons to fire action potentials (APs) after smaller depolarizations. Young Hcrt neurons also exhibited higher-amplitude APs than those of aged Hcrt neurons (young, 56.2 ± 5.2 mV versus aged, 42.3 ± 1.8 mV) (Fig. 3, B, C and H), although other AP properties did not significantly differ (Fig. 3, I to L).

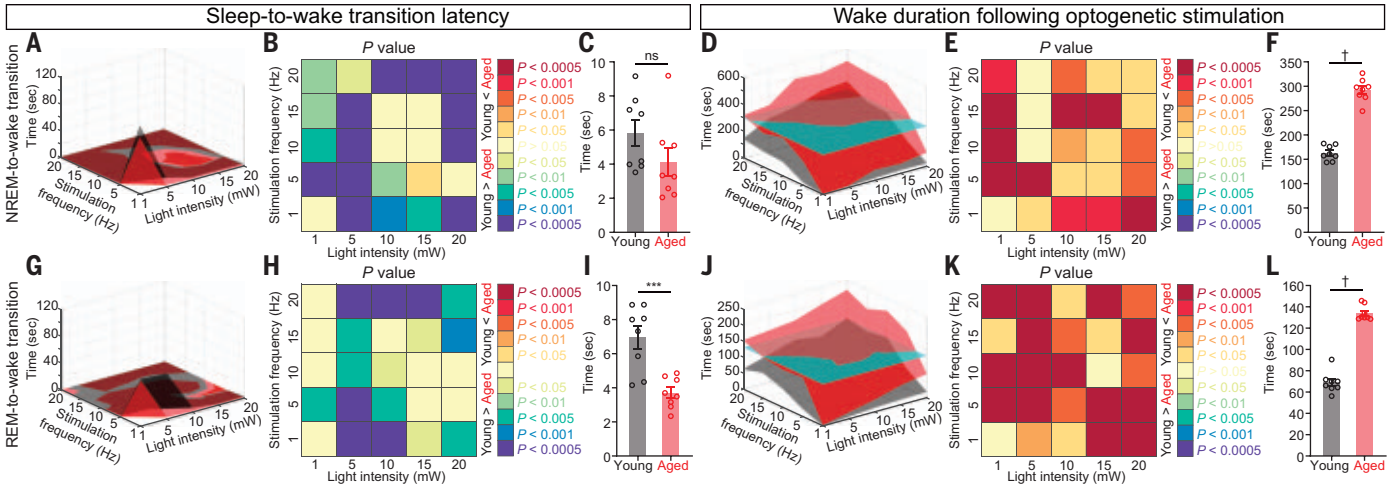


Fig. 2. More prolonged wake bouts upon optogenetic stimulation of Hcrt neurons expressing ChR2-eYFP in aged mice. (**A**) Surface plot of NREM-to-wake transition latency based on the mean value of each stimulation condition. (**B** and **C**) Comparison of NREM-to-wake transition latency based on (B) each stimulation condition and (C) the mean value for each animal. (**D**) Surface plot of wake duration based on the mean value of each stimulation condition. The cyan cutaway surface indicates the mean value for the aged group. (**E** and **F**) Comparison of wake duration based on (E) each stimulation condition and (F) the mean value for each animal. (**G**) Surface plot of REM-to-wake transition latency based on the mean value of each stimulation condition. (**H** and **I**) Comparison of REM-to-wake transition latency based on (H) each stimulation condition and (I) the mean value for each animal. (**J**) Surface plot of wake duration based on the mean value of each stimulation condition. The cyan cutaway surface indicates the mean value for the aged group. (**K** and **L**) Comparison of wake duration based on (K) each stimulation condition and (L) the mean value for each animal. In (B), (C), (E), (F), (H), (I), (K), and (L): Mann-Whitney *U* test; ***$P < 0.005$, †$P < 0.0005$. Statistical details are available in the supplementary text.

We next compared light-evoked firing activity between the young and aged Hcrt neurons expressing ChR2-eYFP. We tested different stimulation frequencies and compared the response attenuation, which is defined as the amplitude difference between the first and last light pulse–evoked responses after a train of blue light stimulations. The response attenuation was significantly smaller in aged Hcrt neurons than in young Hcrt neurons (Fig. 3, M and N). Recordings from non-Hcrt neurons postsynaptic to Hcrt neurons (fig. S4A) demonstrated that optogenetic stimulation of Hcrt neurons expressing ChR2-eYFP reliably evoked time-locked postsynaptic currents (PSCs) after optogenetic stimulation more often in the aged group than in the young group (young, 3 of 15 versus aged, 6 of 18) (fig. S4B). More neurons in slices from young mice exhibited PSC failures compared with those from aged mice (fig. S4, C and D). To test whether differences in excitability could be attributed to differential expression of ChR2-eYFP, we performed step-current injection in both young and aged Hcrt neurons. More spikelets were evoked in aged Hcrt neurons by the same current injection protocol (Fig. 3, O and P), again indicating hyperexcitability of aged Hcrt neurons.

Impaired M-current with loss of KCNQ2 channels in aged Hcrt neurons

Hyperexcitability in aged Hcrt neurons with depolarized RMPs suggested a change in ionic conductance such as K^+ conductance mediated by voltage-gated potassium channels (KCNQ). There are five mammalian subtypes named KCNQ1 to -5 (Kv7.1 to Kv7.5) (*22*, *23*), and KCNQ2 pairs with the KCNQ3 subunit to form KCNQ2/3 heterotetramers, constituting primarily the molecular substrate of the M-current (I_M) (*24*), which plays a critical role in governing neuronal subthreshold excitability, repolarization, and sensitivity to synaptic inputs (*23*–*25*). To test this idea, we applied KCNQ2/3 channel-selective modulators to Hcrt neurons expressing eYFP in brain slices from either young or aged mice (Fig. 4, A-F). Perfusion of a KCNQ2/3-selective blocker, XE991 (50 μM), significantly depolarized the RMP and increased the firing frequency in young Hcrt neurons (Fig. 4, A to C). Reciprocally, application of a KCNQ2/3-selective activator, flupirtine (50 μM), hyperpolarized the RMP and reduced the firing frequency in aged Hcrt neurons (Fig. 4, D to F). XE991 reduced I_M in young Hcrt neurons (before, −11.2 ± 1.3 pA versus after, −5.2 ± 0.8 pA) (Fig. 4G, top). Conversely, flupirtine increased I_M in both young (before, −16.9 ± 3.8 pA versus after, −22.6 ± 5.2 pA) (Fig. 4G, bottom) and aged (before, −14.6 ± 1.1 pA versus after: −18.0 ± 1.5 pA) (Fig. 4H, bottom) Hcrt neurons. The basal I_M in aged Hcrt neurons was significantly smaller than in young Hcrt neurons (young, −17.1 ± 1.9 pA versus aged, −11.8 ± 1.2 pA) (Fig. 4I). These results were validated with array tomography at ultrastructural resolution (*26*), which revealed a significant reduction in KCNQ2 immunoreactivity in aged Hcrt neurons (Fig. 4J).

To determine the extent of differences between young and aged Hcrt neurons at the transcriptomic level, we performed single-nucleus RNA-sequencing (snRNA-seq). Aged Hcrt neurons developed adaptive up-regulation of prepro-Hcrt mRNA expression in both male (fig. S5) and female (fig. S6) mice, suggesting potential compensatory syntheses of Hcrt neuropeptides by individual Hcrt neurons. Although the normalized expression level of *Kcnq* subtypes was not significantly different between the young and aged groups, the percentage of aged Hcrt neurons actively expressing *Kcnq1/2/3/5* mRNAs, the dominant subtypes, was lower (figs. S5E and S6E) and expected to contribute to the hyperexcitability of aged Hcrt neurons.

CRISPR/SaCas9–mediated disruption of Kcnq2/3 genes in young Hcrt neurons destabilizes NREM sleep

Given the broad expression of KCNQ channels in the brain (*25*), what is the contribution of I_M in Hcrt neurons to the overall sleep architecture? To answer this question, we used CRISPR/SaCas9–mediated disruption (*27*) of *Kcnq2/3* genes specifically in Hcrt neurons in young mice to mirror the impaired I_M observed in aged Hcrt neurons. We designed AAV vectors for Cre-dependent expression of SaCas9 (*28*), sgControl, and sgKcnq2/3 targeting *Kcnq2/3* genes in Hcrt neurons (Fig. 5). Young Hcrt::Cre mice from different litters were randomly separated into two groups. We delivered a viral mixture of SaCas9 and sgControl to the Hcrt field bilaterally in the control group, whereas the other group received bilateral injection of a SaCas9 and

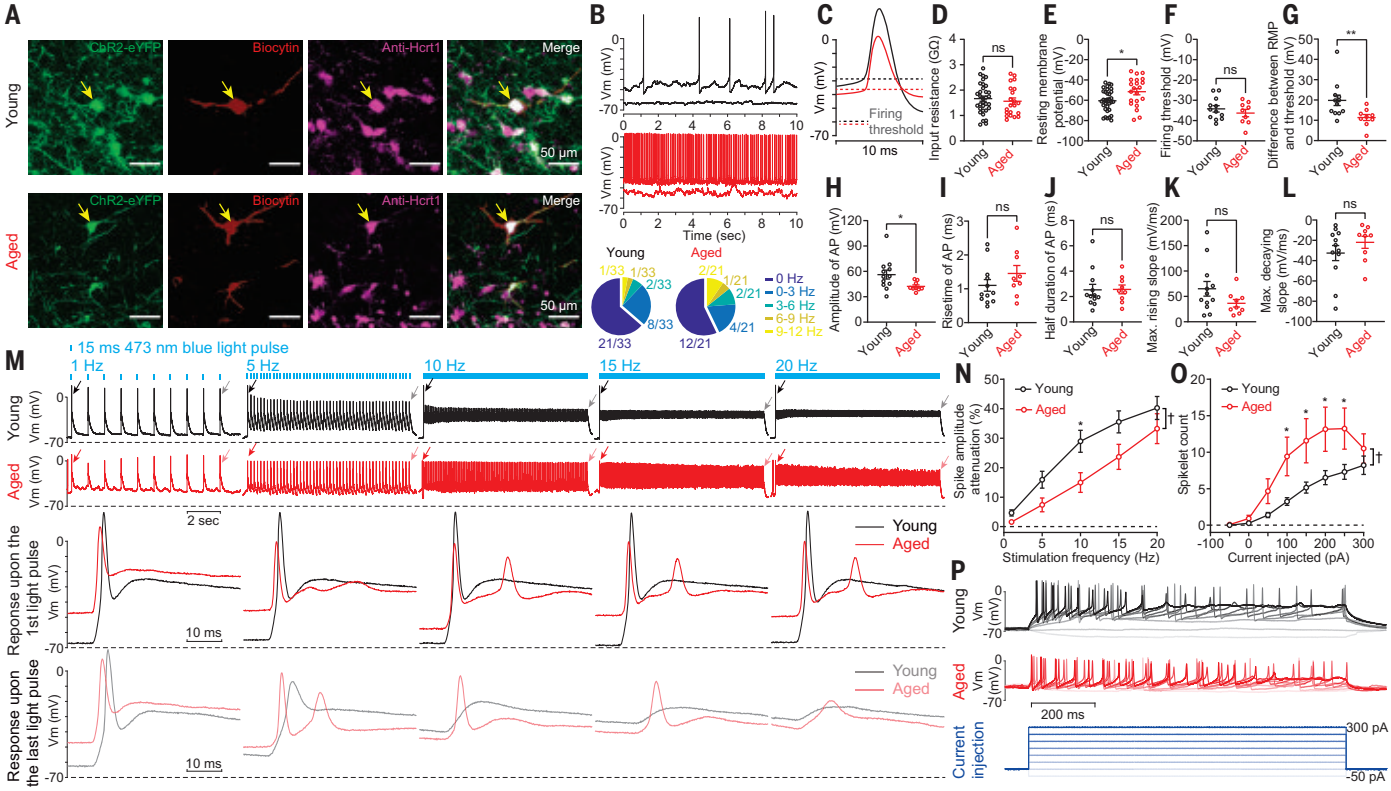


Fig. 3. Hyperexcitability in aged Hcrt neurons revealed with whole-cell patch clamp recording. (**A**) Representative slices containing recorded ChR2-eYFP–labeled Hcrt neurons infused with biocytin. (**B**) Representative traces and fractions of young and aged Hcrt neurons with and without spontaneous firing activities. (**C**) Averaged traces of spontaneous APs shown in (B). (**D** to **L**) Comparison of basic electrophysiological properties between young and aged Hcrt neurons. (D) Input resistance and (E) RMP of all the recorded young and aged Hcrt neurons (young, n = 33 neurons versus aged, n = 21 neurons from eight mice each group). Comparison of other parameters including (F) firing threshold, (G) difference between RMP and firing threshold, (H) AP peak amplitude, (I) AP rising time, (J) AP half duration, (K) maximum rising slope, and (L) decaying slope of spontaneous APs between young and aged Hcrt neurons (young, n = 12 neurons versus aged, n = 9 neurons from eight mice each group). (**M**) (Top) Representative traces of young and aged Hcrt neurons expressing ChR2-eYFP upon optogenetic stimulation. (Bottom) The same responses on a slower time base, illustrating the response to the first and last light pulse stimulations at each stimulation frequency (membrane voltage/Vm). (**N**) Significant reduction of response attenuation calculated based on the first and the last response from trains as in M (young, n = 23 neurons versus aged, n = 21 neurons from eight mice each group). (**O** and **P**) Step current injections triggered more spikelets in aged Hcrt neurons than in young Hcrt neurons [(O) young, n = 33 neurons versus aged, n = 26 neurons from eight mice each group; (P) representative traces and current injection protocol]. In (D) to (L): Mann-Whitney U test; (N) and (O): two-way ANOVA followed by post hoc Šidák's multiple comparisons; $^{*}P < 0.05$, $^{**}P < 0.01$, †$P < 0.0005$. Statistical details are available in the supplementary text.

sgKcnq2/3 viral mixture for disruption of *Kcnq2/3* genes (Fig. 5A). All the mice were implanted with EEG-EMG electrodes for sleep/wake pattern monitoring for a 2-day consecutive recording of EEG-EMG signals weekly for 8 weeks. CRISPR/SaCas9–mediated deactivation of *Kcnq2/3* genes in Hcrt neurons was sufficient to generate NREM sleep fragmentation in young mice (NREM mean bout length at 8 weeks after virus injection, 48 hours; sgControl, 2.1 ± 0.04 min versus sgKcnq2/3, 1.7 ± 0.1 min; light phase, sgControl, 2.2 ± 0.1 min versus sgKcnq2/3, 1.9 ± 0.1 min; dark phase, sgControl, 2.0 ± 0.1 min versus sgKcnq2/3, 1.6 ± 0.1 min) (Fig. 5B). We then performed whole-cell recording from individual mCherry-labeled Hcrt neurons (Fig. 5C) after EEG-EMG recording at 8 weeks after virus injection and found that the Hcrt neurons with *Kcnq2/3* gene disruptions showed a depolarized RMP (sgControl, −67.0 ± 2.4 mV versus sgKcnq2/3, −55.9 ± 3.3 mV) (Fig. 5D) and spontaneous firing activity in higher proportion (Fig. 5E), mimicking the aged Hcrt neurons. EEG-EMG recording up to 12 weeks after virus infection in a subset of these mice (fig. S7) further validated our observations at 8 weeks after virus injection. Analyses of the basic electrophysiological properties of the spontaneous APs revealed that artificial disruption of KCNQ2/3 channels in young Hcrt neurons (fig. S7, E and F) mimicked some features observed in the aged Hcrt neurons, including a trend of reduction in the maximum rising/decaying slope of spontaneous APs (Fig. 3, D to L).

In vivo evaluation of KCNQ2/3-selective ligands

To further test the role of KCNQ2/3 channels in sleep modulation, we administered (intraperitoneally) either the KCNQ2/3-selective blocker XE991 (2 mg/kg) or the saline vehicle as control to young (3 to 5 months) WT mice at the beginning of the light phase, when there is a strong sleep pressure. XE991 significantly increased the wake amount during the first hour after injection compared with that of the control group (Fig. 6A) without affecting the power spectra (Fig. 6, C, E, and G). Reciprocally, we injected the KCNQ2/3–selective activator, flupirtine (intraperitoneally, 20 mg/kg) or 0.3% dimethyl sulfoxide (DMSO) in saline (v/v) as vehicle to aged (18 to 22 months) WT mice at the beginning of the light phase. Flupirtine significantly increased the amount and stability of NREM sleep compared with the control group (Fig. 6B). Flupirtine also increased the theta band power during NREM sleep and the initial REM sleep segment after drug administration (Fig. 6, D, F and H). Sleep quality is correlated with cognitive functions (*1*, *2*), and flupirtine administered to aged mice at the

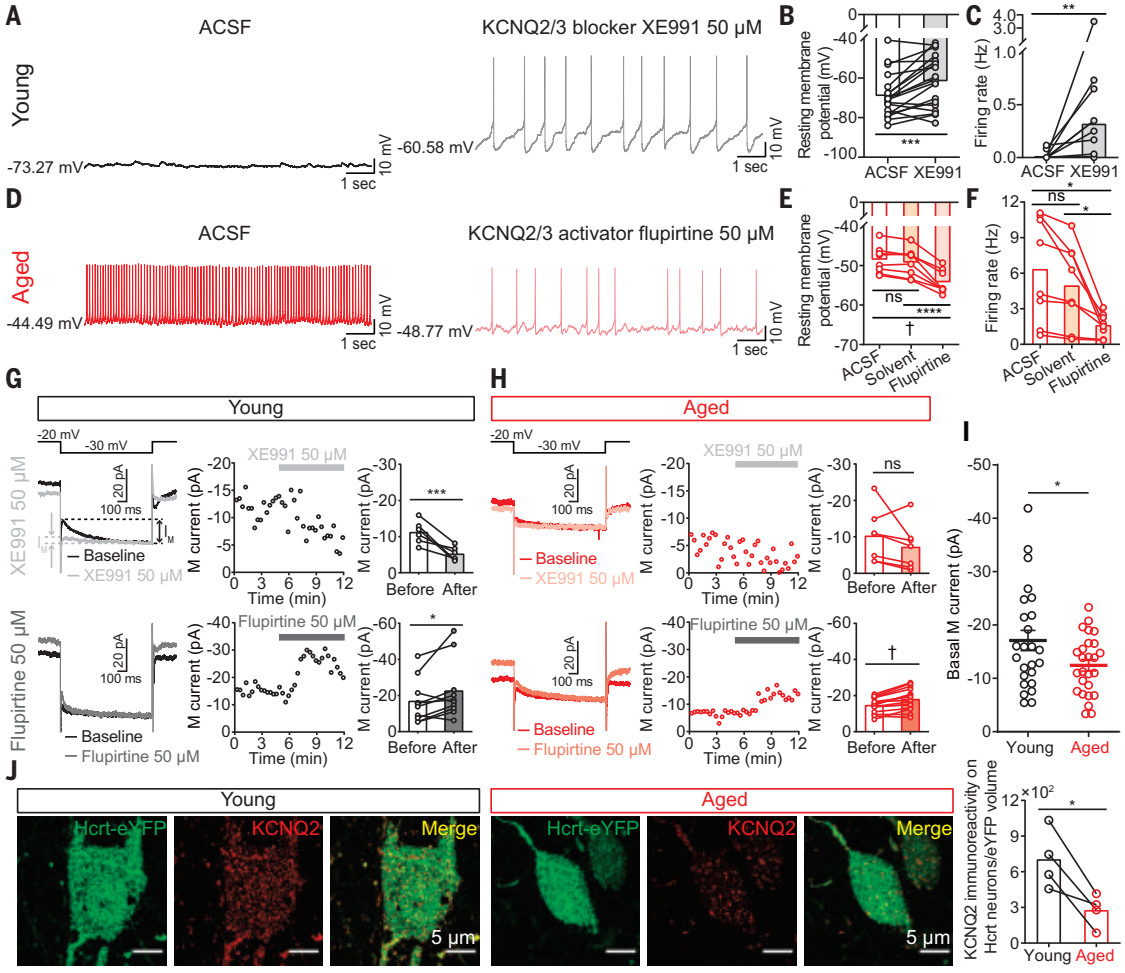


Fig. 4. Impaired I_M associated with loss of KCNQ2 in aged Hcrt neurons. (**A**) Representative traces from a young Hcrt neuron (left) before or (right) in the presence of a KCNQ2/3 blocker XE991 (50 μM). (**B**) XE991 depolarized RMP and (**C**) increased firing frequency in young Hcrt neurons (n = 19 neurons from seven mice). (**D**) Representative traces from an aged Hcrt neuron (left) before or (right) in the presence of a KCNQ2/3 activator flupirtine (50 μM). (**E**) Flupirtine hyperpolarized RMP and (**F**) decreased firing frequency in aged Hcrt neurons (n = 8 neurons from five mice). (**G**) I_M in young Hcrt neurons modulated by XE991 (top; n = 6 neurons from three mice) and flupirtine (bottom; n = 10 neurons from five mice). (**H**) I_M in aged Hcrt neurons modulated by XE991 (top; n = 7 neurons from three mice) and flupirtine (bottom; n = 15 neurons from five mice). (**I**) Basal I_M in young Hcrt neurons (n = 25 neurons from nine mice) versus in aged Hcrt neurons (n = 26 neurons from nine mice). (**J**) Array tomography revealed reduced KCNQ2 expression in aged Hcrt neurons (n = 4 mice/group). In (B) and (C), Wilcoxon matched-pairs signed rank test; (E) and (F), RM one-way ANOVA followed by post hoc Tukey's multiple comparisons; (G), (H), and (J), paired t test; (I) unpaired t test with Welch's correction; statistical details are available in the supplementary text.

beginning of light phase after the familiarization session in the object-recognition task also improved the subsequent exploration of the new object (fig. S8).

Sleep instability in a narcolepsy mouse model with genetic ablation of Hcrt neurons

Abrupt Hcrt neuron loss in pathological conditions at young ages causes type I narcolepsy, a condition characterized by excessive daytime sleepiness and a sudden loss of muscle tone with EEG pattern resembling REM sleep, known as cataplexy, as well as sleep fragmentation (*17*). We crossed OX(Hcrt)–enhanced green fluorescent protein (eGFP) mice (*29*) with OX(Hcrt)-ataxin3 mice, a narcolepsy mouse model (*15*), to generate mice with Hcrt neurons that express both eGFP and ataxin3, allowing us to examine the activity of these neurons while monitoring EEG-EMG patterns of their littermates (figs. S9 and S10). EEG-EMG recording from 5-week-old mice expressing ataxin3 exhibited mild NREM sleep fragmentation, with three of six mice showing cataplexy-like EEGEMG epochs compared with their control group with intact Hcrt neurons (fig. S9, A to C), according to established criteria (*30*). In recordings from brain slices, although Hcrt cells from the ataxin3-expressing group had a more depolarized RMP—a smaller difference between RMP and firing threshold—as well as a higher fraction of spontaneously firing neurons compared with that of age-matched controls, other basic electrophysiological properties were similar (fig. S9, D to G). Ataxin3-expressing mice at an age of 12 weeks showed obvious NREM sleep fragmentation with a severe cataplexy-like EEG-EMG pattern (six of six mice) (fig. S10A). Immunostaining against Hcrt1 showed a near complete Hcrt neuron degeneration at the age of 12 weeks in mice expressing ataxin3 (fig. S10B), confirming Hcrt neuron loss around a similar age in this narcolepsy mouse model (*15*). Thus, although both healthy aged WT mice and young mice expressing ataxin3 show sleep fragmentation, the underlying mechanisms are not identical.

Discussion

Sleep quality decline—in particular, fragmented nocturnal sleep during aging—impairs daytime

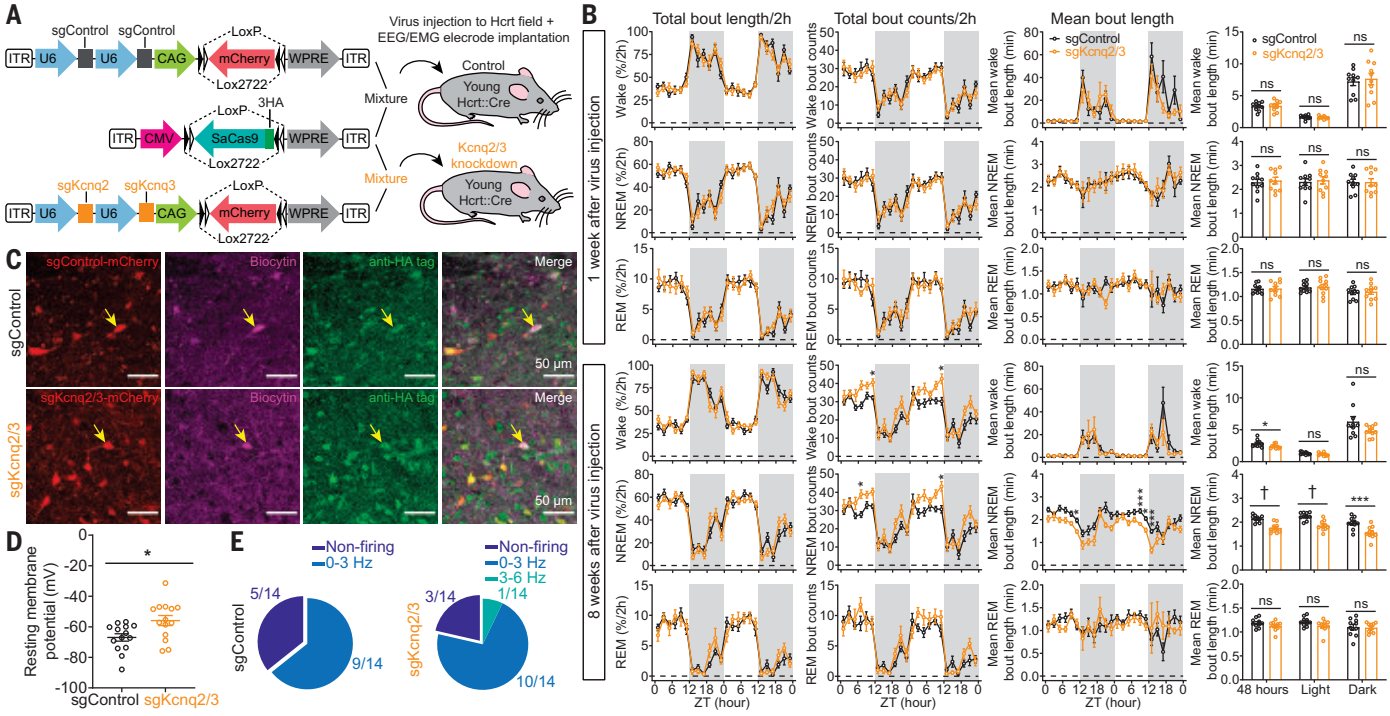


Fig. 5. CRISPR/SaCas9–mediated disruption of *Kcnq2/3* genes in Hcrt neurons leads to NREM sleep fragmentation in young mice. (**A**) Schematic of AAV sgControl, AAV SaCas9, AAV sgKcnq2/3 vector design, and bilateral viral infection of Hcrt neurons in young Hcrt::Cre mice. (**B**) Two-hour (left) binned percentage, (middle left) bout counts, (middle right) mean bout length and (right) mean bout length based on circadian phase for wake, NREM, and REM sleep at 1 week (top) and 8 weeks (bottom) after injection of a virus mixture, as illustrated in (A) (n = 10 mice/group, dark phase indicated by gray shielding). (**C**) Representative slices expressing sgRNA with fluorescent mCherry flag and SaCas9-3HA for sgControl and sgKcnq2/3 group, respectively. Patch clamp recorded cells were labeled with biocytin, and post hoc antibody staining against HA tag confirmed the cells expressing SaCas9 for data analyses. (**D**) Comparison of RMPs between sgControl and sgKcnq2/3 group (n = 14 neurons from three mice each group). (**E**) Fractions of neurons with different firing frequencies in the (left) sgControl and (right) sgKcnq2/3 groups. Data indicate mean ± SEM [(B) left to middle right, two-way RM ANOVA followed by Šidák's multiple comparisons; (B) right, Holm-Šidák; (D) Mann-Whitney U test; *P < 0.05, ***P < 0.005, †P < 0.0005; statistical details are avialable in the supplementary text].

well-being in elderly individuals (*3*). However, the mechanistic underpinnings of aging-related sleep fragmentation are unknown. In this study, we report a mechanism underlying sleep instability during aging. We found a generally fragmented sleep/wake pattern in aged mice with reduced wakefulness during their active phase (fig. S1), replicating the sleep traits in aged populations (*3*). We further observed more frequent Hcrt GCaMP6f activity epochs driving the sleep fragmentation in aged mice (Fig. 1). Despite a reduction in the number of wake-promoting Hcrt neurons in aged mice (fig. S2), these mice paradoxically manifested significantly longer wake bouts in response to Hcrt neuron optogenetic stimulation (Fig. 2 and fig. S3). Immunostaining against Hcrt1 confirmed that the majority of the virus-infected neurons are hypocretinergic (fig. S3, B and C), and the small fraction of non-Hcrt neurons may be assigned to the ~30 cell types described in the LH (*31*), none of which are likely to affect bout length directly (*32*–*34*). Aged Hcrt neurons exhibited increased intrinsic excitability, with more depolarized RMPs (Fig. 3), more spikelets per unit current (Fig. 3, O and P), and up-regulated prepro-Hcrt nuclear mRNA expression (figs. S5 and S6).

To understand the molecular mechanisms underlying the phenotypes described above, we focused on the ion channels that regulate the intrinsic excitability of neurons. Potassium channels play an important role in governing the excitability of neurons through repolarizing action potentials (*22*, *25*). Specifically, KCNQ2/3 channels are expressed broadly in brain regions controlling neuronal network oscillations and synchronization (*35*), and a moderate loss of function of these channels causes epilepsy in humans (*36*, *37*) and mice (*38*). In aged Hcrt neurons, we discovered impaired KCNQ2/3–mediated I_M associated with lower KCNQ2 channel density (Fig. 4, I and J). The loss of KCNQ2 may be due to oxidation, a known factor for potassium conductance impairment during aging (*39*). Decreased levels of transcription factor specificity protein 1 (sp1) in senescent cells (*40*) might be another reason for impaired I_M in aged Hcrt neurons because sp1 has been shown to activate the expression of KCNQ2/3 and augment I_M (*41*). Our data support the hypothesis that the arousal circuitry, and particularly the Hcrt system, becomes hyperexcitable during aging. Selective disruption of *Kcnq2/3* genes in young Hcrt neurons was sufficient to depolarize these neurons and cause sleep fragmentation (Fig. 5 and fig. S7), mimicking the sleep instability observed in aged mice (fig. S1). Further advancing these findings, systemic administration of a KCNQ2/3 blocker increased wakefulness (Fig. 6A), whereas a KCNQ2/3 activator consolidated NREM sleep (Fig. 6B). Specifically targeting the Hcrt system with a pharmacological tool, application of a dual Hcrt/OX receptor antagonist MK6096 (filorexant, 20 mg/kg, intraperitoneally) also increased the amount of NREM sleep and mean NREM bout length within 6 hours after drug administration (fig. S11). Our pharmacological data may open a new approach for conquering sleep quality decline during aging.

On the basis of our scRNA-seq data (figs. S5 and S6), KCNQ1/5 mRNA are expressed in Hcrt neurons and are expected to have a lower KCNQ subunit expression level in aged Hcrt neurons both in male (fig. S5E) and female mice (fig. S6E). Factors other than impaired

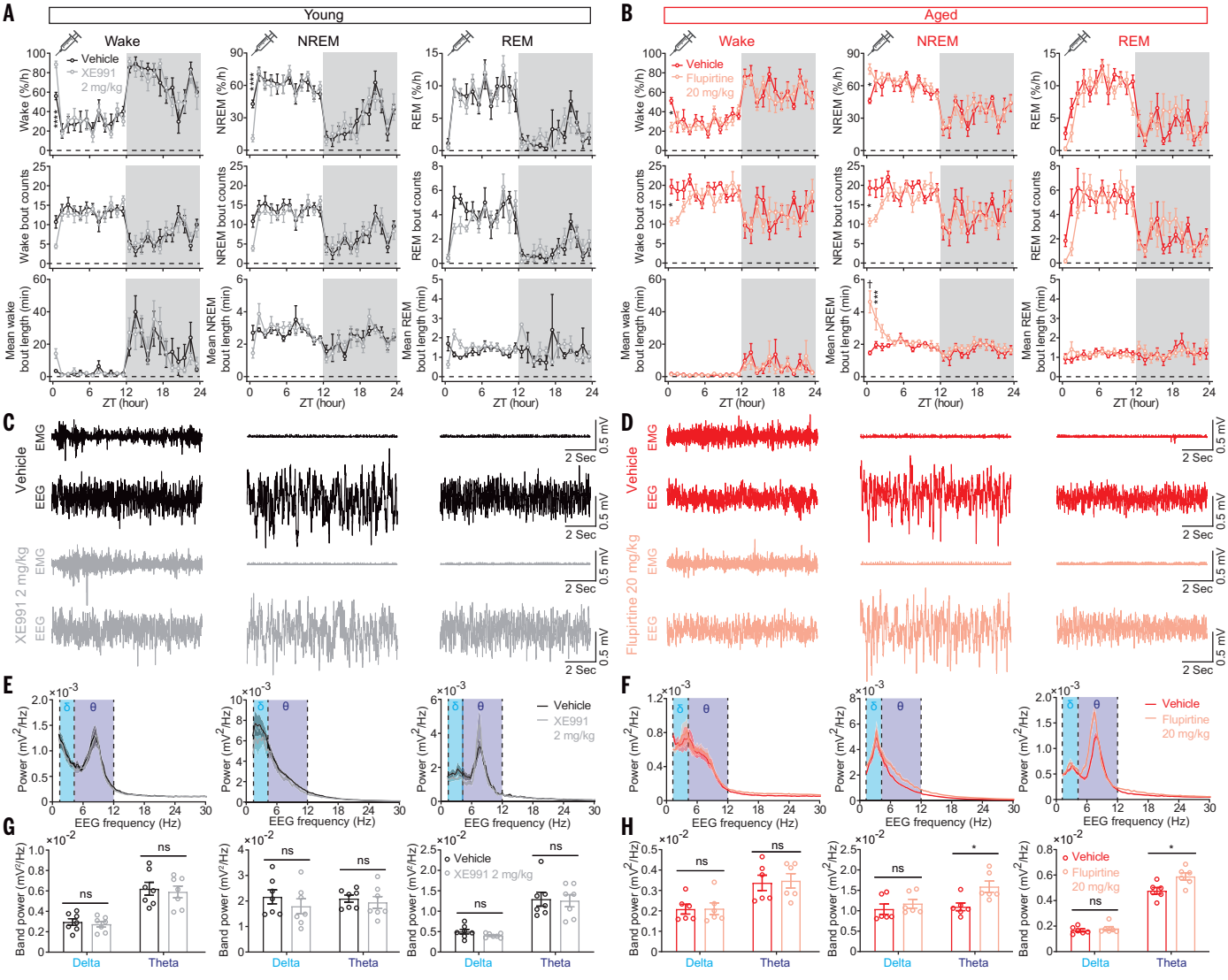


Fig. 6. Pharmacological manipulation of sleep/wake states with KCNQ2/3 ligands. (**A**) Significantly increased wake amount by the KCNQ2/3 blocker XE991 (2 mg/kg) in young mice. (**B**) Significantly increased NREM amount and mean bout length by the KCNQ2/3 activator flupirtine (20 mg/kg) in aged mice. (**C**) Representative EMG-EEG raw traces from vehicle- and XE991-treated (2 mg/kg) young mice. (**D**) Representative EMG-EEG raw traces from vehicle- and flupirtine-treated (20 mg/kg) aged mice. (**E**) Power spectra of EEG for vehicle- and XE991-treated young mice and (**F**) power spectra of EEG for vehicle- and flupirtine-treated aged mice. (**G**) Comparison of delta, theta band power between vehicle- and XE991-treated young mice and (**H**) between vehicle- and flupirtine-treated aged mice. Data indicate mean ± SEM [young, n = 7 mice each group; aged, n = 6 mice each group; (A) and (B) two-way liner mixed-effects model followed by Šidák's multiple comparisons, dark phase indicated by gray shielding; (G) and (H) Holm-Šidák, $^{*}P < 0.05$, $^{***}P < 0.005$, $^{****}P < 0.001$, †$P < 0.0005$; statistical details are available in the supplementary text].

M-current with a key role in neuron repolarization may also contribute to increased excitability of arousal-promoting circuits during aging. Together with KCNQ family, G protein–gated inward rectifying K^+ channels (Girks) are expressed in the brain and mediate outward potassium current in hyperpolarizing neurons and decreasing intrinsic excitability (*42*).

Our findings in aged animals may extend to neurodegenerative conditions such as Alzheimer's disease (AD). The level of amyloid-β (Aβ, a marker of AD) in brain interstitial fluid correlates with wakefulness and increases with elevated hypocretinergic tone in AD mouse models (*43*). Aβ reduces gene expression of *Kcnq2/3* and *Girk2/3/4* in hippocampal slices incubated with Aβ fragment $Aβ_{25-35}$ (*44*) in line with a deleterious cycle of hyperactivation, with multiple excitatory elements implicating Aβ-induced hyperexcitation in hippocampal neurons (*45*), which links AD pathology–mediated down-regulation of K^+ channels to neuronal excitability. Loss of hyperexcitable arousal-promoting neurons destabilizing sleep during aging could be drastically exacerbated by AD pathology, as evidenced by a study of post mortem brains from AD patients that demonstrate a ~32% Hcrt neuron loss compared with their age-matched controls without AD (*46*).

Among the main downstream targets of Hcrt neurons (*47*, *48*), locus coeruleus noradrenergic (LC NA) neurons displayed a milder cell count loss (~15%) (fig. S12) compared with Hcrt neuron loss (~38%) (fig. S2) in the same group of aged mice. Optogenetic activation of LC NA neurons elicited sleep-to-wake transitions and maintained wakefulness more robustly, as indicated by shorter sleep-to-wake transition latencies and longer wake bout

durations in aged mice with the same optogenetic stimulations in young and aged mice (fig. S13). Electrophysiological recordings revealed a more depolarized RMP and a higher proportion of neurons with spontaneous firing activity in aged LC NA neurons (fig. S14). These results suggested a potential up-regulation of excitability in other arousal-promoting brain nuclei during aging.

Sleep instability and fragmentation not only appears in the elderly but also have been observed in type I narcolepsy patients with loss of Hcrt neurons at young ages, yet the pathology may develop gradually (*17*), which raises the question that whether the spontaneous activity of the remaining Hcrt neurons are up-regulated to compensate for the rapid Hcrt neuron loss in the narcolepsy pathological condition. With a narcolepsy mouse model, we found that the remaining Hcrt neurons exhibited depolarized RMPs and a higher fraction with spontaneous firing activity (fig. S9, D to G), despite other AP properties being similar to those of age-matched controls around 5 weeks of age. Yet because the 12-week-old ataxin3^{+} mice have almost completely lost their Hcrt neurons, the even more fragmented sleep features in these mice (compared with the sleep pattern around 5 weeks) (figs. S9 and S10) cannot be attributed to alteration of Hcrt/OX neuronal excitability. Increased depolarization of the remaining Hcrt neurons in ataxin3-expressing mice may result from toxicity introduced by ataxin3 expression or neural circuit reorganization or malfunction during rapid Hcrt neuron loss, whereas elevated depolarization in aged mice is the result of an altered complement of membrane ion channels. Although it is possible that there is also neural circuit reorganization or malfunction accompanying chronic Hcrt neuron loss during natural healthy aging, the absence of a cataplexy-like EEG-EMG pattern in healthy aged WT mice highlighted that the mechanisms underlying sleep fragmentation in young OX(Hcrt)-ataxin3 mice and healthy aged WT mice are not identical.

Collectively, our study delineates that elevated Hcrt neuron excitability is associated with sleep fragmentation during aging. A lower threshold defining sleep-to-wake transitions driven by hyperexcitable Hcrt neurons accounts for sleep fragmentation and yields longer wake bouts upon optogenetic stimulation of these neurons in aged mice. The restoration of sleep stability in aged mice upon manipulation of KCNQ channels may lead to the development of potential therapeutic strategies in aged individuals whose sleep fragmentation contributes to aging-related neurodegeneration.

Materials and methods

Animals

Experiments with mice were performed following the protocols approved by the Stanford University Animal Care and Use Committee in accordance with the *National Institutes of Health Guide for the Care and Use of Laboratory Animals*.

Discomfort, distress, and pain were minimized with anesthesia and analgesic medications. Mice were housed in a temperature- and humidity-controlled animal facility with a 12-hours/12-hours light/dark cycle (9 am light on, Zeitgeber time 0/ZT 0), unless otherwise specified. Mice had ad libitum access to standard laboratory mouse food pellets and water. 2-3 month young male adult wild type (WT) mice were acquired from Jackson Laboratory (Jax) and 18 month old WT male mice were acquired from National Institute on Aging (NIA). OX(Hcrt)-ataxin3 heterozygotes (*15*), Hcrt-IRES-Cre knock-in (Hcrt::Cre) heterozygotes (*20*), OX(Hcrt)-eGFP heterozygotes (*29*) and tyrosine hydroxylase (TH)-IRES-Cre knock-in (TH::Cre) heterozygotes (European Mouse Mutant Archive; EMMA ID: EM:00254) (*49*) were backcrossed onto C57BL/6J background. Male mice were used in the experiments, unless otherwise specified. Mice at an age younger than 5 months belonged to the young group, whereas mice older than 18 months were considered as aged. Animals from multiple litters were randomly assigned to control or experimental group under each experimental paradigm. Group sizes were determined based on earlier publications (*13*, *50*, *51*).

EEG-EMG electrode preparation and implantation

Mini-screw (US Micro Screw) was soldered to one tip of an insulated mini-wire with two tips exposed, and the other tip of the mini-wire was soldered to a golden pin aligned in an electrode socket. A micro-ring was made on one side of an insulated mini-wire with the other end soldered to a separate golden pin in the electrode socket. Each electrode socket contained 4 channels with 2 mini-screw channels for EEG recording and 2 micro-ring channels for EMG recording as described in earlier work from our lab (*12*, *47*, *50*). The resistance of all the channels was controlled with a digital Multimeter (Fluke) to be lower than 1.5 ohms for ideal conductance. Mice were mounted onto an animal stereotaxic frame (David Kopf Instruments) under anesthesia with intraperitoneal injection of a mixture of ketamine (100 mg/kg) and xylazine (20 mg/kg). Two mini-screws were placed in the skull above the frontal (AP: −2 mm; ML: ± 1 mm) and temporal (AP: 3 mm, ML: ± 2.5 mm) cortices for EEG signal sampling and two micro-rings were placed in the neck muscles for EMG signal acquisition. Electrode socket was secured with Metabond (Parkell, Japan) and dental acrylic on skull for recording in freely moving mice. Buprenorphine SR (0.5 mg/kg) was administered subcutaneously to mice before and after surgery for pain relief. After surgery, revertidine (5 mg/kg) was administered (intraperitoneally) to mice to facilitate recovery from anesthesia.

Virus injection with and without fiber optic implantation

Optogenetic experiments

0.3 μl AAV-DJ-EF1α-DIO-hChR2(H134R)-eYFP viruses (ChR2-eYFP, 6.5×10^{12} gc/ml, Stanford Virus Core, Lot no. 4176) was delivered to LH (AP: −1.35 mm, ML: ± 0.95 mm, DV: −5.15 mm) of anesthetized young (3 to 5 months) or aged (18 to 22 months) Hcrt::Cre mice with a 5 μl Hamilton microsyringe according to stereotaxic coordinates determined on a Kopf stereotaxic frame. AAV-DJ-EF1α- DIO-eYFP viruses (eYFP, 6.9×10^{12} gc/ml, Stanford Virus Core, Lot no. 3010) was used as control or for in vitro pharmacology experiments. A glass fiber (200 μm core diameter, Doric Lenses, Franquet, Québec, Canada) was implanted with the tip right above the injection site for optogenetic stimulations later on. After fixing the glass fiber with Metabond, the EEG/EMG electrodes were implanted with dental acrylic fixation. Similar procedure was performed for virus injection in TH::Cre mice targeting LC NA neurons (AP: −5.46 mm, ML: ± 1.2 mm, DV: −3.6 mm). Mice were allowed to recover for at least 2 weeks to get sufficient virus expression before connecting to the EEG/EMG recording cables and optical stimulation patch cord. EEG/EMG electrode and fiber optic implantation were omitted in the mice infected with ChR2-eYFP or eYFP viruses used for in vitro electrophysiology experiments.

Fiber photometry

For fiber photometry, 0.3 μl AAV vectors encoding GCaMP6f (AAV-DJ-EF1α-DIO- GCaMP6f, 1.1×10^{12} gc/ml, Stanford Virus Core, Lot no. 3725) were delivered to LH (AP: −1.35 mm, ML: ± 0.95 mm, DV: −5.15 mm) of young (3 to 5 months) or aged (18 to 22 months) Hcrt::Cre mice with a 5 μl Hamilton micro-syringe. A glass fiber (400 μm core diameter, Doric Lenses) was implanted with the tip at the injection site for GCaMP6f signal acquisition afterwards. EEG/EMG electrodes were implanted following fixation of fiber optic and secured with Metabond and dental acrylic. Mice were allowed to recover for at least 2 weeks to get sufficient virus expression before connecting to the EEG-EMG recording cables and fiber photometry recording patch cord.

Single-nucleus RNA-sequencing (snRNA-seq)

To label telomeres in the nuclei, 0.3 μl AAV vectors encoding Cre-dependent DsRed-hTRF2 (*52*) (AAV-DJ-DIO-DsRed-hTRF2, 1.95×10^{12} gc/ml, customer viruses packaged at Stanford Virus Core, Lot no. 4422) were bilaterally injected to

the LH (AP: −1.35 mm, ML: ± 0.95 mm, DV: −5.15 mm) of young (3 months) and aged (18 months) male and female Hcrt::Cre mice [3 mice per condition (young/aged male/female)].

EEG/EMG recording and analysis

Mice were singly-housed after surgery and allowed to recover for 1 week with access to food and water ad libitum before EEG/EMG recording. EEG/EMG signals were amplified through a multiple channel amplifier (Grass Instruments) and acquired with VitalRecorder (Kissei Comtec Co.) with a sampling frequency of 256 Hz followed by offline signal analysis. The bandpass was set between 0.1 and 120 Hz. Raw EEG/EMG data were exported to Matlab (MathWorks, Natick, MA, USA) and analyzed with custom scripts and Matlab built- in tools based on described criteria (*12*) to determine behavioral states. Cataplexy-like EEG/EMG pattern was determined based on the criteria described in the original publication reporting the OX(Hcrt)-ataxin3 narcolepsy mouse model (*15*) and the consensus definition of cataplexy in mouse models of narcolepsy: (i) ≥ 10 s of EMG atonia; (ii) EEG with theta band domination; (iii) behavioral immobility preceded by ≥ 40 s of wakefulness (*30*). For optogenetic and fiber photometry recording experiments, simultaneous EEG/EMG signals were recorded to determine behavioral states. The latency of sleep-to-wake transition and the duration of wakefulness following optogenetic stimulation during sleep were determined in SleepSign (Kissei Comtec Co.) with indication of stimulation timestamps on the raw EEG/EMG signals. EEG power spectral analysis was performed with the same method as described earlier (*13*). EEG band power calculation was based on: delta (1 to 4 Hz); theta (4 to 12 Hz). EEG band power comparison between vehicle- and KCNQ2/3 ligand-treated groups was conducted based on signals during 1 hour (for vehicle versus XE991) and 3 hours (for vehicle versus flupirtine) following injection for wakefulness and NREM sleep based on the dynamic of drug's effect. As both XE991 and flupirtine postponed REM sleep onset, EEG band power was computed based on the initial REM sleep epoch after injection of vehicle/drug. The investigator was blind to the group information while conducting the EEG/EMG data analysis.

In vivo optogenetic stimulation

After recovery and sufficient virus expression (>2 weeks), mice injected with viruses expressing Cre- dependent ChR2-eYFP were connected to EEG/EMG recording cables and fiber optic patch cords (200 μm core diameter, Doric Lenses) for one week acclimation in special cages with open top which allowed mice to move freely. Following acclimation, optogenetic stimulation with a range of frequencies (1, 5, 10, 15, and 20 Hz, controlled by A.M.P.I. Master 8) and a range of blue light (473 nm) intensities (1, 5, 10, 15, and 20 mW, Laserglow Technologies, calibrated with Thorlabs light meter) was performed. Each stimulation train consisted of 15 ms light pulses for 10 s with a given light intensity and frequency according to a randomized 5 (light intensities) × 5 (frequencies) matrix generated in Matlab. Sleep-to-wake transition experiments were performed between ZT5-ZT9 of their inactive phase when mice have a strong sleep pressure. Light stimulations were delivered to mice within 30 s of NREM or REM sleep onset to determine the latency of sleep-to-wake transition and duration of wake bout following optogenetic stimulation. The onset of light stimulation was time-stamped during recording for offline analysis afterwards.

Fiber photometry signal acquisition and analysis

After recovery, sufficient virus expression (>2 weeks), and habituation to EEG/EMG cable and fiber optic patch cord (400 μm core diameter, Doric Lenses), mice injected with AAV viruses expressing Cre-dependent GCaMP6f were connected to EEG/EMG recording setup and a custom-built fiber photometry setup (*50*). Briefly, a 470-nm LED (M470D3, Thorlabs, NJ, USA) was sinusoidally modulated at 211 Hz and passed through a GFP excitation filter followed by a dichroic mirror (MD 498, ThorLabs) for reflection. The light stream was sent through a high NA (0.48), large core (400 μm) optical fiber patch cord (Doric Lenses, Québec, Canada), which was connected with a zirconia connector (Doric Lenses, Québec, Canada) to the dental acrylic-secured fiber optic implant (0.48NA, 400 μm, Doric Lenses, Québec, Canada) with the tip on the injection site. Separately, a 405-nm LED was modulated at 531 Hz and filtered by a 405-nm bandpass filter and sent through the optical fiber patch cord to mouse brain to evoke reference fluorescence, which was independent of Ca^{2+} release. GCaMP6f fluorescence and reference fluorescence were sampled by the same fiber patch cord through a GFP emission filter (MF525-39, ThorLabs), and center-aligned to a photodetector (Model 2151, Newport, Irvine, CA, USA) with a lens (LA1540-A, ThorLabs). The analog signals were amplified by two lock-in amplifiers for GFP fluorescence and reference fluorescence respectively (30 ms time constant, model SR380, Stanford Research Systems, Sunnyvale, CA, USA). Matlab-based custom software was used to control the LEDs and sample both the GFP fluorescence and reference fluorescence through a multifunction data acquisition device (National Instruments, Austin, TX, USA) with 256 Hz sampling frequency in a real-time manner. ΔF/F was obtained by subtracting the reference fluorescence signal from the 470-nm excited GFP emission signal to remove the system interference. The optical fiber patch cord was photobleached to minimize autofluorescence prior to recording according to the user manual (Doric Lenses, Québec, Canada). The recording was conducted between ZT5-ZT9 of their inactive phase when mice have a strong sleep pressure.

To reveal the Hcrt neuronal activity in driving behavioral pattern changes, we used a bottom-up analysis strategy, i.e., GCaMP6f data were staged independent of simultaneous EEG/EMG signals. We then separated the increased GCaMP6f into two categories: GCaMP6f transients during sleep (G^S) and GCaMP6f epochs associated with wakefulness (G^W) (Fig. 1). All the G^S and G^W were staged from the same amount of recording conducted during ZT5-ZT9 from equal group size (1 hour/each mouse, $n = 6$ mice each group) for comparison of Hcrt neuronal activity between young and aged mice. All the GCaMP ΔF/F transients with a Z score >1% (equals GCaMP6f ΔF/F value ~0.3-0.6 for individual animal) of the highest ΔF/F value of the entire trace were staged. After data staging, each GCaMP6f epoch was normalized to its own 5 s baseline with time 0 defined for the beginning of GCaMP6f rising phase. Heatmaps were generated for each category based on 10 s of normalized GCaMP6f epochs with 5 s prior to and 5 s after time 0. A Z score was calculated by subtracting the mean value of GCaMP6f trace prior to time 0 from the mean value of GCaMP6f after time 0 and an averaged Z score based on each animal was used for statistical comparisons. As the G^S Z score was generally small, only the G^S transients with Z score > mean (G^S Z score) − 3 × SEM (G^S Z score) were included with ideal signal-to-noise ratio for subsequent analyses. By definition, all the G^W epochs were qualified for analyses. G^S scatter plot was generated with the duration of G^S against its peak value, and G^W scatter plot was generated with the duration of wake-associated G^W epoch against its maximum peak value (maximum GCaMP6f ΔF/F, if given epoch appeared with multi-peaks). Animal-based frequencies of G^S and G^W were compared between the young and aged groups. Durations of sleep, wake, and S-W epochs were compared. Spearman correlation analysis with a linear fit was perform between G^W frequency (counts/hour) and mean sleep bout duration. The investigator was blind to the group information while conducting the GCaMP6f data staging.

Chemical preparation and application

XE991 dihydrochloride (Cat. no. 2000, referred to as XE991) and flupirtine maleate (Cat. no. 2867, referred to as flupirtine) were purchased from Tocris. XE991 was prepared in saline with a concentration of 50 μM for in vitro electrophysiology and prepared in saline

with a concentration of 0.2 mg/ml for in vivo experiment with a dosage of 2 mg/kg (0.1 ml/10 g, intraperitoneally). 5 mM flupirtine stock solution (0.9% saline containing 0.3% dimethyl sulfoxide/DMSO, v/v) was added to artificial cerebrospinal fluid (ACSF) to reach a concentration of 50 μM for in vitro electrophysiology. Flupirtine was prepared at a concentration of 2 mg/ml in 0.9% saline containing 0.3% DMSO (v/v, vehicle) for in vivo experiments with a dosage of 20 mg/kg (0.1 ml/10 g, intraperitoneally). Flupirtine solution was ultrasonicated prior to application. Counterbalanced crossover design was used for in vivo pharmacology experiments to reveal the drug's effect. Two rounds of drug administrations were separated by at least one week for a complete wash-out of drug's effect. 4-Aminopyridine (4-AP) was purchased from Sigma-Aldrich (Cat. no. 275875). 100 mM 4-AP stock solution (0.9% sodium chloride/saline as vehicle) was added to ACSF to reach a concentration of 50 μM for in vitro electrophysiology of *I*M experiment. MK6096 (Merck) was prepared at a concentration of 2 mg/ml in a mixture (v/v, vehicle) of 50% 0.9% saline and 50% Poly ethylene glycol (average Mn 400, PEG400, Sigma-Aldrich Cat. no. 202398) for in vivo pharmacology experiment as previously described (*13*).

In vitro electrophysiology

All the in vitro electrophysiology experiments were performed during the light phase (ZT3-ZT9). 3-9 mice were used each group. Slices were randomly assigned to groups examining effects of XE991 or flupirtine on M current in the in vitro pharmacology experiments.

Slice preparation

Mice from both groups were decapitated after anesthesia with sevoflurane or perfused with ice-cold slicing solution under anesthesia. To increase the chances of acquiring a healthy slice, we used a sucrose-based or choline-based ACSF for brain slice preparation to reduce the cell excitotoxicity and loss during slice preparation (*53*). After decapitation, the brain was rapidly dissected and immersed in ice-cold sucrose/choline-based ACSF slicing solution (pH 7.4, 95% O_2 / 5% CO_2). 300 μm-thick coronal brain slices containing Hcrt neurons with eYFP fluorescence were sectioned using a VT1200s vibratome (Leica Microsystems). After ~20 min incubation at ~35°C, the slices were stored at room temperature. Slices were used for maximally 5 hours after dissection. Experiments were performed at room temperature 21° to 24°C.

Recording and data analysis

During experiments, slices were superfused with a physiological extracellular solution containing: 125 mM NaCl, 2.5 mM KCl, 25 mM NaHCO3, 1.25 mM NaH2PO4, 25 mM D-glucose, 2 mM CaCl2, and 1 mM MgCl2 (pH 7.4 in 95% O_2/5% CO_2, ~325 mOsm). Neurons were chosen based on eYFP expression and visualized with an Olympus BX51WI with Nomarski optics connected to a camera (Q-imaging). Thick wall borosilicate pipettes (1B150F-4, World Precision Instruments Inc.) were pulled using a P-97 puller (Sutter Instruments) and electrodes with a resistance of 3-6 megohms were used for recording. Intracellular solution used for whole-cell recording contained: 120 mM K-methyl-sulfonate, 10 mM NaCl, 10 mM EGTA, 1 mM CaCl2, 10 mM HEPES, 0.5 mM NaGTP, 5 mM MgATP, pH adjusted to 7.2 with KOH, osmolarity adjusted to 305 mOsm with sucrose; 0.2% biocytin was added for post-hoc staining. Neurons were recorded under current-clamp to examine excitability, or under voltage-clamp to examine PSCs. 1 s step currents from −50 pA to 300 pA were used to evoke AP firing. For optogenetic stimuli, a 15-ms blue light pulse (3.4 mW, calibrated with Thorlab light meter) was given at 1 Hz, 5 Hz, 10 Hz, 15 Hz, and 20 Hz in a randomized manner for 10 s to compare light-induced activity between the young and aged groups, and the interval between sweeps was 20 s. Data were acquired with a Multiclamp 700B amplifier (Axon Instruments, USA), and sampled at 10 kHz. Stimulus generation and data acquisition were performed using pClamp 10. Data were analyzed using Stimfit 0.14.9 (www.stimfit.org) and R 3.5.1 (the R project for statistical computing). RMP values were measured and averaged from temporal windows (at least 50 ms prior to the peak of a given AP for spontaneously firing neurons) with minimal membrane potential variance (*54*). The RMPs were determined without predicted/measured junction potential correction. All the amplitudes of APs and spikelets were calculated from RMPs. Depolarization events with a peak value above −20 mV, and with a half width shorter than 6 ms were qualified for spikelet analyses. PSC recording from non-fluorescent neuron innervated by fluorescent Hcrt neuron expressing ChR2-eYFP was performed as illustrated in fig. S4A. For the PSC failure analysis, a success PSC was considered when a current deflection bigger than 10 pA occurred time-locked to the light pulse. The investigators were blind to the group information while conducting the data analyses.

LC neurons were recorded in slices prepared from WT young (2 to 3 months) and aged (18 to 21 months) mice, infused with biocytin, followed by antibody staining against tyrosine hydroxylase (TH). Only the neurons positive for both biocytin and TH were included for data analyses.

I_M recording

For recording of the slowly deactivating M-current (I_M) mediated by KCNQ2/3, perforated patch recordings were used to maintain the integrity of second messenger signaling cascades and minimize current rundown. The pore-forming antibiotic nystatin was dissolved in DMSO at 50 mg/ml. This stock solution was diluted in an internal pipette solution and vortexed and ultrasonicated for a final concentration of 100 to 200 μg/ml. Pipette tips were prefilled by brief immersion into antibiotic-free solution and then pipettes were back filled with nystatin. After the cell-attached configuration was attained, the access resistance was periodically monitored with hyperpolarizing voltage steps (10 mV, 20 ms) and capacitative transients were cancelled. After 10 to 20 min, recording was started once the access resistance stabilized. The recording was terminated if a sudden change in access resistance occurred. Extracellular solution contained 4-AP (5 mM) to minimize contamination by other potassium currents, and AMPARs, glycine receptors and GABAA receptors were blocked by 6,7-dinitroquinoxaline-2,3-dione (DNQX, Tocris Cat. no. 0189, 10 μM), strychnine (Sigma-Aldrich Cat. no. S0532, 1 μM), (2R)-amino-5-phosphonopentanoate (APV, Tocris Cat. no. 0106, 100 μM) and bicuculline (Sigma-Aldrich Cat. no. 285269, 10 μM). I_M was recorded using a standard deactivation protocol (1000 ms hyperpolarizing steps to -30 mV from a holding potential of −20 mV every 10 s, intersweep holding potential −20 mV). I_M did not inactivate with this protocol, while contamination by other voltage-gated currents was minimized. I_M was measured as the inward relaxation current caused by deactivation of I_M during this voltage step (Fig. 4, G and H). After obtaining at least a stable 5 min baseline, XE991 (50 μM) or flupirtine (50 μM) was applied. The effect of XE991 or flupirtine was determined by comparing averaged I_M amplitudes over a 5 min period just before XE991 or flupirtine application with averaged I_M amplitudes during the 5 to 10 min period after XE991 or flupirtine application.

Array tomography (AT)

Tissue preparation

Array creation and immunohistochemistry were described in detail in a previous publication (*55*). In short, a small piece of tissue (~2 mm high by 1 mm wide by 1 mm deep), covering the LH containing eYFP-labeled Hcrt neurons, was microwave-fixed in 4% Paraformaldehyde (PFA). The fixed tissue was then dehydrated in graded steps of ethanol, and then embedded in LR White resin overnight at 50°C. The embedded tissue was sectioned on an ultramicrotome at a thickness of 70 nm and placed as a ribbon array directly on gelatin or carbon coated glass coverslips. The ultrathin physical sectioning allows AT to achieve true isotropic voxels of ~100 nm. To assure that the brain tissue from animals were

prepared and imaged in as similar conditions as possible, all samples were paired starting at the tissue preparation step. Thus, young and aged animals were prepared in tandem, placed on the same coverslip, stained together and imaged together. Furthermore, to minimize the impact of locational differences in the gathered tissue, multiple blocks were generated from LH of each mouse, and screened at 20× using 4′,6-diamidino-2-phenylindole (DAPI) fluorescence. Then similar tissue blocks were used for further analysis.

Immunohistochemistry

Immunohistochemistry was then carried out on the arrays using primary antibody against KCNQ2 (Alomone Cat. no. AGP-065). The primary antibodies were visualized via fluorescence-labeled secondary antibody (Alexa 594, Invitrogen Cat. no. A11076), and mounted in SlowFade Gold antifade with DAPI (Invitrogen Cat. no. S36938).

Microscopy

Wide-field imaging of ribbons were accomplished on a *Zeiss* Axio Imager.Z1 Upright Fluorescence Microscope with motorized stage and Axiocam HR Digital Camera as previously described (*56*). A position list was generated for each ribbon array of ultrathin sections using custom software modules written for Axiovision. Single fields of view were imaged for each position in the position list using a *Zeiss* 63×/1.4 NA Plan-Apochromat objective.

Image registration and processing

Image stacks from AT were imported into Fiji (ImageJ) and aligned using both rigid and affine transformations with the Register Virtual Stacks plugin. The aligned image stacks were further registered across image sessions using Fiji and TrackEM. The aligned and registered image stacks were imported into Matlab and deconvolved using the native implementation of Richardson-Lucy deconvolution with empirical or theoretical PSFs with 10 iterations (*56*). Custom functions were written to automate and facilitate this workflow.

eYFP segmentation

eYFP delimited protein amount was calculated using custom Matlab software. eYFP volumes were slightly dilated via morphological operations and used to segment protein data in image space. Segmentation custom functions were used to quantify the number and amount of proteins encapsulated by eYFP.

Single-nucleus isolation, FACS sorting, RNA library preparation and sequencing

3 weeks after virus injection, mice were deeply anesthetized using isoflurane and perfused with 1× PBS. The brains were rapidly dissected and transferred to a chilled metal Brain Slicer Matrix (Zivic Instruments, 500 μm coronal slice intervals), and the brain sections containing Hcrt neurons (AP: −1.0 ~ −2.0 mm) were sliced and transferred to 1× PBS on ice. Bilateral hypothalamic areas (LH) were identified and dissected under a stereoscope. LH tissue blocks were then transferred to a glass dounce homogenizer (Sigma-Aldrich) on ice and homogenized in 1 ml Homogenization Buffer (*57*) containing Tris (pH 8.0, 10 mM), sucrose (250 mM), KCl (25 mM), MgCl2 (5 mM), Triton-X100 (0.1%), RNasin Plus RNase Inhibitor (0.5%, Promega Cat. no. N2615), SUPERase·In RNase Inhibitor (0.5%, ThermoFisher Cat. no. AM2694), Protease Inhibitor Cocktail (1×, Promega Cat. no. G6521), DTT (0.1 mM) and DAPI (1:1000, Invitrogen Cat. no. D3571). LH tissue blocks from 3 mice per condition (young/aged male/female) were pooled each condition for isolation of nuclei. The nuclei were released by sequentially applying 10 to 12 strokes of the loose dounce pestle and 10 to 12 strokes of the tight dounce pestle on ice, followed by filtering the suspension through a 35 μm cell strainer (Falcon). The nuclei were then spun down by centrifugation (10 min, 900× g at 4°C) and resuspended in the Wash Buffer (1× PBS containing 0.8% BSA, 0.5% RNasin Plus RNase Inhibitor and 0.5% SUPERase·In RNase Inhibitor). The single-nucleus suspension was further washed twice in Wash Buffer by centrifugation (10 min, 900× g at 4°C). Fluorescence activated cell sorting (FACS) was performed using the 70-μm nozzle and optimal gates collecting the DsRed/DAPI double positive events and excluding debris and doublets. Sorted DsRed+ single nuclei were confirmed using a fluorescence microscope, and manually counted using a hemocytometer. snRNA-seq libraries were prepared using 10x Genomics Chromium Single Cell 3′ Reagents v3 following manufacturer's instructions. Briefly, the concentration of single nuclei solution prepared from dissected LH tissue was determined using DAPI staining and Trypan Blue staining. The nuclei solution was loaded onto a Chromium Chip B to capture seven to ten thousand nuclei in droplets containing the reverse transcription reagents. After reverse transcription, the now barcoded cDNA was recovered and amplified for 12 polymerase chain reaction (PCR) cycles. After qualitative and quantitative control of the cDNA, the final libraries were constructed by fragmenting the cDNA, End Repair, and A-Tailing. After adapter ligation, the libraries were amplified for 11 PCR cycles. The libraries were sequenced using an Illumina MiSeq v3 150-cycle kit to check library quality and confirm the number of captured nuclei. Then all the barcoded samples were mixed and deep sequenced on an Illumina HiSeqX sequencing machine across 4 different lanes to avoid lane variability and potential lane failure.

snRNA-seq data analysis

Illumina fastq files were processed through the 10x Genomics cellranger pipeline according to the manufacturer's instructions. Briefly, reads were aligned to the mm10 mouse genome using a custom gtf annotation file which labeled all "transcripts" as "exons," thus allowing to count intronic as well as exonic reads. The four libraries were then combined using cellranger *aggr* command to match sequencing depth per cell across libraries. All further processing of the genes X cells count matrix was performed in Seurat V3 (*58*) using scTransform normalization (*59*). First, the population of Hcrt+ neurons were identified out of all sequenced cells by coarse Louvian clustering of the entire sequencing dataset. Only one cluster showed Hcrt expression. This cluster was then separately subclustered, and all doublet clusters were removed. No large batch effects were observed at this level. A core set of three clusters, all of which expressed Hcrt at high levels, served as the basis for the analysis of age related effects.

CRISPR/SaCas9-mediated Kcnq2/3 gene disruption in Hcrt neurons

The target sites of *Kcnq2/3* genes for Staphylococcus aureus CRISPR/Cas9 (CRISPR/SaCas9) were designed by CHOPCHOP (http://chopchop.cbu.uib.no) (*60*). The target sequences were as follows:

sgKcnq2: 5′-CGCGTGTGGAGTCGGGCGCGC-3′, sgKcnq3: 5′-GCGGCCACCGCCCTCCAGCAG-3′.

Oligonucleotides encoding guide sequences were purchased from Sigma-Aldrich and cloned individually into BsaI fragment of pX601 (Addgene plasmid 61591). U6-sgKcnq2 and U6-sgKcnq3 fragments were PCR-amplified, respectively using pX601-sgKcnq as a template. Amplified fragments were cloned tandemly into MluI-digested pAAV CAG FLEX mCherry by Gibson assembly method. The primers used were as follows; Gibson1-F: 5′-TAGGGGTTC-CTGCGGCCGCAGAGGGCCTATTTCCCATG-3′, Gibson1-R: 5′-ATAGGCCCTCTCTAGAAAAA-ATCTCGCCAAC-3′, Gibson2-F: 5′- TTTTTCTA-GAGAGGGCCTATTTCCCATG-3′, Gibson2-R: 5′-TCATTATTGACGTCAATGGAAAAAATCTCG-CCAACAAGTTG-3′. AAV constructs carrying nontargeting guide sequences (5′-GCGAGG-TATTCGGCTCCGCGT-3′) were used as control. For the Cre- dependent SaCas9 construct, SaCas9 fused with 3× HA tag was PCR amplified using pX601 as a template. Amplified fragment was cloned into AscI/NheI-double digested pAAV-U6-SaCas9gRNA(SapI)-CMV-SaCas9-DIO-pA (Addgene plasmid 113691). Next, the plasmid was digested by MluI and applied to self- ligation to remove U6 promoter and single-guide RNA (sgRNA) scaffold sequences. pAAV CMV-DIO-SaCas9-3HA (SaCas9), pAAV U6 sgKcnq2-U6 sgKcnq3 CAG FLEX mCherry (sgKcnq2/3) and pAAV U6 sgControl-U6 sgControl

CAG FLEX mCherry (sgControl) were packaged into AAV-DJ by the Wu Tsai Neurosciences Institute Gene Vector and Virus Core at Stanford University.

20 young (6 to 8 weeks old) Hcrt::Cre mice were separated into two groups in a random manner (n = 10/group). Under anesthetics and analgesic, according to the Hcrt neuron field coordinates as described above, one group received bilateral stereotaxic injection of a 0.6 μl (each side, 0.3 mm apart in depth) mixture of SaCas9 (2.4×10^{13} gc/ml) and sgControl (6.24×10^{12} gc/ml) and implanted with EEG/EMG electrodes to serve as the control group. The other group received bilateral stereotaxic injection of a 0.6 μl mixture of SaCas9 and sgKcnq2/3 (2.97×10^{12} gc/ml) and implanted with EEG/EMG electrodes to monitor the effect of Hcrt neuron- selective *Kcnq2/3* gene disruption on sleep architecture. After surgery, mice were connected to EEG/EMG recording cables and singly-housed with food and water ad libitum to recover, and for EEG/EMG signal recording. EEG/EMG signals were recorded continuously on day 6 and day 7 weekly up to 8 weeks (EEG/EMG recording lasted until 12 weeks in half of each group) after surgery. Following recording in week 8/12 after virus injection, slices were prepared from each group for in vitro electrophysiology experiment to determine RMP and firing property of the Hcrt neurons labeled by mCherry flag. Patch clamp recorded cells were infused with biocytin for subsequent immunostaining. The data were used for statistical analysis only if the recorded neurons were stained to co-express biocytin and HA tag.

Histology

For in vivo experiments, upon accomplishment of recordings, mice were perfused under anesthesia described above with ice-cold 1× PBS and followed by 4% PFA for immunostaining against Hcrt1/OXA for Hcrt neurons, and TH for LC NA neurons. Brains were rapidly extracted, postfixed with 4% PFA at 4°C overnight, and equilibrated in 30% sucrose in 1× PBS containing 0.1% NaN3. Then, brains were sectioned at −22°C with a cryostat (Leica Microsystems) at a thickness of 35 μm. Slices were collected from anterior to posterior consecutively to 24-well plates containing PBS with 0.1% NaN3, covered with aluminum foil, and stored at 4°C until immunostaining and imaging. Primary antibody against OXA/Hcrt1 (SC-8070, Lot no. A2915, Goat polyclonal IgG) was purchased from Santa Cruz Biotechnology. Primary antibody against TH (Chicken polyclonal anti-peptide, Cat. TYH, Lot no. TYH1897983) was purchased from Avēs. Primary antibody against HA tag (Rabbit Anti-HA tag pAb, Item no. 561, Lot no. 067) was purchased from MBL International Corporation. Secondary antibodies: Alexa Fluor 488 Goat anti-chicken IgG (H+L, Ref. no. A11039, Lot no. 1094413), Alexa Fluor 488 donkey anti-goat IgG (H+L, Ref. no. A11055, Lot no. 1869589), Alexa Fluor 488 donkey anti-rabbit IgG (H+L, Ref. no. A21206, Lot no. 1910751), Alexa Fluor 647 donkey anti-goat IgG (H+L, Ref. no. A21447, Lot no. 2175459), were purchased from Invitrogen (Manufacturer: Life Technologies). Alexa Fluor 594 streptavidin conjugate (Ref. no. S11227, Lot no. 1991448) and Alexa Fluor 647 streptavidin conjugate (Ref. no. S32357, Lot no. 1738557) to label neurons infused with biocytin were purchased from Invitrogen. For the WT mice used for comparison of sleep patterns, sections around LH and LC were washed in 1× PBS for 5 min, 3 times and incubated in a blocking solution of PBS with 0.3% Triton X-100 (PBST) and 4% bovine serum albumin (BSA) for 1 hour. Following that, OXA/Hcrt1 primary antibody was added to the blocking solution (1:800) overnight. On the second day, sections were washed in 1× PBS for 3 times (5 min/time), and incubated in blocking buffer for 2 hours. After blocking, secondary antibody was added to the blocking buffer for 2 hours (dilution 1:800). After 3 times of 5-min 1× PBS washing, brain sections were mounted onto gelatin-coated slides, covered with Fluoroshield containing DAPI mounting media (Sigma-Aldrich, F6057) and cover glass for imaging with wild field microscope (Zeiss AxioImager, Germany) for entire section or LSM710 Confocal Microscope for enlarged visualization (Zeiss, Germany). For brain slices infected with Cre-dependent viruses, slices around the injection site were collected and stained with appropriate antibodies as described above. Alexa Fluor 594 streptavidin conjugate or Alexa Fluor 647 streptavidin conjugate for staining of biocytin was added together with the secondary fluorescent antibody for Hcrt1, TH or HA tag on the second staining day for in vitro experiment slices.

Object recognition test

Aged mice (~20 months, singly-housed with a reversed 12 hours/12 hours light/dark cycle, 9 pm light on, Zeitgeber time 0/ZT 0) were used to evaluate flupirtine's effect on memory ability in the object recognition task. The object recognition task was performed according to a protocol described by Leger *et al.* (*61*). The protocol consisted of habituation, familiarization and test sessions (fig. S8). During each habituation session, an individual mouse was released to the arena (34 cm × 17 cm, non-transparent open field filled with Sani-Chip pine bedding floor) for habituation of 5 min. Each mouse underwent two habituation sessions conducted during ZT16-18 and ZT22-24 for 3 consecutive days. During the familiarization session (Day 4: ZT22-24), each mouse was allowed to explore two identical objects for a total of 5 min. Each object was placed at the same distance from the walls and corners of the field without spatial or odor cues (bedding was changed; arena and objects were cleaned with 70% ethanol before each exposure). After the familiarization session, mice were intraperitoneally injected with either vehicle or flupirtine (20 mg/kg) at the beginning of the following light phase. During the test session (Day 5: ZT22-24), mice were placed in the same arena with one of the familiar objects from the familiarization session replaced by a similar size novel object. The position of the novel object (left or right) was randomized for each mouse and each group tested. Time spent facing away from object within the 7 cm radius or climbing on object was not qualified as exploration. Mice were randomly assigned to control/flupirtine group through a counterbalanced crossover design. Two rounds of object recognition task (with two sets of familiar and novel objects) were separated by one week for a complete drug wash-out. Animal-based averaged value of two rounds of familiarization was presented. Mouse with over 65% preference for either object during the familiarization session was not qualified to proceed to the next session.

Statistics

One/two hour-binned sleep comparisons were analyzed by two-way repeated measure (RM) analysis of variance (ANOVA) (linear mixed-effects model for counterbalanced crossover design) followed by Šidák's multiple comparisons. Holm-Šidák was used for comparison based on 24 hours/light/dark phase. Unpaired *t*-test with Welch's correction was used for GCaMP6f data and in vivo optogenetic data analyses. For slice electrophysiology, Mann-Whitney *U* test, RM one-way ANOVA, two-way ANOVA were used to analyze appropriate datasets. Paired test was used for data analyses of experiments with paired design. Spearman correlation with a linear fit was performed for 2-demensional data correlation analysis. For snRNA-seq data, differentially expressed genes across ages were determined using the Wilcoxon rank-sum test, considering only those genes with a Bonferroni adjusted $P < 0.05$. Differences with $P < 0.05$ were considered significant for all experiments. In figures, *, **, ***, ****, and † indicate $P < 0.05$, $P < 0.01$, $P < 0.005$, $P < 0.001$, and $P < 0.0005$, respectively, and ns indicates not significant. Data with error bars were reported as mean ± SEM. Details on statistical analyses have been described in the supplementary text.

REFERENCES AND NOTES

1. M. K. Scullin, D. L. Bliwise, Sleep, cognition, and normal aging: Integrating a half century of multidisciplinary research. *Perspect. Psychol. Sci.* **10**, 97–137 (2015). doi: 10.1177/1745691614556680; pmid: 25620997
2. K. Yaffe, C. M. Falvey, T. Hoang, Connections between sleep and cognition in older adults. *Lancet Neurol.* **13**, 1017–1028 (2014). doi: 10.1016/S1474-4422(14)70172-3; pmid: 25231524
3. M. A. Carskadon, E. D. Brown, W. C. Dement, Sleep fragmentation in the elderly: Relationship to daytime sleep

tendency. *Neurobiol. Aging* **3**, 321–327 (1982). doi: 10.1016/0197-4580(82)90020-3; pmid: 7170049
4. B. A. Mander, J. R. Winer, M. P. Walker, Sleep and human aging. *Neuron* **94**, 19–36 (2017). doi: 10.1016/j.neuron.2017.02.004; pmid: 28384471
5. J. C. Rodriguez, J. M. Dzierzewski, C. A. Alessi, Sleep problems in the elderly. *Med. Clin. North Am.* **99**, 431–439 (2015). doi: 10.1016/j.mcna.2014.11.013; pmid: 25700593
6. K. Koh, J. M. Evans, J. C. Hendricks, A. Sehgal, A *Drosophila* model for age-associated changes in sleep:wake cycles. *Proc. Natl. Acad. Sci. U.S.A.* **103**, 13843–13847 (2006). doi: 10.1073/pnas.0605903103; pmid: 16938867
7. M. E. Wimmer *et al*., Aging in mice reduces the ability to sustain sleep/wake states. *PLOS ONE* **8**, e81880 (2013). doi: 10.1371/journal.pone.0081880; pmid: 24358130
8. L. de Lecea *et al*., The hypocretins: Hypothalamus-specific peptides with neuroexcitatory activity. *Proc. Natl. Acad. Sci. U.S.A.* **95**, 322–327 (1998). doi: 10.1073/pnas.95.1.322; pmid: 9419374
9. T. Sakurai *et al*., Orexins and orexin receptors: A family of hypothalamic neuropeptides and G protein–coupled receptors that regulate feeding behavior. *Cell* **92**, 573–585 (1998). doi: 10.1016/S0092-8674(00)80949-6; pmid: 9491897
10. C. E. Mahoney, A. Cogswell, I. J. Koralnik, T. E. Scammell, The neurobiological basis of narcolepsy. *Nat. Rev. Neurosci.* **20**, 83–93 (2019). doi: 10.1038/s41583-018-0097-x; pmid: 30546103
11. T. Sakurai, The neural circuit of orexin (hypocretin): Maintaining sleep and wakefulness. *Nat. Rev. Neurosci.* **8**, 171–181 (2007). doi: 10.1038/nrn2092; pmid: 17299454
12. A. R. Adamantidis, F. Zhang, A. M. Aravanis, K. Deisseroth, L. de Lecea, Neural substrates of awakening probed with optogenetic control of hypocretin neurons. *Nature* **450**, 420–424 (2007). doi: 10.1038/nature06310; pmid: 17943086
13. S. B. Li, N. Nevárez, W. J. Giardino, L. de Lecea, Optical probing of orexin/hypocretin receptor antagonists. *Sleep* **41**, (2018). doi: 10.1093/sleep/zsy141; pmid: 30060151
14. T. Tsunematsu *et al*., Acute optogenetic silencing of orexin/hypocretin neurons induces slow-wave sleep in mice. *J. Neurosci.* **31**, 10529–10539 (2011). doi: 10.1523/JNEUROSCI.0784-11.2011; pmid: 21775598
15. J. Hara *et al*., Genetic ablation of orexin neurons in mice results in narcolepsy, hypophagia, and obesity. *Neuron* **30**, 345–354 (2001). doi: 10.1016/S0896-6273(01)00293-8; pmid: 11394998
16. L. Lin *et al*., The sleep disorder canine narcolepsy is caused by a mutation in the hypocretin (orexin) receptor 2 gene. *Cell* **98**, 365–376 (1999). doi: 10.1016/S0092-8674(00)81965-0; pmid: 10458611
17. T. E. Scammell, Narcolepsy. *N. Engl. J. Med.* **373**, 2654–2662 (2015). doi: 10.1056/NEJMra1500587; pmid: 26716917
18. M. G. Lee, O. K. Hassani, B. E. Jones, Discharge of identified orexin/hypocretin neurons across the sleep-waking cycle. *J. Neurosci.* **25**, 6716–6720 (2005). doi: 10.1523/JNEUROSCI.1887-05.2005; pmid: 16014733
19. B. Y. Mileykovskiy, L. I. Kiyashchenko, J. M. Siegel, Behavioral correlates of activity in identified hypocretin/orexin neurons. *Neuron* **46**, 787–798 (2005). doi: 10.1016/j.neuron.2005.04.035; pmid: 15924864
20. W. J. Giardino *et al*., Parallel circuits from the bed nuclei of stria terminalis to the lateral hypothalamus drive opposing emotional states. *Nat. Neurosci.* **21**, 1084–1095 (2018). doi: 10.1038/s41593-018-0198-x; pmid: 30038273
21. B. P. Bean, The action potential in mammalian central neurons. *Nat. Rev. Neurosci.* **8**, 451–465 (2007). doi: 10.1038/nrn2148; pmid: 17514198
22. D. L. Greene, N. Hoshi, Modulation of Kv7 channels and excitability in the brain. *Cell. Mol. Life Sci.* **74**, 495–508 (2017). doi: 10.1007/s00018-016-2359-y; pmid: 27645822
23. R. J. Howard, K. A. Clark, J. M. Holton, D. L. Minor Jr., Structural insight into KCNQ (Kv7) channel assembly and channelopathy. *Neuron* **53**, 663–675 (2007). doi: 10.1016/j.neuron.2007.02.010; pmid: 17329207
24. H. S. Wang *et al*., KCNQ2 and KCNQ3 potassium channel subunits: Molecular correlates of the M-channel. *Science* **282**, 1890–1893 (1998). doi: 10.1126/science.282.5395.1890; pmid: 9836639
25. T. J. Jentsch, Neuronal KCNQ potassium channels: Physiology and role in disease. *Nat. Rev. Neurosci.* **1**, 21–30 (2000). doi: 10.1038/35036198; pmid: 11252765
26. G. X. Wang, S. J. Smith, P. Mourrain, Fmr1 KO and fenobam treatment differentially impact distinct synapse populations of mouse neocortex. *Neuron* **84**, 1273–1286 (2014). doi: 10.1016/j.neuron.2014.11.016; pmid: 25521380
27. F. A. Ran *et al*., In vivo genome editing using *Staphylococcus aureus* Cas9. *Nature* **520**, 186–191 (2015). doi: 10.1038/nature14299; pmid: 25830891
28. N. Kumar *et al*., The development of an AAV-based CRISPR SaCas9 genome editing system that can be delivered to neurons in vivo and regulated via doxycycline and cre-recombinase. *Front. Mol. Neurosci.* **11**, 413 (2018). doi: 10.3389/fnmol.2018.00413; pmid: 30483052
29. A. Yamanaka *et al*., Hypothalamic orexin neurons regulate arousal according to energy balance in mice. *Neuron* **38**, 701–713 (2003). doi: 10.1016/S0896-6273(03)00331-3; pmid: 12797956
30. T. E. Scammell, J. T. Willie, C. Guilleminault, J. M. Siegel, International Working Group on Rodent Models of Narcolepsy, A consensus definition of cataplexy in mouse models of narcolepsy. *Sleep* **32**, 111–116 (2009). doi: 10.5665/sleep/32.1.111; pmid: 19189786
31. L. E. Mickelsen *et al*., Single-cell transcriptomic analysis of the lateral hypothalamic area reveals molecularly distinct populations of inhibitory and excitatory neurons. *Nat. Neurosci.* **22**, 642–656 (2019). doi: 10.1038/s41593-019-0349-8; pmid: 30858605
32. S. Izawa *et al*., REM sleep-active MCH neurons are involved in forgetting hippocampus-dependent memories. *Science* **365**, 1308–1313 (2019). doi: 10.1126/science.aax9238; pmid: 31604241
33. C. Kosse, C. Schöne, E. Bracey, D. Burdakov, Orexin-driven GAD65 network of the lateral hypothalamus sets physical activity in mice. *Proc. Natl. Acad. Sci. U.S.A.* **114**, 4525–4530 (2017). doi: 10.1073/pnas.1619700114; pmid: 28396414
34. F. Naganuma *et al*., Lateral hypothalamic neurotensin neurons promote arousal and hyperthermia. *PLOS Biol.* **17**, e3000172 (2019). doi: 10.1371/journal.pbio.3000172; pmid: 30893297
35. E. C. Cooper, E. Harrington, Y. N. Jan, L. Y. Jan, M channel KCNQ2 subunits are localized to key sites for control of neuronal network oscillations and synchronization in mouse brain. *J. Neurosci.* **21**, 9529–9540 (2001). doi: 10.1523/JNEUROSCI.21-24-09529.2001; pmid: 11739564
36. C. Biervert *et al*., A potassium channel mutation in neonatal human epilepsy. *Science* **279**, 403–406 (1998). doi: 10.1126/science.279.5349.403; pmid: 9430594
37. B. C. Schroeder, C. Kubisch, V. Stein, T. J. Jentsch, Moderate loss of function of cyclic-AMP-modulated KCNQ2/KCNQ3 K^+ channels causes epilepsy. *Nature* **396**, 687–690 (1998). doi: 10.1038/25367; pmid: 9872318
38. N. A. Singh *et al*., Mouse models of human KCNQ2 and KCNQ3 mutations for benign familial neonatal convulsions show seizures and neuronal plasticity without synaptic reorganization. *J. Physiol.* **586**, 3405–3423 (2008). doi: 10.1113/jphysiol.2008.154971; pmid: 18483067
39. F. Sesti, Oxidation of K^+ channels in aging and neurodegeneration. *Aging Dis.* **7**, 130–135 (2016). doi: 10.14336/AD.2015.0901; pmid: 27114846
40. S. Y. Kim, H. T. Kang, J. A. Han, S. C. Park, The transcription factor Sp1 is responsible for aging-dependent altered nucleocytoplasmic trafficking. *Aging Cell* **11**, 1102–1109 (2012). doi: 10.1111/acel.12012; pmid: 23013401
41. M. Mucha *et al*., Transcriptional control of KCNQ channel genes and the regulation of neuronal excitability. *J. Neurosci.* **30**, 13235–13245 (2010). doi: 10.1523/JNEUROSCI.1981-10.2010; pmid: 20926649
42. C. Lüscher, P. A. Slesinger, Emerging roles for G protein–gated inwardly rectifying potassium (GIRK) channels in health and disease. *Nat. Rev. Neurosci.* **11**, 301–315 (2010). doi: 10.1038/nrn2834; pmid: 20389305
43. J. E. Kang *et al*., Amyloid-β dynamics are regulated by orexin and the sleep-wake cycle. *Science* **326**, 1005–1007 (2009). doi: 10.1126/science.1180962; pmid: 19779148
44. J. Mayordomo-Cava, J. Yajeya, J. D. Navarro-López, L. Jiménez-Díaz, Amyloid-β(25-35) modulates the expression of GirK and KCNQ channel genes in the hippocampus. *PLOS ONE* **10**, e0134385 (2015). doi: 10.1371/journal.pone.0134385; pmid: 26218288
45. B. Zott *et al*., A vicious cycle of β amyloid-dependent neuronal hyperactivation. *Science* **365**, 559–565 (2019). doi: 10.1126/science.aay0198; pmid: 31395777
46. J. Oh *et al*., Profound degeneration of wake-promoting neurons in Alzheimer's disease. *Alzheimers Dement.* **15**, 1253–1263 (2019). doi: 10.1016/j.jalz.2019.06.3916; pmid: 31416793
47. M. E. Carter *et al*., Tuning arousal with optogenetic modulation of locus coeruleus neurons. *Nat. Neurosci.* **13**, 1526–1533 (2010). doi: 10.1038/nn.2682; pmid: 21037585
48. C. Peyron *et al*., Neurons containing hypocretin (orexin) project to multiple neuronal systems. *J. Neurosci.* **18**, 9996–10015 (1998). doi: 10.1523/JNEUROSCI.18-23-09996.1998; pmid: 9822755
49. J. Lindeberg *et al*., Transgenic expression of Cre recombinase from the tyrosine hydroxylase locus. *Genesis* **40**, 67–73 (2004). doi: 10.1002/gene.20065; pmid: 15452869
50. A. Eban-Rothschild, G. Rothschild, W. J. Giardino, J. R. Jones, L. de Lecea, VTA dopaminergic neurons regulate ethologically relevant sleep-wake behaviors. *Nat. Neurosci.* **19**, 1356–1366 (2016). doi: 10.1038/nn.4377; pmid: 27595385
51. S. B. Li *et al*., Hypothalamic circuitry underlying stress-induced insomnia and peripheral immunosuppression. *Sci. Adv.* **6**, eabc2590 (2020). doi: 10.1126/sciadv.abc2590; pmid: 32917689
52. D. Zada, I. Bronshtein, T. Lerer-Goldshtein, Y. Garini, L. Appelbaum, Sleep increases chromosome dynamics to enable reduction of accumulating DNA damage in single neurons. *Nat. Commun.* **10**, 895 (2019). doi: 10.1038/s41467-019-08806-w; pmid: 30837464
53. G. K. Aghajanian, K. Rasmussen, Intracellular studies in the facial nucleus illustrating a simple new method for obtaining viable motoneurons in adult rat brain slices. *Synapse* **3**, 331–338 (1989). doi: 10.1002/syn.890030406; pmid: 2740992
54. A. J. Pernía-Andrade, P. Jonas, Theta-gamma-modulated synaptic currents in hippocampal granule cells in vivo define a mechanism for network oscillations. *Neuron* **81**, 140–152 (2014). doi: 10.1016/j.neuron.2013.09.046; pmid: 24333053
55. K. D. Micheva, S. J. Smith, Array tomography: A new tool for imaging the molecular architecture and ultrastructure of neural circuits. *Neuron* **55**, 25–36 (2007). doi: 10.1016/j.neuron.2007.06.014; pmid: 17610815
56. G. Wang, S. J. Smith, Sub-diffraction limit localization of proteins in volumetric space using Bayesian restoration of fluorescence images from ultrathin specimens. *PLOS Comput. Biol.* **8**, e1002671 (2012). doi: 10.1371/journal.pcbi.1002671; pmid: 22956902
57. T. E. Bakken *et al*., Single-nucleus and single-cell transcriptomes compared in matched cortical cell types. *PLOS ONE* **13**, e0209648 (2018). doi: 10.1371/journal.pone.0209648; pmid: 30586455
58. T. Stuart *et al*., Comprehensive integration of single-cell data. *Cell* **177**, 1888–1902.e21 (2019). doi: 10.1016/j.cell.2019.05.031; pmid: 31178118
59. C. Hafemeister, R. Satija, Normalization and variance stabilization of single-cell RNA-seq data using regularized negative binomial regression. *Genome Biol.* **20**, 296 (2019). doi: 10.1186/s13059-019-1874-1; pmid: 31870423
60. K. Labun, T. G. Montague, J. A. Gagnon, S. B. Thyme, E. Valen, CHOPCHOP v2: A web tool for the next generation of CRISPR genome engineering. *Nucleic Acids Res.* **44** (W1), W272-6 (2016). doi: 10.1093/nar/gkw398; pmid: 27185894
61. M. Leger *et al*., Object recognition test in mice. *Nat. Protoc.* **8**, 2531–2537 (2013). doi: 10.1038/nprot.2013.155; pmid: 24263092

ACKNOWLEDGMENTS

We thank T. Sakurai and X. (Simon) Xie for providing OX(Hcrt)-eGFP mice and OX(Hcrt)-ataxin3 mice. We thank L. Luo for facilitating snRNA-seq data analysis. We thank Stanford Wu Tsai Neuroscience Microscopy Service for imaging. **Funding:** This work was supported in part by National Institutes of Health grants R01AG047671 (L.d.L.), R01MH116470 (L.d.L.), R01NS104950 (L.d.L. and P.M.), K01AG061230 (G.X.W.), P30EY026877 (G.X.W. and P.M.), R01DA011289 (J.A.K.), R01NS106301 (G.S.), Sleep Research Society Foundation Career Development Award 030-JP-21 (S.-B.L.), Stanford Alzheimer's Disease Center-Scully Family Seed Grant P50AG047366 (L.d.L. and P.M.), and the New York Stem Cell Foundation (G.S.). G.S. is a New York Stem Cell Foundation–Robertson Investigator. **Author contributions:** S.-B.L. and L.d.L. conceptualized and designed this research. S.-B.L. performed all the in vivo and histological experiments and analyzed data. V.M.D. performed in vitro electrophysiology experiments with Hcrt::Cre and other neurons, I_M, and CRISPR reagents. C.C. performed in vitro electrophysiology with Hcrt::Cre neurons. V.M.D., C.C., and S.-B.L. analyzed in vitro electrophysiology data. G.X.W. performed AT experiments and analyzed data. J.M.K. analyzed snRNA-seq data. H.Y. designed and prepared CRISPR constructs. W.-J.B. contributed to snRNA-seq experiments. C.P. and R.P. prepared the RNA library. A.E.U. supervised RNA library preparation. P.M. supervised G.X.W.'s work. J.A.K. supervised

V.M.D.'s work. G.S. supervised C.C.'s work. L.d.L. supervised the entire project. S.-B.L. prepared figures and wrote the manuscript. S.-B.L. and L.d.L. edited the manuscript, with input from other coauthors. All authors discussed the results and commented on the manuscript. **Competing interests:** L.d.L. and S.-B.L. are co-inventors on a WIPO (World Intellectual Property Organization) patent WO/2021/119018 related to the work described in this manuscript. L.d.L. is a Chief Scientific Advisor to and receives consulting fees from Attune Neurosciences. L.d.L. is a paid consultant to Eisai Pharmaceuticals and Idorsia Pharmaceuticals. G.S. is a cofounder of Epiodyne, a drug discovery company, an inventor on a patent application (US application no. 62/962,581) related to imaging of neural dynamics to discover analgesics, and a member of the NIH PSPP (Preclinical Screening Platform for Pain) External Consulting Board. The remaining authors declare that they have no competing interests. **Data and materials availability:** The sequencing reads and preprocessed data are available from NCBI Gene Expression Omnibus (GSE160581). Code is freely available on Github (https://github.com/justuskebschull/Hyprocretin_Li2020). All other data are available in the main text or the supplementary materials. All materials are available from the corresponding author upon reasonable request.

SUPPLEMENTARY MATERIALS

science.org/doi/10.1126/science.abh3021
Materials and Methods
Supplementary Text
Figs. S1 to S14
MDAR Reproducibility Checklist

9 March 2021; accepted 14 January 2022
10.1126/science.abh3021

RESEARCH ARTICLES

PROTEIN TARGETING

Mechanism of signal sequence handover from NAC to SRP on ribosomes during ER-protein targeting

Ahmad Jomaa[1]†, Martin Gamerdinger[2]†, Hao-Hsuan Hsieh[3]†, Annalena Wallisch[2], Viswanathan Chandrasekaran[4], Zeynel Ulusoy[2], Alain Scaiola[1], Ramanujan S. Hegde[4], Shu-ou Shan[3]*, Nenad Ban[1]*, Elke Deuerling[2]*

The nascent polypeptide–associated complex (NAC) interacts with newly synthesized proteins at the ribosomal tunnel exit and competes with the signal recognition particle (SRP) to prevent mistargeting of cytosolic and mitochondrial polypeptides to the endoplasmic reticulum (ER). How NAC antagonizes SRP and how this is overcome by ER targeting signals are unknown. Here, we found that NAC uses two domains with opposing effects to control SRP access. The core globular domain prevented SRP from binding to signal-less ribosomes, whereas a flexibly attached domain transiently captured SRP to permit scanning of nascent chains. The emergence of an ER-targeting signal destabilized NAC's globular domain and facilitated SRP access to the nascent chain. These findings elucidate how NAC hands over the signal sequence to SRP and imparts specificity of protein localization.

Localization of nascent proteins to the appropriate organelle is essential for cell function and homeostasis. The accuracy of cotranslational targeting to the endoplasmic reticulum (ER) relies on two ribosome-binding factors. Signal recognition particle (SRP) uses its M domain to engage hydrophobic ER-targeting signals as they emerge from the ribosomal tunnel and delivers the ribosome-nascent chain complex (RNC) to the SRP receptor (SR) at the ER membrane using its GTPase (NG) domain (*1*–*4*). SRP is far less abundant than ribosomes in the cell and has high affinity for all ribosomes. Thus, its access must be regulated to selectively target ribosomes displaying the ER signal sequence (*5*–*7*). The nascent polypeptide–associated complex (NAC) (composed of NACα and NACβ) prevents SRP from promiscuously targeting ribosomes without an ER-targeting signal (*8*–*12*). NAC consists of a central globular domain from which flexible N- and C-terminal tails extend (*13*–*15*). Cross-linking studies have suggested that the N-terminal tails are used for a range of interactions and participate in ribosome binding (*16*, *17*). The function of the C-terminal tails, including a conserved ubiquitin-associated domain (UBA) in NACα, is unknown. NAC and SRP share overlapping ribosome-binding sites, which may give rise to their antagonism (*16*). However, biochemical experiments have shown that NAC and SRP bind simultaneously to RNCs translating ER proteins (*9*, *11*, *12*), suggesting that there is a handoff intermediate in the poorly understood NAC-to-SRP exchange reaction. Thus, we set out to explain how NAC binds the ribosome to prevent SRP access and how this inhibition is preferentially overcome for ER-targeting signals.

[1]Department of Biology, Institute of Molecular Biology and Biophysics, ETH Zurich, 8093 Zurich, Switzerland. [2]Department of Biology, Molecular Microbiology, University of Konstanz, 78457 Konstanz, Germany. [3]Division of Chemistry and Chemical Engineering, California Institute of Technology, Pasadena, CA 91125, USA. [4]MRC Laboratory of Molecular Biology, Cambridge, UK.
*Corresponding author. Email: elke.deuerling@uni-konstanz.de (E.D.); ban@mol.biol.ethz.ch (N.B.); sshan@caltech.edu (S.S.)
†These authors contributed equally to this work.

Structures of NAC in complex with translating ribosome

We reconstituted in vitro a reaction with signal-containing RNC (RNC_{SS}) mixed with both NAC and SRP and analyzed the complexes formed using cryo–electron microscopy (cryo-EM) (fig. S1). This reaction was likely to contain intermediates at critical steps of cargo recognition and handover, which could be deconvoluted by in silico classification. We resolved two complexes within the particles, a pre-cargo handover RNCss•NAC complex, which we will discuss first, and a ternary post-cargo handover RNCss•NAC•SRP complex, which is discussed later.

The structure of the RNC_{SS}•NAC complex was similar to the RNC•NAC structure obtained from reanalysis of an RNC intermediate during translation of the cytosolic protein tubulin (TUBB) (figs. S2 and S3), on which NAC copurified (*18*). This suggests that NAC initially engages both signal-containing and signal-lacking RNCs but would be expected to hand over to SRP only in the presence of an ER signal sequence.

The structure of the RNCss•NAC complex (Fig. 1, A to D and G) revealed the interactions between the N-terminal tail of NACβ and the ribosome at 3.5 Å resolution (Fig. 1C and fig. S4). The tail, containing an RRKKK motif, formed an α-helix followed by a loop in an anchor-shaped turn wrapping around eL22 while also contacting eL19 and the ribosomal RNA (rRNA) (Fig. 1C and fig. S4). The structure rationalizes the key role of this domain in ribosome binding established previously (*16*, *17*, *19*). To validate the role of this tail as an anchor to the ribosome, we measured NAC-ribosome binding affinity using Förster resonance energy transfer (FRET) between a donor dye placed near the signal sequence on the nascent chain and an acceptor dye placed on NAC. Point mutations of the NAC tail weakened NAC-RNC binding by 10- to 40-fold (Fig. 1, E and F), consistent with its important role in ribosome binding.

The globular domain of NAC was resolved to ~8 Å resolution, which allowed rigid-body fitting of an AlphaFold-predicted structure (*20*) (Fig. 1, A and B, and fig. S5). On the basis of this interpretation, two positively charged α-helices contributed by both NAC subunits contacted rRNA on the surface of the ribosome (Fig. 1G and fig. S5). Charge reversal mutations of a positively charged residue in each helix (K78E-NACα or K43E-NACβ) weakened ribosome binding of NAC in vitro (fig. S6A) and in vivo (fig. S6B).

The binding site of the NAC globular domain overlapped with that of the SRP M domain and was mutually exclusive with SRP binding (Fig. 1G and fig. S6C) (*3*, *4*), consistent with a low-resolution cryo-EM map of NAC in complex with inactive ribosomes (*16*). This finding suggests that NAC interaction at the ribosome exit site is the basis of SRP inhibition. In agreement with this hypothesis, a ribosome-binding mutant in the globular domain (K78E-NACα combined with K43E-NACβ, named NAC KK-EE) was impaired in its ability to compete with SRP binding in vitro (Fig. 1H). The residual binding of NAC KK-EE to the ribosome is likely mediated by the N terminus of NACβ, the position of which would not interfere with SRP binding (fig. S6C).

The corresponding NAC KK-EE mutations in *Caenorhabditis elegans* showed reduced competition of SRP binding by NAC, as shown by elevated levels of ribosome-bound SRP (Fig. 1I and fig. S6D), as well as increased recovery of mRNAs coding for non-ER proteins in SRP pull-downs (fig. S6E). The reduction in SRP competition correlated with elevated levels of a green fluorescent protein (GFP) reporter of ER stress driven by the hsp-4 promoter (hsp-4p::GFP) (*21*), particularly in highly secretory intestinal cells (fig. S6F). Moreover, worms expressing mutant NAC showed reduced embryonic viability (fig. S6G) and a shortened adult life span (fig. S6H).

NAC is destabilized by ER signal sequences, allowing access of SRP to the ribosome exit

SRP antagonism by NAC must be relieved when an ER-targeting signal emerges from the ribosome. One possible explanation for this is that

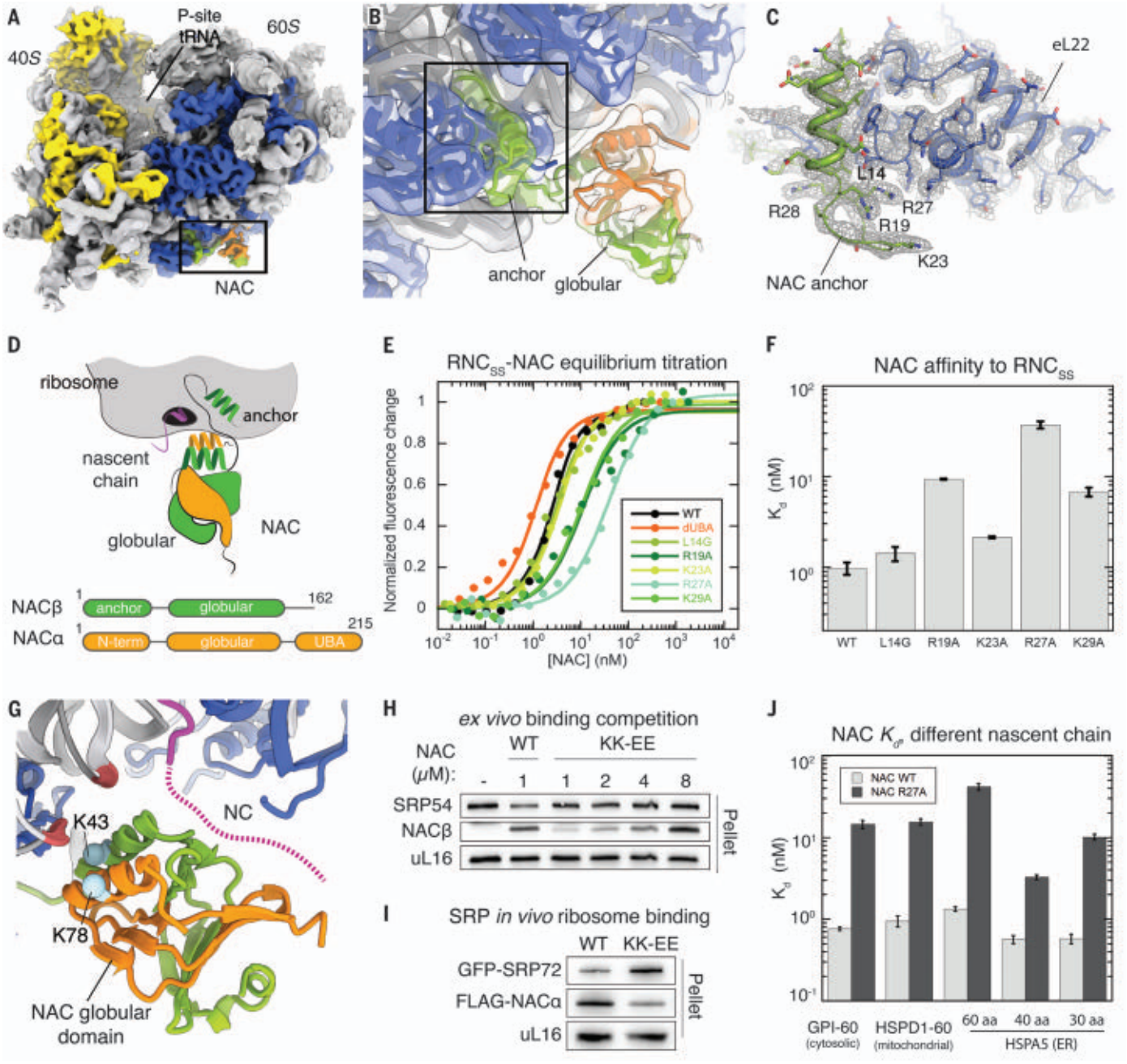


Fig. 1. Structure of the ribosome•NAC complex reveals interactions between the NAC globular and anchor domains with the nascent chain and the ribosome. (**A**) Cryo-EM structure of the RNCss•NAC complex. Boxed region indicates the magnified region shown in (B). (**B**) Closeup of the ribosome tunnel exit region. NACβ is colored green and NACα is colored orange. Anchor and globular domains of NAC are indicated. (**C**) Closeup of the N terminus of NACβ fitted into cryo-EM densities shown as mesh. Ribosomal protein eL22 is shown as a blue cartoon ribbon. (**D**) Schematic of the RNC•NAC complex with a domain structure of NAC. (**E**) Equilibrium titrations to measure the binding of the indicated NAC mutants to RNC_{SS}. The fluorescence signal changes were normalized to the end point of each titration for comparison. The lines are fits of the data to Equation 2. (**F**) Summary of the dissociation constant (K_d) values from (E). (**G**) Closeup of the NAC globular domain highlighting the two antiparallel α-helices, with residues K78 (NACα) and K43 (NACβ) shown as spheres (blue) interacting with the backbone of the rRNA (red). Dashed line indicates the flexible nascent chain (NC, magenta). (**H**) Crude cellular RNCs were incubated with purified NAC proteins and pelleted by sucrose cushion centrifugation. Proteins were detected by immunoblotting. (**I**) Sucrose cushion centrifugation of ribosomes in *C. elegans* expressing the indicated NAC variants and GFP-tagged SRP72. Proteins in the pellet fraction were detected by immunoblotting. (**J**) Summary of the K_d values of NAC R27A for RNCs displaying the nascent chains of GPI (cytosolic), HSPD1 (mitochondrial), and HSPA5 (ER) at the indicated nascent chain lengths. K_d values were from analysis of the data shown in fig. S8, C and D. Error bars are covariances of the fitted K_d values.

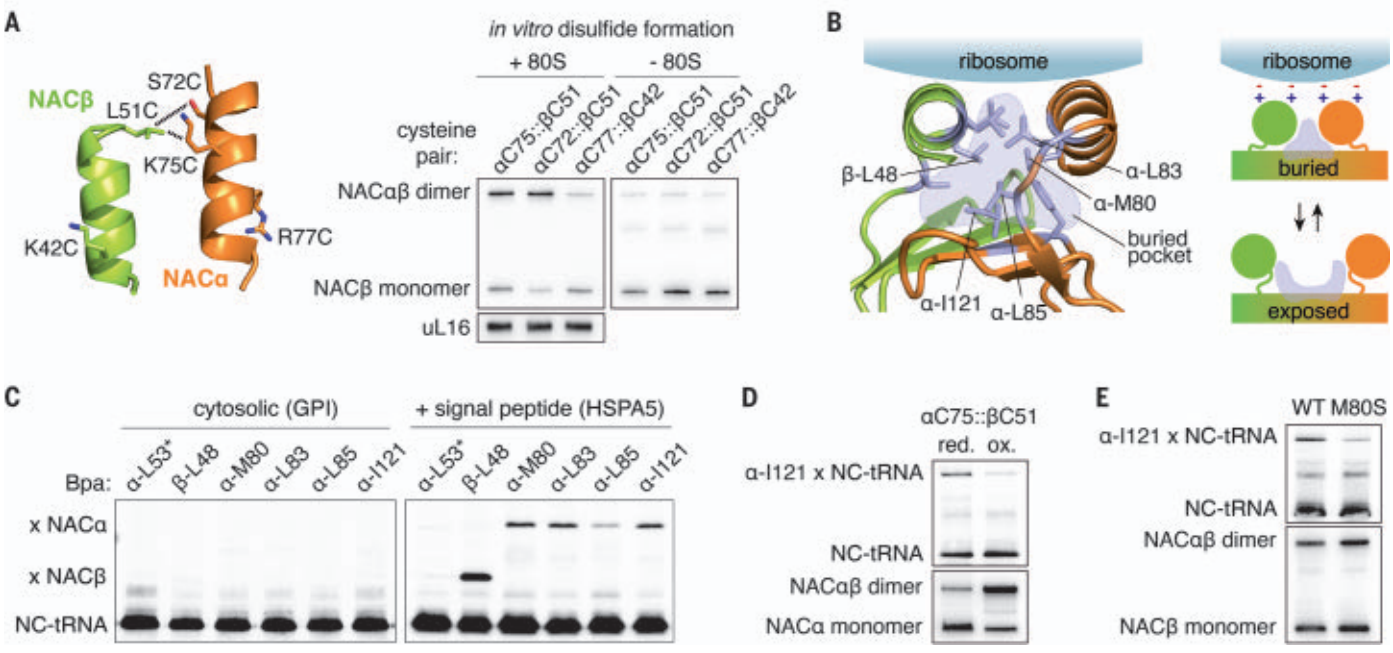


Fig. 2. ER signal sequences are sensed by the ribosome-binding helices of NAC. (**A**) NAC's ribosome-binding helices showing the positions of pairwise cysteine mutants tested for disulfide bond formation. Side chains shown are based on AlphaFold prediction. Dashed lines indicate pairs sufficiently close to form a disulfide bond revealed by immunoblotting (right panel) in the presence of inactive 80*S* ribosomes. (**B**) Residues contributing to the hydrophobic pocket between the two α-helices of NAC (purple). The right side shows a model where ribosome dissociation leads to separation of the helices, thereby exposing a hydrophobic pocket. (**C**) Autoradiograph of photo-cross-linking of Bpa-NAC variants to stalled RNCs carrying 50–amino acid S^{35}-labeled nascent chains of cytosolic GPI (left) or a GPI fusion protein containing the N-terminal signal peptide of HSPA5 (right). The positions of the tRNA-attached nascent chain (NC-tRNA) and its cross-links to NACα and NACβ are indicated. Asterisk indicates a position outside the hydrophobic region. (**D**) Autoradiograph of photo-cross-linking of the αC75-βC51 cysteine variant carrying Bpa at α-I121 to HSPA5-RNCs (55 amino acids), performed in the reduced (red.) and oxidized (ox.) state. (**E**) Autoradiograph and immunoblotting of 55–amino acid HSPA5-RNC photo-cross-linking of the indicated α-I121 Bpa-NAC variants.

hydrophobic ER-targeting signals somehow weaken the interaction between the NAC globular domain and the ribosome to allow SRP access. To test this, we compared the affinity of NAC for RNCs displaying either an ER signal sequence (RNC_{SS}) or a mutated signal sequence that inhibits ER targeting (RNC_{SSmt}) (fig. S7) (*7*). Because the NACβ anchor tail would mask the affinity differences, we performed FRET measurements with NAC mutants with a disrupted RRKKK motif. These mutants, NAC-R27A and NAC-K29A, bound to RNC_{SS} with ~3.5-fold and ~5-fold weaker affinity, respectively, compared with RNC_{SSmt} (fig. S8, A and B).

We then measured NAC binding to purified RNCs bearing ER, cytosolic, and mitochondrial nascent chains (HSPA5, GPI, and HSPD1, respectively) stalled at residue 60, exposing short N-terminal sequences (~30 amino acids) at the tunnel exit (fig. S7). In agreement with our hypothesis, NAC R27A bound 5-fold more weakly to RNC_{HSPA5} exposing an ER signal sequence than to RNC_{GPI} and RNC_{HSPD1} (Fig. 1J and fig. S8, C and D).

We repeated the binding measurements with purified RNCs bearing an ER signal sequence at nascent chain lengths of 30, 40, and 60 amino acids (Fig. 1J and fig. S8, C and D). NAC showed the strongest interaction with the ribosome when the signal sequence was in the tunnel (30 and 40 amino acids), and binding was weakened by >10-fold when the ER signal peptide was exposed (60 amino acids). Thus, the emergence of a hydrophobic signal peptide, but not another type of nascent chain, weakens the interaction of the NAC globular domain with the ribosome.

We then investigated the role of the two ribosome-binding antiparallel helices that dock the globular domain on the ribosome in proximity to the emerging nascent chain. The helices are amphipathic and orient the positively charged side toward the ribosome surface, whereas the hydrophobic side contributes to a buried hydrophobic pocket (fig. S5). These helices were sensitive to proteolysis when human NAC was subjected to crystallization (*15*), suggesting that they are flexibly disposed in solution but are apparently stabilized in the ribosome-bound state. To test this, we engineered two cysteines in the helices such that they would be apposed to each other in the ribosome-bound NAC structure. Consistent with our hypothesis, the engineered cysteines formed a disulfide bond after oxidant treatment only in the presence of the ribosome (Fig. 2A and fig. S9).

To investigate whether the emergence of the signaling peptides may destabilize and release the globular domain of NAC from the ribosome (Fig. 2B), we incorporated photo-cross-linking probes both inside and outside the hydrophobic pocket (Fig. 2B) and tested their proximity to nascent chains coding for a cytosolic, mitochondrial, or ER protein. NAC variants carrying the probe within the hydrophobic pocket (e.g., NACα-I121) cross-linked to ER targeting signals (Fig. 2C and fig. S10, A to C). Cross-linking was dependent on nascent chain length and was only seen once the targeting signal was fully exposed outside the exit tunnel (fig. S10A). Cross-linking was prevented when the helices were covalently linked by disulfide bond formation, demonstrating that destabilization of the NAC globular domain by the ER signal peptide requires separation of the helices (Fig. 2D). Furthermore, cross-linking to the pocket residues NACα-I121 and NACβ-L48, but not the less buried NACα-M80, was modulated by changing targeting signal hydrophobicity (fig. S10D). Mutating M80 to serine impaired nascent chain photo-cross-linking to NACα-I121 (Fig. 2E), which suggests that this residue also contributes to nascent chain sensing.

These results indicate that an ER signal sequence destabilizes the NAC globular domain. The NACβ N-terminal tail remains anchored to the ribosomal surface regardless of the nascent

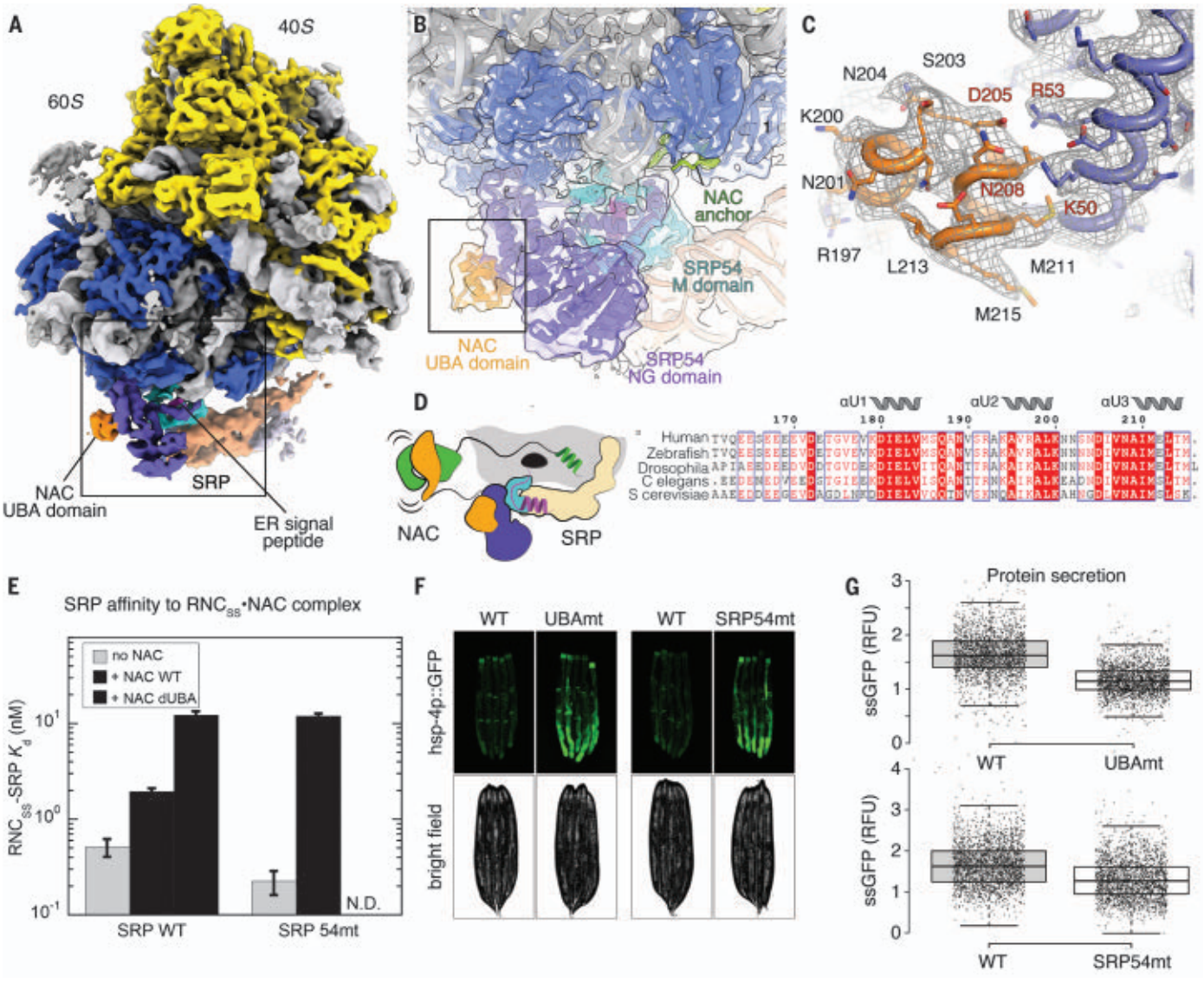


Fig. 3. Structure of the ribosome•SRP•NAC complex. (**A**) Cryo-EM structure of the RNCss•NAC•SRP complex. Boxed region indicates the closeup shown in (B). (**B**) Ribosome tunnel exit regions depicting the SRP54 NG and M domains, the NACα UBA domain, and the NACβ anchor domain are colored slate, cyan, orange, and green, respectively. Underlying EM density is shown as a transparent surface. (**C**) Closeup on the UBA interactions with SRP54 NG domain shown as cartoon and sticks, fitted into cryo-EM densities shown as mesh. (**D**) Schematic representation of the ternary complex. Boxed region shows sequence alignment of NACα UBA domain in eukaryotes. (**E**) Summary of the K_d values for the binding of wild-type and mutant SRPs to RNC_{SS}•NAC, based on fitting of the data in fig. S17A. N.D., not determined. (**F**) and (**G**) Fluorescence microscope images of hsp-4p::GFP worms (F) and worm flow cytometry analysis of ssGFP (G) in worms carrying the indicated RNA interference (RNAi)–resistant genes in the endogenous RNAi background. Box plot center line indicates the median, box length the upper and lower quartile, and whiskers the minimum/maximum quartile ($N \geq 2000$).

chain, as evidenced by cross-linking between a residue in the NACβ anchor and the ribosomal protein eL22, whereas a probe in the N terminus of NACα changed its location only for the ER substrate (fig. S11). Combined, these results suggest that NAC interactions with the ribosome are remodeled as the signal peptide emerges from the ribosome tunnel.

Flexibly tethered UBA domain of NAC recruits SRP

The cryo-EM data on RNC_{SS} mixed with both NAC and SRP also allowed us to visualize the complex with NAC and SRP simultaneously bound to the ribosome (RNCss•NAC•SRP) (Fig. 3A and figs. S1 and S12). The conformation of SRP in the ternary complex was similar to that of previously observed SRP-ribosome complexes (*3*, *4*). The density for the NACβ anchor was observed in a similar position as in the RNC•NAC complexes (fig. S12C). However, the globular domain of NAC was no longer resolved, because its binding position at the tunnel exit was occupied by the SRP54 M domain (Figs. 1G and 3, A to D).

In addition, we observed density for the flexibly tethered C-terminal UBA domain of NACα bound to the N domain of SRP54 (Fig. 3, B and C, and figs. S12 and S13). The interactions occupied two patches of contact points and involved a number of salt bridges and specific hydrogen bonds between highly conserved residues (Fig. 3, C and D, and fig. S14). The UBA-binding site on SRP54 overlapped with the binding site of the NG domain of SR (fig. S15), which suggests that formation of the SRP•SR complex will displace NAC from SRP at the ER membrane (*22*–*24*). The direct interaction of the UBA domain of NAC with SRP raises questions as to whether it plays a role in ER targeting.

To address this, we generated the following: (i) a NAC mutant in which the UBA is deleted (dUBA), (ii) a NAC mutant (D205R/N208R-NACα, named UBAmt), and (iii) an SRP mutant (K50E/R53E-SRP54, named SRP54mt on the basis of human sequence numbering). UBAmt and SRP54mt contain charge reversal mutations at contact points between the UBA and the NG domain of SRP54. We measured the effects of these mutations on the binding affinity of SRP for NAC-engaged RNC_{SS} displaying the ER signal sequence. Although none of the above-described mutations changed the affinity of NAC or SRP for SR or RNCs (figs. S16 and S17), they all decreased the affinity of SRP for the RNC_{SS}•NAC complex by >5-fold (Fig. 3E and fig. S17A). The same effect was observed in reciprocal experiments when NAC was titrated to a preformed RNC_{SS}•SRP complex (fig. S17, B and C). Thus, the contact between NAC UBA and SRP54 NG domains stabilizes the cobinding of SRP and NAC on signal sequence–displaying ribosomes.

To test whether the UBA domain mediates the initial recruitment of SRP to the ribosome, we used total internal reflection fluorescence microscopy to study single-molecule events in which SRP binds to surface-immobilized RNC_{SS} prebound with NAC (Fig. 4A). If SRP is captured by NAC through the UBA domain before stable engagement with the ribosome, then the arrival of SRP on NAC-bound RNC_{SS} would be synchronous with the onset of FRET between a dye pair engineered on the SRP54 NG and NACα UBA domains. The results were consistent with this model: The initiation of colocalized fluorescence signals from NAC and SRP was synchronous with the onset of FRET in every single-molecule fluorescence time trace (Fig. 4, B and C), even in recruitment events that did not lead to a long-lived SRP association with the RNC (for an example, see Fig. 4B). Statistical analysis, in which the FRET time traces were aligned to the start of the SRP fluorescence signal (n = 45), showed that peak FRET efficiency was coincident with SRP arrival (Fig. 4D). Once a stable RNC•NAC•SRP ternary complex was formed, NACα UBA dynamically associated with and dissociated from SRP54, as shown by the frequent transitions between low- and high-FRET states (Fig. 4E). Thus, the contact between UBA and NG initiates before the productive docking of SRP at the exit of the ribosomal tunnel and signal sequence handover.

C. elegans mutants with impaired NAC UBA-SRP54 NG interactions showed elevated levels of the ER stress reporter hsp-4p::GFP, particularly in highly secretory intestinal cells (Fig. 3F and fig. S18, A and B). Furthermore, the levels of a secreted GFP reporter containing a signal sequence (ssGFP) (*25*) were significantly lower in NAC UBA and SRP54 NG mutant worms (Fig. 3G and fig. S18, C and D). The mutant worms also showed a cytosolic stress response, suggesting a possible accumulation of misfolded ER proteins in the cytosol caused by failed targeting (fig. S18E). As mentioned above, the defects observed with SRP54mt were not caused by the impaired interaction with the SR NG domain (figs. S15 and S16). Thus, the contacts between SRP and the UBA domain of NAC are critical for the successful SRP targeting of proteins to the ER.

Mechanism of the NAC-SRP interplay on the ribosome to initiate ER targeting

We propose a molecular mechanism for the interplay of NAC and SRP at the ribosome that controls and initiates cotranslational protein targeting to ER: NAC acts as "gatekeeper" to shield emerging nascent chains from nonphysiological interactions with SRP (Fig. 5). Because of its abundance and high affinity for the ribosome, NAC is bound to most ribosomes at early stages of translation through a high-affinity anchor and a weakly bound globular domain that blocks SRP access to nascent polypeptides. The flexibly tethered UBA domain recruits SRP and increases its local concentration at the tunnel exit region to initiate sampling of nascent chains. The emergence of an

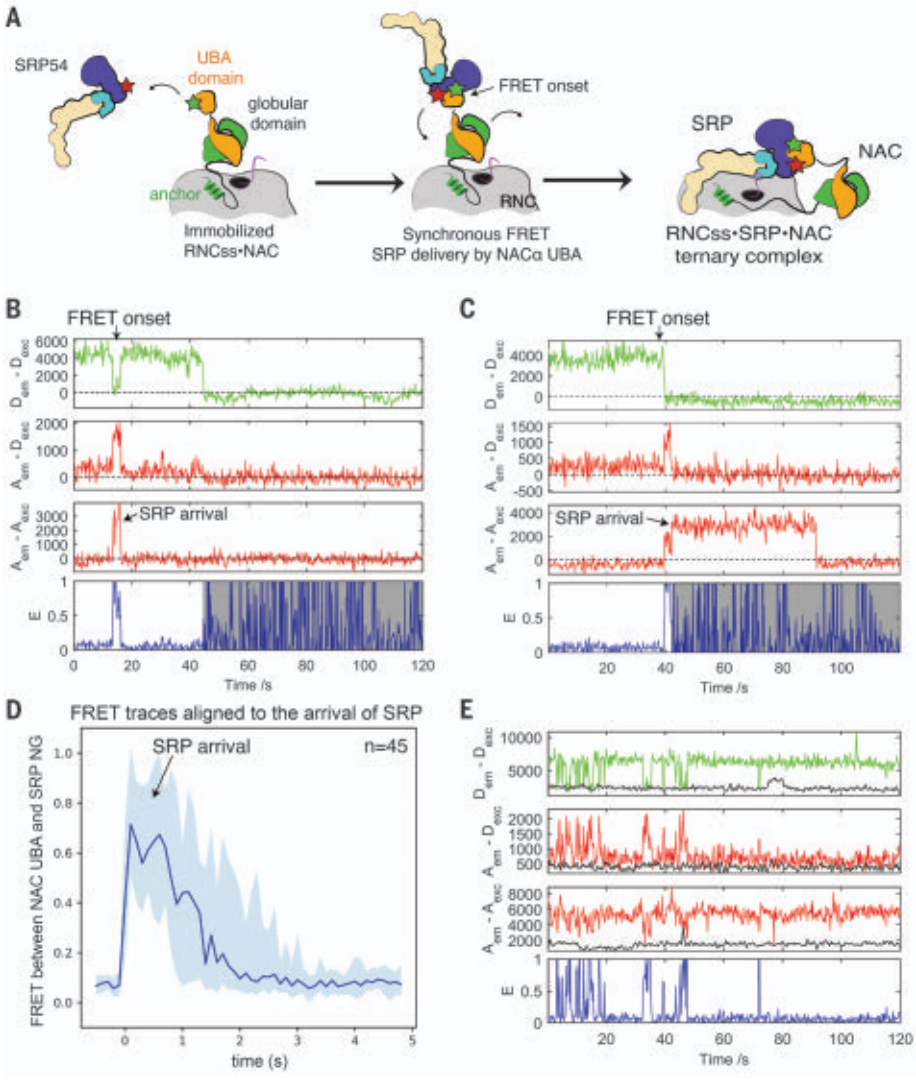


Fig. 4. Interaction between SRP54 and NACα UBA domain mediates initial SRP recruitment to the ribosome. (**A**) Scheme of the single-molecule experiment. RNC is immobilized on the glass coverslip surface through 3′ biotinylated mRNA (not shown). NAC was labeled with Cy3b (green star) in the UBA domain, and SRP is labeled with Atto647N (red star) in the SRP54 NG domain. (**B**) and (**C**) Representative single-molecule fluorescence time traces. $D_{em} - D_{ex}$, donor emission during donor excitation; $A_{em} - D_{ex}$, acceptor emission during donor excitation; $A_{em} - A_{ex}$, acceptor emission during acceptor excitation; and E, apparent FRET efficiency calculated from the $A_{em} - D_{ex}$ and $D_{em} - D_{ex}$ traces. The region after donor photobleaching is masked. (**D**) Time traces of FRET efficiency (n = 45) aligned to the start of the SRP (acceptor) signal. The median FRET value of all traces at each time frame is plotted as a solid blue line. The blue shaded area encloses the FRET range that includes the first to third quartile of data at each frame. (**E**) Representative time trace after a stable NAC•SRP•RNC ternary complex is formed.

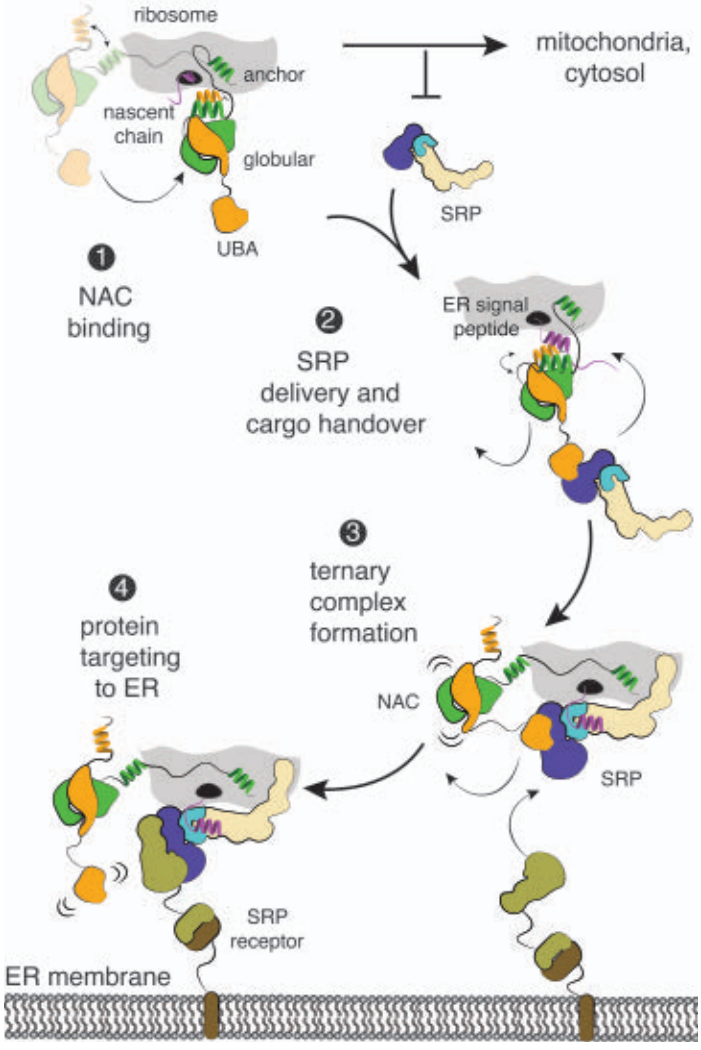


Fig. 5. Model for cotranslational signal sequence handover from NAC to SRP during ER-protein targeting.

ER signal sequence weakens the interactions of NAC's globular domain with the ribosome. This allows SRP to bind the signal sequence at the exit of the ribosomal tunnel, displacing the globular domain of NAC. NAC remains associated with both the ribosome and SRP through the respective NACβ anchor and UBA contacts until it reaches the ER membrane, where SR displaces the UBA domain from SRP.

This study resolves the molecular function of NAC as a sorting factor for nascent chains and the nature of its spatiotemporal coordination with SRP on the ribosome. Our results explain how NAC, which binds to virtually all ribosomes, prevents sub-stoichiometric SRP from forming tight but unproductive complexes with signal-less ribosomes while at the same time keeping SRP tethered to allow it to scan for the presence of the ER signal sequence. Because degenerate and highly diverse targeting sequences cannot be recognized with sufficient specificity in a single step and/or by individual targeting factors, stepwise recognition by NAC followed by SRP, coupled with quality control pathways (*26*–*29*), increases the overall fidelity of protein targeting. The exit region of the ribosomal tunnel is a crowded environment where multiple binding factors compete for the nascent chain. Therefore, it is possible that NAC's role as a sorting factor extends beyond the recruitment of SRP to orchestrate a multitude of nascent chain–processing events.

REFERENCES AND NOTES

1. R. Gilmore, G. Blobel, P. Walter, *J. Cell Biol.* **95**, 463–469 (1982).
2. M. Halic *et al.*, *Nature* **444**, 507–511 (2006).
3. R. M. Voorhees, R. S. Hegde, *eLife* **4**, e07975 (2015).
4. A. Jomaa *et al.*, *Cell Rep.* **36**, 109350 (2021).
5. E. A. Costa, K. Subramanian, J. Nunnari, J. S. Weissman, *Science* **359**, 689–692 (2018).
6. M. Gamerdinger, M. A. Hanebuth, T. Frickey, E. Deuerling, *Science* **348**, 201–207 (2015).
7. J. H. Lee *et al.*, *Proc. Natl. Acad. Sci. U.S.A.* **115**, E5487–E5496 (2018).
8. B. Wiedmann, H. Sakai, T. A. Davis, M. Wiedmann, *Nature* **370**, 434–440 (1994).
9. M. del Alamo *et al.*, *PLOS Biol.* **9**, e1001100 (2011).
10. Y. Nyathi, M. R. Pool, *J. Cell Biol.* **210**, 287–301 (2015).
11. Y. Zhang *et al.*, *Mol. Biol. Cell* **23**, 3027–3040 (2012).
12. H.-H. Hsieh, J. H. Lee, S. Chandrasekar, S. O. Shan, *Nat. Commun.* **11**, 5840 (2020).
13. Y. Liu, Y. Hu, X. Li, L. Niu, M. Teng, *Biochemistry* **49**, 2890–2896 (2010).
14. L. Wang *et al.*, *Protein Cell* **1**, 406–416 (2010).
15. T. Spreter, M. Pech, B. Beatrix, *J. Biol. Chem.* **280**, 15849–15854 (2005).
16. M. Gamerdinger *et al.*, *Mol. Cell* **75**, 996–1006.e8 (2019).
17. R. D. Wegrzyn *et al.*, *J. Biol. Chem.* **281**, 2847–2857 (2006).
18. Z. Lin *et al.*, *Science* **367**, 100–104 (2020).
19. M. Pech, T. Spreter, R. Beckmann, B. Beatrix, *J. Biol. Chem.* **285**, 19679–19687 (2010).
20. J. Jumper *et al.*, *Nature* **596**, 583–589 (2021).
21. M. Calfon *et al.*, *Nature* **415**, 92–96 (2002).
22. K. Wild *et al.*, *J. Mol. Biol.* **428**, 2880–2897 (2016).
23. J. H. Lee *et al.*, *Sci. Adv.* **7**, eabg0942 (2021).
24. K. Kobayashi *et al.*, *Science* **360**, 323–327 (2018).
25. H. Fares, I. Greenwald, *Nat. Genet.* **28**, 64–68 (2001).
26. Y. C. Chen *et al.*, *EMBO J.* **33**, 1548–1564 (2014).
27. R. S. Hegde, E. Zavodszky, *Cold Spring Harb. Perspect. Biol.* **11**, a033902 (2019).
28. T. Hessa *et al.*, *Nature* **475**, 394–397 (2011).
29. V. Okreglak, P. Walter, *Proc. Natl. Acad. Sci. U.S.A.* **111**, 8019–8024 (2014).

ACKNOWLEDGMENTS

We thank M. Leibundgut, T. Lenarcic, and M. Jaskolowski for discussions; R. Schloemer and E. Coellen for technical assistance; and S. Kreft for help with in vitro cysteine cross-linking experiments. Cryo-EM was collected at ScopeM at the ETH Zurich. We acknowledge the MRC - LMB Electron Microscopy Facility for access and support of electron microscopy sample preparation and data collection for NAC-TTC5-RNC and the Caenorhabditis Genetics Center for strains. **Funding:** This work was supported by the Swiss National Science Foundation (grant no. 310030B_163478); the National Center of Excellence in Research RNA & Disease Program of the SNSF (grant no. 51NF40_141735); a Roessler Prize, Ernst Jung Prize, and Otto Naegeli Prize for Medical Research (to N.B.); the German Science Foundation (grant nos. SFB969/A01 and A07 to E.D. and M.G.); the National Institutes of Health (grant no. R35 GM136321 to S.S.); the National Science Foundation (grant no. MCB-1929452 to S.-o.S); and the UK Medical Research Council (MRC grant MC_UP_A022_1007 to R.S.H.). V.C. was supported by V. Ramakrishnan, whose funding was from the MRC (grant no. MC_U105184332), the Wellcome Trust (grant no. WT096570), the Agouron Institute, and the Louis-Jeantet Foundation. We also acknowledge the support of the NVIDIA Corporation for the Titan Xp GPU through a grant awarded to A.J. **Author contributions:** A.J., M.G., H.-H.H., R.S.H., S.S., N.B., and E.D. conceived the project. A.J. and A.S. performed cryo-EM data collection for ER-targeting complexes containing NAC and SRP. A.J. determined the cryo-EM structures of NAC-RNC and NAC-SRP-RNC. M.G. and A.W. performed *C. elegans* in vivo and A.W. cross-linking experiments. H.-H.H. performed FRET titrations and single-molecule experiments. V.C. performed structural analysis of the NAC-TTC5-RNC. Z.U. characterized NAC cysteine variants. A.J., M.G., H.-H.H., S.S., E.D., and N.B. wrote the manuscript. All authors contributed to data analysis and the final version of the manuscript. **Competing interests:** The authors declare no competing interests. **Data and materials availability:** Cryo-EM maps and model coordinates are deposited in the EMDB as EMD-14191, EMD-14192, and EMD-14193 and in the PDB as PDB ID 7QWQ, 7QWR, and 7QWS for the NAC-SRP-RNC$_{SS}$, NAC-RNC$_{SS}$, and NAC-TTC5-RNC$_{TUBE}$, respectively. All other data are available in the main text or the supplementary materials.

SUPPLEMENTARY MATERIALS

science.org/doi/10.1126/science.abl6459
Materials and Methods
Figs. S1 to S18
Tables S1 to S3
References (*30*–*42*)
MDAR Reproducibility Checklist

27 July 2021; resubmitted 3 December 2021
Accepted 27 January 2022
10.1126/science.abl6459

STRUCTURAL BIOLOGY

Dynamics and mechanism of a light-driven chloride pump

Sandra Mous[1], Guillaume Gotthard[1,2], David Ehrenberg[3], Saumik Sen[4]†, Tobias Weinert[2], Philip J. M. Johnson[5], Daniel James[2]‡, Karol Nass[6], Antonia Furrer[2], Demet Kekilli[2]§, Pikyee Ma[2]¶, Steffen Brünle[2]#, Cecilia Maria Casadei[1,2], Isabelle Martiel[7], Florian Dworkowski[7], Dardan Gashi[2,6], Petr Skopintsev[2]**, Maximilian Wranik[2], Gregor Knopp[6], Ezequiel Panepucci[7], Valerie Panneels[2], Claudio Cirelli[6], Dmitry Ozerov[8], Gebhard F. X. Schertler[1,2], Meitian Wang[7], Chris Milne[6]††, Joerg Standfuss[2], Igor Schapiro[4], Joachim Heberle[3], Przemyslaw Nogly[1]*

Chloride transport by microbial rhodopsins is an essential process for which molecular details such as the mechanisms that convert light energy to drive ion pumping and ensure the unidirectionality of the transport have remained elusive. We combined time-resolved serial crystallography with time-resolved spectroscopy and multiscale simulations to elucidate the molecular mechanism of a chloride-pumping rhodopsin and the structural dynamics throughout the transport cycle. We traced transient anion-binding sites, obtained evidence for how light energy is used in the pumping mechanism, and identified steric and electrostatic molecular gates ensuring unidirectional transport. An interaction with the π-electron system of the retinal supports transient chloride ion binding across a major bottleneck in the transport pathway. These results allow us to propose key mechanistic features enabling finely controlled chloride transport across the cell membrane in this light-powered chloride ion pump.

Chloride transport is a fundamental process in biology, regulating osmotic pressure, cell growth, and membrane potential (*1*). In halophilic Archaea, inward halide-pumping rhodopsins (halorhodopsin; HR) from *Halobacterium salinarum* (*Hs*HR) and *Natromonas pharaonis* (*Np*HR) help to generate the membrane potential to produce ATP through the proton motive force, together with the outward proton-pumping bacteriorhodopsin (*2*–*4*). The role of halorhodopsin in marine bacteria, such as rhodopsin 3 from *Nonlabens marinus* (*Nm*HR), remains unclear, but it has been speculated that these chloride pumps are involved in producing ATP and maintaining the osmotic balance of the cell (*5*). Ion gradients are also involved in the generation and propagation of neuronal signals, which has enabled the application of these photoactive chloride-pumping rhodopsins as optogenetic tools in the control of neuronal activity (*6*). Chloride-pumping rhodopsins bind a retinal chromophore in all-*trans* configuration, which, upon photoisomerization, initiates the transport cycle (fig. S1) through a mechanism that is still not well understood. The main transport events can be described following a modified Jardetzky alternate access model (*7*) in which a high-affinity substrate-binding site is transformed into a low-affinity site with light-induced structural changes enabling access to the cytoplasmic release pathway (fig. S2).

The first structure of a halide-pumping rhodopsin from halophilic Archaea was reported 20 years ago (*8*), revealing a chloride-binding site close to the protonated Schiff base (PSB) of the retinal. However, it is essential to determine transient chloride-binding sites to decipher details of the ion transport mechanism. These remained elusive, except for one transient site that was identified in cryo-trapped photointermediate states of the archaeal halorhodopsins *Hs*HR (*9*) and *Np*HR (*10*). Recently, the resting structure of the chloride pump *Nm*HR from marine bacteria was published (*11*, *12*). Although the latter shares only 21% sequence identity with *Hs*HR and *Np*HR, it is conceivable that these structurally similar proteins may use comparable elements in their transport mechanism. Similarities are also evident in the photocycle. The classical bacteriorhodopsin photocycle is usually described by the following scheme: dark + hν → K→ L → M→ N → O → dark. Halorhodopsins do not display the M state intermediate, indicating the lack of a PSB deprotonation stage [for a detailed photocycle comparison, see fig. S3 (*13*–*17*)].

Understanding the molecular mechanism of ion transport requires a methodology with near-atomic spatial resolution and up to picosecond temporal resolution (*13*, *15*, *18*–*26*). Recent years have witnessed rapid development in the field of time-resolved serial femtosecond crystallography (TR-SFX) at x-ray free electron laser (XFEL) facilities with a similar strategy adapted to synchrotrons: time-resolved serial synchrotron crystallography (TR-SSX). The ability to photoactivate rhodopsins renders *Nm*HR an ideal target for time-resolved pump-probe experiments to elucidate the structural dynamics of chloride transport. The ion transport in halorhodopsin contrasts in charge and direction with the studied with TR-SFX bacteriorhodopsin (*13*, *23*, *25*) and the sodium-pumping rhodopsin *Krokinobacter eikastus* rhodopsin 2 [KR2 (*15*)], thus presenting an interesting opportunity for mechanistic comparison of transport strategies in nature.

In this work, we used an approach based on the detection of anomalous signals in the photostationary state using the serial crystallography method to identify transient anion-binding sites inside *Nm*HR. In addition, to provide a comprehensive view of the anion transport mechanism in *Nm*HR, structural intermediates from Δt = 10 ps until 50 ms were determined using a combination of TR-SFX and TR-SSX for resolving structural intermediates of the early and late photocycle, respectively. Our structural data were complemented with crystal spectroscopy and hybrid quantum mechanics/molecular mechanics (QM/MM) simulations. The time-resolved crystallography experiments allowed us to describe two molecular gates orchestrating the unidirectional chloride transport and analyze the mechanism of light energy utilization in transport initiation proceeding through an interaction of the retinal π-electron system with the chloride.

Results and discussion

Tracing the chloride transport pathway

A chloride-binding site named Cl^{351} was identified on the extracellular side of the retinal-binding pocket in the resting state of *Nm*HR (*11*, *12*) (fig. S4C). Chloride transport to the cytoplasm would thus require transfer across the retinal. The presence of such an early transport bottleneck ensures tight light control, enabling transport only upon photoactivation. The resting-state structure of *Nm*HR revealed three water cavities formed by conserved residues (fig. S4, A and B, and S5) that may be involved in the transport pathway. However, a prominent tunnel that would allow for the passage of the anion was not identified. Previous biochemical studies showed that *Nm*HR can transport (*5*) and bind bromide with a

[1]Institute of Molecular Biology and Biophysics, Department of Biology, ETH Zürich, Zürich, Switzerland. [2]Laboratory of Biomolecular Research, Biology and Chemistry Division, Paul Scherrer Institute, Villigen PSI, Switzerland. [3]Experimental Molecular Biophysics, Department of Physics, Freie Universität Berlin, Berlin, Germany. [4]Fritz Haber Center for Molecular Dynamics, Institute of Chemistry, The Hebrew University of Jerusalem, Jerusalem, Israel. [5]Laboratory of Nonlinear Optics, Photon Science Division, Paul Scherrer Institute, Villigen PSI, Switzerland. [6]Laboratory of Femtochemistry, Photon Science Division, Paul Scherrer Institute, Villigen PSI, Switzerland. [7]Laboratory for Macromolecules and Bioimaging, Photon Science Division, Paul Scherrer Institute, Villigen PSI, Switzerland. [8]Science IT, Paul Scherrer Institute, Villigen PSI, Switzerland.
***Corresponding author. Email: przemyslaw.nogly@mol.biol.ethz.ch**
†Present address: Condensed Matter Theory Group, Laboratory for Theoretical and Computational Physics, Paul Scherrer Institute, CH-5232 Villigen PSI, Switzerland.
‡Present address: Department of Physics, Utah Valley University, Orem, UT 84058, USA.
§Present address: Celerion Switzerland AG, CH-8320 Fehraltorf, Switzerland.
¶Present address: Viromotix AG, CH-8952 Schlieren, Switzerland.
#Present address: Leiden Institute of Chemistry, Leiden University, 2333 CC Leiden, The Netherlands.
**Present address: California Institute for Quantitative Biosciences (QB3), University of California, Berkeley, Berkeley, CA, USA.
††Present address: European XFEL GmbH, 22869 Schenefeld, Germany.

similar affinity as chloride [Cl^-: K_d = 24 mM; Br^-: K_d = 10 mM (*17*)]. Furthermore, structural studies show that a bromide ion is coordinated by the retinal PSB in the resting-state Br^{351}-binding site (*11*). We have assumed that bromide can mimic the transport pathway of chloride ions. Therefore, to detect transient anion-binding sites across the protein, we replaced chloride with bromide, which can be localized by anomalous dispersion in x-ray diffraction. Bromide-soaked crystals were continuously illuminated with a 520-nm laser diode while being delivered for serial crystallographic data collection at the Swiss Light Source (*26*). Perpetually activating *Nm*HR within the crystals results in a photostationary state with a mixture of photocycle intermediates (Fig. 1B) and partial occupancies of possible anion-binding sites. However, the O spectroscopic intermediate was predominantly accumulated (fig. S6). Molecular replacement combined with single-wavelength anomalous dispersion enabled us to identify four intramolecular sites overlapping with internal water molecules (Fig. 1A, all scatterers listed in fig. S7, and tables S1 and S2): one corresponding to the resting state (Br^{351}), one in a hydrophilic cavity on the cytoplasmic half of the protein (Br^{353}), and two in hydrophilic cavities in the extracellular half of the protein (Br^{354} and Br^{355}).

To complement the steady-state experiments and to resolve the structural intermediates of the consecutive steps of transport, we collected time-resolved serial crystallography data. Time delays from picoseconds to microseconds were recorded at the SwissFEL X-ray Free Electron Laser (*27*) and complemented with millisecond data from the Swiss Light Source synchrotron (*26*) (fig. S8).

As discussed in the following sections, the time-resolved crystallography experiments allowed the temporal assignment of the transient binding sites identified in the photostationary state.

*Nm*HR photocycle in crystals

*Nm*HR was crystallized in a lipidic cubic phase that mimics the amphipathic environment of cellular membranes. Nevertheless, crystal contacts and crystallization conditions may influence protein kinetics in the crystalline state

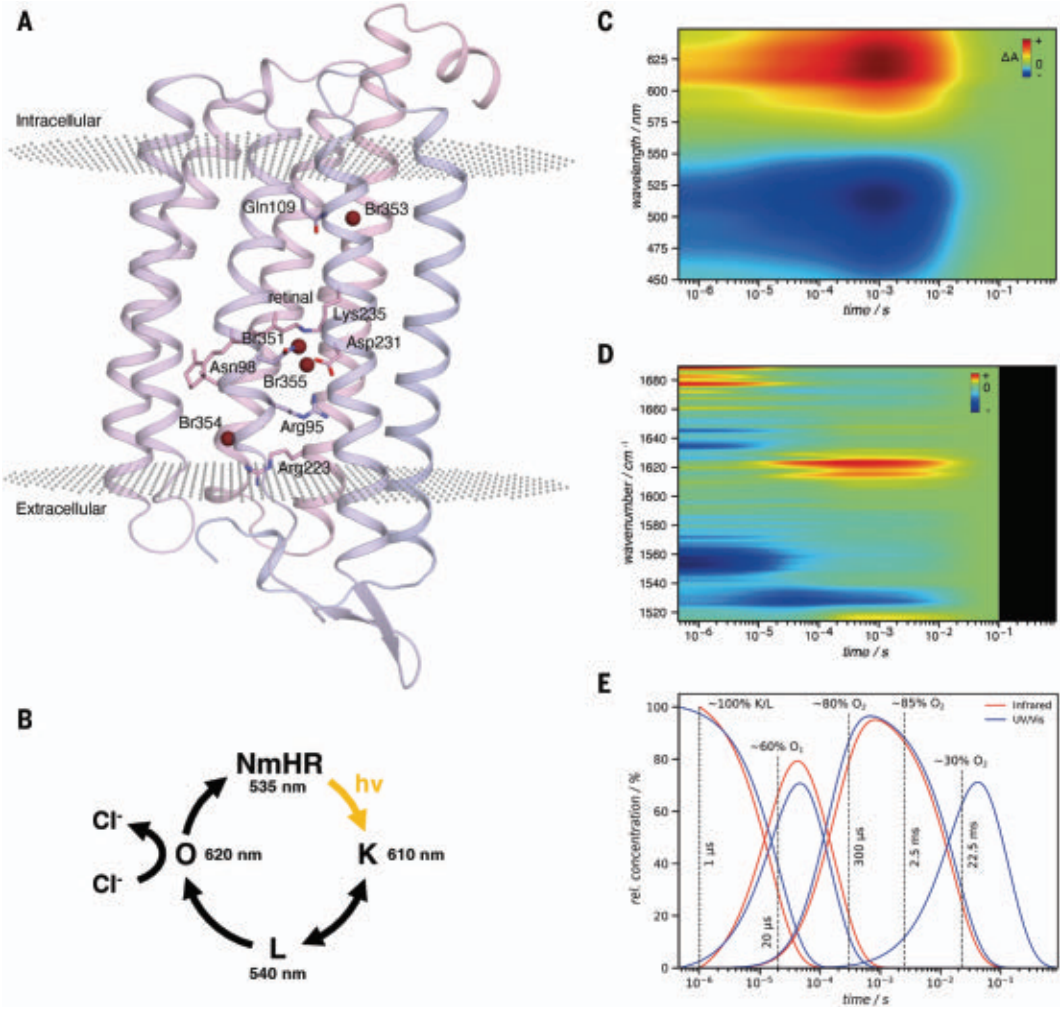
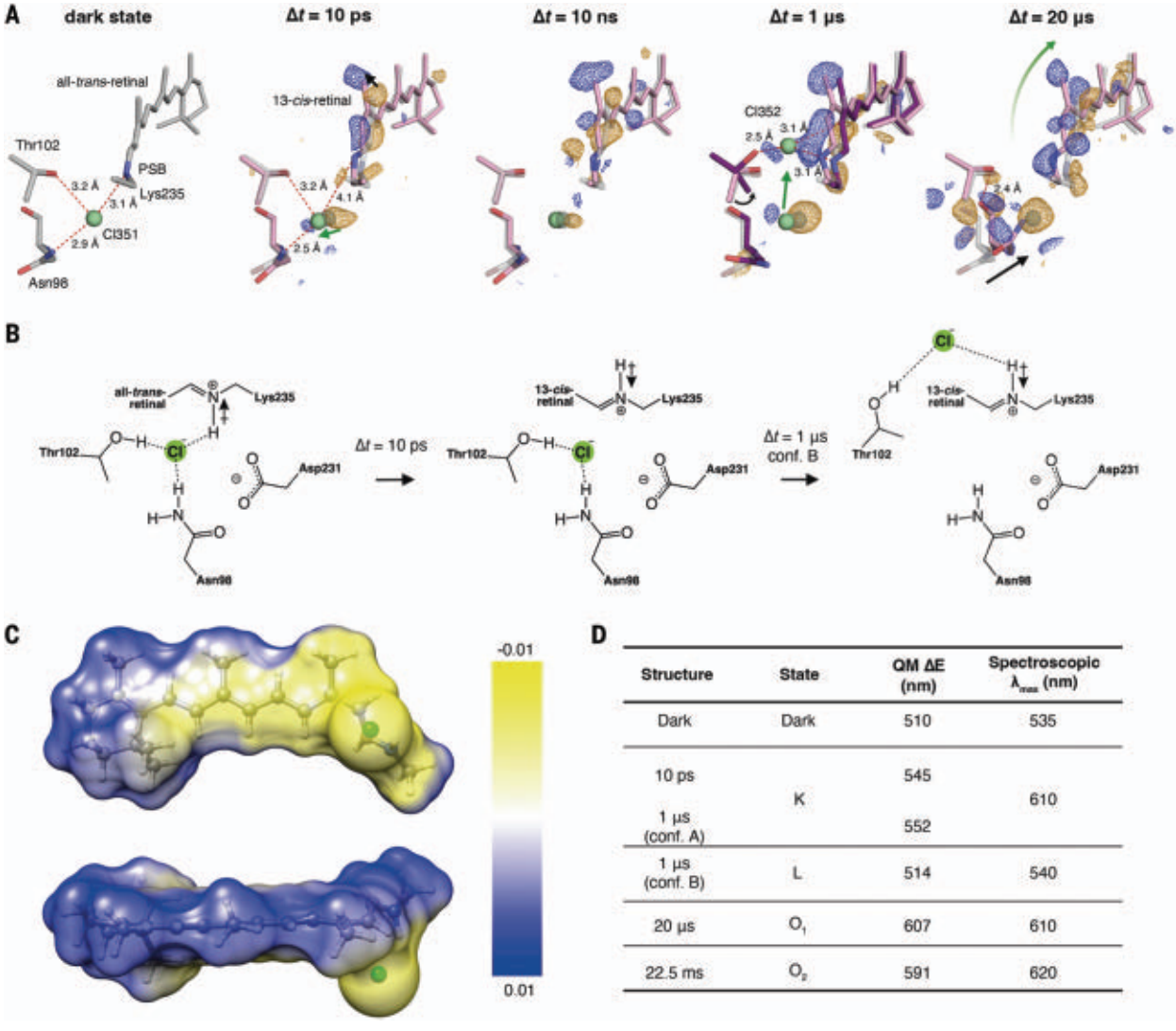


Fig. 1. Halide-binding sites and photocycle of *Nm*HR. (**A**) Ribbon model of *Nm*HR showing the overall secondary structure. Locations of bromide-binding sites, as determined by anomalous scattering, are shown as brown spheres. (**B**) Schematic representation of the *Nm*HR photocycle with the corresponding absorption maxima. (**C**) Two-dimensional representation of transient UV/Vis absorption experiments of *Nm*HR crystals after pulsed photoexcitation. Negative absorption changes (blue areas) correspond to the depletion of ground-state *Nm*HR and positive absorption (red areas) to the rise of intermediate states. (**D**) Kinetic data from time-resolved IR spectroscopy on the crystals. (**E**) Data in (C) and (D) have been subjected to global fit analysis by applying a model of sequential intermediate states. The analysis yielded the concentration profiles of the intermediate states, which were four states for the UV/Vis data (blue traces) and three states for the IR data (red traces), assigned to a mixture of the spectroscopic K/L state, the O_1 state, the O_2 state, and *Nm*HR′ (for which a signal was only observed in the UV/Vis data). The dashed vertical lines indicate the relative concentrations of intermediate states at delay times applied in the SFX experiments.

(*28*). We therefore probed the rise and decay of spectroscopic states (Fig. 1B) in crystals by time-resolved absorption spectroscopy in the infrared (IR) and in the ultraviolet/visible (UV/Vis) region (Fig. 1, C and D). In the nanoseconds to early microseconds, we observed a mixture of K (with λ_{max} at 610 nm) and L intermediates (with λ_{max} at 540 nm; table S3). The L intermediate decays into a red-shifted O intermediate (λ_{max} at 610 nm), which is predominant in the late microseconds until milliseconds (Fig. 1E). The photocycle of *Nm*HR probed in solution (*17*) indicated the rise of the early O_1 to be accompanied by chloride release and the decay of the subsequent O_2 state to be limited by chloride uptake. Compared with *Nm*HR in solution, the kinetics in the crystalline state are slightly altered with a faster decay rate of the spectroscopic intermediates up to the O_1 state and a slower decay rate of the O_2 state. These changes, however, can also be attributed to an increased chloride concentration (*17*).

*Nm*HR activation

Light-driven ion transport by microbial rhodopsins is initiated by the all-*trans* to 13-*cis* photoisomerization of the retinal chromophore. Time-resolved difference Fourier maps ($F_{o(10ps)} - F_{o(dark)}$) of our fastest TR-SFX time delay at Δt = 10 ps show that the retinal has isomerized (Fig. 2A and fig. S9). Structural refinement results in a nearly planar 13-*cis* configuration, however, the chromophore is tilted by 17° compared with the all-*trans*-retinal of the resting state (fig. S10, A



Structure	State	QM ΔE (nm)	Spectroscopic λ_{max} (nm)
Dark	Dark	510	535
10 ps	K	545	610
1 µs (conf. A)		552	
1 µs (conf. B)	L	514	540
20 µs	O_1	607	610
22.5 ms	O_2	591	620

Fig. 2. *Nm*HR activation and initiation of transport. (**A**) Chloride ion–binding site in the resting state and its evolution in the early active states. In the presence of photoisomerized retinal at Δt = 10 ps, when the spectroscopic K intermediate is accumulated, the Cl^{351} is shifted away from the PSB. At Δt = 1 µs, when a mixture of the K and L spectroscopic intermediates is accumulated, an additional Cl^{352}-binding site forms in the proximity of the PSB. Difference Fourier electron density ($F_{light} - F_{dark}$) contoured at 3.0 σ is shown as a blue (positive) mesh and a golden (negative) mesh. The corresponding extrapolated electron density maps can be found in figs. S11 and S12. The chloride ion is depicted as green sphere; the C atom sticks are colored gray (resting state) and pink (active states; Δt = 1 µs conformation B in dark purple). At Δt = 20 µs, when the O_1 spectroscopic intermediate is accumulated, the anion has passed over the retinal chromophore and the resting-state Cl^{351}-binding site has been depleted. (**B**) Schematic overview of the PSB flipping dipole (Δt = 10 ps), dragging the chloride over the retinal chromophore (Δt = 1 µs). (**C**) Molecular electrostatic potential surface of the retinal chromophore (with the nitrogen of the PSB shown as a blue sphere) and Cl^{352} (green sphere) of the 1-µs intermediate. The isocontour value of the surface is 0.005 e $Bohr^{-3}$. Blue and yellow colors correspond to regions of positive and negative electrostatic potential (in atomic units), respectively. Comparison with absent chloride is provided in fig. S15. (**D**) Absorption maxima of the resting state and the photocycle intermediates (excitation energy ΔE, in nanometers) as determined by QM/MM simulations and UV/Vis spectroscopy. The calculated values are consistently blue shifted, including the reference resting state. More details can be found in tables S6 and S7.

to C). The C20 methyl group of the isomerized retinal pushes against Trp^{201}, shifting it away by 0.4 Å. Trp^{99} shifts by 0.3 Å toward 13-*cis*-retinal, filling in the newly created space (fig. S11). The geometry of 13-*cis*-retinal resembles more closely that observed for sodium-pumping rhodopsin KR2 than that of bacteriorhodopsin (fig. S10D).

The PSB changes its orientation upon retinal isomerization. In the resting state, the proton of the PSB points toward the extracellular side and forms an H bond with Cl^{351} (Cl^{351}-PSB distance: 3.1 Å; Fig. 2, A and B). At Δt = 10 ps, the PSB flips, with its proton pointing toward the cytoplasm. Cl^{351} shifts away from the PSB, increasing the distance to 4.1 Å and breaking the H bond between the anion and the PSB, resulting in a destabilization of this binding site. Our QM/MM simulations indicate that 28.2 kcal mol^{-1} of energy is stored upon charge separation between the PSB and Cl^{351} at Δt = 10 ps. This energy corresponds to more than half of a green light photon (530 nm or 53.9 kcal mol^{-1}) to drive the subsequent reactions. Here, the stored energy is attributed to the photon energy that remains in the protein after the isomerization and subsequent return to the ground state. It is calculated as the difference between the resting state of *Nm*HR and the K intermediate.

A recent study complements our results, describing the ultrafast structural changes in *Nm*HR preceding chloride transport, including the retinal geometry evolution during the isomerization (*29*). Our 10-ps time delay provides a single time point overlap with the previous study, which shows overall agreement of the early structural changes.

First step of chloride transport

Upon depletion of the Cl^{351} site observed at Δt = 1 μs (Fig. 2A), we noted a positive difference density between the retinal PSB and Thr^{102}. We modeled it as chloride Cl^{352} in an alternate position to the still partially occupied Cl^{351} site (fig. S12). The partially formed Cl^{352}-binding site is stabilized by interactions with the retinal PSB (3.1 Å to Nζ), the π system (3.1 Å to C14 and C15 of the retinal), and the newly adopted 80° rotamer of Thr^{102} (2.5 Å to Oγ). We analyzed these interactions using quantum-chemical calculations and found that the stabilization is dominated by the electrostatic component between chloride and PSB (table S4). In addition, we have found a contribution from the C14–C15=N fragment of the retinal (fig. S13 and table S5). We identified an anion-π interaction between the conjugated π system of the retinal and Cl^{352} in which the negative charge of the anion polarizes the π-electron density of the chromophore (fig. S14). The polarization resembles the common interaction between anions and π electrons of aromatic rings (*30*–*35*). The polarization effect of the anion is also evident from the electrostatic potential maps of the retinal PSB in the presence of the chloride anion, with a negative potential extending up to the β-ionone ring of the retinal (Fig. 2C and fig. S15). Further validation stems from the calculated QM/MM excitation energy, which is in quantitative agreement with the experimental counterpart obtained from spectroscopy (Fig. 2D and tables S6 and S7). The red shift of the 1-μs intermediate with the anion in the Cl^{352}-binding site with respect to the resting state is 4 nm for the QM/MM simulation and 5 nm for the spectroscopic measurement. By contrast, when Cl^{352} is omitted or replaced by a water molecule, the computed shift is 164 or 187 nm, respectively.

On the basis of the archaeal *Hs*HR resting-state structure (*8*), it was hypothesized that the anion could be "dragged" by the moving PSB, but the passage across the retinal remained unknown. Our *Nm*HR data provide experimental evidence that, upon charge separation between photoisomerized retinal and Cl^{351} (leading to 28.2 kcal mol^{-1} of stored energy), the anion follows the PSB in microseconds, creating a pathway between the retinal and helix C. The identified anion-π interaction appears to be an essential step in the transport process. The first step of the chloride transport brings the anion 4.0 Å closer toward the cytoplasm.

Steric molecular gate

In the resting state, helix C exhibits a kink next to Cl^{351} [Fig. 3, B and C (*36*)]. Upon depletion of Cl^{351}, the kink on helix C relaxes from 38° ± 6° in the resting state to 22° ± 7° in the structure at Δt = 20 μs after light excitation. The kink relaxes even further, reaching a minimum angle of 16° ± 7° at Δt = 2.5 ms. A shift of helix C was also observed in active states of the homologous sodium-pumping rhodopsin KR2 (*15*). However, the observed changes do not lead to kink formation (fig. S16). We may infer

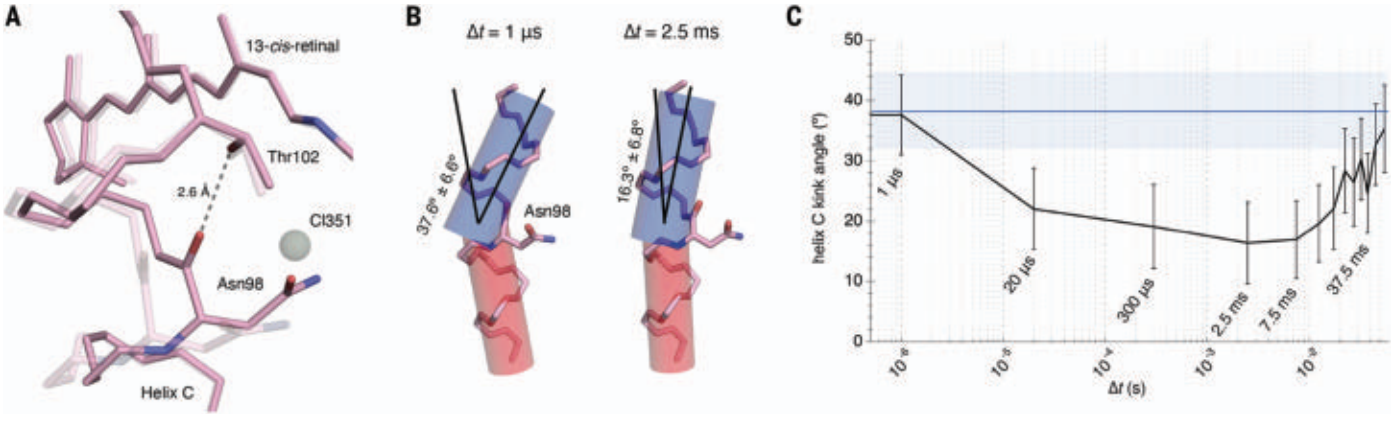


Fig. 3. Steric gate prevents chloride backflow. (**A**) Straightening of helix C at Δt = 20 μs to 7.5 ms, during which the spectroscopic O intermediates are accumulated, allows Asn^{98} to enter the resting-state chloride-binding site (intermediate Δt = 1 μs conformation A with the Cl^{351}-binding site shown in gray, intermediate Δt = 2.5 ms with a straightened helix C shown as pink sticks). The straightening of helix C is stabilized by the formation of a hydrogen bond between the backbone carbonyl group of Asn^{98} and the Thr^{102} side chain, shown by dashed lines with the distance measured in angstroms. (**B**) Two cylinders are fitted, from Asn^{92} to Asn^{98} and from Asn^{98} to Pro^{104}, from which the kink angle at Asn^{98} can be calculated (*36*). The fitted cylinders and calculated angle are shown for the Δt = 1 μs and Δt = 2.5 ms. (**C**) Change in the helix C kink angle over time, calculated using KinkFinder (*36*). One should consider that the apparent linear motion of the helix may be a result of changes in the populations of the intermediates. Error bars indicate the heuristically determined 95% confidence interval of the calculated kink angle (*36*). The blue line indicates the kink angle determined for the resting-state structure of 38.1°, with an estimated error of ± 6.3° represented in light blue.

that an intermediate state with sodium captured between retinal and helix C could lead to similar kink formation in KR2. In *Nm*HR, the relaxation of the kink moves the side chain of Asn^{98} into the chloride-free Cl^{351} site. This movement is rationalized as a sterically closing molecular gate preventing reverse flow of chloride. The Asn^{98} side chain, while replacing Cl^{351}, interacts only with the waters Wat^{484} (3.1 Å) and Wat^{407} (3.5 Å). Additional stabilization of this closed steric molecular gate is achieved by a new H bond between Thr^{102} and the carbonyl group of the Asn^{98} backbone (Fig. 3A), which seals the gate. Thr^{102}, which is part of the conserved NTQ motif defining the rhodopsin family to which *Nm*HR belongs (fig. S5), seems to play multiple roles in the early transport stages. In the resting state, it coordinates Cl^{351}, whereas at Δt = 1 µs, the Thr^{102} side chain assists in transferring the chloride to the Cl^{352} position by rotamerization. Finally, Thr^{102} seals the molecular gate, preventing chloride backflow from Δt = 20 µs once the anion is on its way toward the cytoplasm. The equivalent residue in sodium-pumping rhodopsin KR2 is Asp^{116}, which provides an electrostatic driving force for the cation and neutralizes the positive charge of the PSB (*15*), demonstrating substantial evolutionary adaptation of rhodopsins to different substrates.

Chloride release through Gln^{109} of the NTQ motif

At Δt = 20 µs, the Cl^{351}- and Cl^{352}-binding sites are depleted, and the Cl^{353} may emerge above the retinal by replacing Wat^{485}, which adds another 14 Å distance toward the cytoplasm on the transport pathway (Fig. 4A). The proposed transient Cl^{353}-binding site is characterized by a positive peak in $F_{o(20\mu s)} - F_{o(dark)}$ and displays an anomalous signal in the Br-soaked 13.7 keV photostationary SSX data (Fig. 1A). It should be noted that the anomalous difference density peak for the transient Cl^{353}-binding site is of limited strength (table S1 and fig. S7), likely because of the low occupancy of the transient binding site in the photostationary state. The Cl^{353}-binding site is accessed through Wat^{401} and Wat^{402} and formed by Gln^{109} of the conserved NTQ motif, Ser^{54} and Thr^{243} (Fig. 4A). We also observed a weak anomalous signal between Wat^{402} and Leu^{106} in the photostationary data (table S1). However, the site could not be modeled in our TR-SFX data. A conformational change of the residue corresponding to Leu^{106} (Ile^{134}) is needed to form a transient chloride-binding site in the *Np*HR structure of the N intermediate (*10*).

Gln^{109} of *Nm*HR is found at a strategic position for ion pumps. The equivalent residue of outward proton-pumping bacteriorhodopsin is Asp^{96}, which is the internal proton donor to the retinal Schiff base (*26*). In KR2, the equivalent residue is Gln^{123}, which is involved in the outward transport of sodium (*15*). These analogies suggest that pumping rhodopsins share sections of the transport pathway despite the different charge and size of the translocated ion and even in cases of opposite ion flow.

In the final stage, chloride is possibly released through the Wat^{482}-binding site on the surface, which is formed at Δt = 300 µs and within 8 Å from Cl^{353} (Fig. 4, B to D). It is accompanied by ordering of Thr^{51} and a rotameric change of Ser^{40}, both pointing toward Wat^{482}.

Chloride uptake

*Nm*HR appears to form an electric dipole (Fig. 5A) with the extracellular surface of predominantly negative charge and the cytoplasmic surface of predominantly positive charge. The resulting dipole moment presents an additional driving force for charge transport across the cell membrane, rendering directionality to those transitions that rely on passive anion diffusion.

The net negative charge on the extracellular solvent accessible surface creates a barrier for anion uptake (Fig. 5A), the exception being a water cavity enclosed by Asn^{3} (Fig. 5B). The anion entry into this cavity is driven by the positive charge of conserved Arg^{223}. We identified an anomalous site in the photostationary SSX data and a positive peak in the $F_{o(20\mu s)} - F_{o(dark)}$ map of the TR-SFX experiments, which we modeled as Cl^{354} (Fig. 1A and fig. S17). The latter is coordinated by Arg^{223}, Tyr^{96}, Wat^{403}, and Wat^{404}.

Passing of the chloride further toward the retinal is facilitated by the positive charge of the conserved Arg^{95}, likely through Wat^{429} (fig. S18A). To enter another water cavity consisting of Wat^{409} and Wat^{416} (from Δt = 1 µs, additionally Wat^{481}; fig. S19), the anion needs to pass Gln^{68}, where we observed a rotamer change only

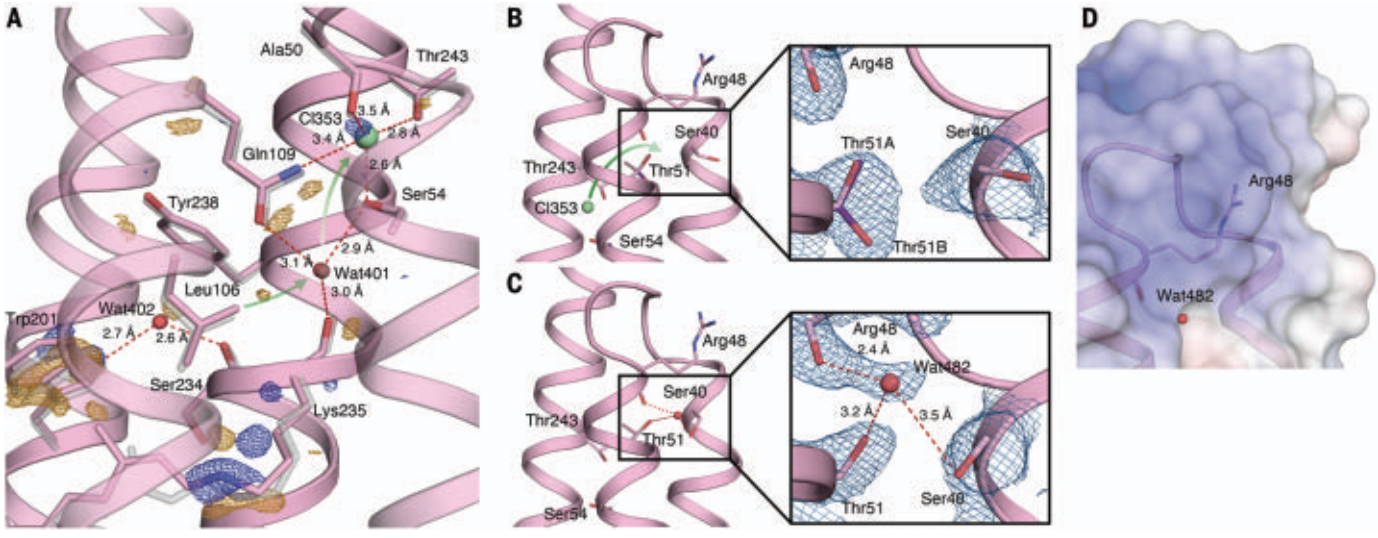


Fig. 4. Chloride transport and release. (**A**) A new chloride-binding site is identified after the anion is transferred over the retinal chromophore in the light-activated intermediate at Δt = 20 µs. Dashed lines indicate hydrogen-bonding interactions in the Cl^{353}-binding pocket with measurements in angstroms. Difference Fourier electron density [$F_{obs(20\ \mu s)} - F_{obs(dark)}$] contoured at 3.0 σ is shown as a blue (positive) mesh and a golden (negative) mesh. (**B**) Exit site at Δt = 20 µs. Conformation B of the Thr^{51} side chain is shown as purple sticks. The panel on the right shows a magnified view of the exit site with the extrapolated electron density ($2F_{ex} - F_{calc}$) as a blue mesh at 1.0 σ (carved at 1.8 Å from the side chains). (**C**) At Δt = 300 µs, the residue Ser^{40} changes conformation, whereas Thr^{51} adopts a single conformation to bind Wat^{482} (shown as a red sphere), which is only observed from Δt = 300 µs to 2.5 ms. At the same time, Cl^{353} and Wat^{485} are both absent at Δt = 300 µs. (**D**) Mapping the electrostatic potential (at ± 5 kT/e) on the solvent-accessible surface shows that the exit site is surrounded by a positive electrostatic potential.

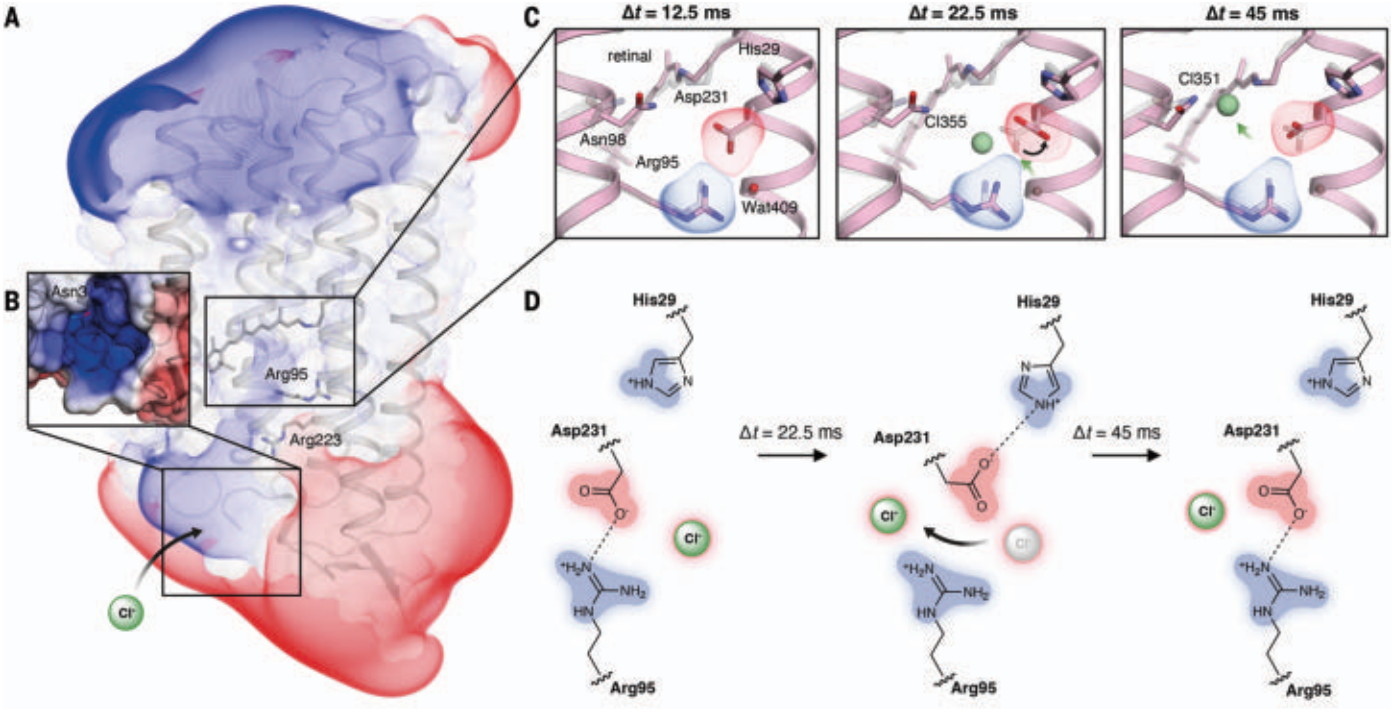


Fig. 5. Chloride uptake and electrostatic gate. (**A**) Ribbon model of *Nm*HR with surface electrostatics shown as an electrostatic potential isocontour at ±1 kT/e, with positive potential shown in blue and negative in red. (**B**) Solvent-accessible surface near the proposed chloride entrance site, with the electrostatic potential projected on the surface at ±3 kT/e. (**C**) Evolution of the accessibility to the retinal-binding pocket at Δt = 12.5 to 45 ms. The light-activated conformations are shown as light pink sticks overlaid on the resting-state structure shown as transparent gray sticks. The electrostatic potential isocontour at ±3 kT/e is shown around the Arg^{95} and Asp^{231} side chains. See fig. S20 for the corresponding electron densities. (**D**) Schematic representation of the electrostatic gate. As the chloride ion approaches residues Asp^{231} and Arg^{95} (step 1), the charge interaction between the residues is shielded, allowing Asp^{231} to interact with His^{29} instead (step 2). This creates a pathway for chloride to proceed toward the resting-state binding site (step 3).

at Δt = 12.5 ms (fig. S18B). Once the halide diffuses into the Wat^{409} position, the transport pathway is occluded by Asp^{231} (Fig. 5C and fig. S20).

Electrostatic gate enables recharging of the resting state

We calculated the excitation energy for different protonation states of Asp^{231} using hybrid QM/MM simulations to determine the form in which it is present. Only the anionic form of Asp^{231} results in the excitation energy consistent with the experimental value (table S8). Along with an interaction distance of 2.9 Å, it supports the presence of a salt bridge between Asp^{231} and Arg^{95}.

We propose that after diffusion into the Wat^{409} position, the halide interferes with the electrostatic attraction between Arg^{95} and Asp^{231} (Fig. 5C). We observed that the conformation of the side chain of Asp^{231} rotates from Δt = 22.5 to 37.5 ms, thereby interacting with the nearby His^{29} instead of Arg^{95} (Fig. 5, C and D). This opens the electrostatic gate and creates a pathway for the halide to the Cl^{355}-binding site, a convenient position for recharging of the Cl^{351} site 4 Å away. Before recovery of the resting state, the electrostatic gate closes again, preventing anion leakage back into the bulk solvent. In this way, the electrostatic gate ensures vectorial transport.

From Δt = 12.5 ms, the kink angle in helix C increases again (likely due to a shift in the populations of intermediates) until ~Δt = 45 ms, where helix C resembles the resting-state conformation (Fig. 3C). With the shift of helix C, the side chain of Asn^{98} also leaves the Cl^{351} site, and the retinal isomerizes back to all-*trans* configuration. It is plausible that the chloride pushes the side chain of Asn^{98} aside and breaks the steric gate seal driven by the energy gained from a strong electrostatic interaction with PSB.

Conclusions

We have traced several possible transient anion-binding sites buried inside *Nm*HR, allowing us to propose the chloride transport pathway (summarized in fig. S21 and movie S1). The time-resolved experiments enabled us to describe in atomic detail how the photonic energy absorbed by the retinal is stored in the form of charge separation between the isomerized retinal and its chloride counterion. In the early microseconds after protein activation, this excess energy drives the very first step of anion transport through an anion-π interaction. Comparing our results with the insights from previous TR-SFX studies of light-driven ion pumps (*13*, *15*), it becomes clear that rhodopsin pumps with different substrate affinities adopt diverse strategies to overcome the retinal bottleneck in ion transport. Whereas in bacteriorhodopsin and KR2, deprotonation of the Schiff base by the counterion (Asp^{85} and Asp^{116}, respectively) is required for successful transport, in *Nm*HR, no residue side chain acts as the proton acceptor, and the positively charged PSB drives the transfer of the anion over the chromophore.

In the steps after the initiation of anion transport, we propose that the steric molecular gate closes over the original anion-binding site accompanied by relaxation of helix C, which finally prevents a backflow. Anion release in the late microseconds is diffusion driven and assisted by the macroscopic dipole moment across the membrane created by the negative extracellular and positive cytoplasmic surface charges. The exit side to cytoplasm that we propose in this work aligns with the suggested ion selectivity filter in KR2 (*37*, *38*).

On the extracellular side, the anion uptake is likely guided by a positive patch in the otherwise negatively charged protein surface. The transient sodium release site in KR2 identified at Δt = 20 ms and created by a shift of the Arg^{243} (*15*) is located 5 Å away from the transient Cl^{354}-binding site in the triple water cluster (coordinated by the corresponding Arg^{223})

of *Nm*HR (fig. S22D), indicating that the sodium and chloride transport pathways may partially overlap on the extracellular side of the protein. Through consecutive steps driven by the charge of two arginine residues, the halide is proposed to arrive at an electrostatic molecular gate, a bottleneck in the anion uptake pathway. The gate likely opens upon interaction with the negative charge, allowing the anion to access the retinal-binding pocket. The subsequent closure of the electrostatic gate prevents anion backflow, imparting a directionality that is a characteristic feature of ion pumps. The counterparts of Arg^{95} and Asp^{231} forming the electrostatic gate in bacteriorhodopsin (Asp^{212} and Arg^{82}) play important functional roles as part of the complex counterion of the retinal and in the proton transfer pathway (*13*).

When comparing the proposed anion transport pathway of *Nm*HR with available archaeal HR structures, it becomes apparent that the anion-binding site coordinated by Gln^{105} identified in the *Hs*HR resting state (Asn^{92} in *Nm*HR) (*9*, *39*) does not align with the anion uptake pathway in *Nm*HR. Although in *Hs*HR, this anion-binding site is directly accessible from the bulk solvent, in *Nm*HR, the site is occluded from solvent by the extended N terminus and the different position of the B-C loop (fig. S22B). Conversely, the anion-binding site in the *Np*HR N state (*10*) is located over the retinal and in the proximity of Ile^{134} (Leu^{106} in *Nm*HR), ~4 Å away from Cl^{352} in *Nm*HR, indicating a plausible pathway toward the Cl^{353} site (fig. S22C). In addition, we observed how retinal isomerization increases the affinity for the anion in the transient Cl^{352}-binding site, allowing access to the cytoplasmic half of the protein and driving ion transfer (*40*–*42*); however, we have not found a clear conformational change switching the accessibility of the exit and uptake tunnel in the late photocycle, as has been proposed for *Np*HR (*10*, *16*). Although differences in the ion transport mechanism of archaeal and bacterial halorhodopsins may exist, the chloride pumps also share many commonalities. The large conformational changes in helix C of *Np*HR in the anion-free (O-like) state (*10*, *43*) and the existence of a salt bridge next to the resting-state chloride-binding site of the archaeal *Hs*HR and *Np*HR (*8*, *44*) suggest that the molecular gates may be a general feature of halorhodopsin ion pumps.

In summary, we have proposed the ion transfer pathway in bacterial halorhodopsin and discussed the interplay between the driving force created by the protein dipole moment and the control of transport by molecular gates. Furthermore, we have provided details about how light energy is converted into kinetic energy for chloride translocation. The resulting charge separation represents a fundamental feature for light energy conversion in nature as well as in technology.

REFERENCES AND NOTES

1. C. Miller, *Nature* **440**, 484–489 (2006).
2. A. Matsuno-Yagi, Y. Mukohata, *Biochem. Biophys. Res. Commun.* **78**, 237–243 (1977).
3. B. Schobert, J. K. Lanyi, *J. Biol. Chem.* **257**, 10306–10313 (1982).
4. C. Engelhard, I. Chizhov, F. Siebert, M. Engelhard, *Chem. Rev.* **118**, 10629–10645 (2018).
5. S. Yoshizawa *et al*., *Proc. Natl. Acad. Sci. U.S.A.* **111**, 6732–6737 (2014).
6. F. Zhang *et al*., *Nature* **446**, 633–639 (2007).
7. O. Jardetzky, *Nature* **211**, 969–970 (1966).
8. M. Kolbe, H. Besir, L.-O. Essen, D. Oesterhelt, *Science* **288**, 1390–1396 (2000).
9. W. Gmelin *et al*., *Photochem. Photobiol.* **83**, 369–377 (2007).
10. T. Kouyama, H. Kawaguchi, T. Nakanishi, H. Kubo, M. Murakami, *Biophys. J.* **108**, 2680–2690 (2015).
11. K. Kim *et al*., *Nat. Commun.* **7**, 12677 (2016).
12. T. Hosaka *et al*., *J. Biol. Chem.* **291**, 17488–17495 (2016).
13. E. Nango *et al*., *Science* **354**, 1552–1557 (2016).
14. K. Inoue *et al*., *Nat. Commun.* **4**, 1678 (2013).
15. P. Skopintsev *et al*., *Nature* **583**, 314–318 (2020).
16. I. Chizhov, M. Engelhard, *Biophys. J.* **81**, 1600–1612 (2001).
17. T. Tsukamoto, S. Yoshizawa, T. Kikukawa, M. Demura, Y. Sudo, *J. Phys. Chem. B* **121**, 2027–2038 (2017).
18. J. Tenboer *et al*., *Science* **346**, 1242–1246 (2014).
19. K. Pande *et al*., *Science* **352**, 725–729 (2016).
20. T. R. M. Barends *et al*., *Science* **350**, 445–450 (2015).
21. N. Coquelle *et al*., *Nat. Chem.* **10**, 31–37 (2018).
22. E. Claesson *et al*., *eLife* **9**, e53514 (2020).
23. P. Nogly *et al*., *Science* **361**, eaat0094 (2018).
24. P. Nogly *et al*., *Nat. Commun.* **7**, 12314 (2016).
25. G. Nass Kovacs *et al*., *Nat. Commun.* **10**, 3177 (2019).
26. T. Weinert *et al*., *Science* **365**, 61–65 (2019).
27. E. Prat *et al*., *Nat. Photonics* **14**, 748–754 (2020).
28. R. Efremov, V. I. Gordeliy, J. Heberle, G. Büldt, *Biophys. J.* **91**, 1441–1451 (2006).
29. J.-H. Yun *et al*., *Proc. Natl. Acad. Sci. U.S.A.* **118**, e2020486118 (2021).
30. A. Robertazzi, F. Krull, E.-W. Knapp, P. Gamez, *CrystEngComm* **13**, 3293–3300 (2011).
31. X. Lucas, A. Bauzá, A. Frontera, D. Quiñonero, *Chem. Sci.* **7**, 1038–1050 (2016).
32. S. Z. Borozan, M. V. Zlatović, S. Đ. Stojanović, *Eur. J. Biochem.* **21**, 357–368 (2016).
33. M. S. Smith *et al*., *ACS Chem. Biol.* **12**, 2535–2537 (2017).
34. C. Estarellas, A. Frontera, D. Quiñonero, P. M. Deyà, *Angew. Chem. Int. Ed.* **50**, 415–418 (2011).
35. L. M. Breberina, M. K. Milčić, M. R. Nikolić, S. Đ. Stojanović, *Eur. J. Biochem.* **20**, 475–485 (2015).
36. E. C. Law, H. R. Wilman, S. Kelm, J. Shi, C. M. Deane, *PLOS ONE* **11**, e0157553 (2016).
37. I. Gushchin *et al*., *Nat. Struct. Mol. Biol.* **22**, 390–395 (2015).
38. H. E. Kato *et al*., *Nature* **521**, 48–53 (2015).
39. M. Schreiner, R. Schlesinger, J. Heberle, H. H. Niemann, *J. Struct. Biol.* **190**, 373–378 (2015).
40. J. K. Lanyi, *FEBS Lett.* **175**, 337–342 (1984).
41. J. K. Lanyi, *FEBS Lett.* **464**, 103–107 (1999).
42. U. Haupts, J. Tittor, E. Bamberg, D. Oesterhelt, *Biochemistry* **36**, 2–7 (1997).
43. S. Kanada, Y. Takeguchi, M. Murakami, K. Ihara, T. Kouyama, *J. Mol. Biol.* **413**, 162–176 (2011).
44. T. Kouyama *et al*., *J. Mol. Biol.* **396**, 564–579 (2010).
45. S. Mous *et al*., SFX raw data for: Dynamics and mechanism of a light-driven chloride pump, PSI Public Data Repository (2022); https://doi.org/doi.psi.ch/detail/10.16907/8ecae5fe-4c00-4d59-be3d-5274f06188c2.
46. S. Mous *et al*., SSX raw data for: Dynamics and mechanism of a light-driven chloride pump, PSI Public Data Repository (2022); https://doi.org/doi.psi.ch/detail/10.16907/12079b73-6563-467a-890a-2ab43e678343.
47. S. Mous *et al*., 13.7 keV anomalous data for: Dynamics and mechanism of a light-driven chloride pump, PSI Public Data Repository (2022); https://doi.org/doi.psi.ch/detail/10.16907/14c30658-cc0b-41fe-b25b-240a9790d5ec.

ACKNOWLEDGMENTS

We thank the Macromolecular Crystallography group for support during the testing of crystals at the Swiss Light Source and the access and support of the Crystallization Facility at Swiss Light Source; the Paul Scherrer Institute, Villigen, Switzerland, for provision of XFEL and synchrotron radiation beamtime at beamlines X06SA (PXI) of the Swiss Light Source and Alvra at SwissFEL; everybody involved in ensuring the smooth operation of the SwissFEL X-ray Free Electron Laser and Swiss Light Source during our experiments; and F. Allain, S. Jonas, and A. Gossert for access to the office, laboratory space, and equipment at L floor of HPP building of ETH Zurich and for the supportive working environment provided. **Funding:** This work was supported by the Swiss National Science Foundation (Ambizione grant PZ00P3_174169 to P.N.; project grant 31003A_179351 to J.S.; and project grant 310030B_173335 to G.F.X.S.); the National Centre of Competence in Research: Molecular Ultrafast Science and Technology (C.M. and J.S.); the German Research Foundation via SFB 1078, projects B3 (J.H.), C6 (I.S.) and via EXC 2008/1 UniSysCat 390540038 (J.H.); Holcim Stiftung (P.M.); European Union's Horizon 2020 research and innovation program (Marie-Sklodowska-Curie grant agreements 701646 and 701647 to G.G., D.K., and S.B.); and the European Research Council (ERC) European Union's Horizon 2020 research and innovation program (grant 678169 'PhotoMutant' to I.S.). **Author contributions:** P.N. designed and coordinated the project. I.S. and S.S. coordinated quantum chemical calculations. C.M. coordinated the pump-probe experiments at the Alvra endstation. J.H. coordinated time-resolved spectroscopy. G.F.X.S. coordinated and supported crystallographic applications at SwissFEL and contributed to discussions throughout the project. S.M. expressed, purified, and crystallized *Nm*HR. S.M., A.F., D.K., and P.M. secured a constant supply of sample during the SFX beamtime. S.M. and D.J. optimized crystal injection. D.J., G.G., F.D., I.M., D.G., and P.S. operated and aligned the lipidic cubic phase injector during the beamtime. P.J., M.J., K.N., G.K., C.C., C.A., M.J., and C.M. aligned and operated the endstation, including the laser system, and designed the Alvra prime pump-probe station. D.O. and K.N. built and operated the SFX data analysis pipeline. T.W., C.M.C., and S.B. performed data processing during the beamtime. S.B., J.S., V.P., and M.W. recorded progress during data collection. J.S. supported P.N. in coordination of the experiment at SwissFEL. S.M. and P.N. optimized data processing. S.M., G.G., and P.N. refined and interpreted structures. S.S. and I.S. performed quantum-chemical calculations. D.E. and S.M. performed the time-resolved spectroscopic experiments and interpreted them together with J.H. E.P. synchronized diode and detector triggering at the synchrotron. D.J., F.D., and T.W. built the pump-probe setup at the synchrotron. S.M., G.G., P.N., and D.J. collected synchrotron data with suggestions on anomalous data collection and analysis from T.W. P.N. wrote the manuscript with direct contributions from S.M., G.G., D.E., J.H., S.S., and I.S. with further suggestions from most of the other authors. All authors read and approved the manuscript. **Competing interests:** The authors declare no competing interests. **Data and materials availability:** Resting-state coordinates and structure factors have been deposited in the PDB database under accession codes 708F (SFX), 708L (SSX), and 708Y (13.7 keV anomalous data). For the light-activated datasets, coordinates, light amplitudes, dark amplitudes, and extrapolated structure factors have been deposited in the PDB database under accession codes 708G (10 ps), 708H (10 ns), 708I (1 μs), 708J (20 μs), 708K (300 μs), 708M (2.5 ms), 708N (7.5 ms), 708O (12.5 ms), 708P (17.5 ms), 708Q (22.5 ms), 708R (27.5 ms), 708S (32.5 ms), 708T (37.5 ms), 708U (45 ms), 708V (55 ms), and 708Z (photostationary; 13.7 keV anomalous data). SFX raw data (*45*), SSX raw data (*46*), and 13.7 keV anomalous data (*47*) are available at the PSI Public Data Repository.

SUPPLEMENTARY MATERIALS

science.org/doi/10.1126/science.abj6663
Materials and Methods
Supplementary Text S1 to S3
Figs. S1 to S29
Tables S1 to S13
References (*48*–*81*)
Movie S1
MDAR Reproducibility Checklist

29 May 2021; accepted 26 January 2022
Published online 3 February 2022
10.1126/science.abj6663

NANOMATERIALS

Highly stretchable van der Waals thin films for adaptable and breathable electronic membranes

Zhuocheng Yan[1], Dong Xu[2], Zhaoyang Lin[1], Peiqi Wang[1], Bocheng Cao[1], Huaying Ren[1], Frank Song[1], Chengzhang Wan[1], Laiyuan Wang[2], Jingxuan Zhou[2], Xun Zhao[3], Jun Chen[3], Yu Huang[2,4]*, Xiangfeng Duan[1,4]*

The conformal integration of electronic systems with irregular, soft objects is essential for many emerging technologies. We report the design of van der Waals thin films consisting of staggered two-dimensional nanosheets with bond-free van der Waals interfaces. The films feature sliding and rotation degrees of freedom among the staggered nanosheets to ensure mechanical stretchability and malleability, as well as a percolating network of nanochannels to endow permeability and breathability. With an excellent mechanical match to soft biological tissues, the freestanding films can naturally adapt to local surface topographies and seamlessly merge with living organisms with highly conformal interfaces, rendering living organisms with electronic functions, including leaf-gate and skin-gate transistors. On-skin transistors allow high-fidelity monitoring and local amplification of skin potentials and electrophysiological signals.

The integration of electronic systems with irregular, soft objects is of increasing importance for many emerging technologies, including electronics for the Internet of Things and bioelectronics for monitoring dynamic living organisms and for diagnosing and treating human diseases in the context of personalized medicine and telehealth (*1*). A robust bioelectronic system requires intimate interaction with biological structures to perform specific operations, such as biological signal recording (*2*–*4*), amplification (*5*–*7*), and extraction (*8*), as well as delivering electrical (*9*, *10*) or chemical stimulation (*11*). Thus, the implementation of bioelectronics hinges on a number of unusual material and device characteristics, including electronic performance; mechanical flexibility, stretchability, or malleability to ensure conformal and adaptable interfaces with dynamically evolving microscopic surface topographies; and permeability or breathability for gas and/or nutrient exchange between living organisms and their surroundings to lessen perturbation of natural biofunctions.

Conventional hard electronic materials exhibit an intrinsic mismatch with soft biological tissues in terms of electrical conductivity, mechanical response, permeability, and environmental adaptability. Hard inorganic semiconductors can be made flexible in an ultrathin membrane format but are barely stretchable and cannot form a conformal interface with irregular geometries with nonzero Gaussian curvatures owing to their fundamental topological limitations (*12*). The development of specifically designed deformation-tolerant structures, such as wrinkled (*13*), buckled (*14*), waved (*15*), or serpentine structures (*16*–*18*), bring macroscopic stretchability but not microscopic conformability, because of the intrinsic microscopic structural undulation. Organic or composite semiconductor thin films can be made stretchable or conformal (*19*) but usually exhibit insufficient electronic performance (*12*, *20*) or limited stability in a typical wet biological environment.

Additionally, traditional inorganic membranes or organic thin films typically exhibit limited mechanical robustness in the ultrathin freestanding format and require a polymer [e.g., polydimethylsiloxane (PDMS) and polyimide (PI)] substrate support to retain structural integrity (*12*) and specific porous architecture design to achieve breathability (*21*). The polymer substrate is typically much thicker (≫1 μm) than a cell membrane (~10 nm), with a large bending stiffness (*22*) and poor conformability and adaptability to the dynamically evolving biological structures (*23*).

Inspired by van der Waals (VDW) interactions in biological assemblies, we exploited these interactions to assemble two-dimensional (2D) nanosheets (*24*–*27*) into freestanding VDW thin films (VDWTFs) with an excellent mechanical match to soft biological tissues that can directly adapt to and merge with living organisms with ultraconformal and breathable membrane–tissue interfaces. The VDWTFs feature bond-free VDW interfaces between the staggered 2D nanosheets, opening sliding and rotation degrees of freedom between neighboring nanosheets to endow unusual mechanical flexibility, stretchability, and malleability. The staggered VDWTFs also feature a percolating network of nanochannels for permeability or breathability.

Topological and mechanical limitations of a conformal interface

Although the flexibility of intrinsically stiff materials (e.g., a silicon wafer or hard cardboard) can be increased in the ultrathin membrane format (e.g., a silicon membrane or paper) (*28*), stretchability is fundamentally limited by the covalent chemical bonds and barely changes with reduced thickness (*29*). Owing to intrinsic topological limitations, it is impossible to use such flexible yet unstretchable membranes to make a conformal interface with local topographies with nonzero Gaussian curvatures (e.g., wrapping a piece of paper around a pen; Fig. 1A) (*30*). To achieve a conformal interface with irregular geometries, stretchability is essential to allow necessary deformation to adapt to the local surface topographies. Specific polymeric materials with intermolecular slippages between polymer chains can be made stretchable (*31*, *32*) and adaptable to local topographies under sufficient tensile stress (e.g., wrapping parafilm around a pen; Fig. 1B) (*29*).

To achieve a conformal interface with a stretchable membrane, external pressure is needed to induce sufficient deformation to match the local surface topography, which results in a contact pressure that can cause tissue deformation or damage (e.g., tightly wrapping parafilm around a fingertip). A 3D geometric model is constructed to visualize the conformal adapting process of a stretchable membrane on spherical topographies and to explore the evolution of the local deformation with the contact pressure (Fig. 1C). With increasing load, the membrane gradually adapts to the spherical indentations, with the membrane grid stretched and expanded to accommodate the local strain and deformation during the conformal adapting process.

We use a simplified spherical indentation model to evaluate the maximum contact pressure needed for forming a conformal interface with a surface topography of a given curvature. The indentation strain, ε, is given by

$$\varepsilon = k\frac{r_{\text{contact}}}{r_{\text{curve}}} \quad (1)$$

where r_{contact} and r_{curve} are the contact radius and the topography radius, respectively (Fig. 1D), and k is a constant associated with indentation strain (*33*). Overall, the contact radius and indentation strain increase with increasing load until a conformal interface between the membrane and the hemisphere is achieved. The maximum contact pressure needed for achieving a conformal interface is determined

[1]Department of Chemistry and Biochemistry, University of California, Los Angeles, CA 90095, USA. [2]Department of Materials Science and Engineering, University of California, Los Angeles, CA 90095, USA. [3]Department of Bioengineering, University of California, Los Angeles, CA 90095, USA. [4]California NanoSystems Institute, University of California, Los Angeles, CA 90095, USA.
*Corresponding author. Email: xduan@chem.ucla.edu (X.D.); yhuang@seas.ucla.edu (Y.H.)

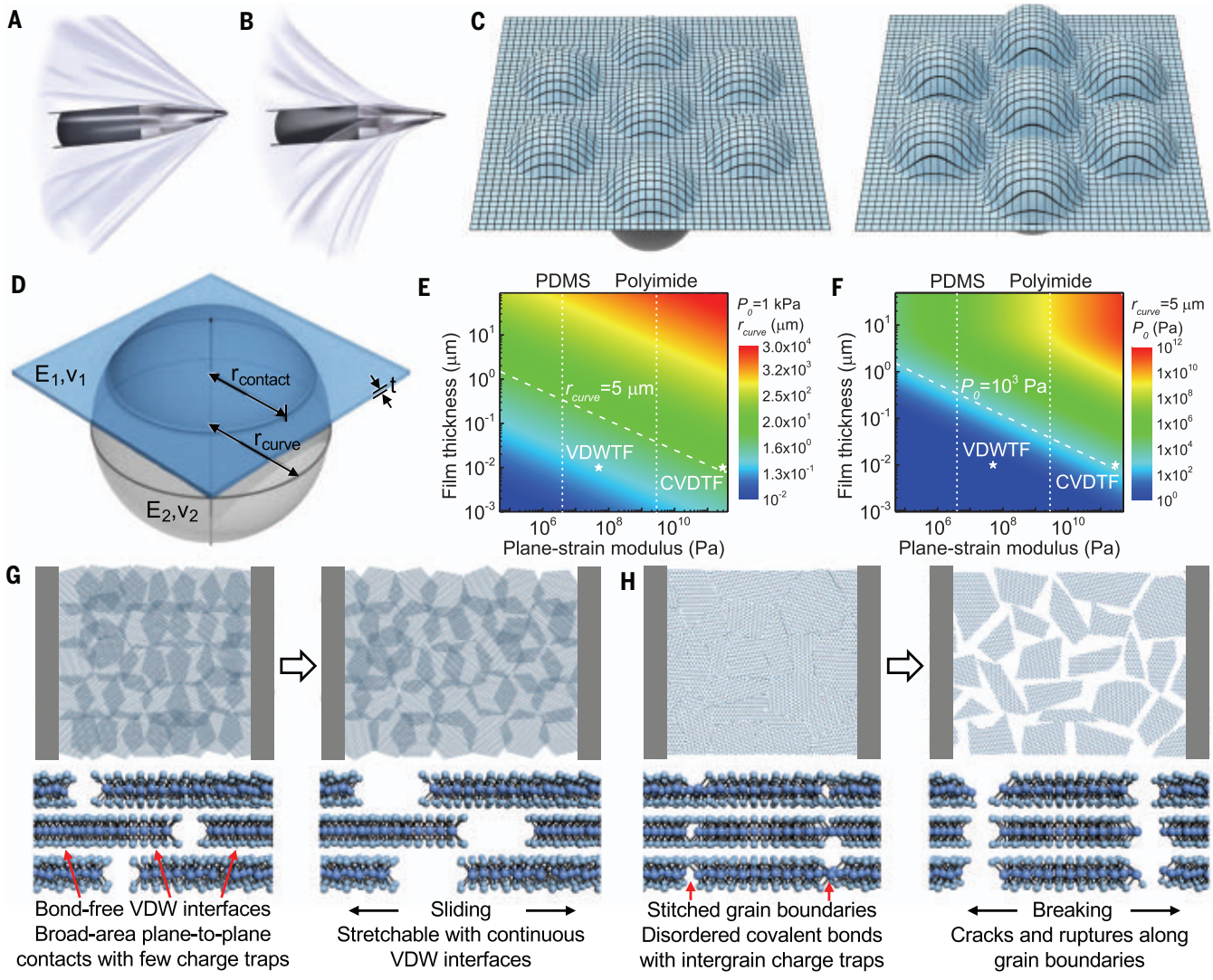


Fig. 1. Conceptual comparison of unstretchable and stretchable membranes. (**A** and **B**) Illustrations showing the wrapping of a piece of (A) unstretchable and (B) stretchable membrane around a pen. (**C**) Illustrations showing stretchable membranes with grid lines gradually conforming to a curved surface topography. (**D**) Diagram of a spherical indentation model and relevant parameters. (**E** and **F**) Contour maps showing the relationship between plane-strain modulus, film thickness, and (E) contact radius at a contact pressure of 1 kPa or (F) maximum contact pressure for a contact radius of 5 μm, highlighting that reducing thickness and plane-strain modulus favors a conformal interface. (**G** and **H**) Schematic diagram of (G) VDWTFs and (H) CVDTFs before and after stretching.

by the Young's modulus and the membrane thickness following the relationship

$$\left[\frac{\pi^2}{4}P_0^2\left(\frac{1-v_1^2}{E_1}+\frac{1-v_2^2}{E_2}\right)^2\right]^{1/3}+\frac{\pi^2}{8}P_0\left(\frac{1-v_1^2}{E_1}\right)\frac{{r_{\text{curve}}}^3}{t^3}=1 \quad (2)$$

where P_0 is the maximum contact pressure; E_1 and v_1 are the Young's modulus and Poisson's ratio of the membrane, respectively; t is the membrane thickness; and E_2 and v_2 are the Young's modulus and Poisson's ratio of the sphere, respectively (*34*, *35*). The $E/(1-v^2)$ is regarded as the plane-strain modulus, which is 130 kPa for human skin (*36*), 4 MPa for PDMS (*37*), and 2.8 GPa for polyimide (*22*). The difference in plane-strain modulus illustrates the large mechanical mismatch between human skin and the soft polymeric elastomer or typical plastics.

Using Eqs. 1 and 2, we can calculate the maximum film thickness allowed to achieve a conformal interface with a topography of a given r_{curve} under a certain contact pressure for materials with a different plane-strain modulus (Fig. 1E). For example, to achieve a conformal interface with a skin topography of $r_{\text{curve}} \sim 5$ μm under a maximum contact pressure P_0 of 1 kPa (the gentlest touch that a human can feel is 1 kPa) (*38*), the maximum allowed thickness is 0.3 μm for PDMS and 39 nm for polyimide. Similarly, we can also calculate the maximum contact pressure needed to form a conformal interface with a given r_{curve} of 5 μm for materials with a different plane-strain modulus and thickness (Fig. 1F).

These analyses highlight that the contact pressure needed to achieve a conformal interface is proportional to the Young's modulus and thickness of the membrane and inversely proportional to the curvature of the radius of the surface topography. Although, in principle, the contact pressure on biological tissue can be minimized by reducing membrane thickness, the thickness cannot be reduced indefinitely for most polymeric materials owing to the limitation of the characteristic size of individual polymer chains and a precipitous decrease in mechanical properties below a critical thickness (e.g., 25 nm) (*23*). Conducting polymers that are suitable for electronic

applications usually show worse mechanical properties owing to their specific structural properties, such as chain length, regioregularity, and degree of polymerization.

Adaptable and breathable VDWTFs

In our design of VDWTFs (Fig. 1G), the dangling bond–free nanosheets are staggered butted up against each other to establish broad-area plane-to-plane VDW contacts with minimum interfacial trapping states to ensure excellent charge transport across the intersheet grain boundaries. With the bond-free VDW interactions between the nanosheets, the VDWTFs offer a natural mechanical match to soft biological assemblies typically characterized by VDW interactions. When deformed, the bonding-free VDW interfaces allow nanosheets to slide or rotate against each other to accommodate the local tension or compression without breaking the broad-area VDW interfaces and conductive pathways (movie S1), which is essential for achieving unusual stretchability and structural stability in the ultrathin freestanding format. The mechanical deformation of VDWTFs is readily transformed into intersheet sliding or rotation to accommodate local strains and deformations and overcome topological limitations, thus endowing exceptional malleability and adaptability to irregular and dynamically changing surface topographies. Lastly, the VDWTFs feature a percolating network of nanochannels (dictated by nanosheet thickness: ~3 nm) winding around the staggered nanosheets for gas and/or nutrient permeation, which is critical for the breathability of bioelectronics (movie S2).

This combination of electronic and mechanical properties originates from the VDW interactions among the staggered 2D nanosheets and is difficult to achieve in typical chemical vapor deposition–grown thin films (CVDTFs) (Fig. 1H). The electrical and mechanical properties of CVDTFs—with their typical polycrystalline structure consisting of laterally stitched domains—are strongly influenced by the grain size, grain orientation, shape, and density of grain boundary defects. The stiff and strong covalent bonding within the grains and disordered bonds at the grain boundaries of the CVDTFs (marked with red arrows in Fig. 1H) can result in the formation of cracks and ruptures that propagate along the grain boundaries when they are deformed, thereby causing mechanical fragmentation and electronic disintegration under minimal strain (movie S1).

Structural and mechanical properties of VDWTFs

Molybdenum disulfide (MoS_2) nanosheet ink was prepared using an intercalation-exfoliation process and assembled into VDWTFs using a spin coating process (see supplementary materials). Scanning electron microscopy (SEM) and transmission electron microscopy (TEM) studies show a staggered nanosheet thin film (Fig. 2, A and B) with an overall film thickness of ~10 nm (fig. S1A). The MoS_2 nanosheets, with a thickness of ~3 nm and lateral dimensions ranging from less than one to several micrometers, are staggered butted up against each

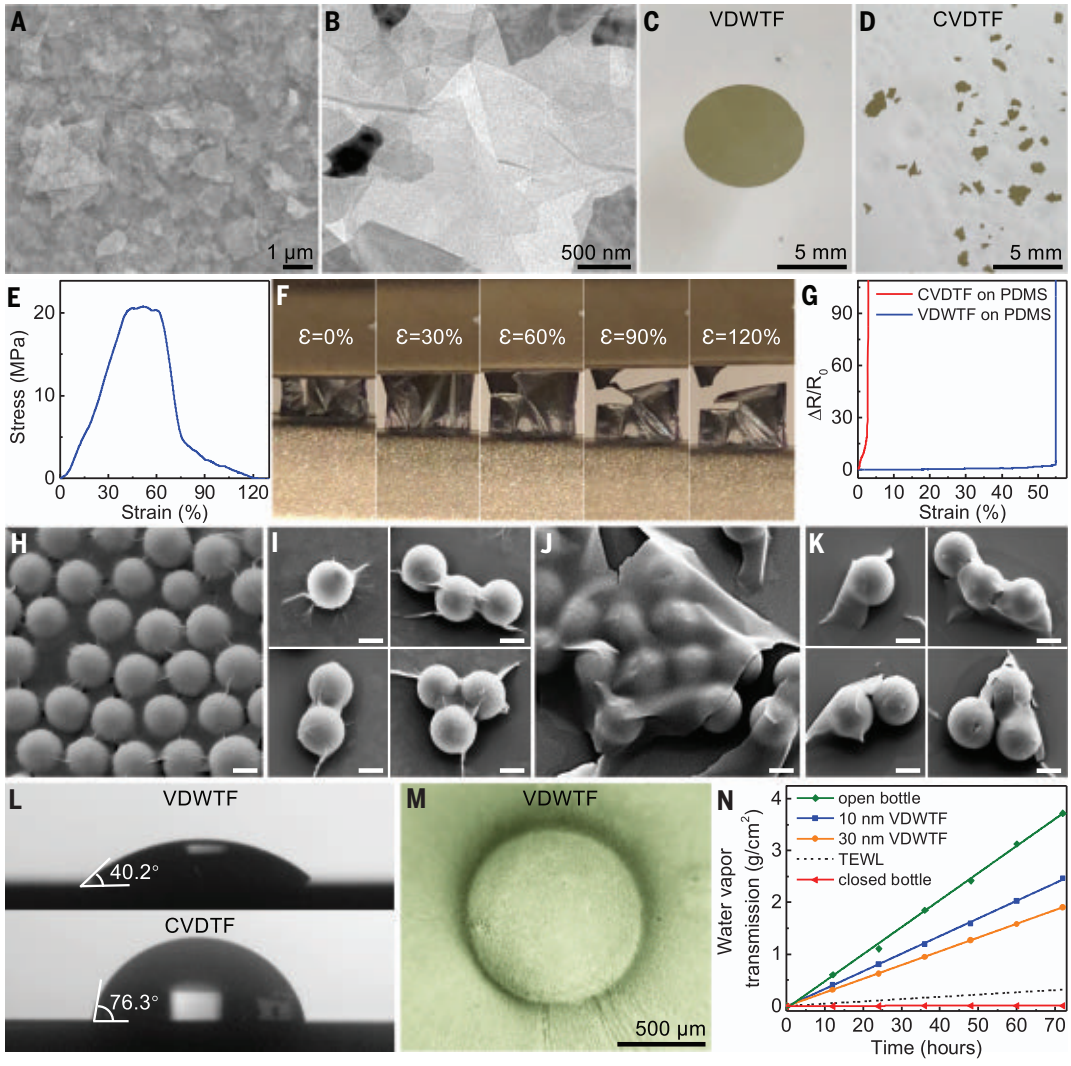


Fig. 2. Material characteristics of VDWTFs and CVDTFs. (**A**) SEM and (**B**) TEM images showing VDWTFs assembled from staggered 2D nanosheets. (**C** and **D**) Photograph of the (C) VDWTFs and (D) CVDTFs floating on water. (**E**) Stress–strain curve of a freestanding VDWTF. Tensile loads cause 2D nanosheets in VDWTFs to slide or rotate against each other, resulting in unusual stretchability. (**F**) Photographs of the VDWTF at different tensile strains. (**G**) Resistance–strain curve of the VDWTF and CVDTF on a PDMS substrate. (**H** to **K**) SEM images showing the contact interface between the 4.3-μm-diameter silica microspheres of different configurations with [(H) and (I)] VDWTFs or [(J) and (K)] CVDTFs. Scale bars, 2 μm. (**L**) Water contact angles of a VDWTF (top) and a CVDTF (bottom). (**M**) Optical micrographs of a VDWTF suspended over a polyimide substrate with circular holes, confirming structural robustness of the freestanding VDWTFs. (**N**) Water vapor transmission through VDWTFs of different thickness versus transepidermal water loss (TEWL). See the supplementary materials for a description of the "open bottle" and "closed bottle" conditions.

other to form broad-area plane-to-plane VDW interfaces with an average of ~3 to 4 nanosheets staggered in a crisscross manner in the vertical direction. The broad-area bond-free VDW interfaces allow adjacent nanosheets to slide or rotate against each other to accommodate local structural perturbation and reduce the strain-induced cracks and fractures, thus ensuring structural integrity even in the freestanding format. For example, the continuous freestanding VDWTFs can be readily floated on water (Fig. 2C and movie S3), completely folded repeatedly without tearing (movie S4), and suspended over open holes without rupturing (Fig. 2M). In comparison, the freestanding polycrystalline CVDTFs (fig. S1B) easily fragment on water (Fig. 2D and movie S3) and are too fragile to suspend over open holes (fig. S2).

The stress–strain curve of the freestanding VDWTFs shows a well-behaved linear relationship up to a tensile strain of 43% (Fig. 2E), with a Young's modulus (~47.3 MPa) about three orders of magnitude smaller than that of bulk MoS_2 (~200 GPa). The greatly reduced modulus indicates that the film deformation is transformed into interlayer sliding or rotation among nanosheets rather than an intrinsic lattice expansion (Fig. 2F). Beyond the linear regime, the stress shows little increase with further increasing of the tensile strain to ~62%, indicating that interlayer sliding or rotation gradually reaches the limit and begins to initiate local rupture, which further aggravates at higher tensile strain and leads to complete rupture at a tensile strain of >120%.

We compared the electronic properties of the VDWTFs and CVDTFs as a function of the applied strain (Fig. 2G). Because CVDTFs cannot maintain macroscopic structural integrity in the freestanding form, the measurement was done on films supported on PDMS substrates to ensure a robust comparison. For CVDTFs, the relative resistance exhibits a gradual linear increase at a tensile strain of <2.5%, followed by a steep increase beyond 2.5%, indicating that the CVDTFs start to macroscopically break apart. In contrast, the VDWTFs do not exhibit a rapid resistance increase until a tensile strain of >55%, with a stable recoverable resistance under repeated strain cycles (fig. S3). When the tensile strain is >55%, the resistance increases sharply, indicating the formation of microscopic cracks and substantially reduced conductive pathways.

Adaptability, wettability, and permeability of VDWTFs

We evaluated the adaptability and conformability of the VDWTFs to microscopic surface topographies. SEM studies revealed that the VDWTFs exhibit highly conformal interfaces with not only the microsphere (4.3-μm-diameter) arrays (Fig. 2H) but also the isolated single microspheres, two- or three-microsphere clusters (Fig. 2I), conformally wrapping around the microspheres without tearing. By comparison, the CVDTFs on the same surface topography are much less conformal and show abundant microcracks (Fig. 2, J and K), particularly at the high strain or stress concentration region (e.g., the foot of the microspheres or the space between two adjacent microspheres).

Surface wettability is essential for ensuring proper adhesion between electronic membranes and living organisms (Fig. 2L). With abundant edge structures in individual nanosheet building blocks, the VDWTFs exhibit better wettability (with a water contact angle of 40.2°) than CVDTFs (water contact angle of 76.3°), which is desirable for intimately interfacing with wet biological tissues.

Lastly, membrane permeability or breathability is required for gas or nutrient exchange with the environment in bioelectronic applications. Water vapor transmission studies (see supplementary materials) reveal water vapor transmission rates of 34 and 26 mg cm^{-2} $hour^{-1}$ for the 10-nm-thick and 30-nm-thick freestanding VDWTFs, respectively, suspended over an open hole (Fig. 2, M and N), about six to eight times higher than the typical transepidermal water loss (TEWL) rate (4.4 mg cm^{-2} $hour^{-1}$) (*39*). Such permeability of the continuous VDWTFs is attributed to the staggered nanosheet structures, with a highly interconnected network of nanochannels (with the channel thickness dictated by the nanosheet thickness: ~3 nm) winding around the staggered nanosheets (movie S2).

Leaf-gate VDWTF transistors

Given their exceptional stretchability, conformability, and breathability, the VDWTFs can directly merge with living organisms to form seamless electronic-bio hybrids. Whereas previous attempts sought to augment plant function with electroactive materials or to simply use the plant as an unconventional supporting substrate, our approach was to transfer the VDWTFs onto a leaf to form a leaf-gate transistor, in which the plant leaf functions as a modulating gate and constitutes an active part of the device. We chose the *Senecio mandraliscae* leaf (Fig. 3A), which contains abundant electrolyte in mesophyll, as a model system to study the leaf-gate transistors. For the leaf-gate transistor operations (Fig. 3B), the VDWTF channel is contacted with serpentine-mesh Au electrodes (Fig. 3C, top) to prevent breaking of the Au thin-film electrodes by local strain on the rough leaf surface, while an inserted tungsten probe establishes electrical contact to the electrolyte within the leaf to form the gate electrode. The transferred VDWTFs form a highly conformal interface with complete compliance, as confirmed by the optical microscopy (Fig. 3D) and SEM studies (Fig. 3E).

The function of the leaf-gate transistor relies on the ionic gating effect (in the electrolyte of the leaf gate) to modulate the electronic properties of the VDWTFs, for which the microscopically conformal interface is essential for efficient gating. The leaf-gate transistor shows a typical *n*-channel transfer curve with an on/off ratio of ~100 (Fig. 3, F to H). The relatively low on/off ratio is limited by the direct leakage into the transistor channel from the leaf gate through direct resistive coupling. With a highly conformal interface and efficient gate coupling, the leaf-gate transistor can operate at a low operating voltage amenable to biological systems.

Skin-gate VDWTF transistors

VDWTFs can be transferred onto human skin with a highly conformal interface to form skin-gate transistors (fig. S4). In the skin, electrolytes help conduct electricity, regulate pH levels, and keep the body's hydration system in check. The conformal integration of VDWTFs with the skin textures (fig. S5, A to C) results in skin-gate transistors in which the electrolyte in human skin effectively modulates the conduction in VDWTFs (Fig. 4, A and B). Proper skin-gate transistor function requires a conformal interface with an intimate interaction between the VDWTF channel and the epidermis, in which the epidermis can be modeled by a parallel circuit consisting of a capacitor and a resistor, and the dermis and underlying subcutaneous tissues modeled by a resistor (Fig. 4B).

We investigated the conformability of the freestanding VDWTFs on a forearm skin replica made of Ecoflex silicone rubber and compared it with the same VDWTF supported on a 1.6-μm-thick PI substrate (Fig. 4C). The freestanding VDWTF adapts to the skin textures and makes an excellent conformal interface without apparent cracking or tearing. In contrast, the 1.6-μm-thick PI substrate and the VDWTF with the PI substrate show much less conformal contact, with most of the fine skin textures, such as the surface wrinkles and pits, hidden (Fig. 4C, right side). A profilometry height profile analysis shows that surface topography of the skin replica covered with the freestanding VDWTF is essentially the same as that without the VDWTF (Fig. 4, D and E), suggesting a fully conformal interface. In contrast, for the area covered with the VDWTF supported by the 1.6-μm-thick PI substrate (Fig. 4, F and G), the surface topography is largely flattened, suggesting that the 1.6-μm-thick PI substrate is already too thick to naturally adapt to the skin textures to form microscopically conformal interfaces.

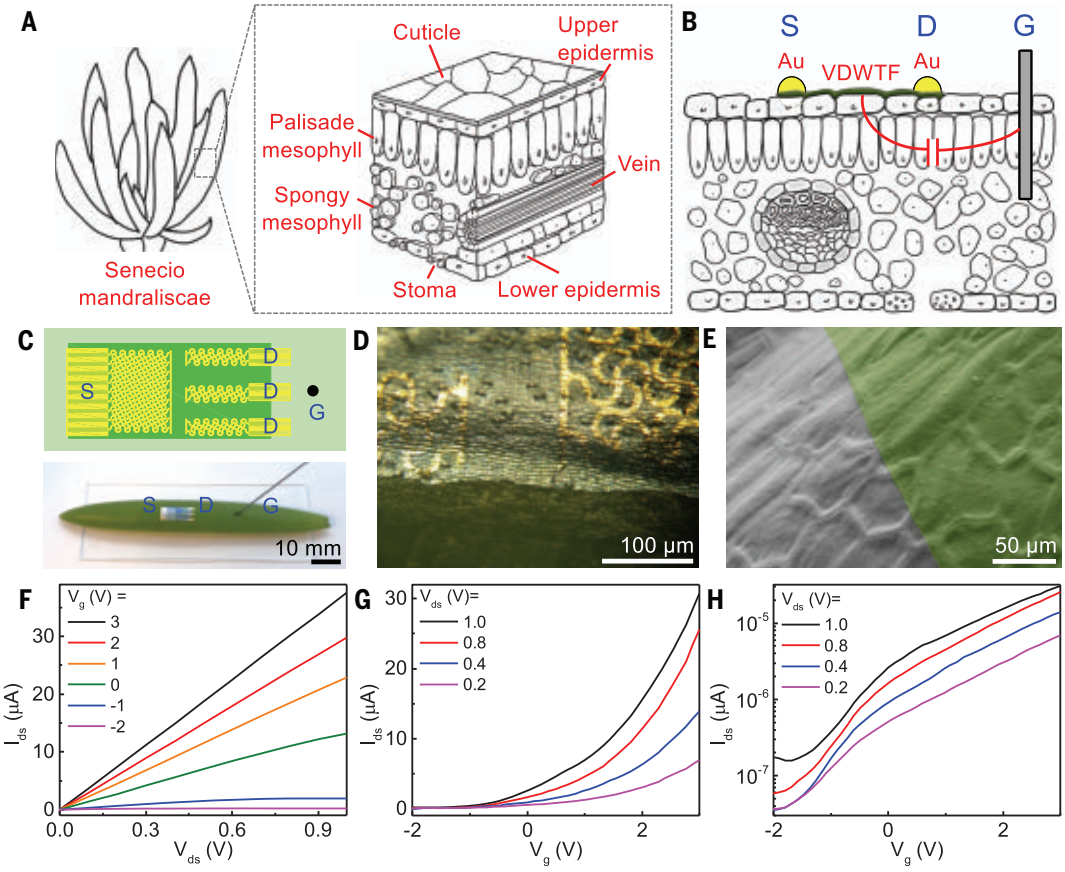


Fig. 3. Leaf-gate VDWTF transistors. (**A**) Diagram of a *Senecio mandraliscae* leaf. (**B**) Cross-sectional view of the leaf-gate transistor with Au source and drain electrodes ("S" and "D," respectively) and an inserted tungsten gate electrode ("G"). (**C**) Schematic illustration (top; leaf, light green; VDWTF, dark green; Au electrodes, yellow; tungsten probe, black dot) and photograph of the leaf-gate transistor (bottom). (**D**) Optical image of a VDWTF with serpentine Au electrodes transferred onto the plant leaf. (**E**) Colorized SEM image of the VDWTF on the leaf. (**F**) Output characteristics of a leaf-gate transistor. V_{ds}, drain-source voltage; I_{ds}, drain-source current. (**G** and **H**) Transfer curves with (G) linear and (H) logarithmic axis. V_g, gate voltage.

The ability of a membrane to make a conformal interface with the surface topography can be determined by bending stiffness (*22*). The effective bending stiffness (*EI*) for a multilayer membrane can be described as

$$EI = \sum_{i=1}^{N} \frac{E_i}{1-v_i^2} h_i \left\{ \frac{1}{3}h_i^2 + \left[\left(\sum_{j=1}^{i} h_j \right) - h_{\text{neutral}} \right]^2 - h_i \left[\left(\sum_{j=1}^{i} h_j \right) - h_{\text{neutral}} \right] \right\} \quad (3)$$

$$h_{\text{neutral}} = \frac{\sum_{i=1}^{N} \frac{E_i}{1-v_i^2} h_i \left[\left(\sum_{j=1}^{i} h_j \right) - \frac{1}{2}h_i \right]}{\sum_{i=1}^{N} \frac{E_i}{1-v_i^2} h_i} \quad (4)$$

where h_{neutral} denotes the neutral mechanical plane; i represents the ith layer of the film; h_i, E_i, and v_i represent the thickness, the elastic modulus, and Poisson's ratio, respectively; and N is the number of layers (*40*). Notably, with its ultrasmall thickness and low elastic modulus, the freestanding 10-nm-thick VDWTF exhibits a bending stiffness of 4.2×10^{-9} GPa·μm^3, which is about eight orders of magnitude smaller than that of the 1.6-μm-thick VDWTF/PI film (0.97 GPa·μm^3).

The VDWTFs transferred onto human skin show excellent natural adaptability to changing skin textures and retain conformal contact without apparent fracturing or flaking throughout stretching, squeezing, and relaxing cycles (Fig. 4H), highlighting the highly adaptable nature of the VDWTFs to dynamically evolving biological substrates. In contrast, the CVDTFs transferred onto human skin easily fracture and flake off when the skin is subjected to similar deformation. Figure 4I shows the remaining area of both films on the skin replica versus the number of squeezing-and-stretching cycles. Because the freestanding CVDTFs are not strong enough for processing and transferring, they are transferred onto the skin replica with methyl methacrylate (MMA) support. After the transfer process, the CVDTFs quickly flake off once the MMA is dissolved away with acetone vapor. The remaining area instantly decreases to ~50% of the original area and, after 100 stretching cycles, further decreases to 40% of the original area, with mostly fractured domains. The fracturing and flaking are attributed to the unstable membrane–skin interface, which is associated with their limited stretchability, conformability, and poor wettability. In contrast, the VDWTFs show superior stretchability and conformability to the dynamically changing skin replica with no apparent fracturing or flaking, retaining essentially 100% surface coverage after the repeated squeezing-and-stretching cycles.

The output and transfer curves of the skin-gate VDWTF transistor demonstrate expected transistor functions (Fig. 4, J and K) with a low operating voltage suitable for biological systems. Furthermore, the skin-gate VDWTF transistor can maintain stable operation while undergoing various mechanical deformations (Fig. 4L), establishing a foundation for applications in probing and amplifying electrophysiological signals.

Monitoring electrophysiological signals with skin-gate VDWTF transistors

Given that many biopotential signals show transient responses, we have evaluated the frequency response of the skin-gate transistors. The response times, τ, of the skin-gate transistors are probed by measuring the current response under a 20-μs pulse of 100-mV gate voltage (Fig. 5A). A response time of 7 μs is achieved by fitting experimental data with an exponential function (Fig. 5B). Furthermore, the skin-gate transistors show a cut-off frequency (at which the transconductance drops by 3 dB from its plateau value) of ~100 kHz (Fig. 5C), which is sufficient for monitoring most electrophysiological signals from the human body.

We explored the skin-gate VDWTF transistors for monitoring electrocardiography (ECG).

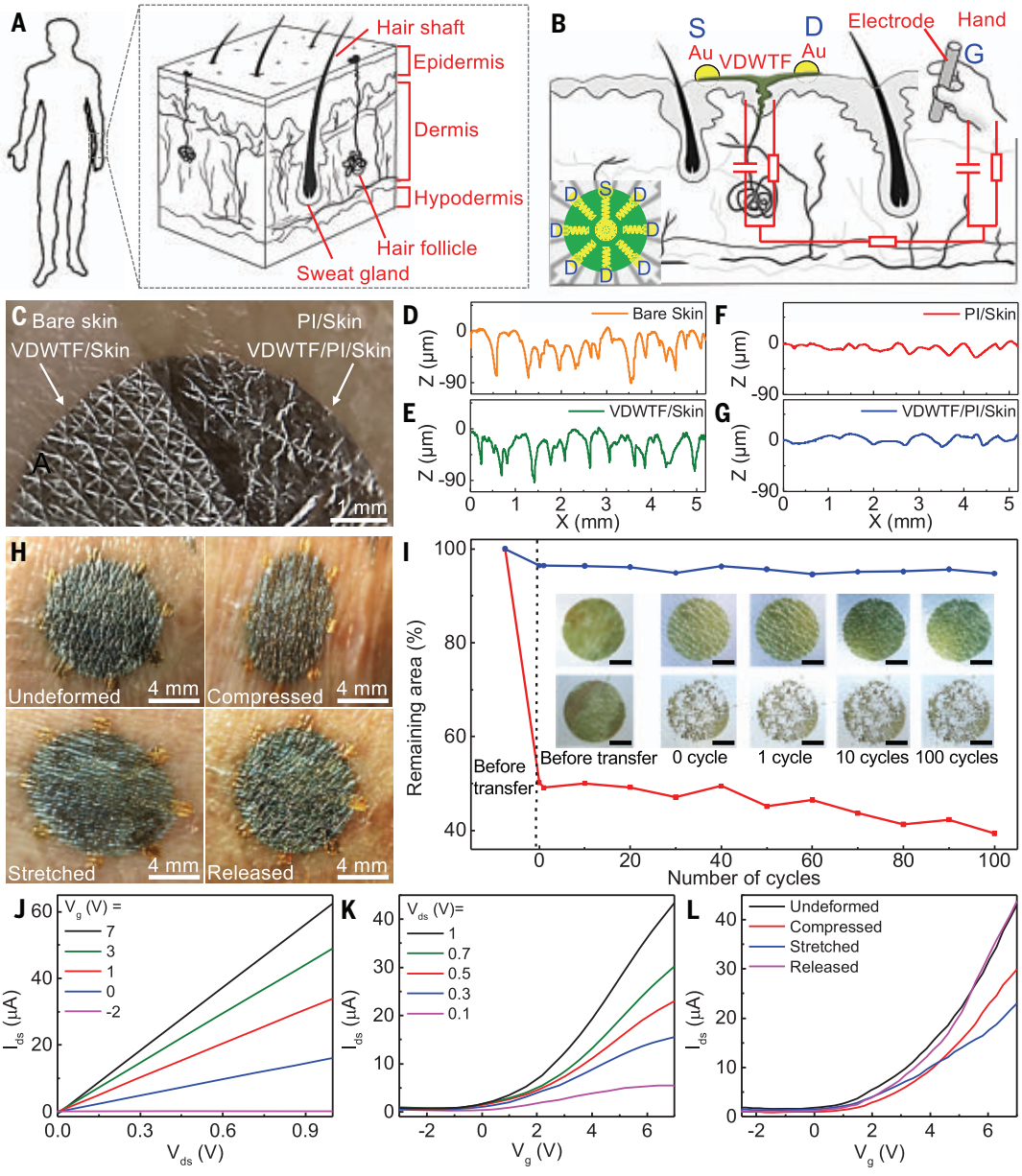


Fig. 4. Skin-gate VDWTF transistors. (**A**) The structure of human skin. (**B**) Schematic of a skin-gate VDWTF transistor with Au source and drain electrodes and an iron rod gate electrode held by a human subject. (**C**) Photograph of the freestanding VDWTF on a replica of human skin (left) and the VDWTF supported by a 1.6-μm-thick polyimide substrate on a replica of human skin (right). (**D** to **G**) Height profiles corresponding to the line scan in different areas of (C). (**H**) Skin-gate VDWTF transistor on human skin under different types of mechanical deformation. (**I**) Remaining area of VDWTFs and CVDTFs on skin replicas as a function of stretching cycles (10% tensile strain). Scale bars, 2 mm. (**J**) Output and (**K**) transfer curves of a skin-gate VDWTF transistor. (**L**) Transfer curves under different types of deformation.

In this measurement, the VDWTF pad is placed on the left forearm and the gate electrode is adhered on the symmetrical position (right forearm) (Fig. 5D), and each VDWTF pad works with an Ag/AgCl electrode nearby for comparison. Among the common challenges in measuring ECG with conventional Ag/AgCl electrodes are the motion artifacts due to sliding, inconsistent adhesion, and a mechanical mismatch at the electrode–skin interface induced by skin deformation, leading to a greatly reduced signal-to-noise ratio (SNR), from 44.3 dB before motion (Fig. 5E) down to 28.5 dB during motion (Fig. 5, F and G). With the conformal skin-gate transistors, motion artifacts are mitigated, achieving an essentially comparable SNR of 49.8 dB before human motion (Fig. 5E and fig. S6) and 49.2 dB during human motion (Fig. 5, F and G). With reduced motion artifacts, the ECG signals recorded by the skin-gate transistors (red line) show clear P, QRS, and T waves, with no abnormal deviations and relatively stable baseline during human motion (Fig. 5, F and G). In contrast, such fine signals are less resolvable by the Ag/AgCl electrodes (Fig. 5G).

High-fidelity, real-time electroencephalogram (EEG) recording is important for monitoring cerebral activities, studying cognitive behaviors, and developing insights into various neurological disorders. Cerebral activities can be divided into five frequency bands: delta wave (0 to 4 Hz), theta wave (4 to 8 Hz), alpha wave (8 to 12 Hz), beta wave (12 to 30 Hz), and gamma wave (>30 Hz), with each frequency band associated with different mental states. To test the ability to acquire high-quality neurophysiological signals, we placed the VDWTF transistor over the left side of the forehead (Fp1) according to the international 10-20 system of EEG electrode placement (*17*) and recorded voltage differences relative to a reference electrode placed over the left occipital region (O1) (Fig. 5H). When the human subject is relaxed with eyes closed, the EEG background is usually characterized by the posteriorly dominant alpha rhythm (posterior dominant rhythm) with a prominent 8- to 12-Hz (alpha) oscillation (Fig. 5, I and J), corresponding to brain activities such as meditation and mindfulness that can reduce stress levels. The alpha rhythm typically attenuates considerably upon eye opening, as clearly seen in the spectrogram of the EEG

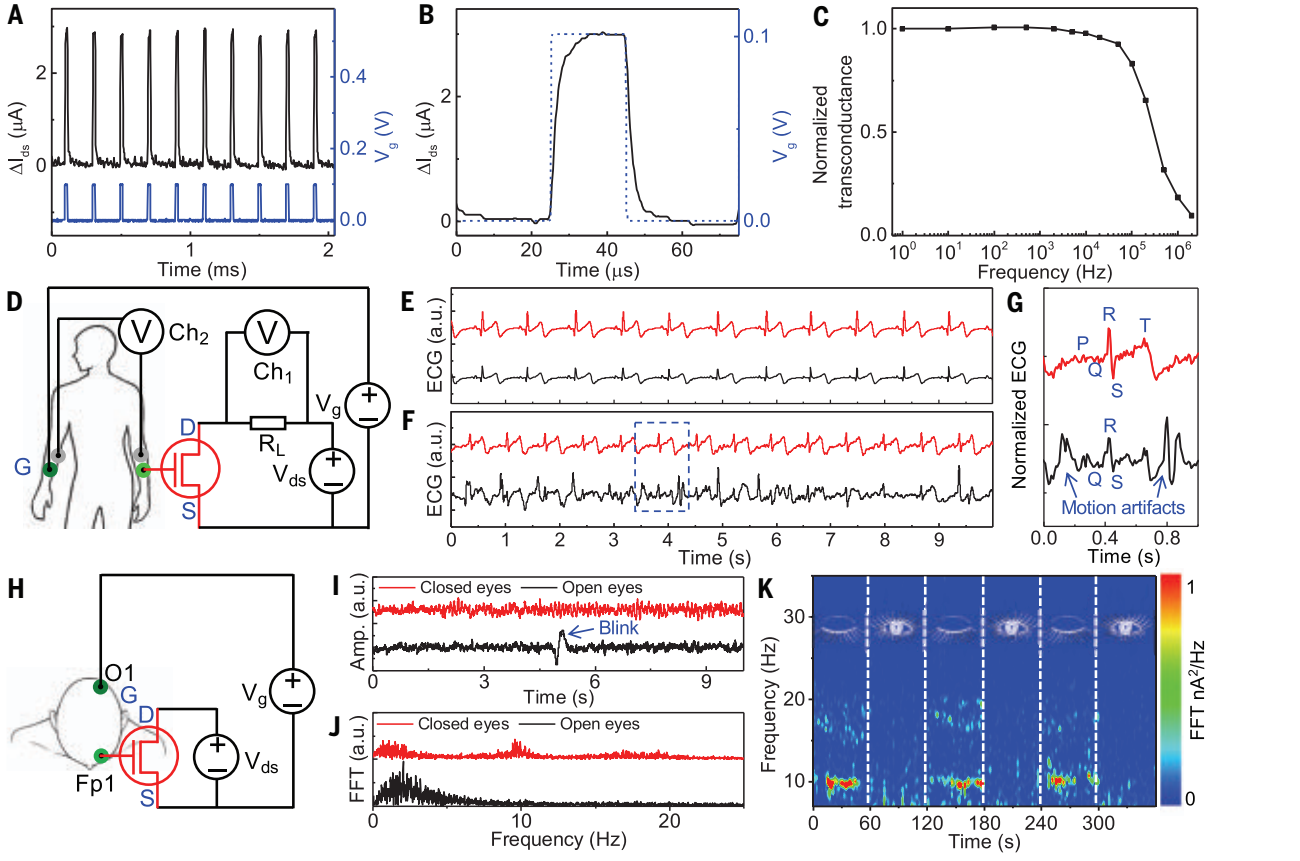


Fig. 5. Skin-gate VDWTF transistors for monitoring transient skin potentials. (**A**) Relative drain current (ΔI_{ds}) of a skin-gate VDWTF transistor stimulated by 5 kHz 0.1-V 20-μs-wide gate pulses at a V_{ds} of 0.1 V. (**B**) The response time of the skin-gate VDWTF transistor to a square gate pulse (blue dashed line). (**C**) Normalized transconductance at various frequencies. (**D**) Schematic diagram of the ECG measurement with a V_{ds} of 0.5 V and a V_g of 0.5 V. (**E** and **F**) The ECG signals measured by the skin-gate transistor (red line) and Ag/AgCl electrode (black line) (E) before and (F) during human exercise. a.u., arbitrary units. (**G**) Zoomed-in view of boxed portion in (F), showing clear P, QRS, and T waves from the skin-gate transistor but only a QRS wave and motion artifacts from the Ag/AgCl electrodes. (**H**) Schematic diagram of the EEG measurement. (**I**) Recorded EEG signals using a skin-gate transistor when a human subject was engaged in two mental states (closed eyes and open eyes). Eye blink artifacts are also visible. (**J**) Fast Fourier transform (FFT)–processed frequency distributions of the EEG signals in (I). (**K**) Time-frequency spectrograms of the EEG signals recorded during cyclic eye closing and opening, showing dynamic activity of the alpha rhythm at ~10 Hz.

signal measured by the skin-gate transistor (Fig. 5K), showing the dynamic activity of the alpha rhythm coupled with cyclic eye closing and opening.

Conclusions

Here, we report on mechanically robust freestanding VDWTFs assembled from 2D nanosheets for highly stretchable, adaptable, conformal, and breathable membrane electronics. The bond-free VDW interfaces among the nanosheets enable sliding and rotating degrees of freedom to render extraordinary mechanical flexibility, stretchability, and malleability. The staggered nanosheet architecture also features a percolation network of nanochannels for excellent permeability or breathability. The ultrathin freestanding VDWTFs are structurally robust with an excellent mechanical match to soft biological tissues, naturally adapting to microscopic topographies and directly integrating with living organisms through highly conformal interfaces, endowing living organisms with electronic functions. The VDWTFs can thus function as versatile electronic membranes that actively adapt to the environment while retaining sufficient electronic performance for sensing, signal amplification, processing, and communication.

REFERENCES AND NOTES

1. G. D. Spyropoulos, J. N. Gelinas, D. Khodagholy, *Sci. Adv.* **5**, eaau7378 (2019).
2. I. You *et al.*, *Science* **370**, 961–965 (2020).
3. F. Ershad *et al.*, *Nat. Commun.* **11**, 3823 (2020).
4. Q. Li *et al.*, *Nano Lett.* **19**, 5781–5789 (2019).
5. S. Wang *et al.*, *Nature* **555**, 83–88 (2018).
6. K. Sim *et al.*, *Sci. Adv.* **5**, eaav5749 (2019).
7. E. Stavrinidou *et al.*, *Sci. Adv.* **1**, e1501136 (2015).
8. K. Kwon *et al.*, *Nat. Electron.* **4**, 302–312 (2021).
9. J. Koo *et al.*, *Nat. Med.* **24**, 1830–1836 (2018).
10. M. Han *et al.*, *Nat. Biomed. Eng.* **4**, 997–1009 (2020).
11. M. Bariya, H. Y. Y. Nyein, A. Javey, *Nat. Electron.* **1**, 160–171 (2018).
12. J. A. Rogers, R. Ghaffari, D.-H. Kim, Eds., *Stretchable Bioelectronics for Medical Devices and Systems* (Springer, 2016).
13. S. H. Chae *et al.*, *Nat. Mater.* **12**, 403–409 (2013).
14. J. Yoon *et al.*, *Nat. Mater.* **7**, 907–915 (2008).
15. D.-Y. Khang, H. Jiang, Y. Huang, J. A. Rogers, *Science* **311**, 208–212 (2006).
16. D.-H. Kim *et al.*, *Science* **333**, 838–843 (2011).
17. L. Tian *et al.*, *Nat. Biomed. Eng.* **3**, 194–205 (2019).
18. Z. Huang *et al.*, *Nat. Electron.* **1**, 473–480 (2018).
19. J. Rivnay *et al.*, *Nat. Rev. Mater.* **3**, 17086 (2018).
20. Y. Fang, X. Li, Y. Fang, *J. Mater. Chem. C* **3**, 6424–6430 (2015).
21. L. Cai *et al.*, *Nat. Commun.* **8**, 496 (2017).
22. Z. Yan *et al.*, *Adv. Sci.* **4**, 1700251 (2017).
23. Y. Liu *et al.*, *Macromolecules* **48**, 6534–6540 (2015).
24. J. N. Coleman *et al.*, *Science* **331**, 568–571 (2011).
25. Z. Lin *et al.*, *Nature* **562**, 254–258 (2018).
26. Z. Lin, Y. Huang, X. Duan, *Nat. Electron.* **2**, 378–388 (2019).
27. D. McManus *et al.*, *Nat. Nanotechnol.* **12**, 343–350 (2017).
28. J. W. Jeong *et al.*, *Adv. Mater.* **25**, 6839–6846 (2013).
29. J. A. Rogers, T. Someya, Y. Huang, *Science* **327**, 1603–1607 (2010).
30. Y.-K. Lee *et al.*, *Sci. Adv.* **6**, eaax6212 (2020).
31. C. E. Carraher Jr., *Giant Molecules: Essential Materials for Everyday Living and Problem Solving* (Wiley, ed. 2, 2003).
32. Y.-Q. Zheng *et al.*, *Science* **373**, 88–94 (2021).
33. B. Xu, X. Chen, *J. Mater. Res.* **25**, 2297–2307 (2010).
34. O. Scott, M. Begley, U. Komaragiri, T. Mackin, *Acta Mater.* **52**, 4877–4885 (2004).

35. X. Fang, C. Zhang, X. Chen, Y. Wang, Y. Tan, *Acta Mech.* **226**, 1657–1672 (2015).
36. S. Wang *et al.*, *J. Appl. Mech.* **79**, 031022 (2012).
37. Y. Yu, D. Sanchez, N. Lu, *J. Mater. Res.* **30**, 2702–2712 (2015).
38. J. J. Boland, *Nat. Mater.* **9**, 790–792 (2010).
39. J. Kottner, A. Lichterfeld, U. Blume-Peytavi, *Arch. Dermatol. Res.* **305**, 315–323 (2013).
40. T. Pan *et al.*, *Adv. Funct. Mater.* **27**, 1702589 (2017).

ACKNOWLEDGMENTS

We acknowledge the Electron Imaging Center at UCLA for STEM and TEM technical support, as well as the Nanoelectronics Research Facility at UCLA for device fabrication technical support. We thank M. Liu for chemical vapor deposition thin-film samples and Sphere Studio for assistance with animations in movies S1 and S2. **Funding:** X.D. acknowledges the UCLA Physical Sciences Entrepreneurship and Innovation Fund and partial support from CNSI Noble Family Innovation Fund. **Author contributions:** X.D. and Y.H. conceived of the research. X.D. and Z.Y. designed all experiments. Z.Y. fabricated the electronic devices and analyzed the results. Z.Y., Z.L., D.X., and F.S. fabricated the solution-processable VDWTFs. D.X. and P.W. assisted with the electronic device fabrication. Z.Y. and P.W. performed the electronic measurements. Z.Y., J.Z., and D.X. conducted the mechanical measurements. Z.Y., B.C., Z.L., and C.W. performed the electron microscopy analyses on VDWTFs. Z.Y. and D.X. conducted the test of water vapor transmission rate for VDWTFs. Z.Y. and H.R. took optical images for organism-gated electronic devices. Z.Y., D.X., P.W., X.Z., and J.C. conducted and participated in the on-body measurements. L.W., H.R., and P.W. assisted with e-beam evaporation. X.D. and Z.Y. co-wrote the paper. X.D. and Y.H. supervised the research. All authors discussed the results and commented on the manuscript. **Competing interests:** A provisional patent application (no. 63/308,028) has been filed on the stretchable van der Waals thin films. The authors declare no other competing interests. **Data and materials availability:** All data are available in the manuscript or the supplementary materials.

SUPPLEMENTARY MATERIALS

science.org/doi/10.1126/science.abl8941
Materials and Methods
Supplementary Text
Figs. S1 to S7
References
Movies S1 to S4

12 August 2021; accepted 20 January 2022
10.1126/science.abl8941

REPORTS

IMMUNOLOGY

Trained ILC3 responses promote intestinal defense

Nicolas Serafini[1], Angélique Jarade[1], Laura Surace[1], Pedro Goncalves[1], Odile Sismeiro[2], Hugo Varet[2,3], Rachel Legendre[2,3], Jean-Yves Coppee[2], Olivier Disson[4], Scott K. Durum[5], Gad Frankel[6], James P. Di Santo[1]*

Group 3 innate lymphoid cells (ILC3s) are innate immune effectors that contribute to host defense. Whether ILC3 functions are stably modified after pathogen encounter is unknown. Here, we assess the impact of a time-restricted enterobacterial challenge to long-term ILC3 activation in mice. We found that intestinal ILC3s persist for months in an activated state after exposure to *Citrobacter rodentium*. Upon rechallenge, these "trained" ILC3s proliferate, display enhanced interleukin-22 (IL-22) responses, and have a superior capacity to control infection compared with naïve ILC3s. Metabolic changes occur in *C. rodentium*–exposed ILC3s, but only trained ILC3s have an enhanced proliferative capacity that contributes to increased IL-22 production. Accordingly, a limited encounter with a pathogen can promote durable phenotypic and functional changes in intestinal ILC3s that contribute to long-term mucosal defense.

Specialized immune cells promote barrier function and maintain microbial tolerance at mucosal surfaces (*1*); these include effector and memory T cells that provide long-term immune-surveillance and recall responses as well as diverse innate lymphoid cells (ILCs) (*2*, *3*). Group 3 ILCs (ILC3s) are highly enriched in the gut where they orchestrate lymphoid tissue development and mucosal defense (*3*, *4*). Largely devoid of pattern recognition receptors (*5*), ILC3s are indirectly activated after infection by soluble factors [interleukin-1β (IL-1β) and IL-23] derived from epithelial and hematopoietic sentinel cells (*4*) and, in turn, secrete IL-17 and IL-22 to protect the host (*6*–*9*). ILC3s are active during fetal lymphoid tissue organogenesis (*10*, *11*), and initial encounters with microbial flora in early postnatal life modifies ILC3 subset distribution and cytokine production (*6*, *12*). Whether ILC3s exhibit any degree of long-term adaptation to a commensal or pathogen encounter that results in heightened immunological function remains to be demonstrated.

To study whether persistent functional changes occur in intestinal ILC3s after microbial encounter, we used *Citrobacter rodentium*, a mouse pathogen that provokes an enterocolitis with disease similarities to human enteropathogenic *Escherichia coli* infection (*13*). *C. rodentium* attaches and effaces the distal small intestine and colon, provoking innate dendritic cell (DC)–induced ILC3 activation as well as generation of adaptive antigen-specific B and T cells (*6*, *9*, *14*). To focus on intestinal ILC3 responses to *C. rodentium* that are independent of adaptive immune priming (*14*) and infection-associated dysbiosis (*13*, *15*), we limited the infection window using antibiotics (Abx) (*15*) (fig. S1, A to E). Indeed, a short course of ciprofloxacin was sufficient to restrict adaptive T helper type 22 (T_H22) responses, whereas innate ILC3-dependent IL-22 responses were activated normally (fig. S1, F to H). Although Abx treatment alone transiently modified intestinal bacterial communities (fig. S2, A to C), no long-term impact on ILC3 function (fig. S2, D to F) or on microbial diversity (fig. S3) was observed.

We characterized innate ILC3 and adaptive T_H22 immune responses in this modified *C. rodentium* infection model using *Rorc*^{GFP} and *Il22*^{TdT} reporter mice (*16*, *17*) (Fig. 1, A and B; and fig. S4) (GFP, green fluorescent protein; TdT, tdTomato). T cell and ILC3 populations were generally stable during the initial infection, but *C. rodentium* reinfection 1 month after Abx treatment resulted in a rapid increase in intestinal NKp46$^+$ and CCR6$^+$ ILC3 subsets with little effect on T cells (Fig. 1, B and C). Absolute numbers and frequencies of IL-22–expressing ILC3s increased in a similar fashion, whereas IL-22–expressing T cells were largely unchanged (Fig. 1, D to F; and fig. S5). *C. rodentium* challenge and rechallenge experiments in mice not treated with ciprofloxacin showed similar ILC3 responses, indicating the innocuous effects of the Abx treatment (fig. S6, A to C). CD4$^+$ T cell numbers and frequencies of IL-17A–, IL-22–, and interferon-γ (IFN-γ)–producing T cells were not affected (fig. S6, B to E). Thus, the homeostasis and function of intestinal IL-22–producing ILC3s can be selectively modified after an Abx-controlled subclinical *C. rodentium* infection.

Mucosal IL-22 production activates epithelial responses during pathogen infection and is required for resistance to *C. rodentium* (*18*, *19*). Bacterial growth after first infection (denoted "CR") was not observed after reinfection of Abx-cleared infected mice (denoted CR-Abx-CR or "CRACR") (Fig. 1, G and H), suggesting that enhanced ILC3 function in CRACR mice might play a role in the resistance to bacterial rechallenge. DC activation was noted during rechallenge, whereas monocytes, macrophages, and granulocytes were largely unchanged (fig. S7). Taken together, a limited initial exposure of intestinal ILC3s to pathogenic bacteria can

[1]Institut Pasteur, Université de Paris, Inserm U1223, Innate Immunity Unit, Paris, France. [2]Institut Pasteur, Université de Paris, Transcriptome and Epigenome Platform–Biomics Pole, Paris, France. [3]Institut Pasteur, Université de Paris, Bioinformatics and Biostatistics Hub, Paris, France. [4]Institut Pasteur, Université de Paris, Inserm U1117, Biology of Infection Unit, Paris, France. [5]Laboratory of Cancer and Immunometabolism, Center for Cancer Research, National Cancer Institute, National Institutes of Health, Frederick, MD, USA. [6]MRC Centre for Molecular Bacteriology and Infection, Department of Life Sciences, Imperial College London, London, UK.
***Corresponding author: Email: james.di-santo@pasteur.fr**

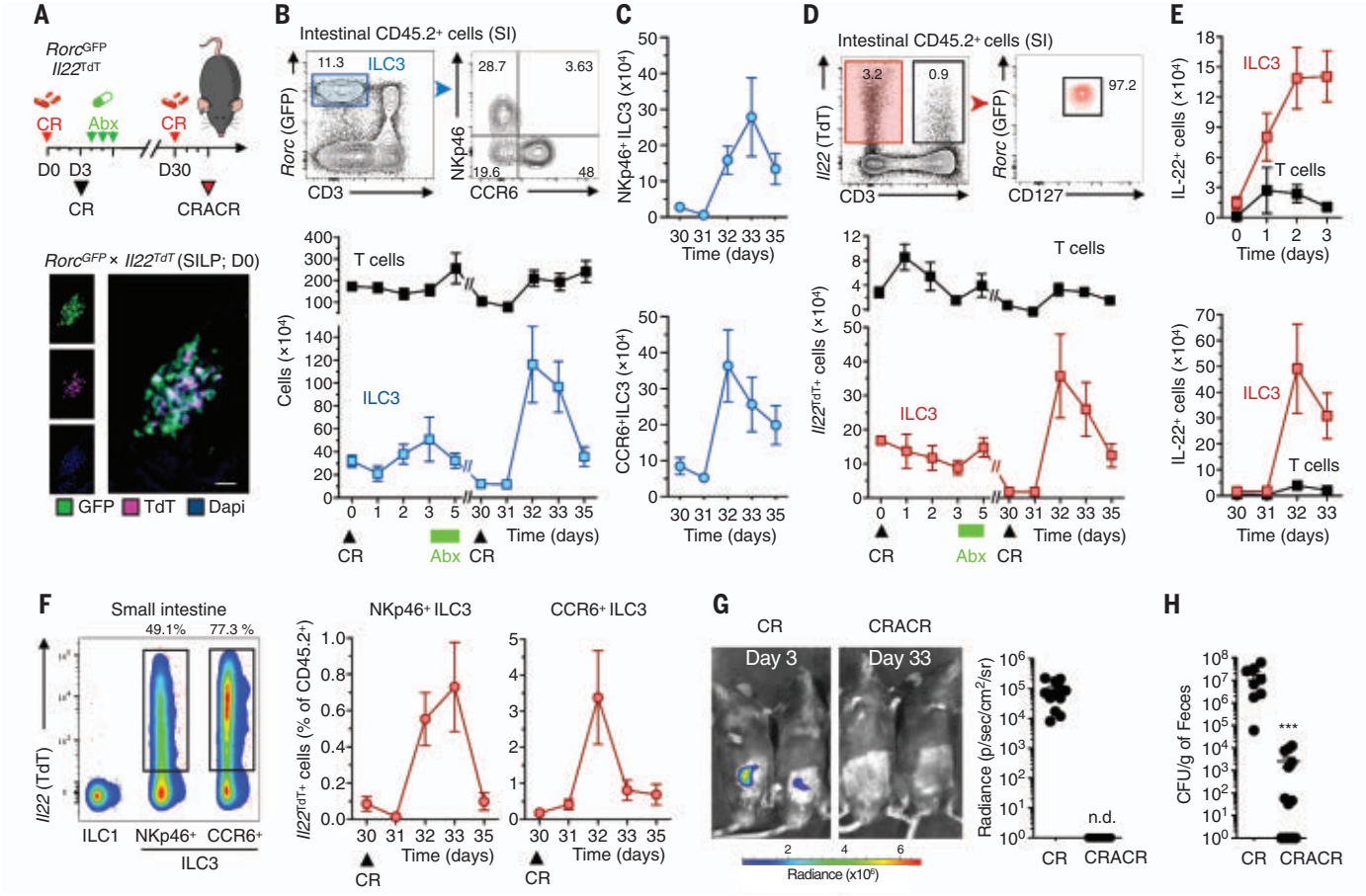


Fig. 1. Tr-ILC3s efficiently control pathogenic bacteria rechallenge. (**A**) The experimental design for (B) to (H) is shown at the top. *Rorc*^{GFP}*Il22*^{TdT} mice received ciprofloxacin (Abx; 100 mg kg^{-1} day^{-1}) after *C. rodentium* infection (CR). One month later, the mice were reinfected with *C. rodentium* (CRACR). A representative steady-state immunofluorescence analysis of RORγt^{+} (green) and *Il22*$^{TdT+}$ (magenta) cells in the small intestine is shown at the bottom. Nuclei were stained with 4′,6-diamidino-2-phenylindole (DAPI) (blue) (scale bar, 20 μm). SILP, small intestine lamina propria; D0, day 0. (**B**) Intestinal NKp46^{+} and CCR6^{+} ILC3s were analyzed by flow cytometry (top). Absolute numbers of ILC3s and T cells in the small intestine lamina propria (n = 4 to 12 for each time point) are shown at the bottom. (**C**) Absolute numbers of intestinal NKp46^{+} (top) and CCR6^{+} (bottom) ILC3s determined with representative data from three independent analyses (n = 3 to 7 for each time point). (**D**) Small intestinal *Il22*$^{TdT+}$ ILC3 (CD45^{+}CD3^{-}*Rorc*$^{GFP+}$) and T cell (CD45^{+}CD3^{+}) frequencies at day 0 (top). Absolute numbers of *Il22*$^{TdT+}$ cells were determined with representative data from six independent analyses (n = 4 to 12 for each time point) (bottom). (**E**) Absolute numbers of IL-22^{+} (protein) cells were analyzed after ex vivo IL-23 (top) and IL-1β (bottom) stimulation (n = 4 to 9 for each time point). (**F**) *Il22*^{TdT} expression in ILC1s (CD3^{-}NKp46^{+}NK1.1^{+}), NKp46^{+} ILC3s, and CCR6^{+} ILC3s (left). Representative data are from three independent analyses. The frequencies of *Il22*$^{TdT+}$NKp46^{+} and NKp46^{-} ILC3 subsets in the small intestine lamina propria after reinfection are shown on the right (CRACR; n = 3 to 7 for each time point). (**G**) *C. rodentium* growth monitored by IVIS imaging (CR, n = 12; CRACR, n = 12). Representative pseudocolor images are shown (color scale in photons s^{-1} cm^{-2} sr^{-1}). (**H**) Fecal *C. rodentium* counts (CR, n = 8; CRACR, n = 13). Data are representative of three independent experiments. Each graph corresponds to the mean ± SEM of the values obtained. n.d. indicates not detected and ***P < 0.001 using two-tailed Mann-Whitney test.

generate a highly functional and persistent ILC3 subset, which we refer to hereafter as "trained ILC3s" (Tr-ILC3s).

Enhanced Tr-ILC3 responses persisted 4 months after *C. rodentium* reinfection of Abx-cleared mice (Fig. 2A), with reduced bacterial loads upon reinfection (Fig. 2B). Absolute numbers of total ILC3s (Fig. 2C) and IL-22^{+} ILC3s (Fig. 2, D and E) were significantly increased in CRACR mice that were reinfected 4 months later with diverse ILC3 subsets as dominant IL-22 producers (Fig. 2, F and G). Because the DNA-binding protein inhibitor ID2 is highly expressed in differentiated ILCs (*20*, *21*), we used *Id2*-regulated inducible fate-mapping (*22*) to track ILCs under steady state and after infection (Fig. 2H). All ILCs were red fluorescent protein (RFP)–labeled, with a somewhat higher percentage of RFP^{+} ILC3s after *C. rodentium* infection (CR and CRA conditions; Fig. 2I). By contrast, most RFP^{+} ILC1s and ILC2s were lost in CRACR mice, whereas labeled RFP^{+} ILC3 subsets were maintained (Fig. 2I). These results indicate that diverse Tr-ILC3s can persist after a limited exposure to *C. rodentium* and may preferentially expand after pathogen reencounter.

We determined if Tr-ILC3s could be generated in the absence of adaptive immunity (Fig. 3A). Absolute numbers of IL-22^{+} ILC3s were significantly increased in CRACR *Rag2*$^{-/-}$ mice (Fig. 3B), which had reduced bacterial loads compared with the CR-infected *Rag2*$^{-/-}$ mice (Fig. 3C). IL-22 production was required for Tr-ILC3–mediated protection against *C. rodentium* (Fig. 3A) because *Rag2*$^{-/-}$*Il22*$^{-/-}$ CRACR mice did not survive reinfection (Fig. 3, D and E). We next compared the protective capacity of adoptively transferred naïve versus Tr-ILC3s in vivo (Fig. 3F). CR-infected *Il22*$^{-/-}$ mice that received naïve ILC3s exhibited body weight loss and succumbed about 2 weeks after infection (Fig. 3G). By contrast, CR-infected *Il22*$^{-/-}$ mice that received Tr-ILC3s recovered and survived (Fig. 3G). Thus, the enhanced functional capacity of Tr-ILC3s

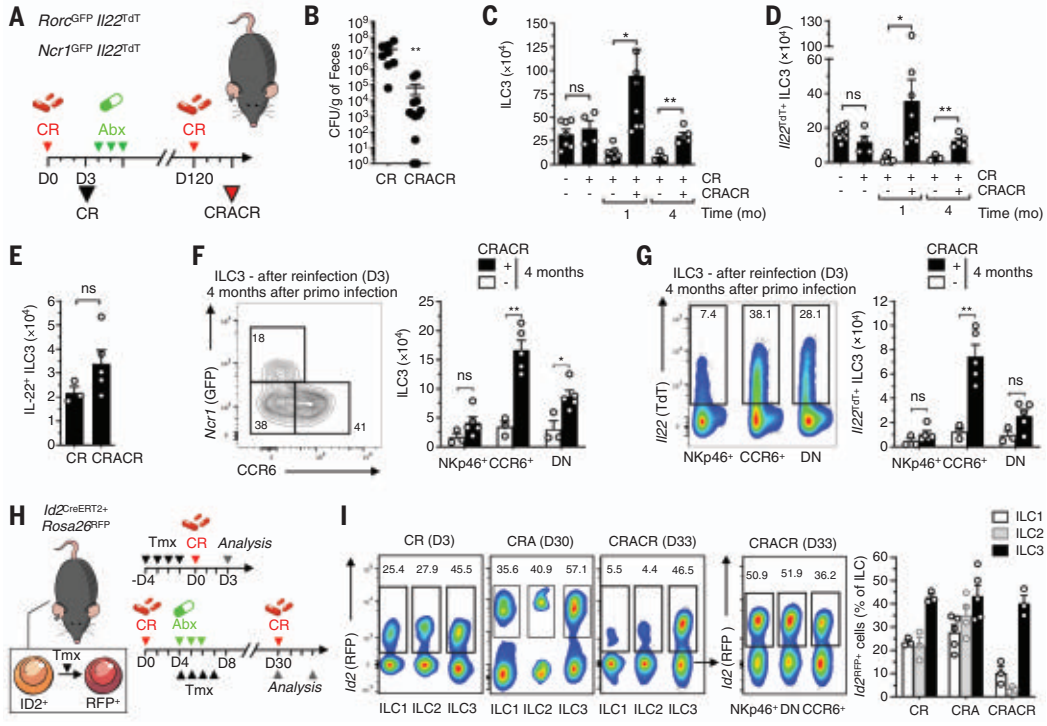


Fig. 2. Tr-ILC3s show long-term persistence. (**A**) Experimental design for (B) to (H). *Rorc*^{GFP}×*Il22*^{TdT} and *Ncr1*^{GFP}×*Il22*^{TdT} mice received ciprofloxacin (Abx; 100 mg kg^{-1} day^{-1}) after *C. rodentium* infection. Four months later, the mice were reinfected with *C. rodentium* (CRACR). (**B**) Fecal *C. rodentium* counts (CR, *n* = 8; CRACR, *n* = 12). CFU, colony forming units. (**C** and **D**) Absolute numbers of total (C) (*n* = 3 to 8) and *Il22*$^{TdT+}$ (D) (*n* = 3 to 9) ILC3s in the small intestine lamina propria. (**E**) Absolute numbers of intestinal IL-22$^+$ ILC3s (protein; *n* = 3 to 5) after ex vivo IL-23 and IL-1β stimulation 3 days after infection or reinfection. (**F** and **G**) Frequency and absolute numbers of ILC3s (F) and *Il22*$^{TdT+}$ ILC3 (G) subsets in CRACR mice were determined (*n* = 3 to 5). DN, double negative. (**H**) Fate-mapping protocol. *Id2*$^{CreERT2+}$×*Rosa26*^{RFP} mice received ciprofloxacin (Abx; 100 mg kg^{-1} day^{-1}) 3 days after *C. rodentium* infection. Mice received tamoxifen (Tmx) by intraperitoneal injection and were analyzed as shown. (**I**) Analysis of *Id2*$^{RFP+}$ cells in ILC1 (CD3$^-$NKp46$^+$NK1.1$^+$), ILC2 (CD3$^-$CD127$^+$CD90.2$^+$KLRG1$^+$), and ILC3 subsets (left) for the protocol shown in (H). Percentages of *Id2*$^{RFP+}$ cells of the total ILCs in CR, CRA, and CRACR mice were determined (*n* = 3 to 5) (right). Each graph corresponds to the mean ± SEM of the values obtained. ns indicates not significant, **P* < 0.05, and ***P* < 0.01 using two-tailed Mann-Whitney test.

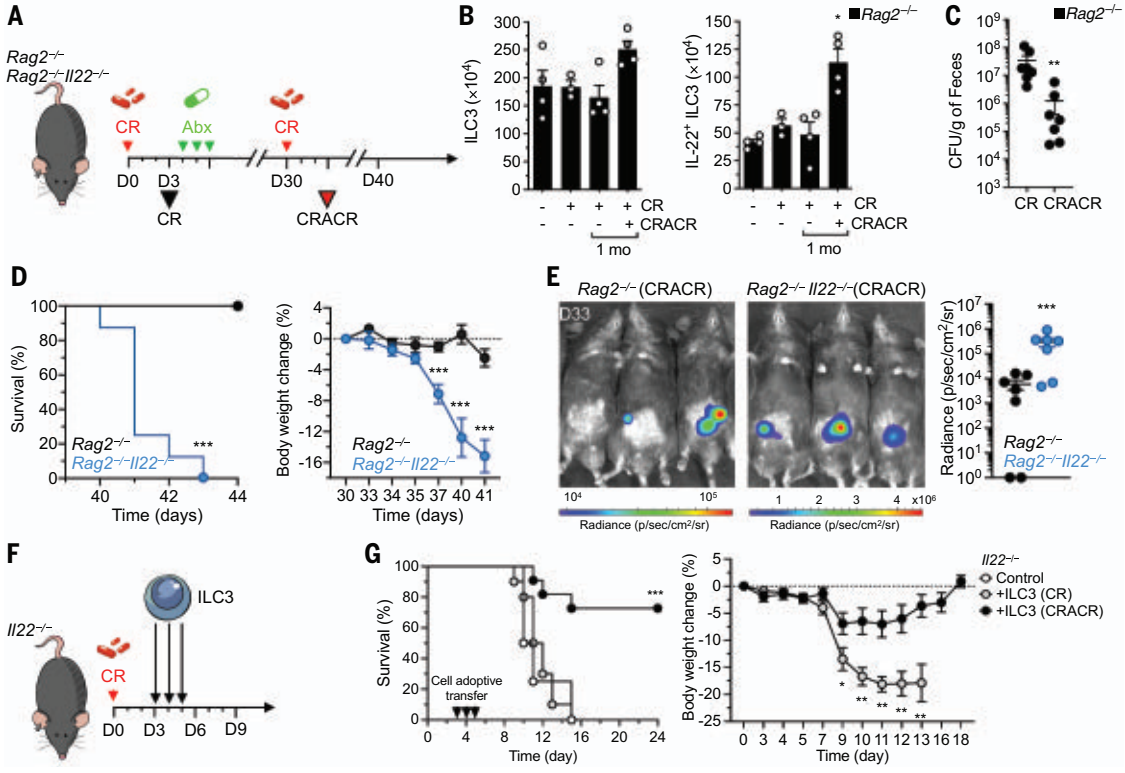


Fig. 3. Tr-ILC3s show enhanced IL-22–mediated protection. (**A**) Experimental design for (B) to (E). *Rag2*$^{-/-}$ and *Rag2*$^{-/-}$*Il22*$^{-/-}$ mice received ciprofloxacin (Abx; 100 mg kg^{-1} day^{-1}) after *C. rodentium* infection. One month later, the mice were reinfected with CR (CRACR). (**B**) Analysis of ILC3s (left) and IL-22$^+$ ILC3s (right) in *Rag2*$^{-/-}$ mice (*n* = 3 to 4). (**C**) Fecal *C. rodentium* counts (*n* = 7). (**D**) Survival (left) and body weight (right) in reinfected *Rag2*$^{-/-}$ and *Rag2*$^{-/-}$*IL22*$^{-/-}$ mice (*n* = 7). (**E**) *C. rodentium* growth monitored by IVIS imaging 3 days after reinfection (left). Relative *C. rodentium* growth was determined in *Rag2*$^{-/-}$ and *Rag2*$^{-/-}$*IL22*$^{-/-}$ mice (*n* = 7) (right). (**F**) Experimental design for (G). ILC3s were purified from infected (CR) or reinfected (CRACR) mice 3 days after infection and transferred into *C. rodentium*–infected *Il22*$^{-/-}$ mice. (**G**) Survival and body weight were assessed at the indicated times after infection [*n* = 4 for *Il22*$^{-/-}$ and ILC3 (CR); *n* = 10 for *Il22*$^{-/-}$ and ILC3 (CRACR); *n* = 11 for *Il22*$^{-/-}$ per group, pool of two independent experiments]. Each graph corresponds to the mean ± SEM of the values obtained. **P* < 0.05, ***P* < 0.01, and ****P* < 0.001 using Krustal-Wallis test (B), two-tailed Mann-Whitney test [(C) to (G)], or log-rank (Mantel-Cox) test [(D) and (G)].

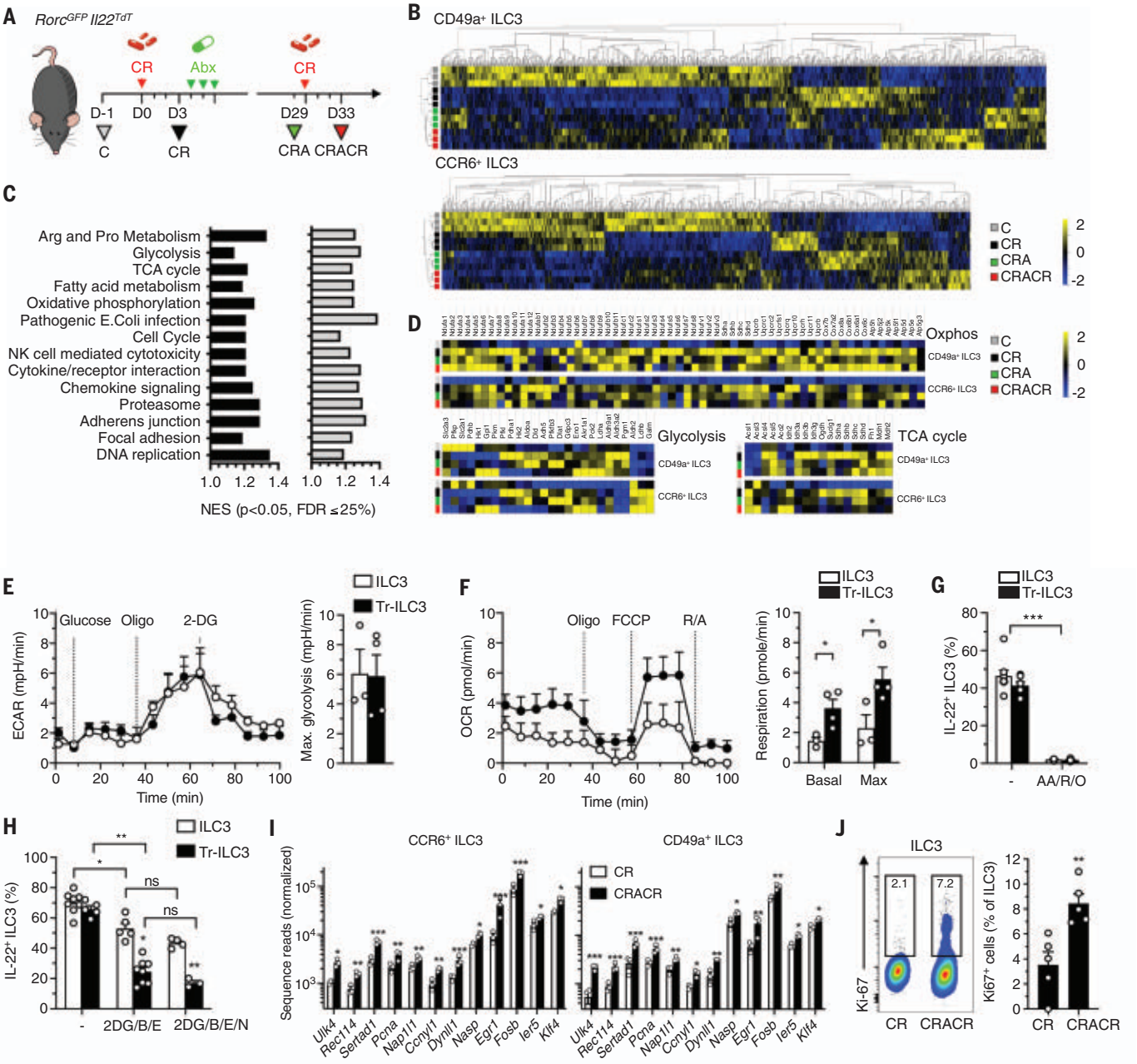


Fig. 4. Gene expression analysis and metabolic profiles of Tr-ILC3s. (**A**) CCR6$^+$ and CD49a$^+$ ILC3 from naïve (C) and infected mice (CR, CRA, and CRACR) were sorted for RNA-seq analysis. (**B** and **C**) A heatmap showing the relative expression levels of differentially expressed genes is shown in (B). In (C), pathway analysis was performed and gene pathways were organized into clusters to compare CR, CRA, and CRACR conditions to C (n = 3). FDR, false discovery rate; NES, normalized enrichment score. (**D**) Heatmap with clustering of differentially expressed metabolism-associated genes (n = 3). (**E** and **F**) Seahorse analysis of freshly sorted ILC3s (C) and Tr-ILC3s (CRACR) in response to a mitochondrial uncoupler [fluoro-carbonylcyanide phenylhydrazone (FCCP)], oligomycin (oligo), rotenone and antimycin (R/A), and 2-DG. Representative metabolic profiles (OCR and ECAR), glycolysis, and respiration were determined (three independent experiments; n = 3 to 4). (**G**) Effect of OXPHOS inhibition (18 hours) on IL-22 production by intestinal ILC3s (n = 5). AA, antimycin; R, rotenone; O, oligomycin. (**H**) Effect of metabolic pathway inhibition (2 hours) on IL-22 production by intestinal ILC3s (two independent experiments; n = 3 to 8). B, BPTES; E, etomoxir; N, Nor-NOHA. (**I**) Differentially expressed genes in CR and CRACR ILC3s (n = 3). (**J**) Frequency of Ki67$^+$ ILC3 from infected (CR) and reinfected (CRACR) mice (two independent experiments; n = 5). Each graph corresponds to the mean ± SEM of the values obtained. ns indicates not significant, $^*P < 0.05$, $^{**}P < 0.01$, and $^{***}P < 0.001$ using two-tailed unpaired Student's t test [(E) and (F)], two-tailed Mann-Whitney test [(G) and (J)], or Krustal-Wallis test (H).

can be adoptively transferred and can operate in a T cell–independent fashion during pathogen rechallenge.

Although antigen specificity has long been considered as a cardinal feature of adaptive B and T cell memory (*23*), innate populations such as myeloid cells (*24*), natural killer (NK) cells (*25*, *26*), and ILC2s (*27*) have been shown to have "memory-like" properties. To investigate pathogen-specific properties of Tr-ILC3s, we analyzed whether *C. rodentium*–activated Tr-ILC3s could protect against *Listeria monocytogenes*. *L. monocytogenes* infection (LM) elicits IL-23 release that can trigger ILC3 activation and IL-22 production, which is

involved in the intestinal epithelial response (*28*). We found enhanced ILC3 responses after rechallenge with *L. monocytogenes* (CRALM compared with LM) (fig. S9, A and B). Thus, Tr-ILC3 responses are not restricted to *C. rodentium* and can potentially extend protection to unrelated pathogens. We also assessed whether Tr-ILC3s can be generated by cytokines alone. Although repeated IL-23 and IL-1β injection triggered higher IL-22 production in intestinal ILC3s (fig. S9, C and D), we failed to detect increased ILC3 numbers in this noninfectious context (fig. S9E). Tr-ILC3s therefore lack antigen specificity and require tissue-dependent signals beyond IL-1β and IL-23 for their generation.

RNA sequencing (RNA-seq) analysis on intestinal ILC3 subsets from naïve (C), *C. rodentium*–infected (CR), *C. rodentium*–infected and ciprofloxacin-treated (CRA), and CRACR mice allowed us to validate previous ILC3 datasets (*5*) and to identify more than 1000 genes in CCR6$^+$ ILC3s and 500 genes in CD49a$^+$ ILC3s modified by *C. rodentium* infection (Fig. 4, A and B; fig. S10A; and table S1). By contrast, comparison of CR and CRACR ILC3 profiles revealed only 152 differentially expressed genes in CCR6$^+$ ILC3s and 138 genes in CD49a$^+$ ILC3s, suggesting that altered transcriptomic profiles stably persist in ILC3s after *C. rodentium* infection (fig. S10, A and B). We documented increased effector functions in ILC3 subsets in *C. rodentium*–exposed mice compared with control naïve mice (Fig. 4C), with Tr-ILC3s strongly expressing transcripts for *Il22*, *Il17f*, *Gzmb*, and *Gzmc* (fig. S10C).

Classical and innate immunological memory requires metabolic rewiring (*29*, *30*) that orchestrates cell survival, proliferation, differentiation, and long-term persistence of these cells. ILC3 subsets demonstrated a profound metabolic shift from glycolysis and glutaminolysis to enhanced tricarboxylic acid (TCA) cycle, oxidative phosphorylation (OXPHOS), fatty acid synthesis, and oxidation-associated gene expression after *C. rodentium* infection, which was preserved in CRA and CRACR mice (Fig. 4, C and D; and fig. S10C). As such, intestinal ILC3s experience durable metabolic rewiring after pathogen encounter.

Bioenergetic profiles, including extracellular acidification rate (ECAR) and cellular oxygen-consumption rate (OCR), define mitochondrial respiration and aerobic glycolytic activity, respectively. Tr-ILC3s showed higher OCRs, indicating increased mitochondrial fitness compared with naïve ILC3s (Fig. 4, E and F), although both required OXPHOS for IL-22 production (Fig. 4G). Diverse nutrients (including glucose, glumatine, and fatty acids) fuel immune cell metabolism and mitochondrial bioenergetic pathways (*31*). In addition, urea cycle–associated genes [arginase-1 (*Arg1*)] can drive ILC2 and T cell proliferation as well as proinflammatory functions (*32*, *33*). Inhibition of glycolysis [2-deoxy-D-glucose (2-DG)], glutamine conversion [bis-2-(5-phenylacetamido-1,3,4–thiadiazol-2-yl)ethyl sulfide (BPTES)], arginine metabolism [N^{ω}-hydroxy-nor-L-arginine (Nor-NOHA)], or fatty acid β-oxidation (etomoxir) did not differentially affect IL-22 production from naïve versus Tr-ILC3s (fig. S10, D to F). However, combined treatment with 2-DG–BPTES and etomoxir significantly decreased IL-22 production from Tr-ILC3s, whereas Arg1 inhibition synergized with 2-DG, BPTES, and etomoxir to significantly reduce IL-22 production from naïve ILC3s (Fig. 4H). Therefore, L-arginine may act as a metabolic source for naïve ILC3s but not Tr-ILC3s.

We further focused our attention on transcripts that were selectively modified in CRACR ILC3s (table S1). From the 51 transcripts that were up-regulated in both CD49$^+$ and CCR6$^+$ ILC3s, 12 were associated with the regulation of cell proliferation (Fig. 4I). Higher Ki67 levels were detected in ILC3s from CRACR compared with CR mice (Fig. 4J), consistent with rapid Tr-ILC3 proliferation after activation. Our results suggest that pathogen encounter is accompanied by durable metabolic changes in intestinal ILC3s, generating Tr-ILC3 subsets with enhanced proliferative capacity and contributing to long-term mucosal defense.

Adaptive immune responses are classically associated with the development of immunological memory. The innate immune system can likewise adapt to environmental inflammatory signals that generate NK and myeloid cells with new long-lived phenotypes (*24*, *26*). Here, we describe intestinal "trained" ILC3s that emerge and persist after initial pathogen encounter. Upon reinfection, Tr-ILC3s proliferate and robustly produce IL-22, thus promoting mucosal defense. The distinct metabolic activity in memory T cells (*34*, *35*) and trained monocytes and macrophages (*24*) is associated with epigenetic reprogramming. The precise mechanisms that underlie the distinct functional features of Tr-ILC3s and the signals that promote them remain to be defined. Tr-ILC3 targeting may provide an avenue for prevention or treatment of disease caused by inflammation or pathogens that invade barrier surfaces.

REFERENCES AND NOTES

1. L. V. Hooper, A. J. Macpherson, *Nat. Rev. Immunol.* **10**, 159–169 (2010).
2. H. Spits *et al.*, *Nat. Rev. Immunol.* **13**, 145–149 (2013).
3. G. F. Sonnenberg, D. Artis, *Nat. Med.* **21**, 698–708 (2015).
4. C. S. N. Klose, D. Artis, *Nat. Immunol.* **17**, 765–774 (2016).
5. M. L. Robinette *et al.*, *Nat. Immunol.* **16**, 306–317 (2015).
6. N. Satoh-Takayama *et al.*, *Immunity* **29**, 958–970 (2008).
7. G. F. Sonnenberg, L. A. Monticelli, M. M. Elloso, L. A. Fouser, D. Artis, *Immunity* **34**, 122–134 (2011).
8. S. Buonocore *et al.*, *Nature* **464**, 1371–1375 (2010).
9. M. Cella *et al.*, *Nature* **457**, 722–725 (2009).
10. H. Yoshida *et al.*, *Int. Immunol.* **11**, 643–655 (1999).
11. R. E. Mebius, P. Rennert, I. L. Weissman, *Immunity* **7**, 493–504 (1997).
12. S. Sawa *et al.*, *Nat. Immunol.* **12**, 320–326 (2011).
13. J. W. Collins *et al.*, *Nat. Rev. Microbiol.* **12**, 612–623 (2014).
14. R. Basu *et al.*, *Immunity* **37**, 1061–1075 (2012).
15. C. Mullineaux-Sanders *et al.*, *Cell Rep.* **21**, 3381–3389 (2017).
16. G. Eberl *et al.*, *Nat. Immunol.* **5**, 64–73 (2004).
17. W. Shen, J. A. Hixon, M. H. McLean, W. Q. Li, S. K. Durum, *Front. Immunol.* **6**, 662 (2016).
18. K. Wolk *et al.*, *Immunity* **21**, 241–254 (2004).
19. Y. Zheng *et al.*, *Nat. Med.* **14**, 282–289 (2008).
20. M. Cherrier, S. Sawa, G. Eberl, *J. Exp. Med.* **209**, 729–740 (2012).
21. W. Xu *et al.*, *Immunity* **50**, 1054–1068.e3 (2019).
22. E. L. Rawlins, C. P. Clark, Y. Xue, B. L. Hogan, *Development* **136**, 3741–3745 (2009).
23. J. Ordovas-Montanes, S. Beyaz, S. Rakoff-Nahoum, A. K. Shalek, *Nat. Rev. Immunol.* **20**, 308–320 (2020).
24. S. Saeed *et al.*, *Science* **345**, 1251086 (2014).
25. M. A. Cooper *et al.*, *Proc. Natl. Acad. Sci. U.S.A.* **106**, 1915–1919 (2009).
26. J. C. Sun, J. N. Beilke, L. L. Lanier, *Nature* **457**, 557–561 (2009).
27. I. Martinez-Gonzalez *et al.*, *Immunity* **45**, 198–208 (2016).
28. O. Disson *et al.*, *J. Exp. Med.* **215**, 2936–2954 (2018).
29. R. J. W. Arts, L. A. B. Joosten, M. G. Netea, *Semin. Immunol.* **28**, 425–430 (2016).
30. G. R. Bantug, L. Galluzzi, G. Kroemer, C. Hess, *Nat. Rev. Immunol.* **18**, 19–34 (2018).
31. J. Muri, M. Kopf, *Nat. Rev. Immunol.* **21**, 363–381 (2021).
32. R. Geiger *et al.*, *Cell* **167**, 829–842.e13 (2016).
33. L. A. Monticelli *et al.*, *Nat. Immunol.* **17**, 656–665 (2016).
34. G. Caputa, A. Castoldi, E. J. Pearce, *Nat. Immunol.* **20**, 793–801 (2019).
35. M. D. Buck, D. O'Sullivan, E. L. Pearce, *J. Exp. Med.* **212**, 1345–1360 (2015).

ACKNOWLEDGMENTS

We thank all the members of the Di Santo laboratory for critical review of the manuscript, helpful discussions, and support. We thank G. Eberl (Institut Pasteur, France) and O. Mandelboim (Hebrew University, Israel) for providing *Rorc*^{GFP} and *Ncr1*^{GFP} mice, respectively. We are indebted to S. Novault (Technology Core of the Center for Translational Science at Institut Pasteur, France) for cell sorting and M. Berard, R. Chennouf (Institut Pasteur, France, animal facilities), and M. Lecuit (Institut Pasteur, France) for support. We thank P. Bousso (Institut Pasteur, France) for critical comments on the manuscript. **Funding:** This work is supported by grants from the Institut National de la Santé et de la Recherche Médicale (INSERM), the Institut Pasteur, the Agence National pour le Recherche (ANR - ILC_MEMORY), and the European Research Council (ERC) under the European Union's Horizon 2020 research and innovation program (695467 – ILC_REACTIVITY). A.J. is supported by the French Ministry of Higher Education, Research, and Innovation and by the Fondation pour la recherche médicale. **Author contributions:** N.S. and J.P.D. designed the study and wrote the manuscript. N.S. and A.J. designed, performed, and analyzed the experiments. O.D. assisted with the *Listeria* experiments. P.G. analyzed the microbiota. N.S., O.S., H.V., R.L., and J.-Y.C. performed RNA-seq analysis. L.S. provided metabolism expertise. G.F. provided microbiology expertise. J.P.D. directed the study. **Competing interests:** The authors declare no competing financial interests. **Data and materials availability:** All data are available in the main text, supplementary materials, or public data repositories [16S rRNA at the NCBI Sequence Read Archive (SUB10763153/BioProject ID: PRJNA786093; RNA-seq datasets: GSE191167)].

SUPPLEMENTARY MATERIALS

science.org/doi/10.1126/science.aaz8777
Materials and Methods
Figs. S1 to S10
Table S1
References (*36*–*41*)
MDAR Reproducibility Checklist

18 October 2019; resubmitted 12 March 2021
Accepted 27 January 2022
10.1126/science.aaz8777

CORONAVIRUS

Structural basis of SARS-CoV-2 Omicron immune evasion and receptor engagement

Matthew McCallum[1]†, Nadine Czudnochowski[2]†, Laura E. Rosen[2], Samantha K. Zepeda[1], John E. Bowen[1], Alexandra C. Walls[1,3], Kevin Hauser[2], Anshu Joshi[1], Cameron Stewart[1], Josh R. Dillen[2], Abigail E. Powell[2], Tristan I. Croll[4], Jay Nix[5], Herbert W. Virgin[2,6,7], Davide Corti[8], Gyorgy Snell[2]*, David Veesler[1,3]*

The severe acute respiratory syndrome coronavirus 2 (SARS-CoV-2) Omicron variant of concern evades antibody-mediated immunity that comes from vaccination or infection with earlier variants due to accumulation of numerous spike mutations. To understand the Omicron antigenic shift, we determined cryo–electron microscopy and x-ray crystal structures of the spike protein and the receptor-binding domain bound to the broadly neutralizing sarbecovirus monoclonal antibody (mAb) S309 (the parent mAb of sotrovimab) and to the human ACE2 receptor. We provide a blueprint for understanding the marked reduction of binding of other therapeutic mAbs that leads to dampened neutralizing activity. Remodeling of interactions between the Omicron receptor-binding domain and human ACE2 likely explains the enhanced affinity for the host receptor relative to the ancestral virus.

Although sequential COVID-19 waves have swept the world, no variants have accumulated mutations and mediated immune evasion to the extent observed for the severe acute respiratory syndrome coronavirus 2 (SARS-CoV-2) Omicron (B.1.1.529) variant of concern (VOC). This variant was first identified in late November 2021 in South Africa and was quickly designated a VOC by the World Health Organization (*1*). Omicron has spread worldwide at a rapid pace relative to previous SARS-CoV-2 variants (*2*, *3*). The Omicron spike (S) glycoprotein, which promotes viral entry into cells (*4*, *5*), harbors 37 residue mutations in the predominant haplotype relative to Wuhan-Hu-1 S (*4*), whereas SARS-CoV-2 Alpha and Delta VOC display ~10 substitutions (*2*, *6*). The Omicron receptor-binding domain (RBD) and N-terminal domain (NTD) contain 15 and 11 mutations, respectively, which lead to severe dampening of plasma-neutralizing activity in previously infected or vaccinated individuals (*7*–*11*). Although the Omicron RBD harbors 15 residue mutations, it binds to the human ACE2 entry receptor with high affinity and can efficiently recognize mouse ACE2 (*7*). As a result of this antigenic shift, the only authorized or approved therapeutic monoclonal antibodies (mAbs) with neutralizing activity against Omicron are S309 (sotrovimab parent) and the COV2-2196/COV2-2130 cocktail (cilgavimab/tixagevimab parents). Even these mAbs had reduced potency (by a factor of 2 to 3 and by a factor of 12 to 200, respectively), according to pseudovirus or authentic virus assays (*7*–*11*). This extent of evasion of humoral responses has important consequences for therapy and prevention of both the current pandemic and future pandemics.

To define the molecular mechanisms involved in Omicron immune evasion and altered receptor recognition, we determined cryo–electron microscopy (cryo-EM) structures of the prefusion-stabilized SARS-CoV-2 Omicron S ectodomain trimer bound to S309 and S2L20 (NTD-specific mAb) Fab fragments (Fig. 1, fig. S1, and table S1) and the x-ray crystal structure of the Omicron RBD in complex with human ACE2 and the Fab fragments of S309 and S304 at 2.85 Å resolution (table S2). S309 recognizes antigenic site IV (*12*), whereas S304 binds to site

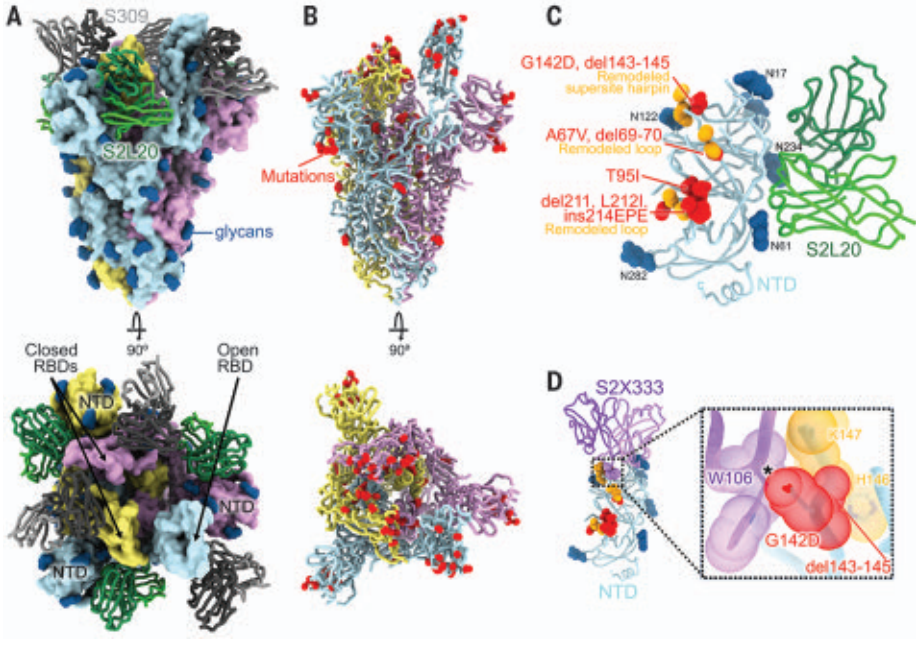


Fig. 1. Cryo-EM structure of the SARS-CoV-2 Omicron S trimer reveals a remodeling of the NTD antigenic supersite. (**A**) Surface rendering in two orthogonal orientations of the Omicron S trimer with one open RBD bound to the S309 (gray) and S2L20 (green) Fabs shown as ribbons. The three S protomers are colored light blue, pink, and gold. N-linked glycans are shown as dark blue surfaces. (**B**) Ribbon diagrams in two orthogonal orientations of the S trimer with one open RBD. Omicron residues mutated relative to Wuhan-Hu-1 are shown as red spheres (except D614G, which is not shown). (**C**) The S2L20-bound Omicron NTD with mutated, deleted, or inserted residues rendered or indicated as red spheres. Segments with notable structural changes are shown in orange and labeled. (**D**) Zoomed-in view of the Omicron NTD antigenic supersite overlaid with the S2X333 Fab [used here as an example of a prototypical NTD-neutralizing mAb (*22*)], highlighting the binding incompatibility; the modeled clash between S2X333 Trp^{106} and NTD G142D is indicated with an asterisk.

[1]Department of Biochemistry, University of Washington, Seattle, WA 98195, USA. [2]Vir Biotechnology, San Francisco, CA 94158, USA. [3]Howard Hughes Medical Institute, University of Washington, Seattle, WA 98195, USA. [4]Cambridge Institute for Medical Research, Department of Haematology, University of Cambridge, Cambridge, UK. [5]Molecular Biology Consortium, Advanced Light Source, Lawrence Berkeley National Laboratory, Berkeley, CA, USA. [6]Department of Pathology and Immunology, Washington University School of Medicine, St. Louis, MO 63110, USA. [7]Department of Internal Medicine, UT Southwestern Medical Center, Dallas, TX 75390, USA. [8]Humabs Biomed SA, a subsidiary of Vir Biotechnology, 6500 Bellinzona, Switzerland.
***Corresponding author. Email: dveesler@uw.edu (D.V.); gsnell@vir.bio (G.S.)**
†These authors contributed equally to this work.

IIc (*13*) and was used to assist crystallization. Furthermore, we used surface plasmon resonance (SPR) to evaluate the binding of clinical mAbs to the Omicron RBD and S ectodomain trimer.

Three-dimensional classification of the cryo-EM data revealed the presence of two conformational states with one (45% of selected particles) or two (55% of selected particles) RBDs in the open conformation, for which we determined structures at 3.1 Å and 3.2 Å resolution, respectively (Fig. 1, A and B, figs. S1 and S2, and table S1). The larger fraction of open RBDs, relative to the apo (*4*, *5*) and S309-bound (*12*) Wuhan-Hu-1 S ectodomain trimer structures, could result from the Omicron mutations, the prefusion-stabilizing mutations (*14*, *15*), or S2L20 binding. Focused classification and local refinement of the S309-bound RBD (domain B) and of the S2L20-bound NTD (domain A) were used to account for their conformational dynamics and led to improved local resolution of these regions (to 3.0 and 3.3 Å resolution, respectively).

Whereas most VOCs have only a few mutations beyond the NTD, RBD, and furin cleavage site regions, the Omicron spike harbors eight substitutions outside of these areas: T547K, H655Y, N764K, D796Y, N856K, Q954H, N969K, and L981F, which could all be modeled in the map (Fig. 1, A and B, and Fig. 2). Three of these mutations introduce interprotomer electrostatic contacts between the S_2 and S_1 subunits: N764K binds Gln^{314} (in domain D), Ser^{982} binds T547K (in domain C of protomers with closed RBDs), and N856K binds Asp^{568} and Thr^{572} (in domain C, the former residue is closer to N856K in protomers with closed RBDs) (Fig. 2) (*16*, *17*). Furthermore, N969K forms interprotomer electrostatic contacts with Q755, and L981F improves intraprotomer hydrophobic packing in the prefusion conformation (Fig. 2). The latter mutation is close to the prefusion-stabilizing 2P mutations (K986P and V987P) used in all three vaccines deployed in the US (Fig. 2). Consistent with recent studies (*18*–*20*), S_1 shedding might be reduced by enhanced interactions between the S_1 and S_2 subunits in Omicron S along with prefusion stabilization, or by altered processing at the S_1-S_2 cleavage site due to the N679K and P681H mutations. Dampened S_1 subunit shedding might enhance the effector function activity of vaccine- or infection-elicited Abs along with that of therapeutic mAbs (*21*) that retain affinity for Omicron S.

The Omicron NTD carries numerous mutations, deletions (del), and an insertion (ins) including A67V, del69-70, T95I, G142D, del143-145, del211, L212I, and ins214EPE (Fig. 1C and fig. S3). Many of these mutations have been described in previously emerged VOCs: del69-70 was found in Alpha, T95I was present in Kappa and Iota, and G142D was present in Kappa and Delta. T95I, del211, L212I, and ins214EPE are outside the NTD antigenic supersite but in the vicinity of the epitope targeted by the P008_056 mAb, which suggests that these mutations could putatively modulate recognition of similar mAbs or have another functional relevance. Although the region comprising del143-145 is weakly resolved in the map, it is expected to alter antibody recognition as a result of the introduced sequence register shift, whereas G142D is incompatible with binding of several potent NTD-neutralizing mAbs (such as S2X333) because of steric hindrance (Fig. 1D) (*2*, *22*). Moreover, del143-145 is reminiscent of Alpha del144, which was also isolated as an escape mutation in the presence of mAb S2X333 and led to viral breakthrough in a hamster challenge model (*22*). These data suggest that G142D and del143-145 account for the observed SARS-CoV-2 Omicron evasion

Table 1. Omicron RBD mutations with a demonstrated (X) or expected (x) reduction of binding or neutralization and based on our structural analyses.
Total GISAID counts are as of 9 January 2022. Entries with >5% Ns are excluded; n/a, not applicable. VOI, variant of interest; VUM, variant under monitoring.

	REGN10933	REGN10987	COV2-2196	COV2-2130	LY-CoV555	LY-CoV016	CT-P59	S309	ADI-58125	Total GISAID counts	Omicron counts	VOC, VOI, VUM harboring mutation
G339D										196,756	192,125	
S371L										182,692	179,486	
S373P										185,025	181,374	
S375F										184,990	181,461	
K417N	X					X	X			116,510	70,903	Beta, K417T in Gamma
N440K										92,338	79,859	
G446S		X		x						83,953	80,518	
S477N	x		X			x				262,216	187,081	
T478K			X							3,976,461	187,859	Delta
E484A	X			X	X		X			192,062	186,965	E484K in Beta, Gamma, Mu, Iota, Eta, Zeta, Theta; E484Q in Kappa
Q493R	X		X	x	X	x	X			191,484	188,353	
G496S							X			187,583	184,575	
Q498R							X			188,462	185,805	
N501Y										1,434,752	186,285	Alpha, Beta, Theta, N501K in Mu
Y505H									X*	188,250	185,491	
PDB ID	6XDG	6XDG	7L7D	7L7E	7KMG	7C01	7CM4	This study	n/a			

*For ADI-58125, the impact on binding of C, N, and S substitutions is shown at position Tyr^{505} according to mutagenesis studies [J. Belk *et al*., WO2021207597 - Compounds Specific to Coronavirus S Protein and Uses Thereof. Adagio Therapeutics Inc. (2021)].

from neutralization mediated by a panel of NTD mAbs (*7*, *9*).

The RBD is the main target of plasma-neutralizing activity in convalescent and vaccinated individuals and comprises several antigenic sites recognized by neutralizing Abs with a range of neutralization potencies and breadth (*12*, *13*, *21*, *23*–*36*) (Fig. 3A). Our structures provide a high-resolution blueprint of the residue substitutions found in this variant (Fig. 3B) and their impact on binding of clinical mAbs (Table 1). Several individual mutations or subsets of mutations occurring in the Omicron RBD have been reported to affect neutralizing antibody binding or neutralization (*37*). The K417N, G446S, S477N, T478K, E484A, Q493R, G496S, Q498R, N501Y. and Y505H mutations are part of antigenic site I, which is immunodominant in previous variants (*13*, *24*). K417N, E484A, S477N, and Q493R would lead to loss of electrostatic interactions and steric clashes with REGN10933 whereas G446S would lead to steric clashes with REGN10987, consistent with the dampened binding to the Omicron RBD and S trimer (Fig. 3, C and D, fig. S3, and table S3) and with previous analyses of the impact of individual mutations on neutralization by each of these two mAbs (*9*, *38*–*40*). Moreover, N440K was reported to dampen REGN10987 neutralization severely (*9*). Reduced binding of the Omicron RBD to COV2-2196 and COV2-2130, relative to the Wuhan-Hu-1 RBD, likely results from T478K [based on Delta S (*2*)], Q493R, and putatively S477N for COV2-2196, as well as G446S and E484A for COV2-2130 (Fig. 3, E and F, fig. S4, and table S3). Integrating these data with neutralization assays suggests that although each point mutation only imparts a small reduction of COV2-2196– or COV2-2130–mediated neutralization (*9*), the constellation of Omicron mutations leads to more pronounced loss of activity (*7*–*11*). E484A abrogates electrostatic interactions with LY-CoV555 heavy and light chains, whereas Q493R would prevent binding through steric hindrance (Fig. 3G, fig. S4, and table S3), as supported by neutralization data (*9*). K417N is expected to negatively affect the constellation of electrostatic interactions formed between the Omicron RBD and LY-CoV16 heavy chain, thereby abolishing binding (Fig. 3H, fig. S4, and table S3) and neutralization of single-mutant S pseudoviruses (*9*, *40*, *41*). Furthermore, S477N and Q493R have been shown to dampen binding of and neutralization mediated by LY-CoV16 (*9*, *41*). Finally, K417N, E484A, and Q493R hinder CT-P59 engagement through a combination of steric hindrance and remodeling of electrostatic contacts, thereby preventing binding (Fig. 3I, fig. S4, and tables S1 and S3).

The SARS-CoV-2 Omicron G339D and N440K mutations are within or near antigenic site IV, which is recognized by the S309 mAb (*12*). Nonetheless, relative to Wuhan-Hu-1 pseudovirus or Washington-1 authentic virus, S309 undergoes only a factor of 2 to 3 reduction of neutralizing activity against Omicron (*7*, *9*–*11*). The Lys side chain introduced by the N440K substitution points away from the S309 epitope and does not affect binding. The Asp side chain introduced by the G339D substitution does not interfere with the S309 epitope, although not all rotamers are compatible with mAb binding (fig. S2). This finding likely explains the similarly moderate reduction of S309 potency against the single G339D S mutant (*9*) or the full constellation of Omicron S mutations (*7*, *9*–*11*). The modest reduction of the Omicron RBD binding to S309 (Fig. 3J, fig. S4, and table S3) mirrors the reduced neutralization potency of this VOC (by a factor of 2 to 3 relative to ancestral viruses) and concurs with deep-mutational scanning analysis of individual mutations on S309 recognition (*24*). Overall, the S309 binding mode remains unaltered by the Omicron mutations, including recognition of the N343 glycan (fig. S5).

The Omicron RBD is structurally similar to the Wuhan-Hu-1 RBD, and both structures can be superimposed with an RMSD of 0.8 Å over 183 aligned Cα residues [as compared to PDB 6m0j (*42*)]. However, the region comprising residues *366* to *375*, which harbors the S371L/S373P/S375F substitutions, deviates markedly from the conformation observed for the Wuhan-Hu-1 RBD, irrespective of the presence of bound linoleic acid (*4*, *42*, *43*). Although this region is weakly resolved in the cryo-EM and x-ray structures, the conformation adopted in the latter structure is incompatible with binding of some cross-reactive site II mAbs such as S2X35, consistent with our observation of dampened binding (fig. S6). We therefore propose that these mutations participate in rendering this region of the RBD dynamic and mediate immune evasion from some site II mAbs.

We recently reported that the SARS-CoV-2 Omicron RBD binds human ACE2 with a factor of ~2.4 enhanced affinity relative to the Wuhan-Hu-1 RBD (*7*). Our crystal structure of the human ACE2-bound Omicron RBD elucidates how the constellation of RBD mutations found in this VOC affect receptor recognition

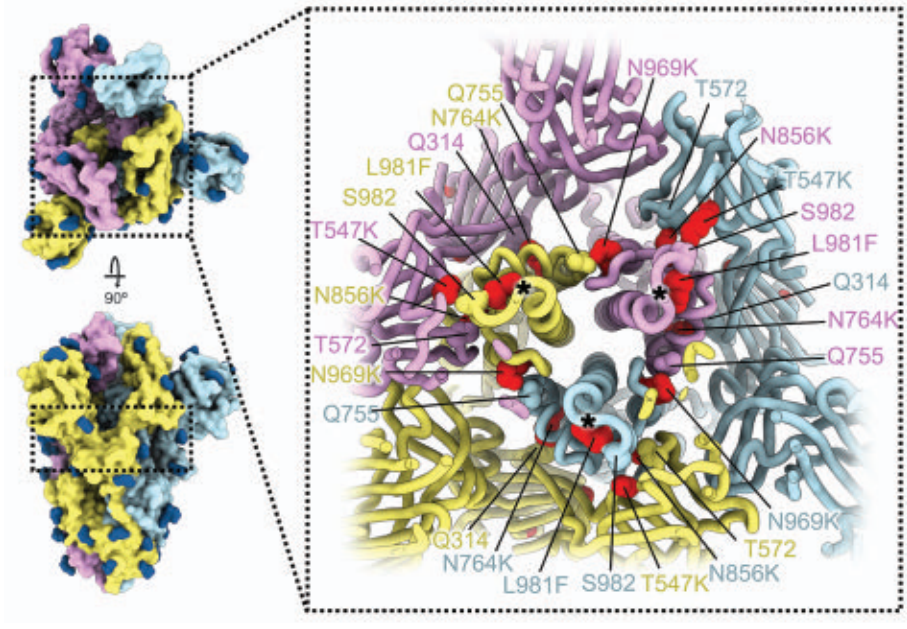


Fig. 2. SARS-CoV-2 Omicron S mutations outside the NTD and RBD. Ribbon diagram shows a cross section of the Omicron S glycoprotein (the location of this slice on the S trimer is indicated at left). Mutated residues T547K, N764K, N856K, N969K, and L981F are shown as red spheres, whereas the residues they contact are shown as spheres colored as the protomer to which they belong. Black asterisks show the positions of residues involved in the prefusion-stabilizing 2P mutations (K986P and V987P) used in all three vaccines deployed in the US. The three S protomers are colored light blue, pink, and gold. N-linked glycans are shown as dark blue surfaces.

(Fig. 4A and table S2). The N501Y mutation alone enhances ACE2 binding to the RBD by a factor of 6 relative to the Wuhan-Hu-1 RBD, as reported for the Alpha variant (*6*), likely as a result of increased shape complementarity between the introduced Tyr side chain and the ACE2 Tyr^{41} and Lys^{353} side chains (Fig. 4B). Omicron S residue Tyr^{501} and ACE2 residue Tyr^{41} form a T-shaped π-π stacking interaction, as previously observed for an N501Y-harboring S structure in complex with ACE2 (*44*). The K417N mutation dampens receptor recognition by a factor of ~3 (*2*, *6*, *39*, *45*) likely through loss of a salt bridge with ACE2 Asp^{30} (Fig. 4C). The Q493R and Q498R mutations introduce two new salt bridges with Glu^{35} and Glu^{38}, respectively, replacing hydrogen bonds formed with the Wuhan-Hu-1 RBD and thereby remodeling the electrostatic interactions with ACE2 (Fig. 4D). Both of these individual mutations were reported to reduce ACE2 binding avidity slightly by deep-mutational scanning studies of the yeast-displayed SARS-CoV-2 RBD (*46*). Finally, S477N leads to formation of new hydrogen bonds between the introduced Asn side chain and the ACE2 Ser^{19} backbone amine and carbonyl groups (Fig. 4E). Collectively, these mutations have a net enhancing effect on binding of the Omicron RBD to human ACE2 relative to Wuhan-Hu-1, which suggests that structural epistasis enables immune evasion while retaining efficient receptor engagement. The large number of Omicron mutations in the immunodominant receptor-binding motif likely explains a substantial proportion of the loss of neutralization by convalescent and vaccine-elicited polyclonal antibodies, and is in line with the known plasticity of this subdomain (*24*).

Although the N501Y mutation has previously been described as enabling some SARS-CoV-2 VOCs to infect and replicate in mice, the Alpha and Beta variant RBDs only weakly bound mouse ACE2 (*47*, *48*). The SARS-CoV-2 Omicron RBD, however, interacts more strongly with mouse ACE2 than do the Alpha and Beta variant RBDs when evaluated side-by-side (fig. S7A) and can use mouse ACE2 as an entry receptor for S-mediated entry (*7*, *49*). We propose that the Q493R mutation plays a key role in enabling efficient mouse ACE2 binding, which occurs through formation of a new electrostatic interaction with the Asn^{31} side chain amide (Lys^{31} in human ACE2); this is supported by in silico modeling based on our human ACE2-bound crystal structure (fig. S7B). These findings concur with the emergence and fixation of the Q493K RBD mutation upon serial passaging in mice to yield a mouse-adapted virus designated SARS-CoV-2 MA10 (*50*).

This work defines the molecular basis for the broad evasion of humoral immunity exhibited

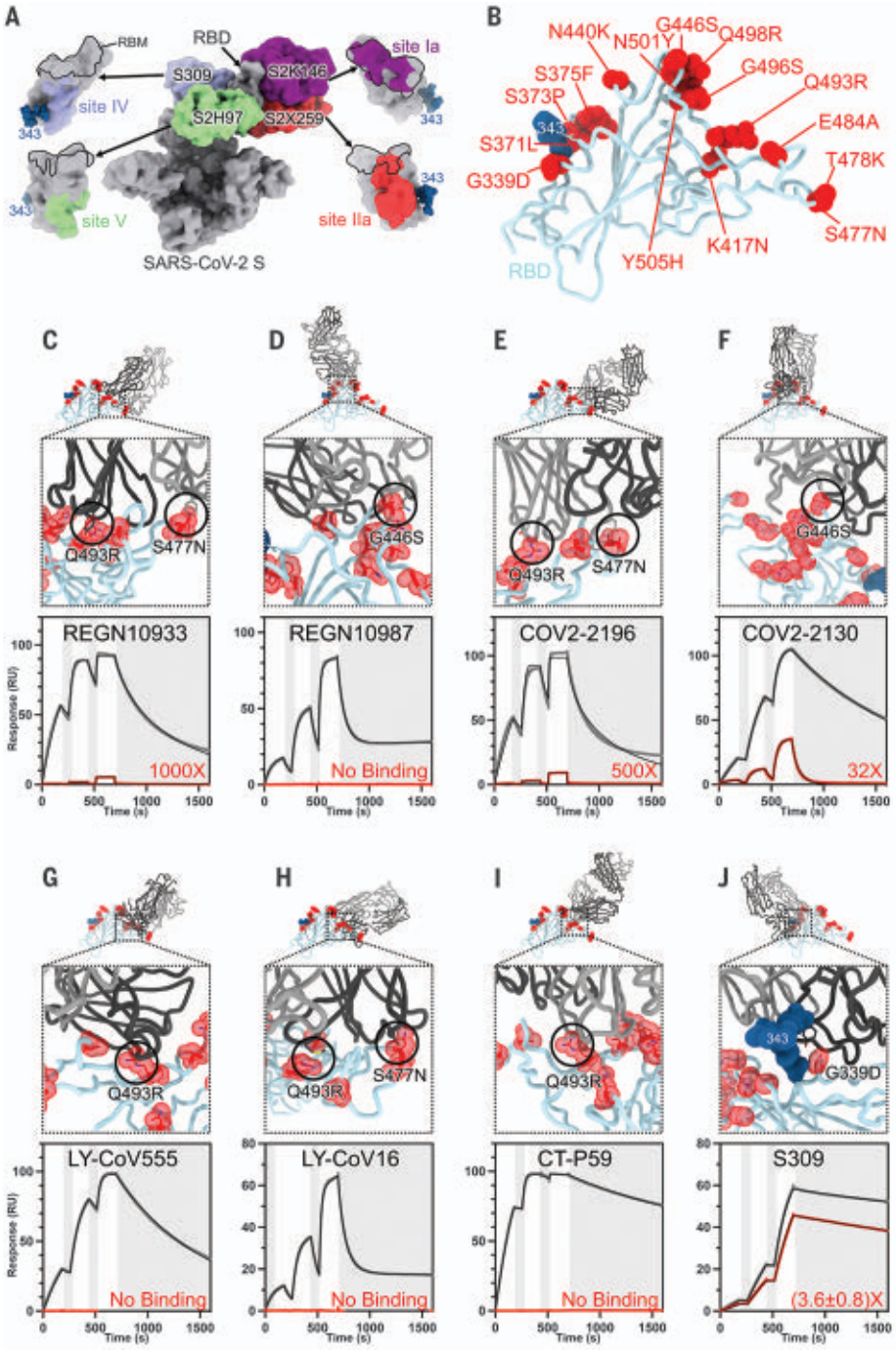


Fig. 3. SARS-CoV-2 Omicron RBD mutations promote escape from a panel of clinical mAbs. (**A**) RBD antigenic map as determined in (*13*). (**B**) Ribbon diagram of the RBD crystal structure, with residues mutated relative to the Wuhan-Hu-1 RBD shown as red spheres. The N343 glycan is rendered as blue spheres. (**C** to **J**) Zoomed-in views of the Omicron RBD (blue) superimposed on structures of clinical mAbs (gray). Selected residues that interfere with the following mAbs are circled: (C) REGN10933, (D) REGN10987, (E) COV2-2196, (F) COV2-2130, (G) LY-CoV555, (H) LY-CoV16, (I) CT-P59, and (J) S309, which does not clash with G339D. All panels were rendered with the crystal structure except (J), which was generated with the cryo-EM model. Binding of the Wuhan-Hu-1 (gray line) or Omicron (red line) RBD to the corresponding mAb was evaluated using surface plasmon resonance (single-cycle kinetics) and is shown underneath each structural superimposition. White and gray stripes are association and dissociation phases, respectively. The thin black line is a fit to a kinetic model. The decrease in affinity between Wuhan-Hu-1 and Omicron binding is indicated in red. Results are consistent with immunoglobulin G binding to S ectodomains (fig. S3).

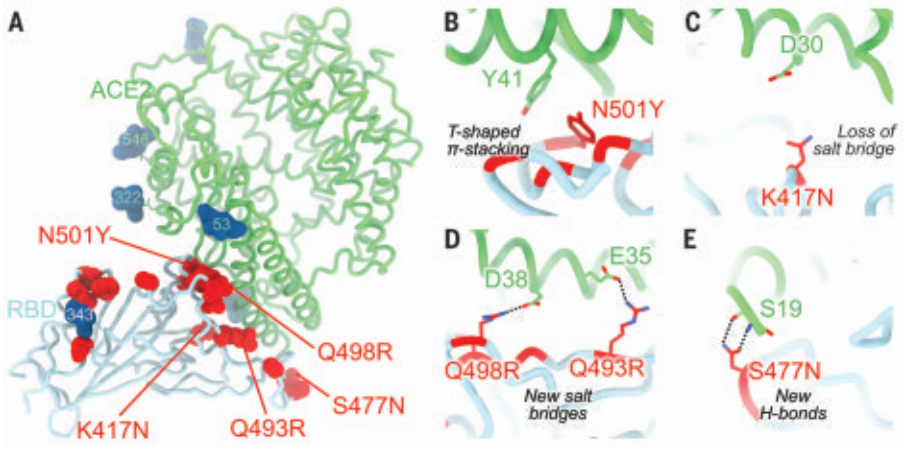


Fig. 4. Molecular basis of human ACE2 recognition by the SARS-CoV-2 Omicron RBD. (**A**) Ribbon diagram of the crystal structure of the Omicron RBD in complex with the ACE2 ectodomain. The S309 and S304 Fab fragments are not shown for clarity. (**B** to **E**) Zoomed-in views of the RBD-ACE2 interface. highlighting modulation of interactions due to introduction of the N501Y (B), K417N (C), Q493R/Q498R (D), and S477N (E) residue substitutions.

by SARS-CoV-2 Omicron and underscores the SARS-CoV-2 S mutational plasticity as well as the importance of targeting conserved epitopes in the design and development of vaccines and therapeutics. The S309 mAb (the parent of sotrovimab) neutralizes Omicron with one-half to one-third the potency with which it neutralizes Wuhan-Hu-1 or Washington-1, whereas the seven other clinical mAbs or mAb cocktails undergo reduction of neutralizing activity of one to two orders of magnitude or greater. Furthermore, some Omicron isolates (≈9%) harbor the R346K substitution, which, in conjunction with N440K (present in the main haplotype), leads to escape from C135 mAb-mediated neutralization (*25*, *51*). R346K does not affect S309 whether in isolation or in the context of the full constellation of Omicron mutations; hence, mAbs targeting antigenic site IV can be differently affected by Omicron (*7*, *9*, *46*). Whereas C135 was identified from a SARS-CoV-2 convalescent donor (*25*), S309 was isolated from a subject who recovered from a SARS-CoV infection in 2003 (*12*); the latter strategy increased the likelihood of finding mAbs that recognize epitopes that are mutationally constrained throughout sarbecovirus evolution. The identification of broadly reactive mAbs that neutralize multiple distinct sarbecoviruses, including SARS-CoV-2 variants, paves the way for designing vaccines that elicit broad sarbecovirus immunity (*52*–*56*). These efforts offer hope that the same strategies that contribute to solving the current pandemic will prepare us for possible future sarbecovirus pandemics.

REFERENCES AND NOTES

1. R. Viana *et al.*, *Nature* 10.1038/s41586-022-04411-y (2022).
2. M. McCallum *et al.*, *Science* **374**, 1621–1626 (2021).
3. M. McCallum *et al.*, *Science* **373**, 648–654 (2021).
4. A. C. Walls *et al.*, *Cell* **181**, 281–292.e6 (2020).
5. D. Wrapp *et al.*, *Science* **367**, 1260–1263 (2020).
6. D. A. Collier *et al.*, *Nature* **593**, 136–141 (2021).
7. E. Cameroni *et al.*, *Nature* 10.1038/s41586-021-04386-2 (2021).
8. Y. Cao *et al.*, *Nature* 10.1038/s41586-021-04385-3 (2021).
9. L. Liu *et al.*, *Nature* 10.1038/s41586-021-04388-0 (2021).
10. D. Planas *et al.*, *Nature* 10.1038/s41586-021-04389-z (2021).
11. L. A. VanBlargan *et al.*, bioRxiv 472828 [preprint] (2021).
12. D. Pinto *et al.*, *Nature* **583**, 290–295 (2020).
13. L. Piccoli *et al.*, *Cell* **183**, 1024–1042.e21 (2020).
14. C. L. Hsieh *et al.*, *Science* **369**, 1501–1505 (2020).
15. E. Olmedillas *et al.*, bioRxiv 441046 [preprint] (2021).
16. A. C. Walls *et al.*, *Nature* **531**, 114–117 (2016).
17. M. A. Tortorici, D. Veesler, *Adv. Virus Res.* **105**, 93–116 (2019).
18. Z. Cong *et al.*, bioRxiv 472934 [preprint] (2021).
19. B. Meng *et al.*, bioRxiv 473248 [preprint] (2021).
20. K. Sato *et al.*, Research Square 10.21203/rs.3.rs-1207670/v1 [preprint] (2022).
21. M. A. Tortorici *et al.*, *Nature* **597**, 103–108 (2021).
22. M. McCallum *et al.*, *Cell* **184**, 2332–2347.e16 (2021).
23. L. Stamatatos *et al.*, *Science* **372**, 1413–1418 (2021).
24. T. N. Starr *et al.*, *Nature* **597**, 97–102 (2021).
25. C. O. Barnes *et al.*, *Nature* **588**, 682–687 (2020).
26. C. A. Jette *et al.*, *Cell Rep.* **36**, 109760 (2021).
27. C. O. Barnes *et al.*, *Cell* **182**, 828–842.e16 (2020).
28. S. J. Zost *et al.*, *Nature* **584**, 443–449 (2020).
29. D. R. Martinez *et al.*, *Sci. Transl. Med.* eabj7125 (2021).
30. J. Dong *et al.*, *Nat. Microbiol.* **6**, 1233–1244 (2021).
31. A. J. Greaney *et al.*, *Sci. Transl. Med.* **13**, eabi9915 (2021).
32. J. Hansen *et al.*, *Science* **369**, 1010–1014 (2020).
33. C. G. Rappazzo *et al.*, *Science* **371**, 823–829 (2021).
34. A. Z. Wec *et al.*, *Science* **369**, 731–736 (2020).
35. Y.-J. Park *et al.*, *Science* eabm8143 (2022).
36. J. E. Bowen *et al.*, bioRxiv 473391 [preprint] (2021).
37. D. Corti, L. A. Purcell, G. Snell, D. Veesler, *Cell* **184**, 3086–3108 (2021).
38. T. Tada *et al.*, *mBio* **12**, e0069621 (2021).
39. M. Yuan *et al.*, *Science* **373**, 818–823 (2021).
40. P. Wang *et al.*, *Nature* **593**, 130–135 (2021).
41. T. N. Starr *et al.*, *Science* **371**, 850–854 (2021).
42. J. Lan *et al.*, *Nature* **581**, 215–220 (2020).
43. C. Toelzer *et al.*, *Science* **370**, 725–730 (2020).
44. X. Zhu *et al.*, *PLOS Biol.* **19**, e3001237 (2021).
45. E. C. Thomson *et al.*, *Cell* **184**, 1171–1187.e20 (2021).
46. T. N. Starr *et al.*, *Cell* **182**, 1295–1310.e20 (2020).
47. H. Shuai *et al.*, *EBioMedicine* **73**, 103643 (2021).
48. T. Pan *et al.*, *Signal Transduct. Target. Ther.* **6**, 420 (2021).
49. M. Hoffmann *et al.*, *Cell* 10.1016/j.cell.2021.12.032 (2022).
50. S. R. Leist *et al.*, *Cell* **183**, 1070–1085.e12 (2020).
51. Y. Weisblum *et al.*, *eLife* **9**, e61312 (2020).
52. A. C. Walls *et al.*, *Cell* **184**, 5432–5447.e16 (2021).
53. A. C. Walls *et al.*, *Cell* **183**, 1367–1382.e17 (2020).
54. P. S. Arunachalam *et al.*, *Nature* **594**, 253–258 (2021).
55. D. R. Martinez *et al.*, *Science* **373**, 991–998 (2021).
56. A. A. Cohen *et al.*, *Science* **371**, 735–741 (2021).

ACKNOWLEDGMENTS

Funding: Supported by National Institute of Allergy and Infectious Diseases grants DP1AI158186 and HHSN272201700059C (D.V.), a Pew Biomedical Scholars Award (D.V.), an Investigators in the Pathogenesis of Infectious Disease Awards from the Burroughs Wellcome Fund (D.V.), Fast Grants (D.V.), NIH grant S10OD032290 (D.V.), the University of Washington Arnold and Mabel Beckman Cryo-EM Center, and Wellcome Trust grant 209407/Z/17/Z. D.V. is an Investigator of the Howard Hughes Medical Institute. Beamline 4.2.2 of the Advanced Light Source, a US DOE Office of Science User Facility under contract DE-AC02-05CH11231, is supported in part by the ALS-ENABLE program funded by National Institute of General Medical Sciences grant P30 GM124169-01. For the purpose of open access, the author has applied a CC BY public copyright license to any Author Accepted Manuscript version arising from this submission. **Author contributions:** M.M., J.E.B., A.C.W., H.W.V., D.C., G.S., and D.V. conceived the project; M.M., L.E.R., S.K.Z., G.S., and D.V. designed experiments; M.M., N.C., S.K.Z., J.E.B., A.J., J.R.D., and A.E.P. expressed and purified proteins; L.E.R. and J.R.D. performed SPR analysis; S.K.Z. performed biolayer interferometry analysis; M.M. carried out cryo-EM sample preparation, data collection, and processing; M.M. and D.V. carried out cryo-EM model building and refinement; N.C. and J.R.D. carried out crystallization experiments; J.N. collected and processed x-ray diffraction data; M.M., T.I.C., G.S., and D.V. built and refined the crystal structure; and M.M. and D.V. wrote an initial draft of the manuscript with input from all authors. **Competing interests:** N.C., L.E.R., J.R.D., A.E.P., H.W.V., D.C., and G.S. are employees of Vir Biotechnology Inc. and may hold shares in Vir Biotechnology Inc. D.C. is currently listed as an inventor on multiple patent applications, which disclose the subject matter described in this manuscript. A.C.W., G.S., D.C., and D.V. are listed as inventors on patent 49230.03US1 describing the S309 epitope. H.W.V. is a founder and hold shares in PierianDx and Casma Therapeutics. Neither company provided resources. The Veesler laboratory has received a sponsored research agreement from Vir Biotechnology Inc. T.C.'s contribution was made under terms of a paid consultancy from Vir Biotechnology Inc. The remaining authors declare that the research was conducted in the absence of any commercial or financial relationships that could be construed as a potential conflict of interest. **Data and materials availability:** The cryo-EM map and coordinates have been deposited to the Electron Microscopy Databank and Protein Data Bank with the following accession numbers: 2 open/1 closed RBD EMD-25993; 2 closed/1 open RBD EMD-25992, EMD-25990, EMD-25991, PDB numbers 7TM0, 7TLY, 7TLZ. The crystal structure has been deposited to the Protein Data Bank with accession number 7TN0. Materials generated in this study will be made available on request, but we may require a completed materials transfer agreement signed with Vir Biotechnology or the University of Washington. This work is licensed under a Creative Commons Attribution 4.0 International (CC BY 4.0) license, which permits unrestricted use, distribution, and reproduction in any medium, provided the original work is properly cited. To view a copy of this license, visit https://creativecommons.org/licenses/by/4.0/. This license does not apply to figures/photos/artwork or other content included in the article that is credited to a third party; obtain authorization from the rights holder before using such material.

SUPPLEMENTARY MATERIALS

science.org/doi/10.1126/science.abn8652
Materials and Methods
Figs. S1 to S7
Tables S1 to S3
References (*57*–*77*)

24 December 2021; accepted 20 January 2022
Published online 25 January 2022
10.1126/science.abn8652

ORGANIC CHEMISTRY

Deracemization through photochemical *E/Z* isomerization of enamines

Mouxin Huang[1]†, Long Zhang[1,2]†, Tianrun Pan[1], Sanzhong Luo[1,2]*

Catalytic deracemization of α-branched aldehydes is a direct strategy to construct enantiopure α-tertiary carbonyls, which are essential to pharmaceutical applications. Here, we report a photochemical *E/Z* isomerization strategy for the deracemization of α-branched aldehydes by using simple aminocatalysts and readily available photosensitizers. A variety of racemic α-branched aldehydes could be directly transformed into either enantiomer with high selectivity. Rapid photodynamic *E/Z* isomerization and highly stereospecific iminium/enamine tautomerization are two key factors that underlie the enantioenrichment. This study presents a distinctive photochemical *E/Z* isomerization strategy for externally tuning enamine catalysis.

Carbonyl transformations are textbook chemical reactions, and subjecting them to asymmetric catalysis can provide enantiomerically pure products essential to pharmaceutical applications (*1*, *2*). Most of these methods involve stereogenic C–C/C–X bond formations featuring enol(ate)- or enamine-based processes, in which the geometry of the intermediate and associated facial selectivity during bond formation dictate the stereoselectivity (Fig. 1A) (*3*, *4*). In the construction of enantiopure α-tertiary carbonyls, catalytic deracemization is arguably the most atom-economical strategy (*5*). However, this transformation remains elusive despite tremendous progress in steering stereogenic carbonyl reactivity more generally (*6*, *7*). The challenges are threefold. First, deracemization is inherently endergonic with a negative entropy change. In addition, according to the principle of microscopic reversibility (*8*), the backward and forward pathways are identical for a given chiral catalyst cycle. Hence, the degree of enantioenrichment of the starting material cannot be adjusted without exogenous chemical or physical inputs (Fig. 1A). Recent seminal works by Bach (*9*, *10*) and Knowles and Miller (*11*) have demonstrated that light absorption can supply the necessary external perturbation to surmount the thermodynamic and kinetic constraints. Accordingly, photomediated energy transfer and electron transfer were found to work effectively in tandem with chiral catalysts to facilitate enantioselective deracemization of allenes or cyclic ureas, respectively (Fig. 1B). The final challenge is that α-tertiary carbonyls are easily racemized through undesired alternative pathways, adding a potentially complex time constraint to catalytic deracemization strategies (*12*, *13*).

Bearing these challenges in mind, we report a photochemical *E/Z* isomerization strategy for the deracemization of α-branched aldehydes by using simple aminocatalysts and readily available photosensitizers (Fig. 1C). Photoisomerization was found to perturb the *E/Z* distribution of the in situ generated enamine intermediates. This photochemical strategy together with our previous finding (*14*, *15*), that enamine of certain configuration (*E* or *Z*) could be stereospecifically formed from the corresponding enantiopure aldehyde with chiral primary amine catalysts such as **1a**, makes possible a highly enantioselective deracemization process. Although visible light–promoted *E/Z* isomerization of double bonds has been widely applied in chemical (*16*) and materials science (*17*), such a process with a transient catalytic intermediate in the pursuit of stereoselective catalysis has not been reported. Photochemical tuning of enamine intermediates has been explored in pioneering studies by MacMillan (*18*, *19*) and Melchiorre (*20*, *21*) using photoinduced electron transfer, which greatly expanded the capacity of nucleophilic enamine catalysis. Our current strategy complements these known processes by harnessing the *E/Z* photoisomerization of an enamine double bond.

We first investigated the deracemization of 2-phenylpropionaldehyde **2a** using a chiral primary amine catalyst (*14*). Screening of photocatalysts showed large variations of optical enrichment outcomes (table S3), and $Ir(ppy)_3$ was identified as the optimal one. The addition of a weak acid such as benzoic acid could significantly improve the enantioselectivity (table S1, entry 2), which is consistent with our previous finding on stereoselective enamine protonation (*15*). With $Ir(ppy)_3$, benzoic acid, and primary-tertiary amine (*S*)-**1a**/$HNTf_2$, the deracemization proceeded rapidly in 1 hour to afford (*R*)-**2a** in 77% yield (73% isolated yield) and 94% enantiomeric excess (ee). Control experiments indicated that aminocatalyst, photocatalyst, and light irradiation were all essential, and their absence led to no enrichment or rather poor enantioselectivity (table S1, entry 1 versus entries 3 and 4). The minor yet noticeable enantioselectivity observed under thermodynamic conditions (table S1, entries 3 and 4) could be accounted for by considering kinetic resolution through selective trapping of aldehyde by aminocatalyst (~10%) (figs. S12 and S13). A small extent of homo-coupling side-reaction (~3%), (fig. S11) was also observed, which may explain the loss of aldehyde during deracemization. We next examined the reactions with optically pure aldehydes. Both (*R*)- and (*S*)-**2a** led to (*R*)-selectivity with comparable enantioselectivity (table S1, entries 7 and 8). By contrast, racemization was observed without light irradiation in these cases. This observation strongly suggests that light supplies the major driving force for the current deracemization reaction. Addition of *E*-stilbene or the presence of ambient oxygen, well-known energy transfer quenchers, completely inhibited the deracemization (table S1, entries 5 and 6), which is a strong indication of the energy transfer mechanism.

The scope of this deracemization was next examined (Fig. 2A). 2-Arylpropanals bearing alkyl or aryl groups on the aromatic ring—such as Me, *i*-Bu, and Ph (**2a-e**)—gave high enantioselectivities. A 5-mmol-scale reaction of **2a** was also successful. The enantioenriched aldehydes can be isolated by simply filtering through a pad of silica gel without ee erosion (table S6 and figs. S2 and S3). Both electron-deficient substituents—such as halogen, trifluoromethyl, and ester (**2f-m**)—and electron-donating groups—such as alkoxyl, aryloxy, and methylenedioxy (**2n-s**)—gave consistently high enantioselectivity. Functional groups such as methylthio (**2t**) and dimethylamino (**2u**) also worked well. When aldehyde and ketone functionality coexisted in the same compound, deracemization would occur preferentially at the α-carbon of the aldehyde, whereas ketone moiety remained unchanged (**2v**). Expanding the aromatic ring or increasing the size of the branched chain led to a slight reduction of enantioselectivity (**2w-aa**). The deracemization could also be applied to complex arylaldehydes bearing functional groups such as amides and alkynes (**2ab** and **2ac**) and distinct chiral centers as in steroids and amino acids (**2ad** and **2ae**). α-Heteroaromatic groups—such as thiophene, dibenzofuran, and pyridine—were compatible with good to excellent enantioselectivity (**2af-ah**). Aldehydes other than 2-arylacetaldehyde showed low enantioenrichment (**2ai**), which we rationalized on the basis of the need for an aryl alkene chromophore in the enamine to achieve effective photoisomerization (*22*). α-Branched ketones were also examined but unfortunately showed no enantioenrichment (**2aj** and **2ak**). We executed simple oxidation of selected products to obtain nonsteroidal anti-inflammatory drug compounds without loss of enantiopurity. The aldehydes could also

[1]Center of Basic Molecular Science, Department of Chemistry, Tsinghua University, Beijing 100084, China. [2]Haihe Laboratory of Sustainable Chemical Transformations, Tianjin 300192, China.
*Corresponding author. Email: luosz@tsinghua.edu.cn
†These authors contributed equally to this work.

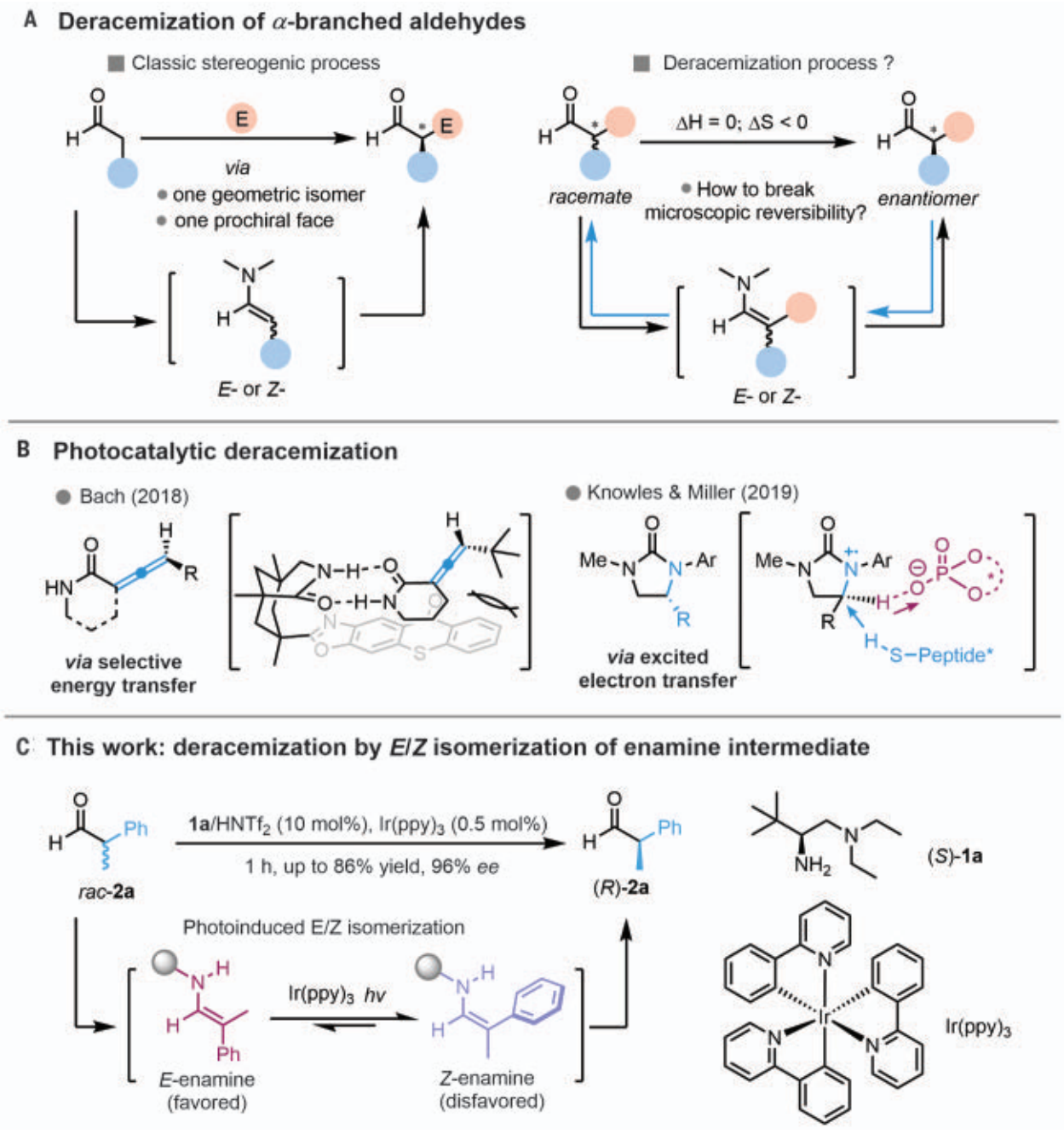


Fig. 1. Deracemization strategies. (**A**) Asymmetric carbonyl transformation. (**B**) Prior works on photocatalytic deracemization. (**C**) Deracemization of α-branched aldehydes through photochemical *E*/*Z* isomerization of enamine intermediate.

undergo reduction and condensation while maintaining enantiopurity (Fig. 2B).

In our deracemization process, the photochemical perturbation may proceed through electron transfer (followed by hydrogen transfer) or energy transfer–induced isomerization. The oxidation potential of the *E*- or *Z*-enamine intermediate was determined to be 0.73 V (*23*), and $Ir(ppy)_3$ has $E_{1/2}^{PC+/PC*}$ = 0.31 V. Although photoinduced electron transfer between enamine and photocatalyst is possible, this was discounted because the obtained enantioselectivity seemed uncorrelated with the excited-state redox potential but rather correlated with the triplet state energy (E_T), as revealed in the screening of different photocatalysts (Fig. 3A). High enantioselectivity was generally obtained by using photocatalysts with triplet-state energies in the 56 to 59 kcal/mol range, which is in line with the triplet-state energy of an enamine intermediate, 54.2 kcal/mol as determined with density functional theory (DFT) calculation (Fig. 4B). The observed inhibition effect with typical triplet-state quenchers such as stilbene or oxygen provides further support for an energy transfer mechanism (table S1, entries 5 and 6).

Stoichiometric experiments were conducted to examine the enamine formation by means of nuclear magnetic resonance (NMR) spectroscopy (Fig. 3D and figs. S15 to S18). The joint use of a strong acid $HNTf_2$ and a weak benzoic acid could significantly enhance the rate of iminium-enamine tautomerization, as previously reported (fig. S15) (*14*). In the presence of (*S*)-**1a**/$HNTf_2$, (*S*)-**2a** selectively

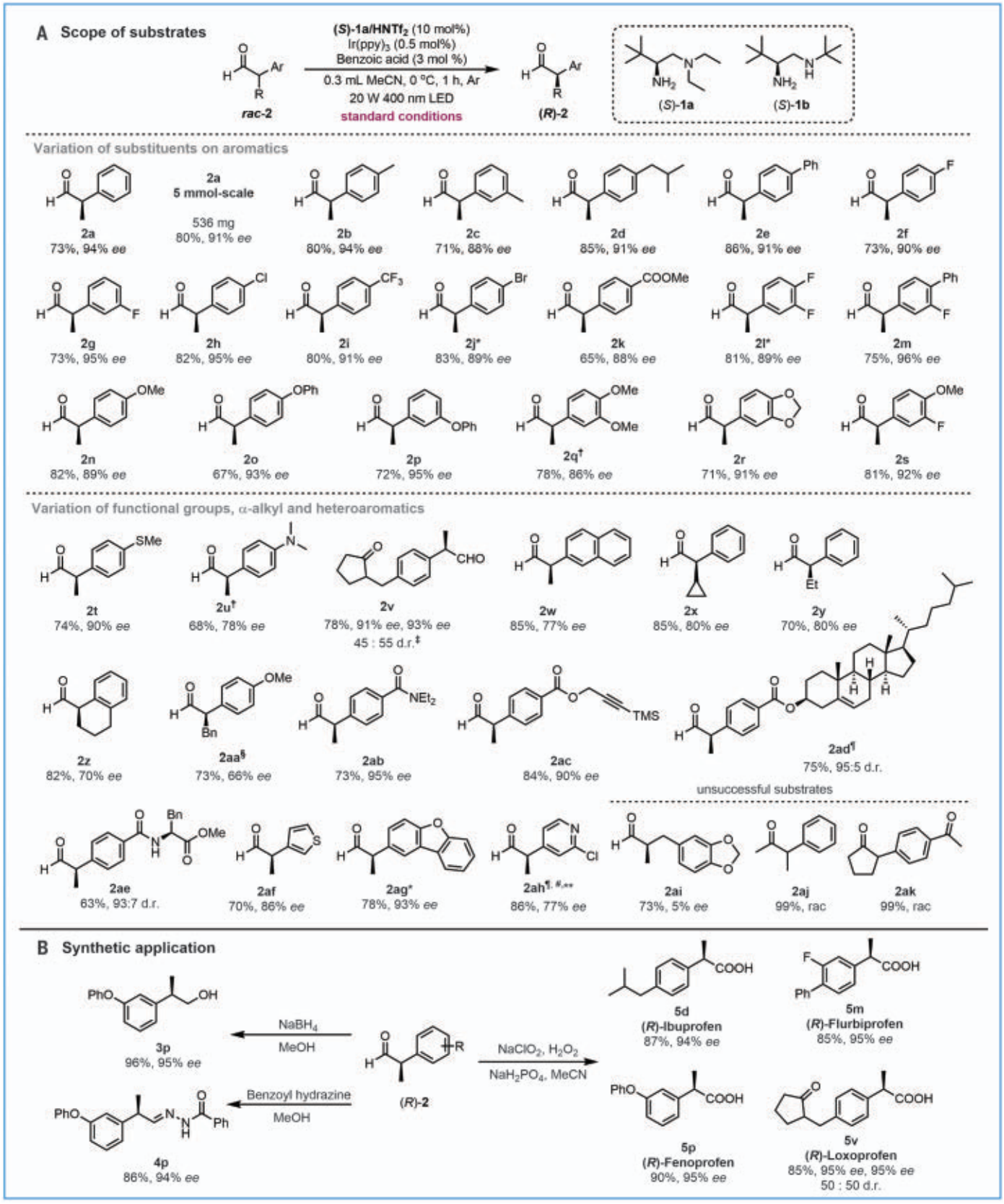


Fig. 2. Substrate scope and synthetic application. (**A**) Substrate scope. Reactions were performed on a 0.2-mmol scale. The yields are of isolated material after purification. The ee values were determined with high-performance liquid chromatography with the isolated products. *$Ir(F\text{-}ppy)_3$ instead of $Ir(ppy)_3$. †(*S*)-**1b**/HOTf instead of (*S*)-**1a**/$HNTf_2$. ‡The ee values were corresponding to the diastereomers as listed, respectively. §Reaction time was 2 hours. ¶CH_2Cl_2 instead of MeCN as the solvent. #$Ir(F\text{-}ppy)_3$ instead of $Ir(ppy)_3$. **The amount of benzoic acid was 15 mol % instead of 3 mol %. (**B**) Synthetic application. Reactions were performed on a 0.5-mmol scale.

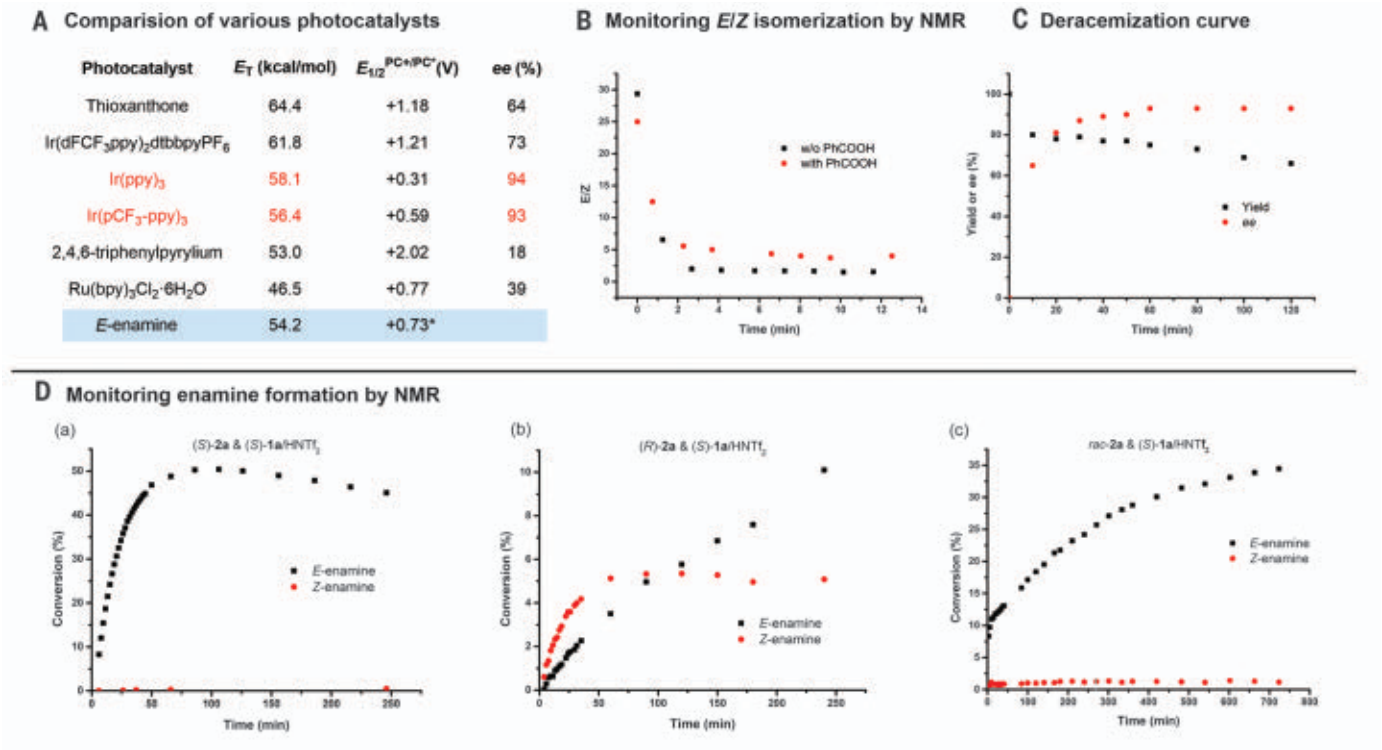


Fig. 3. Mechanistic experiments. (**A**) Investigation of the performance of various photosensitizers. *E_{ox} value instead of $E_{1/2}^{PC+/PC*}$. (**B**) Monitoring the ratio of *E*/*Z*-enamine by means of in situ irradiation in NMR spectrometer. The starting material was preequilibrated to attain an equilibrium ratio of *E*/*Z*-enamine. Conditions were (*S*)-**1a**/$HNTf_2$ (0.067 M), **2a** (0.067 M), benzoic acid (20 mol %), and $Ir(ppy)_3$ (2.5 mol %) in 0.6 mL MeCN-d_3, preequilibrated for 10 hours then exposed to 405-nm laser irradiation inside NMR spectrometer for 20 min. Details are in the supplementary materials (figs. S19 to S23). (**C**) Time-course profile for deracemization under the standard conditions. (**D**) Monitoring the enamine formation process by NMR (a) with (*S*)-**2a**; (b) with (*R*)-**2a**; and (c) with *rac*-**2a**. Conditions were (*S*)-**1a**/$HNTf_2$ (0.067 M) and **2a** (0.067 M) in 0.6 mL MeCN-d_3, with PhCOOBn as the internal standard.

formed *E*-enamine, equilibrating at about 50% conversion (Fig. 3D, a), whereas (*R*)-**2a** preferentially gave *Z*-enamine, which was equilibrated at rather lower conversion (~5%) (Fig. 3D, b), after which overriding formation of *E*-enamine was observed. We also examined enamine formation with *rac*-**2a**, showing a similar kinetic profile to that of (*S*)-**2a**, with *E*-enamine as the major isomer (*E*/*Z* = 30:1, equilibrated at ~35% conversion) (Fig. 3D, c). These results suggested that (*S*)-**2a** and (*S*)-**1a** are stereochemically matched with each other, and their coupling led to the formation of *E*-enamine, which is favored both thermodynamically and kinetically.

Moreover, enamine isomerization was investigated with an in situ irradiative NMR experiment. A 405-nm laser beam was directed into a preequilibrated reaction mixture inside the NMR spectrometer by means of optical fiber. *E*-enamine was found to isomerize into *Z*-enamine rapidly, and a photostationary state was reached within 3 min with a *E*/*Z*-enamine ratio maintained at 1.7:1 or 4:1, depending on the presence of acid additive (Fig. 3B). A quenching study verified that the excited photocatalyst could be selectively quenched by enamine (figs. S25 to S27). We also tracked the reaction progress for deracemization of **2a**, and a photodynamic equilibrium could be established in 1 hour with 94% ee (Fig. 3C). Similar behaviors were observed with other substrates such as **2f**, **2h**, **2w**, **2y**, and **2aa** (figs. S6 to S10). The enantioselectivity did not change upon extending irradiation, but turning off the light source led to immediate racemization (figs. S28 to S30). This observation indicated that the deracemization was driven by photochemical enamine isomerization.

We further rationalized the mechanism with DFT calculations. On the basis of previous work, a weak acid-bridged proton transfer pathway was proposed to account for the iminium-enamine tautomerization (*24*). We calculated all four possible transition states (**TS 1** to **4**) that lead to *E*- and *Z*-enamine (Fig. 4A). The calculations predicted that (*S*)-**2a** would form *E*-enamine selectively (**TS1** versus **TS2**) with $\Delta\Delta G_{21}$ = 4.6 kcal/mol, whereas (*R*)-**2a** showed moderate preference for *Z*-enamine (**TS3** versus **TS4**) with $\Delta\Delta G_{43}$ = 1.2 kcal/mol. These results are fully consistent with the experimentally observed kinetic profile of enamine formation (Fig. 3D). According to the principle of microscopic reversibility (*8*), the backward enamine protonation may proceed by means of **TS1** and **TS4** for *E*-enamine and **TS2** and **TS3** for *Z*-enamine: Both processes show the same selectivity with $\Delta\Delta G_{41}$ and $\Delta\Delta G_{32}$, both equal to 2.9 kcal/mol. Hence, the protonation of *E*- or *Z*-enamine should proceed with high facial selectivity to produce (*S*)-**2a** or (*R*)-**2a**, respectively. The vertical excitation energies ($S_0 \rightarrow T_1$) for *E*/*Z* enamine were calculated to be 71.8 and 74.6 kcal/mol, favoring excitation of *E*-enamine (Fig. 4B). The preferential excitation of *E*-enamine over *Z*-enamine could be explained by the deconjugation of the β-enaminyl phenyl group in the *Z*-geometry because of steric hindrance. Recently, a similar deconjugation effect has also been observed in visible light–promoted isomerization of *E*-alkenes to their thermodynamically disfavored *Z*-isomers (*25*–*27*).

On the basis of the mechanistic investigations above, a plausible mechanism for optical enrichment was proposed (Fig. 4C). Under the ground state, the stereochemically matched enantiomer forms a dominant *E*-configured enamine, which is continuously isomerized to its disfavored *Z*-isomer through photocatalytic energy transfer. Facially selective protonation of the *Z*-enamine then delivers the mismatched enantiomer. Hence, the consumption of the

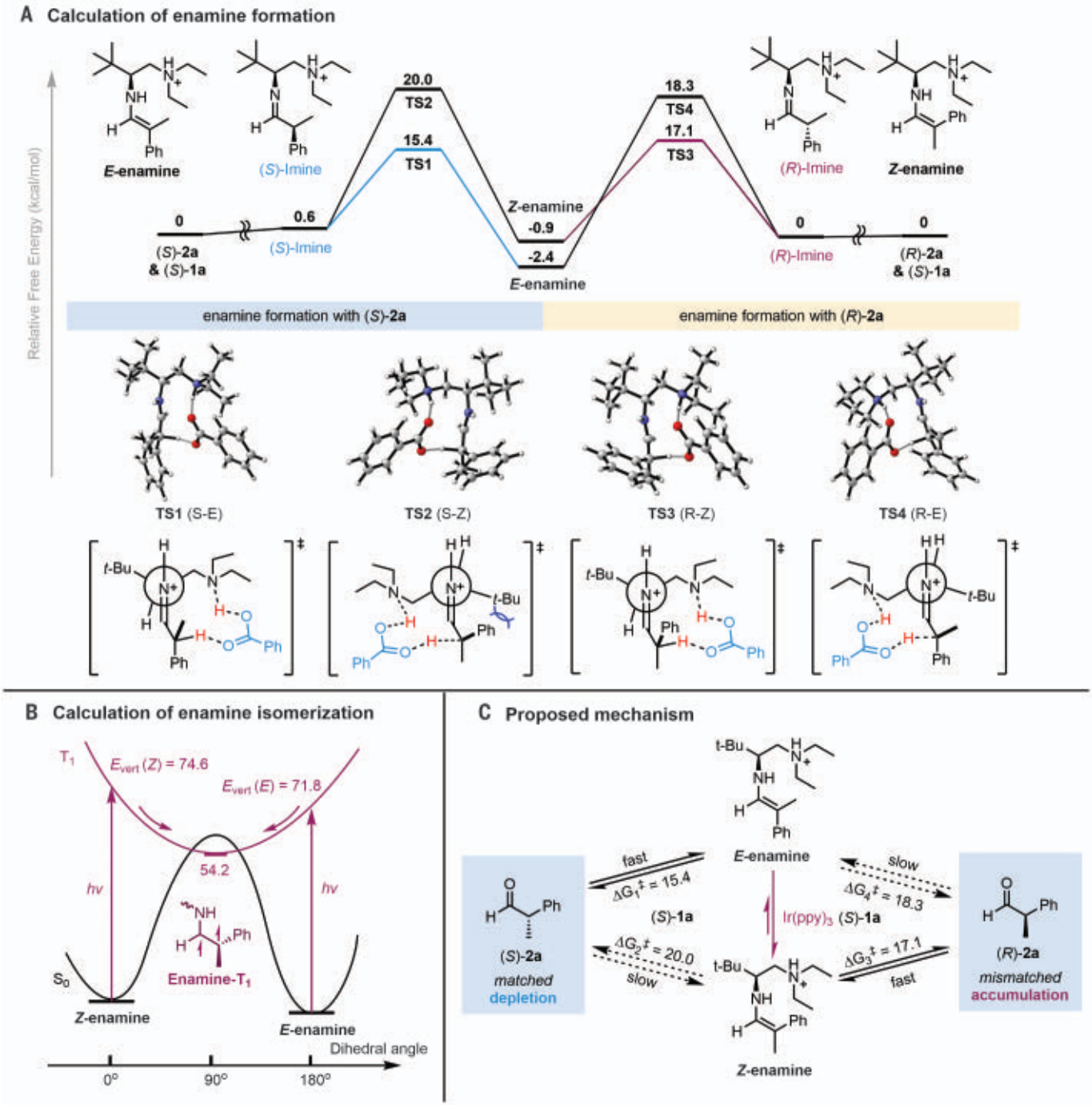


Fig. 4. DFT simulation studies and proposed mechanism. (**A**) Calculated energetics of enamine formation process. (**B**) Calculated energetics of enamine isomerization process. (**C**) Proposed mechanism.

matched enantiomer and accumulation of the mismatched enantiomer are sustained to facilitate effective deracemization. In this process, the stereospecificity of enamine protonation by chiral primary aminocatalysis is also a critical determinant for effective optical enrichment.

REFERENCES AND NOTES

1. S. E. Denmark, J. R. Heemstra Jr., G. L. Beutner, *Angew. Chem. Int. Ed.* **44**, 4682–4698 (2005).
2. B. Schetter, R. Mahrwald, *Angew. Chem. Int. Ed.* **45**, 7506–7525 (2006).
3. S. Mukherjee, J. W. Yang, S. Hoffmann, B. List, *Chem. Rev.* **107**, 5471–5569 (2007).
4. Y. Yamashita, T. Yasukawa, W.-J. Yoo, T. Kitanosono, S. Kobayashi, *Chem. Soc. Rev.* **47**, 4388–4480 (2018).
5. K. Faber, *Chemistry* **7**, 5004–5010 (2001).
6. M. Rueping, A. Kuenkel, I. Atodiresei, *Chem. Soc. Rev.* **40**, 4539–4549 (2011).
7. S. Afewerki, A. Córdova, *Chem. Rev.* **116**, 13512–13570 (2016).
8. D. G. Blackmond, *Angew. Chem. Int. Ed.* **48**, 2648–2654 (2009).
9. A. Hölzl-Hobmeier *et al.*, *Nature* **564**, 240–243 (2018).
10. M. Plaza, C. Jandl, T. Bach, *Angew. Chem. Int. Ed.* **59**, 12785–12788 (2020).
11. N. Y. Shin, J. M. Ryss, X. Zhang, S. J. Miller, R. R. Knowles, *Science* **366**, 364–369 (2019).
12. F. Agbossou, J.-F. Carpentier, A. Mortreux, *Chem. Rev.* **95**, 2485–2506 (1995).
13. J. Burés, A. Armstrong, D. G. Blackmond, *Chem. Sci.* **3**, 1273–1277 (2012).
14. L. Zhang, N. Fu, S. Luo, *Acc. Chem. Res.* **48**, 986–997 (2015).
15. N. Fu, L. Zhang, J. Li, S. Luo, J. P. Cheng, *Angew. Chem. Int. Ed.* **50**, 11451–11455 (2011).
16. V. García-López, D. Liu, J. M. Tour, *Chem. Rev.* **120**, 79–124 (2020).
17. H. K. Bisoyi, Q. Li, *Chem. Rev.* **116**, 15089–15166 (2016).
18. D. A. Nicewicz, D. W. MacMillan, *Science* **322**, 77–80 (2008).
19. M. T. Pirnot, D. A. Rankic, D. B. Martin, D. W. MacMillan, *Science* **339**, 1593–1596 (2013).

20. E. Arceo, I. D. Jurberg, A. Alvarez-Fernández, P. Melchiorre, *Nat. Chem.* **5**, 750–756 (2013).
21. M. Silvi, E. Arceo, I. D. Jurberg, C. Cassani, P. Melchiorre, *J. Am. Chem. Soc.* **137**, 6120–6123 (2015).
22. J. B. Metternich, R. Gilmour, *Synlett* **27**, 2541–2552 (2016).
23. Y. Li, D. Wang, L. Zhang, S. Luo, *J. Org. Chem.* **84**, 12071–12090 (2019).
24. Y. Zhu, L. Zhang, S. Luo, *J. Am. Chem. Soc.* **138**, 3978–3981 (2016).
25. K. Singh, S. J. Staig, J. D. Weaver, *J. Am. Chem. Soc.* **136**, 5275–5278 (2014).
26. J. B. Metternich, R. Gilmour, *J. Am. Chem. Soc.* **137**, 11254–11257 (2015).
27. J. J. Molloy *et al.*, *Science* **369**, 302–306 (2020).

ACKNOWLEDGMENTS

We thank J. Cheng, X. Guo, and L. Jiao for helpful discussions. **Funding:** This work is supported by the Natural Science Foundation of China (91956000, 22031006, and 21861132003), Tsinghua University Initiative Scientific Research Program, and Haihe Laboratory of Sustainable Chemical Transformations. We thank the Tsinghua Xuetang Talents Program for computational support. L.Z. is supported by the National Program of Top-notch Young Professionals. **Author contributions:** S.L. conceived and directed the project. M.H. conducted the experiments, with the help of T.P.; L.Z. performed the computational studies. M.H. and S.L. wrote the manuscript, with contributions from all authors. **Competing interests:** The authors declare that they have no competing interests. **Data and materials availability:** All data are available in the main text or the supplementary materials.

SUPPLEMENTARY MATERIALS

science.org/doi/10.1126/science.abl4922
Materials and Methods
Supplementary Text
Figs. S1 to S33
Tables S1 to S7
References (*28*–*52*)

16 July 2021; resubmitted 4 November 2021
Accepted 25 January 2022
10.1126/science.abl4922

BLACK HOLES

Black hole spin–orbit misalignment in the x-ray binary MAXI J1820+070

Juri Poutanen[1,2,3]*, Alexandra Veledina[1,3,2], Andrei V. Berdyugin[1], Svetlana V. Berdyugina[4], Helen Jermak[5], Peter G. Jonker[6,7], Jari J. E. Kajava[1,8], Ilia A. Kosenkov[1], Vadim Kravtsov[1], Vilppu Piirola[1], Manisha Shrestha[5,9], Manuel A. Perez Torres[10,11], Sergey S. Tsygankov[1,2]

The observational signatures of black holes in x-ray binary systems depend on their masses, spins, accretion rate, and the misalignment angle between the black hole spin and the orbital angular momentum. We present optical polarimetric observations of the black hole x-ray binary MAXI J1820+070, from which we constrain the position angle of the binary orbital. Combining this with previous determinations of the relativistic jet orientation, which traces the black hole spin, and the inclination of the orbit, we determine a lower limit of 40° on the spin-orbit misalignment angle. The misalignment must originate from either the binary evolution or black hole formation stages. If other x-ray binaries have similarly large misalignments, these would bias measurements of black hole masses and spins from x-ray observations.

Black holes can be characterized with just two parameters: mass and spin. When a black hole resides in a binary system, accreting material from a companion donor star through the accretion disk, there are additional parameters that determine its observational signatures: the mass accretion rate and the misalignment angle between the black hole spin and the orbital axis. Standard methods to measure black hole spin from x-ray observations—iron line spectroscopy (*1*) or modeling of the accretion disk spectrum (*2*)—assume that the misalignment angle is small. Conversely, the standard interpretation of low-frequency quasi-periodic oscillations in x-ray and optical observations of black hole x-ray binaries as precession of the accretion disk (*3*–*5*) requires the assumption that the misalignment angle is non-negligible. Substantial misalignment is theoretically predicted for x-ray binaries that received high velocities during formation (*6*). The misalignment angle must be inherited from the formation process, because it can only decrease when the black hole is accreting (*7*). Gravitational wave observations of merging black holes have detected signatures of orbital precession (*8*), indicating nonzero misalignment in these systems (*9*), though they might not be representative of the wider population.

Measuring the misalignment angle in x-ray binaries requires determining the three-dimensional orientation of the black hole spin and orbital axis. Accreting black holes often show relativistic jets, which are launched along an axis determined by the black hole spin direction (*10*). The jet inclination angle can be directly obtained in some cases from radio observations (*11*), whereas the jet position angle can be measured using either radio or x-ray imaging. Combining these two angles allows the black hole spin orientation to be determined. Orbital parameters such as period and orbital inclination can be determined using spectroscopic measurements of radial velocities of the donor star taken during quiescence, the stage at which accretion to the black hole is reduced and optical emission is not dominated by the accretion disk, through orbital modulation of the optical photometry and using constraints from the presence or absence of x-ray and optical disk eclipses (*12*).

The black hole x-ray binary MAXI J1820+070 was discovered as a transient x-ray source on 11 March 2018 (*13*). X-ray quasi-periodic oscillations detected shortly after this discovery were observed for >100 days (*14*). Ejections of material traveling at relativistic velocities have been observed from this source in both radio and x-rays, indicating that the jet inclination (measured from the line of sight) is $i_{\rm jet} = 63°\pm3°$ and the position angle (measured on the plane of the sky from north to east) is $\theta_{\rm jet} = 25.^{\circ}1\pm1.^{\circ}4$ (*15*–*17*). Both angles were determined to be stable over the observed

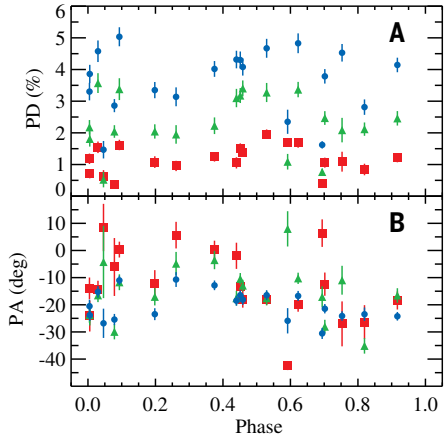


Fig. 1. Observed optical polarization properties of MAXI J1820+070. (**A**) Intrinsic PD and (**B**) PA of MAXI J1820+070 during quiescence are shown as a function of orbital phase (using a published ephemeris) (*23*). The intrinsic values were obtained from the observed ones by subtracting the foreground interstellar polarization, which is measured from nearby field stars. Blue circles, green triangles, and red squares correspond to the B, V, and R bands, respectively, with error bars showing the 68% confidence levels. Polarization is strongest in the B band and weakest in the R band, although the angle does not change substantially.

[1]Department of Physics and Astronomy, FI-20014 University of Turku, Finland. [2]Space Research Institute (IKI) of the Russian Academy of Sciences, 117997 Moscow, Russia. [3]Nordic Institute for Theoretical Physics (Nordita), KTH Royal Institute of Technology and Stockholm University, SE-10691 Stockholm, Sweden. [4]Leibniz-Institut für Sonnenphysik, 79104 Freiburg, Germany. [5]Astrophysics Research Institute, Liverpool John Moores University, L3 5RF Liverpool, UK. [6]Department of Astrophysics, Institute for Mathematics, Astrophysics and Particle Physics (IMAPP), Radboud University, NL-6500 GL Nijmegen, Netherlands. [7]Space Research Organisation of the Netherlands (SRON), Netherlands Institute for Space Research, NL-2333, CA Leiden, Netherlands. [8]Centro de Astrobiología, Villanueva de la Cañada, S-28692 Madrid, Spain. [9]Department of Physics and Astronomy, University of Denver, Denver, CO 80208, USA. [10]Instituto de Astrofísica de Canarias, E-38205 La Laguna, Tenerife, Spain. [11]Departamento de Astrofísica, Universidad de La Laguna, E-38206 La Laguna, Tenerife, Spain.
***Corresponding author. Email: juri.poutanen@utu.fi**

duration of the outburst. The orbital inclination has been constrained to the range $66° < i_{orb} < 81°$ by the lack of x-ray eclipses and the detection of grazing optical eclipses (*12*). Determination of the orientation of the orbital axis requires one further parameter, the orbital position angle θ_{orb}.

We monitored MAXI J1820+070 in the optical B, V, and R photometric bands using double image polarimeters (*18*, *19*) during the 2018 outburst and quiescence. We obtained the source intrinsic linear polarization by subtracting the foreground interstellar polarization, measured from nearby field stars. During the outburst, when the relativistic jets were detected at radio frequencies, the intrinsic linear polarization degree (PD) in the V and R bands reached 0.5% at a polarization angle [(PA), also measured from north to east)] of 23° to 24°, which coincides with the jet position angle within the uncertainties (*20*, *21*). After the source faded in the x-rays, the PD increased by a factor of 5 to 10 and the PA changed by 40°±4° to −17°±4° (Fig. 1 and table S1) (*22*). This increase in PD is most prominent in the B band, which also has the highest PD in the range 1.5 to 5%, whereas the R-band polarization changes from 0.4 to 2%. The PA is most precisely determined in the B band, which also shows the least variability, with the mean being $\langle PA \rangle = -19.^{\circ}7 \pm 1.^{\circ}2$.

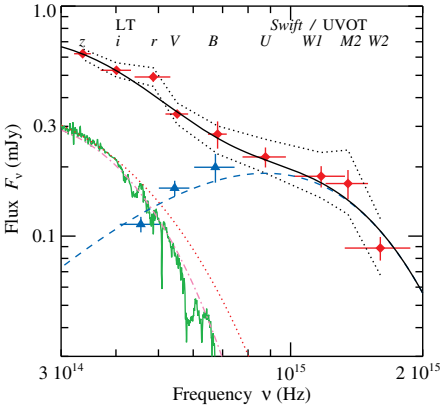


Fig. 2. Spectral energy distribution. The average spectral energy distribution (SED) of MAXI J1820+070 (red diamonds) as observed with the Liverpool Telescope (LT) and Swift UVOT in July 2020 and corrected for reddening, with color excess $E(B-V) = 0.29$. The photometric bands are indicated at the top of the figure. The black dotted lines give the lower and upper limits on the flux for lower and higher extinction with $E(B-V) = 0.25$ and 0.325, respectively. The polarized flux divided by the best-fitting model polarization degree $P_{UV} = 0.055$ (i.e., multiplied by a factor of ~18) is indicated by blue triangles. Error bars show 68% confidence levels. The solid black line gives the total model flux consisting of the companion star modeled as a blackbody (pink dot-dashed line), accretion disk (red dotted line), and a hot blackbody (blue dashed line). The spectrum of a K7 star (*24*) is shown for comparison (solid green line).

We identify three properties of the quiescent-state polarization: (i) It is strongest in the blue part of the optical, with approximate dependence on frequency ν as $PD(\nu) \propto \nu^3$ (Fig. 2 and table S1); (ii) the PD remains high in the range 0.5 to 5% and the PA is stable; and (iii) the PA undergoes apparently stochastic variations with an amplitude of <10° with no dependence on the orbital phase (*23*). These properties constrain the mechanism of the polarized emission. We modeled broadband photometric data obtained with the Liverpool Telescope and the Swift Ultraviolet and Optical Telescope (UVOT) together with the polarized fluxes (Fig. 2). We decomposed the total spectral energy distribution into three components: a companion star (contributing ~25% to the R-band flux) (*24*), an accretion disk with inner temperature $T_d \approx 6200$ K and inner radius $R_d \approx 6 \times 10^{10}$ cm, and an additional ultraviolet (UV) component with blackbody temperature $T_{bb} \approx 15,000$ K and radius $R_{bb} \approx 9 \times 10^9$ cm (table S4). The properties of the polarized flux are consistent with being produced by the UV component with constant PD of 5 to 8%.

The jet cannot be the source of the polarized emission because its optically thin synchrotron spectrum is red, which is inconsistent with the observed blue spectrum of polarized light. Moreover, the PA is offset by ~40° from the jet position angle. The absence of detectable orbital variations in the PA excludes a hot spot origin. An optically thick accretion disk is excluded by the high PD and blue spectrum. A potential source of the polarized emission is scattering of the accretion disk's radiation in the hot, optically thin, geometrically thick accretion flow close to the disk's inner radius (*22*, *25*), which may also be responsible for the observed UV excess. This mechanism would produce polarization parallel to the meridional plane, i.e., the plane formed by the orbital axis and the direction toward the observer. Another possibility is dust scattering, thought to be responsible for the blue polarized spectra observed from accretion disks around some supermassive black holes (*26*). The presence of dust in quiescent-state black hole x-ray binaries has been inferred from the detection of the mid-IR excess in two systems (*27*). If dust is located within a flattened envelope, in the wind around the accretion disk, or in a circumbinary disk, the resulting polarization vector would also be parallel to the meridional plane. However, if dust forms an extended, approximately spherical structure at a high elevation above the accretion disk, the polarization would be perpendicular to the meridional plane. We consider the latter scenario to be implausible, as a nearly spherical envelope cannot produce the high observed PD. A dust scattering mechanism would not explain the UV excess because the disk does not emit in that range and hence there are no photons to be scattered by the dust.

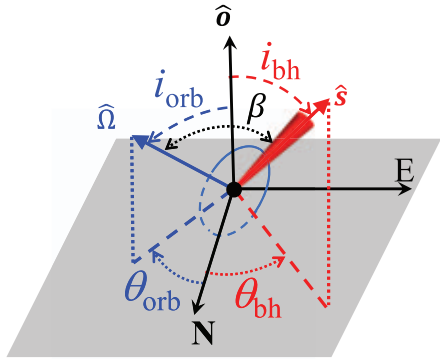


Fig. 3. Geometry of the system from the observer's perspective. The gray plane is the plane of the sky, labelled with north and east axes, perpendicular to the line of sight toward the observer $\hat{o}$. The angles between the line of sight and the vectors of the orbital angular momentum $\hat{\Omega}$ and and the black hole spin $\hat{s}$ are the inclinations i_{orb} and i_{bh}. The corresponding position angles θ_{orb} and θ_{bh} are the azimuthal angles projected onto the sky, measured from north to east. The misalignment angle β is defined as the angle between $\hat{s}$ and $\hat{\Omega}$. The red cone indicates the jet and the blue ellipse indicates the companion star orbit around the black hole, which is at the coordinate center.

Independent of the spectral modeling and geometry of the emission, the stability of the PA (most evident in the B band, Fig. 1) over the orbital phase suggests that the polarization is related to the orbital axis, either parallel or perpendicular to it. Hence, the observed PA provides information about the position angle of the orbital axis. The misalignment angle β can be determined from

$$\cos\beta = \cos i_{bh}\cos i_{orb} + \sin i_{bh}\sin i_{orb}\cos\Delta \quad (1)$$

where i_{bh} is the inclination of the black hole spin vector (measured from the line of sight) and $\Delta = \theta_{bh} - \theta_{orb}$ is the difference between the position angles of the black hole spin vector θ_{bh} and the orbital angular momentum θ_{orb} (the geometry is illustrated in Fig. 3). If the black hole spin vector is directed along the southern approaching jet, then its inclination is $i_{bh} = i_{jet} = 63° \pm 3°$ and its position angle is $\theta_{bh} = 180° + \theta_{jet} = 205.^{\circ}1 \pm 1.^{\circ}4$ (*15*–*17*). The smallest misalignment, $\beta \approx 42°$, is achieved when the orbital spin is also directed south at $\theta_{orb} = \langle PA \rangle + 180° = 160.^{\circ}3 \pm 1.^{\circ}2$ (because the PA has an ambiguity of 180°) at the inclination $i_{orb} \approx 73°$. The probability distribution for β in this case is shown in Fig. 4. The radial velocity measurements (*12*) do not differentiate between orbital inclinations i_{orb} and $180° - i_{orb}$ so there is a second solution with $i_{orb} \approx 107°$ and $\beta \approx 63°$. If either the

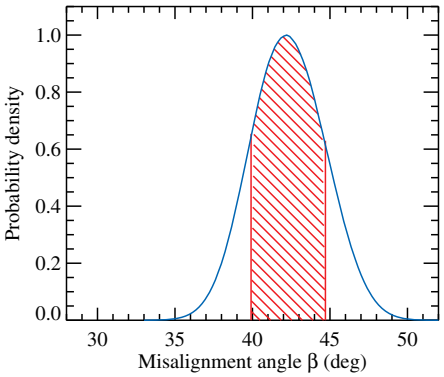


Fig. 4. Probability distribution function for the misalignment angle. The distribution normalized to the peak value is shown for the smallest misalignment angle possible. This case corresponds to the black hole spin directed along the southern approaching jet and the orbital spin being directed south at position angle $\theta_{orb} = \langle PA \rangle + 180°$ and inclination $i_{orb} \approx 73°$. The red hatched region corresponds to the 68% confidence interval (i.e., between 16th and 84th percentiles of the posterior probability distribution). Distributions of β for the other seven possible combinations of θ_{orb}, i_{orb}, and i_{bh} are shown in fig. S4.

orbital angular momentum or the black hole spin is instead directed to the north, the black hole rotation is then retrograde, resulting in $\beta \approx 117°$ or 138° for the same two solutions for the orbital inclination as above.

If the polarization vector is perpendicular to the meridional plane, the orbital position angle can take values $\theta_{orb} = \langle PA \rangle + 90°$ or $\langle PA \rangle + 270°$. This geometrical arrangement leads to nearly identical values for β because the difference between jet position angle and $\langle PA \rangle$ is ~45°. All possible cases for the orientations of the black hole and orbital spins, the resulting values for β, and the azimuthal angle of the black hole spin in the orbital plane are listed in table S5. Corresponding probability distributions are shown in figs. S4 and S5.

The difference of ≈45° between the jet position angle and the PA indicates ≳40° misalignment between the black hole spin and the orbital angular momentum. This result is independent of modeling or geometric ambiguities because it relies only on the observed difference between the polarization angle and jet position angle.

During outbursts, when material reaches the black hole, this misalignment affects the innermost regions of the accretion disk. For a nonzero spin, particles moving around the black hole—in orbits tilted with respect to the black hole equatorial plane—undergo precession at a rate that decreases with radius (*3*). Hence, a tilted disk is subject to twist and warp. A high misalignment adds complications to the models of quasi-periodic oscillations observed in black hole x-ray binaries, which rely on precession of the inner parts of the accretion flow, implying that the whole flow is misaligned by 2β from the orbital axis in some phases (*3*). For $\beta \sim 40°$, the inner parts of the accretion disk would need to become almost perpendicular to its outer parts. Most models assume smaller misalignment angles, typically $\beta \sim 10°$ to 20° (*3*, *4*, *5*) although highly inclined possibilities with $\beta \sim 45°$ to 65° have sometimes been considered (*28*).

High misalignment has previously been suggested on the basis of observations of the gamma-ray light curves produced by the jet in Cyg X-3 (*29*), and differences between orbital and jet inclination angles are ~15° in GRO J1655–40 (*7*) and ~50° in V4641 Sgr (*30*) though the latter is highly uncertain. Misalignment has also been theorized on the basis of the inferred high kick velocities of x-ray binaries acquired during formation (*6*). For the black hole x-ray binary MAXI J1820+070, the high misalignment was identified only after obtaining the constraints on the position angle of the orbital angular momentum θ_{orb}. Without information on the binary plane orientation, we would have obtained only a lower limit on the misalignment angle in MAXI J1820+070 of ≳5° because the orbital inclination is only marginally different from the jet inclination.

Our results demonstrate the need to treat the misalignment angle as a free parameter when measuring black hole masses and spins. Assuming that the black hole spin and the orbital angular momentum are aligned introduces a systematic bias on measurements (*12*, *15*, *31*). A large misalignment angle is expected to drive precession of the binary orbital plane, altering the gravitational waves emitted during a subsequent merger event (*9*). Evidence for orbital precession has been found from population properties of black hole mergers observed using gravitational waves (*8*).

REFERENCES AND NOTES

1. C. S. Reynolds, *Space Sci. Rev.* **183**, 277–294 (2014).
2. J. E. McClintock, R. Narayan, J. F. Steiner, *Space Sci. Rev.* **183**, 295–322 (2014).
3. P. C. Fragile, O. M. Blaes, P. Anninos, J. D. Salmonson, *Astrophys. J.* **668**, 417–429 (2007).
4. A. Ingram, C. Done, P. C. Fragile, *Mon. Not. R. Astron. Soc.* **397**, L101–L105 (2009).
5. A. Veledina, J. Poutanen, A. Ingram, *Astrophys. J.* **778**, 165 (2013).
6. P. Atri *et al.*, *Mon. Not. R. Astron. Soc.* **489**, 3116–3134 (2019).
7. T. J. Maccarone, *Mon. Not. R. Astron. Soc.* **336**, 1371–1376 (2002).
8. R. Abbott *et al.*, *Astrophys. J. Lett.* **913**, L7 (2021).
9. T. A. Apostolatos, C. Cutler, G. J. Sussman, K. S. Thorne, *Phys. Rev. D* **49**, 6274–6297 (1994).
10. J. C. McKinney, A. Tchekhovskoy, R. D. Blandford, *Science* **339**, 49–52 (2013).
11. I. F. Mirabel, L. F. Rodríguez, *Annu. Rev. Astron. Astrophys.* **37**, 409–443 (1999).
12. M. A. P. Torres *et al.*, *Astrophys. J. Lett.* **893**, L37 (2020).
13. T. Kawamuro *et al.*, MAXI/GSC detection of a probable new X-ray transient MAXI J1820+070. The Astronomer's Telegram no. 11399 (2018).
14. H. Stiele, A. K. H. Kong, *Astrophys. J.* **889**, 142 (2020).
15. P. Atri *et al.*, *Mon. Not. R. Astron. Soc.* **493**, L81–L86 (2020).
16. J. S. Bright *et al.*, *Nat. Astron.* **4**, 697–703 (2020).
17. M. Espinasse *et al.*, *Astrophys. J. Lett.* **895**, L31 (2020).
18. V. Piirola, A. Berdyugin, S. Berdyugina, "DIPOL-2: a double image high precision polarimeter" in *Proc. SPIE 9147, Ground-based and Airborne Instrumentation for Astronomy V* (Society of Photo-Optical Instrumentation Engineers, 2014), p. 91478I; doi: 10.1117/12.2055923
19. V. Piirola, I. A. Kosenkov, A. V. Berdyugin, S. V. Berdyugina, J. Poutanen, *Astron. J.* **161**, 20 (2021).
20. A. Veledina *et al.*, *Astron. Astrophys.* **623**, A75 (2019).
21. I. A. Kosenkov *et al.*, *Mon. Not. R. Astron. Soc.* **496**, L96–L100 (2020).
22. Materials and methods are available as supplementary materials.
23. M. A. P. Torres *et al.*, *Astrophys. J. Lett.* **882**, L21 (2019).
24. A. J. Pickles, *Publ. Astron. Soc. Pac.* **110**, 863–878 (1998).
25. R. Narayan, J. E. McClintock, I. Yi, *Astrophys. J.* **457**, 821 (1996).
26. W. Webb, M. Malkan, G. Schmidt, C. Impey, *Astrophys. J.* **419**, 494 (1993).
27. M. P. Muno, J. Mauerhan, *Astrophys. J.* **648**, L135–L138 (2006).
28. M. Liska *et al.*, *Mon. Not. R. Astron. Soc.* **507**, 983–990 (2021).
29. A. A. Zdziarski *et al.*, *Mon. Not. R. Astron. Soc.* **479**, 4399–4415 (2018).
30. J. A. Orosz *et al.*, *Astrophys. J.* **555**, 489–503 (2001).
31. X. Zhao *et al.*, *Astrophys. J.* **916**, 108 (2021).
32. A. V. Berdyugin *et al.*, *Zenodo* (2021); doi: 10.5281/zenodo.5767397
33. J. Poutanen, *Zenodo* (2022); doi: 10.5281/zenodo.5837857

ACKNOWLEDGMENTS

We thank K. Belczynski and A. Zdziarski for comments and suggestions. A.V. thanks the International Space Science Institute (ISSI) in Bern, Switzerland, for providing the environment for stimulating discussions. Our findings are based on observations made with the Nordic Optical Telescope (NOT), owned in collaboration by the University of Turku and Aarhus University, and operated jointly by Aarhus University, the University of Turku, and the University of Oslo, representing Denmark, Finland, and Norway, the University of Iceland and Stockholm University at the Observatorio del Roque de los Muchachos, La Palma, Spain, of the Instituto de Astrofisica de Canarias. We thank the NOT staff for their excellent support. DIPol-UF is a joint effort between University of Turku (Finland) and Leibniz Institute for Solar Physics (Germany). The Liverpool Telescope is operated on the island of La Palma by Liverpool John Moores University in the Spanish Observatorio del Roque de los Muchachos of the Instituto de Astrofisica de Canarias with financial support from the UK Science and Technology Facilities Council. **Funding:** A.V. acknowledges support from the Academy of Finland grant 309308. J.P., A.V., V.K., and S.S.T. received funding from Russian Science Foundation grant 20-12-00364. I.A.K. and V.K. thank the Magnus Ehrnrooth Foundation for support. S.V.B. acknowledges support from ERC Advanced Grant HotMol ERC-2011-AdG-291659. M.A.P.T. acknowledges support from the State Research Agency (AEI) of the Spanish Ministry of Science, Innovation and Universities (MCIU) and the European Regional Development Fund (FEDER) under grant AYA2017-83216-P and a Ramón y Cajal Fellowship (RYC-2015-17854). **Author contributions:** J.P. and A.V. initiated the project, performed modeling, and led writing of the text. A.V.B., V.P., and I.A.K. planned and performed the polarimetric observations. H.J., M.S., and M.A.P.T. planned and executed observations using the Liverpool Telescope and V.K. reduced the photometric data. J.J.E.K. obtained the Swift observations and analyzed the data together with S.S.T., P.G.J., and S.V.B. contributed to the interpretation of the results. All authors provided input and comments on the manuscript. **Competing interests:** We declare no competing interests. **Data and materials availability:** The raw DIPol-UF data are available at Zenodo (*32*). The Liverpool Telescope data are available from https://telescope.livjm.ac.uk/DataProd/ under proposal ID JQ20A01. The Swift data are available at https://heasarc.gsfc.nasa.gov/cgi-bin/W3Browse/swift.pl under Observation IDs 00010627**, with ** being 19 to 22 and 24 to 26. Our software for computing the probability distribution of the misalignment angle and for modelling polarization properties of the hot accretion flow is available at Zenodo (*33*). The parameters of our SED model are listed in table S4 and our derived geometrical parameters are in table S5.

SUPPLEMENTARY MATERIALS

science.org/doi/10.1126/science.abl4679
Materials and Methods
Figs. S1 to S5
Tables S1 to S5
References (*34*–*74*)

15 July 2021; accepted 21 January 2022
10.1126/science.abl4679

CANCER IMMUNOLOGY

Molecular signatures of antitumor neoantigen-reactive T cells from metastatic human cancers

Frank J. Lowery[1]*†, Sri Krishna[1]*†, Rami Yossef[1], Neilesh B. Parikh[1], Praveen D. Chatani[1], Nikolaos Zacharakis[1], Maria R. Parkhurst[1], Noam Levin[1], Sivasish Sindiri[1], Abraham Sachs[1], Kyle J. Hitscherich[1], Zhiya Yu[1], Nolan R. Vale[1], Yong-Chen Lu[1], Zhili Zheng[1], Li Jia[2], Jared J. Gartner[1], Victoria K. Hill[1], Amy R. Copeland[1], Shirley K. Nah[1], Robert V. Masi[1], Billel Gasmi[1], Scott Kivitz[1], Biman C. Paria[1], Maria Florentin[1], Sanghyun P. Kim[1], Ken-ichi Hanada[1], Yong F. Li[1], Lien T. Ngo[1], Satyajit Ray[1], Mackenzie L. Shindorf[1], Shoshana T. Levi[1], Ryan Shepherd[3], Chris Toy[1], Anup Y. Parikh[1], Todd D. Prickett[1], Michael C. Kelly[4], Rachel Beyer[1], Stephanie L. Goff[1], James C. Yang[1], Paul F. Robbins[1], Steven A. Rosenberg[1]*

The accurate identification of antitumor T cell receptors (TCRs) represents a major challenge for the engineering of cell-based cancer immunotherapies. By mapping 55 neoantigen-specific TCR clonotypes (NeoTCRs) from 10 metastatic human tumors to their single-cell transcriptomes, we identified signatures of $CD8^+$ and $CD4^+$ neoantigen-reactive tumor-infiltrating lymphocytes (TILs). Neoantigen-specific TILs exhibited tumor-specific expansion with dysfunctional phenotypes, distinct from blood-emigrant bystanders and regulatory TILs. Prospective prediction and testing of 73 NeoTCR signature–derived clonotypes demonstrated that half of the tested TCRs recognized tumor antigens or autologous tumors. NeoTCR signatures identified TCRs that target driver neoantigens and nonmutated viral or tumor-associated antigens, suggesting a common metastatic TIL exhaustion program. NeoTCR signatures delineate the landscape of TILs across metastatic tumors, enabling successful TCR prediction based purely on TIL transcriptomic states for use in cancer immunotherapy.

Genetic engineering to redirect the antigen specificity of autologous patient immune cells against tumors using T cell receptors (TCRs) and chimeric antigen receptors (CARs) has been effective for the treatment of certain cancer types (*1*–*4*). A major challenge in developing engineered cell therapies against the solid epithelial cancers that are responsible for 90% of cancer deaths (*5*) is the targeting of tumor-specific antigens without destruction of normal cells (*6*–*8*). Tumor neoantigens derived from nonsynonymous somatic cancer mutations presented on human leukocyte antigen (HLA) molecules provide tumor specificity for T cell therapies while obviating toxicities associated with targeting normal tissues (*9*). Tumor neoantigens encoded by somatic mutations present in known cancer driver genes or private mutations specific to individual cancers have emerged as major antigenic targets of $CD8^+$ and $CD4^+$ T cells in immune checkpoint blockade (ICB) and in adoptive cell therapy (ACT) (*9*–*13*). Identification of TCRs capable of recognizing tumor neoantigens can lead to the development of cell-based immunotherapies for patients with metastatic solid malignancies. Neoantigen-reactive TCRs may also help to elucidate factors involved with the generation of antitumor immune responses and provide biomarkers that are useful in monitoring antitumor immune responses to ICB and ACT.

Conventional means of identifying tumor-reactive T cells and their cognate TCRs have generally relied on ex vivo T cell functional assays or, when the minimal epitope is known, single-cell sorting of T cells from bulk populations using antigen-specific HLA multimers and then reconstructing the TCRs expressed by the sorted T cells (*14*–*18*). Approaches to identify cancer-reactive T cells and their receptors from resected tumors that rely on T cell function can be impaired as a result of tumor-mediated T cell exhaustion and dysfunction (*19*, *20*). Expression of cell surface protein markers of T cell activation and dysfunction can provide a tool for isolating tumor-reactive, neoantigen-specific tumor-infiltrating lymphocytes (TILs) and their receptors from tumors and peripheral blood, although these approaches are often hampered by nonspecific enrichment of irrelevant bystander T cells in tumors (*21*–*26*).

Analysis of cellular states can provide insight into the specificity and function of T cells (*17*, *18*). Transcriptomic and epigenetic states of antigen-specific $CD8^+$ T cells from chronic viral infections and tumors have been well established in murine models, but their relevance to the states of human T cells in metastatic tumor samples is unclear (*27*–*29*). Recent studies using single-cell transcriptomic profiling of tumors without in vitro culture have demonstrated the heterogeneity of human TIL states (*20*, *30*–*32*) and explored the phenotypes associated with immunotherapy response in patients (*33*–*36*). However, the lack of focus on cancer antigen-specific human $CD8^+$ and $CD4^+$ TILs in single-cell studies has complicated our understanding of the relevant TIL population involved in antitumor immunity within tumor sites. An additional challenge to the identification of antitumor TCRs is characterized by our recent finding that although natural immune reactions do indeed occur in metastatic epithelial cancer, T cell recognition of such cancers is largely skewed toward private neoantigens specific to each cancer (*11*).

In this study, we evaluated the transcriptomic profiles of neoantigen-reactive TILs within archival metastatic tumor samples from patients to gain insights into intratumoral T cell states. To this end, we performed single-cell RNA sequencing (scRNA-seq) and T cell receptor sequencing (TCR-seq) on $CD8^+$ and $CD4^+$ T cells within metastatic cancers from 10 patients across multiple solid tumor types that included breast, melanoma, colon, and rectal cancers (table S1). We performed unsupervised clustering of 45,676 TILs from tumor digests by using uniform manifold approximation and projection (UMAP) to define 12 distinct transcriptional clusters (Fig. 1A). Patient TILs were distributed across each of the transcriptional phenotypic states regardless of tumor type and whether the patient received prior ICB (table S2 and fig. S1), although some TIL state differences could be attributed to the site of metastasis, as one cluster (C8) was predominantly populated by cells from the sole lymph node metastasis–derived melanoma sample (fig. S1, A to D).

We performed differential gene expression analysis to compare the TIL phenotypes and identify gene sets that represent each transcriptional cluster (table S3). We scored cells by single-cell gene set enrichment analysis (scGSEA) of our cluster-specific markers and more than 100 gene signatures from other recently published scRNA studies (*29*–*39*) and performed cluster correlation analysis to identify TIL cluster phenotypes (Fig. 1A and tables S4 and S5). Phenotypic states ranged from activated TILs (clusters C0, C3, and C10) to resident-memory TILs (TIL_{RM} clusters C2 and C4) and $CD4^+$ regulatory TILs (TIL_{Treg} cluster C9) (Fig. 1, A and B). We also found that clusters C1 and C6 shared genes with dysfunctional $CD4^+$ and $CD8^+$ TIL populations respectively described by other recent single-cell profiling of melanoma and bladder cancer (table S5) (*30*, *31*). A pseudotime trajectory superimposed on the TIL UMAP indicated that the cells within the C6 $CD8^+$ and C1 $CD4^+$ clusters, along with a subset of activated CD4 and CD8 T cells in

[1]Surgery Branch, Center for Cancer Research, National Cancer Institute, National Institutes of Health, Bethesda, MD 20892, USA. [2]National Institutes of Health Library, National Institutes of Health, Bethesda, MD 20892, USA. [3]Vector Production Facility, Clinical Research Directorate, Frederick National Laboratory for Cancer Research, Bethesda, MD 20892, USA. [4]Single Cell Analysis Facility, Cancer Research Technology Program, Frederick National Laboratory, Bethesda, MD 20892, USA.
*Corresponding author. Email: sar@nih.gov (S.A.R.); frank.lowery@nih.gov (F.J.L.); sri.krishna@nih.gov (S.Kr.)
†These authors contributed equally to this work.

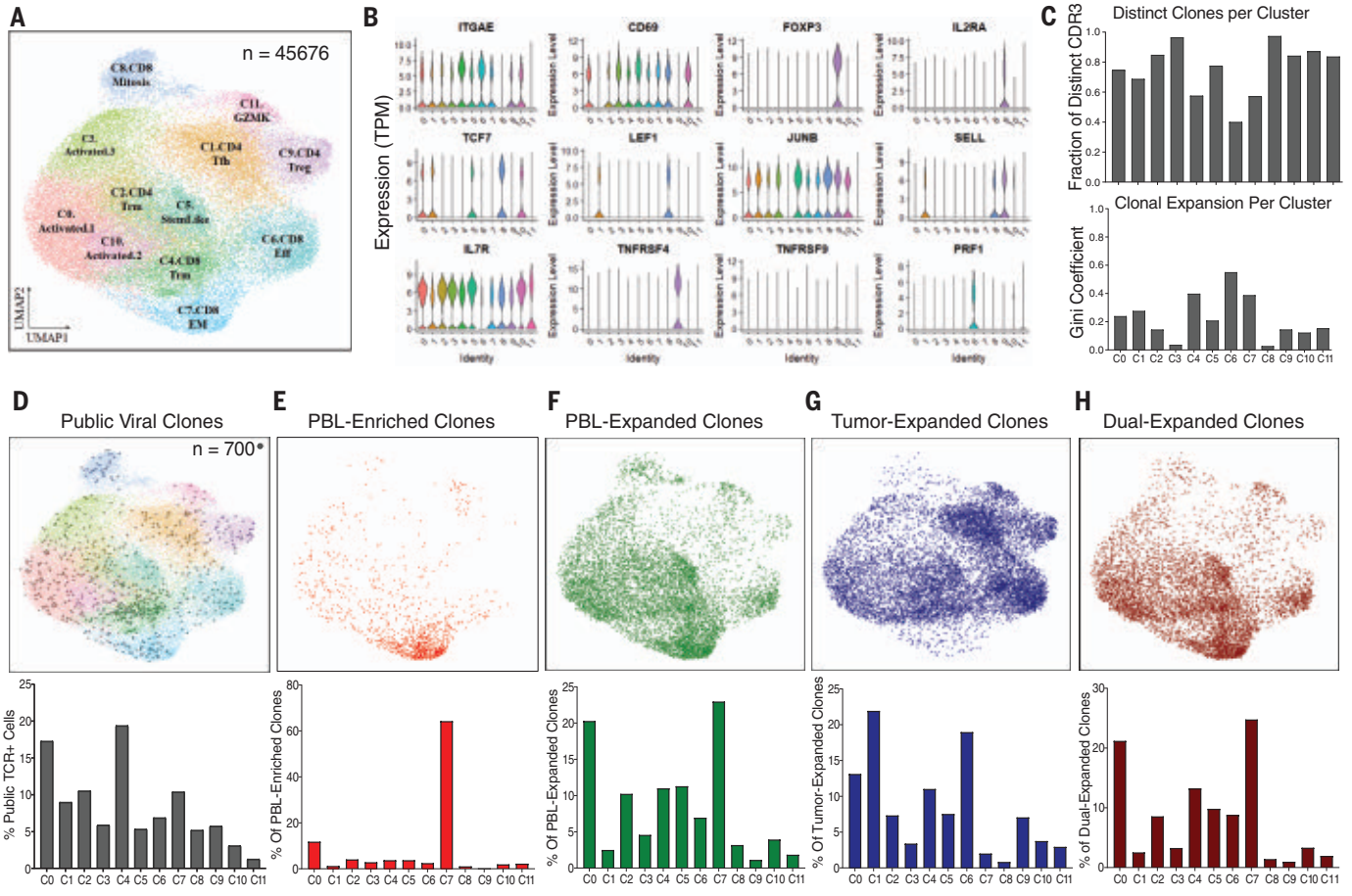


Fig. 1. Transcriptomic landscape of TILs from surgically resected metastatic human cancers. (**A**) UMAP of single-cell transcriptome data from 45,676 T cells sorted from 10 archival tumor specimens. Cluster names are based on names of published scRNA signatures with highest correlations (table S5). (**B**) Violin plots comparing gene expression of common T cell memory and activation markers across UMAP clusters from (A). TPM, transcripts per million. (**C**) (Top) Bar graph showing the fraction of T cells in each cluster that express distinct CDR3s. (Bottom) Bar graph showing Gini coefficients of CDR3 dispersion throughout clusters. Clusters 4, 6, and 7 have the lowest fraction of distinct CDRs and the highest Gini coefficients, indicating greater average clonal expansion and dispersion. (**D** to **H**) (Top) Projection of TCR clonotypes of a given class onto a transcriptomic T cell map. (Bottom) Bar graph showing frequency breakdown by cluster of cells in the corresponding plot. (D) Projection of public TCRs reactive to CMV, EBV, and influenza A (from VDJdb) onto a transcriptomic map from archival patients (n = 700), with the highest frequency in CD8$^+$ TIL$_{RM}$ C4. (E) Projection of cells expressing CDR3s that are peripheral blood (PBL)–enriched (i.e., found at a greater frequency in the PBL than in TILs; n = 1115). The majority of PBL-enriched clones are found in the CD8$^+$ TIL$_{EM}$ C7 state. (F) Projection of cells expressing CDR3s that are PBL expanded (i.e., found at a frequency greater than twice the limit of detection in the PBL; n = 8566). PBL-expanded clones are found in most phenotypic states but are largely absent in the CD4$^+$ C1 dysfunctional differentiated cluster, CD8$^+$C8.Mitosis, CD4$^+$C9.Treg, and C11.GZMK. (G) Projection of cells expressing CDR3s that are tumor expanded but not PBL expanded (i.e., occurring multiple times in tumors but not found at a frequency greater than twice the limit of detection in the PBL; n = 10,631). Tumor-expanded clones are found in most phenotypic states but are largely absent in C7 and C8. (H) Projection of cells expressing CDR3s that are dual expanded (i.e., occurring multiple times in tumors and found at a frequency greater than twice the limit of detection in the PBL; n = 6436). Dual-expanded clones are found most frequently in C0, C4, C5, and C7.

C0, represented the most-differentiated TILs within these cell populations (fig. S1E).

By integrating 23,712 TCR clonotypes within the 12 TIL phenotypic clusters using complementarity-determining region 3β (CDR3β) TCR-seq analysis, we found that the majority of TIL clones were unexpanded singletons (83.2% across all clusters), consistent with previous reports (*40*). Oligoclonal TIL expansion was found mostly within the differentiated dysfunctional CD8$^+$ TIL cluster C6, resident-memory CD8$^+$ TIL$_{RM}$ cluster C4, and effector-memory CD8$^+$ TIL$_{EM}$ cluster C7, consistent with the idea of clonal expansion after T cell activation and differentiation (Fig. 1C). Previous studies indicated that the tumor microenvironment consists of bystander T cells of viral specificities (*23*, *34*). Analyzing public CDR3β TCR clonotypes reactive to common viral antigens from influenza, cytomegalovirus (CMV), and Epstein-Barr virus (EBV) (*41*), we identified 700 T cells that contain bystander viral TCRs distributed across multiple cellular states (table S6), with the majority of them in activated C0 TIL (17.3%), CD8$^+$ TIL$_{RM}$ C4 (19.4%), and CD8$^+$ TIL$_{EM}$ C7 (10.4%) clusters (Fig. 1D).

In parallel, we studied the T cell repertoire in each patient's peripheral blood from the time of tumor resection and coupled it with the TIL scRNA-seq analysis to better understand T cell expansion within tumors. TIL clonotypes that were enriched in the peripheral blood relative to tumors (PBL-enriched clones) were found preferentially in the CD8$^+$ TIL$_{EM}$ C7 state (Fig. 1E), which also contained a large proportion of public viral T cells (Fig. 1D). TIL clonotypes expanded in peripheral blood (PBL-expanded clones) were found within activated C0, TIL$_{RM}$ C2 and C4, C5, and CD8$^+$

C7 TIL_{EM} states but were largely absent in C1, C6, and C9 clusters containing tumor-expanded clones (Fig. 1F). By contrast, TCR clonotypes enriched in tumors (tumor-expanded clones) were mostly enriched in $CD8^+$ C6 and $CD4^+$ C1 dysfunctional differentiated clusters (Fig. 1G). Furthermore, clones that were expanded in both tumors and peripheral blood (dual-expanded clones) were abundant in TIL states C0 and C7 (Fig. 1H). These results indicate that cellular states of tumor-expanded clones (C1 and C6) are distinct from blood-emigrant TILs within metastatic tumors. Additionally, our data suggest that TIL states containing dual-expanded clones (C0 and C7) are largely populated by irrelevant bystander TILs (including viral-specific TILs) that were expanded in blood before arrival at the tumor site.

Given that multiple clonally expanded TIL states were attributable to blood-emigrant bystander T cells, we then sought to define cellular states of antitumor neoantigen-specific TILs. To this end, our group had previously used our tandem minigene and peptide screening platform (*9*, *10*) to identify functional $CD8^+$ and $CD4^+$ neoantigen-specific TILs from 9 of 10 archival patients in the scRNA-seq dataset (*11*, *42*, *43*). Once these reactive TILs were identified, we performed fluorescence-activated cell sorting of activated 4-1BB$^+$ neoantigen-reactive TILs, followed by TCR reconstruction (*14*, *26*, *44*) (fig. S2). We experimentally defined 14 $CD8^+$ and 17 $CD4^+$ neoantigen TCR clonotypes (NeoTCRs) against neoantigens encoded by patient cancer mutations, which also included driver genes such as *PIK3CA*, *KRAS*, and *TP53* (fig. S2, A and B, and table S7). Within the scRNA-seq data across all samples, we identified 325 single T cells (0.9% of all cells) that expressed these 31 experimentally verified NeoTCRs and backprojected them onto the TIL UMAP (Fig. 2A and fig. S2B). The vast majority of NeoTCR$^+$ TILs (84.3%) were distributed between just two clusters: $CD4^+$ C1 and the $CD8^+$ C6 differentiated dysfunctional states from the nine patients (Fig. 2A). Of the $CD4^+$ clonotypes, 91.3% were found in C1 or C6; 78.5% of $CD8^+$ clonotypes were found in C6 (table S7).

We further studied TIL states from tumor 4323, a rectal cancer liver metastasis, which had four previously defined NeoTCRs (tumor 4323 NeoTCRs 1 to 4) recognizing two somatic neoantigens HIATL1mut (p.G380V) and PPP2R1Amut (p.L432S) (table S7). Tumor 4323 $CD8^+$ TILs were broadly distributed across TIL_{EM} C7, TIL_{RM} C4, and C6, whereas $CD4^+$ cells were in TIL_{RM} C2 and TIL_{Treg} C9 (Fig. 2B). The four dominant NeoTCRs that represent 140 single TILs were found almost exclusively in the differentiated $CD8^+$ C6 cluster (91.4%; Fig. 2A). Because dysfunctional and differentiated TIL states could be driven by chronic T cell–tumor neoantigen interaction, we hypothesized that other subdominant clones within the differentiated $CD8^+$ C6 cluster state might also be neoantigen reactive. We therefore reconstructed and tested eight additional TCR clonotypes from tumor 4323 TILs within cluster C6 (table S7, fig. S2B, and materials and methods). Seven of the eight newly predicted TCRs were also found to be reactive against either HIATL1mut or PPP2R1Amut neoantigens (Fig. 2, C and D), and 45 of 48 single cells expressing the newly identified NeoTCRs were found in the $CD8^+$ C6 dysfunctional differentiated cluster. Beyond the ability to capture previously unknown NeoTCRs, $CD8^+$ C6 also demonstrated selectivity for neoantigen reactivity, because other dominant TCR clonotypes from tumor 4323 TILs that had previously screened negative for reactivity against candidate neoantigens ("dominant nonreactive TCRs") were largely found in the $CD8^+$ C4 TIL_{RM} and $CD4^+$ C9 TIL_{Treg} states (Fig. 2B and table S7).

We extended this analysis by reconstructing and experimentally screening candidate TCR clonotypes from other tumor samples that populated the $CD4^+$ C1 and $CD8^+$ C6 dysfunctional differentiated clusters against their autologous tumor mutation–encoded candidate neoantigens. Including those predicted from tumor 4323, we successfully defined 23 NeoTCR clonotypes (expressed by 217 TILs, median: 9 T cells per clonotype, range: 1 to 34) targeting 10 neoantigens (Fig. 2E and table S7). Although many of the newly identified NeoTCRs targeted the same tumor neoantigens defined by in vitro expanded TIL screening, we also identified NeoTCRs targeting previously unknown neoantigens that were not defined by prior screening of cultured TILs (e.g., 10 novel NeoTCRs against four newly identified neoantigens from tumor 4298; Fig. 2E and table S7). Combined backprojection of all 54 (31 previously known plus 23 newly identified) NeoTCR clonotypes representing 542 individual TILs showed that, irrespective of patient tumor histology, clusters C1 and C6 contained the majority (86.5%) of all neoantigen-reactive TILs (Fig. 2F and fig. S3A), suggesting a shared neoantigen-specific TIL program within metastatic cancers. Among 21 $CD8^+$ NeoTCRs expressed by 281 cells, 81.1% of cells were present in C6. Of the 31 $CD4^+$ NeoTCR clones expressed by 261 cells, 60.5% of cells were located within C1, whereas 89.3% were within either C1 or C6. Notably, five $CD4^+$ NeoTCR clones found in C6 were not observed in C1 (table S7), potentially representing CD4 cytotoxic T lymphocytes, as previously observed (*31*). Overall, the frequency of $CD8^+$ NeoTCRs increased 22-fold in C6 compared with the overall frequency, and the frequency of $CD4^+$ NeoTCRs increased fivefold in C1 compared with the overall frequency (fig. S3B). Consistent with our prior study showing that less differentiated T cell states lack enrichment of neoantigen-reactive TILs (*45*), only 7.4% of neoantigen-reactive TILs were found in tumor-resident memory states $CD4^+TIL_{RM}$ (C2) and $CD8^+TIL_{RM}$ (C4) or the stemlike C5 (Fig. 2F and fig. S3A). Additionally, fewer than 1.5% of neoantigen-reactive TILs were found among dual-expanded clonotypes previously reported to be associated with immunotherapy response (*34*), suggesting that only a minority of dual-expanded TILs consist of tumor-relevant clonotypes (Fig. 1H).

Restricting the gene expression analysis to only verified NeoTCR$^+$ TILs within the archival samples enabled us to develop molecular profiles of $CD4^+$ and $CD8^+$ neoantigen-reactive TILs (table S8). $CD4^+$ and $CD8^+$ NeoTCR-expressing cells shared expression of multiple genes—including those encoding the cytokine CXCL13; tissue-homing protein CXCR6; inhibitory markers TIGIT, PD1 (*PDCD1*), CD39 (*ENTPD1*), and LAG3; and TOX, a regulator of T cell exhaustion (Fig. 2, G and H, and table S8)—which have all been previously reported to be expressed by dysfunctional T cells within the tumor microenvironment (*21*–*23*, *29*–*31*). $CD4^+$ and $CD8^+$ NeoTCR-expressing cells also shared expression of several genes that were not previously reported to be associated with intratumoral dysfunctional T cells, including *ADGRG1*, *HMOX1*, *LINC01871*, *DUSP4*, and *ACP5* (Fig. 2H and table S8). $CD4^+$ and $CD8^+$ NeoTCR cells also shared down-regulation of stemness and memory genes *IL7R*, *CD44*, and *KLF2*; lactate dehydrogenase *LDH1*; annexin *ANXA1*; the calcium channel *S100A10*; and cell cycle regulator *RGCC* (table S8). Additionally, $CD8^+$ NeoTCR TILs expressed effector T cell genes *GZMA*, *GZMB*, *GZMK*, *IFNG*, and *PRF1*; exhaustion markers *LAG3*, *HAVCR2* (TIM3), and *ENTPD1* (CD39); and tissue-residency marker *ITGAE* (CD103), which have been previously reported to enrich for neoantigen-specific TILs (Fig. 2H and table S8) (*21*–*23*, *46*).

Pathway analysis of gene networks highlighted several upstream regulators of genes expressed by NeoTCR4$^+$ and NeoTCR8$^+$ cells (table S9). These gene modules implicated a TCR- dependent up-regulation of genes within both $CD4^+$ and $CD8^+$ NeoTCR cells (*CD28*, *TCR*, and *IL2*), in concert with cytokine-encoding genes *IFNA1/2*, *IFNB1*, *IL27*, *IL4*, and *IL6* that are involved in follicular T helper (T_{FH}) cell maintenance and activation (*47*, *48*). The high expression of *CXCL13* by both $CD4^+$ and $CD8^+$ NeoTCRs, in addition to T_{FH} cell activation through type 1 interferons (*47*, *48*) and the implication of B cell receptors in the $CD8^+$ NeoTCR signature (table S9), suggests that antitumor neoantigen-specific TIL activation might involve tertiary lymphoid structures within metastatic deposits of human tumors (*49*, *50*).

We reasoned that the shared neoantigen-specific TIL gene signatures might enable us

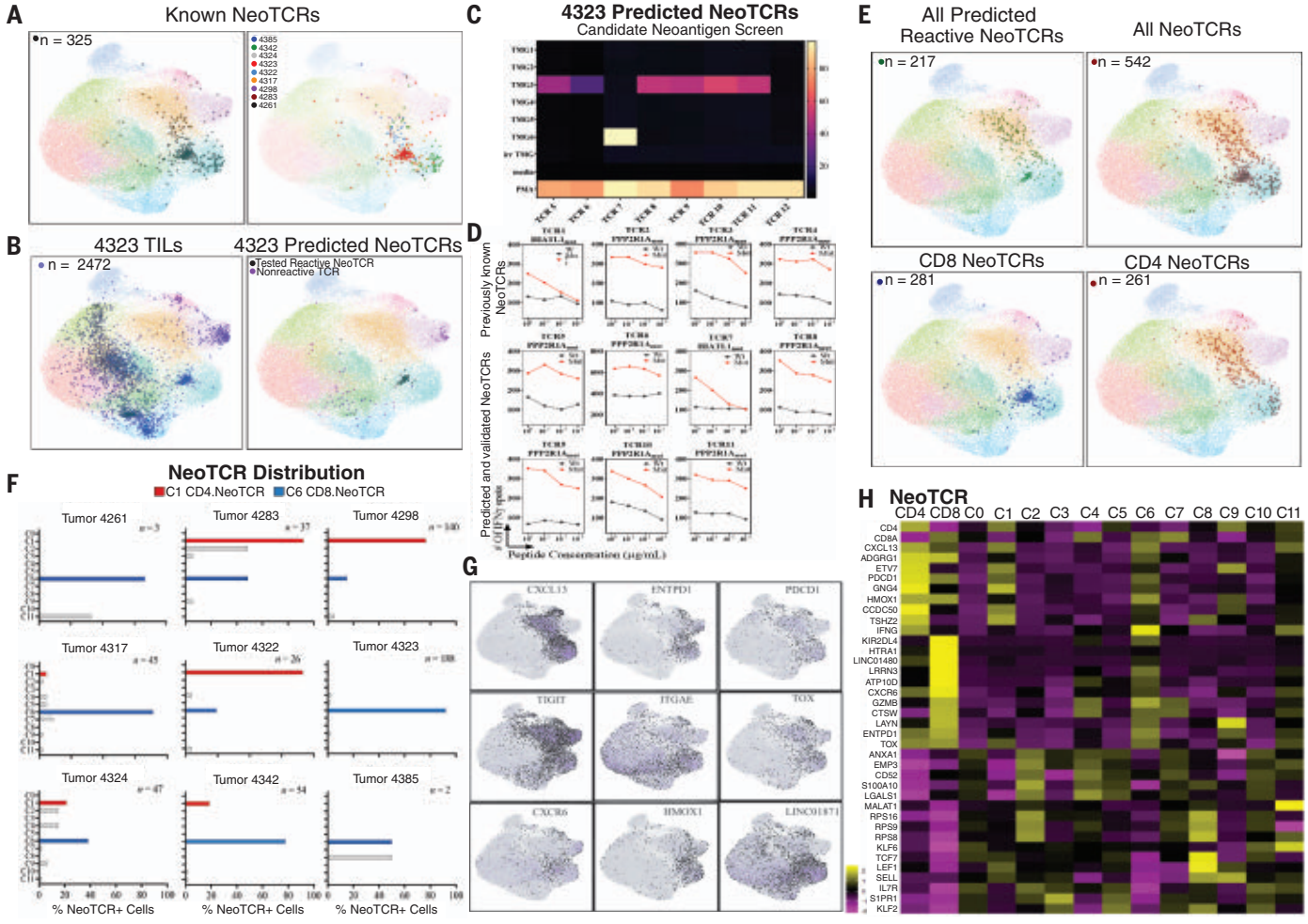


Fig. 2. Neoantigen-reactive CD4 and CD8 T cells exist in common dysfunctional states. (**A**) UMAP of all archival T cells overlaid with known neoantigen-reactive T cells from all patients (left; *n* = 325) and individually by patient (right; see also table S7). (**B**) (Left) Projection of all T cells from tumor 4323 (*n* = 2472) onto a transcriptomic map of T cells from all patients. (Right) Projection of newly predicted, experimentally tested neoantigen-reactive TCR-bearing cells from tumor 4323 (tested reactive NeoTCR, black; *n* = 53) and cells bearing TCRs that were negative in our screening assay (nonreactive TCRs, purple; *n* = 76). (**C**) Heatmap of TCR screening of predicted NeoTCRs from tumor 4323, showing reactivity of seven of eight TCRs to tandem minigenes 3 or 6 (TMG3 or TMG6). The right axis, which shows the percentage of activated T cells, indicates those expressing 4-1BB, as determined by flow cytometry. irr TMG, irrelevant TMG (i.e., TMG expressing candidate neoantigens not present in tumor 4323); PMA, , phorbol 12-myristate 13-acetate and ionomycin. (**D**) Peptide titration curves of TMG-reactive TCRs from tumor 4323, as measured by interferon-γ (IFNγ) ELISpot. (Top row) TCRs 1 to 4 were previously known to be reactive to either HIATL1mut (p.G380V) or PPP2R1Amut (p.L432S). (Bottom rows) Newly identified TCRs showing selectivity for the same neoantigens over the corresponding wild-type peptides. Wt, wild type; Mut, mutant. (**E**) (Top left) Projection of newly identified NeoTCR-expressing cells (*n* = 217) onto a transcriptomic map from all samples. (Top right) Projection of all known NeoTCRs, including previously known NeoTCRs [from (A)] and newly identified NeoTCR clones (*n* = 542). (Bottom left) Projection of all known CD8-restricted NeoTCRs, showing high abundance in C6 (*n* = 281). (Bottom right) Projection of all known CD4-restricted NeoTCRs, showing high abundance in C1 (*n* = 261). (**F**) Bar graphs showing distribution of all known NeoTCR-expressing cells across clusters by patient. Gray bars indicate T cell clones seen outside of NeoTCR clusters C1 and C6. (**G**) Gene expression of representative highly expressed genes from NeoTCR-expressing cells relative to other cells, projected onto a transcriptomic map. (**H**) Heatmap showing gene expression of the most differentially expressed genes from $CD4^+$ NeoTCR-expressing cells (NeoTCR CD4) and $CD8^+$ NeoTCR-expressing cells (NeoTCR CD8) relative to all clusters. A subset of select stemness and memory genes is shown for comparison.

to prospectively predict antitumor, neoantigen-specific TCRs purely on the basis of TIL transcriptomic states. We first tested the sensitivity and specificity of versions of potential NeoTCR4 and NeoTCR8 signatures containing various lengths of gene lists to correctly call known NeoTCRs from the archival specimens (table S10). From these analyses, we found that a 40-gene version of the putative NeoTCR4 signatures and a 243-gene version of the putative NeoTCR8 signatures performed with the highest sensitivity and specificity, and we established these as NeoTCR4 and NeoTCR8 signatures, respectively [area under the curve (AUC) of receiver operator characteristic (ROC) > 0.9; table S10, tab 2]. Additionally, we compared effector and dysfunctional gene sets consisting of different minimal combinations of classical T cell activation or dysfunction markers (*ENTPD1*, *CXCL13*, *PDCD1*, *ITGAE*, *TIGIT*, *TOX*, *LAG3*, *HAVCR2*, and *GZMK*; table S10, tab 3) for their ability to capture $CD4^+$ and $CD8^+$ NeoTCRs. Gene sets that contain *CXCL13* performed well in capturing $CD4^+$ NeoTCR cells (AUC > 0.8) but were inferior (AUC ≤ 0.8) to the NeoTCR8 signature in predicting $CD8^+$ NeoTCRs. Notably, versions of the NeoTCR4 and NeoTCR8 signatures that intentionally excluded these nine genes demonstrated high sensitivity and specificity (NeoTCR4 AUCs > 0.8 and NeoTCR8

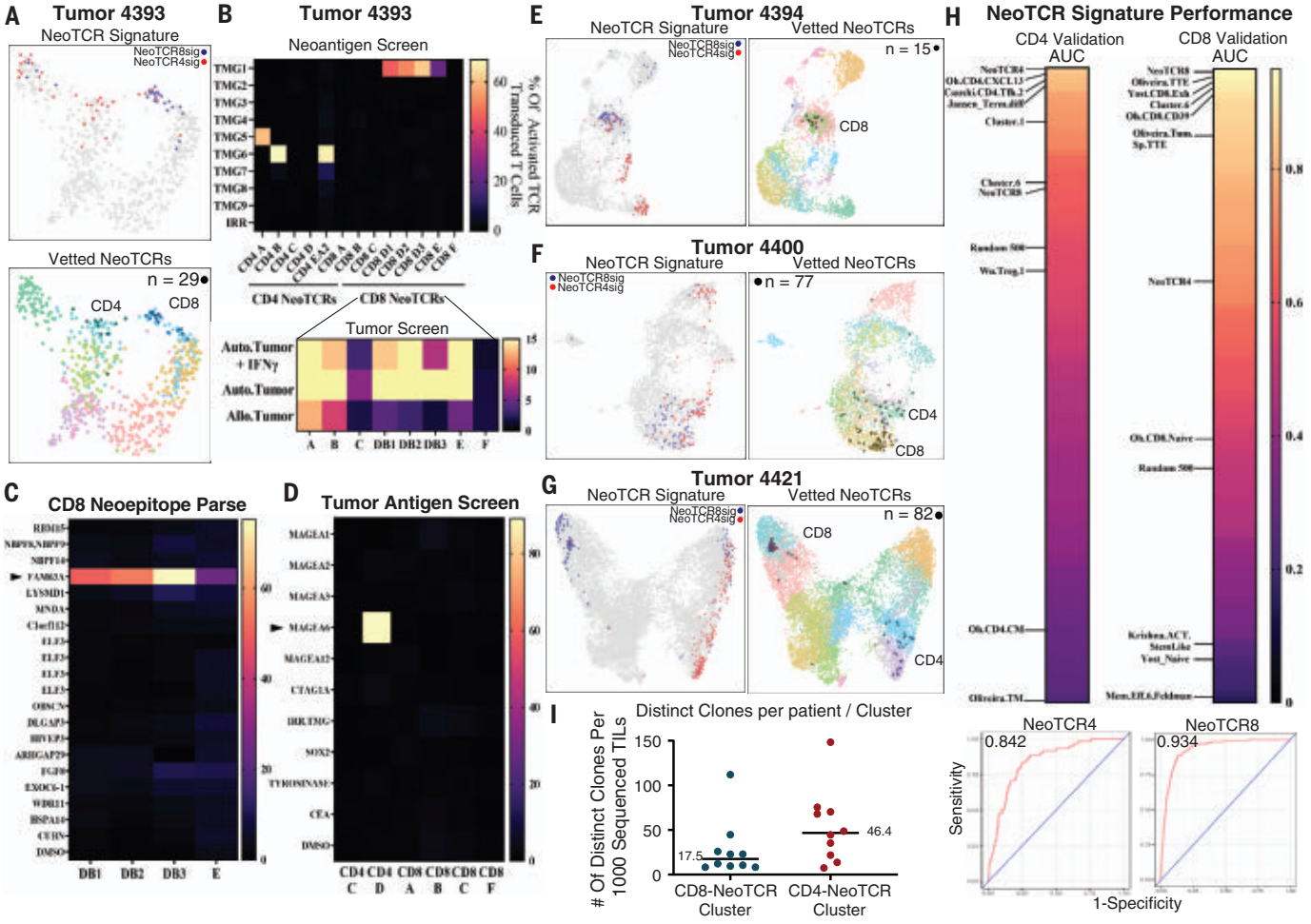


Fig. 3. NeoTCR signatures enable prospective identification of neoantigen-, tumor-associated antigen-, and tumor-reactive CD4 and CD8 TCRs from newly resected tumors. (**A**) (Top) Transcriptomic map of 630 TILs sequenced from tumor 4393 (colon). Cells that score in the 95th percentile of NeoTCR4 and NeoTCR8 signatures are highlighted. (Bottom) Experimentally verified CD4$^+$ and CD8$^+$ NeoTCR-expressing cells (n = 29) backprojected onto a transcriptomic map (black). (**B**) (Top) Screening of eight predicted candidate CD8$^+$ TCRs and six candidate CD4$^+$ TCRs against peptide pools and TMGs that represent 156 tumor mutations identified four TMG- and peptide pool–reactive CD8$^+$ TCRs and three TMG- and peptide pool–reactive CD4$^+$ TCRs. TMGs are shown for clarity. (Bottom) Screening of CD8$^+$ TCRs against corresponding autologous tumors demonstrated selective reactivity toward autologous (Auto.) tumors relative to allogeneic (Allo.) tumors by 7 of 8 TCRs. The right axis, which shows the percentage of activated TCR transduced cells, refers to cells expressing 4-1BB as determined by flow cytometry. (**C**) Reactivity deconvolution data of the TMG-reactive CD8$^+$ TCRs against constituent peptides of their reactive TMGs for newly identified TCRs from tumor 4393. CD8$^+$ TCRs reactive to TMG1 (TCRs DB1, DB2, DB3, and E) demonstrated reactivity to FAM63Amut (p.D460N). (**D**) Screening of neoantigen–nonreactive TCRs from tumor 4393 against autologous dendritic cells expressing TAA RNA or pulsed with TAA peptide pools identified tumor 4393 CD4 TCR D as reactive toward MAGEA6. (**E**) (Left) Transcriptomic map of 2972 TILs sequenced from tumor 4394 (colon). Cells that score in the 95th percentile of NeoTCR4 and NeoTCR8 signatures are highlighted. (Right) Experimentally verified CD8$^+$ NeoTCR-expressing cells (n = 15) backprojected onto a transcriptomic map. (**F**) (Left) Transcriptomic map of 2559 TILs sequenced from tumor 4400 (colon). Cells that score in the 95th percentile of NeoTCR4 and NeoTCR8 signatures are highlighted. (Right) Experimentally verified CD4$^+$ and CD8$^+$ NeoTCR-expressing cells (n = 77) backprojected onto a transcriptomic map. (**G**) (Left) Transcriptomic map of 10,049 TILs sequenced from tumor 4421 (colon). Cells that score in the 98th percentile of NeoTCR4 and NeoTCR8 signatures are highlighted. (Right) Experimentally verified CD4$^+$ and CD8$^+$ NeoTCR-expressing cells (n = 82) backprojected onto a transcriptomic map. (**H**) AUC scores showing the sensitivity and specificity of NeoTCR4, NeoTCR8, and published signatures in calling verified tumor- and neoantigen-reactive TCRs from prospective tumor samples. scGSEA was performed on T cells from samples 4393, 4394, 4400, and 4421, and ROC curves were generated to compare signature sensitivity and specificity. AUC values of all signatures were ranked by their ability to call CD4$^+$ NeoTCRs (top left) and CD8$^+$ NeoTCRs (top right). Selected signatures of interest are highlighted. (Bottom) ROC curves of highest-scoring signatures for CD4 (NeoTCR4; left) and CD8 (NeoTCR8; right) NeoTCRs. (**I**) Dot plots showing numbers of clones present in the C1 NeoTCR4 and C6 NeoTCR8 states per tumor from Fig. 1A, normalized to 1000 sequenced T cells for each tumor. Bars denote median values.

AUCs > 0.9; table S10, tab 4). These data together suggest that the TIL dysfunctional program identified here is not limited to just a few known exhaustion or activation genes but also includes several genes with yet-unidentified functions that together establish a recurrent dysfunctional transcriptional module within neoantigen-specific TILs from human cancers.

Correlation analyses of the NeoTCR4 and NeoTCR8 gene signatures demonstrated that the NeoTCR4 signature was most similar to those of the lung cancer TIL signatures Caushi.CD4.Tfh.2 [Pearson's correlation coefficient (r) = 0.725] and Wu.CD4.IL6ST (Pearson's r = 0.612), whereas the NeoTCR8 signature was most

similar to those of exhausted CD8 cells observed in basal and squamous cell carcinoma (Yost.CD8.Exhausted, Pearson's $r = 0.766$) and melanoma (Oliveira.TTE, Pearson's $r = 0.747$) (table S5) (*34*, *36*, *38*, *39*). These data suggest that the neoantigen-reactive $CD4^+$ and $CD8^+$ dysfunctional TIL states that we identified within colorectal cancer, breast cancer, and melanoma also exist in other tumor histologies. To investigate whether NeoTCR signatures can distinguish bystander viral-reactive TILs from tumor viral antigen–reactive TILs, we performed scRNA and TCR-seq on TILs from a lymph node metastasis from human papilloma virus 16 (HPV16)–positive anal squamous cell cancer (tumor 4397). From the tumor, there was one previously known $CD8^+$ TCR reactive against HPV16 antigen E4 (the only HPV antigen expressed by the tumor; fig. S4, A to C). Despite being observed only once among the 941 sequenced T cells, when scored by scGSEA, the E4-reactive TCR (TCR1) was the fourth-highest NeoTCR8 signature–expressing cell (fig. S4D), which suggests that antitumor viral antigen–specific TILs are similar to neoantigen-reactive dysfunctional TIL states, and that antitumor T cells in metastatic tumors may exist in shared dysfunctional states regardless of antigen class.

We then tested the utility of NeoTCR signatures to prospectively predict antitumor neoantigen-reactive TILs from four independent tumor samples from patients with metastatic colon adenocarcinoma. We performed scRNA-seq and scTCR-seq on patient TILs from single-cell suspensions of surgically resected metastatic tumors and scored each individual T cell using NeoTCR8 and NeoTCR4 signatures to identify putative antitumor NeoTCR TIL states (fig. S5 and table S4). From 630 TILs sequenced from tumor 4393, we reconstructed eight candidate $CD8^+$ TCRs and six candidate $CD4^+$ TCRs using NeoTCR signatures and subsequently screened TCR-transduced T cells for their response to 156 autologous candidate neoantigens, nine candidate tumor-associated antigens (table S11 and materials and methods), and a patient-derived xenograft (PDX) tumor line (Fig. 3, A to D, and fig. S6). The results of the screening assays indicated that four of the candidate $CD8^+$ TCRs recognized a FAM63Amut (p.D460N) neoepitope and the autologous PDX, three $CD8^+$ TCRs recognized the autologous PDX tumor but not any screened candidate neoantigens, one $CD4^+$ TCR recognized a FUT1mut (p.343_344del) neoepitope, two $CD4^+$ TCRs recognized a PCNTmut (p.P2122L) neoepitope, and one $CD4^+$ TCR recognized the highly expressed nonmutated tumor-associated antigen (TAA) MAGEA6 (Fig. 3, B to D, and table S7). Backprojection of these 11 NeoTCRs indicated that they represented 29 single cells (or ~4.6%) of the single-cell map from tumor 4393 TILs (Fig. 3A).

From tumor 4394, we synthesized and tested 12 $CD8^+$ TCRs from the candidate $CD8^+$ NeoTCR cluster against 185 autologous candidate neoantigens (Fig. 3E; no $CD4^+$ clonotypes were tested because the $CD4^+$ NeoTCR cluster comprised highly polyclonal singletons). We identified two $CD8^+$ TCRs against the driver neoantigen KRASmut (p.G12V) and one $CD8^+$ TCR that was nonreactive against screened mutations but did recognize an autologous PDX line (Fig. 3E and table S7). These three NeoTCRs represented 15 cells (0.5% of 2972 TILs) (Fig. 3E). From tumor 4400, we prospectively predicted 15 $CD8^+$ TCRs and 14 $CD4^+$ TCRs on the basis of NeoTCR4 and NeoTCR8 signatures (Fig. 3F). Neoantigen screening against 485 autologous candidate neoantigens and three highly expressed TAAs (table S11) led to the identification of five $CD4^+$ TCRs that mediate recognition of KRASmut (p.G13D driver neoepitope) and nine $CD8^+$ TCRs that were reactive with the tumor PDX line but did not recognize the screened neoantigen candidates (Fig. 3F and table S7). These 14 antitumor TCRs were expressed in 77 cells, representing 3.0% of the total cells captured (Fig. 3F). From tumor 4421, we prospectively predicted 7 $CD8^+$ TCRs and 11 $CD4^+$ TCRs on the basis of candidate NeoTCR clusters and tested them against 239 autologous candidate neoantigens and an autologous tumor organoid (Fig. 3G and fig. S6). Two $CD8^+$ TCRs recognized the ANO9mut p.151_154del neoepitope, one recognized the FLNBmut p.H2539Q neoepitope and organoid, and two recognized the UHRF2mut (p.R212P) neoepitope and organoid, whereas two $CD8^+$ TCRs were exclusively organoid reactive (table S7). Two of the 11 $CD4^+$ TCRs were also neoantigen reactive to ESRP1mut (p.E180D) and THOC6mut (p.R116H). These nine reactive TCRs represented 82 cells (0.8% of 10,049 TILs; Fig. 3G).

From the four prospective patients, 37 of 73 (50.7%) predicted TCRs were reactive to tumors, neoantigens, or TAAs (Table 1). Among predicted CD8 TCRs, this frequency was 60.9%, and predicted CD4 TCRs were positive in our screen 35.4% of the time (Table 1). Notably, though our coculture assays of predicted CD4 TCRs did not show any direct antitumor reactivity, TCR recognition of tumor material through cross-presentation via antigen-presenting cells has not been evaluated. We did not identify any significant gene expression differences between TIL-expressing TCRs that were neoantigen and/or tumor reactive compared with TIL-containing TCRs that were nonreactive in our screens, nor did we find significant differences between gene expression profiles of neoantigen-specific TCR-expressing cells relative to exclusively PDX tumor–reactive TCR-containing cells that did not recognize screened candidate neoantigens (fig. S6).

To assess the sensitivity and specificity of the NeoTCR signatures and compare them to other published T cell signatures in terms of their ability to successfully identify neoantigen-reactive TCRs, we performed scGSEA on individual cells and performed ROC analysis of

Table 1. Summary of prospectively predicted TCRs from four patient tumor TILs to identify antitumor, neoantigen-reactive TCRs using the NeoTCR gene signature. "Tumor" refers to direct organoid or PDX reactivity. NeoAg, neoantigen; TAA, tumor-associated antigen.

	Prospective prediction of TCRs reactive with tumor												
	CD8					CD4					All		
Tumor	Tested	Tumor and NeoAg-reactive	NeoAg only	Tumor only	Total	Tested	NeoAg-reactive	TAA-reactive	Tumor only	Total	Tested	Total	%
4393	8	4	0	3	7	6	3	1	0	4	14	11	79
4394	12	2	0	1	3	0	0	0	0	0	12	3	25
4400	15	0	0	9	9	14	5	0	0	5	29	14	48
4421	7	3	2	2	7	11	2	0	0	2	18	9	50
All	42	9	2	15	26	31	10	1	0	11	73	37	50.7
					61.9%					35.4%			

the ability of given signatures to call $CD4^+$ NeoTCRs, $CD8^+$ NeoTCRs, and public viral TCRs from the archival specimens (training sets; table S12 and fig. S7) and $CD4^+$ NeoTCRs and $CD8^+$ NeoTCRs from the prospective specimens (validation sets; Fig. 3H and table S12). In both the training and validation sets, the NeoTCR4 and NeoTCR8 signatures demonstrated the highest combination of sensitivity and specificity for $CD4^+$ and $CD8^+$ NeoTCRs, respectively (Fig. 3H, fig. S7, and table S12). We also identified TIL phenotypic states from other studies that performed well in our validation sets; namely, the bladder cancer–derived CD4.CXCL13 (*31*) and non–small cell lung cancer–derived CD4.Tfh.2 (*39*) signatures for $CD4^+$ NeoTCRs, and terminally exhausted signatures from melanoma (*38*) and skin carcinoma (*36*) for $CD8^+$ NeoTCRs. Although the studies did not examine the neoantigen reactivity of $CD4^+$ T cells, the conserved phenotypic states shared with the validated $CD4^+$ NeoTCRs identified here likely indicate that those samples also contain $CD4^+$ neoantigen-reactive T cells. Notably, signatures from stemlike T cells associated with ACT response (Krishna.ACT.StemLike) (*45*) and ICB response (CD8_G, Mem.Eff) (*33*) were especially poor at highlighting NeoTCRs, consistent with the majority of antitumor T cells being in a dysfunctional state in progressing metastatic cancer (Fig. 3H and table S12) (*45*). Finally, the relative median AUC values for the NeoTCR4 and NeoTCR8 signatures were low for public virus-reactive T cells, suggesting high specificity of this dysfunctional program for tumor antigen-specific TILs (table S12 and fig. S7). Combining scRNA data from all 15 sequenced tumors, we estimated that a median of 17.5 clonotypes will be present within a given $CD8^+$ NeoTCR cluster, and 46.4 clonotypes will be present within a given $CD4^+$ NeoTCR cluster for every 1000 TILs sequenced per patient (Fig. 3I), which markedly enhances the landscape of possible antitumor T cell clonotypes within solid tumors.

In this Report, we have identified shared gene expression profiles of neoantigen-specific $CD4^+$ and $CD8^+$ T cells within metastatic solid human cancers. Neoantigen-specific TILs largely exhibited tumor-specific clonal expansion, with only limited overlap with dually expanded TILs found in the peripheral blood at the level of our sequencing depth (*33*, *34*). Our results support prior high-dimensional phenotyping studies showing that tumor-reactive T cells are enriched within differentiated dysfunctional cellular states (*23*, *30*, *31*), with very few stemlike antitumor T cells (*38*, *45*). We leveraged the NeoTCR dysfunctional signatures to identify antitumor TCRs with limited TIL material, in some cases identifying even an apparently unexpanded clonotype within the NeoTCR clusters as neoantigen reactive (e.g., tumor 4323 TCR10). Using signatures derived from relatively few neoantigen-reactive clones (54 clonotypes expressed by 542 cells), more than half of all prospectively tested TCRs expressing NeoTCR4 or NeoTCR8 signatures in this analysis were neoantigen and/or tumor reactive, which suggests a high degree of tumor specificity in T cells that exhibit NeoTCR states. These signatures offer the potential to identify antitumor TCRs without the need for functional screening of candidate neoantigens. Further, as the roles of neoantigen-specific $CD4^+$ T cells in establishing an antitumor response by supporting the activation of cytolytic $CD8^+$ T cells have come into view (*51*, *52*), the NeoTCR4 signature identified here will allow for expeditious identification of such $CD4^+$ antitumor TCRs.

Although the identified NeoTCR cells ranged from 0.1 to 9.1% of all TILs within the 14 tumors in which neoantigen reactivity was known, this likely represents an underestimate because we did not synthesize and experimentally determine tumor or mutation specificity for every TCR clonotype within the NeoTCR clusters, nor did we assess tumor or nonmutated TAA reactivity in the archival specimens (Fig. 3I). T cells expressing TCRs that target random mutations, mutations in tumor driver genes (e.g., *KRAS*, *TP53*, and *PIK3CA*), a nonmutated tumor-associated antigen (*MAGEA6*), an oncogenic viral antigen (*HPV16-E4*), and autologous tumor-reactive orphan receptors all converged on the same dysfunctional phenotype. Our results are further evidenced by a recent meta-analysis indicating that expression of *CXCL13*, one of the most differentially expressed genes within the NeoTCR4 and NeoTCR8 signatures, represents an independent variable for predicting responses to ICB (*53*). The existence of several orphan tumor-reactive receptors that are reactive to autologous tumor material but tested negative against candidate neoantigens within the NeoTCR clusters also implies that the landscape of tumor antigens remains broader than that of the somatic mutations we have tested, as has been recently suggested (*54*–*56*). Further evidence for this point is the lack of gene expression differences between NeoTCR signature–expressing cells that tested negative in our screens and those that tested positive. We find it likely that intratumoral T cells that acquire a dysfunctional, clonally expanded phenotype do so because they are reacting to tumor-relevant antigens, although this study did not investigate whether differences in target antigen expression or TCR functional avidity can differentially contribute to T cell dysfunction. We propose that TCRs from cells in the NeoTCR transcriptomic state can be rapidly identified without additional TIL growth, activation, or testing, thus providing opportunities to develop patient-specific neoantigen-targeting TCR immunotherapies against metastatic solid tumors, even when endogenous NeoTCR-expressing cells from those tumors are dysfunctional and/or exhausted. The potential roles of the genes expressed in the NeoTCR signature (including those that have unknown T cell function) in mediating tumor-specific TIL dysfunction in metastatic human cancers also remain to be explored in future studies.

REFERENCES AND NOTES

1. P. F. Robbins *et al*., *J. Clin. Oncol.* **29**, 917–924 (2011).
2. R. A. Morgan *et al*., *Science* **314**, 126–129 (2006).
3. C. H. June, M. Sadelain, *N. Engl. J. Med.* **379**, 64–73 (2018).
4. J. N. Kochenderfer, Z. Yu, D. Frasheri, N. P. Restifo, S. A. Rosenberg, *Blood* **116**, 3875–3886 (2010).
5. R. L. Siegel, K. D. Miller, A. Jemal, *CA Cancer J. Clin.* **70**, 7–30 (2020).
6. R. A. Morgan *et al*., *Mol. Ther.* **18**, 843–851 (2010).
7. M. R. Parkhurst *et al*., *Mol. Ther.* **19**, 620–626 (2011).
8. G. P. Linette *et al*., *Blood* **122**, 863–871 (2013).
9. E. Tran, P. F. Robbins, S. A. Rosenberg, *Nat. Immunol.* **18**, 255–262 (2017).
10. P. F. Robbins *et al*., *Nat. Med.* **19**, 747–752 (2013).
11. M. R. Parkhurst *et al*., *Cancer Discov.* **9**, 1022–1035 (2019).
12. M. M. Gubin *et al*., *Nature* **515**, 577–581 (2014).
13. N. van Rooij *et al*., *J. Clin. Oncol.* **31**, e439–e442 (2013).
14. M. Parkhurst *et al*., *Clin. Cancer Res.* **23**, 2491–2505 (2017).
15. D. B. Keskin *et al*., *Nature* **565**, 234–239 (2019).
16. J. D. Altman *et al*., *Science* **274**, 94–96 (1996).
17. A. Han, J. Glanville, L. Hansmann, M. M. Davis, *Nat. Biotechnol.* **32**, 684–692 (2014).
18. Y.-C. Lu *et al*., *Mol. Ther.* **26**, 379–389 (2018).
19. C. U. Blank *et al*., *Nat. Rev. Immunol.* **19**, 665–674 (2019).
20. A. M. van der Leun, D. S. Thommen, T. N. Schumacher, *Nat. Rev. Cancer* **20**, 218–232 (2020).
21. T. Duhen *et al*., *Nat. Commun.* **9**, 2724 (2018).
22. A. Gros *et al*., *J. Clin. Invest.* **124**, 2246–2259 (2014).
23. Y. Simoni *et al*., *Nature* **557**, 575–579 (2018).
24. R. Yossef *et al*., *JCI Insight* **3**, e122467 (2018).
25. W. Scheper *et al*., *Nat. Med.* **25**, 89–94 (2019).
26. A. Pasetto *et al*., *Cancer Immunol. Res.* **4**, 734–743 (2016).
27. E. J. Wherry *et al*., *Immunity* **27**, 670–684 (2007).
28. D. R. Sen *et al*., *Science* **354**, 1165–1169 (2016).
29. A. C. Scott *et al*., *Nature* **571**, 270–274 (2019).
30. H. Li *et al*., *Cell* **181**, 747 (2020).
31. D. Y. Oh *et al*., *Cell* **181**, 1612–1625.e13 (2020).
32. C. S. Jansen *et al*., *Nature* **576**, 465–470 (2019).
33. M. Sade-Feldman *et al*., *Cell* **176**, 404 (2019).
34. T. D. Wu *et al*., *Nature* **579**, 274–278 (2020).
35. B. C. Miller *et al*., *Nat. Immunol.* **20**, 326–336 (2019).
36. K. E. Yost *et al*., *Nat. Med.* **25**, 1251–1259 (2019).
37. I. Tirosh *et al*., *Science* **352**, 189–196 (2016).
38. G. Oliveira *et al*., *Nature* **596**, 119–125 (2021).
39. J. X. Caushi *et al*., *Nature* **596**, 126–132 (2021).
40. S. Valpione *et al*., *Nat. Commun.* **12**, 4098 (2021).
41. D. V. Bagaev *et al*., *Nucleic Acids Res.* **48**, D1057–D1062 (2020).
42. N. Levin *et al*., *Clin. Cancer Res.* **27**, 5084–5095 (2021).
43. Y.-C. Lu *et al*., *J. Immunother. Cancer* **9**, e002595 (2021).
44. B. C. Paria *et al*., *J. Immunother.* **44**, 1–8 (2021).
45. S. Krishna *et al*., *Science* **370**, 1328–1334 (2020).
46. E. Ghorani *et al*., *Nat. Cancer* **1**, 546–561 (2020).
47. C. Gu-Trantien *et al*., *JCI Insight* **2**, 91487 (2017).
48. A. E. Denton *et al*., *J. Exp. Med.* **216**, 621–637 (2019).
49. R. Cabrita *et al*., *Nature* **577**, 561–565 (2020).
50. N. S. Joshi *et al*., *Immunity* **43**, 579–590 (2015).
51. E. Alspach *et al*., *Nature* **574**, 696–701 (2019).
52. C. Cui *et al*., *Cell* **184**, 6101–6118.e13 (2021).
53. K. Litchfield *et al*., *Cell* **184**, 596–614.e14 (2021).
54. W. Yang *et al*., *Nat. Med.* **25**, 767–775 (2019).
55. V. Roudko *et al*., *Cell* **183**, 1634–1649.e17 (2020).
56. M. H. Gee *et al*., *Cell* **172**, 549–563.e16 (2018).

ACKNOWLEDGMENTS

We thank the Surgery Branch TIL Laboratory and clinical team for generating TIL; we also thank patients enrolled in our clinical protocols. This work utilized the computational resources of the

NIH HPC Biowulf cluster (http://hpc.nih.gov). We also thank NIDAP for providing additional computational support and the CCR Genomics Core for next-generation sequencing support. **Funding:** This research was supported by the Center for Cancer Research intramural research program of the National Cancer Institute. Support from the CCR Single Cell Analysis Facility was funded by FNLCR contract no. HHSN261200800001E. This project has been funded in part with federal funds from the National Cancer Institute, National Institutes of Health, under contract no. 75N91019D00024. The content of this publication does not necessarily reflect the views or policies of the Department of Health and Human Services, nor does mention of trade names, commercial products, or organizations imply endorsement by the US government. **Author contributions:** F.J.L., S.Kr., P.F.R., and S.A.R. conceived the study and designed experiments; F.J.L., S.Kr., N.B.P., and S.L.G. curated patient samples for inclusion; F.J.L., S.Kr., R.Y., N.B.P., P.D.C., N.Z., N.L., M.R.P., Z.Y., N.R.V., K.J.H., Y.C.L., Z.Z., L.J., J.J.G., S.S., V.K.H., A.R.C., A.S., R.V.M., B.G., S.Ki., S.K.N., B.C.P., Y.F.L., M.F., L.T.N., S.R., M.L.S., S.T.L., R.S., C.T., A.P., T.D.P., R.B., and M.C.K. performed experiments; F.J.L., S.Kr., R.Y., S.S., N.B.P., K.H., J.C.Y., and P.D.C. performed data analysis; and F.J.L., S.Kr., and S.A.R. wrote the manuscript, with input from all authors. **Competing interests:** F.J.L., S.Kr., R.Y., K.H., J.C.Y., P.F.R., and S.A.R. are listed as inventors on a patent application (US provisional patent application no. 62/992,701, PCT patent application no. PCT/US2021/023240) submitted by NCI that covers the use of NeoTCR signatures to identify antitumor TCRs. The other authors declare no competing interests. **Data and materials availability:** All data are available in the main text or the supplementary materials. Sequencing data generated as part of this study are available on dbGaP (the Database of Genotypes and Phenotypes) under accession no. phs002748.v1.p1. Previously published tumor exome and RNA-seq data can be found on dbGaP under accession nos. phs002735.v1.p1 and phs001003.v2.p1, respectively.

SUPPLEMENTARY MATERIALS

science.org/doi/10.1126/science.abl5447
Materials and Methods
Figs. S1 to S7
Tables S1 to S12
References (*57*–*69*)
MDAR Reproducibility Checklist

22 July 2021; accepted 20 January 2022
Published online 3 February 2022
10.1126/science.abl5447

OPTICS

Topological modes in a laser cavity through exceptional state transfer

A. Schumer[1,2], Y. G. N. Liu[1], J. Leshin[3], L. Ding[1], Y. Alahmadi[3,4], A. U. Hassan[3], H. Nasari[1,3], S. Rotter[2], D. N. Christodoulides[3], P. LiKamWa[3], M. Khajavikhan[1]*

Shaping the light emission characteristics of laser systems is of great importance in various areas of science and technology. In a typical lasing arrangement, the transverse spatial profile of a laser mode tends to remain self-similar throughout the entire cavity. Going beyond this paradigm, we demonstrate here how to shape a spatially evolving mode such that it faithfully settles into a pair of bi-orthogonal states at the two opposing facets of a laser cavity. This was achieved by purposely designing a structure that allows the lasing mode to encircle a non-Hermitian exceptional point while deliberately avoiding non-adiabatic jumps. The resulting state transfer reflects the unique topology of the associated Riemann surfaces associated with this singularity. Our approach provides a route to developing versatile mode-selective active devices and sheds light on the interesting topological features of exceptional points.

The quantum adiabatic theorem, a corollary of the Schrödinger equation, provides excellent insights into the behavior of slowly varying quantum systems. When the Hamiltonian gradually changes in time, the associated probability densities tend to evolve smoothly, thus allowing a quantum system to remain in its initial eigenstate. If this evolution follows a cyclic path around a spectral degeneracy, then the related eigenvalue can acquire a geometric phase that solely depends on the traversed trajectory in parameter space (*1*, *2*). In condensed-matter physics, when dealing with momentum space, it can be shown that the related concepts of Berry connection and curvature, which lift the path dependency of the observables, give rise to a host of fundamental topological properties such as nonzero Chern number and integer quantum Hall conductance in solids (*3*).

Non-Hermitian systems and their spectral degeneracies, better known as exceptional points (EPs), have attracted attention in various physical disciplines ranging from optics to electronics, optomechanics, and acoustics (*4*–*14*). An interesting feature of these non-Hermitian systems is that, under the appropriate conditions, their eigenvalues and corresponding eigenvectors tend to simultaneously coalesce, forming spectral degeneracies known as EPs (*4*, *15*). The presence of EPs not only affects a configuration that is statically operating in their vicinity but also alters the dynamical response of non-Hermitian systems. In contrast to a quasistatic encirclement of a Hermitian degeneracy (Fig. 1C), cyclic parameter variations in non-Hermitian systems do not necessarily reproduce the input state (apart from a geometric phase) after completing a loop around an EP. Instead, a quasistatic cycle leads to a swap of the instantaneous eigenstates (Fig. 1D) (*3*, *8*, *9*, *16*, *17*). Even more interesting is the behavior of a non-Hermitian system when the EP encirclement is carried out dynamically. In this latter case, the complex nature of the eigenvalues inhibits adiabatic evolution for all eigenvectors except for the one with the largest imaginary part of the corresponding eigenvalue due to non-adiabatic jumps (*17*–*19*). Instead, these jumps produce a chiral behavior unique to non-Hermitian systems, in which the final state after a dynamic loop around an EP depends on the loop's winding direction rather than on the initial state at the loop's outset (Fig. 1F) (*9*, *19*–*25*). Although this chiral behavior has recently been observed in a number of physical systems (*9*, *20*–*22*, *24*, *26*), little has been done to exploit this concept to establish a purely topological state in non-Hermitian configurations (*27*–*29*).

We introduce a type of topological mode appearing in non-Hermitian cavities that feature dynamical EP encirclement. In these systems, the interplay among the Riemann surfaces, the net gain, and gain saturation favors a spatially evolving lasing mode that morphs from one eigenstate profile to another while avoiding the aforementioned non-adiabatic jumps. As a result, we demonstrate a topologically operating single transverse mode laser that is capable of simultaneously emitting in two different, but topologically linked, transverse profiles, each from a different facet. Apart from its counterintuitive behavior, this laser constitutes an adiabatic non-Hermitian cavity that supports a fully topological resonant mode. The implementation of EP encircling with gain additionally avoids the considerable absorption losses that plagued previous reports of chiral state transfer with dissipative elements (*9*, *20*–*22*, *24*, *26*). Furthermore, because the topological energy transfer relies solely on the adiabatic encircling of an EP degeneracy and not on the exact shape of the loop, the resulting lasing mode is robust against defects and fabrication imperfections, as well as fluctuations in gain [see the materials and methods (*30*), sections 5 and 6].

[1]Ming Hsieh Department of Electrical and Computer Engineering, University of Southern California, Los Angeles, CA 90089, USA. [2]Institute for Theoretical Physics, Vienna University of Technology (TU Wien), A-1040 Vienna, Austria. [3]CREOL, The College of Optics and Photonics, University of Central Florida, Orlando, FL 32816, USA. [4]Center of Excellence for Telecomm Applications, Joint Centers of Excellence Program, King Abdul Aziz City for Science and Technology, Riyadh 11442, Saudi Arabia.
***Corresponding author. Email: khajavik@usc.edu**

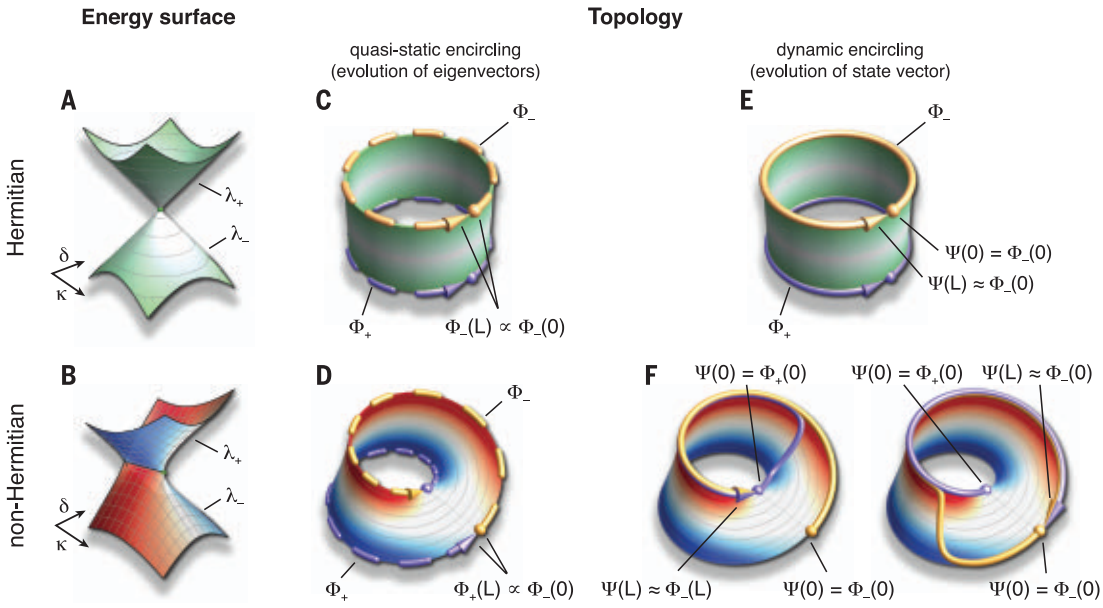


Fig. 1. Encircling a Hermitian or a non-Hermitian degeneracy. Occurrence of the interchange of the instantaneous eigenvectors when cycling around a degeneracy along a closed loop *C* is independent of its shape and only depends on the type of the enclosed degeneracy. (**A** and **B**) Energy surfaces of a Hermitian (top) and of a non-Hermitian degeneracy (bottom). The colors in (B), (D), and (F) are connected to the imaginary part of the eigenvalues indicating the gain [$\Im(\lambda) > 0$; red] and loss [$\Im(\lambda) < 0$; blue] behavior of the respective eigenvectors. (**C** to **F**) Topological equivalent of winding around a degeneracy. A cycle around a Hermitian degeneracy is represented by an untwisted closed sheet, and a loop enclosing a non-Hermitian degeneracy corresponds to a Möbius strip. The eigenvector population $p(z) = \left(|c_+(z)|^2 - |c_-(z)|^2\right) / \left(|c_+(z)|^2 + |c_-(z)|^2\right)$, where $\Psi(z) = c_+(z)\Phi_+(z) + c_-(z)\Phi_-(z)$, is displayed on the vertical axis, such that the two instantaneous eigenstates $\Phi_\pm(z)$ lie on the edges of the sheets. (C) Quasistatically winding around a Hermitian degeneracy along *C* returns each eigenvector to itself. (E) Adiabatic cycling a Hermitian degeneracy starting from an eigenstate, e.g., $\Psi(0) = \Phi_-(0)$ (orange arrow), yields the same eigenvector after traversing *C*, i.e., $\Psi(L) \approx \Phi_-(0)$. (D) Quasistatic evolution around an EP corresponds to the topology of a Möbius strip as the eigenvectors interchange [$\Phi_\pm(0) \propto \Phi_\mp(L)$]. (F) Upon dynamic EP encircling in the CW direction, any initial excitation [orange sphere: $\Psi(0) = \Phi_-(0)$; purple sphere: $\Psi(0) = \Phi_+(0)$] is transferred toward Φ_-, such that after one cycle the state vector yields $\Psi(L) \approx \Phi_-(L) \propto \Phi_+(0)$ (left panel). When looping in CCW direction, every initial state is again drawn to Φ_-, but the state vector then gives $\Psi(L) \approx \Phi_-(0)$ (right panel), leading to a chiral state transfer.

Our laser cavity consists of two transversely coupled waveguides in a parity-time (PT) symmetric configuration, in which one of the elements is subject to gain whereas the other one experiences loss (or a lower level of gain). A schematic of the device is shown in Fig. 2B, and SEM images are shown in the insets of Fig. 2C. The dynamical encircling of the induced EP in time is implemented by modulating certain parameters of the structure along the propagation direction, *z*. Specifically, by varying the coupling and the detuning between the two single-mode waveguides in a continuous fashion, the system's transverse modes are steered around the EP as light circulates in the cavity. Each waveguide is accompanied by a neighboring strip that induces a change in its effective refractive index, providing the required detuning. These loading strips are intentionally designed not to be phase matched to the waveguide elements. The detuning between the two waveguides is thus determined by the distance between each waveguide and its adjacent strip and varies according to $s(z) = s_0 + (s_{\min} - s_0)\sin(2\pi z/L)$ [see the materials and methods (*30*), section 1]. Conversely, the dynamic coupling is attained by modulating the separation between the two primary waveguides, i.e., $d(z) = d_0 + (d_{\max} - d_0)\sin(\pi z/L)$. Using the aforementioned modulation patterns, an EP-encircling loop is realized in parameter space when the light travels through the cavity once (half a cavity roundtrip), as shown in Fig. 2, A and B. The propagation direction of the wave through the cavity then determines the directionality of the EP encircling. During a full cavity roundtrip, the EP is therefore encircled twice, once in each direction. The two loops of opposing directions in parameter space are chosen in such a way that non-adiabatic jumps are avoided (orange/purple line in left/right panel of Fig. 1F). It is this back and forth in the cavity that allows a single topological mode to be formed that is independent of the path taken in parameter space.

When a PT-symmetric pump profile is applied, in the absence of nonlinearities and saturation, the transverse mode evolution in the above active system is governed by a Schrödinger-type equation $i\partial_z\Psi(z) = H(z)\Psi(z)$ with $\Psi(z) = [E_1(z), E_2(z)]^T$, where the *z*-dependent Hamiltonian is given by

$$H(z) = \begin{pmatrix} -\delta(z) - i\gamma + ig & \kappa(z) \\ \kappa(z) & \delta(z) - i\gamma \end{pmatrix} \quad (1)$$

where $\delta(z)$ is the detuning, $\kappa(z)$ is the coupling, γ is the linear absorption loss, and g is the gain provided through pumping. The instantaneous eigenvalues and eigenvectors of the Hamiltonian can be expressed as $\lambda_\pm(z) = i(g/2 - \gamma) \pm \kappa(z)\cos[\theta(z)]$ and $\Phi_\pm(z) = \{2\cos[\theta(z)]\}^{-1/2}\,(e^{\pm i\theta(z)/2}, \pm e^{\mp i\theta(z)/2})^T$, respectively, where $\theta(z) = \arcsin\left[\frac{g/2 + i\delta(z)}{\kappa(z)}\right] \in \mathbb{C}$. The PT-symmetry line is situated along $\delta = 0$, with the EP located at $\kappa_{EP} = g/2$ separating the PT-broken ($g/2 > \kappa$) from the PT-symmetric ($g/2 < \kappa$) phase. The start/end point of the EP-encircling section is at $\delta = 0$ and $\kappa \gg g/2$, and is chosen such that $\theta(0) = \theta_0 \approx g/2\kappa \ll 1$. Consequently, the eigenvector components are approximately equal in magnitude, which implies

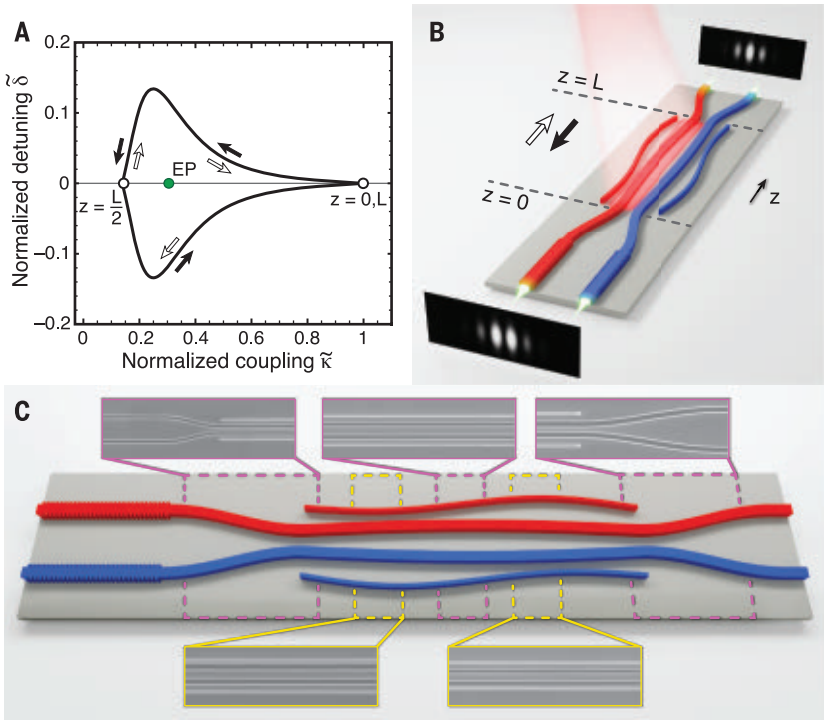


Fig. 2. Operation principle and laser structure. (**A**) Parameter path encircling the EP in the plane spanned by the normalized coupling $\tilde{k}$ and detuning $\tilde{\delta}$. (**B**) Illustration of the EP-encircling laser (not to scale). In addition to the losses caused by absorption in both waveguides, the red waveguide experiences gain by optically pumping the encircling section of the cavity. The separation between the detuners and their respective main waveguides introduces detuning $\delta(z)$, whereas the separation between the two main waveguides generates coupling $\kappa(z)$. The grating reflector on the left end of each main waveguide acts as a wavelength filter. The steady-state topological mode is characterized by the simultaneous emission of the in-phase (right end) and π-out-of-phase (left end) mode, each from one facet. (**C**) SEM images (small panels) of the laser structure demonstrating the variation of the separations between detuners as well as the main waveguides.

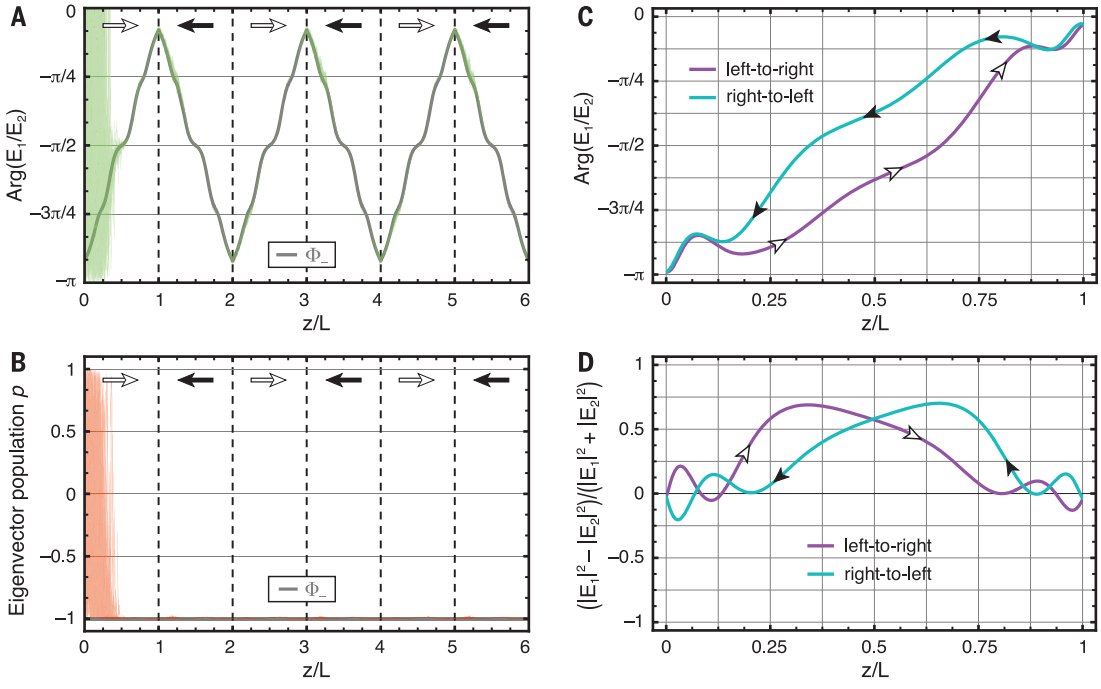


Fig. 3. Numerically simulated transient and steady-state behavior of the encircling part of the cavity. (**A** and **B**) Numerical simulations of the transient field evolution for six passes in alternating directions through the cavity in the presence of gain saturation. In total, 100 individual solutions of Equations 2a and 2b based on purely stochastic excitations are shown as thin green (A) and red (B) lines. The thick gray lines show the instantaneous eigenstate $\Phi_-(z)$ without noise. (A) The relative phase between the two waveguides evolves continuously from $-\pi$ to 0 and back within one round trip. (B) After an initial population transfer toward Φ_-, the normalized eigenvector population p shows that the ensuing adiabatic following of said eigenstate leads to the emission of different supermodes from each facet. (**C** and **D**) Evolution of the relative phase between the two cavities and the normalized intensity difference, respectively, of the left-to-right (purple) and right-to-left (cyan) traveling waves according to a Rigrod-type self-consistent simulation using Equations 3a and 3b. Emissions of different supermodes from each facet are shown. The two spatial supermodes are characterized by equal intensity in both waveguides at the output ports and a phase difference that evolves from $-\pi$ to 0 and back.

that the two supermodes emit with equal intensity in both waveguides at either facet. At $z = 0$, the relative phase φ between the waveguide amplitudes of the supermodes is approximately $\varphi_-(0) \approx -\pi$ (π-out-of-phase) and $\varphi_+(0) \approx 0$ (in-phase) for Φ_- and Φ_+, respectively. This is exactly reversed at the end of the encircling section ($z = L$), i.e., $\varphi_-(L) \approx 0$ and $\varphi_+(L) \approx -\pi$, such that the adiabatic following along the topological mode $\Phi_-(z)$ continuously morphs the transverse mode profile from being π-out-of-phase at one end to being in-phase at the opposite end of the cavity [for details, see the materials and methods (*30*), sections 5 and 6].

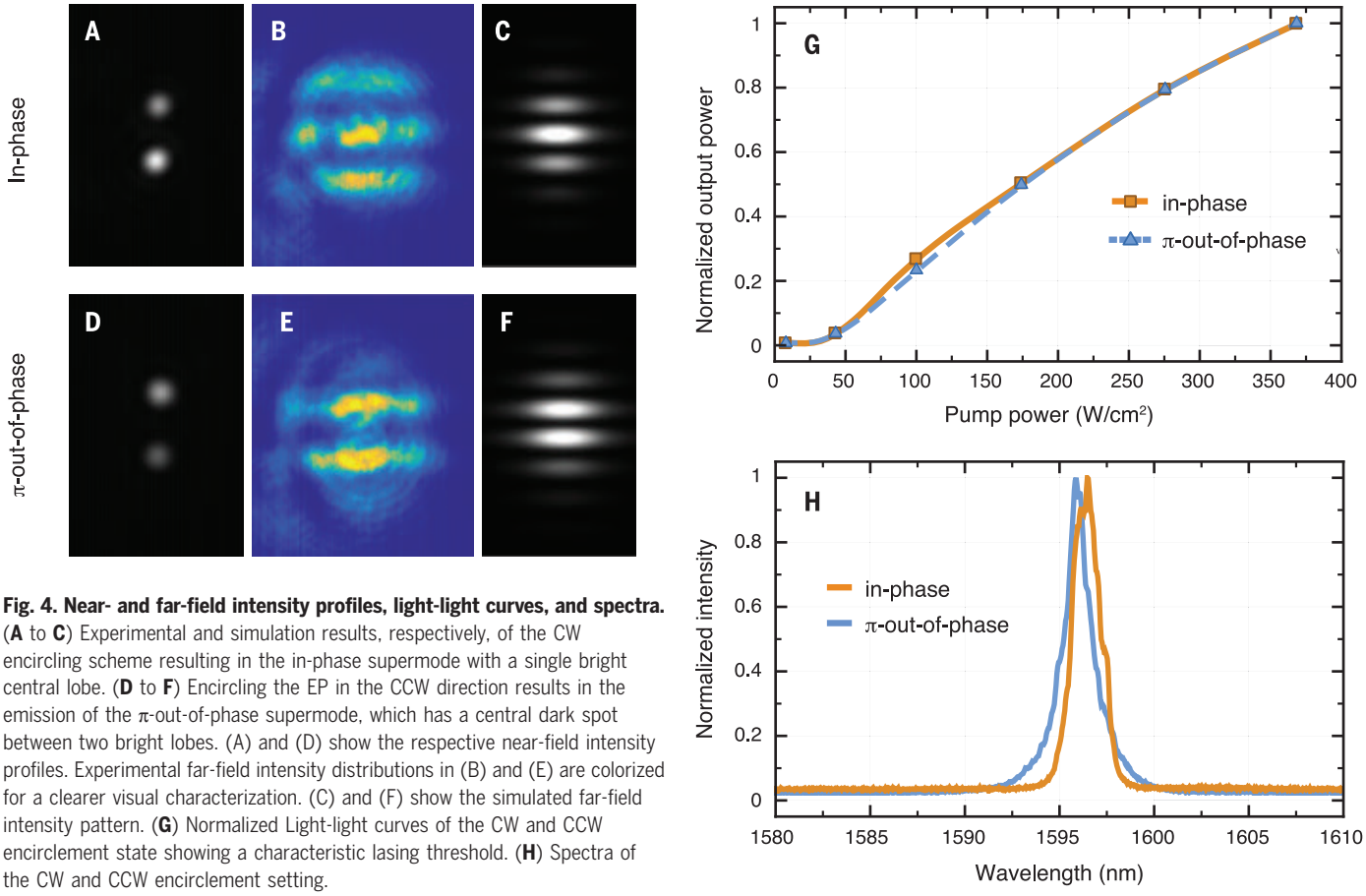


Fig. 4. Near- and far-field intensity profiles, light-light curves, and spectra. (**A** to **C**) Experimental and simulation results, respectively, of the CW encircling scheme resulting in the in-phase supermode with a single bright central lobe. (**D** to **F**) Encircling the EP in the CCW direction results in the emission of the π-out-of-phase supermode, which has a central dark spot between two bright lobes. (A) and (D) show the respective near-field intensity profiles. Experimental far-field intensity distributions in (B) and (E) are colorized for a clearer visual characterization. (C) and (F) show the simulated far-field intensity pattern. (**G**) Normalized Light-light curves of the CW and CCW encirclement state showing a characteristic lasing threshold. (**H**) Spectra of the CW and CCW encirclement setting.

To intuitively understand the topological nature of this process, one may consider a random superposition of the transverse eigenvectors that are excited at one end of the encircling section of the device after establishing the desired PT-symmetric pump profile. Irrespective of the initial excitation, by the end of a roundtrip in the cavity, the state vector has undergone (at most) a single non-adiabatic transition toward the eigenvector subject to gain (purple/orange line in left/right panel of Fig. 1F) and is then caught in the adiabatic (fully topological) cycle, traveling back and forth between the facets. In fact, additional non-adiabatic transitions are forbidden because Φ_- is the amplified supermode throughout the entire length of the cavity. This transient behavior is simulated using the following nonlinear coupled stochastic differential equations, when excited through white noise $|\tilde{\eta}_1| \gg |\tilde{\eta}_2|$

$$\frac{dE_1(\tilde{z})}{d\tilde{z}} = \frac{\tilde{g}_1 E_1(\tilde{z})}{1+|E_1(\tilde{z})/E_s|^2} - \tilde{\gamma}E_1(\tilde{z}) + i\tilde{\delta}(\tilde{z})E_1(\tilde{z}) - i\tilde{\kappa}(\tilde{z})E_2(\tilde{z}) + \tilde{\eta}_1(\tilde{z}) \quad (2a)$$

$$\frac{dE_2(\tilde{z})}{d\tilde{z}} = -\tilde{\gamma}E_2(\tilde{z}) - i\tilde{\delta}(\tilde{z})E_2(\tilde{z}) - i\tilde{\kappa}(\tilde{z})E_1(\tilde{z}) + \tilde{\eta}_2(\tilde{z}) \quad (2b)$$

where $E_1(\tilde{z})$ and $E_2(\tilde{z})$ are the field amplitude in the waveguide subject to gain and loss, respectively, and E_s is the saturation field. All of the parameters are normalized with respect to the maximum coupling $\kappa_0 = \kappa(0) = \kappa(L)$, i.e., $\tilde{\gamma} = \gamma/\kappa_0$, $\tilde{\delta} = \delta/\kappa_0$, $\tilde{g}_1 = g_1/\kappa_0$, $\tilde{\kappa} = \kappa/\kappa_0$, and $\tilde{z} = \kappa_0 z$. After each passage through the cavity, the field amplitudes are reflected by the facets and travel through the system in the opposite direction. The back-and-forth propagation of 100 individual solutions to Equations 2a and 2b for a total of six cycles is shown in Fig. 3, A and B. We observed that any initial excitation was transferred toward the instantaneous eigenstate Φ_- within one cycle, and the ensuing propagation follows this eigenvector adiabatically as the EP is repeatedly encircled in opposite direction. The relative phase between the waveguide amplitudes changes continuously from $-\pi$ to 0 and back during a full roundtrip.

Finally, to obtain a self-consistent steady state lasing solution, a Rigrod-type model was used that considers the waves in both cavities traveling left to right and right to left simultaneously (*31*)

$$\frac{dE_1^{\pm}(\tilde{z})}{d\tilde{z}} = \pm\left[\frac{\tilde{g}_1 E_1^{\pm}(\tilde{z})}{1+\left(|E_1^{+}(\tilde{z})/E_s|^2 + |E_1^{-}(\tilde{z})/E_s|^2\right)} - \tilde{\gamma}E_1^{\pm}(\tilde{z}) + i\tilde{\delta}(\tilde{z})E_1^{\pm}(\tilde{z}) - i\tilde{\kappa}(\tilde{z})E_2^{\pm}(\tilde{z})\right] \quad (3a)$$

$$\frac{dE_2^{\pm}(\tilde{z})}{d\tilde{z}} = \pm\left[-\tilde{\gamma}E_2^{\pm}(\tilde{z}) - i\tilde{\delta}(\tilde{z})E_2^{\pm}(\tilde{z}) - i\tilde{\kappa}(\tilde{z})E_1^{\pm}(\tilde{z})\right] \quad (3b)$$

Here, the subscripts 1 and 2 refer to the first and second waveguide, respectively, and the superscripts correspond to the wave propagating from left to right (+) and right to left (−). The lasing modes have to replicate after each roundtrip within the resonator and obey the boundary conditions $E_i^{+}(0) = R_L E_i^{-}(0)$ and $E_i^{-}(\kappa_0 L) = R_R E_i^{+}(\kappa_0 L)$, where R_L and R_R are the reflectances at the left and right facet, respectively. After the transient behavior has settled in the instantaneous eigenvector Φ_-, the dynamical encircling process is characterized solely by the topological adiabatic energy

transfer between the two mode profiles at the output ports. The ratios of the field intensities in the two waveguides are equal at each facet (Fig. 3D), whereas the relative phase of the state vector changes from $\varphi \approx -\pi$ at $z = 0$ to $\varphi \approx 0$ at $z = L$ (Fig. 3C), corroborating that the system is lasing in the topological mode Φ_- [also see the materials and methods (*30*), section 9].

The laser structures are fabricated on an InP substrate wafer containing a 300-nm InGaAsP multiple quantum well active region that is covered with 500 nm of an epitaxially grown InP layer. The fabrication procedure for realizing the devices is described in the materials and methods (*30*), section 2. The structure comprises a 2-mm-long encircling path, after which the two loaded-strip waveguides are separated further to prevent additional coupling. In the main part, the width of each waveguide is 900 nm, and the separation between the two waveguides varies between 600 and 1500 nm. The width of the detuning strips is 400 nm, and their distance to the waveguides changes between 300 and 900 nm. The electromagnetic simulations of the modes, coupling strengths, and detunings can be found in the materials and methods (*30*), section 1. Because of the short free spectral range of the cavities, 2-mm-long grating mirrors based on sidewall modulation are incorporated at one end of the two waveguides to limit the number of longitudinal modes (Fig. 2, B and C). The gratings are identical (ridge widths: 1200 nm; period: 246 nm; duty cycle: 50%) and designed to promote spectrally narrow emission at ~1596 nm [see the materials and methods (*30*), section 3].

The fabricated laser structure is pumped with a 1064-nm pulsed beam, focused by a high-magnification near-infrared (NIR) objective and cylindrical lenses positioned before the sample. This produces a pump beam with a width of 8 μm and a length of 2 mm. By adjusting the position of the beam with respect to the pattern, one waveguide can be pumped with almost constant intensity over the entire length of the device, whereas the other is left with little to no pump energy. A PT-symmetric configuration is thus established, exhibiting an EP at the gain contrast value $g_1/2 = \kappa$. The level of gain contrast can be selected by changing the position of the pump beam. The in-plane emission from the edge facet of the laser is collected and imaged on a NIR camera and a spectrometer for further analysis. By changing the location of the waveguide facets with respect to the objective lens, one can maneuver between observing the near- and far-field intensity patterns in the camera. The details of the measurement station are described in the materials and methods (*30*), section 4.

To factor out the effect of the dissimilarities between the two ends of the structure, we alternately pump either the first or the second waveguide and collect the emission from the same facet. Changing the pump profile switches the order of clockwise (CW) and counterclockwise (CCW) encirclements in a roundtrip, thus enabling us to observe the cavity output from the two ends without requiring us to switch the probed facet. After the encircling section, the two waveguides are gradually separated to a distance of 5 μm at the emitting end, thus allowing the observation of both near-field and far-field through our configuration. Here, when the upper waveguide is pumped, the left-to-right propagating wave corresponds to dynamically encircling the EP in CW direction, leading to an in-phase emission profile at the designated facet, followed by a CCW winding that promotes the π-out-of-phase-mode on the other facet. This difference is particularly evident in the far-field intensity distribution, which shows a bright lobe in the center of the interference pattern for the in-phase mode (Fig. 4, A to C) when the first waveguide is pumped. By shifting the position of the pump light to the second waveguide, the EP-encircling direction is reversed, resulting in a situation equivalent to viewing the opposite facet. In this case, the π-out-of-phase supermode leads to a far-field pattern with a node at the center and two bright lobes around it (Fig. 4, D to F). In both cases, the near-field intensity patterns are similar (Fig. 4, A and D), with the two waveguides emitting with nearly equal intensity (the slight difference is caused by the unequally pumped separated regions). Together with the far-field profile, this confirms that the observed patterns belong to the desired in-phase and π-out-of-phase emission profiles of the corresponding topological mode [also see the materials and methods (*30*), section 10]. Finally, to verify that the structure is indeed lasing, the light-light curves are collected for both pump scenarios (Fig. 4G). The lasing spectra for both outputs are shown in Fig. 4H, with their peak wavelength occurring near 1596 nm. Unlike standard coupled waveguide lasers, which tend to show frequency splitting, here, the conversion from one state to the other along the cavity results in the same phase accumulation and resonance wavelength for both output states.

Our device presents a demonstration of lasing through topological mode transfer. These lasing structures exhibit emission profiles that are robust to various parameter variations that tend to cause instabilities and temporal fluctuations in standard lasers. Extending this concept to larger arrays can result in laser systems with fast switching between various spatial supermodes by appropriately modulating the pump profile. Our work also provides a route to the study of topological effects in non-Hermitian systems by linking the elimination of non-adiabatic jumps to the formation of spatially evolving topological modes in laser cavities.

REFERENCES AND NOTES

1. S. Pancharatnam, *Proc. Indian Acad. Sci. Sect. A Phys. Sci.* **44**, 247–262 (1956).
2. M. V. Berry, *Proc. R. Soc. A Math. Phys. Eng. Sci.* **392**, 45–57 (1984).
3. C. Dembowski *et al*., *Phys. Rev. Lett.* **86**, 787–790 (2001).
4. W. D. Heiss, *J. Phys. A: Math. Gen.* **37**, 2455–2464 (2004).
5. M. P. Hokmabadi, A. Schumer, D. N. Christodoulides, M. Khajavikhan, *Nature* **576**, 70–74 (2019).
6. H. Jing *et al*., *Sci. Rep.* **5**, 9663 (2015).
7. H. Hodaei *et al*., *Nature* **548**, 187–191 (2017).
8. A. Bergman *et al*., *Nat. Commun.* **12**, 486 (2021).
9. J. Feilhauer *et al*., *Phys. Rev. A* **102**, 040201 (2020).
10. H. Hodaei, M. A. Miri, M. Heinrich, D. N. Christodoulides, M. Khajavikhan, *Science* **346**, 975–978 (2014).
11. B. Peng *et al*., *Science* **346**, 328–332 (2014).
12. M. Brandstetter *et al*., *Nat. Commun.* **5**, 4034 (2014).
13. Z. Lin *et al*., *Phys. Rev. Lett.* **106**, 213901 (2011).
14. A. Regensburger *et al*., *Nature* **488**, 167–171 (2012).
15. T. Kato, *Perturbation Theory for Linear Operators* (Springer, ed. 2, 1995), vol. 132 of *Classics in Mathematics*.
16. C. Dembowski *et al*., *Phys. Rev. E* **69**, 056216 (2004).
17. R. Uzdin, A. Mailybaev, N. Moiseyev, *J. Phys. A: Math. Theor.* **44**, 435302 (2011).
18. T. J. Milburn *et al*., *Phys. Rev. A* **92**, 052124 (2015).
19. I. Gilary, A. A. Mailybaev, N. Moiseyev, *Phys. Rev. A* **88**, 010102 (2013).
20. J. Doppler *et al*., *Nature* **537**, 76–79 (2016).
21. H. Xu, D. Mason, L. Jiang, J. G. E. Harris, *Nature* **537**, 80–83 (2016).
22. J. W. Yoon *et al*., *Nature* **562**, 86–90 (2018).
23. X.-L. Zhang, S. Wang, B. Hou, C. T. Chan, *Phys. Rev. X* **8**, 021066 (2018).
24. X.-L. Zhang, T. Jiang, C. T. Chan, *Light Sci. Appl.* **8**, 88 (2019).
25. A. U. Hassan, B. Zhen, M. Soljačić, M. Khajavikhan, D. N. Christodoulides, *Phys. Rev. Lett.* **118**, 093002 (2017).
26. J. B. Khurgin *et al*., *Optica* **8**, 563–569 (2021).
27. L. J. Maczewsky *et al*., *Science* **370**, 701–704 (2020).
28. K. Wang *et al*., *Science* **371**, 1240–1245 (2021).
29. S. Xia *et al*., *Science* **372**, 72–76 (2021).
30. Materials and methods are available as supplementary materials.
31. G. R. Hadley, *J. Appl. Phys.* **58**, 97–100 (1985).

ACKNOWLEDGMENTS

Funding: This work was supported by DARPA (grant D18AP00058), the Office of Naval Research (grants N00014-16-1-2640, N00014-18-1-2347, N00014-19-1-2052, N00014-20-1-2522, and N00014-20-1-2789), the Army Research Office (grant W911NF-17-1-0481), the National Science Foundation (grants ECCS 1454531, DMR 1420620, ECCS 1757025, CBET 1805200, ECCS 2000538, and ECCS 2011171), the Air Force Office of Scientific Research (grants FA9550-14-1-0037, FA9550-20-1-0322, and FA9550-21-1-0202), the US–Israel Binational Science Foundation (BSF grant 2016381), the Jet Propulsion Laboratory (grant 013385-00001), the European Commission project NHQWAVE (grant MSCA-RISE 691209), and the Austrian Science Fund (FWF) project WAVELAND (grant P32300).
Author contributions: M.K., D.N.C., S.R., and P.L. conceived the project. A.S., Y.G.N.L., J.L., L.D., Y.A., A.U.H., and H.N. conducted the theoretical and experimental investigations. All authors contributed to the preparation of the manuscript. **Competing interests:** The authors declare no competing interests. **Data and materials availability:** All data are available in the main text or the supplementary materials.

SUPPLEMENTARY MATERIALS

science.org/doi/10.1126/science.abl571
Materials and Methods
Supplementary Text
Fig S1 to S13
References (*32*–*36*)

28 July 2021; accepted 25 January 2022
10.1126/science.abl6571

ANTIBIOTIC RESISTANCE

Minimizing treatment-induced emergence of antibiotic resistance in bacterial infections

Mathew Stracy[1,2], Olga Snitser[1], Idan Yelin[1], Yara Amer[1], Miriam Parizade[3], Rachel Katz[3], Galit Rimler[3], Tamar Wolf[3], Esma Herzel[4], Gideon Koren[4], Jacob Kuint[4,5], Betsy Foxman[6], Gabriel Chodick[4,5], Varda Shalev[4,5], Roy Kishony[1,7,8]*

Treatment of bacterial infections currently focuses on choosing an antibiotic that matches a pathogen's susceptibility, with less attention paid to the risk that even susceptibility-matched treatments can fail as a result of resistance emerging in response to treatment. Combining whole-genome sequencing of 1113 pre- and posttreatment bacterial isolates with machine-learning analysis of 140,349 urinary tract infections and 7365 wound infections, we found that treatment-induced emergence of resistance could be predicted and minimized at the individual-patient level. Emergence of resistance was common and driven not by de novo resistance evolution but by rapid reinfection with a different strain resistant to the prescribed antibiotic. As most infections are seeded from a patient's own microbiota, these resistance-gaining recurrences can be predicted using the patient's past infection history and minimized by machine learning–personalized antibiotic recommendations, offering a means to reduce the emergence and spread of resistant pathogens.

Urinary tract infections (UTIs) and wound infections are two of the most common conditions for which antibiotics are prescribed (*1*–*3*). These infections are frequently seeded from bacteria from a patient's own microbiota; uropathogens can persist for years in a patient's gut microbiota, which often acts as a reservoir for future infections (*4*–*6*). Wound infections are commonly caused by pathogens from a patient's skin microbiota, as well as pathogens from the gut flora (*7*). Both UTIs and wound infections can be treated by a range of antibiotics, but resistance is widespread among the causative pathogens, and considerable efforts are being made to develop strategies to minimize susceptibility mismatches, where an antibiotic is mistakenly prescribed to treat an infection resistant to it (*8*–*10*).

Yet even when an antibiotic is correctly prescribed to treat a pathogen sensitive to it (i.e., susceptibility-matched), treatment is a double-edged sword: It may clear the ongoing infection, but it may also select for resistant pathogens among a patient's resident microbial population, limiting current and future treatment efficacy (*11*, *12*). Indeed, prior antibiotic use is a strong risk factor for resistant UTIs and wound infections at the individual-patient level (*8*, *13*–*19*). This is especially problematic because these infections are often recurrent or chronic, with patients receiving multiple courses of antibiotics (*3*, *4*, *20*, *21*). Despite the importance of the emergence of resistance during or after treatment, we know very little about the mechanisms by which it occurs, and we lack strategies to prevent it (*22*). Currently, antibiotic choice focuses on avoiding antibiotics to which the ongoing infection is already resistant, however, it remains unknown if it is possible to select among the susceptibility-matched antibiotics in ways that minimize the risk of treatment-induced emergence of resistance at the individual-patient level.

To understand and predict personal risk of treatment-induced gain of resistance, we combined whole-genome sequencing of isolates from same-patient recurrent infections with analysis of a longitudinal dataset of UTIs and wound infections collected by Israel's Maccabi Healthcare Services (MHS) between June 2007 and January 2019. We identified 215,732 MHS patients with at least one record of a UTI (defined as a UTI diagnosis made by a physician followed within 7 days by a positive urine culture with a bacterial count of $>10^5$ colony-forming units per milliliter) (figs. S1 and S2) and 20,373 MHS patients with at least one record of a positive wound infection culture. For these patients, we collected clinical data including antibiotic susceptibilities and species identification from all positive cultures, antibiotic purchases, and patient demographics (age, gender, and pregnancy status). For UTI patients, we also collected potential comorbidities of chronic kidney disease and diabetes (*23*) and records of urinary catheterization (*24*) (tables S1 and S2). Randomly generated patient identifiers were used to link these different patient records. Resistance profiles were classified in accordance with the Clinical and Laboratory Standards Institute guidelines, with intermediate-level resistance grouped as sensitive. We identified 41,769 untreated UTI cases [defined as a UTI with no antibiotic purchases between 7 days before the sample was taken and the next positive sample or 28 days after the sample was taken (whichever comes first)] and 140,349 single-antibiotic treated cases [where, within 4 days of the sample being taken, one of the eight most frequently prescribed systemic antibiotics was purchased: combination trimethoprim/sulfamethoxazole (sulfa), ciprofloxacin, ofloxacin, combination amoxicillin/clavulanic acid (CA), cefuroxime axetil, cephalexin, nitrofurantoin, or fosfomycin] (table S3). Similarly, for wounds, we identified 7365 infections treated with one of the five most frequently prescribed oral systemic antibiotics (amoxicillin/CA, ciprofloxacin, cefuroxime axetil, cephalexin, and trimethoprim/sulfa). We further categorized these infections by their short-term clinical outcomes, indicating whether they resulted in an "early recurrence," defined as a second positive sample recorded within 4 to 28 days after the first positive sample (13,517 treated UTIs, 7933 untreated UTIs, and 442 treated wound infections).

Even for treatments correctly matching the susceptibility of the infection, early recurrence was common and was associated with infections gaining treatment-specific resistance. Cases were categorized into six groups on the basis of whether their initial infection was sensitive or resistant to the specified antibiotic (S→ and R→, respectively) and on the basis of their outcome: recurrence with a sensitive infection, recurrence with a resistant infection, or no recurrence (→S, →R, and →∅, respectively) (Fig. 1A). Although susceptibility-matched antibiotic treatments (S→) had a lower overall rate of recurrence than did mismatched treatments (R→), recurrences were still common (UTIs, 9.2%; wound infections, 5.1%) and frequently gained resistance to the prescribed antibiotic (S→R) (Fig. 1, B and G). Indeed, 30% of all UTI and 19% of all wound infection recurrences gained resistance after antibiotic treatment (S→R), with this fraction strongly varying by antibiotic, reaching as high as 59% (UTIs) and 27% (wounds) of recurrent infections after treatment with the first-line antibiotic ciprofloxacin (Fig. 1, C and H). These gained-resistance cases were strongly associated with treatment, with infections preferentially gaining resistance to the prescribed antibiotic class (Fig. 1, F and I) and temporally peaking soon after the last day of the antibiotic course (Fig. 1E and fig. S4). Compared with untreated cases, susceptibility-matched antibiotic treatment had two counteracting effects: It decreased the overall risk of UTI recurrence (the sum of S→S and S→R) but increased the risk of gained-resistance recurrence (S→R) (Fig. 1D and figs. S5 and S6).

[1]Faculty of Biology, Technion–Israel Institute of Technology, Haifa, Israel. [2]Department of Biochemistry, University of Oxford, Oxford, UK. [3]Maccabi Mega Lab, Maccabi Healthcare Services, Tel Aviv, Israel. [4]Maccabitech, Maccabi Healthcare Services, Tel Aviv, Israel. [5]Sackler Faculty of Medicine, Tel Aviv University, Tel Aviv, Israel. [6]Department of Epidemiology, University of Michigan School of Public Health, Ann Arbor, MI, USA. [7]Department of Computer Science, Technion–Israel Institute of Technology, Haifa, Israel. [8]Lorry I. Lokey Interdisciplinary Center for Life Sciences and Engineering, Technion–Israel Institute of Technology, Haifa, Israel.
*Corresponding author. Email: rkishony@technion.ac.il

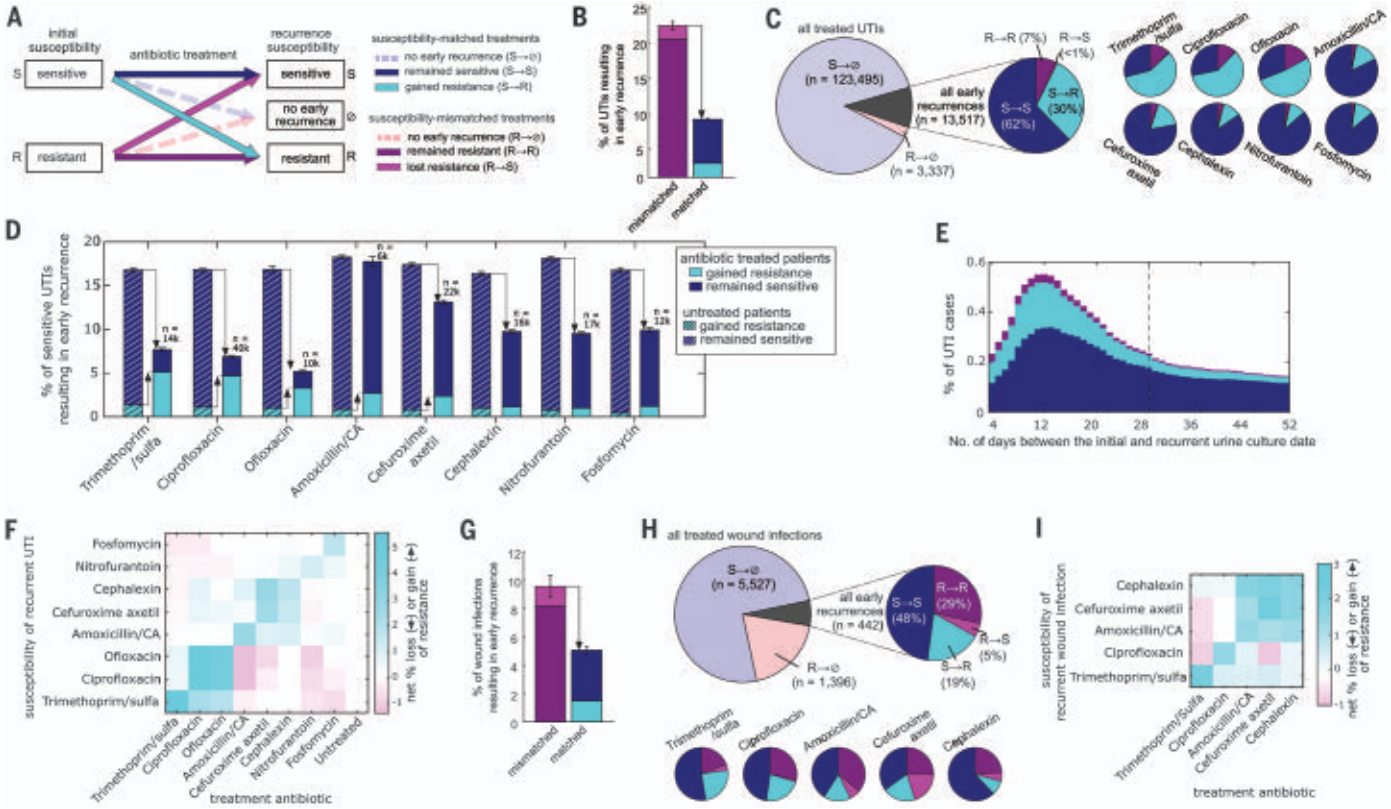


Fig. 1. Posttreatment recurrences are strongly associated with the infection gaining resistance specifically to the treatment antibiotic. (**A**) Each infection case was categorized into one of six possible groups on the basis of the susceptibility and treatment outcome. (**B** and **G**) The overall rate of recurrence for UTIs (B) and wound infections (G) after either susceptibility-matched or susceptibility-mismatched antibiotic treatments. (**C** and **H**) The percentage of all antibiotic-treated UTIs (C) and wound infections (H) resulting in early recurrence, and a breakdown of these early recurrences by their pre- and posttreatment susceptibility to the treatment antibiotic, for all treated cases and for each of the most frequently prescribed antibiotics. (**D**) The rate of early recurrence for UTIs initially sensitive to the specific antibiotic and either treated with this antibiotic (solid bars) or untreated (hashed bars). The cases are further categorized according to whether they recurred still sensitive to the specified antibiotic (dark blue) or recurred while gaining resistance to it (cyan). Susceptibility-matched treatment decreases the overall risk of early recurrences (down-pointing arrows) yet increases the risk of recurrence with gained resistance (up-pointing arrows). (**E**) The rate of UTI recurrences occurring on each day after antibiotic treatment (7-day moving average). Each recurrent case is categorized by pre- and posttreatment susceptibility to the prescribed antibiotic, as shown in (A). The dashed vertical line shows the 28-day threshold used to define early recurrences. (**F** and **I**) The net change in susceptibility of early recurrent UTIs (F) and wound infections (I). For infections treated with each antibiotic (*x* axis) or untreated (UTIs), the percentage of gain of resistance (cyan) minus loss of resistance (magenta) to each specified antibiotic is shown (*y* axis).

The large number of correctly treated infections that subsequently gained resistance could be caused by three possible mechanisms: evolution of resistance through mutations, through dedicated resistance genes, or through reinfection with a different strain resistant to the antibiotic (strain replacement) (Fig. 2A). To distinguish between these possibilities in UTIs, we collected 1113 isolates from 510 patients who experienced early UTI recurrence during a 4.5-month period (30 November 2017 to 16 April 2018). We focused on *Escherichia coli*, which accounts for 70 to 95% of all UTIs (table S4) (*4*, *22*, *25*). Sequencing these *E. coli* isolates, we analyzed the genetic relatedness among same-patient isolates collected before and after treatment and identified any differences in gene content or mutations in antibiotic target and resistance genes (see materials and methods in the supplementary materials).

The genomic analysis showed that while the same *E. coli* strain often persists in early UTI recurrences that do not gain resistance, resistance-gaining recurrences were caused by strain replacement. No cases were identified of resistance appearing through point mutations in the originally infecting strain. Analyzing strain relatedness, we found that while reinfection with a different strain was rare in recurrences that did not change resistance to the treatment (19% of S→S or R→R cases), it was the dominant mode in infections gaining resistance (93% of S→R cases; $P = 1 \times 10^{-27}$ compared with cases that did not gain resistance, Fisher test) (Fig. 2, B and C, and table S5). For example, despite the ability of *E. coli* to readily evolve resistance to ciprofloxacin through point mutations in the target enzymes DNA gyrase subunit A (*gyrA*) and DNA topoisomerase IV subunit A (*parC*) in lab conditions (*26*), we found that all UTI cases that gained resistance were caused by reinfection with a different strain carrying ciprofloxacin-resistant alleles of *gyrA* and *parC* (31 of 31 S→R cases were caused by a different strain compared with 6 of 25 S→S cases; $P = 4 \times 10^{-10}$, Fisher test) (fig. S7) (*27*). Similarly, while trimethoprim resistance can be acquired through point mutations in the target enzyme dihydrofolate reductase (DHRF) (*28*), posttreatment resistance was instead conferred by strain replacement (9 of 12 cases) or by the acquisition of a gene encoding a trimethoprim-resistant DHFR enzyme (3 of 12 cases; table S6) (*29*). Consistent with untreated cases having a much lower rate of gained-resistance recurrence, we found that strain replacement was rare in untreated cases (13%; Fig. 2, D and E). Furthermore, even for antibiotics for which *E. coli* resistance is rare, such as fosfomycin and nitrofurantoin (fig. S8),

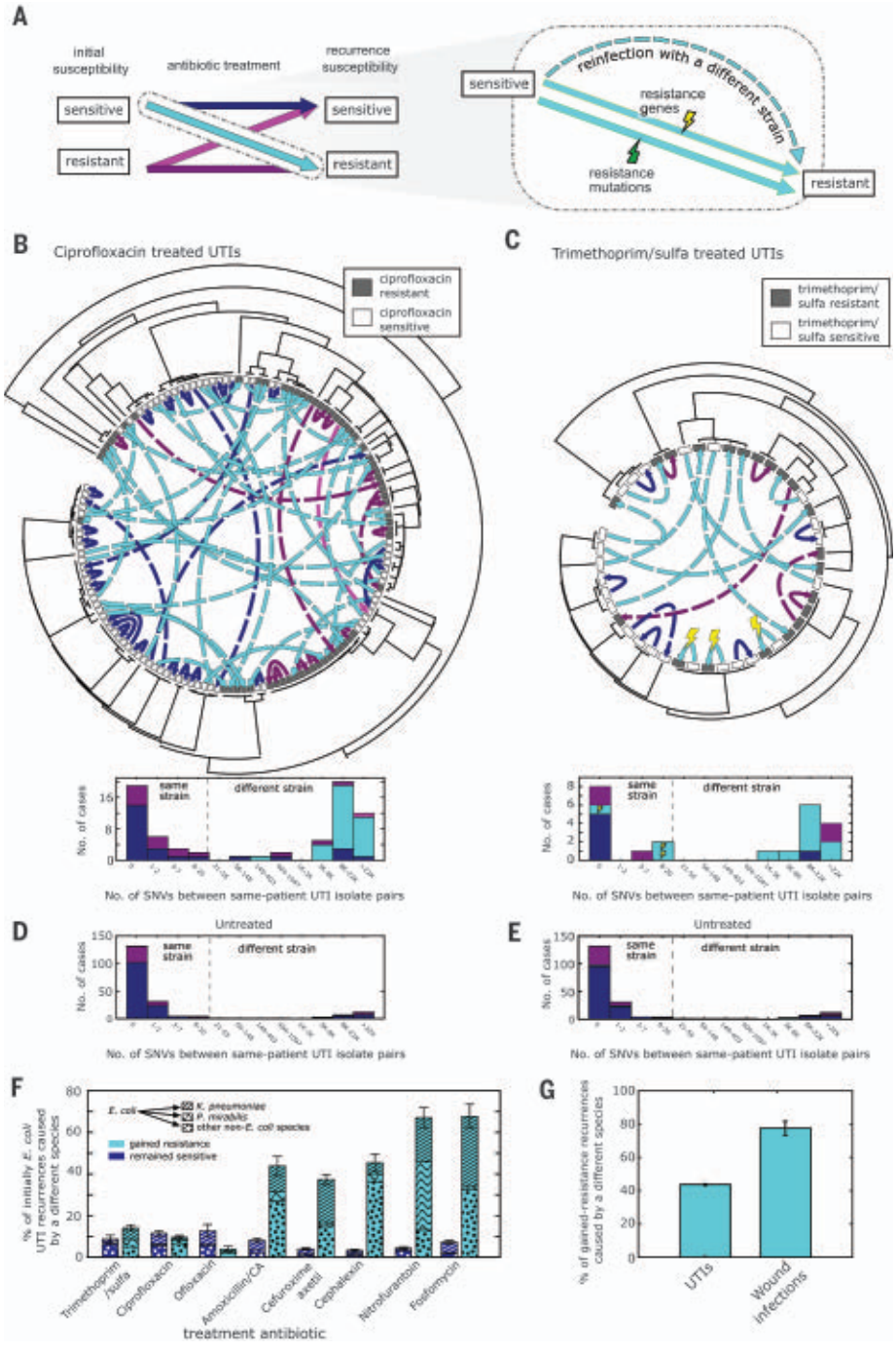


Fig. 2. Genomic analysis of infecting pathogens before and after antibiotic treatment. (**A**) Infections that recurred with gained resistance after treatment (cyan) could be a consequence of acquiring resistance-conferring mutations (green lightning bolt), resistance-conferring genes (yellow lightning bolt), or reinfection with a different strain resistant to the antibiotic (dashed arrow). (**B** and **C**) Phylogenetic trees of *E. coli* urine culture isolates collected from patients who experienced early recurrence after treatment with ciprofloxacin (B) or trimethoprim/sulfa (C), with isolate resistance and sensitivity to the prescribed antibiotic indicated by gray and white boxes, respectively. Same-patient isolates are connected with arrows whose color and style represent change in infection susceptibility and mechanism of gain of resistance [as defined in (A)]. Histograms show the genetic distance, in number of single-nucleotide variations (SNVs), between these same patient isolate pairs, again categorized by infection susceptibility and mechanism of gain of resistance [as defined in (A)]. Vertical dashed lines represent the threshold used to define same-strain versus different-strain recurrences. (**D** and **E**) Histograms of the genetic distance in SNVs between same-patient isolates in untreated cases categorized by infection susceptibility to ciprofloxacin (D) or trimethoprim/sulfa (E). (**F**) The percentage of *E. coli* infections treated with a susceptibility-matched antibiotic that resulted in early recurrence with different non–*E. coli* species (bar patterns), for recurrences that remained sensitive (dark blue) or gained resistance (cyan) to the prescribed antibiotic. (**G**) The percentage of gained-resistance recurrences in all UTIs and wound infections that were caused by reinfection with a different species.

early recurrence with gained resistance after treatment of an initially sensitive *E. coli* infection was strongly associated with reinfection with a different resistant strain, yet this time of an entirely different species (Fig. 2F). Overall, 44% of gained-resistance UTI recurrences were caused by a different species (Fig. 2G). A similar pattern was observed for wound infections: Although the rate of change of species was low among recurrent wound infections that remained sensitive to the treatment antibiotic (fig. S9), in most infections that gained resistance (78%), the species that caused the gain of resistance was not present in the original infection (Fig. 2G). Together, these results suggest that selection for existing resistant strains rather than de novo evolution is the predominant mechanism of treatment-induced emergence of resistance.

Given that posttreatment resistance was typically caused by strain or species replacement rather than by spontaneous, and therefore unpredictable, mutations, we wondered whether emergence of resistance may in fact be predicted at the individual-patient level. As strains are known to recur across same-patient infections even years apart (*6*), we hypothesized that patients with a history of infections with strains resistant to a given antibiotic are at higher risk of gained-resistance recurrence after susceptibility-matched treatment with that antibiotic (Fig. 3A). To test this hypothesis, we performed multivariate logistic regressions of the risk of recurrence with gained-resistance given patient demographics and past infection history among all infections treated with

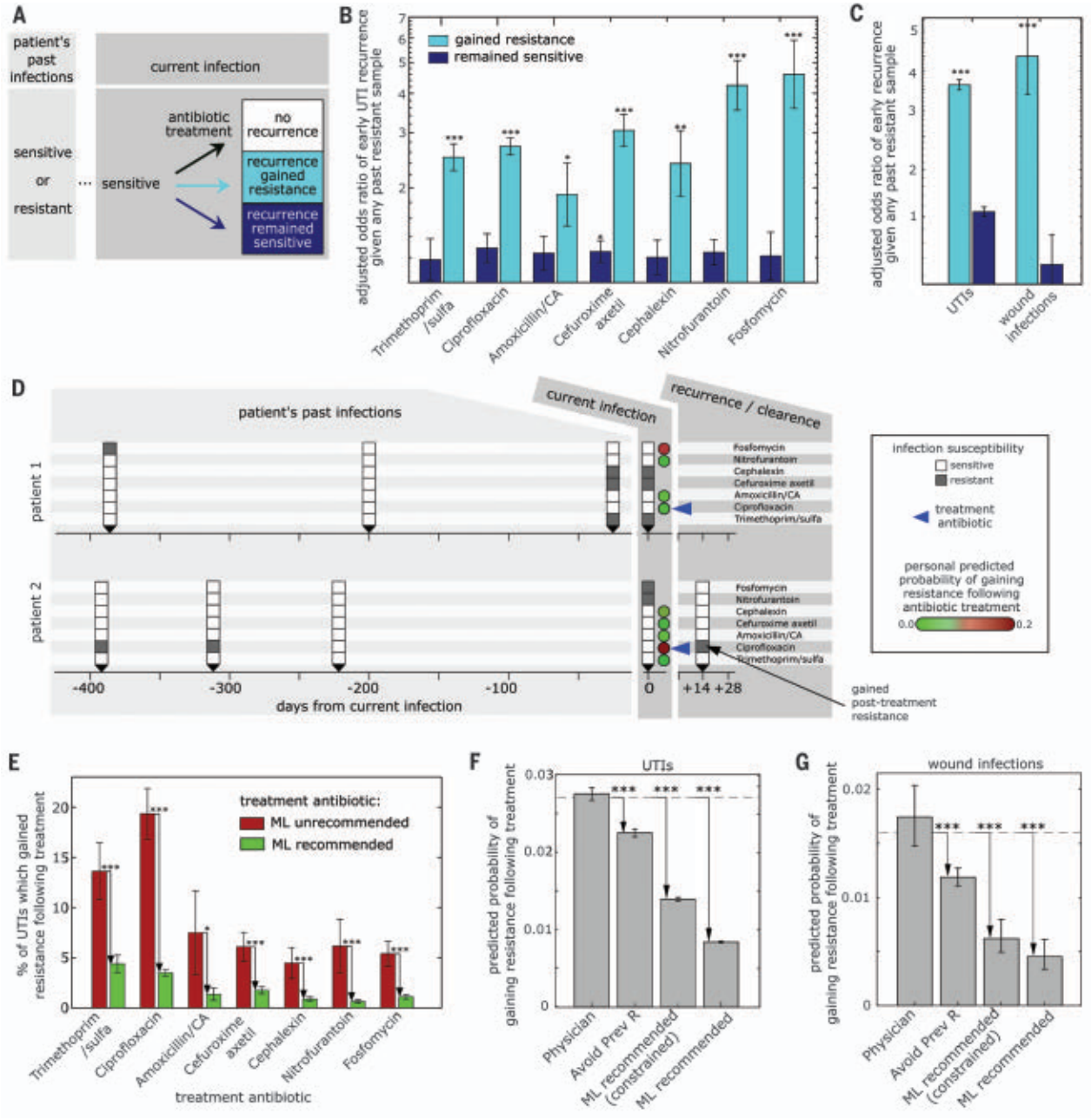


Fig. 3. Personalized, antibiotic-specific predictions of treatment-induced emergence of antibiotic resistance. (**A**) Schematic showing the possible outcomes of susceptibility-matched antibiotic treatment for patients with a recorded history of prior infection susceptibility to the currently prescribed antibiotic. (**B**) Odds ratio of risk of early recurrence that gained resistance (cyan) or remained sensitive (dark blue) given the patient's prior history of resistant infections (binary 1/0: any prior resistance to the prescribed antibiotic, or no prior resistance to the prescribed antibiotic). For each antibiotic, all susceptibility-matched treated cases for patients with any prior infections within the past 3 years are considered. Odds ratios are adjusted for demographics (age, gender) and potential risk factors (pregnancy, catheter use). (**C**) The adjusted odds ratio of early recurrence given the patient's prior history of resistant infections for all antibiotic treatments combined for both UTIs and wound infections. (**D**) Timeline of two example patients showing the susceptibilities of their current (t = 0) and prior (t < 0) infections for each antibiotic (white, sensitive; gray, resistant), as well as their ML-predicted probability of recurrence with gained resistance upon treatment of their current infection with each of the antibiotics (circles, green-to-red colormap). Despite both patients being treated with the same antibiotic to which their infection was sensitive, ciprofloxacin (blue arrow), they had very different ML personal predicted risk of gaining posttreatment ciprofloxacin resistance and indeed varied accordingly in their treatment outcome. (**E**) The percentage of UTIs within the 14-month test period that gained resistance after treatment for cases prescribed an antibiotic that was not recommended ("unrecommended," red, 15% highest predicted risk) or recommended (green, 85% lowest predicted risk) by the ML algorithm (these results are robust to the choice of grouping intermediate-level resistance with resistant, fig. S16). (**F** and **G**) The overall predicted probability of gaining resistance for all UTIs (F) and wound infections (G) during the test period for four different antibiotic prescription methods: (i) the actual antibiotic prescribed by the physician, (ii) an algorithm that randomly chooses an antibiotic but avoids antibiotics to which the patient had past resistance, and the ML recommendation either (iii) unconstrained or (iv) constrained such that each antibiotic is recommended at the exact same frequency as prescribed by the physicians. The dashed line represents the actual gained-resistance rate for the physician-prescribed antibiotics during the test period. *P < 0.05; **P < 0.005; ***P < 0.0005.

a susceptibility-matched antibiotic (136,047 UTIs and 5821 wound infections). Despite all of these cases being treated "correctly," that is, with a susceptibility-matched antibiotic, their risk of recurrence with gained resistance was not uniform: Patients with past infections resistant to the currently prescribed antibiotic were at much higher risk of recurring with gained resistance to the treatment than were patients whose previous infections were sensitive (Fig. 3, B and C; see tables S7 and S8 for regression coefficients). The association between the susceptibility of past infection and the risk of resistance emerging remained significant even for prior infections dating up to 4 years before the current UTI (fig. S10). In contrast, there was no or a much weaker association between past infection susceptibility and risk of early recurrence without gain of resistance, showing that this approach specifically predicts the emergence of resistance rather than merely the risk of early recurrence. A patient's past infection susceptibility was much more predictive than their past antibiotic purchases, which is consistent with within-host selection for strains persisting in the microbiota rather than de novo resistance evolution driving treatment-induced gain of resistance (fig. S11). Finally, beyond the important contribution of personal infection history, we also note the contribution of age and gender to risk of treatment-induced gain of resistance (tables S7 and S8).

Because some patients were at high risk of their infection gaining resistance to the treatment antibiotic, we asked whether the risk of such gained-resistance recurrences may be reduced with an alternative antibiotic. We developed machine learning (ML) algorithms for personalized antibiotic recommendations that minimize the predicted risk of treatment-associated emergence of resistance for both UTIs and wound infections (Fig. 3D). For each antibiotic, we trained a logistic regression model to predict the risk of acquiring resistance during or soon after treatment on the basis of patient demographics (age, gender), potential risk factors (pregnancy, catheter use for UTIs), and their record of prior infections, including the number of past sensitive and resistant isolates. Trained on an initial period and then tested on a temporally separated test period (UTIs: 14 months; wound infections: 30 months), the models predict the risk of resistance emergence well (the area under the curve ranged from 0.89 for nitrofurantoin to 0.62 for amoxicillin/CA in UTIs, and from 0.96 for amoxicillin/CA to 0.58 for cefuroxime in wound infections; ofloxacin was not included, because it was not routinely measured during the test period; fig. S12). More practically, binarizing the patient-specific ML predictions for UTIs into high-risk treatments ("unrecommended," 15% highest ML-predicted risk of gained-resistance recurrence) and lower-risk treatments ("recommended," all others), we found that for every antibiotic, patients for whom the prescribed antibiotic was classified as unrecommended by the ML algorithm acquired antibiotic resistance at a significantly higher rate than did those for whom the antibiotic was recommended, even though all of these cases were treated "correctly" with a susceptibility-matched antibiotic (Fig. 3E; the trends are robust with respect to the recommendation threshold; fig. S13).

Analyzing all susceptibility-matched treated cases in the test period, we found that in most cases there was an alternative susceptibility-matched antibiotic that had a lower patient-specific predicted risk of resistance emerging compared with the antibiotic prescribed by the physician (77% of UTIs and 76% of wound infections). Choosing for each patient the antibiotic with the lowest ML-predicted risk of emergence of resistance (ML recommended) reduces the overall risk of emergence of resistance by 70% for UTIs and 74% for wound infections compared with the risk for physician-prescribed treatments (Fig. 3, F and G). Given that many factors contribute to the rate at which physicians prescribe each antibiotic, such as antibiotic efficacy, cost, ease of use, and side effects, we also developed a constrained antibiotic recommendation model that minimizes the risk of emergence of resistance while preserving the same prescription frequency of each antibiotic as prescribed by physicians during the test period (fig. S14) (*14*). Even these constrained antibiotic recommendations, which merely permute the physician-prescribed antibiotics among patients, can reduce the risk of resistance emerging after treatment by 48% for both UTIs and wound infections compared with the physician-prescribed antibiotics (Fig. 3, F and G). To demonstrate that these constrained recommendations could be made on a case-by-case basis, we also show that the model remains effective when constrained to the physician prescription frequency during a temporally separated period before the final model evaluation period (fig. S14). We note that a simpler algorithm that randomly chooses an antibiotic but avoids antibiotics to which the patient had past resistance can still reduce the risk of resistance emerging after treatment, albeit at a lower frequency than either of the ML models, which is consistent with the contribution of other factors including age, gender, and the more quantitative representation of past infections (Fig. 3, F and G). Furthermore, analyzing the distribution of ML-recommended antibiotics for subsets of patients, such as those with past resistance to a specific antibiotic, may help guide treatment recommendations more broadly (fig. S15). Importantly, the constrained ML models also reduce overall predicted risk of early recurrence (the sum of S→S and S→R), showing that this personalized approach not only reduces gained-resistance recurrences but, by doing so, may also reduce the overall recurrence risk (fig. S17).

While much effort is being invested in methodologies for matching antibiotic treatment to infection susceptibility, susceptibility-matched treatments often fail, as they select for emergence of resistance by means of reinfection with different strains specifically resistant to treatment. The strong association between such treatment-induced selection for resistance and personal history of past resistant infections suggests a patient-specific strain reservoir. Given the known role that uropathogens and wound pathogens persisting in a patient's microbiota have in seeding new infections (*4*–*6*, *30*, *31*) and the collateral effect that antibiotics can have on a patient's microbiome (*32*–*34*), it will be interesting to see whether these emerging resistant strains can be detected in a patient's fecal or skin flora. Regardless of the exact source of these reinfecting resistant strains, our results show that a patient's past infection susceptibility data and patient demographics can be used to predict early recurrence with gained resistance after susceptibility-matched antibiotic treatment. We hope these results will serve as a basis for a personalized treatment approach that minimizes the selection and spread of resistant pathogens at both the individual-patient and population levels.

REFERENCES AND NOTES

1. G. K. M. Harding, A. R. Ronald, *Int. J. Antimicrob. Agents* **4**, 83–88 (1994).
2. W. E. Stamm, S. R. Norrby, *J. Infect. Dis.* **183** (suppl. 1), S1–S4 (2001).
3. C. P. Montgomery, M. Z. David, R. S. Daum, *Curr. Opin. Infect. Dis.* **28**, 253–258 (2015).
4. L. E. Nicolle, in *Brenner and Rector's The Kidney*, K. Skorecki, G. M. Chertow, P. A. Marsden, A. S. L. Yu, M. W. Taal, Eds. (Elsevier, ed. 10, 2015), pp. 1231–1256.
5. V. L. Tchesnokova *et al.*, *Clin. Infect. Dis.* **70**, 937–939 (2020).
6. B. M. Forde *et al.*, *Nat. Commun.* **10**, 3643 (2019).
7. V. Ki, C. Rotstein, *Can. J. Infect. Dis. Med. Microbiol.* **19**, 173–184 (2008).
8. P. D. Brown, A. Freeman, B. Foxman, *Clin. Infect. Dis.* **34**, 1061–1066 (2002).
9. T. M. Hooton, R. Besser, B. Foxman, T. R. Fritsche, L. E. Nicolle, *Clin. Infect. Dis.* **39**, 75–80 (2004).
10. Y. G. Kwak *et al.*, *Infect. Chemother.* **49**, 301–325 (2017).
11. H. Goossens, M. Ferech, R. Vander Stichele, M. Elseviers; ESAC Project Group, *Lancet* **365**, 579–587 (2005).
12. C. Costelloe, C. Metcalfe, A. Lovering, D. Mant, A. D. Hay, *BMJ* **340**, c2096 (2010).
13. R. Colodner, I. Kometiani, B. Chazan, R. Raz, *Infection* **36**, 41–45 (2008).
14. I. Yelin *et al.*, *Nat. Med.* **25**, 1143–1152 (2019).
15. J. P. Metlay, B. L. Strom, D. A. Asch, *J. Antimicrob. Chemother.* **51**, 963–970 (2003).
16. U. D. Allen, N. MacDonald, L. Fuite, F. Chan, D. Stephens, *CMAJ* **160**, 1436–1440 (1999).
17. J. Ena, C. Amador, C. Martinez, V. O. de la Tabla, C. M. Kunin, *J. Urol.* **153**, 117–120 (1995).
18. L. Johnson *et al.*, *Am. J. Med.* **121**, 876–884 (2008).
19. H. C. Baggett *et al.*, *J. Infect. Dis.* **189**, 1565–1573 (2004).
20. J. A. Silverman, H. L. Schreiber 4th, T. M. Hooton, S. J. Hultgren, *Curr. Urol. Rep.* **14**, 448–456 (2013).
21. R. Ikäheimo *et al.*, *Clin. Infect. Dis.* **22**, 91–99 (1996).
22. K. Gupta *et al.*, *Clin. Infect. Dis.* **52**, e103–e120 (2011).
23. R. Ikram, R. Psutka, A. Carter, P. Priest, *BMC Infect. Dis.* **15**, 224 (2015).
24. W. J. Burman *et al.*, *Am. J. Med.* **115**, 358–364 (2003).

25. A. L. Flores-Mireles, J. N. Walker, M. Caparon, S. J. Hultgren, *Nat. Rev. Microbiol.* **13**, 269–284 (2015).
26. F. Collin, S. Karkare, A. Maxwell, *Appl. Microbiol. Biotechnol.* **92**, 479–497 (2011).
27. E. Zankari *et al*., *J. Antimicrob. Chemother.* **72**, 2764–2768 (2017).
28. E. Toprak *et al*., *Nat. Genet.* **44**, 101–105 (2011).
29. E. Zankari *et al*., *J. Antimicrob. Chemother.* **67**, 2640–2644 (2012).
30. M. Magruder *et al*., *Nat. Commun.* **10**, 5521 (2019).
31. K. L. Nielsen, P. Dynesen, P. Larsen, N. Frimodt-Møller, *J. Med. Microbiol.* **63**, 582–589 (2014).
32. L. Dethlefsen, S. Huse, M. L. Sogin, D. A. Relman, *PLOS Biol.* **6**, e280 (2008).
33. M. Yassour *et al*., *Sci. Transl. Med.* **8**, 343ra81 (2016).
34. E. G. Pamer, *Science* **352**, 535–538 (2016).
35. M. Stracy, R. Kishony,Technion-Kishony-lab/Antibiotic-treatment-failure: Code for Stracy et al,Science 2022, version 1, Zenodo (2021); https://doi.org/10.5281/zenodo.5799077.

ACKNOWLEDGMENTS

Funding: This work was supported by National Institutes of Health grant R01 GM081617 (R.Ki.); Israel Science Foundation grant 3055/19 within the Israel Precision Medicine Partnership program (R.Ki.);, Ernest and Bonnie Beutler Research Program of Excellence in Genomic Medicine (R.Ki.); European Research Council FP7 ERC grant 281891 (R.Ki.); Wellcome Trust Sir Henry Wellcome fellowship 204684/Z/16/Z (M.S.); and D. Dan and Betty Kahn Foundation's gift to the University of Michigan, Weizmann Institute, and Technion–Israel Institute of Technology Collaboration for Research. **Author contributions:** M.S., O.S., I.Y., G.K., J.K., G.C., V.S., and R.Ki. designed the study. R.Ka. and E.H. curated clinical data. M.P., G.R., T.W., O.S., and Y.A. collected clinical samples. G.R., T.W., G.K., and J.K. handled clinical project administration. M.S., O.S., I.Y., and Y.A. performed whole-genome sequencing. M.S. and R.Ki. analyzed the data. M.S., I.Y., O.S., B.F., M.P., G.C., V.S., and R.Ki. interpreted the results. M.S. and R.Ki. wrote the paper with comments from all authors. **Competing interests:** The authors declare that they have no competing interests. **Data and materials availability:** The clinical data that support the findings of this study are available from Maccabi Healthcare Services, but restrictions apply to the availability of these data, which were used under license for the current study and so are not publicly available. Access to the data is, however, available upon reasonable request and signing a material transfer agreement with Maccabi Healthcare Services. Analysis code is available from https://github.com/Technion-Kishony-lab/Antibiotic-treatment-failure (*35*). All urine culture isolate whole-genome sequencing data generated in this study have been deposited in the Sequence Read Archive database and are available here:www.ncbi.nlm.nih.gov/sra/PRJNA786867. Treatment and susceptibility data for the sequenced isolates are provided in the supplementary materials (data S1).

SUPPLEMENTARY MATERIALS

science.org/doi/10.1126/science.abg9868
Materials and Methods
Supplementary Text
Figs. S1 to S17
Tables S1 to S8
References (*36*–*38*)
MDAR Reproducibility Checklist
Data S1

10 February 2021; resubmitted 7 September 2021
Accepted 23 December 2021
10.1126/science.abg9868

ORGANIC CHEMISTRY

Total synthesis of himastatin

Kyan A. D'Angelo[1], Carly K. Schissel[1], Bradley L. Pentelute[1,2,3,4]*, Mohammad Movassaghi[1]*

The natural product himastatin has an unusual homodimeric structure that presents a substantial synthetic challenge. We report the concise total synthesis of himastatin from readily accessible precursors, incorporating a final-stage dimerization strategy that was inspired by a detailed consideration of the compound's biogenesis. Combining this approach with a modular synthesis enabled expedient access to more than a dozen designed derivatives of himastatin, including synthetic probes that provide insight into its antibiotic activity.

The proliferation of multidrug-resistant pathogenic bacteria is widely recognized as a threat to global health (*1*, *2*). Natural products have served as the primary inspiration for new antibiotics to treat bacterial infections (*3*). (–)-Himastatin (**1**) is a macrocyclic peptide with a homodimeric structure isolated from *Streptomyces himastatinicus* (Fig. 1) that demonstrates antibiotic and antitumor activity (*4*–*6*). Although (–)-himastatin's (**1**) mechanism of action is not known, an early investigation demonstrated that its antibiotic activity was reduced in the presence of sodium salts of phospholipids and fatty acids, leading to speculation that (–)-himastatin (**1**) may target the bacterial membrane (*7*). (–)-Himastatin's (**1**) homodimeric structure does not resemble those of any well-characterized antibiotic class, including known membrane-disrupting cyclic peptides. The most distinctive structural feature of (–)-himastatin (**1**) is the central C5–C5′ linkage between cyclotryptophan residues that is formed in the final biosynthetic step (*8*) and is critical for the observed Gram-positive antibiotic activity (*9*). Related monomeric natural products discovered after (–)-himastatin (**1**), including (–)-NW-G01 (**S2**), show a substantial enhancement in antibiotic activity upon chemoenzymatic dimerization (*10*) (fig. S1). Other notable structural features of (–)-himastatin (**1**) include the alternating sequence of D- and L-amino acids, a depsipeptide linkage, and the piperazic acid residue with γ-hydroxylation.

Danishefsky's landmark synthesis of (–)-himastatin (**1**), which clarified the Cα stereochemistry of the cyclotryptophan residue, featured an early-stage Stille coupling to form the central C5–C5′ linkage followed by bidirectional elaboration of a dimeric cyclotryptophan (*9*). Early-stage formation of this linkage also featured in total syntheses of the related natural product (–)-chloptosin (**S1**) by Yao (*11*) and Ley (*12*) and their co-workers, who found that cross-coupling approaches to achieve a more attractive late-stage dimerization (which would also offer access to heterodimeric derivatives) were not successful (*12*). Motivated by the distinctive structure, established synthetic challenge, and antibiotic activity, we became interested in developing a concise total synthesis of (–)-himastatin (**1**) that would offer rapid access to derivatives for chemical biology studies.

The key unaddressed challenge of uniting two complex fragments to form the C5–C5′ bond at the center of (–)-himastatin's (**1**) dimeric structure encouraged us to consider the development of a new synthetic methodology. To address the C_{sp2}–C_{sp2} linkage present in (–)-himastatin (**1**), we needed to identify a strategy that stands apart from our group's prior approaches based on reductive or photolytic radical generation and coupling to secure C_{sp3}–C_{sp3} linkages and C_{sp3}–C_{sp2} linkages between similar (*13*) and dissimilar fragments (*14*). We began with a detailed examination of (–)-himastatin's (**1**) biosynthesis from a linear peptide **4** that is cyclized and then subjected to oxidative tailoring by three cytochrome P450 enzymes (*8*). The final step, catalyzed by HmtS, forges the central C5–C5′ bond by oxidative dimerization of (+)-himastatin monomer (**2**). On the basis of recent theoretical studies of P450-catalyzed C–C bond formation, we envisioned that this enzymatic dimerization may take place via radical–radical coupling of two cyclotryptophan radicals (fig. S2) (*15*, *16*). These radical species are likely generated in rapid succession via indoline N–H hydrogen-atom abstraction at the heme active site, before undergoing combination in its vicinity (*16*, *17*).

We envisioned that a biosynthetically inspired chemical method for the oxidative dimerization of cyclotryptophans could follow the same radical–radical coupling blueprint. As opposed to hydrogen atom abstraction, we planned to generate an analogous open-shell cyclotryptophan species via single-electron oxidation of the embedded aniline substructure. Consistent with studies of aniline dimerization via single-electron oxidation (*18*–*20*), we predicted that the resulting arylamine radical cation would rapidly dimerize at the most accessible position, forming the desired C5–C5′ linkage. Late-stage application of this chemistry to dimerization of (+)-himastatin monomer (**2**) permits a straightforward modular assembly of linear hexadepsipeptide **5** akin to native precursor **4**, without the constraints imposed

[1]Department of Chemistry, Massachusetts Institute of Technology, Cambridge, MA 02139, USA. [2]The Koch Institute for Integrative Cancer Research, MIT, Cambridge, MA 02142, USA. [3]Broad Institute of MIT and Harvard, Cambridge, MA 02142, USA. [4]Center for Environmental Health Sciences, MIT, Cambridge, MA 02139, USA.
***Corresponding author. Email: movassag@mit.edu (M.M.); blp@mit.edu (B.L.P.)**

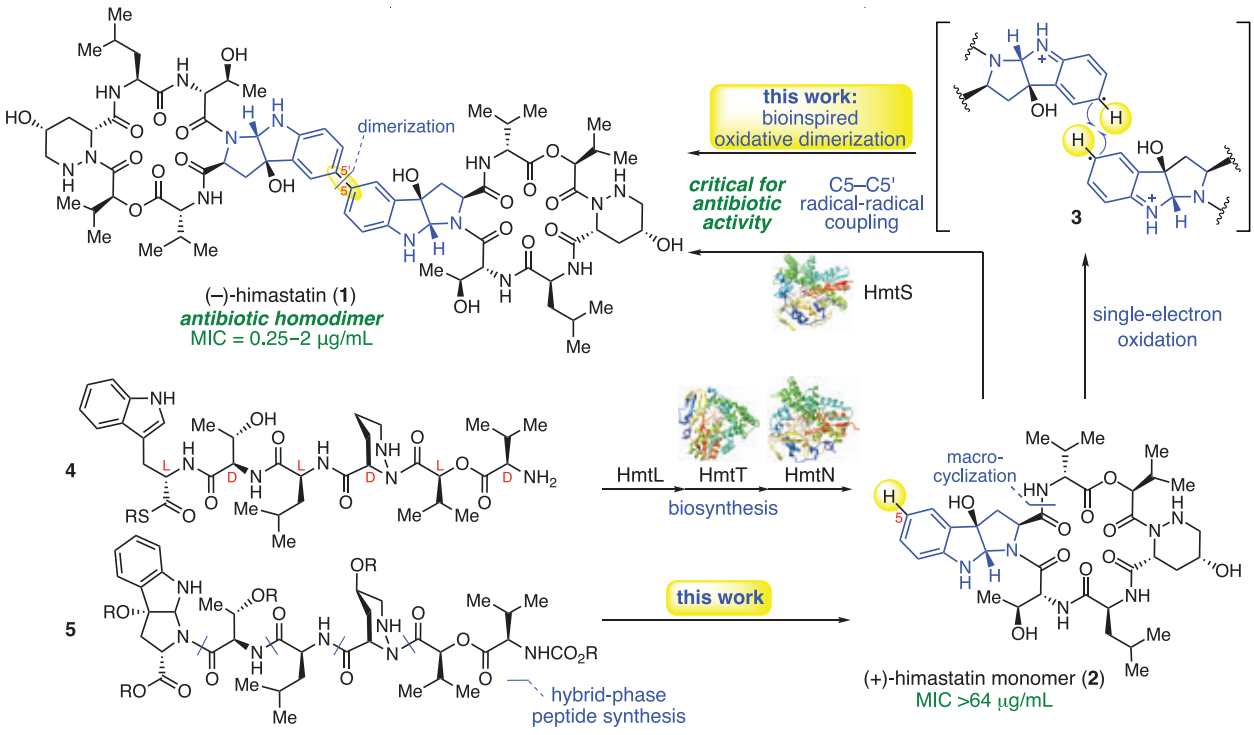


Fig. 1. Comparison of the biogenesis of himastatin and our bioinspired synthetic strategy. MIC values for (–)-himastatin (**1**) are taken from (*4*) against Gram-positive bacteria. MIC, minimum inhibitory concentration. Protein Data Bank identification codes: HmtT, 4GGV; HmtN, 5WX2; HmtS, 5Z9I.

by bidirectional elaboration of a simple dimeric cyclotryptophan (*9*, *11*, *12*). Direct union of complex peptide macrocycles also offers the elusive opportunity to access heterodimeric derivatives of (–)-himastatin (**1**).

Our dimerization method required the identification of a single-electron oxidant that would target the aniline substructure within a complex cyclotryptophan precursor (*21*). Existing precedent for the use of inorganic oxidants for generation of aniline radical cations (*20*) ultimately guided our initial selection of reagents. We found that excess silver(I) hexafluoroantimonate [5 equivalents (equiv.)], in combination with the non-nucleophilic pyrimidine base TTBP (*22*) in 1,2-dichloroethane, could effect C5–C5′ dimerization of cyclotryptophan, cyclotryptamine, and indoline derivatives (Fig. 2A). In each case, a single regioisomer consistent with a symmetric C5–C5′ linked homodimer was isolated. Single-crystal x-ray diffraction of dimeric *endo*-diketopiperazine (+)-**7h** verified the expected connectivity. The use of an aqueous sodium thiosulfate reductive workup was critical for optimal isolation of the dimers, as a second equivalent of oxidant is consumed owing to their sensitivity toward further oxidation under the reaction conditions (*23*, *24*). We found that *exo*-configured diketopiperazines **6e** and **6g** were subject to complete oxidation in approximately half the time of their corresponding *endo*-derivatives **6f** and **6h**, respectively. This finding correlates with the increased accessibility of the N1 locus in substrates **6e** and **6g**, the site of initial oxidation (*25*). Substitution of N1 with a methyl group in the case of indoline **6k** did not inhibit the dimerization, consistent with a radical intermediate as opposed to a closed-shell arenium cation (*26*). As part of our optimization efforts (table S1) (*23*) and to expand the range of reagents that could be used in more complex applications of our dimerization method, we also investigated the use of copper(II) salts as single-electron oxidants (*20*). Cyclotryptophan dimer (–)-**7a** could be obtained by using catalytic copper(II) trifluoromethanesulfonate and silver(I) carbonate as the terminal oxidant, albeit in lower yield (34%, 18% recovered starting material) compared to stoichiometric $AgSbF_6$ (54%, 53% on a 0.50-mmol scale).

To investigate the mechanism of this C–C bond–forming dimerization reaction, we devised a series of experiments using indoline substrates (Fig. 2B and fig. S3) (*23*). When an equimolar mixture of C2-methyl and C2-phenyl indolines **6i** and **6j**, respectively, was subjected to our dimerization conditions, we observed a statistical mixture of homo- and heterodimers arising from similar rates of single-electron oxidation (Fig. 2B, green; fig. S3, eq. 1). However, oxidative dimerization of an equal mixture of indolines **6j** and **6k** gave predominantly (90%) homodimer formation, along with a trace (4%) amount of heterodimer **7n** (fig. S3, eq. 2). When a limiting quantity of oxidant was used, we determined that these indoline substrates were consumed sequentially, with N1-methyl indoline **6k** dimerizing selectively over NH indoline **6j** (Fig. 2B, blue, and fig. S3, eq. 3). Having observed homodimerization of a more readily oxidized monomer in the presence of a similarly nucleophilic but less readily oxidized monomer, we conclude that C5–C5′ bond formation preferentially occurs through radical–radical coupling rather than nucleophilic capture. This conclusion is consistent with the absence of adduct formation in the homodimerization of cyclotryptophan **6a** despite the presence of external π-nucleophiles (e.g., methallyltrimethylsilane, dimethylketene silyl acetal, *N*-trimethylsilylindoline) and is reinforced by prior studies demonstrating that radical–radical coupling between aniline radical cations is fast (k = ~10^7 M^{-1}•s^{-1} for the dimerization of $PhNMe_2^{\bullet+}$) (*18*–*20*). We postulate that the high local concentration of radical species near the surface of the oxidant favors their direct combination over nucleophilic pathways (*14*, *20*). In the context of our synthetic efforts, the rapid rate and apparent insensitivity of the radical–radical coupling manifold to nucleophilic interference bode well for the application of this chemistry to complex substrates. These findings highlight a possible underlying parallel between our oxidative dimerization methodology and our mechanistic proposal for the biosynthetic dimerization catalyzed by HmtS (fig. S2), involving

successive generation of radical species in close proximity to each other.

For the synthesis of (+)-himastatin monomer (**2**), we sought to leverage the practical advantages of solid-phase peptide synthesis (*27*), offering rapid and customizable access to complex peptides by minimizing repetitive purification and isolation steps. In contrast to the reported solution-based approach to intermediates en route to (−)-himastatin (**1**) (*9*), we relied on a hybrid solution–solid phase synthetic strategy. The resin-bound D-threonine **9** (Fig. 3) was elaborated with L-leucine (−)-**10** and tridepsipeptide fragment (+)-**8**, the latter being prepared in one step (*23*) (78% yield) from a depsipeptide block (*23*, *28*) (three steps from commercial carboxylic acids) and known *N*ε, *O*-protected D-5-hydroxypiperazic acid **S8** (*9*) (nine steps from 4-pentenoic acid). The crude pentadepsipeptide acid (+)-**11** obtained upon cleavage was then coupled with cyclotryptophan (−)-**12** [fig. S4; five steps from commercial tryptophan derivative (−)-**S3**, 60% yield], affording linear hexadepsipeptide (−)-**13** in 64% overall yield from threonine resin **9** (*23*). The efficient hybrid synthetic strategy we have developed enabled convergent assembly of intermediate hexadepsipeptide (−)-**13** with only a single chromatographic purification, which compares favorably to linear solution-phase synthesis, which requires at least 10 separate steps to access an intermediate of similar complexity (*9*). Furthermore, our modular strategy allows for conducting difficult couplings in solution (*28*) and introducing the tryptophan residue as a cyclotryptophan to bypass stereoselectivity concerns that would arise from late-stage oxidation (*29*). Following termini deprotection, linear peptide (−)-**13** was cyclized to (+)-himastatin monomer (**2**) in 49% overall yield (Fig. 3), affording the immediate biosynthetic precursor to (−)-himastatin (**1**). All ^{1}H and ^{13}C nuclear magnetic resonance (NMR) data, as well as optical rotation for synthetic monomer (+)-**2**, were consistent with literature values (*8*, *9*).

Having accessed (+)-himastatin monomer (**2**), we focused on the application of our biosynthetically inspired oxidative dimerization methodology to complete the total synthesis of (−)-himastatin (**1**) (Fig. 3). Although silver(I) hexafluoroantimonate and copper(II) trifluoromethanesulfonate were effective for the dimerization of simpler cyclotryptophans (Fig. 2A), they gave little to no oxidation of the cyclotryptophan incorporated within the more complex (+)-himastatin monomer (**2**). We hypothesized that aggregation and inactivation of these insoluble oxidants, combined with the lower reactivity of complex macrocyclic peptide substrates, may be responsible for the low conversion, and we sought to address the challenge posed by evaluating other single-electron oxidants. Consistent with this hypothesis, insoluble oxidants such as other Ag(I,II) and Cu(II) salts were generally ineffective. However, soluble oxidants, including organic radical cations such as magic blue [(4-BrPh)$_3$N$^{\bullet+}$SbF$_6$], did provide oxidation, but products derived from nucleophilic substitution of the C–Br bond (S_NAr) by the peptide dominated (*21*). Informed by our prior use of Cu(II) for the dimerization of simpler substrates and in search of an oxidant with both good solubility and low propensity toward nucleophilic capture, we identified copper(II) hexafluoroantimonate. Our isolation of freshly prepared Cu(SbF$_6$)$_2$, commonly used as a soluble Lewis acid catalyst (*30*), provided us with an opportunity to investigate its use as a stoichiometric oxidant. In the event, exposure of (+)-himastatin monomer (**2**) to excess Cu(SbF$_6$)$_2$ (20 equiv.) and DTBMP (4 equiv.) in 1,2-dichloroethane afforded (−)-himastatin (**1**) in 40% yield (3 mg), with only trace (<5%) amounts of recovered starting material. The remainder of the mass balance consisted of minor undesired products, including dimers and oligomers. Our convergent synthesis of the natural product (−)-**1** is enabled by the

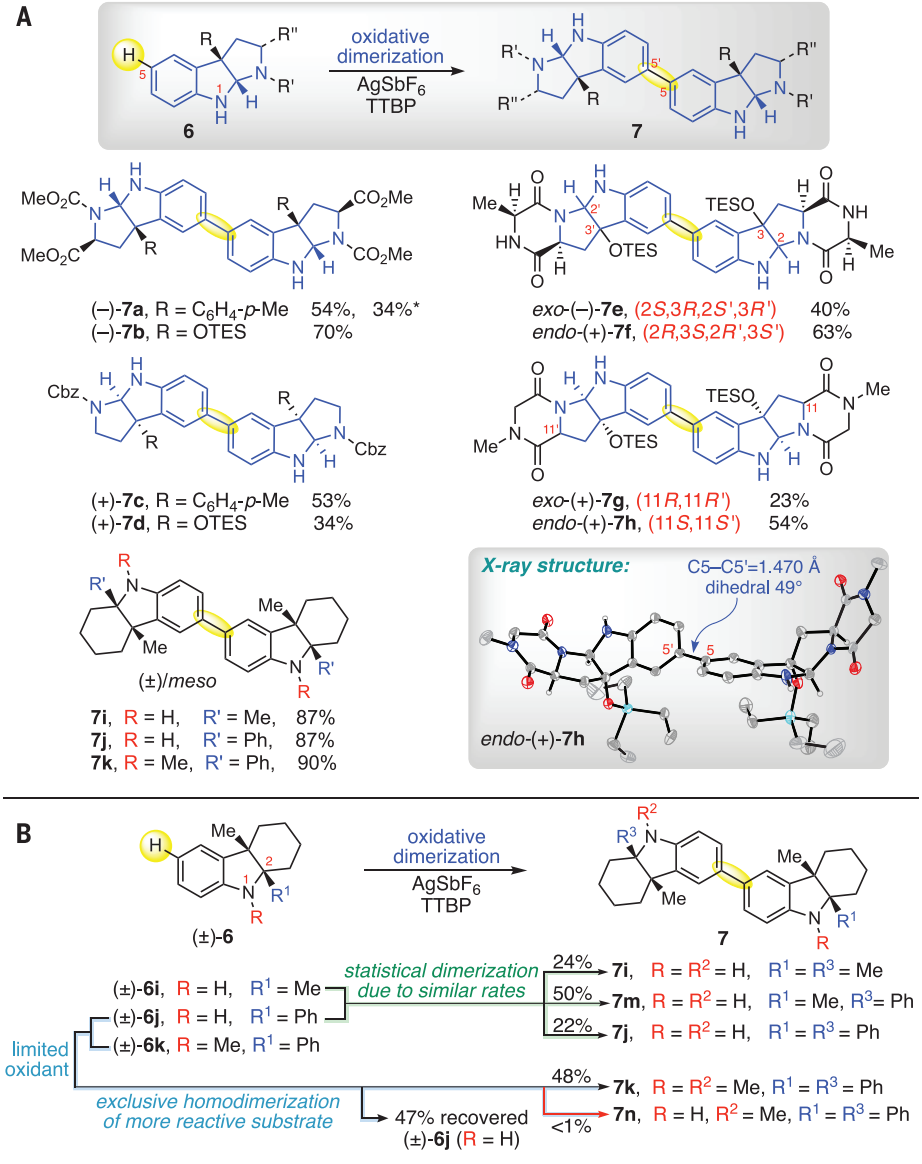


Fig. 2. Oxidative dimerization of cyclotryptophan, cyclotryptamine, and indolines. (**A**) Substrate scope of our oxidative dimerization reaction. In the ORTEP representation of dimeric *endo*-diketopiperazine (+)-**7h**, the thermal ellipsoids are drawn at 30% probability, and only selected hydrogen atoms are shown. (**B**) Mechanistic studies using equimolar mixtures of differentially substituted indolines provide evidence for a radical–radical coupling mechanism. Reagents and conditions: $AgSbF_6$, TTBP, $ClCH_2CH_2Cl$, 23°C; * copper (II)-catalyzed conditions: $Cu(OTf)_2$ (20 mol %), Ag_2CO_3, $ClCH_2CH_2Cl$, 23°C. TES, triethylsilyl; TTBP, 2,4,6-tri-*tert*-butylpyrimidine.

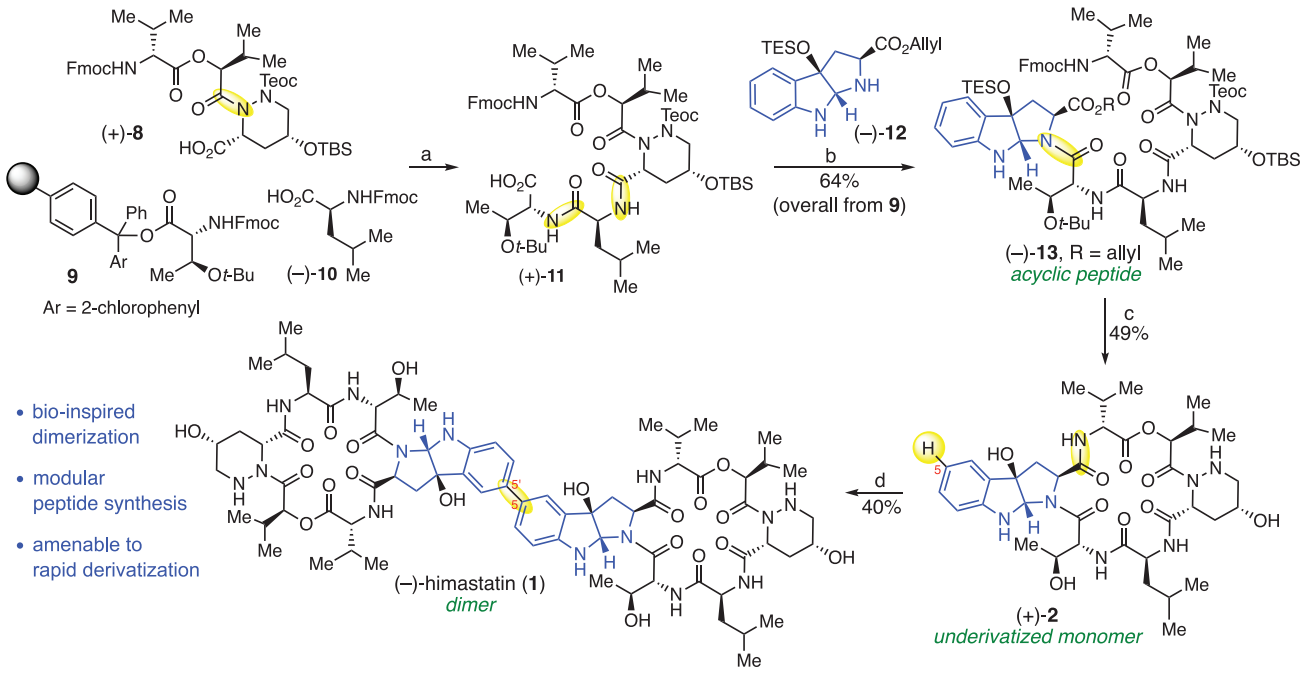


Fig. 3. Concise total synthesis of (–)-himastatin (1). Reagents and conditions: (a) (i) piperidine, DMF, 23°C; (ii) (–)-**10**, HATU, *i*-Pr_2NEt, DMF, 23°C; (iii) piperidine, DMF, 23°C; (iv) (+)-**8**, HATU, *i*-Pr_2NEt, DMF, 23°C; (v) TFA, CH_2Cl_2, 23°C. (b) (–)-**12**, HATU, HOAt, 2,4,6-collidine, CH_2Cl_2, 0 → 23°C. (c) (i) $Pd(PPh_3)_4$, *N*-methylaniline, THF, 23°C; (ii) *i*-Pr_2NH, MeCN, 23°C; (iii) HATU, HOAt, *i*-Pr_2NEt, CH_2Cl_2, 23°C; (iv) TFA, H_2O, anisole; Et_3N, MeOH, 23°C. (d) $Cu(SbF_6)_2$, DTBMP, $ClCH_2CH_2Cl$, 23°C. Ar, 2-chlorophenyl; DMF, *N*,*N*-dimethylformamide; DTBMP, 2,6-di-*tert*-butyl-4-methylpyridine; Fmoc, 9-fluorenylmethoxycarbonyl; HATU, hexafluorophosphate azabenzotriazole tetramethyl uronium; HOAt, 1-hydroxy-7-azabenzotriazole; Leu, leucine; TBS, *tert*-butyldimethylsilyl; Teoc, 2-trimethylsilylethyloxycarbonyl; TFA, trifluoroacetic acid; THF, tetrahydrofuran.

hybrid solution–solid phase assembly of readily available tridepsipeptide (+)-**8**, resin-bound D-Thr **9**, L-leucine (–)-**10**, and cyclotryptophan (–)-**12**, comprising 11 steps (5 on solid-support, 6 in solution) and requiring only three isolations to access (–)-himastatin (**1**) from D-Thr **9** in 13% overall yield. All spectroscopic data, as well as optical rotation, for synthetic (–)-himastatin (**1**) were consistent with literature values (*6*, *9*).

Our concise and versatile chemical synthesis of himastatin, featuring a biosynthetically inspired final-stage dimerization reaction, presented an opportunity both to interrogate structural characteristics that are important for its bioactivity and to access synthetic probes for chemical biology studies (Fig. 4). We hypothesized that the alternating sequence of D,L-residues present in the macrocyclic rings of (–)-himastatin (**1**) could promote self-assembly (*31*, *32*), inspiring our preparation of both the enantiomer (*ent*-(+)-**1**) and *meso* derivative of himastatin (**1**). These stereochemical probes were prepared from precursors of opposite chirality, and in the case of the heterodimer *meso*-himastatin (**1**), by dimerization of an equal mixture of monomer **2** enantiomers and separation of the resulting heterodimer (*23*). Apart from slight variations in the chemical shifts of aromatic ^{1}H and ^{13}C signals, the spectra of *meso*-himastatin (**1**) were nearly identical to those of the corresponding homodimers. We also selected several derivatives with single-residue substitutions to synthesize, each varying a residue that is specific to himastatin among related antibiotics. In all cases, our modular hybrid peptide synthesis approach was quickly adapted to introduce the substituted residue, and the resulting monomers were effectively dimerized (21 to 37% yield) under the conditions developed for the synthesis of (–)-himastatin (**1**) (Fig. 4A) (*23*). As an orthogonal mechanistic probe that would permit direct visualization of himastatin's interaction with bacteria, we designed a fluorescent heterodimer that we predicted would retain antibiotic activity (see below). TAMRA-himastatin heterodimer (–)-**25** was rapidly prepared through the union of himastatin monomer (+)-**2** and azidolysine monomer (+)-**22** followed by labeling via a reduction–acylation sequence (Fig. 4B). This procedure also provided access to TAMRA-himastatin homodimer (–)-**S17** as a useful control (*23*).

We found that synthetic (–)-himastatin (**1**) showed in vitro antibiotic activity against several Gram-positive species, including antibiotic-resistant strains of public health concern (Table 1 and table S11) (*1*). Our synthetic (–)-himastatin (**1**) showed minimum inhibitory concentration (MIC) values (1 to 2 μg/ml) similar to those reported for natural (–)-himastatin (**1**) in identical species (*4*). All monomeric derivatives prepared in this study had MIC values ≥64 μg/ml across all species tested (*9*, *23*), highlighting the critical role of dimerization for antibiotic activity. Our stereochemical probes revealed that the absolute stereochemistry of himastatin has negligible impact on its antibiotic activity; stereoisomers of himastatin (**1**) were found to have nearly identical MIC values across the *Bacillus subtilis*, *Staphylococcus aureus*, and *Enterococcus faecalis* strains tested. This finding has also been observed among enantiomers of certain membrane-targeting cyclic peptides with alternating stereochemistry (*33*) and is consistent with antibiotic activity depending on achiral as opposed to diastereomeric interactions that would lead to differential activity of each stereoisomer (e.g., with peptides or receptors) (*34*, *35*). By contrast, we found that *ent*-(+)-himastatin (**1**) was four- to eight-fold more active in inhibiting the growth of the producing organism, *Streptomyces himastatinicus*, compared with (–)-himastatin (**1**). This finding might be explained by the presence of known self-resistance mechanisms that have evolved in other species, such as enzymatic degradation and efflux, which would be expected to show differences between stereoisomers (*36*).

The introduction of a strategically positioned functional handle in (–)-himastatin (**1**) was a key goal of our derivative design that would

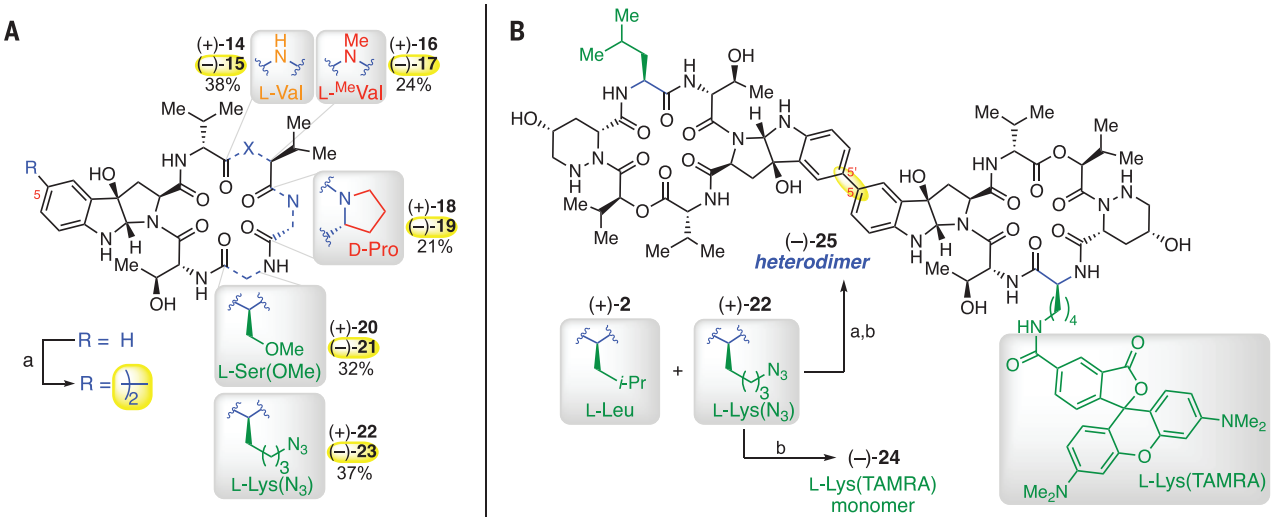


Fig. 4. Synthesis of designed derivatives and probes of himastatin. (**A**) Dimerization of unnatural himastatin derivatives with single-residue substitutions. (**B**) Synthesis of a heterodimeric fluorescent himastatin probe. Reagents and conditions: (a) $Cu(SbF_6)_2$, DTBMP, $ClCH_2CH_2Cl$, 23°C. (b) (i) PMe_3, H_2O, THF, 40°C; (ii) 5-TAMRA succinimidyl ester, *i*-Pr_2NEt, DMF, 23°C. Lys, lysine; Pro, proline; Ser, serine; TAMRA, carboxytetramethylrhodamine; Val, valine.

permit introduction of a fluorescent tag. We focused on L-leucine substitution, given the natural variation of this site among related antibiotics (fig. S1). Replacement with an *O*-methyl serine residue [L-Ser(OMe), dimer (–)-**21**], which is found in (–)-chloptosin (**S1**), had minimal impact on antibiotic activity. A similar finding was observed upon substitution with L-azidolysine [L-Lys(N_3), dimer (–)-**23**], which offered the conjugation site exploited in our synthesis of fluorescent probes. However, unlike serine and azidolysine homodimers (–)-**21** and (–)-**23**, respectively, the corresponding TAMRA-himastatin homodimer (–)-**S17** was inactive (MIC > 64 μg/ml) (fig. S5 and table S11). In addition to TAMRA, homodimeric himastatin analogs derived from other fluorophores were also found to be inactive (fig. S5). Consistent with our expectation that minimizing the overall perturbation of himastatin's structure to only one half of the dimer may preserve antibiotic activity, we found that the MIC of TAMRA-heterodimer (–)-**25** (Fig. 4B) was indeed comparable to that of (–)-himtastatin (**1**) in *B. subtilis* (6 versus 1 μg/ml). Thus, the opportunity for heterodimer formation offered by our biogenetically inspired late-stage dimerization methodology was instrumental to secure access to a fluorescent himastatin probe (*37*), as well as other key derivatives including *meso*-himastatin (**1**) that would otherwise be challenging to prepare by chemoenzymatic or bidirectional synthesis (*9*, *10*).

Other structural features specific to (–)-himastatin (**1**) include a depsipeptide linkage and 5-hydroxypiperazic acid residue. Evaluating the derivatives that we prepared to study these particular structural features, we observed a trend of decreasing antibiotic activity when the ester linkage was replaced with either a secondary amide (–)-**15** or tertiary amide (–)-**17**, consistent with the loss of a hydrogen-bond site (*38*). Furthermore, when the 5-hydroxypiperazic acid residue was replaced with a proline residue, antibiotic activity was completely abolished. Although proline residues are known to induce turn formation, especially when the adjacent amino acid is of opposite α-stereochemistry, they do not exhibit a rigidifying effect as pronounced as that seen in *N*-acyl piperazic acid derivatives (*39*). Consistent with the predicted loss of rigidity upon proline substitution, NMR spectra of homodimer (–)-**19** and monomer (+)-**18** in various solvents at 23°C revealed the presence of minor conformers not observed in the spectra of (–)-himastatin (**1**) or our other derivatives. Taken together, these results provide evidence that structural rigidity, enforced by hydrogen-bonding and conformational restriction, is important to himastatin's antimicrobial mode of action.

Confocal microscopy has been used to observe the biological effects of antibiotics on *B. subtilis*, including the first approved membrane-disrupting lipopeptide, daptomycin (*37*). We sought to use our synthetic compounds in conjunction with this experimental approach to further characterize the antibiotic activity of (–)-himastatin (**1**). Our synthetic heterodimeric probe, TAMRA-himastatin (–)-**25**, offered an opportunity to directly visualize its interaction with bacteria and monitor cellular localization. When *B. subtilis* cells were treated with either 8 or 16 μg of TAMRA-himastatin (–)-**25** per milliliter of solution, we observed substantial accumulation in the bacterial envelope (fig. S6A), with little to no intracellular staining seen at the lower concentration. More cells were stained with TAMRA-himastatin (–)-**25** at the lower concentration than at the higher, but a smaller proportion of the stained cells exhibited visible membrane defects (*23*). The most intense sites of staining were observed at bacterial septa, in addition to patches of stain along sidewalls. At the higher concentration (fig. S6B), defects such as membrane extrusions coincided with lateral accumulation of TAMRA-himastatin (–)-**25**. These sites of curvature appear to reflect areas where the antibiotic has induced changes to membrane morphology.

The staining pattern observed with TAMRA-himastatin (–)-**25** was similar to that of the membrane stain FM4-64 with unmodified himastatin (**1**) (fig. S7). Untreated *B. subtilis* cells have smooth membranes and normal septal rings, but cells treated with a sublethal concentration of either enantiomer of himastatin (**1**) display pronounced membrane defects, notably patches of membrane thickening. Furthermore, the observed similarity in membrane morphology between himastatin (**1**) enantiomers appears to be consistent with their similar antibiotic activity. In a separate experiment, we evaluated the time scale by which (–)-himastatin (**1**) acts on bacteria at lethal concentrations (fig. S8). When treated with (–)-himastatin (**1**) at a concentration twice the MIC value, bacterial membranes were permeabilized within 30 min, as indicated by influx of the viability stain SYTOX Green.

The observations of our microscopy studies are comparable to those seen with daptomycin despite a lack of structural similarity to himastatin (*37*). The membrane defects and localization patterns observed in *B. subtilis* with unmodified (–)-himastatin (**1**) and our fluorescent himastatin derivative (–)-**25** show

Table 1. Antibiotic evaluation of himastatin derivatives and probes against Gram-positive bacteria. MIC values were determined by using the broth-microdilution method; see table S11. MRSA, methicillin-resistant *Staphylococcus aureus*; MSSA, methicillin-sensitive *S. aureus*; VRE, vancomycin-resistant *Enterococcus*; VSE, vancomycin-sensitive *Enterococcus*.

		MIC (μg/ml)		MIC (μg/ml)					
Compound	**Monomer**	***B. subtilis***	**Dimer**	***B. subtilis***	**MRSA**	**MSSA**	**VRE *faecalis***	**VSE *faecalis***	***S. himastatinicus***
(−)-himastatin	(+)-**2**	>64	(−)-**1**	1	2	1	1	1	8
ent-(+)-himastatin	(−)-**2**	>64	(+)-**1**	0.5	2	2	2	1	1
meso-himastatin	–	–	*meso*-**1**	1	2	1	1	1	4
rac-himastatin	(±)-**2**	>64	(±)-**2**	0.5	2	2	1	1	2
			Single-residue substitutions						
L-Val	(+)-**14**	>64	(−)-**15**	8	64	16	32	16	>64
L-^{Me}Val	(+)-**16**	>64	(−)-**17**	>64	>64	>64	>64	>64	>64
D-Pro	(+)-**18**	>64	(−)-**19**	>64	>64	>64	>64	>64	>64
L-Ser(OMe)	(+)-**20**	>64	(−)-**21**	2	4	4	1	2	8
L-Lys(N_3)	(+)-**22**	>64	(−)-**23**	2	2	2	2	1	8
L-Lys(TAMRA)	(+)-**24**	>64	(−)-**25**	6	>64	>64	16	16	–

resemblance to those seen with unmodified and fluorescent forms of daptomycin, respectively (*37*). Furthermore, the short time scale of membrane permeabilization following treatment with himastatin (**1**), like that seen after treatment with daptomycin, is consistent with a mode of action based on physical perturbations (*33*, *37*). This mode of action is distinct from that of certain other Gram-positive peptide antibiotics, such as vancomycin and teixobactin, that interfere with cell-wall biosynthesis and have kill times longer than 30 min (*40*). Separately, the similarity in MIC values and cellular morphology among our series of synthetic himastatin stereoisomers reveals that achiral interactions—for example, with the hydrophobic groups of phospholipids (*34*, *35*)—are largely responsible for the observed antibiotic activity. In summary, our chemical biology studies using our synthetic probes offer findings that are consistent with the hypothesis that (−)-himastatin's (**1**) antibiotic activity is dependent on interaction with bacterial membranes (*7*). It is evident that (−)-himastatin (**1**) is a distinct member among known membrane disruptors (*41*).

Published preclinical studies of (−)-himastatin's (**1**) biological activity are limited to early reports primarily focused on its antitumor activity (*4*, *7*). For instance, it was found that intraperitoneal administration of (−)-himastatin (**1**) prolonged the life span of mice inoculated with leukemia or melanoma cells, with toxicity being observed at the highest doses evaluated (*4*). Against the backdrop of escalating antibiotic resistance, we aim to continue detailed study and evaluation of (−)-himastatin's (**1**) antibiotic activity and application of new insights in the rational design and synthesis of analogs with improved characteristics.

REFERENCES AND NOTES

1. H. W. Boucher *et al*., *Clin. Infect. Dis.* **48**, 1–12 (2009).
2. C. L. Ventola, *P&T* **40**, 277–283 (2015).
3. G. D. Wright, *Can. J. Microbiol.* **60**, 147–154 (2014).
4. K. S. Lam *et al*., *J. Antibiot.* **43**, 956–960 (1990).
5. J. E. Leet, D. R. Schroeder, B. S. Krishnan, J. A. Matson, *J. Antibiot.* **43**, 961–966 (1990).
6. J. E. Leet *et al*., *J. Antibiot.* **49**, 299–311 (1996).
7. S. W. Mamber *et al*., *Antimicrob. Agents Chemother.* **38**, 2633–2642 (1994).
8. J. Ma *et al*., *Angew. Chem. Int. Ed.* **50**, 7797–7802 (2011).
9. T. M. Kamenecka, S. J. Danishefsky, *Chemistry* **7**, 41–63 (2001).
10. Z. Guo *et al*., *J. Am. Chem. Soc.* **140**, 18009–18015 (2018).
11. S.-M. Yu, W.-X. Hong, Y. Wu, C.-L. Zhong, Z.-J. Yao, *Org. Lett.* **12**, 1124–1127 (2010).
12. A. J. Oelke *et al*., *Chemistry* **17**, 4183–4194 (2011).
13. J. Kim, J. A. Ashenhurst, M. Movassaghi, *Science* **324**, 238–241 (2009).
14. M. Movassaghi, O. K. Ahmad, S. P. Lathrop, *J. Am. Chem. Soc.* **133**, 13002–13005 (2011).
15. J. M. Grandner, R. A. Cacho, Y. Tang, K. N. Houk, *ACS Catal.* **6**, 4506–4511 (2016).
16. R. H. Takahashi *et al*., *Drug Metab. Dispos.* **48**, 521–527 (2020).
17. V. V. Shende *et al*., *J. Am. Chem. Soc.* **142**, 17413–17424 (2020).
18. D. Larumbe, I. Gallardo, C. P. Andrieux, *J. Electroanal. Chem. Interfacial Electrochem.* **304**, 241–247 (1991).
19. H. Yang, D. O. Wipf, A. J. Bard, *J. Electroanal. Chem.* **331**, 913–924 (1992).
20. M. Kirchgessner, K. Sreenath, K. R. Gopidas, *J. Org. Chem.* **71**, 9849–9852 (2006).
21. N. G. Connelly, W. E. Geiger, *Chem. Rev.* **96**, 877–910 (1996).
22. D. Crich, M. Smith, Q. Yao, J. Picione, *Synthesis* **2001**, 323–326 (2001).
23. See supplementary materials.
24. O. Ivashenko, J. T. van Herpt, P. Rudolf, B. L. Feringa, W. R. Browne, *Chem. Commun.* **49**, 6737–6739 (2013).
25. B. M. Nelson, R. P. Loach, S. Schiesser, M. Movassaghi, *Org. Biomol. Chem.* **16**, 202–207 (2018).
26. P. G. Gassman, G. A. Campbell, R. C. Frederick, *J. Am. Chem. Soc.* **94**, 3884–3891 (1972).
27. J. S. Albin, B. L. Pentelute, *Aust. J. Chem.* **73**, 380–388 (2020).
28. M. M. Nguyen, N. Ong, L. Suggs, *Org. Biomol. Chem.* **11**, 1167–1170 (2013).
29. K. L. Greenman, D. M. Hach, D. L. Van Vranken, *Org. Lett.* **6**, 1713–1716 (2004).
30. S.-K. Chang, P. Selvaraj, "Copper(II) Hexafluoroantimonate" in *Encyclopedia of Reagents for Organic Synthesis* (Wiley, 2005), pp. 1–4.
31. P. De Santis, S. Morosetti, R. Rizzo, *Macromolecules* **7**, 52–58 (1974).
32. L. Tomasic, G. P. Lorenzi, *Helv. Chim. Acta* **70**, 1012–1016 (1987).
33. S. Fernandez-Lopez *et al*., *Nature* **412**, 452–455 (2001).
34. D. Wade *et al*., *Proc. Natl. Acad. Sci. U.S.A.* **87**, 4761–4765 (1990).
35. C. K. Wang *et al*., *J. Am. Chem. Soc.* **138**, 5706–5713 (2016).
36. E. Peterson, P. Kaur, *Front. Microbiol.* **9**, 2928 (2018).
37. J. Pogliano, N. Pogliano, J. A. Silverman, *J. Bacteriol.* **194**, 4494–4504 (2012).
38. Y. Li *et al*., *ACS Med. Chem. Lett.* **8**, 1171–1176 (2017).
39. N. Xi, L. B. Alemany, M. A. Ciufolini, *J. Am. Chem. Soc.* **120**, 80–86 (1998).
40. L. L. Ling *et al*., *Nature* **517**, 455–459 (2015).

ACKNOWLEDGMENTS

We thank W. C. Salmon at the W. M. Keck Microscopy Facility (Whitehead Institute) for assistance with confocal microscopy; C. Tsay and P. Müller (Massachusetts Institute of Technology) for assistance with single-crystal x-ray diffraction of (+)-**7h**; and R. P. Bhattacharyya (Massachusetts General Hospital) for providing several bacterial strains. We are grateful to J. S. Albin (Massachusetts General Hospital) for helpful discussions. **Funding:** This study was supported by NIH grants GM-089732 and GM-141963 (M.M.); an NSERC postgraduate scholarship, grant PGSD3-502869-2017 (K.A.D.); and an NSF graduate research fellowship, grant 1122374 (C.K.S.). **Author contributions:** K.A.D. and M.M. conceived the project and designed the synthetic routes; K.A.D. performed the chemical synthesis; C.K.S. performed the antibiotic assays and fluorescence microscopy; all coauthors wrote and edited the manuscript. **Competing interests** A patent application covering this work has been filed by MIT (US patent application no. 63/153,286). **Data and materials availability:** Experimental procedures, spectroscopic data, and copies of NMR spectra are available in the supplementary materials. Structural parameters for *endo*-diketopiperazine (+)-**7h** are freely available from the Cambridge Crystallographic Data Centre under CCDC-2099734.

SUPPLEMENTARY MATERIALS

science.org/doi/10.1126/science.abm6509
Materials and Methods
Figs. S1 to S13
Tables S1 to S11
References (*41*–*49*)
Spectral Data

1 October 2021; accepted 21 December 2021
10.1126/science.abm6509



Discussion leaders are noted in bold italics.

Additive Manufacturing of Soft Materials NEW!

Integrating Polymers, Materials and Manufacturing for a Sustainable Future

AUG 7-12, 2022
FOUR POINTS SHERATON, HOLIDAY INN EXPRESS, VENTURA, CA

CHAIRS: Ronald Smaldone and Chenfeng Ke
VICE CHAIRS: Timothy Long and AJ Boydston

- **Additive Manufacturing in Biomaterials** *Shrike Zhang,* Jennifer Lewis, Jason Burdick
- **Volumetric Additive Manufacturing** *Dominic Porcincula,* Hayden Taylor, Grace Gu, Zachariah Page, Johanna Schwartz
- **Technology for Large Scale Additive Manufacturing** *Walter Voit,* Joseph Desimone, Andrew Tilstra
- **New Polymers and Methods for 3D Printing** *Yue (Jessica) Wang,* Nancy Sottos, Xuanhe Zhao, Eva Blasco
- **Therapeutics in Additive Manufacturing** *Hee Jeung Oh,* Sarah Heilshorn, Matthew Becker
- **Applied Additive Manufacturing** *Timothy Long,* Andre Studart, Christopher Williams, Tao Xie
- **Computational and Design Methods in 3D Printing** *Lining Yao,* Ole Sigmund
- **Sustainability in Additive Manufacturing** *Haritz Sardon,* Andrew Dove, Alshakim Nelson, Virginia San Fratello
- **Nanomaterials in Additive Manufacturing** *Emily Pentzer,* Julia Greer, Marcus Worsley
- **The GRC Power Hour™** *Hee Jeung Oh*

Aqueous Corrosion

Precise Measurement, Mechanistic Understanding and Enhanced Avoidance of Corrosion

JUL 10-15, 2022
COLBY-SAWYER COLLEGE, NEW LONDON, NH

CHAIR: Jamie Noel
VICE CHAIR: Mary Ryan

- **Corrosion Mechanisms** *Gerald Frankel,* Sannakaisa Virtanen, Edwin Garcia
- **Analytical Tools** *Dev Chidambaram,* Masayuki Itagaki, Dirk Engelberg, Michael Rohwerder
- **Passive Films** *John Scully,* Philippe Marcus, Xiuliang Ma
- **Localized Corrosion** *Christine Blanc,* Daniel Blackwood, Janine Mauzeroll, Jenifer Locke
- **Corrosion Protection** *Emeka Oguzie,* Tadeja Kosec, Arjan Mol
- **Corrosion in Porous Media** *Francisco Presuel-Moreno,* Ueli Angst, Claire Corkhill, Amir Poursaee
- **Microbiologically Influenced Corrosion** *Jason Lee,* Dmitrij Zagidulin
- **Advanced Materials** *Mary Ryan,* Aleksey Yerokhin, Rebecca Schaller, Pin Lu
- **Pre-Emergent Methods, Mechanisms and Processes in Corrosion Science and Engineering** *Robert Asmussen,* Edouard Asselin, Robert Kelly
- **The GRC Power Hour™** *Oumaïma Gharbi, Yolanda Hedberg*

Aqueous Corrosion GFS

Design of Modern Prediction Tools and Sustainable Corrosion Protection Strategies

JUL 9-10, 2022

CHAIRS: Oumaïma Gharbi and Saba N. Esmaeely

Auditory System

Preventing Loss and Recovering Function of the Auditory System

JUL 10-15, 2022
BRYANT UNIVERSITY, SMITHFIELD, RI

CHAIR: Ruth Litovsky
VICE CHAIR: Allison Coffin

- **Keynote Session: Communication, Music and Hearing Loss** *Mario Svirsky,* Darcy Kelley, Gabriel Corfas, Monita Chatterjee
- **Predictable and Surprising Coding of Auditory Information** *Melissa Caras,* Jerome Bourien, Caroline Niziolek, Maria Chait
- **Immune and Nervous System Cross-Talk** *Yehoash Raphael,* Andrew Groves, Keiko Hirose, Jeffrey Holt
- **Auditory Function and Pathways: Connecting the Ear and the Brain** *Cynthia Moss,* Paul Forlano, Nace Golding, Ross Maddox, Antje Ihlefeld
- **Hearing Without Vision and Vision Without Hearing** *Ingrid Johnsrude,* Ione Fine, Ella Striem-Amit
- **Auditory Experience and Development: Hair Cells, Babies and Brains** *Michael Roberts,* Jason Sanchez, Ana Belen Elgoyhen, Jennifer Stone, Yoko Yazaki-Sugiyama, Aaron Tward
- **Diagnoses and Interventions** *Brandon Cox,* Stefanie Kuchinsky, Konstantina Stankovic, Karen Steel, Katherine Fernandez
- **Cognitive and Attentional Aspects of Hearing** *Blake Butler,* Lori Holt, Matthew McGinley, Jonathan Peelle, Matthew Winn
- **Interconnection of Cells and Tissues** *Catherine Weisz,* Karina Cramer, Sean Megason, Michael Hoa, Dáibhid Ó Maoiléidigh
- **The GRC Power Hour™**

Auditory System GFS

Function and Dysfunction of the Auditory and Vestibular Systems

JUL 9-10, 2022

CHAIR: Travis Babola

Bacterial Cell Surfaces

Altering the Bacterial Cell Envelope: Shaping Fitness in Response to the Host and Environment

JUN 26-JUL 1, 2022
MOUNT SNOW, WEST DOVER, VT

CHAIR: Stephen Trent
VICE CHAIRS: Natividad Ruiz and Jean-Francois Collet

- **Exploring the Bacterial Cell Envelope** *Rut Carballido-Lopez,* Thomas Silhavy, Waldemar Vollmer, Christine Jacobs-Wagner
- **Modifying the Bacterial Cell Surface** *Jean-Francois Collet,* Filippo Mancia, Felipe Cava, Chris Whitfield, Aimee Shen
- **Cell Division and Morphogenesis** *Simon Foster,* Thomas Bernhardt, Erin Goley, Kumaran Ramamurthi
- **Stress Responses and Signaling Across the Cell Envelope** *Marcin Grabowicz,* Sonja-Verena Albers, Tam Mignot, Alexandre Persat, Anna Konovalova
- **Mechanisms of Surface Recognition** *Daniel Wall,* Andrew Lovering, Serge Mostowy, Andrea Wolf
- **Transport through the Envelope** *Natividad Ruiz,* Lori Burrows, Seok-Yong Lee, Jorge Galan, Georgina Cox
- **Protein Secretion and Transport** *Edith Houben,* Melanie Blokesch, Mario Feldman, Tracy Palmer
- **How the Surface Influences Bacterial Communities** *Lotte Sogaard-Andersen,* Peggy Cotter, Urs Jenal, Nicole Koropatkin, Cynthia Whitchurch
- **Biophysical Methods to Improve Antimicrobial Therapies** *Pamela Brown,* Kerwyn Huang, Steven Rutherford, Jie Xiao
- **The GRC Power Hour™** *Erin Goley, Mario Feldman*

Bacterial Cell Surfaces GFS

A Multidimensional View of the Bacterial Cell Envelope: From Molecular Structures to Intracellular Interactions

JUN 25-26, 2022

CHAIRS: Liselot Dewachter and Hannah Smith

Barriers of the CNS

Translating Basic Knowledge About Brain Barriers into Treatments for Neurological Disorders

JUN 12-17, 2022
COLBY-SAWYER COLLEGE, NEW LONDON, NH

CHAIR: William Elmquist
VICE CHAIR: Matthew Campbell

- **Novel Strategies to Overcome Multiple Barriers in the CNS** *Lester Drewes,* Chenghua Gu, Tetsuya Terisaki
- **Experimental Models of Brain Barriers** *Samira Azarin, Eric Shusta,* Choi-Fong Cho, Richard Daneman, Ethan Lippmann, Nur Mustafaoglu, Clive Svendsen

- **Changes in BBB Structure and Function in Disease** *Reina Bendayan, Francesca Cicchetti,* Bjoern Bauer, Richard Keep, Stefan Liebner
- **Delivery of Macromolecular Therapeutics to the Brain** *Danica Stanimirovic, Robert Thorne,* Beverly Davidson, Priti Kumar, Joelle Straehla, Joy Zuchero
- **Understudied Barriers of the CNS** *Stina Syvänen,* Johanna Andrae, David Antonetti, Julie Siegenthaler
- **Methods of Delivery to Overcome Brain Barriers** *Nathalie Agar, Sadhana Jackson,* Krystof Bankiewicz, Adrienne Boire, Kullervo Hynynen, Rachael Sirianni, Mark Souweidane
- **Influence of Neuroinflammation on the BBB** *Chaitali Ghosh,* David Camarillo, Anika Hartz, Joel Patcher
- **CSF and ISF: Fluid Flow and Exchange in the CNS** *Jeffrey Iliff,* Adam Chodobski, Kristopher Kahle, Nanna MacAulay, Ji Hoon Ahn
- **Fluid Flow in the Brain** *Irena Loryan, Steven Proulx,* Cindy Alpinice for Frau Engelhardt, Laura Lewis
- **The GRC Power Hour™** *Martha O'Donnell*

Barriers of the CNS
Exploring the Physiology of CNS Barriers in Health, Aging and Disease
JUN 11-12, 2022
CHAIRS: Michelle Pizzo and Steffen Storck

Bioanalytical Sensors

Interconnecting Biology and Devices to Analyze Microscopic Cells to the Macroscopic World

JUN 26-JUL 1, 2022
SALVE REGINA UNIVERSITY, NEWPORT, RI
CHAIRS: Susan Daniel and Jean-Francois Masson
VICE CHAIRS: Charles Mace and Chenzhong Li

- **Keynote Session: Biosensors for Small to Large Systems** *Christa Brosseau,* Christy Haynes, Jessica Koehne
- **Molecular Recognition at the Nanoscale** *Ling Chao,* Ryan Bailey, Daniel Schwartz, Kaori Sugihara, Heather Clark
- **Sensing for Neuroscience** *Chenzhong Li,* Dan Fu, Susan Lunte
- **Intracellular Biosensing** *Jason Dwyer,* Julie Biteen, Joshua Edel, Neha Kamat, Nicholas Melosh
- **Wearable and Implantable Sensors: Interfacing Sensors with Living Systems** *Charles Mace,* Sahika Inal, Nanshu Lu
- **Pathogen Detection** *Ariel Furst,* Marta Bally, Jaebum Choo, Jacinta Conrad, Michael Serpe
- **Agriculture and Environment: Sensing in the Digital Agriculture Movement** *Miguel Pineros,* Abraham Stroock, Juan Pablo Giraldo
- **Human Health: Detection and Diagnostics** *Angela Brown,* Menno Prins, Zachary Schultz, Roisin Owens, Hadley Sikes
- **Keynote Session: Next Generation Bioanalytical Sensors** *Samuel Hinman, Carine Nemr,* Justin Gooding
- **The GRC Power Hour™** *Matthew Lockett, Rebecca Whelan*

Bioanalytical Sensors
Translational Applications of Sensor Technologies
JUN 25-26, 2022
CHAIRS: Samuel Hinman and Carine Nemr

Biocatalysis

Making Biocatalysis More Predictive: Accelerating Biocatalytic Solutions to Synthetic Challenges

JUL 10-15, 2022
SOUTHERN NEW HAMPSHIRE UNIVERSITY, MANCHESTER, NH
CHAIRS: Gerrit Poelarends and Birgit Kosjek
VICE CHAIRS: Sabine Flitsch and Carlos Martinez

- **Keynote Session: Creating New Activities for Chemical Applications** *Bernhard Hauer,* Don Hilvert, Jeffrey Moore
- **Expanding the Biocatalytic Toolbox with New Enzymes and New Functions** *Mélanie Hall,* Elizabeth Sattely, Brent Dorr, Bo Li
- **Mechanistic Understanding and Innovative Development Strategies to Enable New Applications** *Wilfred van der Donk,* Steven Boxer, Joelle Pelletier, Tobias Erb
- **From Big Data to Enzyme Function via Computational and Bioinformatic Enzyme Design** *Joelle Pelletier,* Rama Ranganathan, Silvia Osuna, Daniela Grabs, Russell Lewis
- **Genome Editing and Genetic Code Expansion to Create New Functions** *Xue Gao,* Anthony Green, John Glass, Chang Liu
- **Radical Biocatalysis** *Caroline Paul,* Todd Hyster, Amie Boal, Mohammad Seyedsayamdost, Shelley Minteer
- **Artificial Metalloenzymes** *Todd Hyster,* Gerard Roelfes, Yi Lu, Thomas Ward
- **Natural Product Biosynthetic Enzymes** *Claudia Schmidt-Dannert,* Hans Renata, Sneha Srikrishnan, Xiaoguang Lei, Wilfred van der Donk
- **Selected Poster Presentations** *Carlos Martinez, Sabine Flitsch*
- **The GRC Power Hour™** *Sabine Flitsch*

Biocatalysis
Biocatalytic Cascades, Pathways and Novel Reactions
JUL 9-10, 2022
Chairs: Matthew McDonald and Thomas Bayer

Biogenic Hydrocarbons and the Atmosphere

Bridging Ecology, Chemistry and Climate

JUN 12-17, 2022
RESIDENCE INN AT OXNARD RIVER RIDGE, OXNARD, CA
CHAIRS: Mark Potosnak and Jaana Back
VICE CHAIRS: Kirsti Ashworth and Zhaozhong Feng

- **Wildfire and Biomass Burning Emissions** *Delphine Farmer,* Vinayak Sinha, Chelsea Stockwell
- **Biogenic Versus Anthropogenic Controls on Urban Aerosols and Ozone** *Neil Donahue,* Tuukka Petäjä, Hai Guo, Yuxuan Wang
- **Sources, Trends and Effects of Reactive Nitrogen** *Ronald Cohen,* Nga Lee Ng, Colette Heald
- **BVOCs and Plant Stress** *Riikka Rinnan,* Meredith Schumann, Federico Brilli, Todd Rosenstiel
- **The Sentient Plant** *Ted Turlings,* Natalia Doudareva, Andre Kessler
- **Early-Career Investigator Presentations** *Kirsti Ashworth*
- **Coupling Climate, Dynamic Vegetation and BVOC Emissions** *Nadine Unger,* Armin Hansel, Danica Lombardozzi
- **Use of High-Resolution Remote Sensing Data to Understand BVOC Emissions and Impacts** *Allison Steiner,* Dylan Millet, Karena McKenna, Jenny Stavrakou
- **Emerging Sources and Sinks** *Alex Guenther,* Chris Geron, Efstratios Bourtsoukidis
- **The GRC Power Hour™**

Biogenic Hydrocarbons and the Atmosphere
Linking Biogenic Hydrocarbon Across Leaf Level, Atmosphere and Earth's Climate
JUN 11-12, 2022
CHAIRS: Ana Yáñez Serrano and Jianhuai Ye

Bioinspired Materials

Designer Materials to Mimic Biology and Manipulate the Immune System

JUN 5-10, 2022
LES DIABLERETS CONFERENCE CENTER, LES DIABLERETS, SWITZERLAND
CHAIR: Daniel Hammer
VICE CHAIRS: Christoph Weder and Molly Stevens

- **Keynote Session: Viruses and Immunity** *Zhibin Guan,* Jeffrey Hubbell, Nicole Steinmetz
- **Peptide and Protein Assembly** *Gregory Hudalla,* Timothy Deming, Ehud Gazit, Roman Jerala
- **Novel Membrane Design** *Abigail Knight,* Atul Parikh, Jeanne Stachowiak, Neha Kamat
- **Active Matter and Motility** *Eric Dufresne,* Zvonimir Dogic, Lauren Zarzar, Peer Fischer, Kim Weirich
- **Protein Coacervation** *Allie Obermeyer,* Ashutosh Chilkoti, Matthew Good, Paolo Arosio
- **Functional Bioinspired Materials** *Cole DeForest,* Ullrich Steiner, Omolola Eniola-Adefeso, Kathryn Uhrich, Anna Balazs
- **New Developments in Synthetic Cells** *Leila Deravi,* Stephen Mann, Cornelia Palivan, Neal Devaraj
- **Tissues and Organoids** *Nuria Montserrat,* Matthias Lutolf, Linda Griffith, David Gracias
- **Keynote Session: Immune Engineering** *Michael Mitchell,* David Mooney, Ankur Singh
- **The GRC Power Hour™**

Bioinspired Materials
Harnessing Biological Principles for Better Materials
JUN 4-5, 2022
CHAIRS: Lee Schnaider and George Degen

Biointerface Science

Functional Assemblies and Biomolecular Information Processing

JUN 12-17, 2022
RENAISSANCE TUSCANY IL CIOCCO, LUCCA (BARGA), ITALY
CHAIR: Jay Groves
VICE CHAIR: Katharina Maniura

- **Keynote Session: Emerging Concepts at the Biointerface** *Kabir Biswas,* Christine Keating
- **Molecular Assemblies to Phase Transitions** *Nam-Joon Cho,* Alf Honigmann, Atul Parikh, Eva Sevcsik
- **Mechanobiology at the Cell Surface** *Simou Sun,* Matthew Paszek, Khalid Salaita, Virgile Viasnoff
- **Signaling Reactions on the Membrane** *William Huang,* Orion Weiner, Cheng-Han Yu, Yan Yu
- **Spatial and Geometric Effects at the Interface** *Hyuneil Kim,* Bianxiao Cui, Daniel Fletcher, Martin Loose, Dimitrios Stamou
- **Synthetic Responsive Systems** *Jey DeGrandchamp,* Sierin Lim, Jwa-Min Nam, Dora Tang, Qiong Yang
- **Emerging Techniques for Interface Characterization** *Kiera Wilhelm,* Daniel Muller, Gerhard Schuetz, Adam Smith
- **Late-Breaking Topics** *Shalini Low-Nam*
- **Functional Assemblies** *Zhongwen Chen,* Patricia Bassereau

Biointerface Science
Mechanical and Physicochemical Properties at Biointerface: Effects on Structure and Function in Cells and Tissues
JUN 11-12, 2022
CHAIRS: Fatma Pir Cakmak and Claudia Bonfio

Biology of Host-Parasite Interactions

Insights Into the Complex Relationships Between Eukaryotic Parasites and Their Hosts

JUN 12-17, 2022
SALVE REGINA UNIVERSITY, NEWPORT, RI
CHAIRS: Kirk Deitsch and Michael Barrett
VICE CHAIRS: Gary Ward and F. Nina Papavasiliou

- **Parasite Motility** *Photini Sinnis,* Freddy Frischknecht, Eva Gluenz, Maryse Lebrun
- **Genome Stability and Genetic Diversity** *Galadriel Hovel-Miner,* Jane Carlton, Jennifer Guler, Gerald Spaeth, Jianbin Wang
- **Immunology and Immuno-Suppression** *Tracey Lamb,* Eva Frickel, P'ng Loke, Meera G. Nair
- **Parasite Dormancy and Persistence** *William Sullivan,* Jon Boyle, Jean-Claude Dujardin, Alexander Paredez, Annmarie Voorberg-Van der Wel
- **Sexual Differentiation and Quorum Sensing** *Manuel Llinas,* Laura Knoll, Isabel Roditi, Andy Waters
- **Host Cell Responses to Manipulation by Parasites** *Ira Blader,* Gordon Langsley, Melissa Lodoen, Alex Loukas, Staffan Svard
- **Molecular Biology and Gene Expression** *Victoria Jeffers,* Lyn-Maria Birkholtz, Iris Bruchhaus, Mohamed-Ali Hakimi
- **Metabolism and Drug Targets** *Sara Lustigman,* Frederick Bringaud, Maria Adelaida Gomez, Karl Hoffman, Maria Mota

- **New Intervention Strategies** *Akhil Vaidya,* Emily Derbyshire, Joerg Moehrle, Boris Striepen, Jennifer Zambriski
- **The GRC Power Hour™**

Biology of Host-Parasite Interactions GFS

The Molecular and Cellular Biology of Eukaryotic Infectious Organisms

JUN 11-12, 2022

CHAIRS: Xu Zhang and Nelson Simwela

Biology of Winter NEW!

Biological Responses to Winter Climate Change

JUN 5-10, 2022

PROCTOR ACADEMY, ANDOVER, NH

CHAIRS: Brent Sinclair and Sapna Sharma
VICE CHAIRS: Pamela Templer and Steven Cooke

- **Keynote Session: Cross-Season Interactions and Nitrogen Oligotrophication in the Northern Hardwood Forest** *Steven Cooke,* Peter Groffman
- **Predicting Snow and Ice Distribution and Quality in a Warming World** *Homa Kheyrolla,* Xiao Yang, Matti Lepparanta, Gesa Weyhenmeyer
- **Late-Breaking Topics** *Raine Kortet*
- **Species and Ecosystem Vulnerability to Changing Winters** *Elisabeth Cooper,* Juergen Kreyling, David Swanson, Christa Mulder, Heidi Steltzer
- **Consequences of Fluctuating Temperatures During Winter** *Chunsen Ma,* Hugh Henry, Katie Marshall
- **Life Under Snow and Ice** *Janneke Hille Ris Lambers,* Hilary Dugan, Sudeep Chandra, Caroline Williams
- **Microbes as Drivers of Winter Biological Processes** *Bjorn Robroek,* Hannah Carey, Mats Oquist
- **Large-Scale Integration of Winter Biology Across Space and Time** *Kath Dickinson,* Emily Stanley, Christian Rixen, Lloyd Peck
- **Keynote Session: Winter as a Driver of Macrophysiological Patterns in the Oceans** *Pamela Templer,* Amanda Bates
- **The GRC Power Hour™** *Dawn Bazely, Bailey McMeans*

Biomineralization

Bridging Scientific Disciplines to Understand Biomineral Formation in Breadth and Depth

AUG 14-19, 2022
REY DON JAIME GRAND HOTEL, CASTELLDEFELS, SPAIN

CHAIR: Janet Moradian-Oldak
VICE CHAIR: Nils Kröger

- **Regulation of Morphogenesis** *Nils Kröger,* Jaroslaw Tyszka, Assaf Gal
- **Cellular and Genetic Control of Mineral Deposition** *Tali Mass, Rivka Elbaum,* Sylvie Tambutte, Monzur Murshed
- **Ion Transport, Signaling and Homeostasis** *Marc McKee,* Rodrigo Lacruz, Alejandro Navarro
- **Chemical and Computational Models of Nucleation, Phase Transformation and Growth** *Wendy Shaw,* Jim Pfaendtner, Thomas Koop, Fiona Meldrum
- **Macromolecules in Biomineralization** *Elia Beniash,* Michiko Nemoto, Andre Scheffel
- **Structure and Biomechanics** *Peter Fratzl,* Derk Joester, Elena Sturm (née Rosseeva), Tamara Alliston
- **Biomineralization Principles Translated** *Maisoon Al-Jawad,* Luiz Bertassoni, Ben Wang
- **Biominerals in Pathology** *Willi Jahnen-Dechent,* Peter Vekilov, Sunita Ho, Eileen Shore
- **Keynote Session: Geochemistry, Proxies and Evolution** *Derk Joester,* Andrew Knoll, Alex Gagnon
- **The GRC Power Hour™** *Netta Vidavsky, Alex Gagnon*

Biomineralization GFS

A Multifaceted Approach Toward Understanding Biomineral Formation Pathways and Purposes

AUG 13-14, 2022

CHAIRS: Dimitra Athanasiadou and Konrad Hedderick

Bioorganic Chemistry

Enabling Technologies in Chemical Biology

JUN 12-17, 2022

PROCTOR ACADEMY, ANDOVER, NH

CHAIRS: Jennifer Heemstra and John Tallarico
VICE CHAIRS: Daniel Nomura and Jason Thomas

- **Keynote Session: Enabling Technologies** *Wenjing Wang,* Lara Mahal
- **Glycobiology in Human Health** *Christina Woo,* Yael David, M.G. Finn, Kamil Godula, Steven Townsend
- **Computational Chemical Biology** *Daniel Nomura,* Alemayehu (Alex) Gorfe, Brian Shoichet
- **Discovery by Mass Spectrometry** *Lars Plate,* Keriann Backus, Vishal Rai, Alan Saghatelian, Laura Sanchez, Markus Schirle
- **Epigenetics and Epitranscriptomics** *Alexis Komor,* Thomas Carell, Chuan He, Heather Hundley, Ralph Kleiner
- **Nucleic Acid Technologies** *Kathryn Mouzakis,* Martin Eastgate, Gwenn Hansen, Andrea Rentmeister, Robert Spitale, Marino Resendiz
- **Microfluidics for High-Throughput Biology** *Alix Chan,* Shuwen Sun, Brian Paegel, Polly Fordyce
- **Biomaterials and Biomimetics** *Olalla Vázquez,* Annelise Barron, Amelia Fuller, Seth Horne, Monika Raj, Ronald Zuckermann
- **Cellular Imaging and Engineering** *Stephen Fried,* Jefferson Chan, Yamuna Krishnan, Paul Richardson, David Savage, Xin Zhang
- **The GRC Power Hour™** *Louise Charkoudian, Alexis Komor*

Bioorganic Chemistry GFS

Molecular Tools for Chemical Biology

JUN 11-12, 2022

CHAIRS: Natalia Milosevich and Pratik Kumar

Calcium Signaling NEW!

Channeling Calcium Signals to Therapeutics

JUN 19-24, 2022
FOUR POINTS SHERATON, HOLIDAY INN EXPRESS, VENTURA, CA

CHAIRS: Jonathan Soboloff and Grace Stutzmann
VICE CHAIRS: Ivan Bogeski and Cristina Mammucari

- **Ca2+ Channels** *Henry Colecraft,* Juan Du, Xiaowei Hou, Jean-Ju Chung
- **STIM-Dependent Signaling** *Gaiti Hasan,* Peter Stathopulos, Rainer Schindl, Yousang Gwack, Khaled Machaca, Paul Rosenberg
- **TRP Channel Function** *Thomas Gudermann,* Mark Nelson, Rudi Vennekens, Ivana Kuo
- **Mitochondrial Ion Channels** *Madesh Muniswamy,* Anna Raffaello, Luca Scorrano, John Elrod, Lan Wei-LaPierre, Dipayan Chaudhuri
- **Intracellular Ion Channels** *Antony Galione,* Sandip Patel, Irina Serysheva, Sebastian Brauchi
- **Calcium Signaling and Neuro(patho)physiology** *Cecilia Hidalgo,* Hilmar Bading, Elizabeth Jonas, Brian Bacskai, Wayne Chen, Claudio Hetz
- **Calcium Sensors** *Loren Looger,* Yubin Zhou, Yan Zhang, Arnab Mukherjee
- **Calcium Signaling and Disease** *Barbara Niemeyer,* Johanna Lanner, Natasha Prevarskaya, Saverio Gentile, Ágnes Enyedi, Michal Hershfinkel
- **Keynote Session: Local Calcium Signaling in Plasticity and Disease** *Ilya Bezprozvanny,* Richard Tsien
- **The GRC Power Hour™**

Cardiac Regulatory Mechanisms

Applying High Resolution Approaches to Complex Cardiac Disorders: Towards Targeted Therapies

JUN 26-JUL 1, 2022
COLBY-SAWYER COLLEGE, NEW LONDON, NH

CHAIRS: Jil Tardiff and Christoph Maack
VICE CHAIRS: Rong Tian and Benjamin Prosser

- **Cardiac Repair and Regeneration** *Bjorn Knollmann, Jop van Berlo,* Bin Zhou, Jennifer Davis, Mauro Giacca, Wolfram Zimmerman
- **Myocellular Structural Dynamics in Health and Disease** *Jolanda van der Velden,* Jennifer Van Eyk, Farah Sheikh, Brett Colson, Maria Kontaridis, Wolfgang Linke
- **Excitation-Contraction Coupling and Arrhythmias** *Donald Bers,* Steven Houser, Isabelle Deschenes, Sara Liin, Xander Wehrens, Matthew Daniels
- **Inflammatory Response in Cardiac Remodeling** *Emilio Hirsch, Jeffery Molkentin,* Gustavo Ramos, Daniela Carnevale, Slava Epelman, Daniela Cihakova, Kory Lavine, Pilar Alcaide
- **Emerging Technologies of Analysis in Cardiac Myocytes and Whole Hearts** *Sarah Franklin, Thomas Thum,* Roger Foo, Federica Accornero, Jan Christoph, Yi Yang
- **Mitochondria and Metabolism: Complex Regulatory Mechanisms** *John Elrod, Elizabeth Murphy,* Danielle Murashige, Mathias Mericskay, Catalina Vasilescu, Johannas Backs, Yibin Wang
- **Cancer and the Heart** *David Eisner, Sumanth Prabhu,* Aarti Asnani, Javid Moslehi, Rudolf de Boer, Anja Karlstaedt
- **Novel Approaches to Targeted Therapies** *Lucie Carrier, Thomas Vondriska,* Laura Zelarayán, Timothy McKinsey, Gabriele Schiattarella, William Pu, Vassilios Bezzerides
- **Keynote Session: From Primary Mechanism to Targeted Therapies for Cardiomyopathies** *Benjamin Prosser, Rong Tian,* Leslie Leinwand, Thomas Eschenhagen
- **The GRC Power Hour™**

Cardiac Regulatory Mechanisms GFS

Unraveling the Complexities of Cardiac Disease by Understanding Basic Mechanisms of Heart Function

JUN 25-26, 2022

CHAIRS: Christopher Johnson and Arica Beisaw

Catalysis

Advancing Sustainable Technologies Through Catalysis

JUN 19-24, 2022
COLBY-SAWYER COLLEGE, NEW LONDON, NH

CHAIR: Susannah Scott
VICE CHAIR: Javier Guzman

- **Sustainability Metrics for Catalysis** *Cathy Tway,* John Holladay, Fabio Ribeiro
- **Applications of Data Science to Enhance Catalysis** *Vassiliki-Alexandra Glezakou,* Karsten Reuter, Joel Schmidt, Toshiaki Taniike, Hongliang Xin
- **Precision Synthesis of Well-Defined Catalysts** *Francisco Zaera,* An-Hui Lu, Charles Sykes, Praveen Bollini
- **Catalysis with Alternative Energy Inputs** *Eranda Nikolla,* Kyoung-Shin Choi, Suljo Linic, William Schneider
- **Dynamic Catalytic Behavior** *Beata Kilos-Reaume,* Anastassia Alexandrova, Norbert Kruse, Omar Abdelrahman
- **Insights from Mechanistic Investigations** *Philippe Sautet,* Rebecca Fushimi, Rachel Getman, Emiel Hensen, Justin Notestein
- **Operando Characterization of Catalysts** *John Lockemeyer,* Juan Bravo-Suarez, Angelika Brückner, Ambarish Kulkarni
- **Alternative Feedstocks for Manufacturing** *Daniel Resasco,* Oliver Gutierrez-Tinoco, Feng Wang, Karen Wilson
- **Keynote Session: Integration of Experiment, Computation and Theory** *Javier Guzman,* Dion Vlachos
- **The GRC Power Hour™** *Beata Kilos-Reaume, Eranda Nikolla*

Catalysis GFS

Designing Catalysts to Advance Sustainable Energy and Chemical Production

JUN 18-19, 2022

CHAIRS: Brandon Bukowski and Sarah Specht

Cell Biology of the Neuron

The Impact of Neuronal Shape, Structure and Size on Neuronal Function in Health and Disease

JUN 26-JUL 1, 2022
WATERVILLE VALLEY, WATERVILLE VALLEY, NH

CHAIRS: Kang Shen and Valeria Cavalli
VICE CHAIRS: Monica Driscoll and Patrik Verstreken

- **Keynote Session: Neuronal Cell Biology and Diseases** *Yishi Jin,* Kelsey Martin, Matthew Rasband
- **Controlling Neuronal Shape, Size and Repair** *Binhai Zheng,* Mike Fainzilber, Alyson Fournier, Oren Schuldiner, Marc Hammarlund
- **Gene Regulation and Phase Transition in Health and Disease** *Pietro De Camilli,* Antonella Riccio, Mingjie Zhang, Lin Mei

- **Synaptic Transmission** *Patrik Verstreken,* Matthew Dalva, Camin Dean, Matthijs Verhage, Ege Kavalali
- **Mitochondria and Cytoskeleton** *Antonina Roll-Mecak,* Richard Youle, Andrew Carter, Lukas Kapitein
- **Membrane Trafficking and Transport** *Thomas Schwarz,* Rejji Kuruvilla, Giampietro Schiavo, Bettina Winckler, Erika Holzbaur
- **Translation and Protein Homeostasis in Health and Disease** *Monica Driscoll,* Andrew Dillin, Anne Bertolotti, Jeffery Twiss
- **Neuron-Glia Interaction and Communication** *Cagla Eroglu,* Nicola Allen, Aiman Saab, Marc Freeman, Michael Granato
- **Keynote Session: New Technologies in Neuronal Cell Biology** *Erik Jorgensen,* Edward Boyden, Xiaowei Zhuang
- **The GRC Power Hour™** *Rejji Kuruvilla, Cagla Eroglu*

Cell Biology of the Neuron

Molecular Understanding of the Neuron: Development, Plasticity and Function

JUN 25-26, 2022

CHAIRS: Chinyere Agbaegbu Iweka and Oshri Avraham

Cell Death

Cell Death-Associated Inflammation in Disease

MAY 15-20, 2022
LES DIABLERETS CONFERENCE CENTER, LES DIABLERETS, SWITZERLAND

CHAIR: Francis Chan
VICE CHAIR: Pascal Meier

- **Keynote Session: Perspectives on the Mechanism and Function of Cell Death in Physiology** *Pascal Meier,* Vishva Dixit, Marion MacFarlane
- **Inflammation and Tissue Homeostasis** *Andrew Oberst,* John Silke, Manolis Pasparakis, Andreas Villunger
- **Immunogenic Cell Death** *Hiroyasu Nakano,* Carla Rothlin, Julie Magarian Blander, Peter Vandenabeele
- **Fundamental Mechanisms of Cell Death** *Carla Rothlin,* Ana Garcia-Saez, Xiaodong Wang, J. Marie Hardwick
- **Cell Death in Neuroinflammation and Neurological disorders** *Stephen Tait,* Junying Yuan, Marc Freeman
- **Cell Death in Immunity** *Elizabeth Hartland,* Seamus Martin, Domagoj Vucic, Henning Walczak
- **Non-Apoptotic Forms of Cell Death** *Ana Garcia-Saez,* Eric Baehrecke, Marcus Conrad, Stephen Tait
- **Harnessing Cell Death Mechanisms in Cancer** *Julie Magarian Blander,* John Abrams, Anne Hamacher-Brady, Andreas Strasser
- **Infectious Diseases and Cell Death** *John Silke,* Elizabeth Hartland, Andrew Oberst, Feng Shao
- **The GRC Power Hour™** *Marion MacFarlane, Anne Hamacher-Brady*

Cell Death

Mechanisms of Cell Death in Homeostasis and Disease

MAY 14-15, 2022

CHAIRS: Katherine Stewart and Florian Bock

Cell Polarity Signaling

Dynamics of Cell Polarity

MAY 29-JUN 3, 2022
COLBY-SAWYER COLLEGE, NEW LONDON, NH

CHAIR: Jeremy Nance
VICE CHAIR: Yukiko Yamashita

- **Polarity Within and Across Cells** *Yukiko Yamashita,* Denise Montell, Geraldine Seydoux
- **Dynamics of Cell Polarization** *Danelle Devenport,* Dominique Bergmann, Clemens Cabernard, Daniel Lew, Edwin Munro
- **Polarity Transitions During Development** *Sander van den Heuvel,* Jessica Feldman, Jean-Léon Maître, Ulrich Tepass
- **Cell Polarization and the Cytoskeleton** *William Bement,* Julie Canman, Gregg Gundersen, Stephanie Gupton, Terry Lechler
- **Polarity and Morphogenesis: Eggs and Embryos** *Jessica Feldman,* Otger Campas, Sally Horne-Badovinac, Yu-Chiun Wang
- **Polarity and Morphogenesis: Tissues and Organs** *Sally Horne-Badovinac,* Michel Bagnat, Danelle Devenport, Shigeo Hayashi, Jeff Rasmussen
- **Polarity Transitions During Disease** *Terry Lechler,* Gillian Griffiths, Carole Parent, Erik Sahai
- **Asymmetric Division and Stem Cells** *Dominique Bergmann,* Renata Basto, Xin Chen, Ahna Skop, Sander van den Heuvel
- **Tissue Homeostasis: Wound Healing and Extrusion** *Carole Parent,* William Bement, Anne Classen, Jody Rosenblatt
- **The GRC Power Hour™**

Cell Polarity Signaling

Cell Polarity Across Developmental Time and Space

MAY 28-29, 2022

CHAIRS: Melissa Pickett and Andrew Tilston-Lunel

Cell-Cell Fusion NEW!

Diverse Organisms and Common Mechanisms in Cell-Cell Fusion

JUN 5-10, 2022
STONEHILL COLLEGE, EASTON, MA

CHAIR: Elizabeth Chen
VICE CHAIR: Mark Rose

- **Keynote Session: Mechanism and Aftermath of Membrane Fusion** *Mark Rose,* Jennifer Lippincott-Schwartz, Axel Brunger
- **Intracellular Membrane Fusion** *Jennifer Lippincott-Schwartz,* Arun Anantharam, Katja Faelber, Junjie Hu, Erdem Karatekin, Ling-Gang Wu
- **Virus-Cell Fusion** *Benjamin Podbilewicz,* Gregory Melikian, Yorgo Modis, James Munro, Felix Rey
- **Cell-Cell Fusogens** *Joshua Zimmerberg,* Roy Duncan, Thomas Krey, Douglas Millay, William Snell, Hongmei Wang, Benjamin Podbilewicz
- **Membrane Adhesion in Cell Fusion** *N. Louise Glass,* Naokazu Inoue, Andrea Pauli, Leonid Chernomordik
- **Actin Cytoskeleton in Cell Fusion** *Stefanie Sprunck,* Ori Avinoam, Mary Baylies, Jean-Francois Cote, Daniel Fletcher, Guangshuo Ou, Sophie Martin
- **Membrane Organization and Lipids** *Leonid Chernomordik,* Michael Kozlov, Harvey McMahon, Huanghe Yang, Joshua Zimmerberg
- **Diverse Cell Fusion Systems** *Sophie Martin,* Sigal Ben-Yehuda, Don Fox, N. Louise Glass, Massimo Hilliard, Vicki Losick, Stefanie Sprunck
- **Cell Fusion and Disease** *Harvey McMahon,* Melissa Wong, Chiara Zurzolo, Fernando Rodriguez-Perez
- **The GRC Power Hour™** *Mary Baylies, Mark Rose*

Cellular and Molecular Fungal Biology

Understanding Fungal Function and Diversity: Complex Communities, Pathogenicity and Bioresources

JUN 26-JUL 1, 2022
HOLDERNESS SCHOOL, HOLDERNESS, NH

CHAIRS: Jason Stajich and Alexandra Brand
VICE CHAIRS: Nick Talbot and Anna Selmecki

- **Fungal Hijacking and Host Manipulation** *João Araújo,* Charissa de Bekker, Carolyn Elya, Pietro Spanu
- **Cellular Organization and Molecular Biology** *James Kronstad,* Amy Gladfelter, Josh Nosanchuk, Gero Steinberg, Duncan Wilson, Lillian Fritz-Laylin, Robert Arkowitz
- **Fungal Mutualism and Symbiotic Interactions** *Christine Voisey,* Gregory Bonito, Jana U'Ren, Anna Rosling
- **Genomic Perspectives on Fungal Evolution** *Christina Cuomo,* David Hibbett, Bridget Barker, Iulian Ene, Daniel Croll, Annegret Kohler, Antonis Rokas
- **Fungi in the Microbiome and Complex Communities** *Anthony Amend,* Nina Gunde-Cimerman, Iliyan Iliev, Teresa Pawlowska, Michelle Afkhami
- **Fungal Virulence and Drug Resistance** *Elaine Bignell,* Antonio Di Pietro, Jeniel Nett, Johanna Rhodes, Carol Munro, Tamara Doering, Mike Bromley
- **Fungi as Bioresources** *Nancy Keller,* Jason Slot, Isabelle Benoit Gelber
- **Sensing, Signaling and Development** *Alexander Idnurm,* Yi Liu, Janet Quinn, Michael Freitag, Neil Brown, Daniel Kornitzer, Lauren Ryder, Julia Schumacher
- **Late-Breaking Topics** *Nick Talbot, Anna Selmecki*
- **The GRC Power Hour™** *Elaine Bignell, Christina Cuomo*

Cellular and Molecular Fungal Biology

Diverse Fungi as Innovative Models for Understanding Genomics, Pathogenicity and Signaling

JUN 25-26, 2022

CHAIRS: Abigail LaBella and Charles Puerner

Centromere Biology

Evolution, Structure, Regulation and Function of Centromeres in Health and Disease

JUL 24-29, 2022
MOUNT SNOW, WEST DOVER, VT

CHAIR: Sylvia Erhardt
VICE CHAIR: Iain Cheeseman

- **Keynote Session: Centromeres: From Evolution to Human Health** *Iain Cheeseman,* Genevieve Almouzni, Harmit Malik
- **Biophysical Properties of Centromeres** *Stephen Harrison,* Ekaterina Grishchuk, Michael Lampson, Andrea Musacchio, David Barford
- **Centromeres in Meiosis and Stem Cell Division** *Arshad Desai,* Julia Cooper, Elaine Dunleavy, Yukiko Yamashita, Binyam Mogessie
- **Centromere Dysfunction: Chromosome Segregation Defects and Disease** *Ben Black,* Daniele Fachinetti, Hironori Funabiki, Beth Sullivan
- **Centromere Genomics, Evolution and Variability** *Steven Henikoff,* Luca Comai, Ines Drinnenberg, Karen Miga
- **Epigenetic Regulation of Centromere Identity** *Patrick Heun,* Daniel Foltz, Fangpu Han, Barbara Mellone, Yael Nechemia-Arbely
- **Transcripts and Transcription Control of Centromere Function** *Claire Francastel,* Robin Allshire, Michael Blower, Dawn Carone, Rachel O'Neill
- **Building Blocks Around and Above the Centromere** *Ann Ehrenhofer-Murray,* Jennifer Deluca, Tatsuo Fukagawa, Dean Dawson
- **New Concepts of Centromere Function and Regulation** *Lars Jansen,* Aaron Straight, Needhi Bhalla, Lilian Kabeche
- **The GRC Power Hour™** *Elaine Dunleavy, Rachel O'Neill*

Centromere Biology

Regulating Centromere Function Through Structure

JUL 23-24, 2022

CHAIRS: Samuel Corless and Maiko Kitaoka

Chemistry and Biology of Tetrapyrroles

The Roles of Tetrapyrroles in Catalysis, Regulation, Metabolism and Disease

JUL 17-22, 2022
SALVE REGINA UNIVERSITY, NEWPORT, RI

CHAIR: Emma Raven
VICE CHAIR: Amy Medlock

- **New Structural Techniques for the Study of Tetrapyrroles** *Syun-Ru Yeh,* Wyatt Yue, Allen Orville, Hitomi Sawai
- **Trafficking, Signalling and Regulation by Heme** *Elizabeth Boon,* Emily Weinert, Hiroaki Kitagishi, Dennis Stuehr, Andrew Hudson
- **The Biogenesis and Functions of Bilins** *J. Clark Lagarias,* Lin Liu, Tammi Richardson, William Lanzilotta
- **Tetrapyrroles in Human Health and Disease** *Peter Meissner,* Makiko Yasuda, Levi Wood, Diane Ward
- **The Biology of Tetrapyrroles: Catalysis, Mechanism and Regulation** *Aimin Liu,* John Groves, Brian Crane
- **B12: Biosynthesis, Transport, Pharmacology and Mechanistic Enzymology** *Stephen Ragsdale,* Dorota Gryko, Alison Smith, Ritimukta Sarangi, Tessa Young
- **Regulation and Biosynthesis of Chlorophyll Pigments** *Jennifer Bridwell-Rabb,* Min Chen, Jean Alric, Neil Hunter
- **Microbial Tetrapyrrole Metabolism** *Mark Shepherd,* Celia Goulding, Stefan Hofbauer, Juliette Lecomte
- **Keynote Session: Tetrapyrrole Regulation and Homeostasis** *Samuel Beale,* Angela Wilks, Mark O'Brian

Chemotactic Cytokines

Orchestrating Cell Migration and Location in Health and Disease

JUN 12-17, 2022
LES DIABLERETS CONFERENCE CENTER, LES DIABLERETS, SWITZERLAND

CHAIR: Marcus Thelen
VICE CHAIR: Ronen Alon

- **Keynote Session: Chemokines in Rare Diseases** *Tracy Handel,* Philip Murphy, Gerry Graham
- **Chemokine Receptor-Dependent Signal Transduction** *Bernhard Moser,* Mario Mellado, Silvano Sozzani, Michel Bouvier, Mette Rosenkilde
- **Structures and In Silico Modeling** *Mette Rosenkilde,* Tracy Handel, Thomas Schall, Brian Volkman
- **Chemokine-Mediated Cell Migration** *Daniel Legler,* Philippe Bousso, Holger Knaut, Carole Parent, Tal Arnon
- **Atypical Chemokine Receptors** *Gerry Graham,* Daniel Legler, Martyna Szpakowska, Ralf Stumm
- **Chemokines in Cancer** *Thomas Schall,* Aleksandra Ozga, Burkhard Ludewig, Adit Ben-Baruch, Ann Richmond
- **Chemokines in Pathologies** *Mariagrazia Uguccioni,* Joanna Groom, Hai Qi, Paul Proost
- **Chemokines in Health and Disease** *Philip Murphy,* Amanda Burkhardt, Davide Robbiani, Christoph Scheiermann, Reinhold Förster
- **Keynote Session: Chemokines in Immune Responses** *Ronen Alon,* Eugene Butcher, Sussan Nourshargh, Antal Rot
- **The GRC Power Hour™** *Ann Richmond*

Chemotactic Cytokines GFS
Chemokine Structure, Function and Receptor Interactions in Homeostasis and Disease
JUN 11-12, 2022
CHAIRS: Acacia Dishman and Gillian Wilson

Chromatin Structure and Function

Chromatin Modifications, RNA and Metabolism

MAY 29-JUN 3, 2022
REY DON JAIME GRAND HOTEL, CASTELLDEFELS, SPAIN

CHAIR: Asifa Akhtar
VICE CHAIR: Geeta Narlikar

- **Remodeling Chromatin Structure** *Ali Shilatifard,* Carl Wu, Karolin Luger, Craig Peterson, Shiv Grewal
- **Chromatin Assembly, Replication and Repair** *Peter Becker,* Thomas Jenuwein, Robert Kingston, Danny Reinberg, Caroline Dean, Steven Jacobsen
- **Histone and RNA Modifications** *Wendy Bickmore,* Jeannie Lee, Claire Rougeulle, Tony Kouzarides, William Greenleaf
- **Chromosomes and Genome Architecture** *Karolin Luger,* Edith Heard, Wendy Bickmore, Peter Fraser, Ting (C-ting) Wu, Peter Becker
- **Chromatin, Metabolism and Physiology** *Robert Kingston,* Oded Rechavi, Raul Mostoslavsky, Shelley Berger, Andreas Ladurner
- **Reprogramming and Regeneration** *Joanna Wysocka,* Anne Ferguson-Smith, Yi Zhang, Bradley Cairns, Amanda Fisher, Alexander Meissner
- **Chromatin and Disease Mechanisms** *Karen Adelman,* Sharon Dent, Ali Shilatifard, Joanna Wysocka, Cigall Kadoch
- **Chromatin Biophysics** *Geeta Narlikar,* Xavier Darzacq, Ibrahim Cisse, Michael Rosen, Leonid Mirny, Zhucheng Chen
- **Transcription and Post-Transcriptional Events** *Ibrahim Cisse,* Karen Adelman, Hiroshi Kimura, Dirk Schubeler, Jerry Workman
- **The GRC Power Hour™** *Claire Rougeulle, Karen Adelman*

Chromatin Structure and Function GFS
Micro to Macro Chromatin Structure in Epigenetics and Disease
MAY 28-29, 2022
CHAIRS: Robert Porter and Jumana AlHaj Abed

> ***"GRC cultivates an environment conducive to interdisciplinary learning and scientific discovery by fostering interactions among senior and junior academics, scientists at government laboratories and industrial associates from all over the globe."***
>
> DR. MONICA OLVERA DE LA CRUZ, Northwestern University

Climate Engineering

Processes and Impacts of Radiation Management Approaches to Climate Change

JUN 26-JUL 1, 2022

GRAND SUMMIT HOTEL AT SUNDAY RIVER, NEWRY, ME

CHAIRS: Douglas MacMartin and Trude Storelvmo
VICE CHAIRS: Simone Tilmes and Ulrike Lohmann

- **Keynote Session: Climate Engineering in Context** *Mark Lawrence,* Piers Forster, Alan Robock
- **Stratospheric Processes** *Valentina Aquila,* Gabriel Chiodo, Jadwiga Richter, Karen Rosenlof
- **Regional Methods** *Olivier Boucher,* Kate Ricke, Sonia Seneviratne
- **Cloud-Mediated Processes** *Thomas Leisner,* Daniel Rosenfeld, Robert Wood, Blaz Gasparini
- **Climate Response** *Ulrike Niemeier,* Peter Irvine, Daniele Visioni
- **Climate Impacts** *Daniel Schrag,* Jonathan Proctor, Long Cao
- **Developing World Impacts** *Michael Taylor,* Ines Camilloni, Izidine Pinto
- **Engineering and Design** *Hugh Hunt,* Frank Keutsch, Ben Kravitz, Wake Smith
- **Keynote Session: Transdisciplinary Research for Climate Engineering** *Holly Buck,* David Keith
- **The GRC Power Hour™** *Simone Tilmes, Ulrike Lohmann*

Climate Engineering GFS
Physical Processes and Impacts of Radiation Management Approaches to Climate Change
JUN 25-26, 2022
CHAIRS: Katie Dagon and Daniele Visioni

Colloidal Semiconductor Nanocrystals

Nanocrystal Chemistry, Physics and Applications

JUL 3-8, 2022
LES DIABLERETS CONFERENCE CENTER, LES DIABLERETS, SWITZERLAND

CHAIRS: Maksym Kovalenko and Matt Law
VICE CHAIRS: Gordana Dukovic and Efrat Lifshitz

- **Synthesis Science** *Brandi Cossairt,* Uri Banin, Elena Shevchenko
- **Bioapplications** *Carlos Toro,* Allison Dennis, Inge Herrmann, Wolfgang Parak, Teresa Pellegrino
- **Assemblies and Collective Phenomena** *Dmitri Talapin,* Sara Bals, Christophe Delerue, Christopher Murray, Nuri Yazdani
- **Charge, Energy and Heat Transport** *Vanessa Wood,* Maria Ibanez, Cherie Kagan, Lea Nienhaus, Marcus Scheele
- **Photophysics** *Mikhail Zamkov,* Daniel Gamelin, Zeger Hens, Patanjali Kambhampati, Victor Klimov
- **Towards Quantum Light Sources** *Matthew Sheldon,* Moungi Bawendi, Yoshihiko Kanemitsu, Brahim Lounis, Peter Sercel
- **Photochemistry and Energy Conversion** *Raffaella Buonsanti,* Jillian Dempsey, Prashant Kamat, Susanna Thon, Emily Weiss
- **Optoelectronics** *Maria Antonietta Loi,* Sergio Brovelli, Hilmi Volkan Demir, Eunjoo Jang, Sohee Jeong
- **Nanocrystals for the Infrared** *Javier Vela,* Philippe Guyot-Sionnest, Wolfgang Heiss, Gerasimos Konstantatos, Emmanuel Lhuillier
- **The GRC Power Hour™** *Gordana Dukovic, Efrat Lifshitz*

Colloidal Semiconductor Nanocrystals GFS
Light-Matter Interactions in Semiconductor Nanomaterials
JUL 2-3, 2022
CHAIRS: Xing Yee Gan and Joo Yeon Roh

Computational Chemistry

Multiscale Modeling of Complex Systems: Methods and Applications

JUL 17-22, 2022
REY DON JAIME GRAND HOTEL, CASTELLDEFELS, SPAIN

CHAIRS: Adrian Roitberg and Zoe Cournia
VICE CHAIR: Natalie Fey

- **Linking Molecular Structure and Dynamics to Function** *Andrea Cavalli,* Adrian Mulholland, Marco De Vivo, Syma Khalid, Darrin York
- **Methods and Applications in Free Energy Calculations** *Chris Chipot,* Hugo Gutierrez-De-Teran, Xinjun Hou, William Jorgensen, Henry Woodcock
- **From Quantum Dynamics to Multiscale Modeling of Materials and Interfaces** *Spiridoula Matsika,* Ana Nicoleta Bondar, Gerald Tanoury, Sotiris Xantheas
- **Modeling Nucleic Acids** *Modesto Orozco,* Thomas Cheatham, Pablo Dans
- **Modeling Functional Materials** *Fernanda Duarte,* Seonah Kim, Edward Sherer
- **Using Machine Learning for Molecular Design** *Natalie Fey,* Tatjana Braun, Gianni De Fabritiis, Olexander isayev, Frank Noe
- **Integrating Big Data in Drug Discovery Applications: From Allostery to Biologics Design** *Kenneth Merz,* Ivet Bahar, Chris de Graaf, Masha Niv, Rebecca Wade
- **Multiscale Modeling for Computer-Aided Drug Design** *Simone Fulle,* Ronald Knegtel, Silvia Lovera, Jeremy Smith
- **Modeling Long-Scale Conformational Dynamics** *Julien Michel,* Cecilia Clementi, Karissa Sanbonmatsu
- **The GRC Power Hour™** *Syma Khalid, Zoe Cournia*

Computational Chemistry GFS
How Computational Method Development Translates into Application
JUL 16-17, 2022
CHAIRS: Anna Kamenik and Taylor Quinn

Computational Materials Science and Engineering NEW!

Comparing Theories, Algorithms and Computation Protocols in Materials Science and Engineering

JUL 31-AUG 5, 2022
GRAND SUMMIT HOTEL AT SUNDAY RIVER, NEWRY, ME

CHAIR: Rampi Ramprasad
VICE CHAIRS: Katsuyo Thornton and Heather Kulik

- **Synthesis Planning Algorithms** *Wenhao Sun,* Elsa A. Olivetti, Connor Coley
- **Machine Learning** *Bryce Meredig,* Subramanian K. R. Sankaranarayanan, Klaus-Robert Müller, Rama Vasudevan
- **Coarse Graining** *James Warren,* Nikolas Provatas, Gregory Voth
- **Concurrent and Hierarchical Multiscale Modeling** *Kaushik Dayal,* David McDowell, Martin Steinhauser, Ellad Tadmor
- **Non-Adiabatic Quantum Mechanics** *Claudia Draxl,* André Schleife, Priya Vashishta
- **Autonomous Robotic Systems** *Christoph Kreisbeck,* Andy Cooper, A. Gilad Kusne, Loïc Roch
- **Calculation of Phase Diagrams (CALPHAD)** *Raymundo Arroyave,* Ursula Kattner, Axel van de Walle
- **Materials by Design** *Alejandro Strachan,* Juan de Pablo, James Saal, Cormac Toher

- **Quantum Computing** *Hanhee Paik,* Alan Aspuru-Guzik, Veera Sundararaghavan
- **The GRC Power Hour™** *Jennifer Carter, Aeriel Leonard*

Correlated Electron Systems

Topology and Correlations: Long-Range Entanglement in Many-Body Systems

JUN 26-JUL 1, 2022

MOUNT HOLYOKE COLLEGE, SOUTH HADLEY, MA

CHAIRS: Nandini Trivedi and James Analytis
VICE CHAIRS: Senthil Todadri and Suchitra Sebastian

- **Magic Angles and Correlations in Moire Materials** *Cory Dean,* Dmitri Efetov, Andrea Young, Ashvin Vishwanath
- **Moire** *Mohit Randeria,* Oskar Vafek, Shahal Ilani, Kwabena Bediako, Jie Shan
- **Quantum Spin Liquids** *Yuan-Ming Lu,* Donna Sheng, Minoru Yamashita, Vesna Mitrovic
- **Quantum Oscillations in Insulators** *Natalia Perkins,* Roser Valenti, Nai Phuan Ong, Hide Takagi, Ciaran Hickey
- **Fractionalization and Anomalous Thermal Hall** *Ehud Altman,* Mitali Banerjee, Gael Grissonnanche, Yuji Matsuda
- **Non-Fermi Liquids** *Subir Sachdev,* Martin Zwierlein, Andy Lucas, Anaëlle Legros, Achim Rosch
- **Non-Equilibrium and Non-Linear Response** *Aashish Clerk,* David Hsieh, Vedika Khemani, Norman Yao
- **Quantum Dynamics and Measurement** *Michel Devoret,* Crystal Noel, Valla Fatemi, Giulia Semeghini, Jason Alicea
- **Late-Breaking Topics** *Senthil Todadri*
- **The GRC Power Hour™** *Colette Patt*

Correlated Electron Systems
Emergent Electronic Order, Fractionalization and Long-Range Entanglement in Quantum Materials
JUN 25-26, 2022
CHAIRS: Ali Husain and Debanjan Chowdhury

Crystal Engineering

Inspired Design, Assembly and Properties of Molecular Materials

JUN 19-24, 2022

GRAND SUMMIT HOTEL AT SUNDAY RIVER, NEWRY, ME

CHAIR: Jennifer Swift
VICE CHAIR: Andy Cooper

- **Order, Disorder and Defects** *Aurora Cruz-Cabeza,* Karena Chapman, Ying Diao
- **Crystal Assembly** *Braulio Rodriguez-Molina,* Katharina Edkins, Matteo Salvalaglio, Jeffrey Rimer, Karah Knope
- **Polymorphs and Mixtures** *Yu-Sheng Chen,* Robert Schurko, Sara Weaver
- **Crystals Under Pressure** *Bruno Hancock,* Iain Oswald, Jack Clegg, Franziska Emmerling, Daniel Hooks
- **Crystal Reactivity** *Pance Naumov,* Kana Sureshan, Jason Benedict
- **Pharmaceuticals and Cocrystals** *Rositza Petrova,* Changquan Sun, Doris Braun, Lynne Taylor
- **Big Data and Informatics** *Susan Reutzel-Edens,* Ian Bruno
- **Porosity and Open Framework Materials** *Brian Smith,* Kim Jelfs, Chenfeng Ke, Craig Brown, Katherine Mirica
- **Engineering Across Length Scales** *Kristin Hutchins,* Benjamin Palmer
- **The GRC Power Hour™** *Susan Reutzel-Edens*

Crystal Engineering
Engineering Crystals in the Fourth Dimension: Monitoring of Structural Changes in Crystals
JUN 18-19, 2022
CHAIRS: Ivana Brekalo and Ren Wiscons

Cyclic Nucleotide Phosphodiesterases

Probing and Targeting PDEs: From Local Control of Signaling Nanodomains to Functional Impact

JUN 19-24, 2022

LES DIABLERETS CONFERENCE CENTER, LES DIABLERETS, SWITZERLAND

CHAIRS: Jos Prickaerts and Jin Zhang
VICE CHAIRS: Viacheslav Nikolaev and Michy Kelly

- **Cyclic Nucleotide Signaling Pathways: From Receptors to Targets** *David Kass,* Carmen Dessauer, Martin Lohse, Susan Taylor, Martina Schmidt
- **Spatiotemporal Regulation of Cyclic Nucleotide Signaling** *Viacheslav Nikolaev,* Manuela Zaccolo, John Scott, Aldebaran Hofer, Mark Gomelsky
- **Structural, Molecular and Systems Dissection of PDE Signaling** *Nikolai Artemyev,* Rick Cote, Ganesh Anand
- **Cyclic Nucleotide Signaling in Cardiovascular Systems** *Rodolphe Fischmeister,* Christina Kruuse, Yang Xiang, Xiaodong Cheng, Chen Yan, David Kass
- **Novel and Atypical Signaling** *Manuela Zaccolo,* Roland Seifert, David Baker, Nikolai Artemyev
- **Selective PDE Targeting of Central Nervous System Functions** *Michy Kelly,* Achim Schmidtko, Dorit Ron, Pierre Vincent, Jan Kehler
- **PDEs in Vascular and Metabolic Processes** *Enno Klussmann,* Donald Maurice, Mary Anna Venneri, Anders Tengholm, Alexander Pfeifer
- **PDE Mediated Signaling in Immunological and Inflammatory Processes** *Joseph Beavo,* Hai-Bin Luo, Gretchen Snyder, Stefan Brocke, Kjetil Tasken, Ralf Hoffmann
- **Therapeutic Considerations and Path to the Clinic** *Gretchen Snyder,* Coleen Atkins, George Baillie
- **The GRC Power Hour™** *Michy Kelly, Viacheslav Nikolaev*

Cyclic Nucleotide Phosphodiesterases
Phosphodiesterases: From Fundamental Insights to Therapeutic Targets
JUN 18-19, 2022
CHAIRS: Melissa Schepers and Amy Tibbo

Cytoskeletal Motors

Molecular Machines: From Biophysics To Physiology To Disease

JUL 10-15, 2022

MOUNT SNOW, WEST DOVER, VT

CHAIR: Steven Rosenfeld
VICE CHAIR: Margaret Titus

- **Keynote Session: Motors Working in a Context** *Margaret Titus,* Vladimir Gelfand, Kathleen Trybus
- **Motors in Cardiovascular Disease** *David Warshaw,* Anne Houdusse, James Spudich, Theresia Kraft, Sanford Bernstein
- **Structure and Regulation** *Carolyn Moores,* Ahmet Yildiz, Anthony Roberts, Hernando Sosa, Stefan Raunser
- **Motors in Cell Motility and Transport** *James Sellers,* David Warshaw, Richard Cheney, Samara Reck-Peterson, Erika Holzbaur
- **Modeling and Analysis of Molecular Motor Systems** *Erkan Tuzel,* David Odde, Tamara Bidone, Michael Murrell, Michael Diehl
- **Motor Generated Forces in Cell Function** *Sarah Heissler,* Michael Ostap, Ewa Paluch, Andre Levchenko, Dylan Burnette
- **Tracks and Filaments** *Antonina Roll-Mecak,* Anna Kashina, Enrique De La Cruz, Jennifer Ross, Casper Hoogenraad
- **Motors in Cancer, Psychiatric, Metabolic, and Infectious Diseases** *Lee Sweeney,* Anne Bresnick, Jonathan Kirk, Dominique Soldati-Favre, Michael Way, Courtney Miller
- **Motors in Mitosis** *Jason Stumpff,* Ekaterina Grishchuk, Tarun Kapoor, Sophie Dumont, William Bement
- **The GRC Power Hour™**

Cytoskeletal Motors
Molecular Motors and Their Tracks: Biophysics, Physiology, and Disease
JUL 9-10, 2022
Chairs: Ashley Arthur and Donte Stevens

Deep Carbon Science

Exploring Fluxes, Forms and Origins of Deep Carbon in Earth and Other Terrestrial Planets

JUN 19-24, 2022
BATES COLLEGE, LEWISTON, ME

CHAIRS: Edward Young and Kai-Uwe Hinrichs
VICE CHAIRS: Tamsin Mather and Doug LaRowe

- **Origins of Carbon in the Solar System** *Mary Voytek,* Bernard Marty, Siyi Xu, Lauren Cleeves
- **Earth's Deep Carbon Cycle** *Michael Walter,* Andrea Giuliani, Graham Pearson, Jonathan Tucker
- **Extreme Physics, Chemistry and Biology of Carbon** *Jie Li,* Razvan Caracas, Susannah Dorfman, Jung-Fu Lin
- **New Tracers of the Provenance of Hydrocarbons** *Jeanine Ash,* Max Lloyd, Thomas Giunta, Jeffrey Marlow, Jill McDermott
- **Serpentinization and Deep Life** *Matthew Schrenk,* Susan Lang, Florence Schubotz
- **Life at its Limits** *Doug LaRowe,* Brandy Toner, Fengping Wang, Daan Speth
- **Connections Between Deep Carbon and Atmospheres** *Tamsin Mather,* Peter Barry, Oliver Shorttle
- **The Fate of Carbon During Subduction** *Terry Plank,* Megan Duncan, Matthieu Galvez, Craig Manning, Paul Wallace
- **Late-Breaking Topics** *Rachel Harris*
- **The GRC Power Hour™**

Deep Carbon Science
Carbon at the Intersection of the Biosphere and Geosphere
JUN 18-19, 2022
Chairs: Jonathan Tucker and Rachel Harris

Defects in Semiconductors

Defect Formation, Characterization, Control and Utilization

AUG 14-19, 2022
COLBY-SAWYER COLLEGE, NEW LONDON, NH

CHAIR: Jeffrey McCallum
VICE CHAIR: Kai-Mei Fu

- **Developments in Defect Spectroscopy and Metrology** *Lasse Vines,* Darshana Wickramaratne, Jean-Philippe Tetienne
- **Color Centers in Wide Band-Gap Semiconductors and 2D Materials for Quantum Applications** *Marina Radulaski,* Cyrus Dreyer, Chitraleema Chakraborty
- **Characteristics of Defects in 2D Materials and Oxide Semiconductors** *Joel Varley,* Matt McCluskey, John Lyons, Prineha Narang
- **Spin Centers: Spectroscopy and Applications** *Takeshi Ohshima,* Sophia Economou, Alexander Weber-Bargioni, Stefania Castelletto
- **Defects in Nitride Semiconductors** *Mary Ellen Zvanut,* Ramon Collazo, Annemarie Exarhos
- **Defects in Photovoltaic Materials and Devices, Identification and Control** *John Murphy,* Hele Savin, Vladan Strevanovic, Wolfram Kwapil
- **Defect Characterization and Control** *Elif Ertekin,* Anyao Liu, Atsushi Oshiyama, Jinwoo Hwang
- **High Resolution Imaging and Characterization of Defects** *Paul Koenraad,* Lorenzo Rigutti
- **Keynote Session: Toward Single Defect Imaging in Layered and 3D Materials** *Kai-Mei Fu,* Jianwei Miao
- **The GRC Power Hour™** *Kai-Mei Fu*

Defects in Semiconductors
Defect Formation, Characterization, Control and Utilization
AUG 13-14, 2022
Chairs: Hongling Lu and Ymir Frodason

Diffraction Methods in Structural Biology

Breaking Down the Barriers in Structural Biology into Defined, Measurable and Solvable Problems

JUL 24-29, 2022
BATES COLLEGE, LEWISTON, ME

CHAIR: James Holton
VICE CHAIR: Janet Newman

- **Artificial Intelligence in Structural Biology** *Airlie McCoy,* Ho Leung Ng, Christopher Watkins
- **Optimal Data Collection Limited by Damage, Equipment and Sample Quality** *Ana Gonzalez,* Elspeth Garman, Kunio Hirata, Gleb Bourenkov
- **Sample Prep with Uncooperative Molecules** *Alex McPherson,* Sarah Bowman, Anchi Cheng
- **Processing Algorithms for Difficult Data** *Kay Diederichs,* Dominika Borek, Loes Kroon-Batenburg, Derek Mendez, Jeney Wierman
- **Massive Radiations: Electrons and Neutrons** *Garib Murshudov,* Wah Chiu, Johan Hattne, Flora Meilleur
- **Interpreting Low-Resolution Maps and Weak Data** *Paul Emsley,* Tristan Croll, Jane Richardson, Isabel Uson
- **Dividing Ligands with Confidence** *Dorothee Liebschner,* Tom Peat, Frank von Delft
- **Selected Poster Presentations** *Edward Snell*
- **The Last Angstrom: Disorder, Dynamics and Function** *Helen Ginn,* Andrea Thorn, Henry van den Bedem, Rozaliya Barabash
- **The GRC Power Hour™** *Elspeth Garman*

Diffraction Methods in Structural Biology

Data-Rich Experiments in Serial Crystallography, Time-Resolved Studies and MicroED

JUL 23-24, 2022

Chairs: Jennifer Wierman and James Parkhurst

DNA Topoisomerases in Biology and Medicine

Topoisomerase Mechanism, Function and Inhibition: From Single-Molecule Analyses to Clinical Trials

AUG 7-12, 2022
BRYANT UNIVERSITY, SMITHFIELD, RI

CHAIRS: Lynn Zechiedrich and Keir Neuman
VICE CHAIRS: Yuk-Ching Tse-Dinh and Dagmar Klostermeier

- **Keynote Session: Molecular Mechanisms to Clinical Trials** *Valakunja Nagaraja,* Sue Jinks-Robertson, Yves Pommier
- **Topoisomerases as Targets for Antimicrobial Agents** *Marc Drolet,* Alexandra Aubry, Pan Chan, Neil Osheroff
- **Processing of Topoisomerase Adducts** *Hannah Klein,* Heidrun Interthal, Robert Van Waardenburg
- **Interplay Between Genome Topology and Topoisomerase Interactions** *David Levens,* Erez Aiden, Laura Baranello, Konstantin Severinov
- **Modeling DNA Topoisomerases and Topology** *Sarah Harris,* Davide Marenduzz, Mariel Vasquez
- **Topoisomerases and DNA Topology in Cancer Chemotherapy** *Scott Kaufmann,* Mary-Ann Bjornsti, Junjie Chen, Karen Vasquez
- **DNA Topology and Topoisomerases at the Single Molecule Level** *Alice Pyne,* Zev Bryant, Michelle Wang
- **Topoisomerases as Cellular Poisons and Essential Enzymes** *Shunichi Takeda,* Anna Bizard, Nayun Kim, Yuh-Hwa Wang
- **Topoisomerase Structure and Function** *Valerie Lamour,* James Berger, Nei-Li Chan

DNA Topoisomerases in Biology and Medicine

Enzymology, Cellular Functions, Roles in Diseases and Therapeutic Targeting

AUG 6-7, 2022

Chairs: Amanda Riccio and Thomas Germe

Drug Carriers in Medicine and Biology

Enabling New Therapies Through Drug Carrier Design

JUL 31-AUG 5, 2022
MOUNT SNOW, WEST DOVER, VT

CHAIRS: Suzie Pun and Samir Mitragotri
VICE CHAIRS: Kathryn Whitehead and Vadim Dudkin

- **Keynote Session: Drug Carriers Revolutionizing Therapeutic Approaches** *Vladimir Muzykantov, Dennis Lee,* Paula Hammond, David Mooney
- **New Materials for Drug Delivery** *Ester Kwon,* Paul Wender, Kristy Ainslie, Jianjun Cheng, Jean-Christophe Leroux
- **Advances Toward Translation and Carrier Interactions with the Immune System** *Elizabeth Nance,* Jinming Gao, Anna Schwendeman
- **Drug Carriers in Oncology** *Rizia Bardhan,* Natalie Artzi, Debra Auguste, Tatiana Novobrantseva, Anand Subramony
- **Cell-Mediated Drug Delivery** *Juliane Nguyen,* Zhen Gu, Elena Batrakova
- **Intracellular Delivery of Biologics** *Michael Mitchell,* Julie Champion, Craig Duvall, Richard Wooster
- **Selected Poster Presentations** *Vadim Dudkin, Kathryn Whitehead*
- **Biological Carriers** *Olivia Merkel,* David Schaffer, Laura Ensign, Don Hilvert, Nicole Steinmetz
- **Overcoming Barriers to Oral Delivery** *Omid Veiseh,* Maria Jose Alonso, Sujatha Sonti, Giovanni Traverso
- **The GRC Power Hour™** *Kristy Ainslie*

Drug Carriers in Medicine and Biology

Exploring Size-Based Delivery Strategies for Biologics and Novel Drug Cargos

JUL 30-31, 2022

Chairs: Anusha Pusuluri and Nicholas Lamson

Drug Metabolism

Drug Discovery to Precision Therapeutics: Novel Mechanisms, Models and Technologies

JUL 10-15, 2022
HOLDERNESS SCHOOL, HOLDERNESS, NH

CHAIR: J. Steven Leeder
VICE CHAIR: Jane Kenny

- **Keynote Session: Integration of Drug Metabolism Science and Big Data to Inform Precision Medicine** *Jane Kenny,* Sir Munir Pirmohamed
- **Drug Transporters: Advancing Drug Development and Precision Therapeutics** *Andrew Goodman,* Nichole Klatt, Matthew Redinbo, Peter Turnbaugh, Michael Zimmermann
- **Drugs of the Future: Probing the ADME Properties of Novel Therapeutics** *Sara Humphreys,* Gaurav Bhardwaj, Diane Ramsden
- **Drug Metabolism by Intestinal Microorganisms** *Kim Brouwer,* Bruno Hagenbuch, Kaspar Locher, Pallabi Mitra, Gauri Rao
- **New Techniques in Drug Metabolism Methodology** *Katherine Elvira,* Xiaomeng Shen, Boyang Zhang
- **Prediction of Drug Metabolism In Vivo from In Vitro Studies** *Cyrus Khojasteh,* Leslie Benet, Murat Cirit, Hiroyuki Mizuguchi, Charity Nofziger
- **Selected Poster Presentations** *Patrick Murphy*
- **Mechanisms of Drug Metabolism** *Emily Scott,* Xinxin Ding, Ruili Huang, Eric Johnson, Richard Auchus
- **Harnessing Technology to Advance Individualized Therapeutics** *Namandje Bumpus,* Netz Arroyo, Catherine Fenselau, Manthena Varma
- **The GRC Power Hour™**

Drug Metabolism

Translational Models and Technologies to Predict Drug Disposition and Response

JUL 9-10, 2022

CHAIR: Chelsea Hosey

Drug Resistance

Strategies to Disrupt Resistance in Infectious Diseases, Cancer and Agriculture

JUN 26-JUL 1, 2022
BRYANT UNIVERSITY, SMITHFIELD, RI

CHAIRS: Lizbeth Hedstrom and Daruka Mahadevan
VICE CHAIRS: Aaron Goldman and Alexis Kaushansky

- **Keynote Session: Protecting New Drugs and Pesticides Against Resistance** *Alexis Kaushansky,* Alina Baum, Seva Rostovtsev
- **The Emergence of Resistance** *Pradipsinh Rathod,* Sophie Helaine, Houra Merrikh, Susan Rosenberg, Sarah Amend
- **Eco-Evolutionary Strategies to Address Resistance** *Andriy Marusyk,* Eugene Shakhnovich, Jacob Scott
- **Combating Resistance with Novel Targets** *Mithila Jugulam,* Emily Derbyshire, Eachan Johnson, Mark Rolfe, Paul Workman
- **Durable Drug Design** *Timothy Wencewicz,* David Epstein, Adam Palmer
- **Systems and Modeling Strategies to Address Resistance** *Adam Palmer,* Nitin Baliga, Funda Meric-Bernstam, Pamela Yeh
- **Threats and Responses** *Funda Meric-Bernstam,* Sarat Chandarlapaty, Pradipsinh Rathod
- **Microbiome and Resistance** *Celia Schiffer,* Christopher Ford, Neha Garg, Yoshitomo Kikuchi, Peter Belenky
- **Keynote Session: Emerging Strategies to Combat Resistance** *Aaron Goldman,* Richard Alm, Paul Turner, James Welsh
- **The GRC Power Hour™**

Drug Resistance

Mechanisms and Approaches to Overcoming Drug Resistance in Cancer, Infectious Disease and Agriculture

JUN 25-26, 2022

CHAIR: Michael Lombardo

Drug Safety

Advances in Models, New Modalities and Clinical Considerations for Drug Safety

JUN 19-24, 2022
STONEHILL COLLEGE, EASTON, MA

CHAIR: Myrtle Davis
VICE CHAIR: Ruth Roberts

- **Keynote Session: Modeling Complex Biological Systems** *David Watson,* Dennis Discher
- **Emerging Applications of Big Data and Machine Learning in Safety Assessment** *James Stevens, Daniel Rudmann,* Melissa Hallow, Laszlo Urban, Erio Barale-Thomas
- **Leveraging Human Genetics and Big Data to Inform Drug Safety** *Blanca Rodriguez,* Danish Saleheen, Lucas Ward, Hao Zhu
- **Biomarker Science in Drug Discovery and Development** *Vishal Vaidya,* Guruprasad Aithal, Holly Soares
- **Microphysiological Models: Advances in Modeling Complex In Vivo Functions and Organ Responses** *Anthony Bahinski, Kyle Kolaja,* Mark Donowitz, Joanna Burdette, Girija Goyal
- **New Paradigms in Translational Safety Science** *Leigh Ann Burns Naas,* Lolke Dehaan, Gary Gilmour, Michael Morton, Eric Sobie
- **Novel Therapeutic Modalities: Challenges and Opportunities in Nonclinical Safety Assessment Strategies** *Wendy Freebern, Jeff Willy,* Fiona Spence, Kathy Meyer, Padma Narayanan
- **Full Utilization of the Clinical Experience in the Nonclinical Space** *Michelle Berny-Lang, Kelly Filipski,* Bonnie Ky, Christine Miaskowski, Yinghong Mimi Wang
- **Keynote Session: Advancing Drug Safety Through Innovation** *Ruth Roberts,* Manasi Nandi
- **The GRC Power Hour™** *Michelle Berny-Lang, Leigh Ann Burns Naas*

Drug Safety

Emerging Technologies and Strategies for Drug Safety Evaluation

JUN 18-19, 2022

CHAIRS: Lauren Lewis and Molly Morgan

Electron Donor-Acceptor Interactions

Electron and Energy Transfer Processes: New Perspectives and Emerging Directions

JUL 31-AUG 5, 2022

SALVE REGINA UNIVERSITY, NEWPORT, RI

Chairs: Felix Castellano and Claudia Turro
Vice Chairs: Lin Chen and Ferdinand Grozema

- **Bio-Inspired Charge Transfer Chemistry** *Sherri McFarland,* Leif Hammarstrom, Hannah Shafaat, Harry Gray
- **Spin Control of Electron Transfer Processes** *Malcolm Forbes,* Natia Frank, Martin Kirk, Stephen Holmes, Danna Freedman
- **Photoredox Driven Chemical Transformations** *James McCusker,* Corey Stephenson, Carsten Milsmann, Oliver Reiser
- **Photonic Materials** *Lea Nienhaus,* Dan Congreve, Xiaosong Li, Nobuhiro Yanai, Justin Caram
- **Molecular Charge Transfer** *Elena Galoppini,* Mark Thompson, Gerald Meyer, Karen Mulfort
- **Catalysis Towards Sustainable Fuels** *Etsuko Fujita,* Clifford Kubiak, Jenny Yang, Elena Jakubikova, Alexander Miller
- **Charge Transport in Complex Architectures and Interfaces** *Dirk Guldi,* Cody Schlenker, Gemma Solomon
- **Energy Transfer, Fusion and Fission** *David Shultz,* Amanda Morris, Justin Johnson, Oliver Wenger, Ken Hanson
- **Keynote Session: Coherence in Charge Transfer Processes** *Niels Damrauer,* Gregory Scholes, Jeffrey Rack, Michael Wasielewski
- **The GRC Power Hour™** *Sherri McFarland, Amanda Morris*

Electron Donor-Acceptor Interactions GRS
From Fundamentals to Applications in Energy Conversion and Beyond
JUL 30-31, 2022
CHAIRS: Alexandria Bredar and Jacob Spies

Endothelial Cell Phenotypes in Health and Disease

Understanding Endothelial Cell Diversity: Regulation and Regenerative Potential

JUN 26-JUL 1, 2022

REY DON JAIME GRAND HOTEL, CASTELLDEFELS, SPAIN

CHAIR: Karen Hirschi
VICE CHAIR: Christiana Ruhrberg

- **Endothelial Cell Heterogeneity** *Hellmut Augustin,* Ralf Adams, Victoria Bautch, Christer Betsholtz
- **Molecular Regulation of Endothelial Phenotypes** *Karina Yaniv,* Martin Schwartz, Natasha Harvey, Mark Kahn, Anne Eichmann
- **Congenital Defects and Clinical Therapy** *Gou Young Koh,* Pia Ostergaard, Miikka Vikkula, Jason Fish, Susan Quaggin
- **Endothelial Cell Damage, Repair and Regeneration** *Joyce Bischoff,* Luisa Iruela-Arispe, Yoshiaki Kubota, Shahin Rafii
- **Aging Endothelium and Impact on Disease Progression** *Eli Keshet,* Jaime Grutzendler, Ebba Brakenhielm, Massimiliano Mazzone
- **Hematovascular Interactions in Development and Disease** *Christiana Ruhrberg,* Stefania Nicoli, Kenneth Walsh, Taija Makinen
- **Advances in Vascular Imaging and Bioengineering** *Mary Dickinson,* Friedemann Kiefer, Rui Benedito, Julien Vermot
- **Vascular Metabolism** *Timothy Hla,* Zoltan Arany, Mariona Graupera, Michael Potente, Michael Simons
- **Emerging Approaches to Understanding Cellular Diversity** *Katie Bentley,* Kari Alitalo, Clint Miller, Bin Zhou, Holger Gerhardt
- **The GRC Power Hour™** *Luisa Iruela-Arispe, Katie Bentley*

Endothelial Cell Phenotypes in Health and Disease GRS
Understanding Endothelial Cell Diversity: Regulation and Regenerative Potential
JUN 25-26, 2022
CHAIRS: Nicholas Chavkin and Gabriela D'Amico

"GRCs are such a positive experience. The conferences are relatively small and very informal. Meeting people and talking shop for a week is better than a vacation."

J. ROBERT DURRWACHTER, Cambrex

Energetic Materials

The Confluence of Science- and Machine-Based Learning Approaches in Energetic Materials Research

JUN 26-JUL 1, 2022
SOUTHERN NEW HAMPSHIRE UNIVERSITY, MANCHESTER, NH

Chair: Joseph Zaug
Vice Chair: Lori Groven

- **From Atomic- to Micro-Scale Phenomena: Beginning at Ignition** *Katharine Tibbetts,* Lee Perry, Rebecca Lindsey, Joseph Olles
- **Meso-Scale Phenomena Illuminated by Science- and Machine-Based Learning** *Santanu Chaudhuri,* David Kittell, Paul Lafourcade, Oishik Sen
- **Machine-Based Learning: Algorithms in Support of Chemical Prescriptions** *Brian Barnes,* Anna Hiszpanski, Koji Tsuda, Bartosz Grzybowski, Anshumali Shrivastava
- **Materials Synthesis: Organic, Inorganic and In Silico** *Qian Yang,* Olexandr Isayev, Virginia Manner, Sili Deng
- **Advanced Manufacturing: Optimizing Performance by Design** *Jena McCollum,* Blair Brettmann, Yoav Eichen
- **Thermodynamics and Kinetics: Tailoring the Power of Energetic Materials** *Matthew Kroonblawd,* Sorin Bastea, Deanna Lacoste, Carole Morrison
- **Thermal-Mechanical Dynamics: Learning from Emergent Response** *Jesus Mares,* Marisol Koslowski, Gary Seidel
- **Intelligently Designed Propellants** *Andrew Demko,* Ralf Kaiser, Joseph Kalman, Devon Swanson
- **Fireball Dynamics** *Michael Soo,* Christopher Goldenstein, Jennifer Gottfried, Mark Phillips
- **The GRC Power Hour™** *Deanna Lacoste*

Energetic Materials GRS
Physicochemical Processes in Reacting Energetic Materials from the Nano to Macro Scale
JUN 25-26, 2022
CHAIRS: Will Bassett and Matthew Kroonblawd

Environmental Endocrine Disruptors

EDCs and the Environment

JUN 19-24, 2022
JORDAN HOTEL AT SUNDAY RIVER, NEWRY, ME

CHAIR: Jodi Flaws
VICE CHAIRS: Juliette Legler and Angel Nadal

- **Keynote Session: Environmental Endocrine Disrupting Chemicals** *Angel Nadal, Bernard Robaire,* Shanna Swan, Gail Prins
- **Evidence for an Mechanisms of EDC-Induced Reproductive Toxicity** *Vasantha Padmanabhan,* Patrick Hannon, Pauliina Damdimopoulou, Aileen Keating, Laura Vandenberg
- **Impacts on the Brain and Behavior** *Andrea Gore, R. Thomas Zoeller,* Heather Patisaul, Sakina Mhaouty-Kodja, Ramendra Saha
- **Social, Cultural, and Political Determinants of Evaluating Risks from EDCs** *Laura Vandenberg,* Kevin Elliott, Katie Boronow, Ami Zota, R. Thomas Zoeller
- **Emerging Exposures, Nonclassical Environmental Endocrine Disruptors, and Safer Alternatives** *Genoa Warner, Thad Schug,* Terrence Collins, Shuo Xiao, Bernard Robaire
- **Short and Long-Term Consequences of Developmental Exposure to EDCs** *Patrick Hannon,* Marisa Bartolomei, Ramji Bhandari, Paola Palanza, Almudena Veiga-Lopez
- **Environmental Endocrine Disruptors in the Marine and Terrestrial Environment** *Juliette Legler, Ramji Bhandari,* Ben Parrott, Turk Rhen
- **EDC Effects in the Context of Human Exposure** *Shanna Swan,* Rita Strakovsky, Jennifer Adibi, Cynthia Curl, Tamarra James-Todd
- **Effects of Environmental Endocrine Disruptors on Energy Balance and Cellular Metabolism** *Almudena Veiga-Lopez, Kylie Rock,* Nikki Posnack, Lindsey Treviño
- **The GRC Power Hour™** *Heather Patisaul, Laura Vandenberg*

Environmental Endocrine Disruptors GRS
Harnessing Interdisciplinary Evidence for Endocrine Disruption to Improve Public Health
JUN 18-19, 2022
CHAIRS: Kylie Rock and Genoa Warner

Environmental Sciences: Water

Innovative Science for the Grand Challenges in Aquatic Environmental Sciences

JUN 19-24, 2022
HOLDERNESS SCHOOL, HOLDERNESS, NH

CHAIR: Heileen Hsu-Kim
VICE CHAIR: Thomas Hofstetter

- **Biodegradable Polymers and Plastic Contamination** *Michael Sander,* Marc Hillmyer, Richard Gross
- **An Updated Look into (Waste) Water Treatment Processes** *Kyle Bibby,* Michael Dodd, Peiying Hong, Krista Wigginton
- **Environmental Metabolomics** *David Wishart,* Pieter Dorrestein, Michael Zimmermann
- **The Continuing Threat of Halogenated Contaminants** *Elizabeth Edwards,* Frank Löffler, Carla Ng, Jinyong Liu
- **The Increasing Complexity of Chemical Pollution: New Avenues for Identifying Unknowns and Assessing Effects** *Beate Escher,* Mingliang Fang, Emma Schymanski
- **New Chemistry and New Materials for Water Treatment** *Marta Hatzell,* Christopher Gorski, T. Alan Hatton, Wendy Queen
- **New Views on Contaminant Transformation Processes** *Thomas Borch,* Huichun Zhang
- **Environmental Biogeochemistry and Anthropogenic Impacts** *Desiree Plata,* Asmeret Asefaw Berhe, Ulf Skyllberg, Lenny Winkel
- **Aquatic Sciences at the Science-Policy Interface** *Rainer Lohmann,* Laurel Schaider
- **The GRC Power Hour™**

Environmental Sciences: Water GRS
Investigating the Status of Water Quality, Technology and Distribution from Glacial Sources to Contaminated Runoff
JUN 18-19, 2022
CHAIRS: Imari Walker Karega and Adam Simpson

Enzymes, Coenzymes and Metabolic Pathways

Enzyme Mechanisms with Applications to Metabolism, Epitranscriptomics and Drug Discovery

JUL 24-29, 2022
WATERVILLE VALLEY, WATERVILLE VALLEY, NH

CHAIRS: Andrew Murkin and Lynn Abell
VICE CHAIRS: Satish Nair and Luiz Pedro Carvalho

- **Enzymology in the Innate Immune System** *Heather Hundley,* Peter Beal, Yorgo Modis, Manal Swairjo
- **Enzyme Evolution and Engineering** *Nicholas Silvaggi,* Tobias Erb, Donald Hilvert, Paola Laurino, David Sherman
- **Enzymes Involved in Post-Translational Modifications** *Walter Fast,* Sonja Lorenz, Minkui Luo, Paul Thompson
- **Inhibitor Design** *Elham Behshad,* Argyrides Argyrou, Andrew Bennet, Caren Freel Meyers
- **Conformational Effects on Catalysis and Inhibition** *Patrick Frantom,* James Fraser, Randy Kipp, John Richard
- **Enzyme Kinetics in Complex Systems** *Dhara Shah,* Swati Nagar, Matthew Robers, Bharath Srinivasan, Peter Tonge
- **Enzyme Mechanisms** *Katherine Hicks,* Squire Booker, Emily Parker, Timothy Wencewicz
- **Methodological Advances for Studying Enzymes** *Audrey Lamb,* Gabriel Lander, David Dulin, Denis Rousseau

- **Perspectives on Modulation of Enzyme Activity** *Catherine Drennan,* Carol Fierke, Paul Fitzpatrick
- **The GRC Power Hour™** *Lynn Abell*

Enzymes, Coenzymes and Metabolic Pathways

The Enzymology of Human Health, Biotechnology and the Environment

JUL 23-24, 2022

CHAIR: Tyler Stack

Epithelial Stem Cells and Niches

Tissue Stem Cell Regulation by Autonomous and Non-Autonomous Mechanisms

JUN 5-10, 2022
VENTURA BEACH MARRIOTT, VENTURA, CA

Chairs: Michael Shen and Valerie Horsley
Vice Chairs: Ophir Klein and Kim Jensen

- **Tissue Stem Cell Function** *Samantha Morris,* Nick Barker, Sarah Knox, Emi Nishimura
- **Niche Interactions** *Anjelica Gonzalez,* Carla Kim, Pantelis Rompolas
- **New Models and Technologies** *Pantelis Rompolas,* Fernando Camargo, Samantha Morris
- **Bioengineering of Stem Cells and Niches** *Rongwen Xi,* Anjelica Gonzalez, Michael Longaker, Sara Wickstrom
- **Regulation of Stem Cell Differentiation** *Shruti Naik,* Ya-chieh Hsu, Rongwen Xi
- **Stem Cell Plasticity in Development and Cancer** *Fernando Camargo,* Cedric Blanpain, Aaron Zorn
- **Immune Microenvironment** *Sara Wickstrom,* Judith Agudo, Calvin Kuo, Shruti Naik
- **Niche Dysregulation in Disease and Cancer** *Ya-chieh Hsu,* Wouter Karthaus, Mark Krasnow, Ilaria Malanchi
- **Keynote Session: Stem Cells, Niches, and Cancer** *Cedric Blanpain,* Fiona Watt, Leonard Zon
- **The GRC Power Hour™**

Epithelial Stem Cells and Niches

Epithelium Dynamics During Development, Regeneration, Disease and Aging

JUN 4-5, 2022

CHAIRS: Francesco Cambuli and David Castillo-Azofeifa

Extracellular Vesicles

Understanding Extracellular Vesicle Biogenesis and Composition for Detection and Treatment of Diseases

JUL 24-29, 2022
GRAND SUMMIT HOTEL AT SUNDAY RIVER, NEWRY, ME

CHAIRS: Paul Robbins and Kenneth Witwer
VICE CHAIRS: Esther Nolte-'t Hoen and Edit Buzas

- **Keynote Session: Physiologic and Pathologic Roles of EVs** *Edit Buzas,* Clotilde Théry, David Lyden
- **Biogenesis and Composition of EVs** *Clotilde Théry,* Deborah Goberdhan, Stanley Lemon, Crislyn D'Souza-Schorey, Anthony Ferrante
- **New Technologies for Quantitating and Analyzing EVs** *Adrian Morelli,* Louise Laurent, Shannon Stott, Juan Falcon-Perez
- **Role of Endogenous EVs in Driving Disease Pathology** *David Lyden,* Andrew Hill, Lucia Languino, Dolores Di Vizio, Jacky Goetz
- **EVs as Delivery Vehicles for Drugs and RNAs** *Andrew Hill,* Pieter Vader, Charles Lai
- **Novel Therapeutic Applications of EVs** *Jacqueline Bromberg,* Adrian Morelli, Bharat Ramratnam
- **EVs in Host-Pathogen Interactions** *Esther Nolte-'t Hoen,* Ana Torrecilhas, Arne Weiberg, Jeff Schorey, Navneet Dhillon
- **Stem Cell EVs for Regenerative Medicine** *Anastasia Khvorova,* Susmita Sahoo, Sai Kiang Lim, Benedetta Bussolati, Ewa Zuba-Surma
- **Current Clinical Trials with EVs** *Sai Kiang Lim,* Maria Brizzi, Eva Rohde
- **The GRC Power Hour™** *Edit Buzas*

Extracellular Vesicles

The Dichotomy of EVs: From Biomarkers and Purveyors of Disease to Potential Therapeutic Agents

JUL 23-24, 2022

CHAIRS: Kilean Lucas and Kyle Mentkowski

Fibroblast Growth Factors in Development and Disease

FGF Signaling: Understanding Function and Devising Therapeutic Tools

MAY 1-6, 2022
RENAISSANCE TUSCANY IL CIOCCO, LUCCA (BARGA), ITALY

CHAIRS: Mohammad Hajihosseini and Mark Lewandoski
VICE CHAIR: Amy Merrill

- **Keynote Session: Early Development, Organogenesis and Evolution** *David Ornitz,* Suzanne Mansour, Didier Stainier
- **Musculoskeletal and Craniofacial Roles** *Amy Merrill,* Marja Hurley, Timothy Saunders, David Ornitz, Andrew Wilkie
- **Interaction of FGFs with Other Signaling Pathways** *Saverio Bellusci,* Joshua Brickman, Igor Stagljar
- **Stem Cells, Tissue Regeneration and Repair** *Joshua Brickman,* Denise Al Alam, Sabine Werner, Saverio Bellusci, Helen Makarenkova
- **Structural Biology of FGFs and Novel Technologies** *Denise Al Alam,* Chiara Francavilla, Moosa Mohammadi
- **FGFs in Cancer: Mechanism, Progression and Therapy** *Fernanda Laezza,* Richard Grose, Florian Siebzehnrubl, Fen Wang
- **Metabolic Homeostasis and Endocrine Functions** *Sabine Werner,* Jarrad Scarlett, Carmine Settembre
- **FGFs in Development and Disease of the Nervous System** *Suzanne Mansour,* Martin Berghoff, Xin Zhang, Hiroshi Kawasaki
- **Intracellular-Acting and Non-Canonical FGFs** *Marja Hurley,* Fernanda Laezza, Geoffrey Pitt

Fibroblast Growth Factors in Development and Disease

Biology, Technology and Translation in FGF Research

APR 30-MAY 1, 2022

CHAIRS: Kel Vin Woo and Theresa Rauschendorfer

Flow and Transport in Permeable Media

Interactions Between Fluids, Elements, Materials, Energy and Life in Porous and Fractured Media

JUL 17-22, 2022
LES DIABLERETS CONFERENCE CENTER, LES DIABLERETS, SWITZERLAND

CHAIR: Tanguy Le Borgne
VICE CHAIR: Marc Hesse

- **Dynamics of Carbon Dioxide in the Subsurface** *Martin Blunt,* Sam Krevor, Benedicte Menez
- **Impact of Fluid and Solid Deformation on Transport and Mixing** *Marco Dentz,* Daniel Lester, Chris MacMinn, Andrew Clarke
- **Controls of Subsurface Flow and Transport on Earth's Hydrological and Geochemical Cycles** *Ilenia Battiato,* Kate Maher, James Kirchner
- **Pore Scale Physics of Multiphase and Complex Flows** *Steffen Berg,* Ryan Armstrong, Marcio Carvalho, Alex Hansen
- **Fluid Mechanics of Droplets and Bacteria** *Dani Or,* François Gallaire, Yohan Davit
- **Coupled Flow and Transport in Ice and Planetary Systems** *Jerome Neufeld,* Kenneth Golden, Christine McCarthy, Christophe Sotin
- **Non-Invasive Methods and Data Assimilation Strategies for Exploring Subsurface Processes** *Stig Niklas Linde,* Haruko Wainwright, Lee Slater
- **Fractures, Hydromechanics and Seismicity** *Ruben Juanes,* Marie Violay, François Renard, Robert Viesca
- **Soil Processes from Micro to Continental Scales** *Insa Neuweiler,* Asmeret Asefaw Berhe, John Selker
- **The GRC Power Hour™**

Flow and Transport in Permeable Media

Active and Passive Transport Processes in Biological and Geophysical Flows

JUL 16-17, 2022

CHAIRS: Amir Pahlavan and Rebecca Liyanage

Forensic Analysis of Human DNA

Leveraging Human Diversity, Data Science and Marker Discovery to Shape Future Forensic Applications

JUN 19-24, 2022
MOUNT SNOW, WEST DOVER, VT

Chairs: Sarah Seashols Williams and Steven Lee
Vice Chairs: Katherine Gettings and Titia Sijen

- **Keynote Session: Forensic Applications of New Genetic and Biomedical Technologies** *Pamela King,* Christopher Mason
- **Haploid and Alternate Autosomal Markers** *Rebecca Just,* Arwin Ralf, Daniele Podini
- **Forensic Genetic Genealogy: Inferring Identity with Long-Range Familial Searches** *Thomas Callaghan,* Fred Bieber, Debbie Kennett
- **Activity Level Research and Impact on Forensic Reporting** *Duncan Taylor, Laurence Devesse,* Roland van Oorschot, Lydie Samie-Foucart
- **Tissue Source Attribution: Epigenetic, microRNA and mRNA Approaches to Attribution** *Robin Cotton,* Cordula Haas, Hwan Lee
- **Age, Ancestry and Appearance Prediction** *Denise Syndercombe Court, Lutz Roewer,* Susan Walsh, Runa Daniel
- **Proteomic, Methylomic and Microbiomics** *Sally Harbison, Glendon Parker,* Zachary Goecker, Athina Vidaki, Baneshwar Singh
- **Bioinformatics and Data Science** *Christopher Phillips,* Rolf Ypma, Noah Rosenberg, Ellen Greytak
- **Addressing Human Factors and Cognitive Bias in Forensic DNA Analysis** *Charlotte Word, Tiffany Layne,* Melissa Taylor, David Kaye, Paul Speaker
- **The GRC Power Hour™** *Katherine Gettings*

Forensic Analysis of Human DNA

New Methods for Human Identification and Investigative Intelligence

JUN 18-19, 2022

CHAIRS: Tiffany Layne and Laurence Devesse

Fragile X and Autism-Related Disorders

Novel Technologies to Advance Discovery of Disease Mechanisms and Therapeutics for Fragile X and Autism

MAY 15-20, 2022
RENAISSANCE TUSCANY IL CIOCCO, LUCCA (BARGA), ITALY

CHAIR: Mustafa Sahin
VICE CHAIR: Kimberly Huber

- **Keynote Session: From Genes to Drugs in Neurodevelopmental Disorders** *Kimberly Huber,* Evdokia Anagnostou, Peter Kind, Tracy King
- **Genetic Heterogeneity** *Alice Luo Clayton,* Catalina Betancur, Jacquemont Jacquemont, Joel Richter
- **Convergence of Molecular Mechanisms** *Jennifer Darnell,* Nicola Allen, Barbara Bardoni, Helen Bateup
- **Human Cellular Models** *Laura Mamounas,* Robin Kleiman, Xinyu Zhao
- **Circuit Biology in Animal Models** *Emily Osterweil,* Andreas Frick, Peter Tsai, Zhaolan (Joe) Zhou
- **Human Physiology and Biomarkers** *Thomas Frazier,* Lauren Ethridge, Shafali Jeste, Charles Nelson
- **Mechanisms and Therapies for Syndromic Autism** *Michael Tranfaglia,* Michela Fagiolini, Mark Zylka, Brielle Ferguson
- **Novel Model Systems and Platforms** *Claudia Bagni,* David Hampson, Devin Binder, Gul Dolen
- **Innovative Approaches to Clinical Outcome Measures and Trial Design** *Elizabeth Berry-Kravis,* Randi Hagerman, Michelle Krishnan
- **The GRC Power Hour™** *Elizabeth Berry-Kravis, Emily Osterweil*

Fragile X and Autism-Related Disorders GRS

Lessons From Differences and Similarities in FXS and Other ASDs

MAY 14-15, 2022

CHAIRS: Sophie Thomson and Elizabeth McCullagh

Frontal Cortex NEW!

Frontal Cortex Structure and Function Across Model Systems

AUG 7-12, 2022
VENTURA BEACH MARRIOTT, VENTURA, CA

CHAIRS: Mark Laubach and Alicia Izquierdo
VICE CHAIRS: Rebecca Shansky and David Moorman

- **Functional Topography of the Frontal Cortex Across Species** *Mark Baxter,* Celine Amiez, Sarah Heilbronner
- **Sex Differences in Structure and Function** *Rebecca Shansky,* Heather Brenhouse, Mohammed Milad, Cara Wellman
- **Insights into Frontal Cortex Function from Neural Recordings** *Matthew Roesch,* Nancy Padilla-Coreano, Erin Rich, Jeremy Seamans
- **Frontal Circuits in Learning and Decision Making** *Peter Rudebeck,* Laura Bradfield, Arif Hamid, Joni Wallis
- **Aversive Processing and the Impact of Chronic Stress** *Bita Moghaddam,* Shannon Gourley, Dean Mobbs, Maria Diehl
- **Reward Processing** *Christopher Lapish,* Xinying Cai, Christine Constantinople, Gorica Petrovich
- **Frontal Cortex in Substance Use** *James Jentsch,* Kathleen Grant, Bruce Hope, Ryan LaLumiere
- **Frontal Cortex and Executive Functions** *Yogita Chudasama,* Verity Brown, Nicola Grissom, Mehdi Khamassi
- **Keynote Session: Frontal Dysfunction in Psychiatric Disease** *David Kupferschmidt,* Laura DeNardo, Nandakumar Narayanan, Angela Roberts
- **The GRC Power Hour™**

Fuel Cells

Integrating Theory, Synthesis, Characterization and Validation for the Advancement of Fuel Cell Research

JUL 24-29, 2022
BRYANT UNIVERSITY, SMITHFIELD, RI

CHAIRS: Marc Secanell and Shanna Knights
VICE CHAIRS: Iryna Zenyuk and Vojislav Stamenkovic

- **A Global Perspective on Fuel Cell Development** *Jonathan Sharman,* Siyu Ye, Rod Borup
- **Novel Oxygen Reduction Reaction Catalysts** *Plamen Atanassov,* Lior Elbaz, Arunima Singh
- **Characterizing Catalyst Activity** *Yu Morimoto,* Kateryna Artyushkova, Anthony Kucernak
- **Designing Better Solid Electrolytes** *Steven Holdcroft,* Wen Liu, Yushan Yan, Stephen Paddison
- **Novel Membrane Fabrication Approaches** *Göran Lindbergh,* Simon Thiele, Marcelo Lozada-Hidalgo
- **Understanding Material-Structure-Performance Interactions in Fuel Cell Electrodes** *Kensaku Kodama,* Adam Weber, Jeff Gostick, Paulo Ferreira
- **Technologies for a Hydrogen Economy** *Huyen Dinh,* Thomas Jaramillo, Nemanja Danilovic
- **Understanding Reactant Transport and Cell Durability** *Jasna Jankovic,* Hubert Gasteiger, Marc-Olivier Coppens, Felix Buchi
- **Advances in Polymer Electrolyte Fuel Cell Design** *Thomas Zawodzinski,* Shimshon Gottesfeld
- **The GRC Power Hour™** *Shanna Knights*

Fuel Cells GRS

Fuel Cells: From Fundamental Electrochemistry to Engineering Applied Materials

JUL 23-24, 2022

CHAIRS: Sadia Kabir and Mayank Sabharwal

Genetic Biocontrol NEW!

New Biological Platforms for Affecting Phenotype Changes for Control

JUN 26-JUL 1, 2022
FOUR POINTS SHERATON, HOLIDAY INN EXPRESS, VENTURA, CA

CHAIRS: David O'Brochta and Alfred Handler
VICE CHAIR: Omar Akbari

- **Keynote Session: Operationalizing Genetic Biocontrol** *Omar Akbari,* Kostas Bourtzis, Scott O'Neill, Andrea Crisanti
- **Inducing and Programming Sterility and Lethality for Genetic Biocontrol** *Marc Schetetig,* Givemore Muhenga, Pablo Liedo, Kevin Gorman, Maxwell Scott
- **Mechanisms and Applications of Natural and Engineered Genetic Incompatibilities** *Jeremy Herren,* Michaei Smanski, Zhiyong Xi
- **Manipulating Microbiomes to Affect Host Phenotypes** *Kostas Bourtzis,* George Dimopoulos, Jeremy Herren, Grant Hughes, Brian Weiss
- **Social and Regulatory Science as Enablers of Genetic Biological Control** *Stephanie James,* Brinda Dass, Abdoulaye Diabate, Willy Tonui, Camilla Beech
- **Manipulating Sex Determination to Affect Genetic Biocontrol** *Maxwell Scott,* Philippos Papathanos, Godana Rašic, Jake Tu, Giuseppe Saccone
- **Soft and Hard Technologies to Enable Genetic Biocontrol** *Jake Tu,* Anna Buchman, Ruth Müller, Jason Rasgon, Ernst Wimmer
- **Gene Drive Genetics and Genetic Engineering** *Ernst Wimmer,* Luke Alphey, Anthony James, Paul Thomas
- **Mathematical Modelling for Successful Genetic Biocontrol** *John Marshall,* Florence Debarre, Fred Gould, Kim Pepin, Toni Piaggio
- **The GRC Power Hour™**

Genomic Instability

Genomic Instability, DNA Repair and Human Diseases

JUL 10-15, 2022
FOUR POINTS SHERATON, HOLIDAY INN EXPRESS, VENTURA, CA

CHAIRS: Lee Zou and Michael Huen
VICE CHAIRS: Agata Smogorzewska and Kyungjae Myung

- **Keynote Session: Genetics and Genomics on Genome Instability** *J. Ross Chapman,* Andre Nussenzweig, Roger Greenberg
- **Repair of Chromosome Breaks** *Travis White,* Patrick Sung, Stephen Kowalczykowski, Maria Jasin, Tanya Paull
- **Genomic Instability and DNA Repair During the Cell Cycle** *Qing Li,* Stephen West, Larraine Symington, Hongtao Yu
- **DNA Replication and Replication Stress** *Shan Zha,* Orlando Schärer, Anindya Dutta, Bik Tye, Xiaolan Zhao
- **Transcription, R-Loops and DNA Repair** *Chetan Rawal,* Gaelle Legube, Li Lan, Dana Branzei, Lei Li
- **Chromatin Dynamics and Epigenetic Regulation of DNA Repair** *Evi Soutoglou,* Qing Li, Kyle Miller, Jun Huang, Jessica Downs
- **Emerging DNA Repair Pathways** *Kyle Miller,* Niels Mailand, Evi Soutoglou, Zhenkun Lou, Kyungjae Myung
- **DNA Repair Defects and Diseases** *Li Lan,* Shan Zha, Robert Weiss, Yosef Shiloh, Agata Smogorzewska, J. Ross Chapman
- **DNA Repair Defects and Cancer Therapy** *Justin Wai Chung Leung,* Junjie Chen, Xiaochun Yu, Binghui Shen
- **The GRC Power Hour™**

Genomic Instability GRS

The Influence of Chromosome Architecture and Cell Cycle on Repair and Maintenance of the Genome

JUL 9-10, 2022

CHAIRS: Travis White and Chetan Rawal

Geochemistry of Mineral Deposits

Geochemical Frontiers, Critical Processes and Value Formation

MAY 22-27, 2022
REY DON JAIME GRAND HOTEL, CASTELLDEFELS, SPAIN

CHAIRS: Sarah Gleeson and David Braxton
VICE CHAIR: Isabelle Chambefort

- **Big Data and Mineral Deposits** *John Vann,* Shaunna Morrison, Shawn Hood
- **Geochemistry and Fundamental Mineral-System-Forming Processes** *John Dilles,* Constantino Mpodozis, Madeleine Humphreys, Santiago Tassara, Nicholas Hayward
- **Next Generation Models** *Koen Torremans,* Juan Carlos Afonso, Stefan Luth
- **Geochemical Processes Contributory to Superior-Grade Development** *Elizabeth Holley,* Katie McFall, Brian Tattich, Alex Gysi, Andrew Wurst
- **Mining Frontiers** *Danielle Schmandt,* Melissa Anderson, Abigail Calzada-Diaz
- **Geochemistry for Discovery** *Christian Ihlenfeld,* Michael Whitbread, Iain Dalrymple, Amanda Stoltze, Simon Griffiths
- **Biological Processes and Ore Deposits** *Sylvia Sander,* Donato Giovannelli, Gordon Southam
- **Geochemistry in Value Realization and Stewardship** *Kathy Ehrig,* Karin Olson Hoal, David Barrie Johnson, Siobhan Wilson, Evelyn Mervine
- **The Future of Geochemistry of Mineral Deposits** *Natalie Caciagli,* John Thompson
- **The GRC Power Hour™**

Geochemistry of Mineral Deposits GRS

Geochemical Frontiers, Critical Processes and Value Creation

MAY 21-22, 2022

CHAIRS: Philip Rieger and Irene del Real Contreras

Graft Preservation in Heart Transplantation NEW!

Prolonged Heart Preservation: The Road From Organ Transport Toward Organ Banks

JUL 17-22, 2022
VENTURA BEACH MARRIOTT, VENTURA, CA

CHAIRS: Robert Bartlett and Cristiano Amarelli
VICE CHAIR: Andreas Zuckermann

- **A Disrupting Technology** *Jamshid Karimov,* Johan Nilsson, Judith Arcidiacono
- **DCD Donation and Ex-Situ Perfusion** *Carmelo Milano,* Stephen Large, Kumud Dhital, Hendrik Tevaearai
- **Ex-Situ Perfusion Over 24 Hours** *Bart Meyns,* Benjamin Kappler, Alvaro Rojas-Pena
- **Reconditioning the Failing Donor Grafts** *Luciano Potena,* Kiran Kush, Arne Neyrinck, Alex Manara
- **Regenerative Medicine Applied to Perfused Grafts** *Sandra Lindstedt,* Dawn Bowles, James Mc Cully
- **Immunoregulation and Regenerative Medicine Applied to Machine Perfusion** *Martin Hoogduijn,* Christine Falk, Darren Freed
- **Ex-Situ Perfusion of Abdominal Organs: Lessons From Under the Diaphragm** *Gabriel Oniscu,* Rutger Ploeg, Peter Friend
- **The Race Toward Organ Banks** *Josef Stehlik, Shaf Keshavjee,* Davide D'Alessandro, Hannah Valantine
- **Ex-Situ Perfusion and New Storage Solutions** *Sebastian Giwa,* David McGiffin, Marcus Granegger
- **The GRC Power Hour™** *Kiran Kush*

Granular Matter

Particulate Systems Across Scales: From Colloidal Science to Geophysics

JUN 26-JUL 1, 2022
STONEHILL COLLEGE, EASTON, MA

CHAIRS: Xiang Cheng and Nathalie Vriend
VICE CHAIRS: Kimberly Hill and Joshua Dijksman

- **Granular Matter in Industrial Processes** *Paul Mort,* Jeremy Lechman, Marty Murtagh
- **Active Suspensions** *Daphne Klotsa,* John Brady, Rajesh Ganapathy, Petia Vlahovska
- **Jamming and Glass Transition** *Eric Corwin,* Eric De Giuli, Jeffrey Morris
- **Dynamics and Structures of Granular Flows** *JC Tsai,* Nathan Keim, Kerstin Nordstrom, Yujie Wang

- **Impact and Cratering** *German Varas,* Hiroaki Katsuragi, Devaraj Van Der Meer
- **Discrete and Continuum Mechanics** *Ted Brzinski,* Karen Daniels, Ken Kamrin, Prabhu Nott
- **Geophysical Granular Flow** *Gert Lube,* Emily Brodsky, Chris Johnson
- **Granular Geotechnical Engineering** *Elisabeth Bowman,* Catherine O'Sullivan, Kenichi Soga, Gordon Zhou
- **Cohesion Between Generations of Granular Matter Researchers** *Cacey Bester,* Olivier Pouliquen

Granular Matter GRS

Particulate Systems Across Scales: From Colloidal Science to Geophysical Flows

JUN 25-26, 2022

CHAIRS: Ishan Srivastava and Jennifer Rieser

Green Chemistry

Chemical Sciences Driving Sustainability

JUL 24-29, 2022
REY DON JAIME GRAND HOTEL, CASTELLDEFELS, SPAIN

CHAIRS: Walter Leitner and Emilio Bunel
VICE CHAIRS: Audrey Moores and Jinlong Gong

- **Keynote Session: A Systems Approach to Green Chemistry** *Steve Howdle, Paul Anastas,* Peter Seeberger, Elsje Alessandra Quadrelli
- **Harvesting Renewable Energy with Green Chemistry** *Marcella Bonchio, John Hansen,* Greta Patzke, Yogesh Surendranath, Gonzalo Prieto
- **Designing Greener Products** *Deryn Fogg,* Christoph Guertler, Silvia Vignolini, Jakub Kostal
- **Chemical Value Chains Based on Biomass and CO2** *Yonas Chebude, David Contreras,* Mahdi Abu-Omar, Francois Jerome, Thomas Schaub
- **Valorization of Waste Material** *Heriberto Cabezas,* Adam Best, Jean-Paul Lange, Timo Repo
- **Molecular Principles and Synthetic Applications** *Carmen Claver, Mika Tamas,* Paul Chirik, Mimi Hii, Aiwen Lei, Hassan Bazzi, Eva Hevia
- **Advanced Materials** *Buxing Han,* Bruno Chaudret, Seth Darling
- **Environmentally Benign Synthesis, Processes and Products** *Martina Peters,* Christophe Darcel, Jason Tedrow, Karen Edler
- **Keynote Session: From Mechanistic Understanding to Industrial Processes** *R. Tom Baker, Philip Jessop,* Avelino Corma
- **The GRC Power Hour™** *Karen Goldberg*

Green Chemistry GRS

Mapping Green Paths to Critical Elements, Molecules and Materials

JUL 23-24, 2022

CHAIRS: Ana Patricia Pacheco and Amit Kumar

Hemostasis

Structure, Biochemistry and Physiology of Hemostasis

JUL 31-AUG 5, 2022
WATERVILLE VALLEY, WATERVILLE VALLEY, NH

CHAIRS: Sidney Whiteheart and Alan Mast
VICE CHAIR: Gow Arepally

- **Coagulation: Signaling and Structure** *Sriram Krishnaswamy,* JoAnn Trejo, Jonas Emsley, Björn Dahlbäck
- **Coagulation and Platelets** *Edward Conway,* Martha Sola-Visner, Justin Hamilton, Nicola Mutch, A. Valance Washington, Zhenyu Li
- **Maintaining Hemostatic Balance** *William Hobbs,* Marie-Christine Bouton, Huanghe Yang, A. Koneti Rao
- **Endothelium and Clotting** *Heyu Ni,* John Hwa, Courtney Griffin, Mark Kahn, Jim Crawley, Audrey Cleuren
- **Lessons of Molecular Hemostasis from Organisms that Feed on Blood** *Joshua Muia,* Mettine Bos, Ivo Francischetti, Diana Imhof
- **Coagulation and Platelets in Diseases** *Ulhas Naik,* Gustaf Edgren, Jill Johnsen, Sidney Strickland, Alisa Wolberg, Aaron Petrey
- **Late-Breaking Topics** *Gow Arepally*
- **Bleeding and Clotting Control** *Sanjana Dayal,* Colin Kretz, Weikai Li, Lindsey George, Walter Kahr, Christopher Ng
- **Keynote Session: Von Willebrand Factor and Kindlins in Bleeding Disorders** *Gary Gilbert,* Robert Montgomery, Edward Plow
- **The GRC Power Hour™** *Gow Arepally, A. Valance Washington*

Hemostasis GRS

Regulation and Molecular Dynamics of Hemostasis and Thrombosis

JUL 30-31, 2022

CHAIRS: Amy Siebert-McKenzie and Xu Han

Heterocyclic Compounds

Design, Synthesis and Application of Biologically Active Heterocycles

JUN 19-24, 2022
SALVE REGINA UNIVERSITY, NEWPORT, RI

CHAIR: R. Jason Herr
VICE CHAIR: Catharine Larsen

- **Strategic Approaches to the Preparation of Heterocyclic Natural Products** *Wei Li,* Ang Li, Margaret Brimble
- **New Approaches to Heterocyclic Compound Construction** *Sudeshna Roy,* Larry Yet, Lee Silverberg, Edward Salaski, Shanina Johnson
- **Design and Synthesis of Biologically Active Heterocycles** *Carmela Molinaro,* Brian Aquila, Stephen Greszler, Donn Wishka
- **Paradigm Shifting Synthesis Technologies** *Kevin Frankowski,* James Beck, Oliver Kappe, Kevin Moeller
- **Catalytic Methods for Heterocyclic Compound Preparation and Functionalization** *Eric Voight,* Todd Hyster, Tanja Gulder, Helene Lebel
- **New Reaction Strategies for Heterocyclic Compound Design** *Jeffrey Gustafson,* Tomas Smejkal, Carmela Molinaro, Thomas Stevenson
- **Total Synthesis of Heterocyclic Natural Products** *Matthew Cook,* Dennis Wright, Tomas Hudlicky
- **Route Optimization of Heterocyclic Compounds of Pharmaceutical Relevance** *David Lathbury,* Aaron Sather, Phillip Inglesby, Austin Smith, Maryll Geherty
- **Keynote Session: Construction of Complex Molecular Architectures** *Daniel Elbaum,* Peter Wipf, Barry Trost
- **The GRC Power Hour™** *Catharine Larsen, Sudeshna Roy*

Human Genetic Variation and Disease

Deciphering Genetic Complexity: Risk Assessment and Treatment Opportunities

JUN 5-10, 2022
SOUTHERN NEW HAMPSHIRE UNIVERSITY, MANCHESTER, NH

CHAIRS: Yana Bromberg and Olivier Lichtarge
VICE CHAIRS: Hannah Carter and Kai Tan

- **Keynote Session: Exploring Genome Perturbations in Health and Disease** *Graham McVicker,* Jean-Laurent Casanova, Adam Godzik
- **Genome Variation and COVID-19** *Benjamin Greenbaum,* Dennis Ko, Dmitry Korkin, Brent Richards, Judith Blake
- **Host Genome and Microbiome Interactions** *Angela Poole,* Emily Davenport, Alexandra Zhernakova
- **Variants in Development and Early Onset Disease** *Gary Hon,* Elizabeth Bhoj, Steven Brenner, Wendy Chung, Lucia Peixoto
- **Human Diversity and Disease** *Valerie Arboleda,* Neil Hanchard
- **Cancer Genomics** *Kuan-lin Huang,* Rachel Karchin, Anna Panchenko, Mona Singh, Itai Yanai
- **Computational Interpretation of Variants in the Clinical Context** *Constantina Bakolitsa,* Sean Mooney, Marylyn Ritchie
- **Genome Variation and Disease** *Laura Conlin,* Douglas Fowler, Martin Kircher, Predrag Radivojac, Janet Thornton
- **Precision Medicine and Genomic Privacy** *Gamze Gursoy,* Yves Moreau, Lucila Ohno-Machado
- **The GRC Power Hour™** *Anna Panchenko, Rachel Karchin*

Human Genetic Variation and Disease GRS

Building Bridges: From Variation Identification to Interpretation and Implementation

JUN 4-5, 2022

CHAIRS: Anh-Thu Lam and Timothy Bergquist

Hypothalamus NEW!

Unraveling the Complexity of the Hypothalamus from Single Molecules to Intricate Behaviors

JUL 24-29, 2022
VENTURA BEACH MARRIOTT, VENTURA, CA

CHAIRS: Michael Krashes and Dayu Lin
VICE CHAIRS: Matt Carter and Alexander Jackson

- **Keynote Session: The Hypothalamus From Individual Molecules to Sophisticated Behaviors** *Charles Bourque,* Seth Blackshaw, Catherine Dulac
- **Hypothalamus and Complex Social and Inter-Species Behavior** *Nirao Shah,* Annegret Falkner, Susana Lima, Xiaohong Xu
- **Hypothalamic Plasticity** *Zheng Li,* Jaideep Bains, Marcelo Dietrich
- **Hypothalamus and Ingestive Behavior** *Garret Stuber,* Amber Alhadeff, Lisa Beutler, Yuki Oka
- **Rhythms in the Hypothalamus** *Luis De Lecea,* Elena Gracheva, David Prober
- **Hypothalamic Development, Cell Type Taxonomy and Architecture** *Larry Swanson,* Tibor Harkany, Deborah Kurrasch, John Campbell
- **Hypothalamic Dysfunction** *Clifford Saper,* Gul Dolen, Giles Yeo
- **The Neuroendocrine Hypothalamus** *Holly Ingraham,* Christian Broberger, Stephanie Correa, Jenna McHenry
- **The Hypothalamus and the Brain-Body Interface** *Sabrina Diano,* Diego Bohorquez, Jeremy Borniger
- **The GRC Power Hour™**

Image Science

Emerging Imaging Techniques at the Intersection of Physics and Data Science

JUN 5-10, 2022
GRAND SUMMIT HOTEL AT SUNDAY RIVER, NEWRY, ME

CHAIR: Rafael Piestun
VICE CHAIR: Jannick Rolland

- **Information Extraction via Computational Imaging** *Matthew Kupinski,* Roarke Horstmeyer, Sjoerd Stallinga
- **Quantum Imaging** *George Barbastathis,* Dan Oron, Nick Vamivakas
- **Artificial Intelligence in Image Science** *Chris Dainty,* George Barbastathis, Aydogan Ozcan
- **Multimodal and Biomedical Imaging** *Kyle Myers,* Sophie Brasselet, Amy Oldenburg, David Sampson
- **Inverse Problems in Imaging** *Richard Paxman,* Mini Das, Demetri Psaltis
- **Imaging in Emerging Consumer Applications** *Joyce Farrel,* Kaan Aksit
- **Astronomical and Space Imaging** *Thomas Bifano,* Jeff Khun, Meredith Kupinski
- **Eyes and Vision** *Jannick Rolland,* Kristina Irsch, Hakan Ürey, Brian Wandell
- **Novel Lensless Imaging** *Sophie Brasselet,* Laura Waller
- **The GRC Power Hour™**

Image Science GRS

Image Acquisition, Processing and Visualization

JUN 4-5, 2022

CHAIRS: Raman Saggu and Dennis Gardner

Immunochemistry and Immunobiology

Immune System in Health, Disease and Therapy

JUN 5-10, 2022
REY DON JAIME GRAND HOTEL, CASTELLDEFELS, SPAIN

CHAIR: Facundo Batista
VICE CHAIR: Alexander Rudensky

- **Keynote Session: Immune Responses** *Alexander Rudensky,* Jason Cyster, Gillian Griffiths
- **Immune Cells Trafficking and Activation** *Jason Cyster, Matteo Iannacone,* Ronald Germain, Hai Qi, Michael Sixt, Gabriel Victora
- **Gene Programming of Immune Cells** *Hai Qi, Alison Ringel,* Thomas Boehm, Laura Mackay, Gioacchino Natoli, Nir Yosef
- **Immunoregulation** *Laura Mackay, Gioacchino Natoli,* Burkhard Becher, Ken Murphy, Jamie Spangler
- **Immune Responses to Vaccine and Infection** *Carola Vinuesa,* Matteo Iannacone, Antonio Lanzavecchia, Federica Sallusto
- **Immunity at Mucosal Sites** *Federica Sallusto,* Janelle Ayres, Douglas Kwon, Dan Littman
- **Sensors, Microbes and Inflammation** *Antonio Lanzavecchia, Andrea Schietinger,* Greg Barton, Sun Hur, Carla Rothlin
- **Integrative Immunology** *Dan Littman, Carla Rothlin,* Ana Domingos, Asya Rolls, Carola Vinuesa
- **Tumor Immunity** *Asya Rolls, Jamie Spangler,* Morgan Huse, Alison Ringel, Andrea Schietinger

Immunochemistry and Immunobiology GRS
Fusing Fields: Cross-Discipline Approaches to Probe and Modulate the Immune System
JUN 4-5, 2022
CHAIRS: Asheley Chapman and Veronica Davé

Immunoengineering NEW!

Immunomodulation Based on Cells, Therapies and Microenvironments

JUL 10-15, 2022
VENTURA BEACH MARRIOTT, VENTURA, CA
CHAIRS: Rebecca Pompano and Bali Pulendran
VICE CHAIRS: Susan Thomas and Madhav Dhodapkar

- **Keynote Session: Modulating Immunity for Human Health** *Susan Thomas, Madhav Dhodapkar,* Kathrin Jansen, Darrell Irvine, Melody Swartz
- **Growth Areas in Immunology: Human Immunity** *Onyinye Iweala,* Mark Davis, Bana Jabri, Marco Colonna
- **Systems and Computational Immunology** *Kathryn Miller-Jensen,* Christina Leslie
- **Molecularly Engineered Immunotherapies** *Bruno Correia,* Janine Schuurman, George Georgiou, Mariana Kaplan
- **In Vitro Models of Immunity** *Hyun Jung Kim,* Britta Engelhardt, Linda Griffith
- **Biomaterials for Vaccines and Immunomodulation** *Jamal Lewis,* Martin Bachmann, Ed Botchwey, Suzie Pun, David Mooney
- **Enabling Micro-Technologies to Assess Immune Cell Function** *Armon Sharei,* Daniel Irimia, Junsang Doh
- **Cellular Immunoengineering** *Elizabeth Wayne,* Wilson Wong, Yvonne Chen, Krishnendu Roy
- **Transformative Tools: Spatially Resolved Analysis for Immunology** *Pamela Chang,* Deborah Fowell, Garry Nolan
- **The GRC Power Hour™**

Immunometabolism in Health and Disease NEW!

Basic and Translational Cellular Metabolism in Immunity

JUN 19-24, 2022
BRYANT UNIVERSITY, SMITHFIELD, RI
CHAIRS: Michael Fessler and Hongbo Chi
VICE CHAIRS: Jeff Rathmell and Catherine Hedrick

- **Repurposing of Bioenergetics in Innate Immunity** *Julie Magarian Blander,* Luke O'Neill, Edward Pearce, Maxim Artyomov
- **Metabolic Programming of Lymphocyte Function** *Peer Karmaus,* Mark Boothby, Vijay Kuchroo, Erika Pearce, Claudia Kemper
- **Metabolic-Epigenetic Crosstalk in Immunity** *Nancie Maciver,* Mihai Netea, Jason Locasale, Russell Jones
- **Sterols in Immunity** *Peter Ghazal,* Steven Bensinger, Alan Tall, Chenqi Xu, Ping-Chih Ho
- **Metabolic Programming in Autoimmune and Inflammatory Diseases** *Erika Pearce,* Laurence Morel, Navdeep Chandel, Cornelia Weyand
- **Immunometabolism of the Tumor Microenvironment** *Brent Hanks,* Juan Cubillos-Ruiz, Ming Li, Weiping Zou
- **Metabolism in Host Defense** *Sebastian Riquelme,* Julie Magarian Blander, Peter Ghazal, Janelle Ayres
- **Cell Fate in Immunity and Metabolic Disease** *Lisa Bouchier-Hayes,* Douglas Green, Gerald Shadel, Ira Tabas, Gokhan Hotamisligil
- **Emerging Opportunities for Intervening Upon Immunometabolism in Disease** *Ana Mora,* Ed Driggers, Richard Siegel, Bruce Blazar
- **The GRC Power Hour™** *Ana Mora, Claudia Kemper*

In Vivo Magnetic Resonance

Identifying the Next 20 Years of Need in In Vivo MR

JUL 17-22, 2022
PROCTOR ACADEMY, ANDOVER, NH
CHAIR: Jeff Dunn
VICE CHAIR: Kim Butts Pauly

- **Keynote Session: Magnetic Resonance: Opportunities for Breakthroughs in New Research Areas** *Michael Smith,* Joseph Ackerman, Charles Springer
- **Engineering the Future of Magnetic Resonance Technology** *Andrew Webb,* Clarissa Cooley, Jan Korvink, Christoph Juchem
- **Multimodal MRI: New Data from New Combinations** *Sharmila Majumdar,* Blaise Frederick, Vesna Sossi
- **Embracing Machine Learning and Graphics for MR Processing and Visualization** *Cornelia Laule,* Nicole Seiberlich, Valentina Pedoia
- **Microimaging: Pushing the Limits with High Field** *Stephen Blackband,* Samuel Grant, Klaus Scheffler
- **Novel Biomedical Targets for the Application of Magnetic Resonance** *Elaine Bearer,* Helene Benveniste, Youssef Zaim Wadghiri, Catherine Lebel
- **Magnetic Resonance for Visualizing the Unusual: MSK from Equine to Mixed Reality** *Joel Garbow,* Sarah Pownder, Brian Hargreaves
- **Methods and Sequences for Acquiring Magnetic Resonance Data** *Jurgen Hennig,* Moritz Zaiss, Claudia Prieto, Jan-Bernd Hovener
- **MRI for Space Research and Medicine** *Daniel Sodickson,* Rachael Seidler, Gordon Sarty
- **The GRC Power Hour™** *Melissa Haskell, Kim Butts Pauly*

In Vivo Magnetic Resonance GRS
Identifying the Next 20 Years of Need in In Vivo MR
JUL 16-17, 2022
CHAIRS: Manushka Vaidya and Melissa Haskell

In Vivo Ultrasound Imaging NEW!

Advances in New Ultrasonic Imaging Modes and Imaging Techniques Undergoing Clinical Evaluation

AUG 14-19, 2022
VENTURA BEACH MARRIOTT, VENTURA, CA
CHAIRS: Michael Oelze and Kenneth Hoyt
VICE CHAIRS: Michael Kolios and Oliver Kripfgans

- **Beamforming and Speckle Reduction** *Jeremy Dahl,* Alfred Yu, Brett Byram, Muyinatu Bell
- **Super-Resolution Ultrasound Imaging** *Mickael Tanter,* Olivier Couture, Kirsten Christensen-Jeffries, Pengfei Song
- **Development of Novel Contrast Agents** *Christy Holland,* Mark Borden, Agata Exner, Klazina Kooiman
- **Tissue Biomarkers and Tissue Characterization** *Kevin Parker,* Gregory Czarnota, Jonathan Mamou, Kibo Nam
- **Ultrasound Elasticity Imaging** *Kathy Nightingale,* Marvin Doyley, Caterina Gallippi, Guy Cloutier
- **Photoacoustic Imaging** *Roger Zemp,* Sarah Burris, Carolyn Bayer, Sarah Bohndiek
- **Ultrasound Tomography** *Roberto Lavarello,* James Wiskin, Neb Duric, Nicole Ruiter
- **Ultrasound Therapy** *Flordeliza Villanueva,* John Eisenbrey, Hong Chen, Kevin Hayworth
- **Neuromodulation Using Ultrasound** *Elisa Konofagou,* Merritt Maduke, Charles Caskey, Emad Ebbini
- **The GRC Power Hour™**

Industrial Ecology

Advancing the Circular Economy for Human and Planetary Wellbeing

JUN 12-17, 2022
GRAND SUMMIT HOTEL AT SUNDAY RIVER, NEWRY, ME
CHAIR: Anu Ramaswami
VICE CHAIR: Ming Xu

- **Frontiers of Industrial Ecology to Inform Sustainable Circular Economy Transitions** *Valerie Thomas,* Stefanie Hellweg
- **Scaling Up a Sustainable Circular Economy: Opportunities and Conundrums** *Nabil Nasr,* Raimund Bleischwitz, Hervé Corvellec
- **Advances in Methods: Circular Flows and Life Cycle Assessment** *Tomer Fishman,* Arnold Tukker, Shweta Singh, Stefan Pauliuk, Weslynne Ashton
- **Advances in Methods: Circular Flows, Socioeconomic Metabolism and Impact Modeling** *Alissa Kendall,* Bing Zhu, Gara Villalba Mendez
- **Circular Economy Concepts for Zero-Carbon Communities** *Shoshanna Saxe,* Heinz Schandl, Kangkang Tong
- **Circular Economy: Food and the Food-Energy-Water Nexus** *Yuanchao Hu,* Bruno Basso, Ramzy Kahhat, Callie Babbitt, Joe Bozeman
- **Implementing the Circular Economy in Industrial Systems and Processes** *Bhavik Bakshi,* Gregory Keoleian, Yuan Yao, Vered Blass
- **Advances of Circular Economy and Plastics Pollution** *Ming Xu,* Sangwon Suh, Yong Sik Ok, Paul Mativenga, Amy Landis
- **Circular Economy and Water Sustainability** *Elias Ayuk,* Ligy Philip, Zhiyong Jason Ren
- **The GRC Power Hour™** *Ming Xu, Callie Babbitt*

Industrial Ecology GRS
Turning Research into Practice: Complexities of Industrial Ecology Implementation
JUN 11-12, 2022
CHAIRS: Joe Bozeman III and Alexandra Westin

Inorganic Chemistry

Using the Versatility of Inorganic Elements to Address Grand Challenges in Health, Energy and the Environment

MAY 29-JUN 3, 2022
SALVE REGINA UNIVERSITY, NEWPORT, RI
CHAIR: Amy Prieto
VICE CHAIR: Jacqueline Veauthier

- **Harnessing Reactivity** *Andrew Borovik,* Fabian Dielmann, George Stanley
- **The Heavy Elements** *Justin Walensky,* Susanne Barth, Stosh Kozimor, Marinella Mazzanti, Eric Schelter
- **Interfacing Metals and Biology** *Elisa Tomat,* Marcetta Darensbourg, Emily Que
- **Modes of Bonding** *Tracy Lohr,* Francois Gabbai, Laurel Schafer, Mitch Smith, Theodore Betley
- **Spanning Molecules to Solids** *Natalia Shustova,* Bart Bartlett, Raffaella Buonsanti
- **Condensed Matter and Its Applications** *Evgeny Dikarev,* Jakoah Brgoch, Susan Kauzlarich, Lisa McElwee-White
- **Physical Inorganic Chemistry** *Nancy Haegel,* Kyle Lancaster, Joshua Vura-Weis, Ping Yang
- **Energy Production and Storage** *Bart Bartlett,* James Mayer, Hailiang Wang
- **Inorganic Chemistry as a Driver of Innovation** *Jacqueline Veauthier,* Polly Arnold, T. Don Tilley
- **The GRC Power Hour™** *Jacqueline Veauthier*

Inorganic Chemistry GRS
Applications of Inorganic Molecules and Materials in Magnetism, Catalysis and Energy Storage
MAY 28-29, 2022
CHAIRS: Avery Baumann and Trevor Latendresse

Intermediate Filaments

Linking the Cytoskeleton and Nucleus in Mechanobiology, Ageing, and Disease

JUN 5-10, 2022
MOUNT SNOW, WEST DOVER, VT

CHAIRS: Jan Lammerding and Roy Quinlan
VICE CHAIRS: Elly Hol and Howard Worman

- **Visualizing Filament Organization and Dynamics at the Nanoscale** *Harald Herrmann,* Birgit Lane, Ohad Medalia, Jennifer Lippincott-Schwartz
- **Functional Insights into the Structure and Biophysics of Intermediate Filaments** *Natasha Snider,* Elaine Fuchs, Christopher Bunick, Sarah Koester, Steve McKnight
- **Signaling and Cytoskeletal Crosstalk by Intermediate Filaments** *Sandrine Etienne-Manneville,* Gaudenz Danuser, Ming Guo, Pierre Thibault, John Eriksson
- **Connecting the Nucleus, Cytoskeleton and Extracellular Environment** *Gregg Gundersen,* Catherine Shanahan, Daniel Starr, Kathleen Green
- **Integration of Muscle Mechanobiology by Intermediate Filaments in Health and Disease** *Dennis Discher,* Benjamin Prosser, Shenhav Cohen, Brian Glancy
- **Linking Intermediate Filaments to Neurodegenerative Diseases** *Ronald Liem*, Pascale Bomont, Sanjay Kumar, Jean-Pierre Julien, Milos Pekny
- **Progenitors, Senescence and Cancer** *Dennis Roop,* Ganna Bilousova, Andy Xiang, Pierre Coulombe
- **Mechanistic Insights into Intermediate Filament Diseases** *Cecilia Sahlgren,* Nicole Schwarz, Dolores Perez-Sala, Kurt Zatloukal, Karen Ridge
- **Emerging Therapeutic Approaches for Intermediate Filament-Based Diseases** *Gisele Bonne,* Lori Wallrath, Stephen Young, Colin Stewart
- **The GRC Power Hour™**

Intermediate Filaments GRS

Bridging the Gap Between Molecules and Tissue: How Intermediate Filaments Affect our Health

JUN 4-5, 2022

CHAIR: Rebecca de Leeuw

Intrinsically Disordered Proteins

The Functional Role of Disorder in Biological Systems

JUN 26-JUL 1, 2022
LES DIABLERETS CONFERENCE CENTER, LES DIABLERETS, SWITZERLAND

CHAIRS: Elizabeth Rhoades and Philipp Selenko
VICE CHAIRS: Birthe Kragelund and Tanja Mittag

- **Keynote Session: Mechanisms of IDPs in Signalling** *Birthe Kragelund,* Vincent Hilser, Martha Cyert
- **Functional Mechanisms of IDPs** *Lucia Chemes,* Carrie Partch, Jennifer Hurley, Antonina Roll-Mecak
- **Tools and Methods for IDPs** *Edward Lemke,* Kresten Lindorff-Larsen, Cesar Cuevas-Velazquez, Andrea Soranno, Samrat Mukhopadhyay
- **IDPs in Disease** *Perdita Barran,* Carlos Castaneda, Lucia Chemes, Hoi Sung Chung, Toby Gibson
- **Evolution and Proteomics** *Toby Gibson,* Allan Drummond, Agnes Toth-Petroczy, Paula Picotti
- **Biomolecular Condensates and Biomaterials** *Samrat Mukhopadhyay,* Ali Miserez, Shana Elbaum-Garfinkle, Lucas Pelkmans, Felipe Quiroz, Joan-Emma Shea
- **Dynamic Ensembles** *Peter Wright,* Shahar Sukenik, Katherine Aurelia Ball, Hagen Hofmann
- **IDPs in the Nucleus** *Keith Dunker,* Ibrahim Cisse, Lucia Strader, Sara Cuylen-Haering, Shasha Chong, Liesbeth Veenhoff
- **Keynote Session: Dynamic Ensembles** *Tanja Mittag,* Martin Blackledge, Jane Dyson
- **The GRC Power Hour™** *Martha Cyert, Lucia Strader*

Intrinsically Disordered Proteins GRS

How Life Harnesses Disorder: Emergent Functions of IDPs in Cells, Materials and Medicine

JUN 25-26, 2022

CHAIRS: Alexander Chin and Erik Martin

Ion Channels

Molecular Mechanisms of Electrical Signaling in Health and Disease

JUL 10-15, 2022
MOUNT HOLYOKE COLLEGE, SOUTH HADLEY, MA

CHAIR: Brad Rothberg
VICE CHAIRS: Teresa Giraldez and Baron Chanda

- **Keynote Session: Ion Channels in Excitable Cells** *Teresa Giraldez,* Sudha Chakrapani, Roderick MacKinnon
- **Anion Channels in Health and Disease** *Alessio Accardi,* Anne Carlson, Merritt Maduke, Zhaozhu Qiu, Jue Chen
- **Mechanisms of Voltage-Sensing and Gating** *Baron Chanda,* Jian Payandeh, Kenton Swartz, Eduardo Perozo, Crina Nimigean
- **Dynamic Approaches to Bridge Structure and Function** *William Kobertz,* Chris Ahern, Stephanie Heusser, Simon Scheuring
- **Cardiac Ion Channels and their Modulation** *David Jones,* Peter Larsson, Cathy Proenza, Jianmin Cui, Gail Robertson
- **Calcium Channel Complexes and Cell Signaling** *Ivy Dick,* Jean-Ju Chung, Henry Colecraft, Amy Lee, Claudia Moreno
- **Channel Pharmacology and Channelopathies** *Valeria Vasquez,* Paul Slesinger, Stephen Tucker, Andrea Bruggemann, Andrea Meredith
- **Glutamate Receptors from Structure to Synapse** *Vasanthi Jayaraman,* Hiro Furukawa, Ingo Greger, Gabriela Popescu, Lonnie Wollmuth, Andrew Plested
- **TRP and Other Sensory Channels** *Vera Moiseenkova-Bell,* Sebastian Brauchi, Vanessa Ruta, Elena Gracheva, Lejla Zubcevic, Martin Chalfie, Julio Cordero-Morales
- **The GRC Power Hour™**

Ion Channels GRS

Molecular Mechanisms of Electrical Signaling in Health and Disease

JUL 9-10, 2022

CHAIRS: Alexandria Miller and Valeria Kalienkova

Ionic Liquids

Linking Ionic Liquid Structure, Reactions and Applications Across Temperature

AUG 7-12, 2022
GRAND SUMMIT HOTEL AT SUNDAY RIVER, NEWRY, ME

CHAIR: Paul Trulove
VICE CHAIR: Jared Anderson

- **Keynote Session: The Future of Ionic Liquids** *Robert Mantz,* Tom Welton, Mark Shiflett
- **Natural and Synthetic Polymers** *Luke Haverhals,* David Durkin, Stephen Paddison
- **Linking Biology and Ionic Liquids** *Paula Berton,* Patrick Dennis, Eden Tanner
- **Electrochemical Applications of Ionic Liquids** *Hunaid Nulwala,* Jesse McDaniel, Cristina Pozo-Gonzalo
- **Ionic Liquids Beyond the Boundaries** *Sheng Dai,* James Davis, Claudio Margulis, Isiah Warner
- **The Interface Between Ionic Liquids and Deep Eutectic Solvents** *Burcu Gurkan,* Isabel Marrucho, Karen Edler, Malgorzata Swadzba-Kwasny
- **Structure-Property Relationships in Ionic Liquids** *Hugh De Long,* Ralf Ludwig, Edward Maginn, Joan Brennecke
- **Ionic Liquids in Future Sustainable Technologies** *Jason Hallett,* Jason Bara, Agnieszka Brandt-Talbot, Nolene Byrne, Elizabeth Biddinger
- **Late-Breaking Topics** *Jared Anderson*
- **The GRC Power Hour™** *Burcu Gurkan, Jared Anderson*

"GRCs are an excellent mechanism for building communities that support career advancement for junior and senior scientists alike. GRCs in recent years have helped promote diversity and inclusion among their participants."

DR. CYNTHIA BURROWS, University of Utah

Ionic Liquids GRS

Linking Ionic Liquid Structure, Reactions and Applications Across Temperatures

AUG 6-7, 2022

CHAIRS: Emmanuel Varona-Torres and Hemant Choudhary

Lignin

Realizing Lignin's Potential in Biorefining by Bridging Plant Biology, Chemistry and Engineering

JUL 31-AUG 5, 2022
STONEHILL COLLEGE, EASTON, MA

CHAIRS: Yuriy Román and Katalin Barta
VICE CHAIRS: Laura Bartley and Jeremy Luterbacher

- **Keynote Session: Converging Disciplines for the Sustainable Valorization of Lignin** *Jeremy Luterbacher,* Lacey Samuels, Bert Weckhuysen
- **Methods to Tailor Lignin Biosynthesis In Planta** *Claire Halpin,* Taku Demura, Aymerick Eudes, Shinya Kajita, Ohkamae Park
- **Designing Enzymatic Systems for Lignin Depolymerization** *Taina Lundell,* Davinia Salvachua, Steven Singer, Takashi Watanabe
- **Catalytic Lignin Depolymerization and Upgrading** *Seema Singh,* Emiel Hensen, Roberto Rinaldi, Chen Zhao
- **Convergent Microbial Lignin Conversion Strategies** *Timothy Donohue,* Tim Bugg, Lindsay Eltis, Guillermina Hernandez Raquet
- **Lignin from an Industrial Perspective** *Jean-Pierre Lindner,* Raymond Buser, Michael Rushton, Karolien Vanbroekhoven, Christian Dahlstrand, Ian Klein, Sander Van den Bosch
- **Tools and Methods for the Analysis, Visualization and Structural Elucidation of Lignin** *Yuki Tobimatsu,* Simon Hawkins, Susannah Scott, Tuo Wang
- **Tailoring Chemical Routes for the Synthesis of Direct and Functional Replacement Products from Lignin** *Pieter Bruijnincx,* Martin Lawoko, Mojgan Nejad, Chris Saffron, Ning Yan
- **Incorporating Process Engineering in the Lignin Upgrading Workflow** *Sankar Nair,* Christos Maravelias, Junyong Zhu
- **The GRC Power Hour™** *Claudia Crestini, Rebecca Smith*

Lipidomics NEW!

Lipidomics and Decoding Life: From the Technology and Biology Landscapes to Clinical Adaptation

AUG 7-12, 2022
JORDAN HOTEL AT SUNDAY RIVER, NEWRY, ME

CHAIRS: John Bowden and Kim Ekroos
VICE CHAIRS: Gerhard Liebisch and Xianlin Han

- **Lipidomics in Decoding Biology** *William Griffith,* Scott Summers, Vytas Bankaitis
- **Lipidomics in Human Health and Disease** *Edward Dennis,* Michal Holcapek, Michael Kiebish, Gilbert Di Paolo
- **Harmonization and Standardization in Lipidomics** *Valerie O'Donnell,* Martin Giera, Markus Wenk, Jeffrey McDonald
- **Novel Lipidomic Mass Spectrometry Strategies** *Christer Ejsing,* Shane Ellis, Christoph Thiele, André Nadler

- **Clinical and Translational Lipidomics** *Veronica Anania,* Daisuke Saigusa, Livia Eberlin
- **Lipidomics Data Dimensions and Biological Interpretation** *John McLean,* Erin Baker, Steffany Bennett, Andrej Shevchenko, Yu Xia
- **Resolving Lipid Metabolic Networks** *Gavin Reid,* Nathan Hatcher, Jace Jones, Charles Serhan
- **Role of the Environment on the Lipidome** *Nancy Denslow,* Laila Abdullah, Jeremy Koelmel, Kuniyuki Kano
- **Integration of Lipidomics with Genomics, Proteomics and Metabolomics** *Harald Koefeler,* Bjoern Titz, Peter Meikle
- **The GRC Power Hour™** *Erin Baker*

Lipoprotein Metabolism

New Lipid and Lipoprotein Genes, Pathways and Therapies

JUN 5-10, 2022
SOUTHBRIDGE HOTEL & CONFERENCE CENTER, SOUTHBRIDGE, MA
CHAIRS: M. Mahmood Hussain and Kiran Musunuru
VICE CHAIRS: Marlys Koschinsky and Daisy Sahoo

- **Keynote Session: Genetics of Lipids and Cardiovascular Disease** *Marlys Koschinsky,* Sekar Kathiresan
- **The Lipoprotein Lipase Pathway** *Ira Goldberg,* Anne Beigneux, Karin Bornfeldt, Sander Kersten, Xiao Wang
- **Therapeutic Approaches to Modulate Plasma Lipids and Lipoproteins** *Mary Sorci-Thomas,* Marina Cuchel, Bruce Given, Viktoria Gusarova, Richard Lee
- **Noncoding RNAs in Lipoprotein Metabolism** *Katey Rayner,* Kathryn Moore, Muredach Reilly, Tamer Sallam, Yajaira Suarez
- **Lipid Metabolism in Adipose Tissue** *Loredana Quadro,* Robert Farese, Susan Fried, Sujith Rajan, Judith Storch
- **The Post-Genomic Era in Lipoprotein Metabolism** *Masahiro Koseki,* Robert Bauer, Mary Haas, Elizabeth Tarling, Noam Zelcer
- **Permanent Modification of Lipid Levels** *Daisy Sahoo,* Alexandra Chadwick, Steven Farber, Lily Hoffman-Andrews, Klaus Ley
- **Lipoproteins** *Gissette Reyes-Soffer,* Ashira Blazer, Edward Fisher, Roop Mallik, Nathalie Pamir, Lloyd Ruddock, Shadab Siddiqi
- **Cutting-Edge Technologies for Lipid and Lipoprotein Research** *Qing Miao,* Chiara Giannarelli, Alan Remaley
- **The GRC Power Hour™** *Marlys Koschinsky, Daisy Sahoo*

Lipoprotein Metabolism GRS

Molecular Mechanisms of Lipid Metabolism in Health and Disease

JUN 4-5, 2022

CHAIR: Paul Li-Hao Huang

Liquid Biopsy for Cancer

JUN 19-24, 2022
MOUNT HOLYOKE COLLEGE, SOUTH HADLEY, MA
CHAIRS: Klaus Pantel and Shana Kelley
VICE CHAIRS: Min Yu and Rosandra Kaplan

- **Grand Challenges in Liquid Biopsy Research** *Min Yu,* Howard Scher
- **The Biology Behind Liquid Biopsy Biomarkers** *Rosandra Kaplan,* John Condeelis, Jacky Goetz, Jean Paul Thiery
- **Genotypic CTC and ctDNA Analysis** *Daniel De Carvalho,* Wai Kei Jacky Lam, Jacqui Shaw, Brian Dougherty
- **Phenotypic and Functional Analysis for Liquid Biopsy** *Wai Kei Jacky Lam,* Nicola Aceto, Matt Trau, Catherine Alix-Panabieres, Ryan Sullivan
- **High Performance Analytical Technologies for Liquid Biopsy** *Shannon Stott,* Amy Herr, Daniel Chiu, Vanessa Jonsson
- **Liquid Biopsy and Clinical Utility** *Harriet Wikman,* Andrew Armstrong, Alison Allan, Ellen Heitzer, Ralph Graeser
- **Early-Career Investigator Presentations** *Amy Herr*
- **Extracellular Vesicles** *Catherine Alix-Panabieres,* David Lyden, Yong Zeng, Shannon Stott
- **New Liquid Biopsy Biomarkers** *Alison Allan,* Michael Sixt, Daniel Chiu, Harriet Wikman
- **The GRC Power Hour™**

Liquid Biopsy for Cancer GRS

Emerging Liquid Biopsy Technologies for Early Detection, Disease Profiling and Monitoring of Cancer

JUN 18-19, 2022

CHAIRS: Fredrik Thege and Nykia Walker

Lysosomes and Endocytosis

Physiological Adaptations of the Endo-Lysosomal System

JUN 19-24, 2022
PROCTOR ACADEMY, ANDOVER, NH
CHAIR: Christopher Burd
VICE CHAIR: Phyllis Hanson

- **Lysosomes and the Control of Cellular Metabolism** *Suzanne Pfeffer, Robert Piper,* Andrea Ballabio, Erik Jorgensen, Jennifer Stow
- **The Endo-Lysosomal System and Disease** *Scott Emr, Leon Murphy,* Rushika Perera, Marco Sardiello, Harald Stenmark, Joseph Mindell
- **Entering Cells** *Lauren Jackson, Frances Brodsky,* Gunther Hollopeter, Min Wu
- **Inter-Organelle and Inter-Cellular Communication** *Philip Stahl,* Sandra Cristina Paiva, Guillaume van Niel, Meng Wang, Lois Weisman, Roberto Zoncu
- **Roles of the Endosomal Network in Organismal Physiology** *Tomas Kirchhausen, Margaret Robinson,* Max Gutierrez, Francesca Peri, Avital Rodal
- **The Lysosome, Autophagy and Cellular Catabolism** *Markus Babst, James Hurley,* Florian Froehlich, Thomas Melia, Anne Simonsen, Michael Overholtzer
- **Late-Breaking Topics** *Alexander Sorkin,* Michael Bassik, Yamuna Krishnan
- **Sorting and Trafficking in the Endosomal Network** *Elizabeth Conibear,* Juan Bonifacino, Michael Marks, Andreas Mayer, Peter Cullen
- **Lysosome-Like Organelles** *Fred Maxfield,* Graca Raposo
- **The GRC Power Hour™** *Sandra Cristina Paiva, Phyllis Hanson*

Lysosomes and Endocytosis GRS

Physiology, Functions and Interactions of the Endo-Lysosomal System in Health and Disease

JUN 18-19, 2022

CHAIR: Roni Levin Konigsberg

Mammalian Reproduction

From Regulatory Mechanisms to Practical Applications

AUG 14-19, 2022
MOUNT SNOW, WEST DOVER, VT
CHAIRS: Margaret Petroff and Kyle Orwig
VICE CHAIRS: Richard Freiman and Joan Jorgensen

- **Building Blocks for Reproduction: Eggs, Sperm and Uterus** *Julie Kim,* Francesca Duncan, Stefan Schlatt, Thomas Spencer
- **Stem Cells in Reproductive Processes** *Robin Hobbs,* Katsuhiko Hayashi, Margherita Turco, Ina Dobrinski
- **Developmental Biology and Sex Determination** *Lane Christenson,* Helen Jones, Diana Laird, Fei Zhao
- **Internal and External Influences on Reproduction** *Miguel Brieño-Enriquez,* Sean Limesand, Sherman Silber, James Turner, Ans Van Pelt
- **Bioengineering for Improving Reproductive Outcomes** *Monica Laronda,* Jon Oatley, Anthony Perry, Ariella Shikanov
- **Immune Function in Reproductive Biology** *Tony De Falco,* Maria Battistone, Jannette Dufour, Tippi MacKenzie, Dorothy Sojka
- **Reproduction in the Age of Omics** *John Schimenti,* Pat Lonergan, Roser Vento-Tormo, Miles Wilkinson
- **Molecular and Genetic Control of Reproduction** *Sue Hammoud,* Nehemia Alvarez, Sarah England, Chen Chen
- **Keynote Session: Determinants of Reproductive Outcomes and Disease** *Richard Freiman, Joan Jorgensen,* Asgerally Fazleabas, Mary Ann Handel
- **The GRC Power Hour™**

Mammalian Reproduction GRS

Safeguarding Fertility for the Present and Future

AUG 13-14, 2022

CHAIRS: Margeaux Marbrey and Klementina Fon Tacer

Mammary Gland Biology

Normal Breast Biology and Its Relationship to Breast Cancer Initiation and Progression

MAY 29-JUN 3, 2022
RENAISSANCE TUSCANY IL CIOCCO, LUCCA (BARGA), ITALY
CHAIRS: Maria Vivanco and Beatrice Howard
VICE CHAIRS: Russell Hovey and Senthil Muthuswamy

- **Keynote Session: Breast Stem Cell Biology** *Barry Gusterson,* Connie Eaves
- **Normal Breast Biology: Progenitor and Stem Cells** *Renee Van Amerongen,* Marja Mikkola, Pamela Cowin, Lone Ronnov-Jessen
- **Abnormal Breast Biology: Precancerous Lesions (DCIS)** *Fariba Behbod,* Louise Jones, Jelle Wesseling
- **Heterogeneity in Breast Cancer** *Walid Khaled,* Rama Khokha, Joan Brugge, Helen Piwnica-Worms
- **Molecular Alterations During Pregnancy and Lactation** *Russell Hovey,* Carles Lerin, Natalie Shenker
- **Residual Disease and Metastasis** *Eva Gonzalez-Suarez,* Marianna Rapsomaniki, Douglas Hanahan, Fatima Mechta-Grigoriou
- **Hormone Receptor Signaling** *Senthil Muthuswamy,* Cathrin Brisken, Leonie Young
- **Novel Approaches to Study Mammary Development and Disease** *Gillian Farnie,* Michael Lewis, Joaquin Arribas, Spiros Linardopoulos
- **Keynote Session: Breast Stem Cell Biology and Translational Breast Cancer Research** *John Stingl,* Geoffrey Lindeman
- **The GRC Power Hour™** *Leonie Young*

Mammary Gland Biology GRS

Molecular and Cellular Processes Driving Mammary Gland Development and Breast Cancer

MAY 28-29, 2022

CHAIRS: Qiang Lan and Giusy Tornillo

Marine Microbes

The Interconnected Microbial Ocean

MAY 29-JUN 3, 2022
LES DIABLERETS CONFERENCE CENTER, LES DIABLERETS, SWITZERLAND
CHAIR: Corina Brussaard
VICE CHAIR: Lasse Riemann

- **Pathogenic Microbe Interactions and Their Influence on Biogeochemical Cycling** *Curtis Suttle,* Steven Wilhelm, Rui Zhang
- **Single Celled Microbes Versus Assembled Microbial Communities** *Martin Ackermann,* Roman Stocker, Knut Drescher, Nicole Dubilier
- **Evolution of Marine Microbes** *Alexandra Worden, Rogier Braakman,* Anja Spang, Kasper Kjeldsen, Gabrielle Rocap
- **Microbial Predator-Prey Interchange in Relation to Marine Ecological Theories** *Thomas Kiorboe,* Susanne Wilken, Selina Vage, Ramon Massana
- **Synergistic Microbe-Microbe and Microbe-Host Connections and Communication** *Justin Seymour Seymour, Hanna Farnelid,* Jonathan Zehr, Torsten Thomas, Michael Sweet
- **The Complex Marine Microbiomes Captured in Networks and Ecosystem Models** *Naomi Levine,* Christian Mueller, Victoria Coles, Marina Levy
- **Environmental Shaping of Microbial Communities and Vice Versa** *Xose Anxelu Moran, Laura Alonso-Saez,* Daniele Bianchi, Ed Hall, Clara Ruiz-González
- **Living at the Ocean's Boundaries** *Anne Dekas,* Filip Meysman, Heide Schulz-Vogt, Sarah Hu
- **A Changing Ocean: Challenges to Overcome for Microbial Functional Success** *Oded Beja, Charmaine Yung,* Stephen Giovannoni, Osvaldo Ulloa, Katherine Mackey
- **The GRC Power Hour™** *Charmaine Yung, Gabrielle Rocap*

Marine Microbes
Integrative Microbial Oceanography
MAY 28-29, 2022
CHAIRS: B. B. Cael and Chase James

Mechanical Systems in the Quantum Regime

Quantum Phononics for Fundamental Measurements and Quantum Technology

JUN 19-24, 2022
VENTURA BEACH MARRIOTT, VENTURA, CA
CHAIRS: Cindy Regal and Klemens Hammerer
VICE CHAIRS: Thomas Purdy and Amir Safavi-Naeini

- **Acoustic Waves and Brillouin Optomechanics** *Amir Safavi-Naeini,* Peter Rakich, Konrad Lehnert
- **Gravitational Wave Detectors** *Thomas Purdy,* Nergis Mavalvala, Martin Hewitson, Yanbei Chen, David McClelland
- **Nonreciprocity and Chirality in Optomechanics** *Ewold Verhagen,* Anja Metelmann, Haitan Xu, Aashish Clerk
- **Levitated Optomechanics and Electromechanics** *Tongcang Li,* Benjamin Stickler, Markus Aspelmeyer, Hendrik Ulbricht, Jack Harris
- **Fundamental Tests with Mechanical Sensors** *Yiwen Chu,* Swati Singh, Holger Mueller, Jacob Taylor
- **Heralding Single Phonons and Quantum Measurements** *Aashish Clerk,* Simon Groeblacher, Magdalena Zych, Christophe Galland, Eugene Polzik
- **Quantum Electromechanical Devices** *Eva Weig,* Adrian Bachtold, John Teufel, Silvia Viola Kusminskiy
- **Spin Coupling to Nanomechanics** *Donghun Lee,* Christian Degen, Ania Bleszynski-Jayich, Raffi Budakian, Philipp Treutlein
- **Late-Breaking Topics** *John Teufel*
- **The GRC Power Hour™** *Jack Harris, Eva Weig*

Mechanical Systems in the Quantum Regime
Optomechanical Systems Enabling Novel Quantum-Enhanced Technologies and Tests of Fundamental Physics
JUN 18-19, 2022
CHAIRS: Charles Brown and Martin Koppenhoefer

Mechanisms of Epilepsy and Neuronal Synchronization

Molecular and Network Complexity in the Epileptic Brain

JUL 31-AUG 5, 2022
REY DON JAIME GRAND HOTEL, CASTELLDEFELS, SPAIN
CHAIRS: Jeffrey Noebels and Chris Dulla
VICE CHAIRS: Helen Scharfman and Viji Santhakumar

- **Complexity in Epilepsy** *Gemma Carvill,* Danielle Bassett, Liset Menendez de la Prida
- **Local and Long-Range Circuitry** *Esther Krook-Magnuson,* Yoav Adam, Peyman Golshani
- **Cell Type-Specific Contributions to Seizures** *Ivan Soltesz,* Mauro Costa-Mattioli, Gordon Fishell
- **Synaptic and Network Homeostasis** *Istvan Mody,* Seth Grant, Eve Marder, Joseph Raimondo
- **Glial Signaling and Epileptogenesis** *Amy Brewster,* Ukpong Eyo, Phil Haydon
- **Developing Circuits** *Heinz Beck,* Arnold Kriegstein, Annapurna Poduri, Beatriz Rico, Elsa Rossignol
- **New Gene Targets and Therapies** *Dimitri Kullmann,* Amy Brooks-Kayal, Stefanie Dedeurwaerdere, Harald Sontheimer
- **Oscillations, Rhythms and Network Dynamics** *Jennifer Gelinas,* Christophe Bernard, Laura Ewell, Vikaas Sohal, Rafael Yuste
- **Epigenetic and Metabolic Targets in Epileptic Brain** *Jeannie Chin,* David Henshall, Katja Kobow
- **The GRC Power Hour™**

Mechanisms of Epilepsy and Neuronal Synchronization
Approaching Complexity in Neuroscience and Epilepsy
JUL 30-31, 2022
CHAIRS: Melanie McNally and Wesley Clawson

Medicinal Chemistry

Innovations in Drug Discovery and Enabling Technologies

AUG 7-12, 2022
COLBY-SAWYER COLLEGE, NEW LONDON, NH
CHAIR: Cynthia Parrish
VICE CHAIR: Michael Ellis

- **Small Molecule Approaches for Immuno-Oncology** *Laura D'Agostino, Julia Haas,* Eric Miller, Louis Chupak, Nigel Swain
- **Emerging Technologies: From In Silico to Implementation** *H. Rachel Lagiakos,* Steve Swann, Jason Burch, Falgun Shah, Heike Schoenherr
- **Therapies Targeting Diseases of the CNS** *Emily Peterson,* Peter Fuller, Duane Burnett, Kevin Guckian
- **Synthetic Technologies to Enable Medicinal Chemistry** *Amy Hart,* Jesus Alcazar, Rachel Grainger, Vincent Colandrea, Alison Wendlandt
- **Recent Advances in Modulators of Protein-Protein Interactions** *Alex Cortez,* Eric Fischer, Jim Henderson
- **Strategies for Overcoming Drug Safety Liabilities** *Izzat Raheem,* Iyassa Sebhat, Michael Rudd, Grace Chuang, Patrizio Mattei
- **New Directions in Beyond 500 Compounds: From PK to the Clinic** *Christopher Nasveschuk, Andrew Scholte,* John Link, Matthew Weiss
- **Late-Breaking Topics: First Disclosures of Clinical Candidates** *Meredeth McGowan,* Michael Graupe, Michelle Garnsey, Scott Edmondson
- **Keynote Session** *Michael Ellis,* Rosana Kapeller
- **The GRC Power Hour™**

Medicinal Chemistry
Principles, Strategies and Case Studies in Medicinal Chemistry and Drug Discovery
AUG 6-7, 2022
CHAIR: Erin DiMauro

Meiosis

Diverse and Conserved Molecular Mechanisms Preventing Aneuploidy During Gamete Production

JUN 5-10, 2022
COLBY-SAWYER COLLEGE, NEW LONDON, NH
CHAIR: Paula Cohen
VICE CHAIR: Jeff Sekelsky

- **Physical Properties and Organization of the Synaptonemal Complex** *Ricardo Benavente,* Scott Hawley, Nancy Kleckner, Ofer Rog
- **Placement and Induction of Double Strand Breaks (DSB)** *Bernard de Massy,* Corentin Claeys Bouuaert, Monica Colaiacovo
- **DSB Processing and Pathway Choice** *Douglas Bishop,* Diana Libuda, Michael Lichten, Mathilde Grelon
- **Chromosome Dynamics, Cohesion and Pairing** *Akira Shinohara,* Nicole Crown, Denise Zickler
- **Chromatin Organization, Gene Expression and Epigenetic Control of Meiosis** *Kevin Corbett,* Florencia Pratto
- **Crossover Designation, Maturation and Homeostasis** *Neil Hunter,* Petr Cejka, Francesca Cole, Ian Henderson
- **Meiotic Drive Mechanisms and Evolution** *Sarah Zanders,* Kirsten Bomblies, Abby Dernburg, Amanda Larracuente, Michael Lampson
- **Spindle Assembly, Chromosome Segregation and Checkpoint Control** *Needhi Bhalla,* Binyam Mogessie
- **Post-Translational Modifications in Meiosis** *Anne Villeneuve,* Peter Carlton, Hiro Ohkura, Yumi Kim

Meiosis
Molecular Mechanisms and Regulation of Sexual Reproduction
JUN 4-5, 2022
CHAIRS: María Angélica Bravo Núñez and Katherine Billmyre

Membrane Transport Proteins

Biomedical Transporters: Physiology, Dysfunction and Targets of Pharmacotherapy

JUN 12-17, 2022
REY DON JAIME GRAND HOTEL, CASTELLDEFELS, SPAIN
CHAIR: Aurelio Galli
VICE CHAIRS: Renae Ryan and Susan Ingram

- **Channelopathies and Transportopathies** *Renae Ryan,* Al George, Hanne Poulsen, Jeffrey Rothstein
- **Targeting Transporters for Pharmacotherapies** *Sandra Hewett, Erin Calipari,* Nancy Carrasco, Amy Newman, Manuel Palacin, Robert Vandenberg
- **Transporter Function and Dysfunction in Metabolism, Diabetes and Obesity** *Habibeh Khoshbouei,* Zachary Freyberg, Sophie Hambleton, Amira Klip, Michael Koettgen
- **Invertebrates as Animal Models to Study Transporter Functions** *Randy Blakely, Freja Herborg,* Susan Amara, Laura Bianchi, Lucia Carvelli, David Krantz
- **Na, K-ATPase and Related Pumps** *Imogen Coe,* Matthias Hediger, Jonathan Javitch, Poul Nissen, Daniela Pietrobon
- **Neurological and Neuropsychiatric Disorders: Transporters at Play** *Rajini Rao,* Heinrich Matthies, Haley Melikian, Gaia Novarino, Harald Sitte
- **New Strategies, Ideas and Techniques to Study Membrane Protein Structure-Function and Trafficking** *Ulrik Gether,* Olga Boudker, Sergio Grinstein, Parastoo Hashemi, Eduardo Perozo
- **Peptides, Hormones, and Neurotransmitter Release: The Importance of Transporters in the Gut and Brain** *Michael Freissmuth, Susan Ingram,* Eric Gouaux, Robert Edwards, Naoki Yamanaka
- **Detailing Mechanisms of Importers and Exporters** *Roxanne Vaughan,* Isabelle Baconguis, Hassane Mchaourab, Christine Ziegler
- **The GRC Power Hour™** *Imogen Coe*

Membrane Transport Proteins
The Structure-Function Relationship of Transporters in Health and Disease
JUN 11-12, 2022
CHAIRS: Susanna Concilio and Eric Figueroa

Membranes: Materials and Processes

Growing Convergence in Membrane Separations Research

JUL 31-AUG 5, 2022
COLBY-SAWYER COLLEGE, NEW LONDON, NH
CHAIRS: Isabel Escobar and William Phillip
VICE CHAIRS: J.R. Johnson and Lucy Camacho

- **Keynote Session: Interfacial Engineering of Membranes for Environmental Applications** *Audie Thompson, Steven Weinman,* Dibakar Bhattacharyya, Lidietta Giorno
- **Rational Design of Membrane Materials** *Jamie Hestekin, Christopher Arges, Hee Oh,* Qilin Li, Zachary Smith, Haiqing Lin
- **Process Optimization and Intensification** *William Tarpeh, Ngai Yin Yip,* Michelle Dose, Uwe Beuscher
- **Membrane Manufacturing** *Ramy Swaidan, Tequila Harris,* Marcus Worsley, Maria Coleman, Glenn Fredrickson
- **Real-Time Process Control and Membrane Fouling** *Shudipto Dishari, Johannes Vrouwenvelder,* Daniel Miller, Jessica Schiffman
- **Composite Membrane Structures** *Cristiana Boi, Marta Hatzell,* Sibudjing Kawi, Andrea Schaefer, Nicholas Kotov
- **Reactive, Emerging and Hybrid Membrane Processes** *Kerri Hickenbottom, Lauren Greenlee,* Suzana Nunes, Seth Darling
- **Emerging Industrial Separations** *TorOve Leiknes, Alexander Lopez,* Chunqing Liu, Stephen Ritchie, Christina Carbrello

- **Keynote Session: From Lab-Scale Discoveries to Industrial Separation Processes** *Ayse Asatekin, Robert Schucker,* William Koros
- **The GRC Power Hour™** *Jamie Hestekin, Christina Carbrello*

Membranes: Materials and Processes GRS

Connecting Pathways Between Molecular Design and Module Commercialization in Membrane Science

JUL 30-31, 2022

CHAIRS: Gabrielle Lawrence and Matthew Rivera

Metallocofactors

Bioinorganic Active Sites that Drive Challenging Chemical Conversions

JUN 5-10, 2022
SALVE REGINA UNIVERSITY, NEWPORT, RI

CHAIR: Serena DeBeer
VICE CHAIR: Kyle Lancaster

- **Frontiers of Metallocofactor Design** *Kelly Chacon,* Yi Lu, Andrew Borovik
- **Hydrogenase: From Models to Enzymes** *R. David Britt,* Alison Parkin, Hannah Shafaat, Jason Shearer, Ulf-Peter Apfel
- **Protein Engineering** *Lisa Olshansky,* Akira Onoda, Ross Anderson, Julie Renner
- **Iron-Sulfur Biochemistry** *Patricia Dos Santos,* Sean Elliott, Daniel Suess, Seigo Shima
- **CO and CO2 Conversion by Enzymes and Models** *Inês Pereira,* Holger Dobbek, Abhishek Dey, Christine Thomas
- **Lanthanide Metallobiochemistry** *Rebecca Abergel,* Cathleen Zeymer, N. Cecilia Martinez-Gomez, Joseph Cotruvo, Jr.
- **Recent Advances in Nitrogenase Research** *Oliver Einsle,* Shelley Minteer, Akif Tezcan, Simone Raugei
- **Water Oxidation in Enzymes and Models** *Theodor Agapie,* Yulia Pushkar, Nicholas Cox, Julio Lloret Fillol, Greta Patzke
- **C-H Activation by Copper** *William Tolman,* Amy Rosenzweig, Paul Walton
- **The GRC Power Hour™**

Metals in Medicine

Advancing the Use of Metal-Based Compounds and Nanotheranostics for Personalized Medicine

JUN 26-JUL 1, 2022
PROCTOR ACADEMY, ANDOVER, NH

CHAIRS: Edith (Phoebe) Glazer and Angela Casini
VICE CHAIRS: Carolyn Anderson and Anne-Kathrin Duhme-Klair

- **Keynote Session: Supramolecular Metal-Based Molecules for Biomedical Applications** *Michael Hannon,* Makoto Fujita, Shawn Chen, Wenbin Lin
- **Clinical Advances for Metals in Medicine** *Walter Berger,* Sherri McFarland, Thomas Meade, Linda Vahdat, Anton Simeonov
- **Catalysis in Cells** *Luca Salassa, Loi Do,* José Luis Mascareñas, Katsunori Tanaka
- **Novel Metallomics Methods and Tools** *Ana Maria Costa Ferreira, Samuel Meier-Menches,* Eric Gale, Alessandra Magistrato, Sarah Michel, Nigel Robinson, Sharon Ruthstein, Janet Morrow
- **Late-Breaking Topics** *Carolyn Anderson, Anne-Kathrin Duhme-Klair,* Camilla Abbehausen, Eszter Boros, Orazio Vittorio
- **Novel Chelation Strategies and Applications for Radionuclides and Contrast Agents** *Eric Gale,* Rebecca Abergel, Peter Caravan, Jason Lewis, Darren Magda, Katherine Vallis
- **Essential Metals in Disease Mechanisms** *Katherine Franz,* Donita Brady, Martin Burke, Matteo Ceccarelli
- **Stimuli-Responsive Materials for Therapy and Imaging** *Zijian Guo, Justin Wilson,* Shuhei Furukawa, Zhuang Liu, Rachela Popovtzer, Anna Cristina Samia
- **Targeted Metal-Based Therapeutics** *Thomas Meade,* Seth Cohen, Maria Contel
- **The GRC Power Hour™**

Microbial Stress Response

Bacterial Mechanisms for Sensing, Responding and Adapting to Stress

JUL 17-22, 2022
MOUNT HOLYOKE COLLEGE, SOUTH HADLEY, MA

CHAIRS: Michael Laub and Jade Wang
VICE CHAIRS: Amy Schmid and Peter Chien

- **Cell Envelope Stress** *Eduardo Groisman,* Jean-Francois Collet, Petra Levin, Natividad Ruiz, Allison Williams
- **Replication Stress** *William Navarre,* Susan Rosenberg, Lyle Simmons, Jan-Willem Veening
- **Stress of Other Cells** *Petra Levin,* Marie Elliot, Daniel Wall, Chris Waters
- **Temperature, Oxidative and Metal Stress** *Joan Slonczewski,* Frederic Barras, Carol Gross, John Helmann, Arash Komeili
- **Energy and Metabolic Stress** *Peter Chien,* Lars Dietrich, N. Cecilia Martinez-Gomez, Caroline Harwood
- **Regulatory Systems for Stress** *Amy Gehring,* Mark Buttner, Sean Crosson, Susan Gottesman, Gisela Storz
- **Stress of Phage and Mobile Genetic Elements** *Lyle Simmons,* Alan Grossman, Kim Seed, Cari Vanderpool
- **Stress of Being in a Host** *Marie Elliot,* Sophie Helaine, William Navarre
- **Proteotoxic and Translational Stress** *Amy Schmid,* Gert Bange, Pierre Genevaux, Daniel Kearns
- **The GRC Power Hour™**

Microbial Stress Response GRS

Microbial Sensing, Signaling and Survival in Stress

JUL 16-17, 2022

CHAIRS: Mona Orr and Jan-Ulrik Dahl

Microbial Toxins and Pathogenicity

Mechanisms of Action, Detection and Evasion of Microbial Toxins

JUL 10-15, 2022
SOUTHBRIDGE HOTEL & CONFERENCE CENTER, SOUTHBRIDGE, MA

CHAIR: Heran Darwin
VICE CHAIR: Mary O'Riordan

- **Keynote Session: Virulence Regulation During Infections** *Andrew Darwin,* Andrew Perault, Britney Hardy, Virginia Miller
- **Bacterial Toxins: Structure, Function and Outcome** *Victor Torres,* Borden Lacy, Isaac Chiu, Jeongmin Song, John Mekalanos, Andreas Peschel
- **Toxic Defense Mechanisms** *Peggy Cotter,* Marek Basler, Christopher Hayes, Alecia Septer
- **Subverting Host Functions with Bacterial Toxins and Effectors** *Eric Skaar,* Jim Cassat, Sophie Helaine, Ralph Isberg, ZhaoQing Luo, Asaf Levy
- **Regulation of Genes and Proteins in Pathogens** *Raphael Valdivia,* Petra Dersch, Aimee Shen, Joshua Woodward
- **Intracellular Problems and Solutions** *Joanne Engel,* Isabelle Derré, Marcia Goldberg, Rebecca Lamason, Renee Tsolis, Sarah Stanley
- **Evolution of Virulence Factors** *Manuela Raffatellu,* Ankur Dalia, Tamara O'Connor, Matthew Waldor
- **Detection and Response to Bacterial Infections** *Russell Vance,* Ivan Dikic, Katrin Mayer-Barber, Edward Miao, Anna Tischler, Sebastian Winter
- **Keynote Session: Innate Sensing of Pathogens** *Kim Orth,* Feng Shao
- **The GRC Power Hour™** *Drusilla Burns*

Microbial Toxins and Pathogenicity GRS

Intercellular Interactions and Pathologic Outcomes

JUL 9-10, 2022

CHAIRS: Britney Hardy and Andrew Perault

Microbiology of the Built Environment

Microbes at the Interface of Water, Air and Human Health in Built Environments

JUN 19-24, 2022
WATERVILLE VALLEY, WATERVILLE VALLEY, NH

CHAIR: Kyle Bibby
VICE CHAIR: Amy Pruden

- **Linking Building Microbiomes and Health** *Karen Dannemiller,* Chuck Gerba, Laura-Isobel McCall
- **Drinking Water Microbiome** *Sarah Haig,* Shantini Gamage, Frederik Hammes, Ameet Pinto
- **Extreme and Confined Environments** *Amy Pruden,* Charlie Ott, Trinity Hamilton
- **Antibiotic Resistance** *Erica Hartmann,* Kerry Hamilton, Tao Yan
- **Microbiology of Sewage Collection Systems** *Jordan Peccia,* Lydia Bourouiba
- **Microbiology of the Built Environment in the Developing World** *Krista Wigginton,* Joe Brown, Kara Nelson, Amy Pickering
- **Microbiologically-Informed Green Engineering Design** *Mark Hernandez,* Timothy Julian, William Rhoads
- **Standardizing Built Environment Microbiological Methods** *Timothy Julian,* Andrew Jackson, Robert McLean, Caitlin Proctor
- **Biofilms** *Robert McLean,* Scott Kelley
- **The GRC Power Hour™** *Amy Pruden*

Mitochondria and Chloroplasts

Semi-Autonomous Organelles: From Fundamental Processes to Translation in Agriculture and Medicine

JUL 17-22, 2022
MOUNT SNOW, WEST DOVER, VT

CHAIR: Zach Adam
VICE CHAIR: Antoni Barrientos

- **Evolution and Dynamics of Organelles and Their Genomes** *Andreas Weber,* Dan Mishmar, Dan Sloan
- **Organelle Gene Expression** *Zofia Chrzanowska-Lightowlers,* Alice Barkan, Brendan Battersby, Flavia Fontanesi, Meng Chen
- **Protein Import, Sorting and Assembly** *Agnieszka Chacinska,* Hsou-Min Li, Peter Rehling, Masato Nakai
- **Organelle Dynamics: Division, Differentiation and Contacts** *Liza Pon,* Yoshiki Nishimura, Maya Schuldiner, Samantha Lewis
- **Structure and Function of Organelle Complexes** *Johannes Herrmann,* Amandine Marechal, Alexey Amunts
- **Organelle Metabolism** *Sabeeha Merchant,* A. Harvey Millar, Veronica Maurino, Ken Nakamura
- **Signaling and Stress Response** *Sally Mackenzie,* Valentina Perissi, Jaakko Kangasjärvi
- **Proteostasis, Mitophagy and Chlorophagy** *Klaas Van Wijk,* Paul Jarvis, Hagai Abeliovich
- **Organelle Biology Translated into Medicine and Agriculture** *Richard Hartley,* Stephen Long, Giovanni Manfredi, Ralph Bock
- **The GRC Power Hour™**

Mitochondria and Chloroplasts GRS

Semi-Autonomous Organelles: From Fundamental Processes to Translation in Agriculture and Medicine

JUL 16-17, 2022

CHAIRS: Florian Schober and Laura Klasek

Molecular and Cellular Neurobiology

Emerging Technologies to Study Nervous System Development, Function and Neurological Disease

JUL 24-29, 2022
FOUR POINTS SHERATON, HOLIDAY INN EXPRESS, VENTURA, CA

CHAIR: Aaron Gitler
VICE CHAIR: Mingjie Zhang

- **Keynote Session: Mechanisms of Neurological Disease** *Katja Brose,* Carla Shatz, Viviana Gradinaru, Hailan Hu
- **Development of the Nervous System** *Kang Shen,* Shen-Ju Chou, Daniel Colón-Ramos, Gordon Fishell, Xuecai Ge, Yukiko Gotoh, Carina Hanashima, Melissa Rolls, Hongyan Wang

- **Synapses and Synaptic Function** *Xiang Yu,* Lu Chen, Camin Dean, Peter Scheiffele, Thomas Sudhof, Johannes Hell
- **Neural Circuits and Behavior** *Shernaz Bamji,* Anna Beyeler, Yang Dan, Steven Flavell, Nirao Shah, Juan Song, Yi Zuo
- **Brain Imaging and Connectomics** *Yimin Zou,* Na Ji, Tianyi Mao
- **Genetics and Epigenetics of the Nervous System** *Louis Reichardt,* Dan Geschwind, Nancy Ip, Bianca Marlin, Coleen Murphy, Theodore Price, Jie Shen
- **Sensory Systems** *John Ngai,* Alexander Chesler, Sandeep Robert Datta, Craig Montell, Amita Sehgal, Fengwei Yu
- **Mechanisms of Neurodegeneration and Regeneration** *Leonard Petrucelli,* Frank Bradke, Jun Ding, Eric Huang, Martin Kampmann, Claire Le Pichon, James Shorter, Michael Ward
- **Advanced Technologies for Neuroscience Research** *Yi Sun,* Ryohei Yasuda, Feng Zhang
- **The GRC Power Hour™**

Molecular and Cellular Neurobiology

Functional Integration of Neural Mechanisms in Health and Disease

JUL 23-24, 2022

CHAIRS: Nicole Leung and Zacharie Taoufiq

Molecular Basis of Microbial One-Carbon Metabolism

Enzymes and Metabolisms Driving the Global Carbon Cycle

AUG 7-12, 2022
SOUTHBRIDGE HOTEL & CONFERENCE CENTER, SOUTHBRIDGE, MA

CHAIR: Seigo Shima
VICE CHAIR: Christopher Marx

- **Methane and the Carbon Cycle** *Thomas Hanson,* Justin North, Andrew Crombie, William Metcalf
- **Biochemistry and Physiology of Aerobic Methylotrophy** *Yasuyoshi Sakai,* Amy Rosenzweig, Alexander Tveit, Marina Kalyuzhnaya, Matthias Steiger
- **Chemoautotrophy and Electrons** *Amelia-Elena Rotaru,* Chris Greening, Bonnie Murphy, Nikhil Malvankar
- **From C1 to C2: Acetogens, Reactions and Applications** *Mirko Basen,* Volker Mueller, Byung-Kwan Cho, Stephen Ragsdale, Hannah Shafaat, Michael Koepke
- **Ecology and Evolution of C1 Metabolism** *Kathleen Scott,* Samantha Joye, Guillaume Borrel, Stephane Vuilleumier
- **CO2 Fixation and Photorespiration** *Tobias Erb,* Cheryl Kerfeld, Manajit Hayer-Hartl, Elke Dittmann, Elizaveta Bonch-Osmolovskaya
- **Key Enzymes of Anaerobic C1 Metabolism** *Silvan Scheller,* Gerrit Schut, Florin Musat, Jan Schuller
- **C1 Metabolism and Physiology** *Cornelia Welte,* Masaru Nobu, N. Cecilia Martinez-Gomez, Takuro Nunoura, Diana Sousa
- **Syntrophy and Eukaryogenesis** *Colleen Cavanaugh,* Manuel Liebeke, Anja Spang, Hiroyuki Imachi
- **The GRC Power Hour™** *Cornelia Welte*

Molecular Basis of Microbial One-Carbon Metabolism

Microbial One-Carbon Conversion from the Microscale to the Global Scale

AUG 6-7, 2022

CHAIRS: Marie Schölmerich and Grayson Chadwick

Molecular Interactions and Dynamics

Dynamics and Spectroscopy of Chemical Systems

JUL 10-15, 2022
STONEHILL COLLEGE, EASTON, MA

CHAIR: Hua Guo
VICE CHAIR: Ricardo Metz

- **Cold and Ultracold Collisions and Reactions** *Andreas Osterwalder,* Nandini Mukherjee, Balakrishnan Naduvalath, Edvardas Narevicius
- **Molecular Interactions and Collisions in the Gas Phase** *Jun Li,* Richard Dawes, Uwe Manthe, Arthur Suits, Roland Wester
- **Kinetics of Combustion, Atmospheric and Interstellar Reactions** *David Osborn,* Stephen Klippenstein, Marsha Lester, Albert Viggiano
- **Molecular Interactions and Dynamics at Interfaces** *Jörg Meyer,* Rainer Beck, Timothy Minton, Gilbert Nathanson, Alec Wodtke
- **Impact of Machine Learning** *Philipp Marquetand,* Roman Krems, Francesco Paesani, David Wilkins
- **Photochemistry and Nonadiabatic Dynamics** *Michael Schuurman,* Joseph Subotnik, David Yarkony, Kaijun Yuan, Benjamin Levine
- **Ultrafast Processes** *Xiaosong Li,* Luis Banares, Marcos Dantus, Irene Burghardt
- **Molecular Interactions and Dynamics in Complex Systems** *Jian Liu,* Vicki Grassian, Wei Kong, Richard Loomis, Caroline Jarrold
- **Keynote Session: Spectroscopy and Dynamics** *Ricardo Metz,* Robert Field, Daniel Neumark, George Schatz

Molecular Interactions and Dynamics

Reactions, Collisions and Energy Transfer on Short to Long Timescales

JUL 9-10, 2022

CHAIR: Matthew Bain

Molecular Structure Elucidation

Recent Advances in Analytical Technologies to Expedite the Development of New Drug Modalities

JUL 31-AUG 5, 2022
JORDAN HOTEL AT SUNDAY RIVER, NEWRY, ME

CHAIRS: Mohammad Al-Sayah and R. Graham Cooks
VICE CHAIRS: Yongchao Su and Gaurav Chopra

- **Keynote Session: Discovery and Development of New Drug Modalities** *Roy Helmy,* Paul Carter, David Brayden
- **Analytical Characterization of New Drug Modalities** *Alexey Makarov,* Wendy Sandoval, Rainer Fischer, Martin Gilar
- **High Throughput Experimentation, Computational Chemistry and Machine Learning** *Michael Wleklinski,* Spencer Dreher
- **Advances in Spectroscopic Techniques** *Eric Munson, Qi Gao,* Mei Hong, Krishna Mallela, Zheng Ouyang
- **Emerging Techniques in Separation Science** *Samuel Yang,* Robert Kennedy, Peter Shoenmakers, Kevin Schug
- **Advancing Pharmaceutical Discovery and Development Through Molecular Structure Elucidation** *Naijun Wu,* Caroline McGregor, Huijuan Li, John Masucci
- **The Dark Metabolome and Lipidome** *Christina Ferreira,* Peter Nemes, Xin Yan, David Wishart
- **Proteins in Unusual States** *David Russell, Vicki Wysocki,* David Clemmer, Jennifer Brodbelt, Arthur Laganowsky, Michael Marty
- **Efficient Development of Novel Analytical Technologies via Collaborations Between Academia and the Pharmaceutical Industry** *Christopher Welch,* Andreas Kaerner, Rebecca Whelan, Paul Bohn, Yong Liu
- **The GRC Power Hour™**

Multiferroic and Magnetoelectric Materials

JUL 31-AUG 5, 2022
BATES COLLEGE, LEWISTON, ME

CHAIRS: Venkatraman Gopalan and Ramamoorthy Ramesh
VICE CHAIR: Tsuyoshi Kimura

- **User Facilities for Materials Synthesis and Probes of Fundamental Phenomena** *Padraic Shafer,* Alan Tennant, John Freeland, Gerrit Vander Laan, Aaron Lindenberg
- **Theoretical Frameworks and Machine Learning Approaches** *Jorge Iniguez,* Javier Junquera, Alexander Balatsky, Long-Qing Chen, Geoffroy Hautier
- **Multiferroic Crystal Synthesis** *Tsuyoshi Kimura,* Ram Seshadri, Shenqiang Ren, Vivien Zapf
- **Thin Films, Heterostructures and Nanostructures** *Lane Martin,* Chang-Beom Eom, Chan-Ho Yang, Pu Yu, Susan Trolier-McKinstry, Susanne Stemmer
- **Applications of Multiferroics and Magnetoelectrics** *Cheng Song,* Nian Sun, Geoffrey Beach, Cewen Nan, YinHao Chu
- **Picoscale Metrology** *Xiaoqing Pan,* Manfred Fiebig, Jan Musfeldt, Jan Seidel, Margaret Murnane
- **Quantum Materials and 2-Dimensional Multiferroics** *Ni Ni,* Zhiqiang Mao, Arzhang Ardavan, Xiaodong Xu, Youtarou Takahashi
- **Symmetry, Topology, Non-Reciprocal and Emergent Phenomena: Real Space and Reciprocal-Space** *Manfred Fiebig,* Shinichiro Seki, Sang-Wook Cheong, Yoshinori Onose, Jirka Hlinka
- **Keynote Session: Fundamental and Applied Science of Multiferroics** *Sang-Wook Cheong,* Ian Young, Jean-Marc Triscone, Darrell Schlom, Ekhard Salje
- **The GRC Power Hour™**

Multiferroic and Magnetoelectric Materials

Multiferroic Coupling Effects and Dynamics of Domains and Domain Walls at the Nanoscale

JUL 30-31, 2022

CHAIRS: Mads Weber and Johanna Nordlander

Multiphoton Processes

Fundamental Electronic and Structural Dynamics

JUN 12-17, 2022
BRYANT UNIVERSITY, SMITHFIELD, RI

CHAIR: Caterina Vozzi
VICE CHAIRS: Nirit Dudovich and Daniel Rolles

- **Keynote Session: Multiphoton Processes** *Marc Vrakking,* Donna Strickland
- **Chirality** *Markus Ilchen,* Valerie Blanchet, Olga Smirnova, Oren Cohen
- **Electronic and Nuclear Dynamics in Complex Systems** *Adam Kirrander,* Matthias Kling, Zhi Heng Loh
- **Solid-State Dynamics** *Hadas Soifer,* Jens Biegert, Ursula Keller, Mette Gaarde
- **Nonlinear XUV and X-Ray Science** *Johan Mauritsson,* James Cryan, Mizuho Fushitani
- **Multidimensional Imaging of Chemical Dynamics** *Maria Novella Piancastelli,* Till Jahnke, Itzik Ben-Itzhak, Albert Stolow
- **Dynamics at Conical Intersections** *Russell Minns,* Heide Ibrahim, Michael Schuurman
- **Attosecond Dynamics** *Jonathan Marangos,* Francesca Calegari, Paul Corkum, Alicia Palacios
- **Emerging Techniques** *Michael Chini,* Giulia Mancini, Jochen Mikosch
- **The GRC Power Hour™** *Valerie Blanchet, Nirit Dudovich*

Multiphoton Processes

Study of Dynamics by Light-Matter Interaction: From Atoms to Complex Systems

JUN 11-12, 2022

CHAIRS: Ruaridh Forbes and Omer Kneller

Multiscale Mechanochemistry and Mechanobiology NEW!

From Molecular Mechanics to Smart Materials

JUL 31-AUG 5, 2022
VENTURA BEACH MARRIOTT, VENTURA, CA

CHAIR: Matthew Harrington
VICE CHAIR: Kerstin Blank

- **Multiscale Mechanics of Biological and Synthetic Materials** *Hermann Gaub,* Viola Vogel, Stephen Craig
- **Mechanosensing in the Different Domains of Life** *Viola Vogel,* Anja Geitmann, Vernita Gordon, Alex Dunn
- **Mechanically Induced Chemical Reactions** *Nancy Sottos,* Evelina Colacino, Robert Göstl
- **Mechanoresponsive Polymeric Materials** *Julia Kalow,* Yi Cao, Andreas Walther
- **Simulations and Mechanisms of Mechanoresponsive Molecules** *Anna Tarakanova,* Frauke Gräter, Jennifer Schwarz
- **Bottom-up Design of Mechanoresponsive Materials** *Niels Holten-Andersen,* Gijsje Koenderink, Oren Scherman, Anna Rising
- **Active Force Generation in Synthetic Systems** *Robert Göstl,* Aranzazu Del Campo, Stephen Schrettl
- **Bio-inspired Materials** *Phillip Messersmith,* Douglas Fudge, Andre Studart
- **Multiscale Methods for Measuring and Applying Forces** *Andreas Walther,* Costantino Creton, Khalid Salaita

Multiscale Plant Vascular Biology

Assessing Plant Vascular Function Through Optical Approaches

JUN 5-10, 2022
JORDAN HOTEL AT SUNDAY RIVER, NEWRY, ME
CHAIRS: Brent Helliker and Jeannine Cavender-Bares
VICE CHAIRS: Anna Sala and Rachel Spicer

- **Keynote Session: Viewing Plant Vascular Function Across Scales** *Noel Holbrook,* Abigail Swann
- **Plant-Atmosphere Connections from Landscapes to Whole Earth** *Yanlan Liu,* Kyla Dahlin, Susan Ustin, Kim Novick
- **Water Movement Through Leaves to Ecosystems** *Yakir Preisler,* Abraham Stroock, Andrew Leakey
- **3D Elucidation of Leaf Structure and Function** *Lawren Sack,* Margaret Barbour, Craig Brodersen, Christine Scoffoni
- **Vascular Transport from Whole Plants to Ecosystems** *Clarissa Fontes,* Kim O'Keefe, Anna Trugman
- **Xylem Structure-Function Relationships** *Francesca Secchi,* Jochen Schenk, Jose Torres-Ruiz, Maciej Zwieniecki
- **Phloem Structure-Function Relationships** *Jozica Gricar,* Jessica Savage, Sanna Sevanto
- **Stomatal and Aquaporin Mediated Water Flux** *Tom Buckley,* Tim Brodribb, Menachem Moshelion
- **Evolution of Plant Vascular Systems** *Adam Roddy,* Charles Boyce, Monica Carvalho
- **The GRC Power Hour™**

Multiscale Plant Vascular Biology
Challenges for Plant Vascular Function in the Anthropocene
JUN 4-5, 2022
CHAIRS: Gerard Sapes and William Hammond

Musculoskeletal Biology and Bioengineering

New Approaches to Accelerate Discovery in the Musculoskeletal System

AUG 7-12, 2022
PROCTOR ACADEMY, ANDOVER, NH
CHAIR: Tamara Alliston
VICE CHAIR: Louis DeFrate

- **Keynote Session: Biology and Bioengineering as a Platform for Change** *Constance Chu,* Kelly Stevens, Izzy Jayasinghe
- **Biology and Bioengineering of Aging in the Musculoskeletal System** *Samuel Ward,* Thomas Rando, Kharma Foucher, Sarah Dallas, Adetola Adesida
- **Musculoskeletal Pain: Causes and Cures** *Anne-Marie Malfait,* A. Vania Apkarian, Tony Yaksh, Gregory Hicks
- **Spatial Context in the Musculoskeletal System** *Catherine Kuo,* Lin Han, Ralph Müller, Stefano Di Talia, Alessandra Sacco
- **Tracking Musculoskeletal Histories Over Time** *Ivo Kalajzic,* Terence Capellini, Qing-Jun Meng, George Muschler
- **Multiscale Metabolism in Musculoskeletal Tissue Crosstalk** *Peter Croucher,* Ronald June, Nancy Lane, Tri Phan, Graham Williams
- **Enlisting the Immune System for Musculoskeletal Health** *Laura McCabe,* Dana Graves, Danièle Noël, Hiroshi Takayanagi
- **Multiscale Musculoskeletal Mechanobiology** *Pen-Hsiu Chao,* Belinda Beck, Melissa Knothe Tate, Alayna Loiselle, Elise Morgan
- **Synthetic Musculoskeletal Biology and Biomaterial** *Alan Grodzinsky,* Robert Bowles, Blanka Sharma, Johnna Temenoff
- **The GRC Power Hour™**

Musculoskeletal Biology and Bioengineering
Multi-Scale Approaches to Understanding Musculoskeletal Tissues
AUG 6-7, 2022
CHAIRS: Sun Peck and Stefaan Verbruggen

Mutagenesis

Fundamental Mechanisms of Genomic Change and Adaptation

JUN 12-17, 2022
JORDAN HOTEL AT SUNDAY RIVER, NEWRY, ME
CHAIR: Julian Sale
VICE CHAIR: Houra Merrikh

- **Keynote Session: Fundamental Mechanisms of Mutagenesis** *Daniel Jarosz,* Sue Jinks-Robertson, Reuben Harris
- **DNA Damage Tolerance by the Replication Fork** *Sarah Lambert,* Helle Ulrich, Susan Lovett, Wei Yang, Dana Branzei
- **Visualizing Mutagenic Mechanisms** *Wei Yang,* Joseph Loparo, Antoine Van Oijen, David Rueda
- **Mutagenesis Arising from Replication Errors** *Susan Lovett,* Thomas Kunkel, Roger Woodgate, David Pellman
- **RNA-Dependent Mutagenesis** *Thomas Kunkel,* Karlene Cimprich, Andres Aguilera, Hannah Klein
- **Repeat and Barrier-Induced Mutagenesis** *Hannah Klein,* Marcel Tijsterman, Catherine Freudenreich, Sarah Lambert, Sergei Mirkin
- **Understanding Mutation Signatures in Cancer and Aging** *K.J. Patel,* Nuria Lopez-Bigas, Ruben van Boxtel
- **Environmental and Endogenous Mutagenesis** *Reuben Harris,* Ivan Matic, K.J. Patel, Bjoern Schwer, Shana Sturla
- **Evolvability and Adaptation** *Houra Merrikh,* Lilach Hadany, Melissa Gymrek, Daniel Jarosz
- **The GRC Power Hour™**

Mutagenesis
Mechanisms of Mutagenesis and Clinical Implications
JUN 11-12, 2022
CHAIRS: Claudia Aloisi and Brandon Case

Myelin

Translational Science of Myelin: From Glial Biology to Repair

MAY 22-27, 2022
RENAISSANCE TUSCANY IL CIOCCO, LUCCA (BARGA), ITALY
CHAIRS: Catherine Lubetzki and Kelly Monk
VICE CHAIRS: Terri Wood and Jonah Chan

- **Remyelination in Multiple Sclerosis and Animal Models** *Anne Baron-Van Evercooren, Jonah Chan,* Christine Stadelmann-Nessler, Benedetta Bodini, Robin Franklin
- **Cell-Cell Interactions in Myelination** *Charles ffrench-Constant, Terri Wood,* Sophie Belin, Peter Brophy, Julia Edgar, Jun Hee Kim, Eva-Maria Kramer-Albers, Elior Peles, Keiichiro Susuki, Anne Desmazieres
- **Oligodendroglial Heterogeneity** *Bernard Zalc, Wendy Macklin,* Goncalo Castelo-Branco, Vahbiz Jokhi, Ragnhildur Karadottir
- **Novel Imaging Tools: From Cells to Human Tissue** *David Lyons, Bruno Stankoff,* Martina Absinta, Emmanuel Beaurepaire, Jaime Grutzendler, Heidi Johansen-Berg, Dies Meijer, Peter Stys, Ethan Hughes
- **Schwann Cell Development and Repair** *Laura Feltri, James Salzer,* Peter Arthur-Farraj, Lydia Daboussi, Claire Jacob, Alison Lloyd, Piotr Topilko
- **Development of Myelinating Glia** *Leda Dimou, Bruce Appel,* Fiona Doetsch, Hyun Kyoung Lee, Jayshree Samanta, Ruth Stassart, Brad Zuchero
- **Multiple Sclerosis: A Therapeutic Perspective** *Marco Salvetti, Frauke Zipp,* Riley Bove, Jeremy Chataway, Gianvito Martino, Mariapia Sormani, V. Wee Yong
- **Innate Immune Cells in Myelin Damage and Repair** *Roberta Magliozzi, William Talbot,* Robert Hill, Inge Huitinga, Hans Lassmann, Veronique Miron, Marco Prinz, Sebastian Werneburg
- **Adaptive Myelination and Remyelination** *Maria Cecilia Angulo, Tobias Merson,* Dwight Bergles, Maarten Kole, Letizia Leocani
- **The GRC Power Hour™** *Jennifer Orthmann-Murphy, Violetta Zujovic*

Myelin
Dynamics of Myelin Formation, Function and Repair
MAY 21-22, 2022
CHAIRS: Meng-meng Fu and Jenea Bin

Nanoscale Science and Engineering for Agriculture and Food Systems

Convergence of Nanotechnology With Food and Agriculture

JUN 19-24, 2022
SOUTHERN NEW HAMPSHIRE UNIVERSITY, MANCHESTER, NH
CHAIRS: Antje Baeumner and Julie Goddard
VICE CHAIRS: Carmen Gomes and Melanie Kah

- **Keynote Session: Convergence of Nanotechnology with Food and Agriculture** *Jason White,* Sharon Walker, Fabio Pulizzi
- **Advances in Nanomaterials** *Margaret Frey,* Brenda Hutton-Prager, Khara Grieger, Tony McNally
- **Translation of Nano-Based Science for Application in Food and Agriculture** *Timothy Duncan, Nick Dokoozlian,* Marie Connett, Rick Shang
- **Nanobiosensor Approaches to Improving Human and Animal Health** *Man Bock Gu,* Susana Campuzano Ruiz, Jenny Emneus, Sundaram Gunasekaran
- **Environmental Nanotechnology** *Greg Lowry,* Leonardo Fraceto, Rebecca Klaper
- **Big Data in Food and Agricultural Nanotechnology: IoT and Predictive Modeling** *Arturo Keller,* Amalia Turner, Riccardo Accolla, Abigail Horn
- **Nanodelivery Approaches to Improving Human and Animal Health** *Gretchen Mahler,* Debora Rodrigues, Ja-an Ho
- **Nanotechnology's Impact on Food Safety** *Richard Canady,* Evangelyn C. Alocilja, Eric McLamore, Maya Al Sid Cheikh
- **Nanotechnology's Role in Agriculture** *David Britt,* Maria DeRosa, Raymond Briñas
- **The GRC Power Hour™** *Carmen Gomes, Melanie Kah*

Nanoscale Science and Engineering for Agriculture and Food Systems
Convergence of Nanotechnology with Food and Agriculture
JUN 18-19, 2022
CHAIRS: Ying Wang and Antonia-Teodora Perju

Nasopharyngeal Carcinoma

Nasopharyngeal Carcinoma and Beyond: Lessons and Learnings from Virus-Associated Carcinomas

MAY 8-13, 2022
REY DON JAIME GRAND HOTEL, CASTELLDEFELS, SPAIN
CHAIRS: Kwok Wai Lo and Quynh-Thu Le
VICE CHAIRS: Mu Sheng Zeng and Alan Chiang

- **Keynote Session: Viruses and Tumor Development** *Lawrence Young,* Joan Steitz, Ian Frazer
- **Cancer Virus as a Target for Therapy and Vaccination** *Henri-Jacques Delecluse,* Paul Lieberman, A. Dimitrios Colevas, Ka-Leung Wong, Jeffrey Cohen, Christian Ottensmeier, Stuart Wong
- **Preclinical Models for NPC and OPC** *Kathy Ho Yen Shair,* Christian Münz, Anna Chi Man Tsang, John Sunwoo
- **Biomarkers for NPC and OPC** *Wei-Hua Jia, Christine Chung,* Allan Hildesheim, Miao Xu, Anna Coghill, Maura Gillison, Benjamin Pinsky, Scott Bratman
- **Translating Genomics to the Clinics: Therapeutic Perspective** *Maria Lung,* Jin-Xin Bei, Vivian Wai Yan Lui, Robert West
- **Tumor Microenvironment of NPC and OPC** *Pierre Busson,* Rajiv Khanna, Robert Ferris, Qian Zhong, Xin-Yuan Guan
- **Advances in Imaging, Pathology, Treatment Planning and Clinical Management** *Sue Yom,* Nasir M. Rajpoot, Jun Ma, Matt Lechner
- **Immunotherapy in NPC and OPC** *Alan Rickinson,* Barbara Burtness, Brigette Ma, Han Chong Toh, Rafi Ahmed
- **Keynote Session: Future Perspectives in NPC Research and Treatment** *Fei-Fei Liu,* Charles Swanton, Garry Nolan
- **The GRC Power Hour™** *Brigette Ma, Kathy Ho Yen Shair*

Natural Products and Bioactive Compounds

The Function of Natural Products at the Interface of Chemistry and Biology

JUL 31-AUG 5, 2022

PROCTOR ACADEMY, ANDOVER, NH

CHAIR: Amber Onorato
VICE CHAIR: Philip Kym

- **Keynote Session: Biomimetic Inspired Synthesis of Natural Products** *Jonathan Scheerer,* Hosea Nelson, Richmond Sarpong, Dirk Trauner
- **Innovative Chemical and Biological Technology** *Cheryl Hayward,* Francis Gosselin, Lisa Marcaurelle, Derek Tan, Michael VanNieuwenhze
- **Chemical Biology of Natural Products and Bioactive Compounds** *Ryan Rafferty,* Amanda Garner, Janet Smith, Gavin Williams
- **Novel Synthetic Strategies and Methodology** *John D'Angelo,* Mark Rizzacasa, Uttam Tambar, Tehshik Yoon
- **Unique Methods for the Discovery of Natural Products** *Katie Garber,* Ikuro Abe, Tadeusz Molinski
- **Medicinal Chemistry of Natural Products and Bioactive Compounds** *Carlos Zepeda,* David Myles, David Limburg, Jamie McCabe Dunn
- **Discovery and Biological Activity of Natural Products** *Jeremy Cody,* Cassandra Quave, Chambers Hughes, Jon Thorson
- **Chemical Modifications and Biological Activity of Natural Products** *Kyle Rugg,* Gregory Dudley, James Leahy, Daniel Appella
- **Keynote Session: Pioneering Synthetic Efforts** *Michael Schmidt,* Margaret Brimble, David Williams
- **The GRC Power Hour™** *Jamie McCabe Dunn, Cheryl Hayward*

Natural Products and Bioactive Compounds

Novel Approaches in Drug Discovery, Synthesis and Biosynthesis of Biological Relevant Natural Products

JUL 30-31, 2022

CHAIRS: Bernhard Kepplinger and Gina Morgan

Neural Development

Building the Nervous System: Insights from Development, Evolution and Disease

AUG 7-12, 2022

SALVE REGINA UNIVERSITY, NEWPORT, RI

CHAIR: Claude Desplan
VICE CHAIR: Debby Silver

- **Keynote Session: Principles of Neurogenesis** *Rosalind Segal,* Fiona Doetsch, Magdalena Goetz, Catarina Homem
- **Neural Cell Fate Specification** *Fiona Doetsch,* Laure Bally-Cuif, Yukiko Gotoh, Bassem Hassan, Alessandra Pierani, Shubha Tole
- **The Generation of Neural Diversity** *Yukiko Gotoh,* Stavros Lomvardas, Song-Hai Shi, Josh Huang
- **Neural Lineages: From Genomics to Imaging** *Laure Bally-Cuif,* Zhirong Bao, Simon Hippenmeyer, Rick Livesey, Christian Mayer, Chris Doe
- **Evolution of Brain Development** *Zhirong Bao,* Detlev Arendt, Victor Borrell, Alejandro Sanchez Alvarado, Maria Tosches
- **Axon Generation and Degeneration** *Maria Tosches,* Stephanie Gupton, Samantha Butler, Dietmar Schmucker, Rosalind Segal, Jessica Treisman
- **Function of Glia in Development** *Samantha Butler,* Vilaiwan Fernandes, Maxwell Heiman, Cody Smith, Dong Yan
- **Development of Neural Circuitry** *Cody Smith,* Yishi Jin, Genevieve Konopka, Richard Mann, Niels Ringstad, Claire Wyart
- **Keynote Session: Human Development and Disease** *Genevieve Konopka,* Arturo Alvarez-Buylla, Flora Vaccarino, Giorgia Quadrato
- **The GRC Power Hour™**

Neural Development

Building the Nervous System: Cell Diversity, Circuit Assembly and Disease

AUG 6-7, 2022

CHAIRS: Daniel Pederick and Stephanie Redmond

Neural Mechanisms of Acoustic Communication

NEW!

Circuits and Specializations for Behavioral Interactions in Acoustic Communication

JUL 31-AUG 5, 2022

MOUNT HOLYOKE COLLEGE, SOUTH HADLEY, MA

CHAIRS: Sarah Woolley and Michael Long
VICE CHAIRS: Mala Murthy and Marc Schmidt

- **Quantitative Approaches to Behavioral Analysis** *Jan Clemens,* Roian Egnor, Catherine Perrodin, Coen Elemans
- **Vocal Development** *Jon Sakata,* Daniel Takahashi, Alison Barker, Michale Fee, Patricia Kuhl
- **Models of Vocal Learning and Production** *Adrienne Fairhall,* Jason Bohland, Ana Amador, Richard Hahnloser
- **Auditory Specializations for Communication** *Ioana Carcea,* Sarah Woolley, Todd Roberts, Lizabeth Marie Romanski, Robert Liu
- **Vocal Interactions** *Xiaoqin Wang,* Yossi Yovel, Arkarup Banerjee, Ofer Tchernichovski
- **Genetics of Communication** *Constance Scharff,* Genevieve Konopka, Hopi Hoekstra, Kate Watkins, Erich Jarvis
- **Predictive Coding in Vocal-Motor Networks** *Andrew Bass,* Vincent Gracco, David Schneider, Berthold Hedwig
- **Comparative Anatomy and Function of Communication Circuits** *Darcy Kelley,* Anne Von Philipsborn, Benjamin Judkewitz, Mimi Kao, Lisa Stowers
- **Cortical Mechanisms of Vocal Production** *Daniela Vallentin,* Michael Brainard, Steffen Hage, Edward Chang
- **The GRC Power Hour™**

Neurobiology of Brain Disorders

Fundamental Mechanisms Leading to Novel Therapeutics and Biomarkers for Neurodegenerative Disease

AUG 7-12, 2022

REY DON JAIME GRAND HOTEL, CASTELLDEFELS, SPAIN

CHAIRS: Leonard Petrucelli and Alison Goate
VICE CHAIRS: Karen Duff and Chris Shaw

- **Keynote Session: Development of Novel Blood-Based Biomarkers for Neurodegenerative Disease** *Karen Duff, Chris Shaw,* Henrik Zetterberg
- **Genetic and Genomic Approaches to Neurodegenerative Disease** *Carlos Cruchaga,* Henne Vrei, Sonja Scholz, Peter Heutink, Hemali Phatnani
- **Epigenetics of Neurodegenerative Disease** *Bess Frost,* Christopher Glass, Sam Sisodia, Leslie Thompson, Anne Schaefer
- **Frontotemporal Dementia and ALS: Mechanisms** *Benjamin Wolozin,* Dorothee Dormann, Mina Gouti, Aaron Gitler, Michael Ward
- **Parkinson's Disease: Mechanisms** *Mark Cookson,* Valina Dawson, Towfique Raj, Patrik Verstreken, Dario Alessi
- **Alzheimer's Disease: Mechanisms** *Soyon Hong,* Beth Stevens, Christian Haass, Mathew Blurton-Jones, Tara Spires-Jones
- **Tauopathies: Mechanisms and Biomarkers** *Celeste Karch,* David Holtzman, Li Gan, Sally Temple, Guojun Bu
- **Biomarkers: Diagnoses and Theranostics** *Fanny Elahi,* Magdalini Polymenidou, Nicholas Seyfried, Donna Wilcock, Tania Gendron
- **Therapeutics Approaches** *Mercedes Prudencio,* Eric McDade, Chris Henderson, Sarah DeVos, Beverly Davidson

Neurobiology of Brain Disorders

Neurodegenerative Disease: From Molecular Mechanisms to Potential Therapies

AUG 6-7, 2022

CHAIRS: Judith Houtman and Brian Lananna

Neurobiology of Cognition

Neural Circuits, Dynamics and Computations of Cognition and Behavior

JUL 24-29, 2022

JORDAN HOTEL AT SUNDAY RIVER, NEWRY, ME

CHAIRS: David Freedman and Sabine Kastner
VICE CHAIRS: Joni Wallis and Aaron Batista

- **Keynote Session: Attention and Working Memory** *Elisabeth Murray,* Robert Desimone, Kia Nobre
- **Subcortical Contributions to Cognition** *Helen Barbas,* Farran Briggs, Michael Halassa, Richard Krauzlis, Yuri Saalmann
- **Cognitive Computations in Brains and Machines** *Xiao-Jing Wang,* Tatiana Engel, Daniel Yamins, Joshua Tenenbaum
- **Beyond the Microelectode: New Approaches for Probing Circuits of Cognition** *Christopher Harvey,* Denise Cai, Jessica Cardin, John Maunsell, Jude Mitchell
- **Neurophysiology of Human Cognition** *Rony Paz,* Randolph Helfrich, Robert Knight, Lila Davachi
- **Neural Mechanisms of Memory** *Tatiana Pasternak,* Christos Constantinidis, Earl Miller, Anna Schapiro
- **Motor Cognition** *Charles Schroeder,* Michele Basso, Mark Churchland, Karel Svoboda
- **Neural Encoding: Convergence and Controversy** *Stephanie Palmer,* Brent Doiron, Ila Fiete, Stefano Fusi, Jennifer Groh
- **Cognitive Maps** *Talia Konkle,* Danielle Bassett, Elizabeth Buffalo, Sylvia Wirth
- **The GRC Power Hour™** *Sabine Kastner, Joni Wallis*

Neurobiology of Cognition

Multidisciplinary Approaches to Understanding the Neural Circuits of Cognition

JUL 23-24, 2022

CHAIRS: Raman Saggu and Sebastien Tremblay

Neurobiology of Drug Addiction

Addiction Research: From Molecules to Circuits to Treatment

AUG 14-19, 2022

GRAND SUMMIT HOTEL AT SUNDAY RIVER, NEWRY, ME

CHAIRS: Yavin Shaham and Marina Wolf
VICE CHAIRS: Marina Picciotto and Serge Ahmed

- **Keynote Session: Advances in Epigenetic and Circuit Mechanisms of Drug Addiction: Implications to Treatment** *Pier Vincenzo Piazza,* Eric Nestler, Nora Volkow
- **Cellular and Circuit Mechanisms of Opioid Addiction and Pain** *Cecilia Flores,* Brigitte Kieffer, Laura Bohn, Stefan Schulz, Nurulain Zaveri, Gregory Scherrer
- **Learning Mechanisms of Drug Addiction** *Karen Ersche,* Rita Fuchs, Geoffrey Schoenbaum, Regina Carelli, Stephanie Groman
- **Synaptic Mechanisms of Drug Addiction** *Paul Kenny,* Yan Dong, Kasia Radwanska, Vincent Pascoli, Carrie Ferrario, Meaghan Creed, Cassandra Gipson-Reichardt
- **Addiction Theories** *Rita Goldstein,* David Epstein, Jane Taylor, Lee Hogarth, Diana Martinez
- **Animal Models of Drug Addiction and Relapse** *Gavan McNally,* Olivier George, Michael Nader, Chris Pierce, Marco Venniro, Nathan Marchant, Morgan James, Erin Calipari
- **Translational Research in Drug Addiction** *Markus Heilig,* Aldo Badiani, Sandra Comer, Courtney Miller, Matt Banks, Hedy Kober
- **Circuitry of Drug Addiction** *Marisela Morales,* John Mantsch, Sara Jones, Kate Wassum, Nii Addy, Drew Kiraly, Kathryn Reissner
- **New Imaging Methods to Visualize the Effect of Addictive Drugs on the Brain** *Veronica Alvarez,* Byungkook Lim, Lin Tian, Ream Al-Hasani, Seksiri Arttamangkul
- **The GRC Power Hour™** *Rajita Sinha, Dorit Ron*

Neurobiology of Drug Addiction

Mechanisms Underlying Development and Persistence of Drug Addiction

AUG 13-14, 2022

CHAIRS: Sam Golden and Megan Fox

New Antibacterial Discovery and Development

Disruptive Antibiotics and Non-Antibiotic Therapies to Combat Drug-Resistant Bacterial Infections

JUL 24-29, 2022

RENAISSANCE TUSCANY IL CIOCCO, LUCCA (BARGA), ITALY

CHAIRS: Ruben Tommasi and Matthew Cooper
VICE CHAIR: Peter Smith

- **Keynote Session: Clinical and Pre-Clinical Successes and Failure Modes in Antibiotic Development** *Heike Broetz-Oesterhelt,* Steven Projan, Ryan Cirz

- **Alternatives to Antibiotics** *Robert Hancock,* Heike Broetz-Oesterhelt, Guilherme Castro, Benjamin Chan, Heather Fairhead, Victor Nizet
- **Unraveling the Requirements for Drug Permeation and Target Engagement** *Olga Lomovskaya,* Helen Zgurskaya, Muriel Masi, David Six, Paul Hergenrother
- **New Approaches to Antibacterial Hits and Leads** *Peter Smith,* Sharookh Kapadia, Nawaz Khan, David Roper, Mark Blaskovich, Andrew Tomaras
- **Advances in Enabling Diagnostics and PK/PD** *Alita Miller,* Eric Stern, George Drusano, William Hope, Valerie Raymond-Schwartzmann
- **Learning from Successes and Failures in Antibacterial Lead Optimization** *Richard Lee,* Thomas Durand-Reville, Claudia Zampaloni, Daniel Obrecht, Scott Hecker, Alastair Parkes
- **Antibiotic Adjuvants** *Gerry Wright,* Ana Rita Brochado, Eric Brown, Olga Lomovskaya, Christian Melander
- **New Results from Clinical Studies** *Troy Lister,* Angela Talley, Katherine Young, Alita Miller
- **Models for Advancing Antibiotics** *Ursula Theuretzbacher,* Daniel Berman, Matthew Todd, Seamus O'Brien, Richard Alm
- **The GRC Power Hour™** *Heike Broetz-Oesterhelt, Alita Miller*

New Antibacterial Discovery and Development
Challenges and Innovative Approaches to Discover and Develop New Antibacterial Agents
JUL 23-24, 2022
CHAIRS: Ashleigh Paparella and Haroon Mohammad

Noble Metal Nanoparticles

Harnessing Designer Metal Nanostructures for Diverse Applications

JUN 12-17, 2022
MOUNT HOLYOKE COLLEGE, SOUTH HADLEY, MA
CHAIR: Sara Skrabalak
VICE CHAIR: Gregory Hartland

- **Keynote Session: Metal Nanostructure Design and Application** *Catherine Murphy,* Christy Haynes, Younan Xia
- **Spectroscopy and Microscopy** *Amanda Haes,* Kenneth Knappenberger, David Masiello, Jennifer Dionne, Utkur Mirsaidov
- **Plasmonics for Energy Conversion** *Marina Leite,* Tamar Seideman, Matthew Sheldon, Christy Landes
- **Synthesis of Designer Nanostructures** *Sen Zhang,* Matthew Jones, Ki Tae Nam, Svetlana Neretina, Richard Tilley
- **On the Nanoparticle Surface** *James Evans,* Jill Millstone, Kristen Fichthorn, Ayman Karim
- **Designer Catalysts** *Christina Li,* Graeme Henkelman, Michelle Personick, Matteo Cargnello, Peng Chen
- **Nanostructures for Diagnosis and Delivery** *Teri Odom,* Xing Yi Ling, Somin Lee, Xiaohu Xia
- **Assembly, Self-Organization and Reconfiguration of Nanoparticles** *Laura Na Liu,* Robert Macfarlane, Xingchen Ye, Michael Engel, Vivian Ferry
- **Selected Poster Presentations** *Gregory Hartland,* Jianping Xie
- **The GRC Power Hour™** *Amanda Haes*

Noble Metal Nanoparticles
Structure-Function Relationships of Noble Metal Nanomaterials from Design Principles to Diverse Applications
JUN 11-12, 2022
CHAIRS: Melissa King and Stephen Lee

Notch Signaling in Development, Regeneration and Disease

Mechanisms of Notch Signaling in Health and Disease

JUL 17-22, 2022
BATES COLLEGE, LEWISTON, ME
CHAIRS: Ivan Maillard and Freddy Radtke
VICE CHAIRS: Jon Aster and Kim Dale

- **Keynote Session: Setting Notch in Context** *Jon Aster, Kim Dale,* Kun-Liang Guan, Nancy Speck
- **Structure and Mechanisms of Notch Activation** *John Ngo,* Stephen Blacklow, Robert Haltiwanger, Penny Handford
- **Notch and Development** *Rachael Kuintzle, Roshana Thambyrajah,* Carmen Birchmeier, Ertugrul Ozbudak, Francois Schweisguth
- **Transcription, Epigenetics and Notch** *Anna Bigas,* Sarah Bray, Robert Faryabi
- **Notch, Cancer and Therapeutics** *Lucio Miele,* Rumela Chakrabarti, Adolfo Ferrando, Frank Kuhnert, Rajwinder Lehal
- **Notch and Liver Disease** *Sarah Bray,* Emma Andersson, Stacey Huppert, Hamed Jafar-Nejad, Utpal Pajvani, David Piccoli, Christian Siebel
- **Signaling Interactions and Modulations** *Daniel Lafkas,* John Ngo, Wendy Gordon, Vincent Luca, David Sprinzak
- **Late-Breaking Topics** *Raphael Kopan,* Nathalie Labrecque, Daniel Lafkas, Marc Vooijs
- **Blood and Vessels** *Irwin Bernstein,* Anna Bigas, Ralf Adams, Julia Mack
- **The GRC Power Hour™**

Notch Signaling in Development, Regeneration and Disease
Mechanisms of Notch Signaling in Health and Disease
JUL 16-17, 2022
CHAIRS: Rachael Kuintzle and Roshana Thambyrajah

NOX Family NADPH Oxidases

NOX Enzymes from Host Defense to Cell Signaling and Metabolic Disease

MAY 29-JUN 3, 2022
MOUNT SNOW, WEST DOVER, VT
CHAIR: Albert Van Der Vliet
VICE CHAIR: Marie Jose Stasia

- **Keynote Session: The NOX Family in Host Defense and Redox Biology** *William Nauseef,* Karl-Heinz Krause, Rafael Radi
- **NOX Structure and Functional Regulation** *Susan Smith,* Francesca Magnani, Ji Sun, Elizabeth Sweeny, David Thomas
- **Novel Tools to Assess NOX Activity and Function** *Louise Hecker,* Edward Chouchani, Hadley Sikes, Thomas Michel
- **NOX in Infection, Immunology and Microbiome Regulation** *Mary Dinauer,* Ulla Knaus, Nathalie Grandvaux, Balazs Rada, Amy Hsu
- **Biological Targets of NOX Biology: Peroxidases, Thiol Proteins and Ion Channels** *Franck Fieschi,* Miklós Geiszt, Ivan Bogeski, Takaaki Akaike
- **NOX in Cellular Metabolism and Metabolic Disease** *Ajay Shah,* Agnes Görlach, Roberto Di Maio, Rhian Touyz, Gerta Hoxhaj
- **Cell and Organelle-Specific Actions of NOX Enzymes** *Francisco R. Laurindo,* Vikas Anathy, Dongmin Kang, Ron Mittler
- **NOX in Cell Differentiation and Stem Cell Function: Implication for Cancer Biology** *Kathy Griendling,* Gareth Thomas, Katrin Schröder, Anna Martner, Lucia Lopes
- **NOX in Translation: Implications for Clinical Application** *Patrick Pagano,* Cristina Furdui, Victor Thannickal
- **The GRC Power Hour™** *Susan Smith*

NOX Family NADPH Oxidases
The Role of NOX-Dependent Oxidant Signaling in Health and Disease: Towards Therapeutic Targets
MAY 28-29, 2022
CHAIRS: Dina Vara and Carmen Veith

Ocean Biogeochemistry

Biogeochemical Processes Across Space and Time

MAY 1-6, 2022
REY DON JAIME GRAND HOTEL, CASTELLDEFELS, SPAIN
CHAIRS: Chuanlun Zhang and Susanne Neuer
VICE CHAIRS: Adina Paytan and Fei Chai

- **The Deoxygenation of the World Oceans** *Denise Breitburg,* Ronnie Glud, Sunke Schmidtko
- **Biological Carbon Pump and Microbial Carbon Pump in Changing Oceans** *Nianzhi Jiao,* Bethanie Edwards, Morten Iversen, Carol Robinson
- **Particle Pumps: Role of Animals and Injections** *Sarah Fawcett,* Herve Claustre, Santiago Hernandez De Leon
- **Carbon and Nitrogen Cycles Mediated by Keystone Organisms and Viruses** *Angelicque White,* Xiao-Hua Zhang, Takuro Nunoura, Jianfang Chen
- **Hydrocarbon Degradation in the Deep-Sea Sediments** *Fengping Wang,* Zhongze Shao, Katherine Dawson
- **Biogeochemistry in Polar High Latitude Oceans** *Wei-Jun Cai,* Jianfang Chen, Patricia Matrai, Walter Geibert
- **Shelf and Estuarine Biogeochemistry Under Anthropogenic Stress** *Celia Marrase,* Jianping Gan, Katja Fennel
- **Biogeochemistry in Ancient Oceans** *Sean Crowe,* Ariel Anbar, Kikki (Helga) Flesche Kleiven, Eva Stueeken
- **Current and Future Oceans** *Galen McKinley,* Tim Lenton, Christopher Sabine

Ocean Biogeochemistry
Biogeochemical Processes Across Space and Time
APR 30-MAY 1, 2022
CHAIRS: Qian (Lydia) Li and Christian Lindemann

Ocean Global Change Biology

Integrating Environmental, Organismal and Community Complexity into Ocean Global Change Research

JUL 17-22, 2022
WATERVILLE VALLEY, WATERVILLE VALLEY, NH
CHAIR: Sinead Collins
VICE CHAIR: Mary Sewell

- **Modeling Different Timescales in Ocean Change Biology** *Andy Ridgwell,* Patricia Sanchez-Baracaldo, Ben Ward
- **Horizon-Scanning in Ocean Global Change Biology** *Francis Chan,* Victoria Coles, David Hutchins, Andreas Osclies
- **Understanding the Role of Environmental Fluctuations in Shaping Organismal Responses** *Luis-Miguel Chevin,* Joanna Bernhardt, Juan Gaitan-Espitia, David Vasseur
- **Epigenetics and Transgenerational Plasticity** *Naomi Levine,* Melanie Heckwolf, Frank Johannes, Katie Lotterhos
- **Organismal Interactions in Changing Oceans** *Paul Renaud,* Corina Brussaard, Fernando Lima
- **Tropicalization** *Chris Harley,* Jason Hall-Spencer, Adriana Verges
- **Biological Variation and Responses to Changing Environments** *C. Elisa Schaum,* Amanda Bates, Colin Kremer, Tatiana Rynearson
- **Life Histories and Ocean Change** *Mary Sewell,* Catriona Clemmesen, Anke Kremp, Jonathan Havenhand
- **Incorporating Conservation and Mitigation Goals into Fundamental Research** *Gretchen Hofmann,* Trisha Atwood, Philip Boyd

Ocean Global Change Biology
Synthesizing Approaches to Predict Species Responses to Global Change
JUL 16-17, 2022
CHAIRS: Mark Bitter and Matthew Sasaki

Ocean Mixing

The Impact of Ocean Mixing on the Earth, Ocean and Atmosphere Systems, Climate and Society

JUN 5-10, 2022
MOUNT HOLYOKE COLLEGE, SOUTH HADLEY, MA
CHAIRS: Jonathan Nash and Kurt Polzin
VICE CHAIRS: Sonya Legg and Alberto Naveira Garabato

- **The Evolving Perspective of Ocean Mixing: Uncertainties in Global Predictions and Assessing Risk and Societal Impact in a Changing Climate** *Sjoerd Groeskamp,* Julie Pullen, Angelique Melet
- **Physics Near the Ice-Ocean Interface: Mixing in Ice-Influenced Oceans** *Mary-Louise Timmermans,* Sylvia Cole, Tom Rippeth, Amelie Meyer
- **Physics Near the Ice-Ocean Interface: Mixing Beneath Ice Shelves, in Fjords and Near Sea Ice** *Satoshi Kimura,* Claudia Cenedese, Bishakhdatta Gayen
- **Mixing in the Interior: Internal Waves and the Next Generation of Parameterizations** *Cynthia Bluteau,* Alexis Kaminski, Friederike Pollmann, Giovanni Dematteis

- **Upper-Ocean Mixing and Impacts on Biogeochemistry** *Peter Franks,* Amala Mahadevan, Laure Resplandy
- **Mesoscale and Submesoscale Processes: Eddies, Eddy-Wave Interactions and Nonlinear Coupling** *Amit Tandon,* Leah Johnson, Jennifer MacKinnon, Hideharu Sasaki
- **Mixing and Its Role in Climate Dynamics** *Eleanor Frajka-Williams,* Camille Lique, David Marshall, Andreas Schmittner
- **Mixing at the Bottom** *Erika McPhee-Shaw,* Ruth Musgrave, Jacob Wenegrat, Bethan Wynne-Cattanach
- **Pathways to Reducing Uncertainty** *Matthew Alford,* Tom Farrar, Eric D'Asaro
- **The GRC Power Hour™** *Alejandra Sanchez-Rios, Sally Warner*

Ocean Mixing

Ocean Mixing from the Smallest to the Largest Scales and its Impact on Ocean Dynamics, Biogeochemistry and the Climate System

JUN 4-5, 2022

CHAIRS: Marion Alberty and Sjoerd Groeskamp

Optics and Photonics in Medicine and Biology

Biophotonics Spanning the Biology-Medicine Continuum

JUL 10-15, 2022
BATES COLLEGE, LEWISTON, ME

CHAIRS: Kristen Maitland and David Sampson
VICE CHAIRS: E. Duco Jansen and Snow Tseng

- **Advanced Microscopy and Imaging** *Stephani Otte,* Winfried Denk, Jonathan Liu, Gabriel Popescu
- **Label-Free Imaging** *Andrew Rollins,* Yongkeun Park, Shalin Mehta, Kimani Toussaint, Irene Georgakoudi
- **Engineering Contrast** *Afrouz Anderson,* Cristina Zavaleta, Daniel Razansky, Summer Gibbs
- **Margin Assessment and Surgical Guidance** *Sylvain Gioux,* Laura Marcu, Muyinatu Bell, Christopher Contag
- **Neuroscience and the Brain** *Anna Devor,* Daniel Cote, Jana Kainerstorfer
- **Imaging in the Circulatory System** *Charles Lin,* Eva Sevick-Muraca, Darren Roblyer, Sarah Bohndiek, Clemens Alt
- **Endoscopy** *Audrey Bowden,* Caroline Boudoux, Eman Namati, Kev Dhaliwal
- **Noninvasive Probing of the Eye** *Ralf Brinkmann,* Iwona Gorczynska, Kirill Larin, Peter Török, Gereon Huettmann
- **Photo-Activation and Inactivation** *Alex Vitkin,* Kaushal Rege, Bryan Spring, Vanderlei Bagnato
- **The GRC Power Hour™** *Caroline Boudoux, Irene Georgakoudi*

Optics and Photonics in Medicine and Biology

Exploring the Role of Machine Learning in the Future of Biophotonics

JUL 9-10, 2022

CHAIRS: Danielle Harper and Madeleine Durkee

Optogenetic Approaches to Understanding Neural Circuits and Behavior

Linking Brain Circuits to Behavior: Novel Methods and Biological Insights Derived from Optogenetic Approaches

JUL 17-22, 2022
GRAND SUMMIT HOTEL AT SUNDAY RIVER, NEWRY, ME

CHAIR: Denise Cai
VICE CHAIR: Ofer Yizhar

- **Keynote Session: Neural Circuits and Neuromodulators in Health and Disease** *Sheena Josselyn,* Kay Tye, Lin Tian, Kafui Dzirasa
- **Circuits for Stress, Pain and Fear** *Conor Liston,* Thomas Kash, Sheena Josselyn, Michael Bruchas, Joshua Gordon
- **Seeing Dynamics and Understanding Circuits** *Joshua Trachtenberg,* Na Ji, Yevgenia Kozorovitskiy, Daniel Aharoni
- **Brain-Wide Dynamics** *Saskia de Vries,* Karl Deisseroth, Anne Churchland, Kanaka Rajan, Yang Dan, Gina Poe
- **Computational Behavior Analysis** *Nadine Gogolla,* Sandeep Robert Datta, Mackenzie Mathis, Mala Murthy
- **Circuits for Reward, Motivation and Addiction** *Steve Ramirez,* Kate Wassum, Paul Kenny, Zayd Khaliq, Veronica Alvarez, Erin Calipari, Christian Luscher
- **Circuits in Action** *Vanessa Ruta,* Adam Hantman, John Tuthill, Gaby Maimon
- **Circuits for Social Behaviors** *Bianca Jones Marlin,* Gul Dolen, Dayu Lin, Garret Stuber, Catherine Dulac, Ishmail Abdus-Saboor
- **Seeing Voltage: Sensors and Imaging** *Christina Kim,* Michael Lin, Luke Lavis
- **The GRC Power Hour™**

Optogenetic Approaches to Understanding Neural Circuits and Behavior

Expanding and Integrating Optogenetic Tools and Techniques

JUL 16-17, 2022

CHAIRS: Kevin Monk and Sarah Stern

Organic Geochemistry

The Formation and Fate of Organic Matter: How It Regulated Earth History and Will Shape Its Future

JUL 31-AUG 5, 2022
HOLDERNESS SCHOOL, HOLDERNESS, NH

CHAIR: Richard Pancost
VICE CHAIR: Anna Martini

- **The Limits of Our Understanding of Organic Matter** *Erdem Idiz,* Lena Vincent, Alon Amrani
- **The Evolutionary and Geological History of Biosynthetic and Metabolic Pathways** *Paula Welander,* Jochen Brocks, Amanda Garcia, Sarah Hurley, Patrick Shih
- **Interfaces Between Organic and Inorganic Chemistry: Preservation, Destruction and Interactions** *Johan Weijers,* Prachi Joshi, Christian Maerz, Sander Van Den Boorn
- **Lipid Membranes: From Biophysics to Adaptation to Novel Proxies** *Nicole Bale, Florence Schubotz,* Phil Oger, Laura Villanueva, Jiasong Fang, Guy Schleyer
- **Big Data Approaches to Obtain New Understanding of Geological Systems** *Jeff Sheremata,* Krista Longnecker, Thomas Abraham, Yishu Song
- **The Myriad Pools and Archives of OM** *Ryan Pereira,* Asmeret Asefaw Berhe, Thomas Blattmann, Anja Engel, Peter Hernes
- **The Organic Geochemistry of the Arctic** *Bart van Dongen,* Lisa Bröder, Carolyn Ruppel, Rémi Amiraux
- **Measuring and Deciphering Intramolecular Isotopes Across Space and Time** *Kate Freeman,* Alexis Gilbert, Barbara Sherwood Lollar
- **Late-Breaking Topics** *Elise Wilkes*
- **The GRC Power Hour™** *Nicole Bale, Richard Pancost*

Organic Geochemistry

Mechanistic and Experimental Insights on Geochemical Archives

JUL 30-31, 2022

CHAIRS: Elise Wilkes and Julie Lattaud

Organic Reactions and Processes

Innovations in Synthesis: Advancing Capabilities and Empowering Industrial Processes

JUL 17-22, 2022
BRYANT UNIVERSITY, SMITHFIELD, RI

CHAIRS: Sriram Naganathan and Jimmie Weaver
VICE CHAIRS: Craig Merlic and Michael Zacuto

- **Stereochemical and Atomic Control in Organic Synthesis** *Mark Biscoe,* Qiu Wang, David Lupton, Cathleen Crudden
- **Installation and Uses of Halogens** *Florence Williams,* Rebecca Green, Mark Kerr, Megan Smyth, Tobias Ritter, Beate Koksch
- **Innovative Strategies in C-C Bond Formation** *Erin Stache,* Debabrata Maiti, Sarah Wengryniuk, Chulbom Lee
- **Proteins and Similars** *Sebastien Laulhe,* Emma McInturff, Jie Xu, Sara Bonderoff, Samuel Gellman, Jennifer Heemstra
- **Behold the Power of Light** *Yalan Xing,* David Nicewicz, Abigail Doyle, Ryan Gilmour
- **More C-C Bond Formation and Methods** *Michael Harmata,* Hongli Bao, Thomas Snaddon
- **Let the Chemistry Flow** *Silas Cook,* Nadine Kuhl, Jessica Herrick, Jason Hein, Timothy Noel, Timothy Jamison
- **Reactions in Motion** *Michael Zacuto,* Robert Flowers, Oliver Kappe, Mary Russell
- **Chemistry on Complex Molecules** *Craig Merlic,* John Jasper, Lukas Goossen, Jeff Johnson
- **The GRC Power Hour™** *Jen Heemstra and Emma McInturff*

Organometallic Chemistry

JUL 10-15, 2022
SALVE REGINA UNIVERSITY, NEWPORT, RI

CHAIR: Mitch Smith
VICE CHAIR: Heather Spinney

- **Bioorganometallic Chemistry** *Paula Diaconescu,* Joan Broderick, Hannah Shafaat
- **Late and Heavy Metal Chemistry** *Selvan Demir,* Aaron Tondreau, Vincent Lavallo, Jennifer Schomaker
- **Harnessing Photons and Electrons** *John Gordon,* Louise Berben, Yogesh Surendranath, Daniel Nocera
- **Synthesis and Catalysis with More Abundant Metals** *Aaron Sadow,* Kyle Lancaster, Corinna Schindler
- **Early-Career Investigator Presentations** *Thomas Cundari,* Hosea Nelson, Neil Tomson, Jenny Yang
- **Main Group Chemistry** *Nora Radu,* Christopher Cummins, Stephen Westcott
- **Organometallic Chemistry at Surfaces** *Odile Eisenstein,* John Roberts, Matthew Conley, Christophe Copéret
- **Bond Activation and Functionalization** *John Walzer,* Robert Phipps, Matthew Sigman
- **Ligands and Metals** *Heather Spinney,* R. Tom Baker, Paul Chirik
- **The GRC Power Hour™** *Nancy Williams, Jenny Yang*

Organometallic Chemistry

Transition Metal and Main Group Synthesis and Catalysis for a Sustainable Future

JUL 9-10, 2022

CHAIRS: Natalia Loewen and Eric Cueny

Oscillations and Dynamic Instabilities in Chemical Systems

Nonequilibrium to Induce and Maintain Spatio-Temporal Patterns

JUL 17-22, 2022
STONEHILL COLLEGE, EASTON, MA

CHAIR: Satoshi Nakata
VICE CHAIR: Marcus Hauser

- **Spatio-Temporal Pattern Based on Reaction-Diffusion Systems** *Tomohiko Yamaguchi,* Annette Taylor, Alberto Munuzuri
- **Self-Organized Active Matter** *Kouichi Asakura,* Raymond Kapral, Masaharu Nagayama, Lee Cronin
- **Electrochemical Control on Oscillations and Patterns** *Katharina Krischer,* Istvan Kiss, Ronald Imbihl
- **Spatio-Temporal Collective Behaviors** *Hiroyuki Kitahata,* Veronique Pimienta, Jeremie Palacci, Nobuhiko Suematsu, Hiraku Nishimor
- **Molecular Design of Self-Organized Structures** *John Pojman,* Anna Balazs, Andreas Walther
- **Biological Oscillations and Patterns** *Takashi Amemiya,* Geneviève Dupont, Takashi Miura
- **Emergence in Signal Transduction and Network Systems** *Toshiyuki Nakagaki,* Castern Beta, Agota Toth
- **Nonlinear Dynamics: Synchronization, Bifurcation and Chaos** *Dezso Horvath,* Irving Epstein, Anne De Wit, Sumana Dutta
- **Pattern Formation Coupled with Mass Transfer and Flow** *Kenneth Showalter,* Jerzy Gorecki, Oliver Steinbock

Oscillations and Dynamic Instabilities in Chemical Systems
Looking at Science and Technology Through the Lens of Nonlinear Chemistry
JUL 16-17, 2022
CHAIRS: Domenico Bullara and Pamela Knoll

Personalized Medicine

From Scientific Basis to Clinical Practice in Individuals and Populations

JUN 26-JUL 1, 2022
VENTURA BEACH MARRIOTT, VENTURA, CA
CHAIRS: Hsing-Jien Kung and Pui-Yan Kwok
VICE CHAIR: Dean Ho

- **Genomic Profiling: Tools and Applications** *Robert Nussbaum,* Nikolaus Schultz, Janina Jeff
- **Precision Oncology: Early Detection** *Dan Robinson,* Colin Collins, Muh-Hwa Yang, Donald Parsons
- **Genomic Approaches to Rare Disease Diagnosis** *Ebony Madden,* Sharon Plon, Stephen Kingsmore
- **Personalized Oncology: Tailored Treatment-1** *Emily Lin,* Dan Robinson, Edward Chow, Victoria Seewaldt
- **Social and Ethical Implications of Personalized Medicine** *Fatima Munoz,* Sara Ackerman, Mildred Cho
- **Personalized Oncology: Tailored Treatment-2** *David Ann,* Whei-Mei Teresa Fan, Kun-Liang Guan, Melanie McReynolds
- **Genomic Approaches to Infectious Disease Diagnosis** *David Engelthaler,* Charles Chiu, Alexander Greninger
- **Common Disease Risk Prediction and Mitigation** *Kelly Frazer,* Natasha Strande, Nancy Cox
- **Personalized Medicine for Large Populations** *Ysabel Duron,* Alicia Zhou, Carlos Bustamante
- **The GRC Power Hour™** *Ebony Madden, Nancy Cox*

Personalized Medicine
Precision Oncology Highlighting Molecular Diagnostics and Experimental Therapeutics
JUN 25-26, 2022
CHAIRS: Chia-Lin Chen and Emine Gunes

Phosphorylation and G-Protein Mediated Signaling Networks

Molecular Mechanisms of Signal Integration in Cellular and Organismal Regulation

JUN 12-17, 2022
SOUTHBRIDGE HOTEL & CONFERENCE CENTER, SOUTHBRIDGE, MA
CHAIR: Rebecca Berdeaux
VICE CHAIR: Alan Smrcka

- **Keynote Session: Regulation of Protein Kinase Signaling** *Anton Bennett,* Alexandra Newton, Robert Screaton, Yonghao Yu
- **Membrane Proximal G-Protein Signaling** *Alan Smrcka,* Heidi Hamm, Ku-Lung Hsu, Nevin Lambert, Angeline Lyon
- **Cyclic Nucleotide Regulated Signaling** *Carmen Dessauer,* Xiaodong Cheng, Lonny Levin, Susan Taylor
- **G-Protein and Kinase Signaling in Physiological Control** *Henrik Dohlman,* Gregory Tall, Melanie Cobb, Carmen Dessauer, Joan Heller Brown, Kirill Martemyanov
- **Physiological and Chemical Regulation of G-Protein Activity** *Kirill Martemyanov,* Kendall Blumer, Evi Kostenis, Roger Sunahara
- **GPCR-Activated Signaling in Control of Cell Proliferation and Cancer** *Melanie Cobb,* Antonio Amelio, Kun-Liang Guan, J. Silvio Gutkind, Michelle Kimple
- **Signaling Beyond the Plasma Membrane** *John Scott,* Jeff Frost, Alan Jones, Carol Williams
- **Integration of Phosphorylation and G-Protein Mediated Signaling** *Joan Heller Brown,* Roshanak Irannejad, Jurgen Wess, Anton Bennett, John Scott
- **Keynote Session: Structural Aspects of G-Protein Signaling** *Roger Sunahara,* Arun Shukla, Stephen Sprang, John Tesmer

Phosphorylation and G-Protein Mediated Signaling Networks
Mechanisms in G-Protein and Kinase-Mediated Signaling
JUN 11-12, 2022
CHAIR: Ankita Jaykumar

Photonuclear Reactions

Frontiers in Nuclear and Hadronic Physics

AUG 7-12, 2022
HOLDERNESS SCHOOL, HOLDERNESS, NH
CHAIR: Huey-Wen Lin
VICE CHAIRS: Douglas Higinbotham and Marc Vanderhaeghen

- **New Results in Precision Hadron Structure with Electromagnetic Probes** *Aldo Antognini,* Sylvester Joosten, Nikolaos Sparveris
- **Femtography of Hadrons** *Barbara Pasquini,* Xiangdong Ji, Julie Roche
- **Electrons for Neutrinos** *Or Hen,* Adi Ashkenazi, Afroditi Papadopoulou, Sam Zeller, Noemi Rocco
- **Hadrons in the Nuclear Medium** *Eliezer Piasetzky,* Efrain Segarra, Igor Korover, Gerald Miller, Ronen Weiss, Dien Nguyen
- **Nuclear Precision Physics and Applications** *Concettina Sfienti,* Chiara Mazzocchi, Saori Pastore
- **Hadron Spectroscopy** *Annalisa D'Angelo,* Justin Stevens
- **From QCD to Gravitational Waves** *Jocelyn Read,* Jorge Piekarewicz, Kenta Kiuchi
- **Nuclear Physics and Quantum Information Science** *Ian Cloet,* Srimoyee Sen, Zohreh Davoudi
- **Physics with an Electron Ion Collider** *Abhay Deshpande,* Elena Long, Todd Satogata
- **The GRC Power Hour™** *Huey-Wen Lin, Elena Long*

Plant and Microbial Cytoskeleton

Cytoskeletal Diversification Across the Domains of Life

AUG 14-19, 2022
PROCTOR ACADEMY, ANDOVER, NH
CHAIRS: Erin Goley and Geoffrey Wasteneys
VICE CHAIRS: Sophie Martin and Alexander Paredez

- **Keynote Session: Evolution of the Cytoskeleton** *Magdalena Bezanilla,* Marko Kaksonen, Nina Salama
- **Proliferation and Reproduction** *Christopher de Graffenried,* Alex Bisson, Rui Li, Simonetta Piatti, Carolyn Rasmussen
- **Interactions with Membranes** *Anthony Vecchiarelli,* Aoife Heaslip, Geraldine Laloux, Snezhka Oliferenko
- **Wall Polymer Placement and Cell Morphogenesis** *Sabine Mueller,* Chris Ambrose, Rut Carballido-Lopez, Nicolas Minc
- **Selected Poster Presentations** *Prachee Avasthi*
- **Cell Polarity and Polar Growth** *Daniel Lew,* Michelle Facette, Shanjin Huang, Liedewij Laan, Luis Vidali
- **Motors and Motility** *Lillian Fritz-Laylin,* Ram Dixit, Freddy Frischknecht, Kent Hill
- **Regulating Cytoskeletal Dynamics** *Marc Edwards,* Bruce Goode, David Kovar, Alphée Michelot, Hiroyasu Motose
- **Keynote Session: Host-Microbe Interactions** *Alexander Paredez,* Dominique Soldati-Favre, Chris Staiger
- **The GRC Power Hour™** *Erin Goley,* Geoffrey Wasteneys

Plant and Microbial Cytoskeleton
An Evolving Cytoskeleton: Diverging Mechanisms and Converging Patterns
AUG 13-14, 2022
CHAIRS: Katrina Velle and Ryan Eng

Plant Molecular Biology

Spatial and Temporal Dynamics in Plant Biology

JUN 12-17, 2022
HOLDERNESS SCHOOL, HOLDERNESS, NH
CHAIR: C. Robertson McClung
VICE CHAIR: Rebecca Mosher

- **Keynote Session: Symbioses** *Cara Haney,* Maria Harrison, Giles Oldroyd
- **Development in Space** *Madelaine Bartlett,* Zach Lippman, Miltos Tsiantis, Minako Ueda
- **Biotic Interactions** *Hua Lu, Hailing Jin,* Sophien Kamoun
- **RNA: Roles Beyond the Message** *Aman Husbands,* Xiaofeng Cao, Blake Meyers
- **Nutrient Regulation and Transport** *Terri Long,* Rodrigo Gutierrez, David Mendoza Cozatl
- **Development in Time** *Stacey Harmer,* Hong Gil Nam, Mark Estelle
- **Modeling and Gene Regulatory Networks** *Gabriel Krouk,* Martin Howard, Joseph Swift
- **Environmental Sensing** *Ullas Pedmale,* Julia Bailey-Serres, Dawn Nagel, Richard Vierstra
- **Keynote Session: Gene and Genome Evolution** *Benjamin Blackman,* Pamela Soltis, Jennifer Wisecaver
- **The GRC Power Hour™** *Stacey Harmer*

Plant Molecular Biology
Diversifying the Plant Molecular Biology Toolkit to Understand and Engineer Plants
JUN 11-12, 2022
CHAIRS: Jennifer Brophy and Sunil Kumar Kenchanmane Raju

Plasma Processing Science

Plasmas and Their Interactions with Matter

JUL 24-29, 2022
PROCTOR ACADEMY, ANDOVER, NH
CHAIR: Anthony Murphy
VICE CHAIR: Lorenzo Mangolini

- **Measuring the Interplay between Plasma and Matter** *Holger Kersten,* Sedina Tsikata, David Pai
- **Plasma Synthesis of Novel Materials** *Elijah Thimsen,* Mohan Sankaran, Scott Walton, Boris Feygelson
- **Linking Plasma Processing and Fusion Plasmas** *Yevgeny Raitses,* David Ruzic, Michael Campanell
- **Plasma Interactions with Biological Materials** *Greg Fridman,* Antoine Rousseau, Nevena Puac
- **Complex Chemical Synthesis Using Plasmas** *Katharina Stapelmann,* Julia Bandow, Felipe Iza
- **Plasmas and Catalysts** *Maria Carreon,* William Schneider, Sankaran Sundaresan
- **Plasma Surface Modification and Deposition** *Michael Gordon,* Sumit Agarwal, Lenka Zajickova
- **The Plasma-Liquid Interface** *Peter Bruggeman,* Dingxin Liu, Fumiyoshi Tochikubo, Ester Marotta
- **Plasmas for the Environment** *Sylvain Coulombe,* Volker Hessel, Mariadriana Creatore
- **The GRC Power Hour™**

Plasma Processing Science
Investigating Multiphase and Multiscale Plasma-Material Interactions
JUL 23-24, 2022
CHAIRS: Judith Golda and Marien Simeni Simeni

Plasmonics and Nanophotonics

Nanoscale Light-Matter Interactions for Sustainability

JUL 10-15, 2022
GRAND SUMMIT HOTEL AT SUNDAY RIVER, NEWRY, ME
CHAIR: Jennifer Dionne
VICE CHAIR: Javier Aizpurua

- **Keynote Session: Dynamic Light-Matter Interactions** *Nader Engheta,* Mark Brongersma, Peter Nordlander, Teri Odom
- **Photochemistry and Catalysis** *Renee Frontiera,* Peng Chen, Prashant Jain, Yousoo Kim, Christy Landes
- **Sustainable Energy and the Environment** *Harry Atwater,* Shanhui Fan, Vivian Ferry, Matthew Sheldon
- **Nanophotonics for Biology and Medicine** *Laura Fabris,* Rizia Bardhan, Gennady Shvets

- **Metasurfaces and Metamaterials** *Jon Schuller,* Andrea Alu, Jason Valentine
- **Active Nanophotonics and Molecular-Scale Optoelectronics** *Carsten Rockstuhl,* Joshua Caldwell, Jeremy Baumberg, Christian Nijhuis, Uriel Levy, Maiken Mikkelsen, Anatoly Zayats
- **Quantum and Nonlinear Nanophotonics** *Aitzol Garcia-Etxarri,* Yuri Kivshar, Prineha Narang, Timur Shegai, Francisco Garcia-Vidal
- **Novel Syntheses and Spectroscopies** *Javier Garcia de Abajo,* Bin Ren, Mathieu Kociak
- **Keynote Session: Technology Translation** *Albert Polman,* Naomi Halas, Vladimir Shalaev, Luat Vuong
- **The GRC Power Hour™** *Teri Odom, Luat Vuong*

Plasmonics and Nanophotonics
Engineering Nanoscale Light-Matter Interactions for Energy, Communication and Biomedical Applications
JUL 9-10, 2022
CHAIRS: Loza Tadesse and Pavlos Pachidis

Polymer Physics

Polymer Physics for Sustainability

JUL 24-29, 2022
MOUNT HOLYOKE COLLEGE, SOUTH HADLEY, MA
CHAIR: Sanat Kumar
VICE CHAIR: Rachel Segalman

- **Polymer Upcycling** *Megan Robertson, Karen Winey,* Gregg Beckham, Linda Broadbelt
- **Solid Polymer Electrolytes** *Nitash Balsara, Jodie Lutkenhaus,* Monika Schoenhoff, Jennifer Schaefer, Emmanouil Glynos, Moon Jeong Park
- **Limits of Macromolecular Self-Assembly** *Arthi Jayaraman, Lynn Walker,* Mahesh Mahanthappa, Oleg Gang
- **Nanocomposites** *Russell Composto, Jane Lipson,* Michael Rubinstein, So Youn Kim, Reika Katsumata, Marc Couty
- **Novel Characterization Methods** *Christopher Soles, Danielle Mai,* Enrique Gomez, Brian Collins, Muzhou Wang
- **Artificial Intelligence and Machine Learning** *Jonathan Whitmer,* Alexander Hexemer, Debra Audus, Venkat Ganesan
- **Dynamic Networks** *Bradley Olsen, Vivek Sharma,* Evelyne van Ruymbeke, Jian Qin
- **Membranes** *Chinedum Osuji, Richard Register,* Benny Freeman, Sangwoo Lee, Miguel Modestino, Ayse Asatekin
- **Biomaterials** *Thomas Epps, Matthew Tirrell,* LaShanda Korley, Sarah Heilshorn
- **The GRC Power Hour™** *Lilo Pozzo, Rodney Priestley, Arthi Jayaraman*

Polymer Physics
Leveraging Polymer Physics for a More Sustainable Future
JUL 23-24, 2022
CHAIRS: Whitney Loo and Konane Bay

Post-Transcriptional Gene Regulation

Coordination and Integration of RNA Processing from Transcription to Translation

JUL 10-15, 2022
JORDAN HOTEL AT SUNDAY RIVER, NEWRY, ME
CHAIRS: Tom Cooper and Kristen Lynch
VICE CHAIRS: Karla Neugebauer and Nicholas Conrad

- **Emerging Concepts in RNA Biology** *Joan Steitz,* Christine Mayr, Mitch Guttman, Benjamin Blencowe, Roy Parker
- **Role of Post-Transcriptional Regulation From Genotype to Phenotype** *Brenton Graveley,* Xinshu Xiao, Juan Valcarcel, Alain Laederach, Angela Brooks, Auinash Kalsotra, William Fairbrother
- **3' End Processing** *Chris Burge,* Eric Wagner, Bin Tian, Yongsheng Shi
- **RNA Decay** *Karla Neugebauer,* Lynne Maquat, Olivia Rissland, Bobby Hogg, Heidi Cook-Andersen, Sujatha Jagannathan
- **RNA Structure and Modifications** *Wendy Gilbert,* Steve Bonilla, Richard Gregory, Kathy Fange Liu, Rui Zhao
- **Regulation of Translation** *Ruth Lehmann,* Katrin Karbstein, Davide Ruggero, Gloria Brar, Joel Neilson, Jeff Coller
- **RNA Localization and Assembly** *Douglas Black,* Kimberly Mowry, Robin Stanley, Lingling Chen, Beatriz Fontoura
- **RNP Function and Disease Implications** *Manuel Ares,* Eric Wang, Sara Cherry, Kathryn Hamilton, Peter Sarnow, Adrian Krainer
- **Integration of RNA Biogenesis Steps** *Nicholas Conrad,* Tracy Johnson, Matthew Simon, David Bentley
- **The GRC Power Hour™** *Kristen Lynch, Karla Neugebauer*

Post-Transcriptional Gene Regulation
Emerging Roles of RNA in Gene Regulation
JUL 9-10, 2022
CHAIRS: Nicole Martinez and Ana Fiszbein

Protein Processing, Trafficking and Secretion

From Cell Biology to Human Disease

JUL 17-22, 2022
COLBY-SAWYER COLLEGE, NEW LONDON, NH
CHAIR: Alan Attie
VICE CHAIR: Julia von Blume

- **Protein Folding in the Secretory Pathway** *Regina Fluhrer,* Jason Gestwicki, Carmine Settembre, Feroz Papa, Feyza Engin
- **Glycosylation and Phosphorylation in the Secretory Pathway** *Melkam Kebede,* Hudson Freeze, Heather Flanagan-Steet, Kelly Ten Hagen, Michael Boyce
- **Nutrient Sensing, Ion Channels and Vesicle Trafficking** *Peter Arvan,* Matthew Merrins, Debbie Thurmond, Samuel Stephens, Melkam Kebede
- **Protein Aggregation, Proteostasis and Autophagy** *Feyza Engin,* Mondira Kundu, Luigi Puglielli, Judith Frydman
- **COVID-19 Entry Into the Cell and Assembly in the Secretory Pathway** *Carmine Settembre,* Gary Whittaker, Nihal Altan-Bonnet, Hector Aguilar-Carreno
- **Visualizing the Secretory Pathway** *Julia von Blume*, Ana Paula Arruda, Anjon Audhya, Michele Solimena, Joerg Bewersdorf
- **Lipid Transport Through the Secretory Pathway** *Michele Solimena,* Anant Menon, Russell Debose-Boyd, Thomas Melia, Elina Ikonen
- **Proteolysis in the Secretory Pathway** *Nabil Seidah*, Thomas Delong, Annik Prat, Regina Fluhrer, Stefan Lichtenthaler
- **Exosomes** *Anjon Audhya,* Carmella Evans-Molina, Philipp Scherer, Wei Guo
- **The GRC Power Hour™** *Julia von Blume,* Iris Lindberg

Protein Processing, Trafficking and Secretion
Insights into the Molecular Mechanisms of Protein Trafficking
JUL 16-17, 2022
CHAIRS: James Checco and Julie Cruanes

Proteoglycans

Frontiers in Basic and Translational Proteoglycan Research to Improve Human Health

JUL 10-15, 2022
PROCTOR ACADEMY, ANDOVER, NH
CHAIRS: Liliana Schaefer and Charles Frevert
VICE CHAIR: Catherine Merry

- **Keynote Session: Recent Progress in Proteoglycan Biology** *Marian Young, Renato Iozzo,* Peter Seeberger
- **Genetic Defects Linking Proteoglycans and Glycosaminoglycans to Clinical Phenotypes and Tissue Pathologies** *Thomas Wight, Suneel Apte,* Fransiska Malfait, Josephina Meester, Eri Arikawa-Hirasawa, Mark Febbraio
- **Proteoglycans and Associated Molecules in Tissue Homeostasis and Disease** *Billy Hudson, Nikos Karamanos,* Nicola Allen, Joseph Hippensteel, Anthony Day
- **Proteoglycan Signaling** *Melanie Simpson, Jeffrey Esko,* Mythreye Karthikeyan, Jorge Filmus, Aaron Petrey, Rashmin Savani
- **Proteoglycans in Development and Regenerative Medicine** *Hideto Watanabe, John Whitelock,* Alyssa Panitch, Tommaso Pizzorusso
- **Proteoglycans and GAGs in Immuno-Oncology** *Karin Forsberg-Nilsson, Stephen Hewitt,* Fotis Asimakopoulos, Mattias Belting, Wantong Yao, Paul Timpson
- **New Technologies to Define the Role of PGs and GAGs in Health and Disease** *Brooke Farrugia, Vincent Hascall,* Sylvie Ricard-Blum, Jamie Thompson, Adam Hall
- **Development of New Drugs Targeting Proteoglycans** *Jin-Ping Li, Ralph Sanderson,* Jeremy Turnbull, Nunzio Bottini, Jian Liu, Mitchell Ho
- **Matrix-Targeted Glycan Therapeutics in Clinical Trials** *Glenn Prestwich, John Paderi,* Li Peng, Sangeetha Srinivasan, Mats Wahlgren, Denis Barritault, Thomas Kennedy, Abigail Pulsipher
- **The GRC Power Hour™** *Catherine Merry*

Proteoglycans
Integrated Proteoglycan Research to Improve Human Health
JUL 9-10, 2022
CHAIRS: Marissa Maciej-Hulme and Ryan Weiss

Proteolytic Enzymes and Their Inhibitors

The Regulation of Proteolysis in Health, Disease and Treatment

JUN 5-10, 2022
RENAISSANCE TUSCANY IL CIOCCO, LUCCA (BARGA), ITALY
CHAIR: James Huntington
VICE CHAIR: Jeanne Hardy

- **Cancer** *Klaudia Brix,* Galia Blum, Donna Small, Boris Turk
- **Coagulation Proteases** *Rodney Camire,* Jim Crawley, Joanna Koziel, Christoph Reinhardt, Thomas Renné
- **Immunity and Inflammation** *James Whisstock,* Charaf Benarafa, F. Xavier Gomis-Rüth, Piet Gros, Guy Salvesen
- **Proteases and Pathogens** *Jan Potempa,* Charles Craik, Ruby Law, Celia Schiffer
- **Therapeutic Targeting of Proteolytic Activity** *Joanne Lemieux,* Grant Blouse, Henry Maun, Dennis Wolan
- **The Ubiquitin-Proteosome System** *Paula Da Fonseca,* Andreas Martin
- **Probing Protease Action In Situ** *Marcin Drag,* Matthew Bogyo, Laura Edgington-Mitchell, Paulina Kasperkiewicz
- **Proteolysis in and on Cell Membranes** *Manu Platt,* Christoph Becker-Pauly, Regina Fluhrer, Rui Zhou
- **SARS-CoV-2 Proteases and Inhibitors** *Jeanne Hardy,* Rolf Hilgenfeld, Christopher Overall, Joanne Lemieux
- **The GRC Power Hour™** *Galia Blum*

Proteolytic Enzymes and Their Inhibitors
The Regulation of Proteolysis in Health, Disease and Treatment
JUN 4-5, 2022
CHAIRS: Paulina Kasperkiewicz and Amy Weeks

Quantum Science

Many-Body Quantum Systems: From Quantum Computing and Simulation to Metrology and Coherent Light-Matter Hybrids

JUL 24-29, 2022
STONEHILL COLLEGE, EASTON, MA
CHAIRS: Markus Greiner and Eugene Demler
VICE CHAIRS: Susanne Yelin and Jonathan Simon

- **Quantum Simulation** *Ana Maria Rey*, Monika Aidelsburger, Fabian Grusdt
- **Progress in Quantum Computing and Algorithms** *Mikhail Lukin,* Andrew Houck, Matthias Troyer
- **Non-Equilibrium Quantum Matter** *Monika Aidelsburger,* Richard Averitt, Waseem Bakr, Ana Maria Rey, Julian Léonard
- **From Quantum Simulation to Quantum Computing** *Eun-Ah Kim,* Rainer Blatt, Dries Sels, Mikhail Lukin
- **Quantum Metrology and Sensing** *Susanne Yelin,* Ania Bleszynski-Jayich, Holger Mueller, Vladan Vuletic
- **Late-Breaking Topics** *Andrew Houck*

- **Quantum Matter** *Andrea Cavalleri,* Amir Yacoby, Andrea Young, Sankar Das Sarma
- **Light-Matter Interactions and Many-Body Quantum Optics** *Jonathan Simon,* Andrea Cavalleri, Angel Rubio, Ephraim Shahmoon
- **Connection Between Quantum Science and Other Fields** *Vladan Vuletic,* Eun-Ah Kim

Quantum Science
Quantum Matter for Communications, Fundamental Investigations, Simulation and Computation
JUL 23-24, 2022
CHAIRS: Julia Cline and Kristine Rezai

Radionuclide Theranostics for the Management of Cancer NEW!

Molecularly Targeted, Radioactive Cancer Diagnosis and Therapy

JUL 17-22, 2022
JORDAN HOTEL AT SUNDAY RIVER, NEWRY, ME
CHAIR: Alan Harris
VICE CHAIR: Yusuf Menda

- **Targets and Radionuclides** *Michael Schultz,* David Bauer, Germo Gericke
- **Radiotherapeutics in Oncologic Diseases** *Daniel Pryma,* Ken Herrmann, Ebrihim Delpassand, Amir Iravani, Michael Schultz
- **Dosimetry-Guided Therapy with Radionuclides** *Stephen Graves,* Robert Hobbs
- **Development of Theranostic Radiopharmaceuticals** *Jonathan McConathy,* Richard Wahl, Andrew Bellizzi, Benjamin Larimer
- **Radionuclide Therapy in Clinical Practice** *Joseph Dillon,* John Buatti, Eric Liu, Daniel Pryma, Stephen Graves
- **Optimizing Therapy** *Kjell Oberg,* Jonathan McConathy, David Bushnell, Josh Mailman
- **Design of Theranostic Clinical Trials** *David Bushnell,* Philip Harris, Charles Kunos, Emily Bergsland
- **Advances in Radionuclide Theranostics** *John Buatti,* Aldo Scarpa, Brian Miller, Chandrasekhar Bal
- **Selected Poster Presentations** *Yusuf Menda*
- **The GRC Power Hour™**

Renewable Energy: Solar Fuels

Advancing Complexity, Selectivity and Efficiency in Artificial Photosynthesis

MAY 8-13, 2022
RENAISSANCE TUSCANY IL CIOCCO, LUCCA (BARGA), ITALY
CHAIRS: Clifford Kubiak and Xile Hu
VICE CHAIRS: Can Li and Jillian Dempsey

- **Solar Fuels at Sunrise** *Jillian Dempsey,* Raffaella Buonsanti, Haotian Wang
- **Biological and Bio-Inspired Systems** *Marc Fontecave,* Tobias Erb, Jenny Yang
- **Merging Molecules with Materials** *Greta Patzke,* Bettina Lotsch, Amanda Morris, Yogesh Surendranath
- **Light Absorbers and Photocatalysts** *Marcella Bonchio,* Kyoung-Shin Choi, Osamu Ishitani, Li-Zhu Wu
- **Water Splitting** *Licheng Sun,* Bin Liu, Peter Strasser
- **Operando Spectroscopy** *Moniek Tromp,* Hao Ming Chen, Beatriz Roldan Cuenya
- **CO2 Reduction** *Alexander Miller,* Karen Chan, Matthew Kanan, Marc Robert
- **Systems and Engineering** *Harry Atwater,* Curtis Berlinguette, Hans Geerlings, Avner Rothschild, Wilson Smith
- **Late-Breaking Topics** *Can Li*

Renewable Energy: Solar Fuels
Catalytic Transformations for Sustainable Chemicals
MAY 7-8, 2022
CHAIRS: Anna Beiler and Shannon Bonke

Research at High Pressure

Exploring High Pressure Science at the Extremes Through Experiment and Computation

JUL 17-22, 2022
HOLDERNESS SCHOOL, HOLDERNESS, NH
CHAIR: Sakura Pascarelli
VICE CHAIR: Chris Pickard

- **Challenges to Our Understanding of Dense Matter** *Russell Hemley,* Paul Loubeyre
- **Hydrogen Rich Systems** *Yanming Ma,* Mikhail Eremets, Audrey Grockowiak, Ashkan Salamat, Dmitrii Semenok
- **Beyond Earth: Pressure as an Experimental Probe** *Amy Jenei,* Stephanie Brygoo, Sara Seager
- **Scientific Opportunities Opened by New Experimental Approaches** *Siegfried Glenzer,* Stewart McWilliams, Thomas Meier, Mohamed Mezouar
- **Earth: From Crust to Inner Core** *Renata Wentzcovitch,* Yanhao Lin, Taku Tsuchiya
- **The Limits of Computation and the Role of Data Driven Approaches** *Maosheng Miao,* Kien Nguyen-Cong, Volker Deringer, Clemens Prescher, Eva Zurek
- **Extreme Bioscience** *Ryo Kitahara,* Catherine Royer, Karen Lloyd
- **New Phenomena at High Density** *Guoyin Shen,* Graeme Ackland, Leonid Dubrovinsky
- **Keynote Session: Extremely Dense Matter** *Chris Pickard,* Jon Eggert, Andrea Kritcher, Burkhard Militzer

Research at High Pressure
Synergy Between Experiment and Computation Within Science at the Extremes
JUL 16-17, 2022
CHAIR: Dean Smith

Rock Deformation

Combining Laboratory Measurements with Observational Constraints to Understand Tectonic Processes

AUG 7-12, 2022
BATES COLLEGE, LEWISTON, ME
CHAIR: Daniel Faulkner
VICE CHAIR: Heather Savage

- **Keynote Session: Lithospheric Rheology from Small-Scale Experiments** *David Kohlstedt,* Brian Evans, Philip England
- **Fundamental Frictional Processes** *Marco Maria Scuderi,* Izabela Szlufarska, David Goldsby, Kathryn Hayward
- **Earthquake Mechanics** *Roland Burgmann,* Nadia Lapusta, Gregory McLaskey
- **Fault Slip in Nature** *Zoe Mildon,* Rachel Abercrombie, Matt Tarling, Marion Thomas
- **Early-Career Investigator Presentations** *Heather Savage*
- **Lower Crustal Dynamics** *Virginia Toy,* William Shinevar, Luca Menegon, Ylona Dinther
- **Mantle Rheology** *Benjamin Holtzman,* Sylvie Demouchy, David Dobson
- **Shallow Subduction Processes** *Christine Regalla,* Noel Bartlow, Rob Skarbek, Demian Saffer
- **Deeper Subduction Processes** *Nadege Hilairet,* Geoff Abers, Greg Hirth
- **The GRC Power Hour™**

Rock Deformation
Integrating Rock Deformation Studies with Geophysics, Field Geology and Modeling
AUG 6-7, 2022
CHAIRS: Taka Kanaya and Carolyn Tewksbury-Christle

Salt and Water Stress in Plants

Mechanisms of Abiotic Stress Resilience and Applications for Agriculture

MAY 22-27, 2022
LES DIABLERETS CONFERENCE CENTER, LES DIABLERETS, SWITZERLAND
CHAIRS: Jose Dinneny and Christa Testerink
VICE CHAIRS: Thomas Juenger and Amelia Henry

- **Keynote Session: Mechanisms of Stress Signaling and Resilience** *Julia Bailey-Serres,* Katayoon Dehesh, David Salt
- **Signaling Mechanisms and Stress Response** *Claudia Jonak,* Zhen-Ming Pei, Rashmi Sasidharan, Liwen Jiang, Sean Cutler
- **Cellular Organization and Stress Response** *Katayoon Dehesh,* Takashi Hashimoto, Staffan Persson, Jürgen Kleine-Vehn
- **Photosynthesis, Climate Change and Agriculture** *Amelia Henry,* Marjorie Lundgren, Moises Exposito-Alonso, Diana Santelia, Andrew Leakey
- **Adaptation to Water Stress and Salinity** *Magdalena Julkowska,* Maheshi Dassanayake, Melvin Oliver
- **Rhizosphere Interfaces with Soil, Water and Ions** *Daniela Dietrich,* Andrea Carminati, Malcolm Bennett, Siobhan Brady, Niko Geldner
- **Interfaces with Soil and Microbes** *Sheng Yang He,* Jennifer Pett-Ridge, Cyril Zipfel, Rumyana Karlova
- **Omic Approaches to Understanding Stress Acclimation** *Robert VanBuren,* Sonia Negrao, David Des Marais, Malia Gehan, Jill Farrant
- **Tissue Hydraulics and Plant Physiology** *Yann Boursiac,* Guillaume Lobet, Matthew Gilliham, Noel Holbrook
- **The GRC Power Hour™** *Thomas Juenger, Julia Bailey-Serres*

Salt and Water Stress in Plants
Unraveling Plant Stress Responses Using Multidisciplinary Approaches
MAY 21-22, 2022
CHAIRS: Stephanie Klein and Abdeljalil Elhabti

Scientific Methods in Cultural Heritage Research

Integrating Multidisciplinary Approaches for Deeper Characterization, Interpretation and Preservation of Heritage

JUL 10-15, 2022
LES DIABLERETS CONFERENCE CENTER, LES DIABLERETS, SWITZERLAND
CHAIRS: Julie Arslanoglu and Loïc Bertrand
VICE CHAIRS: Admir Masic and Costanza Miliani

- **Keynote Session: Insights and Visions Connecting Cultural Heritage Research** *Katrien Keune,* Hartwig Fischer, Caroline Tokarski
- **Artistic and Conservation Practice-Driven Material Study** *Marika Spring,* Daryl Howard, Maartje Stols-Witlox, Ilaria Bonaduce
- **Computational Advances Driving New Interpretations** *Agnès Desolneux,* Michalina Pacholska, Livio de Luca
- **Study of Ancient and Historical Biological Materials** *Clara Granzotto,* Elizabeth Henaff, Theanne Schiros
- **Heritage Material Systems from Nanometric to Macroscopic Scales** *Dominique Derome,* Lara Maldanis, Letizia Monico, Patrick Dietemann
- **Safer Experimental Conditions for Heritage Studies** *Costanza Miliani,* Nathan Wales, Samuel Webb, G. Asher Newsome
- **Engineering and Materials Sciences in Cultural Heritage Research** *Johanna Leissner,* Lukasz Bratasz, Daniel Asmar, Laurence De Viguerie
- **Novel Materials Inspired by Ancient Materials and Practices** *Clément Sanchez,* Marie Jackson, Roberto Giustetto, Romain Bordes
- **Keynote Session: Future Frontiers for Heritage Research by Strengthening Collaboration Between the Humanities and Science** *Barbara Berrie,* Francesca Casadio, Yannick Rochat, Johanna Tummers
- **The GRC Power Hour™** *Teresa Duncan, Alicia McGeachy*

Scientific Methods in Cultural Heritage Research
Innovation in Materials and Technologies for the Analysis and Conservation of Heritage
JUL 9-10, 2022
CHAIRS: Victor Gonzalez and Teresa Duncan

Signal Transduction by Engineered Extracellular Matrices

Microenvironmental Regulation of Stem and Somatic Cells in Organismal Development and Regenerative Medicine

JUL 24-29, 2022
SOUTHERN NEW HAMPSHIRE UNIVERSITY, MANCHESTER, NH
CHAIRS: David Schaffer and Matthias Lutolf
VICE CHAIRS: Shelly Peyton and Sanjay Kumar

- **Keynote Session: Exploring and Manipulating the Cell-Matrix Interface in Health and Disease** *Adam Engler,* Valerie Weaver, Juergen Knoblich
- **Organoids** *Alex Hughes,* Jianping Fu, Nuria Montserrat
- **Organs-on-a-Chip** *Peter Loskill,* Nancy Allbritton, Roger Kamm
- **Advanced Engineered ECMs** *Shyni Varghese,* Sarah Heilshorn, Cole DeForest, Jason Burdick
- **Single Cell Biology and Development** *Karthik Shekhar,* Siddharth Dey, Tom Nowakowski
- **ECM Mechanobiology** *Catherine Kuo,* Xavier Trepat, Ovijit Chaudhuri, Celeste Nelson
- **ECM and Stem Cell Fate Regulation** *Kris Kilian,* Samira Musah, Randy Ashton
- **Bioinspired Fabrication** *Fabien Guillemot,* Jordan Miller, Kelly Stevens, Akhilesh Gaharwar
- **Engineering and Application of Immune-Modulatory Materials** *David Wilson,* Takahsi Kishimoto, Ankur Singh
- **The GRC Power Hour™** *Sarah Heilshorn*

Signal Transduction by Engineered Extracellular Matrices
Nano to Macroscale Engineering in Biology and Regenerative Medicine
JUL 23-24, 2022
CHAIRS: Claudia Loebel and Woojin Han

Signaling by Adhesion Receptors

Adhesion Across Scales: From Molecules to Morphogenesis

JUL 17-22, 2022
SOUTHERN NEW HAMPSHIRE UNIVERSITY, MANCHESTER, NH
CHAIR: Ann Miller
VICE CHAIR: Patrick Derksen

- **Keynote Session: Adhesion Across Scales: From Molecules to Morphogenesis** *Patrick Derksen,* Bob Goldstein, Kathleen Green
- **Mechanotransduction by Adhesion Receptors** *Christopher Chen,* Carl-Philipp Heisenberg, Erin Cram, Patrick Oakes
- **Maintaining Adhesion in Dynamic Environments** *Adam Martin,* Carien Niessen, Yusuke Toyama, Jennifer Zallen
- **Adhesive Control of Cell Division** *Cara Gottardi,* Yohanns Bellaïche, Sarah Woolner, Martijn Gloerich
- **Advances in Adhesion Signaling** *Alpha Yap,* Rafael Garcia-Mata, Tony Koleske, Alexa Mattheyses
- **Adhesion Signaling and Cell Migration** *Tony Koleske,* Danijela Matic Vignjevic, Maddy Parsons, Sally Horne-Badovinac
- **Engineering Adhesion** *Martin Schwartz*, Christopher Chen, Sanjay Kumar, Karen Kasza
- **Adhesion, Morphogenesis and Tissue Remodeling** *Bob Goldstein,* Scott Holley, Adam Martin, Robert Krauss
- **Adhesion and Disease** *Kathleen Green,* Asma Nusrat
- **The GRC Power Hour™**

Signaling by Adhesion Receptors
Examining the Basic Biomechanics and Biomedical Aspects of Cell Adhesion Signaling
JUL 16-17, 2022
CHAIRS: Kate Cavanaugh and Fiona Passanha

Single Molecule Approaches to Biology

Uncovering Physical Principles of Life with Single Molecule Approaches

JUL 3-8, 2022
REY DON JAIME GRAND HOTEL, CASTELLDEFELS, SPAIN
CHAIRS: Erwin Peterman and Olga Dudko
VICE CHAIRS: Samuel Hess and Suliana Manley

- **Keynote Session: Probing the Non-Equilibrium Nature of Life** *Carlos Bustamante,* John Marko, Rob Phillips
- **Diffusion as Transport Mechanism in the Cell** *Samuel Hess,* Julie Biteen, Maria Garcia-Parajo, David Holcman, Cornelis Murre
- **Beating the Diffusion Speed Limit: Biological Motors** *Stefan Diez,* Carlos Bustamante, Cees Dekker, Lukas Kapitein
- **Navigating Energy and Fitness Landscapes** *Hermann Gaub,* Irene Chen, Thomas Perkins, Michael Woodside
- **The Dynamic Nature of Cellular Structures** *Zan Luthey-Schulten,* Ariel Amir, Patricia Bassereau, Daniel Needleman
- **Crossing the Phase Boundary** *Patricia Bassereau,* Ibrahim Cisse, Yaojun Zhang, Gary Karpen
- **Biology in Bits: Information Approaches** *Suliana Manley,* Naama Brenner, Yoav Shechtman, Gasper Tkacik
- **Searching for Principles in Biological Complexity** *Marileen Dogterom,* Toshio Ando, Taekjip Ha, Zan Luthey-Schulten, Antoine Van Oijen
- **Keynote Session: From Single Molecules to Unifying Principles of Life** *Taekjip Ha,* Petra Schwille, Stefan Grill
- **The GRC Power Hour™**

Single Molecule Approaches to Biology
Single Molecule Perspectives for a Deeper Understanding of Biology
JUL 2-3, 2022
CHAIRS: Lukas Milles and Carleen Kluger

Single-Cell Cancer Biology NEW!

Dissecting Evolution and Heterogeneity of Single Cancer Cells

JUN 12-17, 2022
STONEHILL COLLEGE, EASTON, MA
CHAIRS: Kai Tan and Nicholas Navin
VICE CHAIRS: Mario Suva and Sohrab Shah

- **Pre-Malignancies and Early-Stage Tumors** *Samuel Aparicio,* Kai Kessenbrock, Xin Lu, Jorge Reis-Filho
- **Solid Tumors** *Devon Lawson,* Samuel Aparicio, Sam Behjati, Michalina Janiszewska, Peter Van Loo
- **Hematological Tumors** *Iannis Aifantis,* Charles Gawad, Catherine Wu, Koichi Takahashi, Adam Mead
- **Epigenomic Heterogeneity** *Catherine Wu,* Nicola Aceto, Andrew Adey, Ansuman Satpathy, Celine Vallot
- **Tumor-Immune Cell Interactions in Tumor Microenvironment** *Mario Suva,* Iannis Aifantis, Itay Tirosh, Zemin Zhang
- **Computational Methods for Single-Cell Analysis** *Sohrab Shah,* Ken Chen, Dana Pe'er, Rahul Satija, Nancy Zhang
- **Current Advances in Single-Cell Technologies** *Klaus Pantel,* Bernd Bodenmiller, Dario Bressan, Joakim Lundeberg
- **Circulating Tumor Cells and Metastasis** *Xin Lu,* Daniel Haber, James Hicks, Klaus Pantel
- **Therapeutic Resistance** *Michalina Janiszewska,* Maxim Artyomov, Liynat Jerby-Arnon, Devon Lawson, Kornelia Polyak
- **The GRC Power Hour™**

Single-Cell Genomics NEW!

When Stochasticity Meets Precision in a Single Cell

MAY 1-6, 2022
LES DIABLERETS CONFERENCE CENTER, LES DIABLERETS, SWITZERLAND
CHAIRS: Xiaoliang Sunney Xie and Stephen Quake
VICE CHAIRS: Xiaowei Zhuang and Barbara Treutlein

- **Single-Cell Transcriptomics** *Dana Pe'er,* Long Cai, Rickard Sandberg, Jianbin Wang
- **Imaging** *Robert Singer,* Hazen Babcock, Alistair Boettiger, Arjun Raj, Loic Royer
- **Genomes** *Ido Amit,* Paul Blainey, Dong Xing, Chenghang Zong
- **Epigenetics** *Alexander Meissner,* Yunlong Cao, Wolf Reik, Fuchou Tang, Jan Vijg
- **3D Genome Structures and Dynamics** *Amos Tanay,* Peter Fraser, William Greenleaf, Kikue Tachibana
- **Innovations in Genomic Technologies** *Piero Carninci,* Martin Enge, Emma Lundberg, Nikolai Slavov, Jonathan Weissman
- **Applications to Cancer and Immunology** *Michael Clarke,* Charles Gawad, Nicholas Navin, Zemin Zhang
- **Applications to Neurobiology** *Hongkui Zeng,* Michelle Chen, Joseph Ecker, Ge Gao, Bosiljka Tasic
- **Human and Model Organism Cell Atlas** *Michael Levine,* Spyros Darmanis, Camille Ezran, Aki Minoda
- **The GRC Power Hour™**

Solid State Chemistry

Functional Inorganic Materials: Exploratory Synthesis, Advanced Characterization and Computational Methods

JUL 24-29, 2022
COLBY-SAWYER COLLEGE, NEW LONDON, NH
Chair: Shiv Halasyamani
Vice Chair: Arthur Mar

- **Quantum and Layered Materials** *Arthur Mar,* Leslie Schoop, Andrew Grosvenor
- **Energy Materials** *Linda Nazar,* Jakoah Brgoch, Taylor Sparks, Serena Cussen, John Vaughey
- **Advanced Characterization Methods** *Katherine Page,* John Evans, Joke Hadermann
- **Synthesis of Functional Materials** *Simon Clarke,* Michael Hayward, Daniel Shoemaker, Mario Bieringer, Bayram Saparov
- **Computational Methods** *James Rondinelli,* Nicole Benedek, Elsa A. Olivetti
- **Non-Oxide Materials** *Julia Chan,* Paul Canfield, Kanishka Biswas, Oliver Janka, Stefanie Dehnen
- **Chemistry in Industry** *Kenneth Poeppelmeier,* William Sheets, Erin Sorenson
- **Non-Oxide Materials: Superconductors, Hydrides and Magnetocalorics** *Danna Freedman,* Weiwei Xie, Ulrich Häussermann, Bettina Lotsch, Yurij Mozharivskyj
- **Modulated Structures** *Daniel Fredrickson,* Sven Lidin
- **The GRC Power Hour™** *Danna Freedman, Nicole Benedek*

Solid State Chemistry
Functional Inorganic Materials: Exploratory Synthesis, Advanced Characterization and Computational Methods
JUL 23-24, 2022
CHAIRS: Rebecca Smaha and Yuzki Oey

Solid State Studies in Ceramics

Coupled Phenomena in Ceramics Across Length Scales

AUG 7-12, 2022
MOUNT HOLYOKE COLLEGE, SOUTH HADLEY, MA
CHAIR: Ivar Reimanis
VICE CHAIRS: Wayne Kaplan and Edwin Garcia

- **Achieving Exceptional Responses in Structural Materials** *Brian Cox,* Julia Greer, Kevin Hemker
- **Thermo-Mechanical Behavior in Extreme Environments** *William Fahrenholtz,* Alexandra Navrotsky, David Poerschke, Frank Zok

- **Processing Complex Structures** *Lisa Rueschhoff,* Rajendra Bordia, Jennifer Rupp
- **Interfaces and Grain Boundaries** *Fadi Abdeljawad,* Yuichi Ikuhara, Amanda Krause, David Srolovitz
- **Defects in Ceramics** *Nasim Alem,* William Bowman, Elizabeth Dickey
- **Interfaces and Electrical Charge** *Sossina Haile,* Wolfgang Rheinheimer, Klaus van Benthem, Roger De Souza
- **Coupled Phenomena in Oxides** *Kelsey Hatzell,* Nicola Perry, Bilge Yildiz
- **Perovskites for Optoelectronics** *Bryan Huey,* David Cahen, Marina Filip, Annamaria Petrozza
- **Biological Materials in the Extreme** *Olivia Graeve,* David Kisailus
- **The GRC Power Hour™**

Solid State Studies in Ceramics
Fundamental Phenomena in Ceramics from the Atomistic Level to the Microstructure
AUG 6-7, 2022
CHAIRS: Hadas Sternlicht and Jasmin Koldehoff

Stereochemistry

Different Forms of Stereochemistry: From Catalysis and Synthesis to Macromolecules and the Natural World

JUL 24-29, 2022
SALVE REGINA UNIVERSITY, NEWPORT, RI
CHAIRS: Varinder Aggarwal and Eric Ashley
VICE CHAIRS: Eric Jacobsen and Tamas Benkovics

- **Keynote Session: Synthesis and Translation to Medicine** *Eric Jacobsen,* Sarah Reisman, Paul Wender
- **Stereochemistry of Radicals and Peptides** *Alastair Lennox,* Michelle Chang, Ivan Huc, Song Lin, Alison Wendlandt
- **Functionalization of Multiple Bonds** *Santanu Mukherjee,* Keary Engle, Tomislav Rovis, Ryan Shenvi
- **Transition Metals in Asymmetric Catalysis** *Robert Paton,* Gregory Fu, Matthew Gaunt, Kyle Mack, Franziska Schoenebeck
- **Functionalization of Strong Bonds** *Shauna Paradine,* Abby Doyle, Bill Morandi, Corinna Schindler
- **Discovery and Synthesis of Medicinal Molecules** *Juana Du,* Cameron Cowden, Andrew Neel, Robert Singer, Linli Wei
- **Catalysis and Sustainability** *Tian Qin,* Josep Cornella, Daniele Leonori, Alison Narayan
- **Asymmetric Catalysis and Mechanism** *Nicholas Race,* Guy Lloyd-Jones, Keiji Maruoka, James Morken
- **Keynote Session: De Novo Generation of Chirality** *Tamas Benkovics,* Michael Mcbride, Richmond Sarpong
- **The GRC Power Hour™** *Eric Ashley, Sarah Reisman*

Streptococcal Biology

Evolving Genomes, Behavior and Pathogenic Mechanisms of Streptococci and Enterococci

AUG 14-19, 2022
JORDAN HOTEL AT SUNDAY RIVER, NEWRY, ME
CHAIRS: Kelly Doran and Shiranee Sriskandan
VICE CHAIRS: Michael Federle and Jan-Willem Veening

- **Keynote Session: Insights into Pathogen and Host Biology** *Jan-Willem Veening,* Michael Gilmore, Victor Nizet
- **Evolution of Genomes: From Genomics to Function** *Andrew Camilli,* Mark Davies, Bill Hanage
- **Regulation and Virulence Mechanisms** *Elaine Tuomanen,* Michael Wessels, Melanie Hamon, Jose Lemos
- **Host-Pathogen Interactions and the Fight for Survival** *Anna Norrby-Teglund,* Mattias Collin, David Aronoff, Annelies Zinkernagel
- **At the Surface of the Bacterial-Host Encounter** *Lakshmi Rajagopal,* Angela Nobbs, Eric Schmidt, Nina van Sorge
- **Interactions Within the Microbial Community** *Kimberly Kline,* Katherine Lemon, Mohammad Seyedsayamdost, Joseph Zackular
- **Phage and Mobile Genetic Elements** *Breck Duerkop,* Kelli Palmer, Angela Brueggemann
- **Evolving Therapeutic Approaches and Methodologies** *Adam Ratner,* Annaliesa Anderson, Joshua Osowicki
- **Early-Career Investigator Presentations** *Michael Federle*
- **The GRC Power Hour™** *Elaine Tuomanen*

Streptococcal Biology
Physiology, Host-Interactions and Vaccine Development and Epidemiology of Streptococci
AUG 13-14, 2022
CHAIRS: Brady Spencer and Lamar Thomas

Structural Nanomaterials

Design, Microstructure and Mechanical Behavior of Structural Nanomaterials

MAY 8-13, 2022
LES DIABLERETS CONFERENCE CENTER, LES DIABLERETS, SWITZERLAND
CHAIRS: Qing Ping Sun and Andrea Hodge
VICE CHAIRS: Lei Lu and Xun-Li Wang

- **Keynote Session: Materials Design at the Nanoscale** *Ruth Schwaiger,* Christopher Schuh, Diana Farkas
- **Homogeneous and Heterogeneous Nanoscale Microstructures** *Lei Lu,* Wendy Gu, Thomas Waitz, Koichi Tsuchiya
- **Advanced Characterization Techniques** *Aslan Ahadi,* Erica Lilleodden, Jason Trelewicz
- **Mechanics at the Nanoscale** *Chelsea Appleget,* Daniel Kiener, Megan Cordill, Corinne Packard
- **Synthesis of New Nanostructures and Alloys** *Blythe Clark,* Horst Hahn, C. Cem Tasan
- **Advances in Hierarchical Materials Design** *Mingxin Huang,* Lorenzo Valdevit, Christoph Eberl, Yang Lu
- **Atomistic and Nanoscale Simulations** *Paulo Branicio,* Mark Asta, David Srolovitz
- **Heretical Material Design and Properties** *Timothy Rupert,* Alfonso Ngan, Ralph Spolenak, Qiming Wang
- **Non-Equilibrium Structures** *Xun-Li Wang,* Gerhard Dehm, Yilong Han

Synaptic Transmission

Fine-Scale Synaptic Interactions in Space and Time

JUN 19-24, 2022
RENAISSANCE TUSCANY IL CIOCCO, LUCCA (BARGA), ITALY
CHAIR: Alison Barth
VICE CHAIRS: Daniel Choquet and Graeme Davis

- **Synapses and Social Behavior** *Helene Marie,* Robert Malenka
- **Presynaptic Regulation** *Noa Lipstein Lipstein,* Gwyneth Card, Annette Dolphin, Timothy Ryan, Matthijs Verhage
- **Imaging Synaptic Structure** *Thomas Blanpied,* Kristen Harris, Michael Higley, Na Ji, Valentin Nägerl
- **In Vivo Synaptic Transmission** *Mario Penzo,* Johannes Letzkus, James Poulet, Marlene Bartos, Lucy Palmer
- **Synaptic Function in Disease** *Bruce Herring,* Paola Arlotta, Gaia Novarino, Morgan Sheng
- **Multisynaptic Interactions** *Pablo Castillo,* Kevin Bender, Yishi Jin, Thomas Nevian, Inna Slutsky
- **Synaptic Computation and Network Design** *Srikanth Ramaswamy,* Claudia Clopath, Richard Naud, Andreas Tolias, Wei Wei
- **Target-Specific Synaptic Function** *Ralf Schneggenburger,* Peter Jonas, Jeff Magee, Xiang Yu
- **Synaptic Dysfunction in Psychiatric Disorders** *Roger Nicoll,* Guoping Feng
- **The GRC Power Hour™** *Alison Barth*

Synaptic Transmission
Synaptic Function: From Molecules to Networks
JUN 18-19, 2022
CHAIRS: Hannah Monday and Simon Chamberland

Systems Aging NEW!

Systemic Processes, Omics Approaches and Biomarkers in Aging

MAY 29-JUN 3, 2022
GRAND SUMMIT HOTEL AT SUNDAY RIVER, NEWRY, ME
CHAIR: Vadim Gladyshev
VICE CHAIR: Steve Horvath

- **Delaying and Reversing Aging** *Steve Horvath,* Cynthia Kenyon, Richard Miller
- **Epigenetic Reprogramming and Rejuvenation** *Felipe Sierra,* Manuel Serrano, Vittorio Sebastiano, Jacob Kimmel, Morgan Levine
- **Genomics of Aging** *Emma Teeling,* Nicholas Schork, Ed Boyden, Martin Borch Jensen, Joris Deelen
- **Epigenetic Biomarkers** *Kristen Fortney,* Riccardo Marioni, Ake Lu, Daniel Belsky, Sara Hagg
- **Clinical and Molecular Biomarkers** *Meng Wang,* Cavin Ward-Caviness, Morten Scheibye-Knudsen, Brian Kennedy, Paola Sebastiani
- **Artificial Intelligence and Machine Learning** *Marc Kirschner,* Jing-Dong Han, Alex Zhavoronkov, Kristen Fortney, Albert-Laszlo Barabasi
- **Aging as a Systemic Process** *Ned David,* Meng Wang, Danica Chen, Jessica Tyler
- **Comparative Genomics of Aging** *Andrei Seluanov,* Vera Gorbunova, Emma Teeling, João Pedro de Magalhães
- **Fundamental Bases of Aging** *Cynthia Kenyon,* Kenneth Raj, Daniel Promislow
- **The GRC Power Hour™** *Morgan Levine*

Systems Chemistry

Life-Like and Emergent Behavior in Complex Molecules and Ensembles

JUN 26-JUL 1, 2022
JORDAN HOTEL AT SUNDAY RIVER, NEWRY, ME
CHAIRS: Sijbren Otto and Rein Ulijn
VICE CHAIRS: Rebecca Schulman and Rafal Klajn

- **From Self-Assembly to Life Through Modelling and Experiment** *Rebecca Schulman,* David A. Leigh, Ramanarayanan Krishnamurthy
- **Origins and Synthesis of Life** *Ramanarayanan Krishnamurthy,* David Lynn, Gonen Ashkenasy, Eörs Szathmáry, Oliver Trapp, Kerstin Göpfrich
- **Fueled Reaction Networks and Metabolic Materials** *Sergey Semenov,* Kenneth Showalter, Agota Toth, Massimo Baroncini
- **Navigating Shallow Energy Landscapes in Supramolecular Systems** *Julia Ortony,* Allie Obermeyer, Matthew Rosseinsky, Tell Tuttle, Jonathan Nitschke, Sarah Perry, Akif Tezcan
- **Emergent Catalysis, Machines and Motility** *Ivan Korendovych,* Beatriu Escuder, Steve Granick, Daniela Wilson, Nathalie Katsonis
- **Active and Adaptive Materials Through Molecular Self-Assembly** *Rienk Eelkema,* Job Boekhoven, Andreas Walther, Adam Braunschweig, Ronit Freeman
- **Active and Adaptive Materials Based on Nanoparticles or Colloids** *Rafal Klajn,* Anna Balazs, Robert Macfarlane, Willem Noorduin, Alfredo Alexander-Katz
- **Biological Systems Chemistry** *Ayala Lampel,* Wilhelm Huck, Henry Hess, Cecilia Leal, Ilja Voets, Roy Bar-Ziv
- **Systems Chemistry in Flow** *Peter Korevaar,* Lee Cronin, Andrew Griffiths, Steven Benner
- **The GRC Power Hour™** *Ayala Lampel, Julia Ortony*

Systems Chemistry
Fundamental Principles and Emergent Behavior within Networks of Molecules
JUN 25-26, 2022
Chairs: Ignacio Colomer and Meagan Beatty

Thiol-Based Redox Regulation and Signaling

The Chemical Biology of Sulfur

JUL 10-15, 2022
REY DON JAIME GRAND HOTEL, CASTELLDEFELS, SPAIN
CHAIR: Kate Carroll
VICE CHAIR: Joris Messens

- **Keynote Session: Pioneers in Redox Regulation and Signaling** *Ursula Jakob,* Christine Winterbourn, Elias Arner

- **Enabling Technologies for Redox Biology** *Gregory Payne, Vsevolod Belousov,* Cristina Furdui, Derek Pratt, Yimon Aye, Che Pillay, Elizabeth New, Jing Yang
- **Mechanisms of Thiol-Based Regulation** *Elizabeth Veal, Melissa Kemp,* Fernando Antunes, Benoit Boivin, Pat Eyers, Brian Smith, W. Todd Lowther, Beatriz Alvarez
- **Reactive Sulfur Species** *Michael Pluth, Peter Nagy,* Kenneth Olson, Ming Xian, David Giedroc, Takaaki Akaike, Bindu Paul
- **Mechanisms of Thiol-Based Signaling** *Leslie Poole, Albert Van Der Vliet,* James Galligan, Carolyn Sevier, Tobias Dick, Cao Xu, Ana Denicola, Hadley Sikes
- **Redox Medicine** *Ulla Knaus, Philip Eaton,* Yvonne Janssen-Heininger, Pietro Ghezzi, Carmen Wong, Bruce Freeman
- **Redox Metabolism** *Keith Blackwell,* Bruce Morgan, Carolina Greco, Canhua Huang, Oleh Khalimonchuk
- **Selenoproteins and Reversible Methionine Oxidation** *Garry Buettner,* Sina Ghaemmaghami, Robert Hondal, Rodney Levine, Vasanthi Viswanathan, Bruno Manta, Daniel Bak
- **Grand Challenges and New Paradigms in Redox Signaling** *Toren Finkel,* Helmut Sies, Rafael Radi, Ruma Banerjee

Thiol-Based Redox Regulation and Signaling
Redox Signaling Factors: From the Molecular Mechanisms to the Physiological Consequences
JUL 9-10, 2022
CHAIRS: Brandan Pedre Perez and Evanna Mills

Three Dimensional Electron Microscopy

Technical Advances in 3DEM to Study Biological Structures Across Scales

JUN 19-24, 2022
REY DON JAIME GRAND HOTEL, CASTELLDEFELS, SPAIN
CHAIR: Daniela Nicastro
VICE CHAIR: Radostin Danev

- **Keynote Session: The Future of 3DEM in Structural Biology: Beyond Cryo-EM** *Eva Nogales,* Melanie Ohi
- **Advances in Specimen Preparation and Workflows** *Hongwei Wang,* Arjen Jakobi, Doryen Bubeck, Thamiya Vasanthakumar, Abraham Koster, Shengjie Feng
- **3DEM in Translational Research** *Pamela Williams,* Claudio Ciferri, Shee-Mei Lok
- **New Developments in Algorithms and Software** *Joachim Frank, Sjors Scheres,* Jose Carazo, Ricardo Sánchez Loayza, Tristan Bepler
- **Selected Poster Presentations** *Mario Borgnia*
- **Frontiers in Cellular Tomography** *Julia Mahamid,* Alex de Marco, Stefan Raunser, David Agard
- **Structures In Situ: Pushing Resolution Limits** *John Briggs,* Friedrich Foerster
- **Innovations of Instruments and Hardware** *Robert Glaeser,* Holger Mueller, Keiichi Namba, Peiyi Wang, Saori Maki-Yonekura
- **Selected Poster Presentations** *Radostin Danev*
- **The GRC Power Hour™**

Three Dimensional Electron Microscopy
Technical Advances in 3DEM and their Connection to Biological Breakthroughs
JUN 18-19, 2022
CHAIRS: Cristina Puchades and Julia Peukes

Transglutaminases in Human Disease Processes

Known and Emerging Transglutaminase-Related Diseases and New Methods for Detection and Treatment

JUN 12-17, 2022
MOUNT SNOW, WEST DOVER, VT
CHAIR: Jeffrey Keillor
VICE CHAIR: Kiyotaka Hitomi

- **Keynote Session: Clinical Relevance of Tissue Transglutaminase** *Elisabetta Verderio,* Richard Eckert, Ludvig Sollid
- **Emerging Diseases** *Laszlo Fesus,* Mari Kaartinen, ZhaoQing Luo, Ian Maze, Christian Recktenwald
- **Emerging Research Tools** *Reik Loeser,* Diana Imhof, William Katt, Lakshmi Santhanam
- **Cardiovascular Diseases** *Lakshmi Santhanam,* Martin Griffin, In-Gyu Kim, Nicola Mutch, Michal Neeman
- **Neurological Diseases** *Manuela Basso,* Gail Johnson, Xianhua Piao, Anne-Marie Van Dam
- **Cancer and Signaling Disorders** *Daniela Matei,* Nicoletta Bianchi, Salvatore Condello, Soo-Youl Kim, Nicholas Peake
- **Celiac Disease and Inflammation** *Mauro Piacentini,* Xian-Yang Qin, Detlef Schuppan, Yang Xia
- **Fibrosis and Remodeling** *Patricia Sime,* Timothy Johnson, James Luyendyk, Hideki Tatsukawa, Elisabetta Verderio
- **Keynote Session: Activation and Inactivation of Tissue Transglutaminase** *Anne-Marie Van Dam,* Chaitan Khosla
- **The GRC Power Hour™**

Transglutaminases in Human Disease Processes
Pathology, Mechanism and Intervention of Transglutaminases
JUN 11-12, 2022
CHAIR: Estéfano Pinilla Pérez

Tribology

Understanding Sliding Interfaces to Master Tribological Systems Across Length Scales

JUN 26-JUL 1, 2022
BATES COLLEGE, LEWISTON, ME
CHAIR: Judith Harrison
VICE CHAIR: Seong Kim

- **Understanding the Sliding Interface** *Filippo Mangolini,* Nicolas Fillot, Prathima Nalam
- **Adhesive Phenomena in Tribology** *Kathryn Wahl,* Tevis Jacobs, Ramin Aghababaei, Jean Denape
- **Probing the Sliding Interface** *Angela Pitenis,* Antonella Rossi, James Schall
- **Lamellar Solid Lubricants** *Thomas Scharf,* John Curry, Clotilde Minfray, Andreas Rosenkranz
- **Soft Tribology** *David Burris,* Rosa M. Espinosa-Marzal, Alison Dunn
- **Tribology at the Extreme** *Marina Ruths,* Pantcho Stoyanov, Joichi Sugimura, Satish Achanta
- **Tribologically-Induced Surface Changes and Wear** *Richard Chromik,* Alfons Fischer, Christian Greiner
- **Electric Vehicle and Green Tribology** *Brian Borovsky,* Arup Gangopadhyay, Peter Lee, Farrukh Qureshi
- **Keynote Session: Tribology for Health** *Seong Kim,* Robert Carpick
- **The GRC Power Hour™** *Alison Dunn, Jacqueline Krim*

Tribology
Understanding Sliding Interfaces to Master Tribological Systems Across Length Scales
JUN 25-26, 2022
CHAIRS: Nathaniel Hawthorne and Yijue Diao

Two Dimensional Electronics Beyond Graphene

Emerging Complex Phenomena and Applications

JUN 12-17, 2022
SOUTHERN NEW HAMPSHIRE UNIVERSITY, MANCHESTER, NH
CHAIRS: Xiaodong Xu and Deji Akinwande
VICE CHAIRS: Jie Shan and Frank Koppens

- **Synthesis and Characterization** *Anna Isaeva,* James Hone, Jiwoong Park
- **Device Applications** *Fengnian Xia,* Peide Ye, Iluliana Radu
- **Collective Excitation** *Tony Heinz,* Kin Fai Mak, Pablo Jarillo-Herrero, Marco Polini
- **Quantum and Nonlinear Optical Effects** *Hongkun Park,* Hui Deng, Atac Imamoglu
- **Magnets and Heterostructures** *Roland Kawakami,* Alberto Morpurgo, Daniel Ralph, Emanuel Tutuc
- **Modeling Grand Challenges** *Di Xiao,* Vladimir Falko, Allan Macdonald
- **Complex Phenomena** *Feng Wang,* Kenneth Burch, David Cobden, Yuanbo Zhang
- **Tunable Correlated States in Twisted 2D Materials** *Philip Kim,* Cory Dean, Ali Yazdani, Andrea Young
- **Emerging Phenomena** *David Tomanek,* Hyeon-Jin Shin, Andres Castellanos-Gomez
- **The GRC Power Hour™**

Two Dimensional Electronics Beyond Graphene
Fundamentals and Applications of Emerging 2D Crystals
JUN 11-12, 2022
CHAIRS: Zhong Lin and Dmitry Ovchinnikov

Unconventional Semiconductors and Their Applications NEW!

Physics, Chemistry and Applications of Metal-Halide Perovskites

JUN 12-17, 2022
FOUR POINTS SHERATON, HOLIDAY INN EXPRESS, VENTURA, CA
CHAIRS: Matthew Beard and Jinsong Huang
VICE CHAIRS: Hanwei Gao and Iván Mora-Seró

- **Keynote Session: Opportunities and Challenges in Metal-Halide Perovskites** *David Mitzi,* Tsutomu Miyasaka
- **Photovoltaics and Stability** *David Cahen,* Antonio Abate, Kylie Catchpole, Yabin Qi, Yang Yang
- **Ion Migration** *Prashant Kamat,* David Ginger, Mike McGehee, Elizabeth von Hauff
- **Structure-Property Correlation** *Song Jin,* Hemamala Karunadasa, Yanfa Yan, Peidong Yang
- **Interfaces and Defects** *Barry P. Rand,* Filippo De Angelis, Giulia Grancini, Annamaria Petrozza
- **Carrier Dynamics** *Libai Huang,* Laura Herz, Carlos Silva, Tze-Chien Sum, Xiaoyang Zhu
- **Charge Transport** *Yuanyuan Zhou,* Aditya Mohite, Valy Vardeny, Kai Zhu
- **Light Emission** *Samuel Stranks,* Letian Dou, Maksym Kovalenko, Linn Leppert, Qihua Xiong
- **Beyond PV and LED** *Joseph Berry,* Biwu Ma
- **The GRC Power Hour™**

Unifying Ecology Across Scales

Integrating Theory and Empiricism in Ecology and Evolution through Energetics, Elements, and Information

JUL 31-AUG 5, 2022
SOUTHERN NEW HAMPSHIRE UNIVERSITY, MANCHESTER, NH
CHAIR: Angelica Gonzalez
VICE CHAIR: John DeLong

- **Keynote Session: Integration and Synthesis in Ecology and Evolution Through Fundamental Principles** *Helmut Hillebrand,* Pablo Marquet, Elizabeth Borer
- **Causal Links between Temperature, Metabolism and Stoichiometry** *Anita Narwani,* Elena Litchman, Sean Michaletz, Joey Bernhardt, Alexis Synodinos, Daniel Wieczynski
- **Variation in Biological Scaling and the Four Dimensions of Life** *Joanna Bernhardt,* James Brown, Anastassia Makarieva, Ian Hatton
- **Evolutionary Underpinnings of Ecological Physiology** *Theodore Garland,* Lauren Buckley, Christopher Kempes, Jennifer Sunday, Seth Rudman, Juan Vicente Gallego Rubalcaba
- **Integrating Theories to Explain Ecological Patterns and Processes Across Spatial Scales** *Dominique Gravel,* Jordan Okie, Adam Clark, Cristian Roman Palacios, Melissa Guzman
- **Wrapped Hierarchies and Disease Ecology: The Interplay of Ecological and Evolutionary Theories** *Andy Dobson,* Mercedes Pascual, Cynthia Downs, Dedmer Van de Waal, Ann Tate
- **Time Continuum: Synergies Between Paleoecological and Neoecological Perspectives** *Michelle Lawing,* Jessica Blois, Kate Lyons, Graciela Gil-Romera





- **Multitrophic Species Interactions and the Functioning of Ecosystems** *Serguei Saavedra,* Priyanga Amarasekare, Oscar Godoy, Pablo Antiqueira
- **Keynote Session: Challenges and Opportunities for an Integrative Ecology** *Jeremy Fox,* Brian McGill, Felisa Smith
- **The GRC Power Hour™** *Jennifer Sunday, John DeLong*

Unifying Ecology Across Scales
Integrating Ecological Currencies Across Scales From Cells to Ecosystems
JUL 30-31, 2022
CHAIRS: Joey Bernhardt and Daniel Wieczynski

Venom Evolution, Function and Biomedical Applications

Bridging Gaps in Venom Research: From Ecology and Evolution to Socio-Economic Impacts

AUG 7-12, 2022
MOUNT SNOW, WEST DOVER, VT
CHAIRS: Ashlee Rowe and Glenn King
VICE CHAIRS: Stephen Mackessy and Irina Vetter

- **Keynote Session: Functional Ecology and Biodiversity of Venom** *Yehu Moran*, Maria Modica, Kartik Sunagar
- **Ecological and Evolutionary Processes Shaping Venoms: Connecting Basic Research with Downstream Applications** *Ricardo Rodriguez de la Vega,* Darin Rokyta, Maria Peichoto
- **Emerging Models in Venom Research** *Andrew Walker*, Mande Holford
- **Advances in Technological and Methodological Approaches** *Beatrix Ueberheide*, Greg Neely, Eivind Undheim
- **Toxin Structure and Function** *Gregor Anderluh,* R. Manjunatha Kini, Markus Muttenthaler
- **Characterizing Toxin-Target Interactions** *Micaiah Ward*, Jian Payandeh, Ray Norton, Evelyne Deplazes
- **Antivenom: Advances in Development and Production** *Nicholas Casewell*, Andreas Laustsen, Julian White, Leslie Boyer
- **Biomedical and Pesticidal Applications of Venom** *Baldomero Olivera,* Maria Ikonomopoulou, Helena Safavi, Volker Herzig
- **Keynote Session: Socio-Economic and Human Health Impacts of Venom** *Irina Vetter*, José María Gutiérrez, Abdulrazaq Habib, Robert Kennedy
- **The GRC Power Hour™** *Nancy Ryan Gray*

Venom Evolution, Function and Biomedical Applications
Bridging Gaps in Venom Research: From Ecology and Evolution to Socio-Economic Impacts
AUG 6-7, 2022
CHAIRS: Aida Verdes and Micaiah Ward

Vibrational Spectroscopy

Unravelling Chemical Heterogeneity

JUL 31-AUG 5, 2022
BRYANT UNIVERSITY, SMITHFIELD, RI
CHAIRS: Lauren Webb and Aaron Massari
VICE CHAIRS: Judy Kim and Poul Petersen

- **Complex Charged Liquids** *Amber Krummel,* Steven Corcelli, Franz Geiger, Heather Allen
- **Biological Complexity at Surfaces** *Elsa Yan,* Jennifer Lee, Wei Zhuang, Lu Wang, Vicki Grassian
- **Biological Complexity in Solution** *Scott Brewer,* Steven Boxer, Casey Londergan, Carlos Baiz
- **Environmental Applications of Vibrational Spectroscopy** *Amanda Mifflin,* Jana Roithova, Mark Johnson, Cristina Puzzarini, Sharon Hammes-Schiffer
- **Unorthodox Vibrational Spectroscopy** *Melanie Reber,* Jordan Hachtel, Quentin Ramasse, Fancesca Palombo
- **Heterogenous Catalytic Systems** *Jahan Dawlaty,* Sandra Luber, Renee Frontiera, Wei-Tao Liu, Alexander Cowan
- **Vibrational Spectroscopy on the Nanoscale** *Wei Xiong,* George Schatz, Wei Min, Katarzyna Marzec
- **Vibrational Spectroscopy at Charged Interfaces** *John Asbury,* Sylvie Roke, Andrei Tokmakoff, Marie-Pierre Gaigeot, Julianne Gibbs
- **New Approaches to Obtain Vibrational Information** *Thomas Allison,* Aaron Rury, Adam Dunkelberger, Hui Li
- **The GRC Power Hour™** *Elsa Yan, Judy Kim*

Vibrational Spectroscopy
Interrogating Chemical Structures, Functions and Dynamics Using Molecular Vibrations
JUL 30-31, 2022
Chairs: Kajari Bera and Mark Babin

Visual System Development

Building and Rebuilding the Visual System: From Genes to Cells to Circuits

AUG 14-19, 2022
SOUTHBRIDGE HOTEL & CONFERENCE CENTER, SOUTHBRIDGE, MA
CHAIR: Seth Blackshaw
VICE CHAIR: Valerie Wallace

- **Keynote Session: Frontiers in Visual Systems Development and Disease** *Nadean Brown,* Thomas Reh, Masayo Takahashi
- **From Retinal Patterning to Cell Fate Specification** *Kristen Kwan,* Susana da Silva, Vilaiwan Fernandes, Jin Woo Kim, Justin Kumar, Simon Sprecher
- **Genome-Wide Approaches for Studying Visual Development** *Michael Dyer,* Rui Chen, Brian Clark, Xin Li, Xiaoqun Wang
- **Building, Remodeling and Repairing Retinal Circuitry** *Jeremy Kay,* Robin Hiesinger, Melanie Samuel, Enrica Strettoi, Julie Lefebvre, Iris Salecker
- **Non-Neuronal Cells and Tissues** *Ruth Ashery-Padan,* Ruby Shalom-Feuerstein, Monica Vetter, Sumiko Watanabe
- **Central Visual Development and Sensory Integration** *David Feldheim,* Xin Duan, Samer Hattar, Takao Hensch, Chi-hon Lee, Hongkui Zeng
- **Development and Dysfunction of the Primate Retina** *Robert Johnston,* Rod Bremner, Jay Gopalakrishnan, Anna La Torre
- **Cellular Regeneration and Stem Cells** *Michel Cayouette,* Katia Del Rio-Tsonis, Mike Karl, Jeff Mumm, Kapil Bharti, Carol Schuurmans
- **Emerging Systems for Studying Visual Development** *Tiffany Cook,* Belinda Chang, Joseph Corbo, Kristen Koenig, Wei Li
- **The GRC Power Hour™** *Monica Vetter*

Visual System Development
Establishing a Visual System: From Retinal Cell Fate to Higher Order Connectivity and Processing
AUG 13-14, 2022
Chairs: Cameron Prigge and Chi Sun

Water and Aqueous Solutions

Water on Multiple Length Scales From the Molecular Level to the Global Hydrosphere

JUL 24-29, 2022
HOLDERNESS SCHOOL, HOLDERNESS, NH
CHAIR: Mary Jane Shultz
VICE CHAIR: Susan Rempe

- **Smallest Scale: Few Water Clusters** *Michael Duncan,* Mark Johnson, Anne McCoy
- **Nonlinear Surface Probes THz to UV** *Dennis Hore,* Mischa Bonn, Marie-Pierre Gaigeot, Tahei Tahara
- **Modeling Nonlinear Spectra** *Heather Allen*, Francesco Paesani, Richard Saykally
- **Clathrate Hydrates Packaging Water** *Qiang Cui,* Larry Anovitz, Anastasia Ilgen, Tod Pascal
- **Water Mediated Aggregation** *Douglas Tobias,* Heloisa Bordallo, Kenneth Dill
- **Neutron Probes in the Bio Realm** *Lorena Tribe,* Dor Ben-Amotz, Steve Seibner, Nonne Prisle
- **Water in the Atmosphere: Ice Nucleation and Growth** *Emily Asenath-Smith,* Ruth Signorell, Petr Slavicek
- **Selected Poster Presenters** *Revati Kumar,* Bertrand Chazallon, Teresa Head-Gordon
- **Water Enveloping the Earth from the Subsurface to the Stratosphere** *Veronica Vaida,* Antonio Mannino
- **The GRC Power Hour™**

Water and Aqueous Solutions
Water on Multiple Length Scales From the Molecular Level to the Global Hydrosphere
JUL 23-24, 2022
Chairs: Clara-Magdalena Saak and Elise Duboue-Dijon

ScienceCareers online @sciencecareers.org

FACULTY OPPORTUNITY:

Institute for Genomic Medicine at Nationwide Children's Hospital

The Institute for Genomic Medicine (IGM) combines a robust clinical laboratory with cutting-edge research in molecular and computational biology to optimize patient care. The IGM's primary mission is to move genomics-based research results into the mainstream of diagnosis and treatment, making the results accessible and meaningful for patients and families.

About the Faculty Position:

- Seeking Associate or Full Professor
- Candidate should have a research laboratory with a focus on immunology/immunogenetics, cardiac or GI developmental biology or polygenic risk score calculations for predictive complex disease risk

Qualifications Required:

- MD, MD/PhD, or PhD
- Strong track record of publishing in high IF journals
- Current R01 or equivalent federal grant funding is preferred

Send correspondence, including CV, brief statement of research interests, and contact information for three references to: Richard Wilson, PhD, and Elaine Mardis, PhD, c/o Elena.Chiappinelli@NationwideChildrens.org

NATIONWIDE CHILDREN'S
When your child needs a hospital, everything matters.

THE OHIO STATE UNIVERSITY
COLLEGE OF MEDICINE

W552400





KENNESAW STATE UNIVERSITY
COLLEGE OF SCIENCE AND MATHEMATICS

Open Rank Tenure Track Faculty Positions

The College of Science and Mathematics (CSM) at Kennesaw State University, one of the fastest growing universities in Georgia, seeks several new tenure track faculty to join our diverse community of researchers. Positions are available at the Assistant, Associate, or Professor rank for individuals who are committed to contributing to an inclusive and equitable work environment.

Specifically, we are interested in candidates with research programs in:

Microorganism or parasite chemical biology, infection, or drug discovery. Seeking to understand microorganisms or parasites using functional, phenotypic, chemical, genetic, and structure-based methods. (**Job ID# 238131**)

Examples of programs:

Chris Cornelison (**https://bioinnovation.kennesaw.edu/research/**)
Thomas C. Leeper (**https://facultyweb.kennesaw.edu/tleeper/index.php**)
Kojo Mensa-Wilmot (**https://facultyweb.kennesaw.edu/kmensawi/research.php**)

Molecular basis of disease in model systems. Research may integrate genetic, chemical, biophysical, and structural approaches to molecular underpinnings of disease in cellular, tissue, and animal models. (**Job ID# 238108**)

Examples of programs:

Martin Hudson (**https://facultyweb.kennesaw.edu/mhudso28/research.php**)
Scott Nowak (**https://facultyweb.kennesaw.edu/snowak/nowak-lab/research.php**)

Learn more about CSM research at **https://csm.kennesaw.edu/research/research-interest-groups/index.php**

Do you want to…

- Contribute to development of exciting new interdisciplinary programs?
- Work in outstanding research facilities?
- Receive competitive compensation and benefits, relocation assistance and startup research packages?
- Join a college that values inclusive excellence and diversity of faculty?

Then, we want you!

How to apply:

1. Visit **https://hr.kennesaw.edu/careers.php**
2. Click Faculty & Staff Openings
3. Click View all Jobs
4. Search Job ID 238131 or 238108

Science Careers online @sciencecareers.org

By **Julie R. Posselt**

It's not (all) about you

Smiling through the interrogation of an online Ph.D. admission interview, a woman of color confidently answered questions posed by three men huddled around a laptop. I sat behind them, observing as a researcher studying the admissions process. In my view, she handled their questions brilliantly—stressing her qualifications and articulating creative research ideas. But the next week, when her application came up in committee deliberations, the decision to reject her was swift and unanimous. I was shocked. One faculty member commented, "Ugh, I wondered if she'd ever stop smiling." Another replied, "No kidding. Too much sunshine, not enough gravitas."

I've worked in and studied graduate admissions for almost 20 years, and perhaps the most fundamental misconception is that the best applicants win. The truth is that what counts as an "ideal" applicant is a moving target. The process can be unfair—even unjust. Practical considerations also play a role, starting with the reality that programs have limited funding and advising capacity. Either way, the reasons for rejection are often as much about the professors and programs as they are about the applicants. Here are some scenarios I've witnessed.



"In admissions, like any game, you will win some and lose some."

FACULTY HOLD BIASES. Outcomes of graduate admissions can be especially unpredictable for students from marginalized groups. For example, gender bias no doubt contributed to the rejection of the woman whose interview I observed more than 10 years ago; her friendly persona didn't comport with the panel's idea of "gravitas." Bias is a major, multifaceted problem—which is why faculty should reflect on and discuss their admissions priorities, learn what current research says about selection and bias, and develop shared standards.

THE FIT WAS OFF. I have been on committees put in the uncomfortable position of rejecting applicants with stellar grades, mountains of research experience, and powerful personal statements—simply because their research interests didn't align with the specific, immediate needs of a faculty member. Applicants can help their chances by clearly articulating how their interests and experiences match those of prospective advisers.

IT WAS ABOUT THE COHORT. Great applicants are often rejected because faculty are thinking not only about individual students, but also the cohort they want to enroll. It's common to want "balance"—groups of admitted students that are diverse on many dimensions, including their social identities and research interests. Applicants don't know and can't control who else has applied, but they unwittingly affect one another's odds.

COMMITTEES CAN BE RISK AVERSE. I once observed an admissions committee decline an applicant from a top-ranked university who had seven first-authored publications under his belt. The faculty were so convinced he'd be admitted to a higher ranked program that they didn't want to take a chance by giving him an offer. Instead they accepted applicants they thought were more likely to attend. It underscores why applicants should only apply to programs where they can make a compelling case for their interest.

THEY DON'T WANT TO FIGHT. If two professors are keen to advise the same applicant and there are no structures for coadvising, then professors may protect their relationship with each other by simply rejecting the applicant rather than fighting about it. Collegiality is a virtue in academia, but it doesn't always benefit students.

Admissions decisions involve more than a judgment of an applicant's worth and potential. If you're among the thousands of prospective graduate students who receive rejection letters each year, perhaps these insights into the process can help you reframe rejection. It's natural to be frustrated, but keep in mind that in admissions, like any game, you will win some and lose some. Keep playing! ■

Julie R. Posselt is an associate dean of the graduate school at the University of Southern California. Do you have an interesting career story to share? Send it to SciCareerEditor@aaas.org.

ILLUSTRATION: ROBERT NEUBECKER

CALL FOR PAPERS

SPJ
SCIENCE PARTNER JOURNALS

spj.sciencemag.org/bmef



BMEF

OPEN ACCESS

BMEF is a **Science Partner Journal** distributed by the **American Association for the Advancement of Science** (AAAS) in collaboration with the **Suzhou Institute of Biomedical Engineering and Technology, Chinese Academy of Sciences** (SIBET CAS). *BMEF* serves the multidisciplinary community of biomedical engineering by publishing breakthrough original Research Articles, Rapid Reports, Reviews, Perspectives, and Editorials. The journal also publishes research in the fields of pathogenic mechanisms as well as disease prevention, diagnosis, treatment, and assessment.

The Science Partner Journals (SPJ) program was established by the American Association for the Advancement of Science (AAAS), the nonprofit publisher of the *Science* family of journals. The SPJ program features high-quality, online-only, open access publications produced in collaboration with international research institutions, foundations, funders and societies. Through these collaborations, AAAS expands its efforts to communicate science broadly and for the benefit of all people by providing top-tier international research organizations with the technology, visibility and publishing expertise that AAAS is uniquely positioned to **offer as the world's largest general science membership society**.

Submit your research to *BMEF* today!
Learn more at: **spj.sciencemag.org/bmef**

ARTICLE PROCESSING CHARGES WAIVED UNTIL 2023

Cell Therapy Research & Development CRO

Innovative Solutions for Customizing Immune Cells

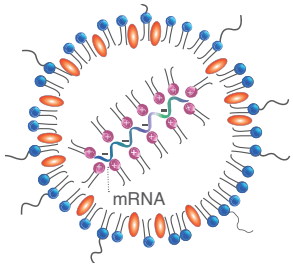
Gene Delivery Methods

mRNA



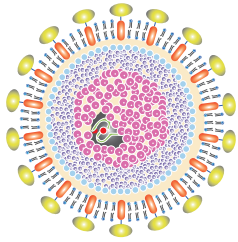
Electroporation

Lipid Nanoparticle



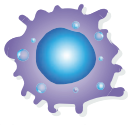
Transfection

Lentivirus/Retrovirus

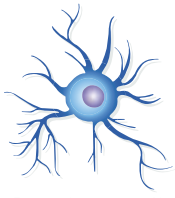


Transduction

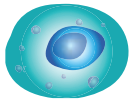
Types of Cells



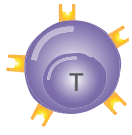
Macrophage



Dendritic cell



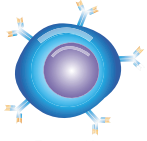
Natural Killer cell



γδ T cell



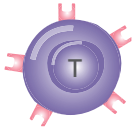
Erythrocyte



B cell



Monocyte



T cell

ProMab Biotechnologies provides many products and services to aid cell therapy research. As the world's first established CAR-T CRO, we bring over 6 years of experience developing lentiviral vectors for integrating novel genes and chimeric antigen receptors into a variety of cell types. Now, we look towards transient methods and expanded our offerings for mRNA transfection and lipid nanoparticle gene delivery. Leverage our platform for your cell therapy research with tailor-made products and service offerings.

Cell Therapy Research Services

- Lentivirus Production: GMP/Non-GMP
- mRNA Production & Lipid Nanoparticle Encapsulation
- CAR-T/NK Cell Generation
- CAR-T/NK Animal Models
- Immune Cell Engineering
- CRISPR Gene Knock-Outs

All products are for research use only

Discover more | www.promab.com

ProMab Biotechnologies, Inc.

2600 Hilltop Dr, Building B, Suite C320, Richmond, CA 94806

1.866.339.0871 | info@promab.com

SCAN ME